TECHNISCHE UNIVERSITÄT MÜNCHEN

Fakultät für Maschinenwesen

Lehrstuhl für Numerische Mechanik

Computational Models and Methods for Molecular Interactions of Deformable Fibers in Complex Biophysical Systems

Maximilian Josef Grill

Vollständiger Abdruck der von der Fakultät für Maschinenwesen der Technischen Universität München zur Erlangung des akademischen Grades eines

Doktor-Ingenieurs (Dr.-Ing.)

genehmigten Dissertation.

Vorsitzende: Prof. Dr. Petra Mela

Prüfer der Dissertation:

      1.   Prof. Dr.-Ing. Wolfgang A. Wall

      2.   Prof. Dr. Philipp J. Thurner

Die Dissertation wurde am 10.02.2020 bei der Technischen Universität München eingereicht und durch die Fakultät für Maschinenwesen am 12.08.2020 angenommen.

Abstract

This work is motivated by the abundance and manifoldness of biological, fiber-like structures on the nano- and microscale such as actin, collagen, and DNA. These slender, deformable fibers form a variety of complex, hierarchical assemblies such as networks (e.g. cytoskeleton, extracellular matrix, mucus) or bundles (e.g. muscle, tendon, ligament), which are crucial for numerous essential processes in the human body. Mainly due to the involved length and time scales and the complex composition of these systems, gaining insights into their fundamental properties and behavior both from experiments and theory often is severely restricted. In particular, the design and working principles mostly remain poorly understood and their significant importance for human physiology and pathophysiology can only be roughly estimated so far.

This thesis tackles one of the great challenges of the simulation-based investigation of these complex biophysical systems caused by the efficient and accurate modeling of molecular interactions such as van der Waals adhesion, electrostatic effects, and steric repulsion. In many cases, these interactions between atoms or charges are the key to the functionality and behavior on the system level. The main achievement of this work is the development of conceptually new computational approaches to account for molecular interactions of fiber-like structures in the simulation of complex biophysical systems. On the one hand, the models are derived from the first principles of molecular interactions, which are formulated as interaction potentials of atoms or unit charges, and on the other hand, they are inspired by (geometrically exact) beam theory, exploiting the dimensionally reduced, slender structure of the fibers. This leads to accurate, highly efficient, and versatile beam-beam interaction formulations that allow for the computational study of so far intractable problems in complex biophysical systems, which is demonstrated in the second half of this work. This class of problems is characterized by involving length and time scales that are inaccessible for molecular dynamics simulations, but require a level of detail, which precludes homogenized continuum models.

The key idea of the novel formulations is to evaluate the two-body interaction potential of arbitrarily deformed and oriented slender fibers in three-dimensional space based on effective section-section interaction potentials (SSIP), i.e., reduced, analytical interaction laws, which effectively reduces the overall dimensionality of the problem from 6D to 2D. While this fundamental approach and the generic form of an SSIP law are universal and therefore capable of describing a broad variety of (molecular) interactions, the present work also proposes specific, ready-to-use SSIP law expressions, which have a pleasantly simple form due to reasonable assumptions, e.g., about the either long or short range of interactions. Further exploiting the rapid decay of the strength of short-ranged interactions also motivated the development of a second fundamental approach based on section-beam interaction potentials (SBIP) including the analytical derivation of the required SBIP law starting from a generic, inverse power law for the point pair potential. This specialized SBIP approach is thus even more efficient than the SSIP approach and the derived interaction law turns out to be also significantly more accurate than the previously considered simple SSIP laws in the intended use case of short-ranged interactions. The first, methodological part of this work furthermore includes a numerical regularization of the characteristic singularity of all the reduced interaction laws, the spatial discretization by means of finite elements and the required linearization of all resulting virtual work contributions.

The second half of this thesis is dedicated to the simulation-based investigation of so far intractable problems by employing the novel models and methods to both abstract systems of universal importance (e.g. the peeling and pull-off of two adhesive elastic fibers) and specific, real biological systems. The obtained insights include the first analysis of conformational changes of the mucin filament due to changes in its effective line charge distribution and the first direct evidence of mechanisms and motion patterns giving rise to the remarkable selective filtering of biological hydrogels such as mucus layers or the extracellular matrix, to name but a few. Beside this immediate gain of knowledge regarding current biophysical research questions, the large number and broad variety of scenarios considered in these applications provide an extensive proof of concept for the novel computational models and methods.

Together with the versatile, modular nature of the approaches and the overall theoretical and computational framework, this should encourage further applications such as the computational reconstitution of collagen (type I) fibrils, which is outlined already in this work. The future fields of applications, however, need not remain limited to biological systems and may be extended along with the technological applications on these small length scales involving e.g. synthetic polymer, glass, and carbon nanofibers. In the long run, further enhancements towards truly predictive, powerful simulation tools could contribute to a streamlined design and manufacturing process of innovative materials and microscale machines. Moreover, such simulation tools could enable innovative medical treatment including, e.g., the patient-specific design of drug delivery objects based on the prediction of its mobility in the selective hydrogels mentioned above. Also an optimal choice of therapeutic options based on individually predicting the occurrence and course of dysregulations in the complex biological microscale systems is conceivable.

Zusammenfassung

Diese Arbeit ist motiviert durch die Fülle und Vielfalt biologischer, faserähnlicher Strukturen auf der Nano- und Mikroebene, wie z.B. Aktin, Kollagen und DNA. Diese schlanken, deformierbaren Fasern bilden eine Vielzahl von komplexen, hierarchischen assemblierten Strukturen wie Netzwerke (z.B. Zytoskelett, extrazelluläre Matrix, Schleim) oder Bündel (z.B. Muskel, Sehnen, Bänder), die für zahlreiche essentielle Prozesse im menschlichen Körper eine entscheidende Rolle spielen. Vor allem aufgrund der involvierten Längen- und Zeitskalen und der komplexen Zusammensetzung dieser Systeme sind Einblicke hinsichtlich deren grundlegender Eigenschaften und deren Verhaltens sowohl aus Experimenten als auch aus der Theorie oft nur sehr eingeschränkt möglich. Insbesondere die Design- und Funktionsprinzipien sind meist noch wenig verstanden und ihre Bedeutung für die menschliche Physiologie und Pathophysiologie kann bisher nur erahnt werden.

Die vorliegende Arbeit befasst sich mit einer der großen Herausforderungen der simulationsbasierten Untersuchung dieser komplexen biophysikalischen Systeme, die darin besteht, die molekularen Wechselwirkungen wie van-der-Waals-Adhäsion, elektrostatische Effekte und sterische Abstoßung effizient und genau zu modellieren. In vielen Fällen sind diese Wechselwirkungen zwischen Atomen oder Ladungen der Schlüssel zu Funktionalität und Verhalten auf der Systemebene. Die wichtigste Errungenschaft dieser Arbeit ist die Entwicklung konzeptionell neuer computergestützer Ansätze zur Berücksichtigung der molekularen Wechselwirkungen faserartiger Strukturen bei der Simulation komplexer biophysikalischer Systeme. Die Modelle sind einerseits von den physikalischen Grundprinzipien der molekularen Wechselwirkungen abgeleitet, die als Interaktionspotential von Atomen oder Einheitsladungen formuliert sind, und andererseits von der (geometrisch exakten) Strahltheorie inspiriert, die die dimensionsreduzierte, schlanke Struktur der Fasern ausnutzt. Dies führt zu akkuraten, hocheffizienten und vielseitigen Formulierungen für Balken-Balken-Interaktionen, die die simulationsbasierte Untersuchung bisher kaum beantwortbarer Fragen in komplexen biophysikalischen Systemen ermöglichen, wie in der zweiten Hälfte dieser Arbeit demonstriert wird. Diese Klasse von Problemen ist dadurch gekennzeichnet, dass sie einerseits Längen- und Zeitskalen betreffen, die für molekulardynamische Simulationen nicht zugänglich sind, andererseits aber einen Detaillierungsgrad erfordern, der homogenisierte Kontinuumsmodelle ausschließt.

Die Kernidee der neuen Formulierungen besteht darin, das Zwei-Körper-Interaktionspotential von beliebig deformierten und orientierten schlanken Fasern im dreidimensionalen Raum auf der Basis resultierender Interaktionspotentiale zweier Querschnitte (SSIP), d.h. reduzierter, analytischer Interaktionsgesetze, zu berechnen, wodurch die Gesamtdimensionalität des Problems von 6D auf 2D reduziert wird. Während dieser grundlegende Ansatz und die generische Form eines SSIP-Gesetzes universell sind und daher in der Lage sind, eine breite Vielfalt von (molekularen) Wechselwirkungen zu beschreiben, schlägt die vorliegende Arbeit auch spezifische, anwendungsbereite SSIP-Gesetz-Ausdrücke vor, die aufgrund plausibler Annahmen, z.B. über die entweder lange oder kurze Reichweite von Wechselwirkungen, eine erfreulich einfache Gestalt haben. Eine weitere Ausnutzung des raschen Abklingens der kurzreichweitigen Wechselwirkungen motivierte auch die Entwicklung eines zweiten grundlegenden Ansatzes basierend auf Querschnitt-Balken-Interaktionspotentialen (SBIP) einschließlich der analytischen Herleitung des erforderlichen SBIP-Gesetzes ausgehend von einem generischen, inversen Potenzge-

setz für das Punkt-Paar-Potential. Dieser spezialisierte SBIP-Ansatz ist somit noch effizienter als der SSIP-Ansatz und das hergeleitete Interaktionsgesetz erweist sich im beabsichtigten Anwendungsfall von kurzreichweitigen Wechselwirkungen zudem als wesentlich genauer als die bisher betrachteten einfachen SSIP-Gesetze. Der erste, methodische Teil dieser Arbeit beinhaltet darüber hinaus eine numerische Regularisierung der charakteristischen Singularität aller reduzierten Interaktionsgesetze, die räumliche Diskretisierung mittels finiter Elemente und die erforderliche Linearisierung aller resultierenden virtuellen Arbeitsbeiträge.

Die zweite Hälfte dieser Arbeit ist der simulationsbasierten Erforschung bisher unerreichbarer Problemstellungen gewidmet, indem die neuartigen Modelle und Methoden sowohl auf abstrakte Systeme von universeller Bedeutung (wie z.B. das Abschälen und Abziehen zweier adhäsiver elastischer Fasern) als auch auf konkrete, reale biologische Systeme angewendet werden. Die gewonnenen Erkenntnisse beinhalten unter anderem die erste Analyse von Konformationsänderungen des Mucin-Filaments aufgrund von nderungen seiner effektiven Ladungsverteilung und den ersten direkten Nachweis von Mechanismen und Bewegungsmustern, die zu den bemerkenswerten selektiven Filtereigenschaften von biologischen Hydrogelen wie Schleimschichten oder der extrazellulären Matrix führen. Neben diesem unmittelbaren Erkenntnisgewinn zu aktuellen biophysikalischen Forschungsfragen liefert die große Anzahl und Vielfalt der in diesen Anwendungen betrachteten Szenarien einen umfassenden Nachweis des allgemeinen praktischen Nutzens der neuen computergestützten Modelle und Methoden.

Zusammen mit der Vielseitigkeit und Modularität sowohl der Ansätze als auch des übergreifenden theoretischen und Code-Frameworks sollte dies weitere Anwendungen wie die simulationsbasierte Rekonstitution von Kollagen (Typ I)-Fibrillen ermutigen, die bereits in dieser Arbeit skizziert wird. Die künftigen Anwendungsbereiche müssen jedoch nicht auf biologische Systeme beschränkt bleiben und können einhergehen mit der Zunahme der technologischen Anwendungen auf diesen kleinen Längenskalen, z.B. mittels synthetischen Polymeren, Glas und Kohlenstoff-Nanofasern. Langfristig könnten Weiterentwicklungen hin zu wahrhaft prädiktiven, leistungsfähigen Simulationswerkzeugen dazu beitragen, den Entwurfs- und Herstellungsprozess innovativer Materialien und Maschinen auf der Mikrometerebene zu vereinfachen. Darüber hinaus könnten solche Simulationswerkzeuge innovative medizinische Behandlungen ermöglichen wie beispielsweise ein patientenindividuelles Design von Wirkstofftransport-Objekten basierend auf der Vorhersage ihrer Mobilität in den oben genannten selektiven Hydrogelen. Auch eine optimale Auswahl von Therapieoptionen auf der Grundlage einer individuellen Vorhersage des Auftretens und des zeitlichen Verlaufs von Störungen in den komplexen biologischen Systemen auf der Mikroskala ist denkbar.

Danksagung

Zu dieser Arbeit haben über die Jahre hinweg so viele Personen auf solch vielfältige Art und Weise beigetragen, dass ihnen diese Danksagung trotz großer Mühen wohl nicht gerecht werden kann. Ich nehme das als Ansporn, dennoch mein Bestes zu geben und zugleich als Erklärung für die längliche Form. Es ist mir immens wichtig, meine Dankbarkeit hier auszudrücken.

Der offensichtlichste Dank gebührt meinem Doktorvater Prof. Wolfgang Wall für die Möglichkeit, dieses Promotionsvorhaben zu bearbeiten. Weit darüber hinaus geht jedoch meine Dankbarkeit für die Inspiration durch seine grenzenlose, nimmermüde Begeisterung für die Wissenschaft wie auch Lehre in der (numerischen) Mechanik, die meine Richtungsentscheidungen während des Studiums und der Promotion maßgeblich beeinflusst hat. Ich bedanke mich auch für das große Vertrauen und die vielen Freiheiten bei gleichzeitiger Rückendeckung, Anregung und auch Zuspruch, wann immer nötig. Die menschliche, offene Art und vielen sehr guten Gespräche weiß ich bis heute sehr zu schätzen.

In seinen Rollen als Betreuer von Bachelor- und Masterarbeit, als erfahrener Kollege und als Postdoc hat Christoph Meier maßgeblich zu meinem Verständnis und damit einhergehend der Leidenschaft für die Strukturmechanik und Balkentheorie beigetragen. Ich ziehe bewundernd den Hut und bedanke mich für entscheidende, tiefgründige fachliche Anregungen sowie die stetige moralische Unterstützung. Gleichzeitig erinnere ich mich gern an unzählige Fußballdiskussionen und sauvui Gaudi bei Müsli- oder Kaffeerunden, Volksfest- oder Schwasibesuchen.

Allgemein habe ich das Beisammensein mit so vielen angenehmen, witzigen und klugen Köpfen am Lehrstuhl als großes Geschenk empfunden und möchte mich bei allen LNM-Weggefährten und -gefährtinnen herzlich bedanken. So viel durfte ich von euch lernen und so viele schöne Stunden am und außerhalb des Lehrstuhls - beim Bouldern, Bergsteigen, Skifahren, Skitouren gehen, Fußball oder Laufen, auf Weihnachtsfeiern, Volksfesten oder ESPs, in täglichen Müsli- und Kaffeepausen - mit euch erleben! All das hat mir die Zeit nicht nur angenehmer, sondern die leidenschaftliche Arbeit in dieser Form erst möglich gemacht. Besonderer Dank geht hier an meinen Bürokollegen Michael Hiermeier, von dem ich insbesondere in der Anfangszeit und zum Thema Coding sehr viel lernen durfte. Ebenfalls bedanke ich mich bei Kei Müller für die anfängliche fachliche Einführung in die Simulation von Biopolymerfasern und -netzwerken. Martin Pfaller danke ich für eine produktive und immer lustige Zusammenarbeit in der TM-Lehre. Fachlich wie zeitlich die größte Überschneidung ergab sich mit Jonas Eichinger - vielen Dank für die mega Zusammenarbeit und die geteilten Mühen vor allem zu Beginn. Auch möchte ich mich bei all meinen Studierenden dafür bedanken, dass sie mit viel Einsatz in Form von Hiwi- oder Studienarbeiten ihren Teil zum Gelingen dieser Arbeit beigetragen haben.

Prof. Alex Levine, Valentin Slepukhin und Jonathan Kernes von der University of California in Los Angeles danke ich herzlich für die großartige Kooperation und den immer spannenden und humorvollen Austausch zwischen theoretischer Biophysik und numerischer Mechanik. Auch für die Gastfreundschaft bei meinen beiden Aufenthalten bedanke ich mich von ganzem Herzen. Für eine weitere erfolgreiche interdisziplinäre Zusammenarbeit geht mein Dank an Theresa Lutz und insbesondere Prof. Oliver Lieleg, der mich durch eine äußerst inspirierende Vorlesung erst zum Thema dieser Arbeit verleitete. Zusätzliche wertvolle Anregungen kamen von Prof. Philipp Thurner, dem ich für das Interesse an dieser Arbeit und den spannenden fachlichen Austausch

Contents

Nomenclature

Abbreviations

1D ... 6D	One- ... six-dimensional
ABC	All-angle beam contact
DNA	Deoxyribonucleic acid
ECM	Extracellular matrix
ID	Identification number
KL	Kirchhoff-Love
LJ	Lennard-Jones
LU	Lower / upper triangular matrix
MD	Molecular dynamics
MSD	Mean squared displacement
SBIP	Section-beam interaction potential
SR	Simo-Reissner
SSIP	section-section interaction potential
SA	Sialic acid
TF	Torsion-free (Kirchhoff-Love)
TUM	Technical University of Munich
UCLA	University of California, Los Angeles
UCI	University of California, Irvine
vdW	Van der Waals

Notation of scalars and tensors

q, Q	Scalar quantity, Euclidean norm of corresponding vector
$\boldsymbol{q}, \boldsymbol{Q}$	Vector / matrix representation of first-/second-order tensor
$\mathbf{q}, \mathbf{Q}$	Vector / matrix of assembled discrete quantities

Operators and symbols

$\cdot$	Inner product
$\times$	Vector product

$\otimes$	Dyadic product
$(.)^T$	Transpose of a tensor
$(.)^{-1}$	Inverse of a tensor
$(.)^{-T}$	Transpose of the inverse of a tensor
$\boldsymbol{I}_{n \times n}$	Identity matrix of dimension $n \times n$
$\mathbf{diag}[(.)]$	Diagonal matrix
$\|(.)\|$	Euclidean norm
$\langle(.)\rangle$	Macaulay brackets
$\dot{(.)}$	Time derivative
$(.)'$	Derivative with respect to the arc-length parameter s
$(.)^{\shortmid}$	Derivative with respect to the element parameter ξ
$\delta(.)$	Variation of a quantity
$\Delta(.)$	Finite increment of a quantity

Beam theory

$\boldsymbol{E}_1, \boldsymbol{E}_2, \boldsymbol{E}_3$	Material base vectors of Cartesian frame
$\boldsymbol{g}_1, \boldsymbol{g}_2, \boldsymbol{g}_3$	Base vectors spanning the cross-section
t	Time
s	Arc-length parameter of the centerline curve in the undeformed configuration
l	Length of the centerline curve in the undeformed configuration
$\boldsymbol{r}$	Centerline curve
$\boldsymbol{t}$	Tangent vector to the centerline curve
$\boldsymbol{\Lambda}$	Material triad with base vectors $\boldsymbol{g}_1, \boldsymbol{g}_2, \boldsymbol{g}_3$, rotation tensor
$\boldsymbol{\psi}$	Spatial (total) rotation vector
$SO(3)$	Special orthogonal group
$\boldsymbol{w}$	Spatial angular velocity
ϵ	Axial tension
κ	Scalar curvature, shear correction factor
$\boldsymbol{\kappa}$	Spatial curvature vector
$\boldsymbol{\gamma}, \boldsymbol{\Gamma}$	Spatial and material deformation measures representing tension and shear
$\boldsymbol{\omega}, \boldsymbol{\Omega}$	Spatial and material deformation measures representing torsion and bending
$\boldsymbol{f}, \boldsymbol{m}$	Spatial force and moment stress resultant
$\boldsymbol{F}, \boldsymbol{M}$	Material force and moment stress resultant
$\boldsymbol{f}_\rho, \boldsymbol{m}_\rho$	Distributed inertia force and moment per unit length
$\tilde{\boldsymbol{f}}, \tilde{\boldsymbol{m}}$	Distributed external force and moment per unit length
$\boldsymbol{C}_F, \boldsymbol{C}_M$	Material constitutive tensor for forces and moments
$\boldsymbol{c}_\rho$	Spatial inertia tensor
A	Cross-section area
A_2, A_3	Reduced cross-section areas
I_T	Torsional moment of inertia

I_P	Polar moment of inertia
I_2, I_3	Principal moments of inertia
E	Young's modulus
G	Shear modulus
ν	Poisson's ratio
ρ	Mass density
EA	Axial stiffness
GA_2, GA_3	Shear stiffnesses
GI_T	Torsional stiffness
EI_2, EI_3	Bending stiffnesses
Π_{int}	Internal, i.e., elastic energy
Π_{kin}	Kinetic energy
W_{ext}	Work of external forces and moments
ζ	Slenderness ratio

Spatial discretization

ξ	Element parameter coordinate
J	Element Jacobian
$\mathbf{r}$	Element residual vector
$\mathbf{R}$	Global residual vector
$\mathbf{k}$	Element tangent stiffness matrix
$\mathbf{K}$	Global tangent stiffness matrix
$\mathbf{x}$	Element vector of all primary degrees of freedom
$\mathbf{X}$	Global vector of all primary variables
n_{ele}	Number of finite elements
l_{ele}	Arc-length of an undeformed finite element
n_{node}	Number of nodes
$\hat{\mathbf{d}}^i$	Position vector at node i
$\hat{\mathbf{t}}^i$	Tangent vector at node i
$\hat{\mathbf{d}}$	Vector of all nodal positions and tangents of one element
H_{d}^i	Hermite polynomial associated with position at node i
H_{t}^i	Hermite polynomial associated with tangent at node i
$\mathbf{H}$	Assembled matrix of Hermite polynomials
$\hat{\boldsymbol{\psi}}^i$	Rotation vector at node i
$\hat{\boldsymbol{\psi}}$	Vector of all rotation vectors of one element
$\delta\hat{\boldsymbol{\theta}}^i$	(Multiplicative) variation of the rotation vector at node i
$\delta\hat{\boldsymbol{\theta}}$	Vector of all (multiplicative) rotation vector variations of one element
L^i	Lagrange polynomial associated with the rotation vector at node i
$\mathbf{L}$	Assembled matrix of Lagrange polynomials

$\Delta\hat{\boldsymbol{\theta}}^i$	(Multiplicative) increment of the rotation vector at node i
$\hat{\varphi}$	Scalar twist angle at node i
$\mathbf{v}_{(.)}$	Auxiliary vectors representing discrete strain variations
$\bar{\mathbf{v}}_{(.)}$	Re-interpolated auxiliary vector $\mathbf{v}_{(.)}$

Temporal discretization

Δt	Time step size
ρ_∞	Spectral radius of the Generalized-α method at infinite frequencies

Macroscopic approaches to beam contact

g	Gap, i.e., surface-to-surface separation
d	Inter-axis separation
$(.)_{\mathrm{bl}}$	Quantity resulting from bilateral closest-point projection
$(.)_{\mathrm{ul}}$	Quantity resulting from unilateral closest-point projection
$\boldsymbol{n}$	Contact normal vector
$\boldsymbol{f}_{\mathrm{c}\varepsilon}$	Contact point force vector
$\tilde{\boldsymbol{f}}_{\mathrm{c}\varepsilon}$	Contact line force vector
ε	Penalty parameter
$\Phi_{\mathrm{c}\varepsilon}$	Penalty potential law
$\Pi_{\mathrm{c}\varepsilon}$	Virtual work contribution from penalty potential
$(.)_{\parallel}$	Quantity associated with line contact
$(.)_{\perp}$	Quantity associated with point contact
α	Scalar angle enclosed by the tangent vectors
z	Abbreviation for the cosine of the angle α
$k(z)$	Scaling factor used for smooth blending of contact forces

Intermolecular forces and potentials

Φ	Interaction potential of two atoms or point charges
r	Scalar separation of two points
$\boldsymbol{f}$	Interaction force
$\boldsymbol{x}$	Position vector
Q	Electric charge
ε	Dielectric permittivity

m	Negative exponent of a generic inverse power law
k_{m}, C	Scalar prefactor of interaction potential laws
$r_{\mathrm{LJ,eq}}$	Equilibrium separation of the Lennard-Jones force law
$\Phi_{\mathrm{LJ,eq}}$	Minimal value of the Lennard-Jones potential law
$f_{\mathrm{LJ,min}}$	Minimal value of the Lennard-Jones force law
$r_{\mathrm{LJ,f}_{min}}$	Separation corresponding to the minimal force value
Π_{ia}	Two-body interaction potential
ρ_i	Atomic density of body i
σ_i	Surface charge density of body i
g	Gap, i.e., surface-surface separation
d	(Cylinder) inter-axis or (sphere) center-center separation
A_{Ham}	Hamaker constant
$\tilde{\pi}$	Interaction potential per unit length
$\tilde{f}$	Interaction force per unit length
$\tilde{\tilde{\pi}}$	Interaction potential per unit length squared
$\tilde{\tilde{f}}$	Interaction force per unit length squared
R	Cylinder radius
A	Cross-section area
L	Cylinder length
α	Mutual angle of two cylinders
r_{c}	Cut-off radius

Section-section and section-beam interaction potential approach

$\tilde{\tilde{\pi}}$	Section-section interaction potential (SSIP) law
$\tilde{\pi}$	Section-beam interaction potential (SBIP) law
c, K	Scalar prefactor of SSIP or SBIP law
$\boldsymbol{r}_{1\text{–}2}$	Separation vector of centroid positions
$\boldsymbol{\psi}_{1\text{–}2}$	Relative rotation vector between the material frames of two cross-sections
g	Gap, i.e., scalar surface-surface separation
d	Scalar inter-axis separation
$\boldsymbol{n}$	Normal vector
α	Scalar angle enclosed by the two tangent vectors
θ, ϑ	Scalar angles describing the mutual orientation of disk and cylinder
λ_i	Linear charge density of beam i
n_{IS}	Number of segments per element used for numerical integration
n_{GP}	Number of integration points per segment used for numerical integration
$\boldsymbol{t}_1, \boldsymbol{u}_1, \boldsymbol{v}_1$	Base vectors of an auxiliary orthonormal triad
a, b, c, β, Δ	Auxiliary scalar coefficients

Applications to biophysical systems

u	Scalar displacement component
F	Scalar reaction force component
D_f	Fiber diameter
D_p	Diameter of a spherical particle
$\boldsymbol{r}_\mathrm{p}$	Midpoint position of a spherical particle
T	Temperature
$k_\mathrm{B}T$	Thermal energy
$\mathcal{W}$	(Two-dimensional) Wiener process
η	Dynamic viscosity of the background fluid
ℓ_p	Persistence length of a semiflexible filament
L_e2e	End-to-end distance
R_g	Radius of gyration
γ_p	Friction coefficients of a spherical particle
Q_p	Electric charge of a spherical particle
$<\Delta r_\mathrm{p}^2>$	Mean squared displacement of a spherical particle
τ	Time interval, External tensile force
N_τ	Number of time intervals
κ	Scalar bending stiffness
V	Background potential field
V_0	Mean value of the background potential
ξ	Correlation length of the background potential
k	Magnitude of the wavenumber of a Fourier mode
$\langle (.) \rangle$	Mean value
n_f	Number of fibers
$\bar{V}_\mathrm{f}$	Fiber volume fraction
n_VP	Number of Voronoi points / particles

Selected subscripts and superscripts

$(.)_\mathrm{adh}$	Adhesive
$(.)_\mathrm{rep}$	Repulsive
$(.)_\mathrm{ls}$	Large separations
$(.)_\mathrm{ss}$	Small separations
$(.)_\mathrm{ul}$	Unilateral
$(.)_\mathrm{bl}$	Bilateral
$(.)_\mathrm{c}$	Closest point
$(.)_\mathrm{reg}$	(Numerical) regularization
$(.)_\parallel$	Parallel orientation or component
$(.)_\perp$	Perpendicular orientation or component

1. Introduction

The aim of this introductory section is to outline both the overarching theme and the specific content of this thesis. In particular, the description of the motivation for this work is directed to a broader audience beyond the experts in the field(s) to foster the comprehensible communication of this research topic to larger parts of the society. The stated long-term, visionary goals will subsequently be broken down and after the specification of requirements in Section 1.2 and a review of fundamental approaches in Section 1.3, the achievements of this work will be listed in Section 1.4. The latter is considered the best way for experts to quickly get an overview of the novelties. The organization of the remainder of this thesis will finally be outlined in Section 1.5.

1.1. Motivation

The content of this section is predominantly grounded on general knowledge and textbook knowledge such that references will only be given where deemed particularly necessary.

The relevance of fibers and fibrous systems in nature   The original motivation for this work lies in the recognition of fiber-like structures as a fundamental, abundant pattern in biological systems. Fibers, fibrils, filaments, strands, threads, rods, and other slender structures can be found across several length scales from meters down to the range of nanometers. Popular examples include hair, muscle fibers, tendons, ligaments, cellulose fibers, collagen, actin, mucin and other biopolymer filaments, DNA, wood fibers, stems, branches, twigs and tendrils, spider silk, tentacles, and limbs. In this work, the focus lies on the fibrous species to be found on the nano- and microscale, which gives rise to the fact that molecular interactions between these fibrous species play a decisive role as will be discussed in further detail below. Typically, these slender structures form fibrous systems such as networks (cytoskeleton, extracellular matrix) or bundles (muscle, tendon), which can be very complex in terms of the large number of fibers and fiber species with a broad variety of properties, their interconnections and especially various kinds of interactions. Often, the fiber-like components can be found even across several levels of a hierarchical architecture (e.g. muscle, tendon, bone), possibly also as part of composite structures [50]. In many cases, such fibrous systems act as load-bearing structures providing mechanical support and protection against environmental influences, and in fact they can be identified as a governing design principle in terms of light-weight design. The range of observed material behaviors hereby varies from soft matter like tissue to stiff structures like bones and include as diverse characteristics as both active and passive behavior. However, they at least contribute to a large number of further purposes such as filtering, transport and energy transfer and play a crucial role in a large number of functions and processes in the human body. The multitude of behaviors and purposes on the system scale can be regarded as a result of the complex interplay of the many

different constituents and for many of the above mentioned systems, especially on the nano- and microscale, the underlying design and working principles and mechanisms still remain unclear.

The relevance of intermolecular forces The interactions between molecules such as electrostatic and -dynamic forces, including adhesive van der Waals and repulsive contact forces, are truly ubiquitous and significantly influence the behavior of (fibrous) systems on the micro- and nanoscale. On these small length scales, such molecular interactions are as fundamental and important as gravity and mass inertia are on the length scales that we experience in our daily life [51, 74]. For some visible effects on the macroscale such as Gecko adhesion and the Lotus effect, the origin and causal link to intermolecular forces are widely known. For others such as contact, friction, and stiction, the effect is just as clearly observable, however, the origin in terms of molecular interactions seems to be less perceived. Also regarding the biological, fibrous systems on cellular and subcellular scale mentioned above, the key to their behavior, functions, and working principles lies in the interactions of the fiber-like constituents. It would thus be highly desirable to gain a better knowledge about the fundamental properties of various kinds of intermolecular interactions, their complex interplay, and finally their influence on the system behavior. In this respect, the important role of the aforementioned fibrous systems in countless body functions needs to be emphasized and it seems appropriate to think of these nano- and microscale systems as the actual machine rooms of our body that substantially contribute to running the entire organism. Even more desirable and promising than the solution for already acknowledged, yet unresolved issues, however, should be the discovery of so far unknown and unexpected phenomena on these length scales.

The opportunities of physics-based, predictive simulations The key value of computer simulations is to foresee the future and thus enable to predict a course of events and their final outcome before they take place in the real world. Generally, humans are quite successful in anticipating the future and even do this subconsciously in everyday situations that are covered well enough by their previous personal experiences. Also regarding some more complicated scenarios requiring conscious action, the human intelligence allows to predict the outcome based on either heuristics or a basic knowledge of physics such as the trajectory of a thrown object. At some point, however, the complexity of the matter prevents any reliable predictions by human individuals. The solution of many important problems for instance in the fields of economy, climate, and medicine would require to predict the outcome of different options, because a trial-and-error approach is impossible due to the fatal, irreversible consequences. In these cases, the use of truly predictive, physics-based computer simulations could contribute and finally lead to optimal decisions with a big impact and great benefit. But also in other situations, where humans are either not able or intended to make the decisions such as in autonomous systems like cars or on flights into outer space, the assessment of different options by means of computer simulations can be of great help. Apart from the just mentioned possibility of automation, computer simulations have a number of further advantageous properties including ideal reproducibility, reusability, controllability of influences, freedom in experimental design (including even unrealistic choices of physical parameters and laws), and the fact that results can directly be processed, stored and shared without much effort and accessed in arbitrary detail. Generally speaking, this

relatively young discipline complements theory and experiment as a third source of knowledge in science and technology. The ongoing, rapid development in terms of computer hardware and software leading to increasing computational resources (high performance clusters, GPUs) and enhanced digital tools (compilers, IDEs, web-based collaboration platforms) is expected to accelerate both the development and use of simulation tools. Altogether, the extension and enhancement of computational solution approaches to physical problems is thus considered to be highly promising.

The visionary goals of this research   Considering the high relevance of complex biophysical systems on the nano- and microscale, involving manifold interactions of fiber-like structures, and in awareness of the great opportunities of computer simulations, the following long-term goals of this research can be stated:

1. Gain knowledge about the yet poorly understood fundamental properties, design and working principles of many complex biological systems by providing useful tools for computational experiments.

2. Enable innovative medical treatment due to an enhanced understanding of human physiology and pathophysiology.

3. Enable case- and patient-specific treatment by predicting the individual course of existing illnesses as a result of different therapeutic options in simulations.

4. Enable case- and patient-specific precaution and diagnosis by predicting the outbreak and severeness of illnesses caused by malfunctions and dysregulations in simulations.

5. Enable and streamline the design and manufacturing of innovative materials, products, and machines on the micro- and nanoscale by providing useful tools for computational experiments.

These ambitious goals showcase the great potential and possibly far-reaching implications of this research in the fields of science, medicine, and (bio-)engineering in the long run.

The short-term goals of this research   In pursuit of the long-term goals stated above, the main objectives of this PhD project and for the near future are given as follows.

1. Develop suitable[1] computational models and methods to enable simulations of complex (biophysical) systems that account for various kinds of molecular interactions between deformable, fiber-like structures.

2. Apply them to first specific biological systems in order to both provide a proof of concept and gain immediate insights with regard to open scientific questions in biophysics.

The two preliminary steps of specifying the requirements for the aspired computational methods and reviewing the existing fundamental approaches will be taken in the following sections.

---

[1]cf. Section 1.2 for the specification of requirements

1.2. Specification of requirements

The following is a list of the key requirements for computational approaches with regard to the objectives of this work and beyond.

Accuracy The feasibility of predicting the quantity of interest with small error and small uncertainty. Mainly influenced by the choice and validity of model assumptions.

Efficiency The feasibility of simulating biologically relevant system sizes and time scales at small computational cost. Mainly influenced by the level of modeling, i.e., the resolution of details, and the implementation.

Generality The validity for a large number and broad range of relevant problems. Mainly influenced by the limitations of model assumptions.

Robustness The ability to avoid failure and yield accurate results despite the occurrence of rare, untypical and unfavorable cases. Mainly influenced by the solution strategy, its implementation, and the composition and interplay of model assumptions.

Simplicity The quality of both theory and code to be easy to understand and convenient to work with.

Modularity The quality of a theoretical and code framework to consist of separable logical units that can be recombined depending on the specific needs.

The applicability and usefulness and in turn the overall value of computational models and methods will be determined by the combination of all these requirements. Trying to meet all requirements will, however, often entail severe conflicts of objectives such that optimal compromises will be searched for in many places throughout this thesis. The necessary decisions between different options in the development but also in the application of models and methods will always be made under consideration of both the short-term and the long-term goals stated above.

1.3. Brief review of fundamental approaches

While a detailed and exhaustive review of literature will later be presented for each specific topic, this section aims to provide a rough overview of existing approaches and a corresponding feasibility analysis based on order-of-magnitude estimates. Most well-established computational approaches to classical problems related to the ones involving complex fibrous systems as described above can be divided into the following two categories. On the one hand, molecular dynamics (MD) simulations generally resolve every single atom and are based on solving Newton's laws of motion to determine the trajectory of all atoms in the system (see e.g. [52, 59]). On the other hand, classical continuum mechanical approaches are based on the formulation and solution of space-continuous equations for a bulk material (see e.g. [11, 68]). The fiber-like, macromolecular species in mind represent structures with diameters starting from several nanometers and typical lengths up to the order of micrometers. As outlined above, the class of

problems at hand is characterized by the interactions of a large number of these fiber-like structures giving rise to a complex system behavior. The great challenges associated with this class of problems comes from the biologically relevant length scales of several nano- to tens of micrometers (in three-dimensional space) in combination with the biologically relevant time scales of at least tenths up to hundreds of seconds. Despite considerable efforts and the use of high performance computers, the current limits of all-atom MD approaches are either on the order of milliseconds for very small systems or on the order of millions of atoms (corresponding to system sizes of approx. $10 - 100\,\mathrm{nm}$ in three-dimensional space) for very short time spans. MD approaches can thus be considered as highly resolved and accurate, yet by orders of magnitude not efficient enough to allow for the combinations of relevant length and time scales specified above. In contrast, applying solid mechanical continuum approaches on the system level does not allow to resolve the required level of detail, which is determined by the fiber-like structures and their interactions, and is therefore not suitable for the described needs. If, on the other hand, these solid mechanical continuum models are applied to fully resolve the three-dimensional volume of the fibers, the solution of the resulting systems would again be computationally infeasible as will turn out also in the remainder of this work.

An alternative approach that overcomes these limitations is to develop models and methods on the level of fibers. The dimensions of the fibers stated above are just beyond the atomistic level and can thus be considered as objects in an intermediate regime where the principles and laws of physics from both atomistic and continuum theory can be relevant and valid. Specifically, a computational micromechanical approach to the Brownian dynamics of biopolymer filaments described by beam theory and corresponding finite element formulations has been proposed by Cyron and Wall [31, 32]. It has been shown to be an accurate and highly efficient approach to this microscale problem. The subsequent application to the simulation of the self-assembly of biopolymer networks has furthermore demonstrated its capability of simulating large and complex systems of fibers [34, 35]. The rheology of such transiently cross-linked biopolymer networks from the high- to the low-frequency regime has in the following been investigated for the first time by Müller et al. [118]. The considered system sizes of hundreds of fibers in a simulation cube of up to $10\,\mathrm{\mu m}$ edge length and the time intervals of several hundreds of seconds prove the unique capabilities of this kind of approach. It is thus chosen as the one to be followed in this thesis and extended towards the important molecular interactions of the fibers that are expected to play a crucial role in many biological systems as outlined above.

1.4. Achievements of this work

The following is a concise list of the most important scientific achievements of this work.

1. Development of a novel beam-beam interaction formulation based on section-section interaction potentials

   a) Proposal of specific expressions for reduced, i.e., disk-disk, interaction laws for generic long-ranged (e.g. Coulomb) and short-ranged (e.g. van der Waals and steric) interactions

   b) Derivation of virtual work contribution, spatial discretization, and linearization

   c) Proposal of a numerical regularization scheme

   d) Validation by means of numerical examples

2. Development of a specialized, more efficient beam-beam interaction formulation for short-ranged interactions based on section-beam interaction potentials

   a) Derivation of a reduced, i.e., disk-cylinder, interaction law for generic short-ranged (e.g. van der Waals and steric) interactions via analytical 5D integration

   b) Derivation of virtual work contribution, spatial discretization, and linearization

   c) Proposal of a numerical regularization scheme

   d) Validation by means of numerical examples

3. Further methodological work

   a) Extension of the well-established Simo-Reissner beam element formulation [29, 76] to a C^1-continuous centerline interpolation using cubic Hermite polynomials

   b) New classification of existing and new beam-beam interaction formulations

   c) Derivation of formulations for a beam interacting with a rigid sphere as special case of the beam-beam interactions

4. Applications to abstract, academic examples with universal importance

   a) Investigation of the peeling and pull-off behavior of adhesive elastic fibers

   b) Study of the conformation of a semiflexible filament in a static random potential field

   c) Proof of principle for nanofiber-grafted adhesive surfaces

5. Applications to specific biological systems

   a) Investigation of the conformations of mucin filaments resulting from changes in its effective line charge distribution

   b) Study of the hindered mobility of charged particles in biological hydrogels including the key influences and mechanisms

   c) Computational reconstitution of collagen (type I) fibrils

1.5. Organization of this thesis

The remainder of this thesis is organized as follows. **Chapter 2** and **Chapter 3** summarize and review the fundamentals of intermolecular forces and beam theory that will be of high relevance for the following chapters. **Chapter 9** and **Chapter 5** are concerned with the development of two computational approaches for molecular interactions of deformable fibers. A subsequent classification and comparison of these novel and existing approaches as well as the derivation of formulations for some special cases is presented in **Chapter 6** and concludes the methodological part of this thesis. The second part consists of the **Chapters 7 to 11** and applies the novel computational approaches to systems that range from rather abstract, academic problems of fundamental importance to specific, real biological systems. Finally, **Chapter 12** concludes the present work by providing a summary and outlook to promising directions for future research.

2. Fundamentals of Intermolecular Forces and Potentials

Interactions between molecules may result from various physical origins and are a complex and highly active field of research within the community of theoretical as well as experimental physics. The methods to be derived in this work make use of the most essential and well established findings as summarized e.g. in the textbooks [74] and [125]. This chapter briefly presents a selection of aspects relevant for this work and shall serve as a valuable source of reference for the later use. The majority of this chapter has previously been published in the author's article [61].

2.1. Characterization, terminology and disambiguation

To begin with, a number of universal aspects characterizing molecular interactions, especially with regard to the numerical methods to be developed in this work, shall be presented. A few simple facts about the examples mostly considered throughout this work, namely electrostatic and vdW interaction, are presented straight away, whereas the details on these and further types of molecular interactions are to be discussed in the subsequent Section 2.2.

A collection of characteristics of molecular interactions with high relevance for this work

- *Type of elementary interaction partners* Interaction may originate from unit charges as in the case of electrostatics. Another popular example are vdW effects that are caused by fluctuating dipole interactions occurring in every molecule and hence are related to the molecular density of the material.

- *Spatial distribution of elementary interaction partners* Thinking of the resulting interaction between two bodies as accumulation of all molecular interactions, the question for the locations of all elementary interaction partners arises. Charges can often be found on the bodies' surfaces whereas molecules relevant for vdW interactions spread over the entire volume of the bodies. This work focuses on solid bodies (i.e. condensed matter) that are non-conducting such that interaction partners will not redistribute, i.e., change their position within a body.

- *Distance-dependency of the fundamental potential law* Generally, the strength of molecular interactions decays with increasing distance. Most frequently, inverse power laws with different exponents or exponential decay can be identified.

- *Range of interactions* As a result of the previous aspects, a range of significant strength of an interaction can be defined. Rather than an inherent property, the classification of long- versus short-ranged interactions is a theoretical concept to judge the perceptible impact in specific scenarios. Moreover, it is a decisive factor in the derivation of well-suited numerical methods.

- *Additivity and higher-order contributions* Many approaches including the one presented in this work make use of superposition, i.e., accumulating all the individual contributions from elementary interaction partners to obtain the total effect of interaction. This assumes that the interactions behave additively, i.e., that the sum of all pair-wise interactions describes the overall interaction sufficiently well. More specifically, the presence of other elementary interaction partners in the surrounding must not have a pronounced effect as compared to an isolated system of an interacting pair. Otherwise, the sum of all pair-wise interactions would need to be extended by contributions from sets of three, four and more elementary interaction partners.

As a matter of course, this list is not exhaustive, but represents a selection of the most relevant aspects considered in the development of the novel computational methods throughout Chapter 4 and 5.

Interaction potential and corresponding force

An interaction potential $\Phi(r)$, also known as (Gibbs) free energy of the interaction, is defined as the amount of energy required to approach the interaction partners starting from a reference configuration with zero energy at infinite separation. Hence, the following relations between the interaction potential $\Phi(r)$ and the magnitude of the force $f(r)$ acting upon each of the partners, each in terms of the distance between both interacting partners r, hold true:

$$\Phi(r) = \int_{\infty}^{r} -f(r)\,\mathrm{d}r \qquad \leftrightarrow \qquad f(r) = -\frac{\mathrm{d}\,\Phi(r)}{\mathrm{d}\,r} \tag{2.1}$$

Although the final quantities of interest are often the resulting, vectorial forces on slender bodies, it is yet convenient and sensible to consider the scalar interaction potential throughout large parts of this work. This is underlined by the fact that nonlinear finite element methods in the context of structural dynamics can be formulated on the basis of energy and work expressions. Equation (2.1) expresses the direct and inherent relation between force and potential. Note that the forces emanating from such interaction potentials are conservative and the integral value in (2.1) is path-independent. Furthermore, the interaction is symmetric in a sense that the force acting upon the first interacting partner $\boldsymbol{f}_1(r)$ has the same magnitude yet opposite direction as compared to the force acting on the second partner $\boldsymbol{f}_2(r)$. Using the partners' position vectors $\boldsymbol{x}_1, \boldsymbol{x}_2 \in \mathbb{R}^3$, we can formulate the vectorial equivalent of the formula above:

$$\boldsymbol{f}_1(r) = -\frac{\mathrm{d}\,\Phi(r)}{\mathrm{d}\,r}\frac{\boldsymbol{x}_1 - \boldsymbol{x}_2}{\|\boldsymbol{x}_1 - \boldsymbol{x}_2\|} \quad \text{and} \quad \boldsymbol{f}_2(r) = \frac{\mathrm{d}\,\Phi(r)}{\mathrm{d}\,r}\frac{\boldsymbol{x}_1 - \boldsymbol{x}_2}{\|\boldsymbol{x}_1 - \boldsymbol{x}_2\|} \quad \text{with} \quad r = \|\boldsymbol{x}_1 - \boldsymbol{x}_2\|$$

$$\tag{2.2}$$

Disambiguation

In order to particularize the very general term *molecular interactions*, we may note that we solely consider interactions between distinct, solid (macro)molecules, i.e., no covalent or other chemical bonds, but rather what is sometimes referred to as *physical bonds*. Thus, we restrict ourselves to *intermolecular* forces as opposed to *intramolecular* ones.

2.2. Interactions between pairs of atoms, small molecules or point charges

First principles describing molecular interactions are formulated for a pair of atoms, molecules or point charges. In the following, all types of interactions to be considered in this work are thus first presented for a minimal system consisting of one pair of these elementary interaction partners.

2.2.1. Electrostatics

Coulomb's law is one of the most fundamental laws in physics and describes the interaction of a pair of point charges under static conditions by

$$\Phi_{\text{elstat}}(r) = \frac{Q_1 Q_2}{4\pi\varepsilon_0\varepsilon}\frac{1}{r}, \qquad \|\boldsymbol{f}_{\text{elstat}}(r)\| = \frac{Q_1 Q_2}{4\pi\varepsilon_0\varepsilon}\frac{1}{r^2}, \qquad \boldsymbol{f}_{\text{elstat},1}(r) = \frac{Q_1 Q_2}{4\pi\varepsilon_0\varepsilon}\frac{\boldsymbol{x}_1 - \boldsymbol{x}_2}{\|\boldsymbol{x}_1 - \boldsymbol{x}_2\|^3} \quad (2.3)$$

where ε_0 and ε are the vacuum and dielectric permittivity, respectively. For the sake of brevity in any later usage, let us define the abbreviation $C_{\text{elstat}} := (4\pi\varepsilon_0\varepsilon)^{-1}$. Depending on the signs of Q_1 and Q_2, electrostatic forces may either be repulsive or attractive. Besides a pair of point charges, Coulomb's law likewise holds for a pair of spherically symmetric charge distributions with resulting charges Q_1 and Q_2, respectively. This is an important insight, since ultimately we are interested in interactions between two bodies with finite extension rather than points. Furthermore, interactions between rigid spheres and rigid bodies are of interest for applications such as particle diffusion in hydrogels. Throughout the entire work, no electrodynamic effects shall be considered. This is a valid assumption as long as bodies are non-conductive and the motion of bodies carrying the attached charges happens on much larger time scales than relevant eigenfrequencies in electrodynamics.

Due to the inverse-first power law, the electrostatic potential has quite a long range, meaning that two point charges at a large distance still experience a considerable interaction force as compared to small distances. This behavior is even more pronounced for the interaction of two extended bodies, where the whole lot of all distant point pairs dominates the total interaction energy as compared to the few closest point pairs. This property is crucially different as compared e.g. to vdW interactions considered in the next section. We will account for and indeed make use of this important property in the development of the methods to be presented in this work.

2.2.2. Van der Waals interactions

VdW forces originate from charge fluctuations, thus being an electrodynamic effect caused by quantum-mechanical uncertainties in positions and orientations of charges. Depending on the interaction partners, three subclasses can be distinguished as Keesom (two permanent dipoles), Debye (one permanent dipole, one induced dipole) and London dispersion interactions (two transient dipoles). The ubiquitous nature of vdW interactions is due to the fact that the latter contribution even arises in neutral, nonpolar, yet polarizable matter that means basically every atom or molecule. All three kinds of dipole interactions can be unified in that their interaction free energy follows an inverse-sixth power law in the separation [125]:

$$\Phi_{\text{vdW}}(r) = -\frac{C_{\text{vdW}}}{r^6} \tag{2.4}$$

This is a pleasantly simple expression, yet intricate when it comes to transferring it to two-body interactions, as we will discuss in Section 2.3.2. In general, vdW forces are always attractive for two identical or similar molecules, yet may be repulsive for other material combinations.

2.2.3. Steric exclusion

Two approaching atoms or molecules will at some very small separation suddenly experience a seemingly infinite repulsive force. This effect is attributed to the overlap of electron clouds and referred to as *steric repulsion*, *steric exclusion* or *hard core repulsion*. Without thorough theoretical foundation, several (almost) infinitely steep repulsive potential laws are empirically used to model this phenomenon. The first option is a *hard wall/core/sphere* potential which has a singularity at zero separation

$$\lim_{r \to 0} \Phi_{\text{c,hs}}(r) = \infty \qquad \text{and} \qquad \Phi_{\text{c,hs}}(r) \equiv 0 \quad \text{for} \quad r > 0. \tag{2.5}$$

Other common choices include a *power-law* potential with a large integer exponent $n_{\text{c,pow}}$

$$\Phi_{\text{c,pow}}(r) = C_{\text{c,pow}} \, r^{-n_{\text{c,pow}}} \tag{2.6}$$

and finally an *exponential* potential

$$\Phi_{\text{c,exp}}(r) = C_{\text{c,exp}} \, e^{-r/r_{\text{c,exp}}}. \tag{2.7}$$

Note that the former two coincide in the limit $n_{\text{c,pow}} \to \infty$ and increase indefinitely for $r \to 0$ while the exponential one does not. Generally, this behavior of steric exclusion is in good agreement with our intuition based on macroscopic solid bodies coming into contact.

2.2.4. Total molecular pair potentials and force fields

In many systems of interest, any two or more of the aforementioned effects may be relevant at the same time such that a combination of the pair potentials is required. This is typically done by summation of the individual potential contributions and leads to a *total intermolecular pair*

potential. Among the large number of possible combinations[1], the *Lennard-Jones* (LJ) potential is probably the most commonly used variant (see Figure 2.1).

$$\Phi_{\text{LJ}}(r) = k_{12}r^{-12} + k_6 r^{-6} = -\Phi_{\text{LJ,eq}} \left(\left(\frac{r_{\text{LJ,eq}}}{r} \right)^{12} - 2 \left(\frac{r_{\text{LJ,eq}}}{r} \right)^6 \right) \tag{2.8}$$

It is a special case of the *Mie potential* $\Phi_{\text{Mie}}(r) = C_{\text{Mie,m}} \, r^{-m} - C_{\text{Mie,n}} \, r^{-n}$ with exponents being
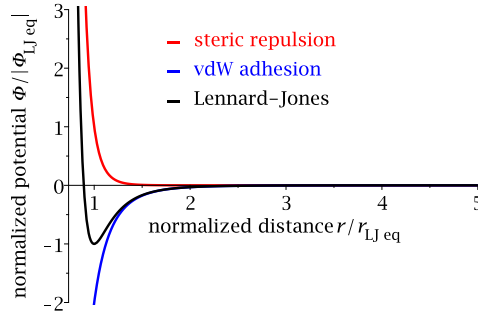
Figure 2.1.: Lennard-Jones interaction potential for a pair of points, i.e. atoms. Figure taken from the author's article [61].

chosen to model the inverse-sixth vdW attraction on the one hand and a strong repulsion on the other hand. The parameters can be identified as the minimal value $\Phi_{\text{LJ,eq}} < 0$ that the LJ potential takes at equilibrium separation $r_{\text{LJ,eq}} > 0$, i.e., at the separation where the resulting force is zero.

Other important quantities characterizing the LJ force law

$$f_{\text{LJ}}(r) = -\frac{12\,\Phi_{\text{LJ,eq}}}{r_{\text{LJ,eq}}} \left(\left(\frac{r_{\text{LJ,eq}}}{r} \right)^{13} - \left(\frac{r_{\text{LJ,eq}}}{r} \right)^7 \right) \tag{2.9}$$

are the minimal force value $f_{\text{LJ,min}}$ and corresponding distance $r_{\text{LJ,f}_{\min}}$

$$f_{\text{LJ,min}} \approx 2.6899 \, \frac{\Phi_{\text{LJ,eq}}}{r_{\text{LJ,eq}}} \qquad \text{and} \qquad r_{\text{LJ,f}_{\min}} = \left(\frac{13}{7} \right)^{1/6} r_{\text{LJ,eq}} \approx 1.1087 \, r_{\text{LJ,eq}}. \tag{2.10}$$

The minimal force, i.e., the maximal adhesive force, is commonly referred to as *pull-off force*. Israelachvili [74] also points out the chance of a fortunate cancellation of errors in total pair potentials, especially close to the limit $r \to 0$. In this regime, attractive forces tend to be underestimated by the simplified inverse-sixth term but likewise the steric repulsion is probably stronger than estimated from the power law. Both errors cancel rather than accumulate and increase the model accuracy.

---

[1]See [74][p. 138] for a comprehensive list of combinations used as total pair potential laws.

Remarks

1. Many of the presented point-point interaction potentials decay rapidly with the distance as shown exemplarily for a law $\Phi(r) \propto r^{-12}$ in Figure 2.2. In anticipation of the numerical methods to be proposed in this work we can already state at this point that these extreme gradients are very challenging for numerical quadrature schemes that will therefore be discussed in a dedicated Section 4.4.4.

2. In molecular dynamics, a *force field* is typically used instead of the potential law to model the total interaction of a pair of atoms. Specific forms are being proposed for (coarse-grained) force fields modeling the interaction of macromolecules such as DNA instead of atoms. Since these all-atom approaches follow an entirely different approach as compared to the continuum model proposed here, we will not discuss force fields any further.
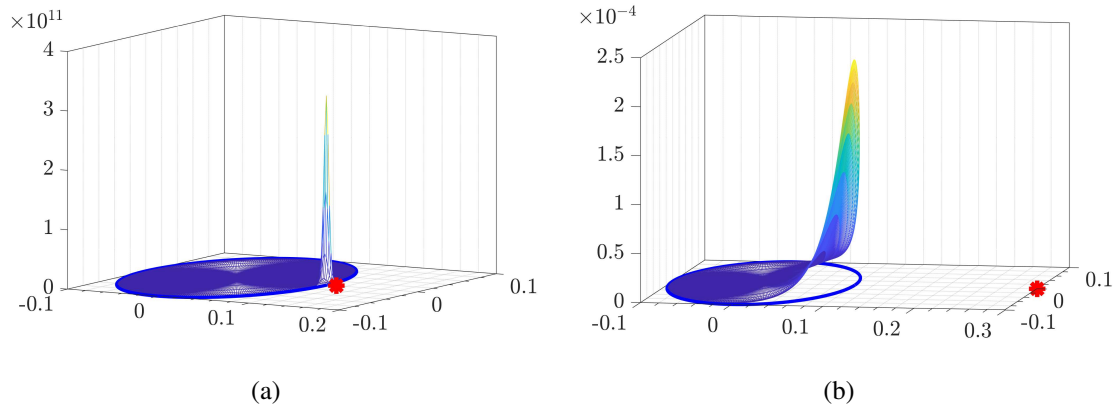
Figure 2.2.: Example of a point-point interaction potential $\Phi(r) \propto r^{-12}$ plotted over a circular domain (blue circle) with (a) small and (b) large distance to the point-like interaction partner (red dot). Note the huge difference in scales. Figure taken from the author's article [61].

2.3. Two-body interaction: Surface vs. volume interaction

In this section, we take the important step from interacting point pairs to interactions between two bodies with defined spatial extension containing many of the fundamental point-like interaction partners considered throughout the preceding Section 2.2. The obvious question for the spatial distribution of the interaction partners leads to the important distinction between *surface* and *volume interactions*. As the name suggests, in the first case, the elementary interaction partners are distributed over the surface of the bodies but not in the interior. The most important example from this category are electrostatic interactions between bodies where the charges sit on the surfaces and are not free to move around. This applies to a large number of charged, non-conductive biopolymer fibers such as actin or DNA. In the second case of volume interactions,

the elementary interacting partners are distributed over the entire volume of the bodies. The most important examples here are vdW interactions and steric exclusion. As compared to surface interactions, this further increases the dimension of the problem making it more challenging to tackle, both by analytical as well as numerical means. In terms of notation one may also find the expressions *body forces* or *bulk interaction* referring to this category of interactions.

Let us briefly look at volume and surface interactions as an abstract concept, leaving aside the specifics of the underlying physical effects that are to be discussed in the subsequent Section 2.3.1 and Section 2.3.2. Likewise, we assume additivity here and discuss the applicability later with the physical type of interaction. Since volume interactions are the more general and challenging case, we will discuss most aspects and approaches first for volume interactions and later only point out the differences considering surface interactions. Figure 2.3 schematically visualizes the distribution of elementary interaction partners within two macromolecular or macroscopic bodies.
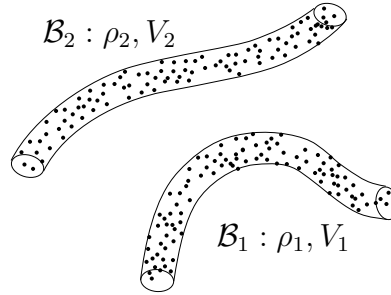
Figure 2.3.: Two arbitrarily shaped, deformable bodies $\mathcal{B}_1$ and $\mathcal{B}_2$ with volumes V_1, V_2 and continuous particle densities ρ_1, ρ_2. Figure taken from the author's article [61].

Assuming additivity, we apply *pairwise summation* to arrive at the two-body interaction potential

$$\Pi_{\mathrm{ia}} = \sum_{i \in \mathcal{B}_1} \sum_{j \in \mathcal{B}_2} \Phi(r_{ij}). \tag{2.11}$$

Further assuming a continuous atomic density ρ_i, $i = 1, 2$, the total interaction potential can alternatively be rewritten as integral over the volumes V_1, V_2 of both bodies $\mathcal{B}_1$ and $\mathcal{B}_2$:

$$\Pi_{\mathrm{ia}} = \iint_{V_1, V_2} \rho_1(\boldsymbol{x}_1)\rho_2(\boldsymbol{x}_2)\Phi(r)\,\mathrm{d}V_2\,\mathrm{d}V_1 \qquad \text{with} \quad r = \|\boldsymbol{x}_1 - \boldsymbol{x}_2\| \tag{2.12}$$

It can be shown that this continuum approach is the result of *coarse-graining*, i.e., smearing-out the discrete positions of atoms in a system into a smooth atomic density function $\rho(\boldsymbol{x})$ [141].

In the case of surface interactions, the dimensionality of the problem reduces and summation or integration is carried out over both bodies' surfaces $\partial\mathcal{B}_1$, $\partial\mathcal{B}_2$:

$$\Pi_{\mathrm{ia}} = \iint_{S_1, S_2} \sigma_1(\boldsymbol{x}_1)\sigma_2(\boldsymbol{x}_2)\Phi(r)\,\mathrm{d}S_2\,\mathrm{d}S_1 \qquad \text{with} \quad r = \|\boldsymbol{x}_1 - \boldsymbol{x}_2\| \tag{2.13}$$

Accordingly, surface densities $\sigma_i(\boldsymbol{x}_i)$, $i = 1, 2$, replace the volume densities in this case.

The range of two-body interaction forces originating from point pair potentials

Let us assume a general inverse power law $\Phi(r) = kr^{-m}$ for the point pair interaction potential. It is obvious, that the potential becomes infinitely large if the separation of the two individual points r approaches zero and, on the other hand, that the potential rapidly decays with increasing distance. Turning to two bodies of finite size, i.e., two clouds of points, things are more involved as the following theoretical considerations demonstrate. In short, it can be shown that there is a fundamental difference between potentials with an exponent $m \leq 3$ on the one hand and $m > 3$ on the other hand. Starting with the case $m > 3$, e.g., vdW interactions, the two-body interaction potential goes to infinity if the bodies approach until their surfaces touch each other. This can be illustrated by the simple example of two spheres of radius R, where the vdW interaction potential scales with $\Pi_{vdW} \propto g^{-1}$ (cf. [74, p.255]) with surface-to-surface separation or gap $g = d - 2R$ and the distance between the spheres' centers d. This singularity of the two-body interaction potential in the limit of zero separation $g \to 0$ is due to the fact that potentials with $m > 3$ decay so rapidly that the few point pairs with smallest separation outweigh the potentially very large number of all other, distant point pairs in terms of their potential contributions. Therefore, we can conclude that potentials with $m > 3$ have no significant large distance contribution and the two-body interaction potential is governed by the separation of any two closest points (and their immediate surrounding). Considering the example of two cylinders later on, we will also see that the vdW interaction potential of two perpendicular cylinders does not change perceptibly if the length of the cylinders is increased (cf. Equation (2.16)), which can again be attributed to the short range of vdW interactions.

The situation is substantially different for potentials with $m \leq 3$, e.g., Coulombic interactions. Here, the total contribution of all distant point pairs dominates over the few closest point pairs and the total interaction potential remains finite even if both bodies are in contact. Looking once again at the simple example of two spheres, Coulomb's law (cf. Equation (2.3)) directly shows $\Pi_{elstat} \propto d^{-1}$ and thus no singularity occurs for (nearly) contacting surfaces $g \to 0$, i.e., $d \to 2R$. Also, in contrast to the case of vdW mentioned above, the Coulomb interaction potential of two perpendicular cylinders would increase if their length is increased. The underlying theoretical derivations revealing also the turning point, i.e., the exponent $m = 3$ were first noted by Newton and can be found e.g. in [74, p. 11]. Due to this crucial difference, potentials with $m > 3$ will be denoted as *short-range* interactions (e.g. repulsive as well as attractive part of LJ) and potentials with $m \leq 3$ as *long-range* interactions (e.g. Coulomb) throughout this work.

2.3.1. Electrostatics of non-conductive bodies: An example for long-range surface interactions

The Coulomb interaction is additive such that the net force acting on an individual point charge in a system of point charges can be calculated from superposition of all pair-wise computed force contributions [74]. Equivalently, the net interaction potential results from summation of all pair potentials. A large body of literature deals with the problem of electrostatic multi-body interaction. One concept of high relevance for the present work is a well-known strategy called multipole expansion, which aims to express the resultant electrostatic potential of a (continuous) charge distribution as an (infinite) series (see e.g. [127] for details). The individual terms of the

series expansion generally are inverse power laws in the distance with increasing exponent and referred to as mono-, di-, quadru-, up to n-pole moments. At points far from the location of the charge cloud, the series converges quickly and can thus be truncated in good approximation. Regarding the total interaction potential of two charged bodies as formulated in (2.12) or (2.13), this already outlines the way how to determine Π_{elstat} for trivial geometries of the interacting bodies, where the integrals can potentially be solved analytically. We will return to this concept in the context of deformable slender fibers when proposing the general SSIP approach in the beginning of Section 4.2 and make use of a (truncated) multi-pole expansion of the charged cross-sections for the (simplified) SSIP law for long-range surface interactions to be proposed in Section 4.3.3.

2.3.2. Van der Waals interaction: An example for short-range volume interactions

Here, we want to discuss vdW interactions as one example of physically relevant volume interactions that is based on the inverse-sixth power law (2.4). However, very similar considerations and formulae apply to steric interactions as well as LJ interactions.

Today, we know that vdW interactions are generally non-additive. The latest and most accurate models for two-body vdW interactions are based on Lifshitz theory and, among other effects, include retardation, anisotropy and differences in polarizability. Nevertheless, a "happy convergence" of old, i.e., Hamaker's pairwise summation, and new, i.e. Lifshitz, theory allows to determine the distance dependency from pairwise summation and then estimate the prefactor, i.e., Hamaker "constant" A_{Ham}, from more advanced modern theory. This approach yielding a so-called Hamaker-Lifshitz hybrid form [125], [74, p. 257] is what motivates us to use pairwise summation in the derivation of the numerical methods to be proposed in the present work. Also, there are some special scenarios (negligible retardation, negligible difference in optical properties of the bodies, interaction in vacuum, ...), where additivity can be assumed as a good approximation even without adaption of the Hamaker constant.

Generally, even the simple approach of pairwise summation requires two nested 3D integrals over both bodies' volumes, i.e., six-dimensional integration. Mainly due to this high dimensionality of the problem, unfortunately, (closed-form) analytical solutions can only be obtained for some simple special cases. Still, careful considerations and selection allow us to exploit some of these analytical expressions in order to develop efficient, reduced methods in Section 4.2.2. To get a concise overview of all expressions relevant for the remainder of this work, we will provide a collection of closed-form analytical solutions in the following.

First, we want to look at two cylinders representing the simplest model for two interacting straight, rigid fibers with circular cross-section. A number of publications consider this scenario and due to the simplicity of the geometry they were able to derive analytical solutions for some special cases. The resulting expressions are summarized in Table 2.1 and will be used for verification purposes in Section 4.5.1. A second, highly relevant scenario is the one considering two disks. These analytical expressions, summarized in Table 2.2, will be beneficial, and in fact provide the main ingredient, for the SSIP approach to describe molecular interactions between *deformable* fibers modeled as 1D Cosserat continua.

Two Cylinders

To begin with, we consider the cases of parallel and perpendicular cylinders before we turn to arbitrary mutual angles further down. Generally, the cylinders are assumed to be infinitely long, such that the boundary effects at its ends may be neglected. As the interaction potential for parallel cylinders would be infinite, one typically considers a length-specific interaction potential $\tilde{\pi}_{\text{vdW,cyl}\|\text{cyl}}$ with dimensions of energy per unit length. This quantity thus describes the interaction of one infinitely long cylinder with a section of unit length of the other infinitely long cylinder. For perpendicular orientation (and all other mutual angles apart from $\alpha = 0$) on the other hand, the total interaction potential $\Pi_{\text{vdW,cyl}\perp\text{cyl}}$ remains finite.

Even for this simple case of two cylinders, no closed-form analytical solution for the vdW interaction energy can be found for all separations. One thus resorts to the consideration of the limits of small and large surface-to-surface separations for which the general solution, an infinite series, converges to the expressions presented in the following Table 2.1.

	Limit of *small* separations $g \ll R_1, R_2$	Limit of *large* separations $g, d \gg R_1, R_2$
parallel $\left[\frac{\text{energy}}{\text{length}}\right]$	$\tilde{\pi}_{\text{vdW,cyl}\|\text{cyl,ss}} = -\frac{A_{\text{Ham}}}{24}\sqrt{\frac{2R_1R_2}{R_1+R_2}}\,g^{-\frac{3}{2}}$ (2.14) see [74][p. 255], [125][p. 172]	$\tilde{\pi}_{\text{vdW,cyl}\|\text{cyl,ls}} = -\frac{3\pi}{8}\,A_{\text{Ham}}\,R_1^2R_2^2\,d^{-5}$ (2.15) see [125][p. 16, p. 172]
perp. [energy]	$\Pi_{\text{vdW,cyl}\perp\text{cyl,ss}} = -\frac{A_{\text{Ham}}}{6}\sqrt{R_1R_2}\,g^{-1}$ (2.16) see [74][p. 255]	$\Pi_{\text{vdW,cyl}\perp\text{cyl,ls}} = -\frac{\pi}{2}\,A_{\text{Ham}}\,R_1^2R_2^2\,d^{-4}$ (2.17) see [125][p. 16]

Table 2.1.: A collection of analytical solutions for the cylinder-cylinder interaction potential derived via pairwise summation. Here, R_i denotes the cylinder radii, d denotes the closest distance between the cylinder axes, g denotes the surface-to-surface separation, i.e., gap, $A_{\text{Ham}} := \pi^2 \rho_1 \rho_2 C_{\text{vdW}}$ is the commonly used abbreviation known as Hamaker constant where ρ_i denotes the particle densities and C_{vdW} denotes the constant prefactor of the point-pair potential law (see Equation (2.4)).

Despite the different dimensions of the quantities for parallel and perpendicular cylinders, we can still compare these expressions as becomes clear by the following thought experiment. Considering two "sufficiently long" cylinders of length L in parallel orientation, the total interaction potential is well described by $\Pi_{\text{vdW,cyl}\|\text{cyl}} = \tilde{\pi}_{\text{vdW,cyl}\|\text{cyl}} \cdot L$ and thus shows the same scaling behavior in the separation as (2.14) and (2.15). In addition, (2.16) and (2.17) are also a good approximation for the perpendicular orientation of these cylinders of finite length L since the difference in the distant point pairs is negligible.

It seems worth to point out a few interesting aspects of these equations. First, it is remarkable how the expressions differ in the exponent of the power law describing the distance dependency of the potential. This relates to a diverse and highly nonlinear behavior already for this simplest model system of fiber-fiber interactions composed of two cylinders. Second, the parallel orientation is a very special orientation that gives rise to the strongest possible adhesive forces between two cylinders and at the same time is the only stable equilibrium configuration. Third, the distance scaling behavior of two parallel cylinders at small separations $\tilde{\pi}_{\mathrm{vdW,cyl\|cyl,ss}} \propto g^{-\frac{3}{2}}$ lies between the fundamental solutions known for two infinite half spaces $\tilde{\tilde{\pi}} \propto g^{-2}$ (double tilde indicates a potential per unit area) and two spheres $\Pi \propto g^{-1}$. Note that again multiplication of these laws by a length or area does not alter the scaling law in the distance. Looking at the equations for large separations, we see similar relations, once again with a stronger distance scaling behavior in the parallel case. Generally, the solutions for large separations are expressed more naturally in the inter-axis separation d rather than the surface-to-surface separation g.

Angle-dependency in the two-cylinder scenario

In the limit of small separations, the vdW interaction potential of two infinitely long cylinders follows the following general relationship valid for all (nonzero) mutual angles $\alpha \in]0, \pi/2]$ as stated e.g. in [125, p. 173]:

$$\Pi_{\mathrm{vdW,cyl\text{-}cyl}} = -\frac{A_{\mathrm{Ham}}}{6}\sqrt{R_1 R_2}\, g^{-1}/\sin\alpha \qquad \text{with} \quad A_{\mathrm{Ham}} := \pi^2 \rho_1 \rho_2 C_{\mathrm{vdW}} \qquad (2.18)$$

For the limiting case of perpendicular cylinders $\alpha = \pi/2$, this coincides with $\Pi_{\mathrm{vdW,cyl\perp cyl,ss}}$ as given before in Equation (2.16) in Table 2.1. For the case of parallel cylinders, however, the total interaction potential of infinitely long cylinders is infinite and we obtain $\tilde{\pi}_{\mathrm{vdW,cyl\|cyl,ss}}$ from Equation (2.14) instead, which is also listed in Table 2.1.

Remark. Interestingly, the $1/\sin\alpha$-scaling behavior also holds true for screened electrostatic interaction of two cylinders [16], [91, p. 23]. Indeed, it is shown in [74, p. 218], that this relation results from fundamental geometric considerations related to the so-called Derjaguin approximation, and is thus independent of the type of interaction, i.e., the specific form of the point interaction potential law $\Phi(r)$.

Two Disks

This problem has been studied in literature on vdW interaction of straight, rigid cylinders of infinite length [90]. In analogy to the cylinder-cylinder scenario, it turns out that not even in the simplest case of parallel orientation, i.e., two disks with parallel normal vectors lying in one plane, a closed analytical solution can be found for all separations. Instead, two expressions for the limit of small and large separations of the disks g as compared to their radii R_1, R_2 are presented in the following Table 2.2, respectively.

To summarize this Section 2.3.2 on two-body vdW interactions, it can be stated that a closed-form expression for the two-body vdW interaction potential is only known for some rare special cases and the ones relevant for fiber-fiber interactions have been identified in the voluminous

	Limit of *small* separations $g \ll R_1, R_2$	Limit of *large* separations $g, d \gg R_1, R_2$
parallel $\left[\frac{\text{energy}}{\text{length}^2}\right]$	$\tilde{\tilde{\pi}}_{\text{vdW,disk}\|\text{disk,ss}} = -\frac{3A_{\text{Ham}}}{256} \sqrt{\frac{2R_1 R_2}{R_1 + R_2}}\, g^{-\frac{5}{2}}$ (2.19) see [90]	$\tilde{\tilde{\pi}}_{\text{vdW,disk}\|\text{disk,ls}} = -A_{\text{Ham}}\, R_1^2\, R_2^2\, d^{-6}$ (2.20) see [90]

Table 2.2.: A collection of analytical solutions for the disk-disk interaction potential derived via pairwise summation. Here, R_i denotes the disk radii, d denotes the closest distance between the disk midpoints, g denotes the surface-to-surface separation, i.e., gap, $A_{\text{Ham}} := \pi^2 \rho_1 \rho_2 C_{\text{vdW}}$ is the commonly used abbreviation known as Hamaker constant where ρ_i denotes the particle densities and C_{vdW} denotes the constant prefactor of the point-pair potential law (see Equation (2.4)).

literature on this topic and presented here in a brief and concise manner and unified notation. In addition to these analytical expressions obtained by means of simple pairwise summation, further theoretical work that relax certain assumptions and consider more advanced aspects like interaction across inhomogeneous or anisotropic media, differences in optical material properties or retardation can be found in the literature. To give but one example, [128] studies cylinders with anisotropic optical properties considering the example of carbon nanotubes. A review of recent research activities on this topic is given in [39]. This work however focuses on the extension towards deformable and thus curved slender fibers with arbitrary mutual separations and orientations due to their possibly large elastic deformations in 3D, and therefore uses the basic pairwise summation approach as discussed and motivated in the beginning of this section.

2.3.3. Steric repulsion – mechanical contact

As a last type of two-body interaction, steric exclusion, i.e., contact interactions, shall be briefly discussed in this section as already done for pairs of atoms or small molecules in Section 2.2.3. The prevailing notion of contact between microscopic bodies (e.g. in biophysics) is most commonly described as excluded volume effect, which means that bodies may approach each other without any influence on each other and only as soon as their surfaces touch, the repulsive contact forces that inhibit any overlap of the bodies' volumes may rise to infinite strength. This class of physical interactions shares the two central properties of being extremely short in range and being volume interactions with the previously considered vdW interactions. Starting e.g. from the inverse-twelve power law as in the repulsive part of the LJ interaction law (2.8), one may apply very similar solution strategies and finally obtain very similar expressions as the ones presented in the previous section. For the sake of brevity, we refer to the derivations in Appendix A and the analysis of the resulting total LJ interaction that will also be used for the regularization of the reduced potential laws in Section 4.4.3 and 5.4.1.

In the field of (computational) mechanics with a focus on applications in engineering, the effect of contact interaction has also been considered a lot, albeit with a slightly different, rather macroscopic perspective. The existing, macroscopic beam contact formulations relevant for this work will thus be briefly summarized in Section 3.3 and a comparison with the novel computational approaches to be developed in Chapter 4 and 5 will be given in Section 6.2. Finally, both the existing, macroscopic approaches and the novel beam interaction formulations based on the repulsive part of the LJ potential will be applied in the remainder of this work depending on the specific use case and e.g. directly compared in the numerical example to be presented in Section 4.5.2.

3. Fundamentals of Beams and Beam Contact

This chapter aims to provide a brief and concise introduction to those well-known concepts of beam theory to be used in the remainder of this work. It shall also serve as a valuable source of reference for the reader of the following chapters and by no means is meant to be an exhaustive overview of the vast body of literature on this topic for which the interested reader is kindly referred e.g. to the recent article [113] and the dissertation by C. Meier [108].

As commonly used in engineering mechanics, we refer to the term *beam* as a mathematical model for a three-dimensional, slender, deformable body for which the following assumption can be made. The much larger extent of the body in its axial direction as compared to all transverse directions often justifies the Bernoulli hypothesis of rigid and therefore undeformable cross-sections. This in turn allows for a reduced dimensional description as a 1D Cosserat continuum embedded in the 3D Euclidian space.

The outline of this chapter is as follows. First, the space-continuous beam theory will be summarized in Section 3.1 before suitable finite element formulations will be presented in Section 3.2. Finally, Section 3.3 will summarize the existing, macroscopic beam contact formulations already mentioned in the context of repulsive steric interactions in the previous chapter.

Generally, this chapter is a review of existing knowledge in this field as previously elaborated e.g. in the dissertation by C. Meier [108]. However, this chapter will also include the following two original contributions of the author. On the one hand, the existing Simo-Reissner beam element formulation proposed by Crisfield and Jelenić [29, 76] is augmented by a C^1-continuous Hermite centerline interpolation in Section 3.2.2 and its optimal spatial convergence behavior is verified by a numerical example in Section 3.2.3. On the other hand, the beam contact formulations recently proposed by Meier et al. [110, 111] are for the first time applied in combination with this Hermitian Simo-Reissner element and also in combination with the Kirchhoff-Love beam element recently proposed by Meier et al. [113] in the numerical examples to be presented in Section 3.3.4. This demonstrates the versatility of the theoretical and computational framework and allows for a comparison of the different types of beam formulations in challenging beam contact scenarios. This original work of the author has previously been published as part of the co-authored article [112].

3.1. Geometrically exact 3D beam theory

Throughout this work, solely the so-called *geometrically exact* beam theory will be applied. Its name aims to underline the fact that this category of beam theory uses deformation measures that

are consistent with the strong and weak form of the balance equations for arbitrary translated, rotated, and deformed configurations of the beam.

Since the theory of Simo and Reissner, which accounts for the deformation modes of axial tension, bending, torsion and shear deformation, is the most general representative of geometrically exact beam theories, it will be predominantly applied throughout this work. However, Kirchhoff-Love beam formulations are known to be advantageous in the regime of high slenderness ratios where the underlying assumption of negligible shear deformation is met [112, 113]. This work thus aims to develop novel approaches to molecular interactions of beams that are not restricted to a specific beam formulation and can be applied to different beam formulations depending on the specific use case. Thus, the fundamentals of both types of beam theories will be briefly presented in the following.

3.1.1. Simo-Reissner beam theory

The Simo-Reissner beam theory dates back to the works of Reissner [129], Simo [150], and Simo and Vu-Quoc [151], who generalized the linear Timoshenko beam theory [159] to the geometrically nonlinear regime.

Geometry representation

A certain configuration of the 1D Cosserat continuum is uniquely defined by the centroid position and the orientation of the cross-section at every point of the continuum. The set of all centroid positions is referred to as *centerline* or *neutral axis* and expressed by the curve

$$s, t \mapsto \boldsymbol{r}(s, t) \in \mathbb{R}^3 \tag{3.1}$$

in space and time $t \in \mathbb{R}$. Each material point along the centerline is represented by a corresponding value of the arc-length parameter $s \in [0, l_0] =: \Omega_l \subset \mathbb{R}$. Note that this arc-length parameter s is defined in the stress-free, initial configuration of the centerline curve $\boldsymbol{r}_0(s) = \boldsymbol{r}(s, t{=}0)$. Thus, the norm of the initial centerline tangent vector yields

$$\|\boldsymbol{r}_0'(s)\| := \|\frac{\partial \boldsymbol{r}_0(s)}{\partial s}\| \equiv 1, \tag{3.2}$$

but generally, in presence of axial tension, $\|\boldsymbol{r}'(s, t)\| = \|\partial \boldsymbol{r}(s, t)/\partial s\| \neq 1$.

Furthermore, the cross-section orientation at each of these material points is expressed by a right-handed orthonormal frame often denoted as *material triad*:

$$s, t \mapsto \boldsymbol{\Lambda}(s, t) := [\boldsymbol{g}_1(s, t), \boldsymbol{g}_2(s, t), \boldsymbol{g}_3(s, t)] \in SO^3 \tag{3.3}$$

The second and third base vector follow those material fibers representing the principal axes of inertia of area. Such a triad can equivalently be interpreted as rotation tensor transforming the base vectors of a global Cartesian frame $\boldsymbol{E}_i \in \mathbb{R}^3, i \in 1, 2, 3$ into the base vectors of the material triad $\boldsymbol{g}_i \in \mathbb{R}^3, i \in 1, 2, 3$ via

$$\boldsymbol{g}_i(s, t) = \boldsymbol{\Lambda}(s, t) \, \boldsymbol{E}_i(s, t). \tag{3.4}$$

In summary, a beam's configuration may be uniquely described by a field of centroid positions $\boldsymbol{r}(s, t)$ and a field of associated material triads $\boldsymbol{\Lambda}(s, t)$, altogether constituting a 1D Cosserat
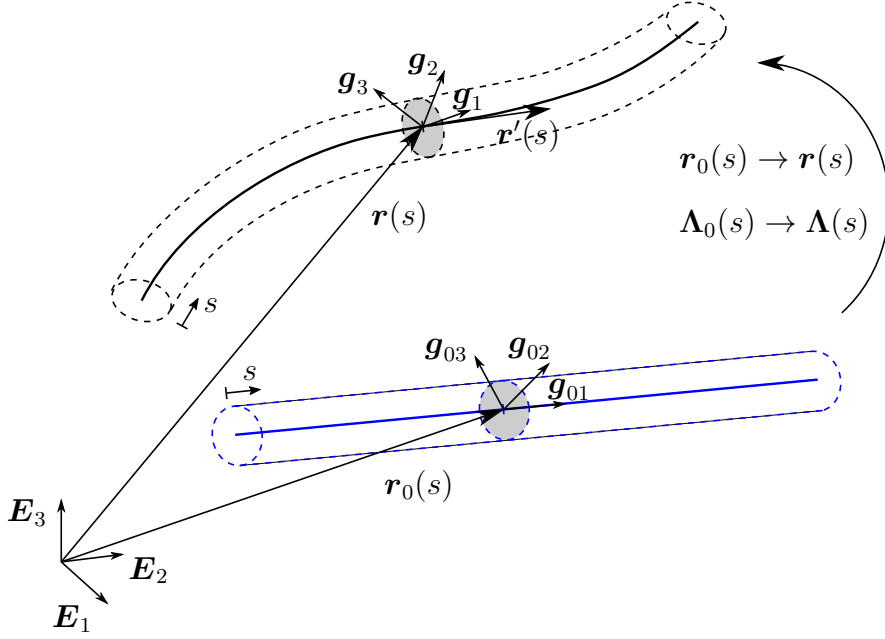
Figure 3.1.: Geometry description and kinematics of the Cosserat continuum formulation of a beam: Initial, i.e., stress-free (blue) and deformed (black) configuration. The straight configuration in the initial state is chosen exemplarily here without loss of generality. Figure taken from the author's article [61].

continuum (see Figure 3.1). According to this concept of geometry representation, the position $\boldsymbol{x}$ of an arbitrary material point P of the slender body is obtained from

$$\boldsymbol{x}_{\mathrm{P}}(s, s_2, s_3, t) = \boldsymbol{r}(s, t) + s_2\, \boldsymbol{g}_2(s, t) + s_3\, \boldsymbol{g}_3(s, t). \tag{3.5}$$

Here, the additional convective coordinates s_2 and s_3 specify the location of P within the cross-section, i.e., as linear combination of the unit direction vectors $\boldsymbol{g}_2$ and $\boldsymbol{g}_3$. For a minimal parameterization of the triad, e.g. the three-component rotation pseudo-vector $\boldsymbol{\psi}$ may be used such that we end up with six independent degrees of freedom $(\boldsymbol{r}, \boldsymbol{\psi})$ to define the position of each material point in the body by means of (3.5).

Remark on notation. Unless otherwise specified, all vector and matrix quantities are expressed in the global Cartesian basis $\boldsymbol{E}_i$. Differing bases as e.g. the material frame are indicated by a subscript $[.]_{\boldsymbol{g}_i}$. Quantities evaluated at time $t = 0$, i.e., the initial stress-free configuration, are indicated by a subscript 0 as e.g. in $\boldsymbol{r}_0(s)$. Differentiation with respect to the arc-length coordinate s is indicated by a prime, e.g., for the centerline tangent vector $\boldsymbol{r}'(s, t) = \mathrm{d}\,\boldsymbol{r}(s, t)/\mathrm{d}\,s$. Differentiation with respect to time t is indicated by a dot, e.g., for the centerline velocity vector $\dot{\boldsymbol{r}}(s, t) = \mathrm{d}\,\boldsymbol{r}(s, t)/\mathrm{d}\,t$. For the sake of brevity, the arguments s, t will often be omitted in the following.

Remark on finite 3D rotations. To a large extent, the challenges and complexity in the numerical treatment of the geometrically exact beam theory can be traced back to the presence of large

rotations. In contrast to common *vector spaces*, the rotation group $SO(3)$ is a *nonlinear manifold* (with Lie group structure) and lacks essential properties such as additivity and commutativity, which makes standard procedures such as interpolation or update of configurations much more involved. This also carries over to the novel beam interaction formulations to be developed in Chapter 4 and 5 and thus motivates to avoid the handling of finite rotations wherever possible in order to achieve simpler and more compact numerical formulations.

Kinematics and deformation measures

Figure 3.1 summarizes the kinematics of geometrically exact beam theory. Based on these kinematic quantities, translational and rotational deformation measures as well as constitutive laws relating these deformation measures to resulting forces and moments can be defined. Particularly the objectivity and path-independence of deformation measures should be mentioned as essential requirements for a consistent formulation at this point. See e.g. [29, 76, 113] for a detailed presentation of these steps.

Finally, the potential energy of the internal (elastic) forces and moments Π_{int} is expressed uniquely by means of the set of six degrees of freedom $(\boldsymbol{r}, \boldsymbol{\psi})$ at each point of the 1D Cosserat continuum as will be outlined in the following. In addition to the internal elastic energy, the contributions from kinetic energy and the work of external forces and moments can be included in the balance equations.

Strong and weak form of equilibrium equations

The internal energy, i.e. the contribution from elastic forces and moments, reads

$$\Pi_{\text{int}} = \int_0^l \frac{1}{2}\boldsymbol{\Omega}^T\boldsymbol{C}_M\boldsymbol{\Omega} + \frac{1}{2}\boldsymbol{\Gamma}^T\boldsymbol{C}_F\boldsymbol{\Gamma}\,\mathrm{d}s. \tag{3.6}$$

It results from an assumed hyperelastic stored energy function relating the material deformation measures $\boldsymbol{\Omega}$ and $\boldsymbol{\Gamma}$ to material stress resultants $\boldsymbol{M}$ and $\boldsymbol{F}$ via constitutive matrices $\boldsymbol{C}_M$ and $\boldsymbol{C}_F$:

$$\boldsymbol{M} = \underbrace{\mathbf{diag}\big[GI_T, EI_2, EI_3\big]}_{\boldsymbol{C}_M}\boldsymbol{\Omega}, \qquad \boldsymbol{F} = \underbrace{\mathbf{diag}\big[EA, GA_2, GA_3\big]}_{\boldsymbol{C}_F}\boldsymbol{\Gamma} \tag{3.7}$$

The required scalar values for torsional rigidity GI_T, bending rigidities EI_2, EI_3, axial rigidity EA and shear rigidities GA_2, GA_3 may either be obtained from experiments or calculated from geometrical as well as constitutive parameters of the 3D continuum such as Young's modulus E, shear modulus G, and Poisson's ratio ν. For the latter approach, the cross-section geometry is well defined via the torsional moment of inertia I_T, principal moments of inertia I_2, I_3, cross-section area A and reduced cross-section areas A_2, A_3, which are related to the cross-section area via the shear correction factor κ.

Based on the spatial angular velocity $\boldsymbol{w}$ and the centerline velocity $\dot{\boldsymbol{r}}$, the kinetic energy may be expressed as the sum of rotational and translational inertia terms:

$$\Pi_{\text{kin}} = \int_0^l \frac{1}{2}\boldsymbol{w}^T\boldsymbol{c}_\rho\boldsymbol{w} + \frac{1}{2}\rho A\dot{\boldsymbol{r}}^T\dot{\boldsymbol{r}}\,\mathrm{d}s \tag{3.8}$$

Again, the values for the inertia tensor

$$\boldsymbol{c}_\rho = \mathbf{diag}\big[\rho(\underbrace{I_2 + I_3}_{=:I_P}), \rho I_2, \rho I_3\big] \tag{3.9}$$

involve cross-section moments of inertia as well as material specification in terms of the mass density ρ.

Finally, external forces $\boldsymbol{f}_\sigma$ and moments $\boldsymbol{m}_\sigma$ specified at the Neumann boundary Γ_σ as well as distributed external forces $\tilde{\boldsymbol{f}}$ and moments $\tilde{\boldsymbol{m}}$ contribute to the virtual work via

$$\delta W_{\text{ext}} = \int\limits_0^l \Big(\delta\boldsymbol{\theta}^T \tilde{\boldsymbol{m}} + \delta\boldsymbol{r}^T \tilde{\boldsymbol{f}} \Big)\, \mathrm{d}s + \Big[\delta\boldsymbol{r}^T \boldsymbol{f}_\sigma \Big]_{\Gamma_\sigma} + \Big[\delta\boldsymbol{\theta}^T \boldsymbol{m}_\sigma \Big]_{\Gamma_\sigma}. \tag{3.10}$$

Here, $\delta\boldsymbol{r}$ and $\delta\boldsymbol{\theta}$ denote the virtual displacements and the (multiplicative) variation of the rotation vector, respectively.

According to the Principle of Virtual Work, the total virtual work of a system must vanish in the state of (either static or dynamic) equilibrium and we end up with the weak form of the balance equations:

$$\delta W = \delta\Pi_{\text{int}} + \delta\Pi_{\text{kin}} - \delta W_{\text{ext}} \overset{!}{=} 0 \tag{3.11}$$

Alternatively, the *strong*, i.e., point-wise form of equilibrium can be expressed as balance of all yet considered forces and moments:

$$\boldsymbol{f}' + \tilde{\boldsymbol{f}} + \boldsymbol{f}_\rho = \boldsymbol{0} \tag{3.12}$$

$$\boldsymbol{m}' + \boldsymbol{r}' \times \boldsymbol{f} + \tilde{\boldsymbol{m}} + \boldsymbol{m}_\rho = \boldsymbol{0} \tag{3.13}$$

3.1.2. Kirchhoff-Love beam theory

Euler's theory neglecting shear deformation marks the beginning in the long history of beam theory. A shear-free model in the geometrically linear regime assuming small deformations today is referred to as Euler-Bernoulli beam. Kirchhoff and Love later refined this theory to be geometrically exact, i.e., hold for arbitrary geometrical configurations as a result of rigid body translations, rotations and deformations. The effect of shear deformation is known to decrease with increasing slenderness of the beam. Thus, the slenderness ratio $\zeta = l/R$ defined via the length l and cross-section radius R of the beam is the key parameter to judge the applicability of shear-free Kirchhoff-Love beam theory.

Vanishing shear deformation can be mathematically described as

$$\boldsymbol{g}_2^T \boldsymbol{r}' = 0 \qquad \text{and} \qquad \boldsymbol{g}_3^T \boldsymbol{r}' = 0 \qquad \text{or, equivalently,} \qquad \boldsymbol{g}_1 \equiv \frac{\boldsymbol{r}'}{\|\boldsymbol{r}'\|}, \tag{3.14}$$

i.e., the cross-section plane remains perpendicular to the centerline tangent vector in every point along the beam centerline. This additional constraint reduces the number of rotational degrees of freedom that parameterize the cross-section orientation and couples it to the centerline geometry.

In contrast to Simo-Reissner theory using three independent parameters, e.g., the components of a rotation pseudo-vector, the Kirchhoff-Love theory thus features one scalar degree of freedom representing rotation around the tangent vector. This additional degree of freedom relates to the twist deformation.

Introducing the additional constraint equations, the governing equations for Kirchhoff beam theory can be derived from the Simo-Reissner theory presented above. As an example, the contribution from internal elastic forces and moments is obtained as

$$\Pi_{int} = \int_0^l \frac{1}{2}\mathbf{\Omega}^T \mathbf{C}_M \mathbf{\Omega} + \frac{1}{2} E A \epsilon^2 \, \mathrm{d}s. \tag{3.15}$$

The comparison with Equation (3.6) illustrates that energy contributions from shear forces vanish due to zero shear deformations. However, Equation (3.8) for the kinetic energy remains unchanged.

Instead of strongly enforcing the Kirchhoff constraint (3.14) at every point of the 1D continuum, we will follow the approach proposed by Meier et al [113] to include this constraint in a weak sense. As it turns out that this exclusively affects the rotation interpolation strategy, further details on this approach will be discussed along with the spatial discretization scheme in Section 3.2.4. Alternatively, a geometrically exact method following a strong, point-wise enforcement of the Kirchhoff constraint has been proposed in [107, 109]. A detailed analysis of both approaches can be found in [113].

3.1.3. Torsion-free Kirchhoff-Love beam theory

As shown in [108], rod-like structures remain torsion-free under specific loading and boundary conditions. It turns out that the assumption of vanishing torsion and initially straight beams with isotropic cross-section allows for a specifically simple and elegant beam theory exclusively based on the beam centerline curve. Hence, the mathematical description of finite 3D rotations and corresponding interpolation schemes can be avoided. This combination of a significantly simplified theory and the applicability in many practically relevant scenarios is the motivation to include this torsion-free beam theory in the versatile computational framework outlined in Appendix F.

The internal energy contributions from the remaining deformation modes axial tension and bending and the kinetic energy read

$$\Pi_{\text{int}} = \int_0^l \frac{1}{2} \left(E A \epsilon^2 + E I \kappa^2 \right) \mathrm{d}s \quad \text{and} \quad \Pi_{\text{kin}} = \int_0^l \frac{1}{2} \rho A \dot{\mathbf{r}}^2 \, \mathrm{d}s, \tag{3.16}$$

respectively. This formulation thus includes isotropic bending quantified via the scalar curvature κ that can directly be expressed via the curvature of the Frenet-Serret frame

$$\kappa := \frac{\mathbf{r}' \times \mathbf{r}''}{\|\mathbf{r}'\|^2}. \tag{3.17}$$

3.1.4. Concluding overview of the applied beam theories

To conclude this brief summary of the fundamentals of beam theory, Figure 3.2 shows a graphical overview of the three presented categories of beam theory that have been applied in the scope of this work. This categorization illustrates the underlying assumptions and thus applicability
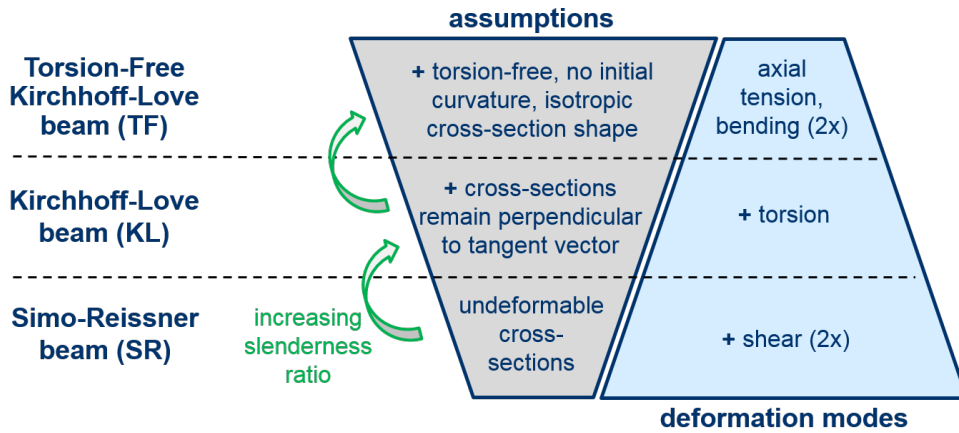
Figure 3.2.: Graphical overview of the three categories of beam theory that have been used in the scope of this work. Simo-Reissner (SR), Kirchhoff-Love (KL), and torsion-free Kirchhoff-Love (TF) theory are categorized by the underlying assumptions and corresponding deformation modes, which in turn determine the number of physical degrees of freedom of the 1D continuum.

on the one hand and the resulting deformation modes and thus number of physical degrees of freedom on the other hand. Due to these conflicting fundamental objectives of generality and simplicity/efficiency, all three beam theories are considered to be valuable in distinct areas of applications. We will revisit and extend this comparison of beam models after the presentation of the corresponding finite element formulations at the end of the following section.

3.2. Finite element formulations

This section briefly outlines the general solution strategy for the set of space- and time-continuous partial differential equations presented so far. The fundamentals of the applied finite element method can be found in textbooks such as [12, 170].

In order to solve the governing equations presented in the preceding Section 3.1, discretization in space and time is inevitable except for very rare cases. The resulting nonlinear system of equations is solved iteratively by Newton's method or modified variants thereof until specified convergence criteria are met. We therefore need to repeatedly evaluate the residual $\mathbf{R}$ as well as the corresponding Jacobian $\mathbf{K}$, resulting from linearization with respect to the discrete degrees of freedom $\mathbf{X}$:

$$\mathbf{K}(\mathbf{X}) := \frac{\partial \mathbf{R}(\mathbf{X})}{\partial \mathbf{X}} \tag{3.18}$$

The Jacobian is commonly referred to as tangent stiffness matrix expressing its interpretation in continuum solid mechanics.

In the following, we will first briefly discuss the applied temporal discretization schemes in Section 3.2.1 before turning to the spatial discretization by means of the finite element method. A key concept of the latter is the subdivision of the spatial domain $[0; l]$ into a finite number of elements n_{ele} and the geometry description in a local, element-wise manner. It is therefore sufficient to discuss the spatial discretization of a single beam finite element. As for the space-continuous theory in the last section, once again all three element formulations of Simo-Reissner (SR), Kirchhoff-Love (KL) and torsion-free Kirchhoff-Love (TF) type will be briefly presented in the remainder of this section.

3.2.1. Temporal Discretization

Throughout this work, finite difference schemes will be applied as temporal discretization for dynamic problems. As commonly used in the context of structural finite element simulations, the Generalized-α method as originally proposed by [25] is chosen for its second-order accuracy, unconditional stability and optimized damping characteristics. However, in case of finite rotations, an extension to Lie groups as proposed by [20] is required and thus applied in combination with Simo-Reissner and Kirchhoff-Love beam elements throughout this work. Accordingly, the original Generalized-α method is only used along with the torsion-free Kirchhoff-Love beam model. Refer to [108, 113] for further details on this topic.

Additionally, the Brownian motion of slender fibers modeled as beams will be considered in some of the applications to be presented e.g. in Chapter 8 and 9. In this scenario to be found on the nano- to micrometer scale, inertia can generally neglected in good approximation resulting in a system of first order (stochastic) partial differential equations in time. The Brownian dynamics finite element formulation that has been developed specifically for this application in [32] is based on a Backward Euler scheme to discretize in time. For further details, the reader is kindly referred to the original publication [32].

3.2.2. Hermitian Simo-Reissner beam element

As presented in Section 3.1, the centerline position r and the triad Λ arise as the two primary fields of unknowns. Within Simo-Reissner beam theory, both fields are uncorrelated and their discretization can hence be considered independently as follows.

Centerline field
The Simo-Reissner beam element used throughout this work originates from [29, 76], although we apply a different centerline interpolation scheme here. We employ cubic Hermite polynomials based on nodal position vectors $\hat{\mathbf{d}}^1, \hat{\mathbf{d}}^2$ and tangent vectors $\hat{\mathbf{t}}^1, \hat{\mathbf{t}}^2$ as the primary variables. See [109] for a detailed discussion of Hermite centerline interpolation in the closely related context of geometrically exact Kirchhoff-Love beams.

Applying the cubic Hermite interpolation scheme results in the following discretized center-line geometry and variation thereof:

$$\boldsymbol{r}(\xi) \approx \boldsymbol{r}_{\mathrm{h}}(\xi) = \sum_{i=1}^{2} H_d^i(\xi)\, \hat{\mathbf{d}}^i + \frac{l}{2} \sum_{i=1}^{2} H_t^i(\xi)\, \hat{\mathbf{t}}^i =: \mathbf{H}\, \hat{\mathbf{d}}, \tag{3.19}$$

$$\delta\boldsymbol{r}(\xi) \approx \delta\boldsymbol{r}_{\mathrm{h}}(\xi) = \sum_{i=1}^{2} H_d^i(\xi)\, \delta\hat{\mathbf{d}}^i + \frac{l}{2} \sum_{i=1}^{2} H_t^i(\xi)\, \delta\hat{\mathbf{t}}^i =: \mathbf{H}\, \delta\hat{\mathbf{d}} \tag{3.20}$$

Here, all the degrees of freedom of one element relevant for the centerline interpolation, i.e., nodal positions $\hat{\mathbf{d}}^i$ and tangents $\hat{\mathbf{t}}^i$, $i = 1, 2$ are collected in one vector $\hat{\mathbf{d}}$. Thus, $\mathbf{H}$ denotes the accordingly assembled matrix of shape functions, i.e., Hermite polynomials H_d^i and H_t^i. The newly introduced element-local parameter $\xi \in [-1; 1]$ is biuniquely related to the arc-length parameter $s \in [s_{\mathrm{ele,min}}; s_{\mathrm{ele,max}}]$ describing the very same physical domain of the beam as follows and the scalar factor defining this mapping between both infinite length measures is called the element *Jacobian* $J(\xi)$:

$$\mathrm{d}s = \frac{\mathrm{d}\,s}{\mathrm{d}\,\xi}\, \mathrm{d}\xi =: J(\xi)\, \mathrm{d}\xi \qquad \text{with} \qquad J(\xi) := \|\frac{\mathrm{d}\,\boldsymbol{r}_{0,\mathrm{h}}(\xi)}{\mathrm{d}\,\xi}\|\,. \tag{3.21}$$

The definition of the cubic Hermite polynomials is finally given as

$$H_d^1 = \frac{1}{4}(2 + \xi)(1 - \xi)^2, \;\; H_d^2 = \frac{1}{4}(2 - \xi)(1 + \xi)^2, \tag{3.22}$$

$$H_t^1 = \frac{1}{4}(1 + \xi)(1 - \xi)^2, \;\; H_t^2 = -\frac{1}{4}(1 - \xi)(1 + \xi)^2. \tag{3.23}$$

Refer to [109] for a discussion of the interpolation properties of Hermite polynomials.

The motivation to use (cubic) Hermite interpolation originates from the fact that it ensures C^1-continuity, i.e., a smooth geometry representation even across element boundaries. This property turned out to be crucial for the robustness of simulations in the context of macroscopic beam contact methods [112], and is just as important if we include molecular interactions as proposed in this work. See [136] for a comprehensive discussion of (non-)smooth geometries and adhesive, molecular interactions using 2D solid elements. Note however that neither the general SSIP and SBIP approaches to be proposed in Chapter 4 and Chapter 5 nor the specific expressions for the interaction free energy and the virtual work are restricted to this Hermite interpolation scheme. In fact, all of the discrete expressions to be presented throughout these chapters will be equally valid for a large number of other beam formulations, where the discrete centerline geometry is defined by polynomial interpolation, which can generally be expressed in terms of a generic shape function matrix $\mathbf{H}$ introduced above.

Triad field

The correct interpolation of large rotations is the crux of geometrically exact beam finite elements. We follow the approach of [29, 76], thus ensuring objectivity based on the definition of an element-local reference triad and the interpolation of local rotation vectors. More specifically,

the three-noded variant, i.e., using quadratic Lagrange polynomials L^i, is applied throughout this work as this turns out to ideally complement the cubic centerline interpolation in terms of numerical efficiency. Without going into detail, the procedure can be summarized as determining the interpolated triad $\mathbf{\Lambda}(\xi)$ from all nodal triads $\mathbf{\Lambda}^i$ in a nonlinear manner:

$$\mathbf{\Lambda}(\xi) \approx \mathbf{\Lambda}_{\mathrm{h}}(\xi) = \mathrm{nl}(\mathbf{\Lambda}^1, \mathbf{\Lambda}^2, \mathbf{\Lambda}^3, \xi) \tag{3.24}$$

In contrast, the virtual rotation vector $\delta\boldsymbol{\theta}(\xi)$ is linearly interpolated from nodal quantities following a Petrov-Galerkin scheme:

$$\delta\boldsymbol{\theta}_{\mathrm{h}}(\xi) = \sum_{i=1}^{3} L^i(\xi)\,\delta\hat{\boldsymbol{\theta}}^i =: \mathbf{L}\,\delta\hat{\boldsymbol{\theta}} \tag{3.25}$$

In analogy to the previously considered matrix of Hermite polynomials $\mathbf{H}$, here $\mathbf{L}$ has been introduced as the properly assembled matrix of Lagrange shape functions. In terms of primary degrees of freedom, we choose a minimal parameterization of the nodal triads $\mathbf{\Lambda}^i(\boldsymbol{\psi}^i)$ via rotation vectors $\hat{\boldsymbol{\psi}}^i \in \mathbb{R}^3$, $i = 1, 2, 3$ and transform between triads and rotation vectors by means of the Rodrigues formula and Spurrier's algorithm.

Nodal degrees of freedom

To summarize, the applied Hermitian Simo-Reissner element thus features the following set of primary degrees of freedom defined at three nodes $i = 1, 2, 3$ located at $\xi = \{-1, 1, 0\}$:

$$\hat{\mathbf{x}}_{\mathrm{SR}} := \left[\hat{\mathbf{d}}^{1T},\, \hat{\mathbf{t}}^{1T},\, \hat{\boldsymbol{\psi}}^{1T},\, \hat{\mathbf{d}}^{2T},\, \hat{\mathbf{t}}^{2T},\, \hat{\boldsymbol{\psi}}^{2T},\, \hat{\boldsymbol{\psi}}^{3T}\right]^T \tag{3.26}$$

For convenience in later notation and since the centerline description is independent of the rotational degrees of freedom, the following split into one vector collecting the primary degrees of freedom that is sufficient to describe the centerline geometry $\hat{\mathbf{d}}_{\mathrm{SR}}$ and another vector holding the rotational primary degrees of freedom $\hat{\boldsymbol{\psi}}_{\mathrm{SR}}$ shall be defined:

$$\hat{\mathbf{d}}_{\mathrm{SR}} := \left[\hat{\mathbf{d}}^{1T},\, \hat{\mathbf{t}}^{1T},\, \hat{\mathbf{d}}^{2T},\, \hat{\mathbf{t}}^{2T}\right]^T \tag{3.27}$$

$$\hat{\boldsymbol{\psi}}_{\mathrm{SR}} := \left[\hat{\boldsymbol{\psi}}^{1T},\, \hat{\boldsymbol{\psi}}^{2T},\, \hat{\boldsymbol{\psi}}^{3T}\right]^T \tag{3.28}$$

This has already been used in Equation (3.19). With respect to the required variations $\delta\hat{\mathbf{x}}_{\mathrm{SR}}$ and increments $\Delta\hat{\mathbf{x}}_{\mathrm{SR}}$ of these degrees of freedom, it seems worth to highlight the consistent use of multiplicative rotation vector variations $\delta\hat{\boldsymbol{\theta}}^i$, also known as spin vectors, and corresponding multiplicative increments $\Delta\hat{\boldsymbol{\theta}}^i$, $i = 1, 2, 3$, in the computational framework used in this work:

$$\delta\hat{\mathbf{x}}_{\mathrm{SR}} := \left[\delta\hat{\mathbf{d}}^{1T},\, \delta\hat{\mathbf{t}}^{1T},\, \delta\hat{\boldsymbol{\theta}}^{1T},\, \delta\hat{\mathbf{d}}^{2T},\, \delta\hat{\mathbf{t}}^{2T},\, \delta\hat{\boldsymbol{\theta}}^{2T},\, \delta\hat{\boldsymbol{\theta}}^{3T}\right]^T \tag{3.29}$$

$$\Delta\hat{\mathbf{x}}_{\mathrm{SR}} := \left[\Delta\hat{\mathbf{d}}^{1T},\, \Delta\hat{\mathbf{t}}^{1T},\, \Delta\hat{\boldsymbol{\theta}}^{1T},\, \Delta\hat{\mathbf{d}}^{2T},\, \Delta\hat{\mathbf{t}}^{2T},\, \Delta\hat{\boldsymbol{\theta}}^{2T},\, \Delta\hat{\boldsymbol{\theta}}^{3T}\right]^T \tag{3.30}$$

Discrete element residual vector

The combination of cubic Hermite interpolation for the centerline geometry as well as its variations and quadratic Lagrange interpolation for the triad field yields fourth order spatial convergence in the L^2-error as will be verified numerically in the following section. Finally, the discrete element residual vectors $\mathbf{r}_{\text{SR}}$ resulting for the internal, inertia, and external forces and moments of this Hermitian Simo-Reissner element are obtained as

$$\mathbf{r}_{\text{SR},\hat{\mathbf{d}}} = \int\limits_{-1}^{1} \left(\mathbf{H}'^T \boldsymbol{f} + \mathbf{H}^T \boldsymbol{f}_\rho - \mathbf{H}^T \tilde{\boldsymbol{f}} \right) J \, \mathrm{d}\xi - \left[\mathbf{H}^T \boldsymbol{f}_\sigma \right]_{\Gamma_\sigma} \tag{3.31}$$

$$\mathbf{r}_{\text{SR},\hat{\boldsymbol{\theta}}} = \int\limits_{-1}^{1} \left(\mathbf{L}'^T \boldsymbol{m} - \mathbf{L}^T \mathbf{S}(r') \boldsymbol{f} + \mathbf{L}^T \boldsymbol{m}_\rho - \mathbf{L}^T \tilde{\boldsymbol{m}} \right) J \, \mathrm{d}\xi - \left[\mathbf{L}^T \boldsymbol{m}_\sigma \right]_{\Gamma_\sigma}. \tag{3.32}$$

In order to avoid shear and membrane locking effects, the contributions including the deformation measure $\boldsymbol{\Gamma}$ are computed with reduced integration, whereas all other contributions are integrated by means of a four point Gauss-Legendre scheme. Specifically, a three point Gauss-Lobatto integration scheme featuring integration points at the boundary nodes as well as the element midpoint is applied for the reduced integration. The effectiveness of this strategy grounds on a discrete constraint ratio of two, thus matching that of the space-continuous problem, and has been verified by means of a convergence study using a standard numerical example to be presented in the following section.

3.2.3. Verification of the Hermitian Simo-Reissner beam element

This study has previously been published in the author's contribution [112]. The initial geometry is represented by a 45°-degree circular arc-segment with curvature radius $r_0 = 100$ that lies completely in the global x-y-plane and that is clamped at one end. The section constitutive parameters of the beam result from a quadratic cross-section shape with side length $R = 1$ and a Young's modulus of $E = 10^7$ as well as a shear modulus of $G = 0.5 \cdot 10^7$. This initial geometry is loaded by an out-of-plane force $\boldsymbol{f} = (0, 0, f_z)^T$ in global z-direction with magnitude $f_z = 600$. This example has initially been proposed by Bathe and Bolourchi [13] and can meanwhile be considered as a standard benchmark test for geometrically exact beam element formulations that has been investigated by many authors (see e.g. [22, 28, 30, 46, 72, 76, 130, 131, 147, 151]). While the original definition of the slenderness ratio yields a value of $\zeta = l/R = 100\pi/4$ for this example, a slightly modified definition of the slenderness ratio according to $\tilde{\zeta} = r_0/R = 100$ is employed here.

For comparison reasons, also a second variant of this example with increased slenderness ratio $\tilde{\zeta} = r_0/R = 10000$, i.e. $R = 0.01$, and adapted force $f_z = 6 \cdot 10^{-6}$ will be investigated. The initial and deformed geometry are illustrated in Figure 3.3(a). In Figure 3.3(b), the relative L^2-error (see e.g. [109] for the exact definition of the applied error norm) has been plotted over the total number of degrees of freedom for the two different slenderness ratios $\tilde{\zeta} = 100$ and $\tilde{\zeta} = 10000$ as well as for discretizations with $1, 2, 4, 8, 16, 32, 64$ and 128 Hermitian Simo-Reissner (SR) elements. In order to investigate the effectiveness of the employed reduced integration procedure
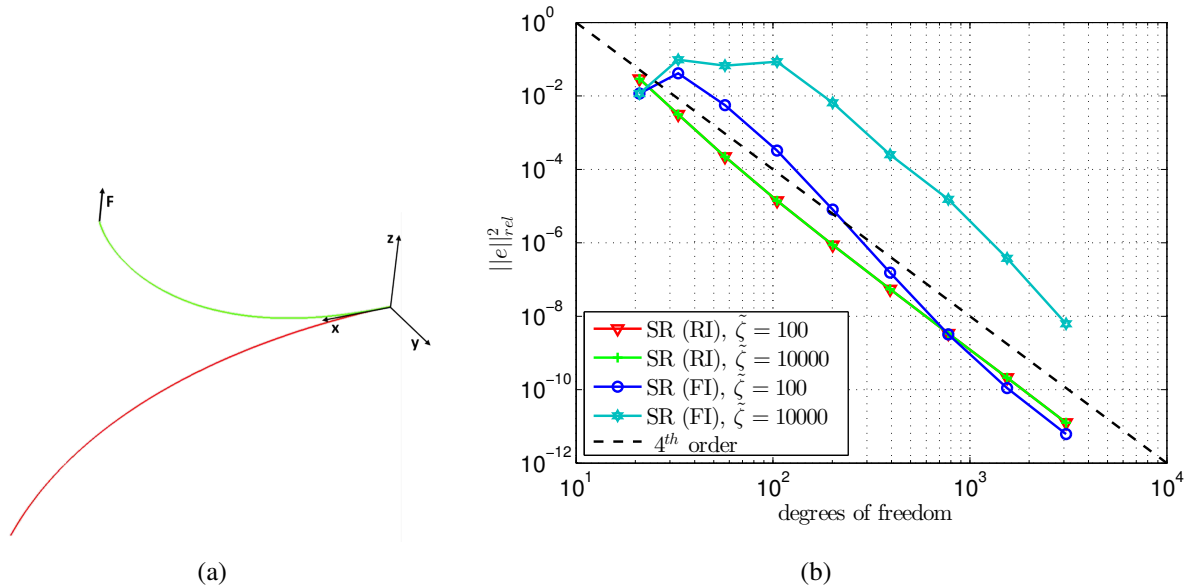
Figure 3.3.: (a) Initial, stress-free (red) and final (green) configuration. (b) L^2-error resulting for low and high value of the slenderness ratio $\tilde{\zeta}$ and using full or reduced integration (FI/RI) each. 512 SR elements are used to determine the numerical reference solution. Taken from the co-authored article [112].

(RI) based on a three-point Gauss-Lobatto integration scheme (integration points at the element boundary nodes and the element mid-point), also the L^2-error resulting from a full integration (FI) by means of a four-point Gauss-Legendre integration scheme is presented in Figure 3.3(b). Similar to the observations made in [107], the full integration leads to a clearly visible decline in the spatial convergence rate that can be attributed to membrane and shear locking. The deterioration of the convergence order increases with increasing beam slenderness ratio $\tilde{\zeta}$ and decreases with mesh refinement as a consequence of an decreasing element slenderness ratio (see also [107]). On the contrary, the proposed reduced Gauss-Lobatto integration scheme successfully avoids membrane and shear locking, thus leading to the optimal convergence order of four for both investigated beam slenderness ratios. Furthermore, it has been verified numerically (not plotted in Figure 3.3(b)) that a reduced integration approach based on a three-point Gauss-Legendre integration scheme (three integration points in the elements interior) barely improves the spatial convergence behavior as compared to the four-point scheme plotted in Figure 3.3(b). This observation underlines the importance of the special choice of Gauss-Lobatto integration points, which are identical to the collocation points applied by the so-called *minimally constrained strains* method as proposed in [107] for the avoidance of membrane locking.

3.2.4. Kirchhoff-Love beam element

Throughout this work, the element formulation developed in [113] is applied. To be more precise, the variant based on a weak enforcement of the Kirchhoff constraint and nodal tangents as primary degrees of freedom is chosen (denoted as WK-TAN in the original publication).

The same C^1-continuous Hermite centerline interpolation scheme as for the Simo-Reissner beam element is applied for the Kirchhoff-Love element. Due to the Kirchhoff constraint (3.14), the centerline tangent vector at the same time determines the first base vector of the material triad. Assuming a strong enforcement of the Kirchhoff constraint, it would thus be sufficient to introduce one additional scalar rotational degree of freedom φ to keep track of the triad orientation. The weak enforcement of the Kirchhoff constraint, however, only requires the first base vector and centerline tangent vector to be identical at the so-called collocation points. It is therefore most convenient to apply also the same triad interpolation scheme that is well known from the Simo-Reissner element and has been proposed originally in [29, 76].

At the two boundary nodes used for centerline interpolation, the first base vector of the nodal triad is directly determined from the tangent degrees of freedom $\hat{\boldsymbol{t}}^i$, $i = 1, 2$. At the interior node $i = 3$, however, the first base vector and hence the nodal triad depends on the normalized interpolated centerline tangent vector $\boldsymbol{r}'_{\mathrm{h}} / \|\boldsymbol{r}'_{\mathrm{h}}\|$ at this point $\xi^3 = 0$. Further details on the definition of the triads by means of first base vector and scalar twist degree of freedom $\hat{\varphi}^i$ can be found in the original publication [113] and are omitted here for the sake of brevity.

Nodal degrees of freedom
The resulting nodal degrees of freedom for this Kirchhoff-Love beam element are summarized as follows:

$$\hat{\mathbf{x}}_{\mathrm{KL}} := \left[\hat{\mathbf{d}}^{1T}, \, \hat{\mathbf{t}}^{1T}, \, \hat{\varphi}^1, \, \hat{\mathbf{d}}^{2T}, \, \hat{\mathbf{t}}^{2T}, \, \hat{\varphi}^2, \, \hat{\varphi}^3 \right]^T \tag{3.33}$$

Once again, it is emphasized that the centerline representation is identical to the employed Simo-Reissner element: $\hat{\mathbf{d}}_{\mathrm{KL}} = \hat{\mathbf{d}}_{\mathrm{SR}}$. Moreover, the vector of variations and increments of the primary degrees of freedom are given as

$$\delta\hat{\mathbf{x}}_{\mathrm{KL}} := \left[\delta\hat{\mathbf{d}}^{1T}, \, \delta\hat{\mathbf{t}}^{1T}, \, \delta\hat{\Theta}_1^1, \, \delta\hat{\mathbf{d}}^{2T}, \, \delta\hat{\mathbf{t}}^{2T}, \, \delta\hat{\Theta}_1^2, \, \delta\hat{\Theta}_1^3 \right]^T \tag{3.34}$$

$$\Delta\hat{\mathbf{x}}_{\mathrm{KL}} := \left[\Delta\hat{\mathbf{d}}^{1T}, \, \Delta\hat{\mathbf{t}}^{1T}, \, \Delta\hat{\varphi}^1, \, \Delta\hat{\mathbf{d}}^{2T}, \, \Delta\hat{\mathbf{t}}^{2T}, \, \Delta\hat{\varphi}^2, \, \Delta\hat{\varphi}^3 \right]^T \tag{3.35}$$

Note that $\delta\hat{\Theta}_1^i$ denotes the first component of the multiplicative material spin vector at each of the three nodes $i = 1, 2, 3$, whereas the increment of the scalar twist angle $\Delta\hat{\varphi}^i$ is an additive increment.

Discrete element residual vector
The resulting discrete element residual vectors of the employed Kirchhoff-Love beam element

are given as

$$\mathbf{r}_{\mathrm{KL},\hat{\mathbf{d}}} = \int\limits_{-1}^{1} \left(\bar{\mathbf{v}}'_{\theta_\perp} \bar{\boldsymbol{m}} + \bar{\mathbf{v}}_\epsilon \bar{F}_1 + \mathbf{H}^T \boldsymbol{f}_\rho - \mathbf{H}^T \tilde{\boldsymbol{f}} + \bar{\mathbf{v}}_{\theta_\perp} \boldsymbol{m}_\rho - \bar{\mathbf{v}}_{\theta_\perp} \tilde{\boldsymbol{m}} \right) J \, \mathrm{d}\xi - \left[\mathbf{H}^T \boldsymbol{f}_\sigma + \bar{\mathbf{v}}_{\theta_\perp} \boldsymbol{m}_\sigma \right]_{\Gamma_\sigma}$$

(3.36)

$$\mathbf{r}_{\mathrm{KL},\hat{\mathbf{\Theta}}_1} = \int\limits_{-1}^{1} \left(\bar{\mathbf{v}}'_{\theta_{\|\Theta}} \bar{\boldsymbol{m}} + \bar{\mathbf{v}}_{\theta_{\|\Theta}} \boldsymbol{m}_\rho - \bar{\mathbf{v}}_{\theta_{\|\Theta}} \tilde{\boldsymbol{m}} \right) J \, \mathrm{d}\xi - \left[\bar{\mathbf{v}}_{\theta_{\|\Theta}} \boldsymbol{m}_\sigma \right]_{\Gamma_\sigma}.$$

(3.37)

Here, the quantities denoted as $\mathbf{v}_{(.)}$ are vectors representing discrete strain variations. The bars over these quantities indicate that a re-interpolation of these quantities based on collocation point values is applied in order to fulfill the Kirchhoff constraint in a weak sense. A similar re-interpolation technique called *minimally constrained strains* (originally proposed in [107]) is applied to the axial force term to avoid membrane locking. The re-interpolation process can be summarized as

$$\bar{\mathbf{v}}_{(.)}(\xi) = \sum_{i=1}^{3} L^i(\xi) \, \mathbf{v}_{(.)}(\xi^i).$$

(3.38)

Once again, refer to the original publication [113] for further details.

3.2.5. Torsion-free Kirchhoff-Love beam element

In the special case of the torsion-free Kirchhoff-Love beam element as proposed in [107], no triad field needs to be discretized such that only the centerline field remains to be discretized in space. Once again, the C^1-continuous cubic Hermite interpolation as applied before to the Simo-Reissner and Kirchhoff-Love elements is chosen here. All components of the vector of nodal degrees of freedom for this element hence are already known from the previous sections since $\hat{\mathbf{d}}_{\mathrm{TF}} = \hat{\mathbf{d}}_{\mathrm{KL}} = \hat{\mathbf{d}}_{\mathrm{SR}} = \hat{\mathbf{d}}$:

$$\hat{\mathbf{x}}_{\mathrm{TF}} := \hat{\mathbf{d}}_{\mathrm{TF}} = \left[\hat{\mathbf{d}}^{1T}, \, \hat{\mathbf{t}}^{1T}, \, \hat{\mathbf{d}}^{2T}, \, \hat{\mathbf{t}}^{2T} \right]^T$$

(3.39)

Here, the structure of the discrete element residual vector is reproduced for convenience and again the reader is kindly referred to the original publication [107] for further details:

$$\mathbf{r}_{\mathrm{TF},\hat{\mathbf{d}}} = \int\limits_{-1}^{1} \left(\bar{\mathbf{v}}_\epsilon \bar{F}_1 + \mathbf{v}_\kappa \boldsymbol{m} + \mathbf{H}^T \boldsymbol{f}_\rho - \mathbf{H}^T \tilde{\boldsymbol{f}} - \mathbf{v}_\kappa \tilde{\boldsymbol{m}} \right) J \, \mathrm{d}\xi - \left[\mathbf{H}^T \boldsymbol{f}_\sigma + \mathbf{v}_{\theta_\perp} \boldsymbol{m}_{\sigma\perp} \right]_{\Gamma_\sigma} \quad (3.40)$$

3.2.6. Concluding comparison of beam element formulations

Figure 3.4 provides a brief assessment and comparison of the presented beam element formulations that have been used in the scope of this work. Simo-Reissner (SR), Kirchhoff-Love (KL),
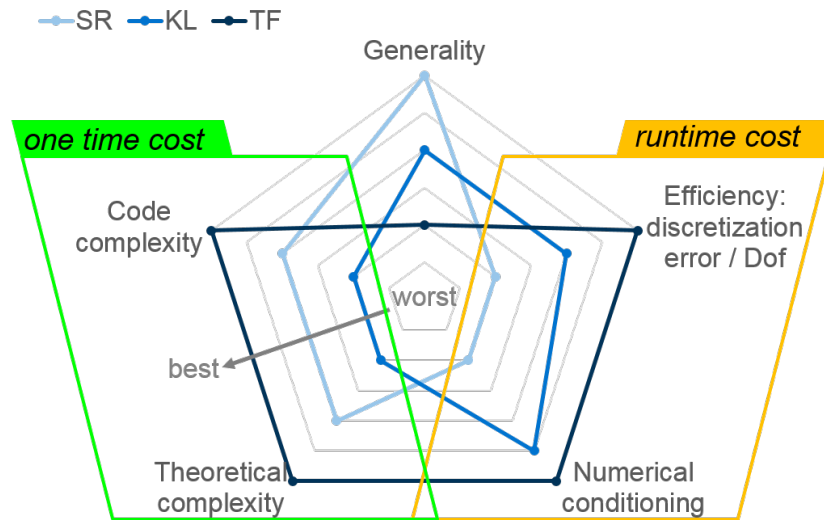
Figure 3.4.: Comparison of the three beam element formulations that have been used in the scope of this work. Simo-Reissner (SR), Kirchhoff-Love (KL), and torsion-free Kirchhoff-Love (TF) theory are judged based on the five criteria of generality, efficiency, theoretical complexity, theoretical complexity, and numerical conditioning.

and torsion-free Kirchhoff-Love (TF) theory are judged based on five criteria that are considered to be important for the optimal choice of the beam formulation depending on the specific use case. Recall from the first comparison of the underlying space-continuous beam theories in Section 3.1.4 that there is a fundamental tradeoff between the generality and thus applicability on the one hand and the efficiency in terms of required physical degrees of freedom on the other hand. Figure 3.4 illustrates that the additional assumptions of shear-free and torsion-free theory moreover has a beneficial effect on the numerical conditioning of the problem due to the characteristic high stiffness associated with the shear and torsion mode. This in turn reduces the computational cost by decreasing the number of nonlinear iterations and/or increasing the feasible time step size. In addition, the one-time cost to comprehend a theory in the first place and implement it in a code framework is compared in this diagram. Refer to the recent article [113] for a more comprehensive comparison of SR and KL beam theory and corresponding geometrically exact finite element formulations.

To conclude, the TF beam element is considered to be the most efficient and at the same time pleasantly simple formulation such that it should be used whenever the underlying assumptions are met in the specific use case. If, however, a more general scenario including for example torsion or initially curved beams is considered, the KL formulation should be the method of choice as long as the slenderness of the beam is large enough to fulfill the assumption of vanishing shear deformations. Finally, the SR beam element formulation is the most general one that should be chosen whenever shear deformation is expected to play a role or if numerical performance of the beam formulation is not critical e.g. due to a small system size or another part of the computational model dominating the overall computational cost.

3.3. Macroscopic approaches for beam contact

Existing approaches to beam-to-beam contact are motivated by the macroscopic perspective to not allow for any penetration (see e.g. [23, 43, 56, 86, 87, 98, 110, 111, 161, 163]). This agrees with the perception of a hard core model on the atomistic level as discussed in Section 2.2.3. Following a similar key idea, one category of existing beam-to-beam contact formulations – commonly referred to as *penalty methods* – use heuristic contact potentials to model the strong repulsion. Most often, these contact potentials are formulated for a pair of closest points thus yielding discrete point forces. As becomes clear from the illustrative example of two parallel straight beams, such *point contact* formulations fail whenever no unique closest-point pair between deformable slender bodies exists. Recently, a number of so-called *line contact* formulations have thus been proposed to overcome this deficiency (cf. e.g. [110]). Moreover, a unification of both approaches to combine the advantages of both formulations in different regimes of mutual orientations has been suggested in [111]. It is a distinct characteristic of penalty approaches that small penetrations are conceded in order to get a repulsive potential contribution from the penalty law.

In strong contrast, a second category of (beam) contact formulations based on *Lagrange multipliers* enforces the positions of the contacting surface points to coincide by means of equality constraints (cf. e.g. [98]). The main drawbacks associated with this approach are an increased system size due to additional degrees of freedom for the Lagrange multipliers and the resulting saddle-point structure of the overall system of equations.

At this point, recall that the beam theory presented in Section 3.1 generally neglects cross-section deformations. It is therefore appealing to use penalty methods for beam contact and implicitly model the cross-section compliance via the penalty potential. In this way, the simpler and at first glance less accurate approach can be exploited to achieve an overall more realistic model for cross-section characteristics. Throughout this work, only the penalty approach will be applied to model macroscopic contact between beams. It can also be considered as one of the basic theoretical concepts based on which this work has set out to develop the novel methods for molecular interactions between beams that are to be proposed in Chapter 4 and 5.

Note that in the following we restrict ourselves to beams with circular cross-sections and beam radii R_i, $i = 1, 2$. Some extensions to more general cross-section shapes can be found in the literature and will be briefly discussed in a remark at the end of this section.

Remark on the search for interaction partners. Identifying all pairs of beam elements that potentially interact with each other is an essential step that turns out to even be critical in terms of the total computational effort for large systems. The basic concept of the applied search algorithm and its role in partitioning the problem to allow for parallel computing will be briefly presented in Section 4.4.6 in the context of the novel beam interaction formulation for molecular interactions to be developed. For all methods to be presented, it is sufficient to look at one pair of beam elements at a time and apply the formulation subsequently for all pairs obtained from the search algorithm.

3.3.1. Point penalty contact

The applied point contact formulation has been proposed by Wriggers and Zavarise in [163]. See Figure 3.5 for an overview of the kinematic quantities. We aim at fulfilling the following
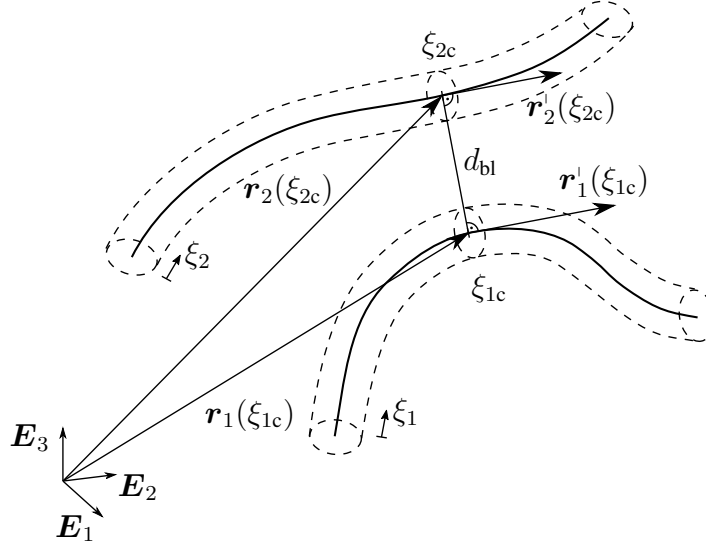
Figure 3.5.: Illustration of the geometric quantities used in the point contact formulation.

contact constraint formulated for a pair of material points ξ_1, ξ_2 anywhere along the considered pair of beams

$$g(\xi_1, \xi_2) \geq 0 \tag{3.41}$$

where the so-called gap g is defined as the surface-to-surface separation computed via $g := d_{bl} - R_1 - R_2$. A bilateral closest-point projection yields the minimum centerline separation

$$d_{\mathrm{bl}} := \min_{\xi_1, \xi_2} d(\xi_1, \xi_2) = d(\xi_{1c}, \xi_{2c}) \tag{3.42}$$

and parameter coordinates of the corresponding two contacting points ξ_{1c}, ξ_{2c}. Using the spatial curves $\boldsymbol{r}_i(\xi_i)$, $i = 1, 2$ representing the beams' centerlines, the nonlinear orthogonality conditions

$$
\begin{aligned}
\boldsymbol{r}_1'^T(\xi_1)\left(\boldsymbol{r}_1(\xi_1) - \boldsymbol{r}_2(\xi_2)\right) &\doteq 0, \\
\boldsymbol{r}_2'^T(\xi_2)\left(\boldsymbol{r}_1(\xi_1) - \boldsymbol{r}_2(\xi_2)\right) &\doteq 0
\end{aligned}
\tag{3.43}
$$

need to be solved. Note that here the short prime has been introduced and denotes a differentiation with respect to the element parameter coordinate, i.e., $\boldsymbol{r}_i'(\xi_i) = \mathrm{d}\,\boldsymbol{r}_i(\xi_i)/\mathrm{d}\,\xi_i$. For this special pair of points ξ_{1c}, ξ_{2c}, a penalty potential law is defined for instance as

$$\Phi_{\mathrm{c}\varepsilon_\perp} = \frac{1}{2}\varepsilon_\perp \langle g(\xi_{1c}, \xi_{2c})\rangle^2 \quad \text{with} \quad \langle x \rangle := \left\{ \begin{array}{ll} x, & x \leq 0 \\ 0, & x > 0 \end{array} \right. . \tag{3.44}$$

The point penalty parameter $\varepsilon_\perp$ determines the slope of this linear force law (i.e. quadratic potential law). Variation of this point potential yields the contributions to the weak form

$$\delta\Pi_{c\varepsilon_\perp} = \varepsilon_\perp \langle g \rangle \, \delta g = \varepsilon_\perp \langle g \rangle \, \left(\delta\boldsymbol{r}_1(\xi_{1c}) - \delta\boldsymbol{r}_2(\xi_{2c})\right)^T \boldsymbol{n} \tag{3.45}$$

and the point contact forces can be identified as

$$\boldsymbol{f}_{c\varepsilon_\perp} = \pm\varepsilon_\perp \langle g \rangle \, \boldsymbol{n}, \quad \boldsymbol{n} := \frac{\boldsymbol{r}_1(\xi_{1c}) - \boldsymbol{r}_2(\xi_{2c})}{\|\boldsymbol{r}_1(\xi_{1c}) - \boldsymbol{r}_2(\xi_{2c})\|}. \tag{3.46}$$

Note that the centerline field is sufficient to compute the contributions from beam contact and no triad information is required. Discretization of (3.45) by means of (3.19) hence yields the contributions to the discrete residual vectors and stiffness matrices of the two interacting elements. In addition, off-diagonal entries coupling the centerline degrees of freedom of both elements result from the linearization of one element's residual vector with respect to the other element's degrees of freedom. All required expressions as well as further details are given in [110, 163].

3.3.2. Line penalty contact

As mentioned earlier, the point contact formulation suffers from the non-uniqueness of the closest-point projection in certain geometric configurations. The most obvious and practically relevant example is the scenario of parallel, straight beams. Therefore, a specific formulation for beams coming into contact at a small mutual angle as proposed by [110] is outlined in the following. See Figure 3.6 for an overview of the kinematic quantities.
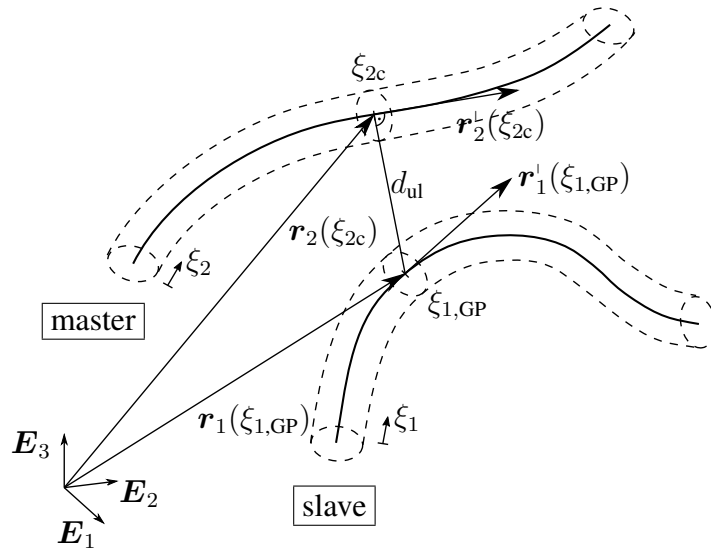
Figure 3.6.: Illustration of the geometric quantities used in the line contact formulation [110].

As the name of the line-to-line contact approach suggests, the contact constraint is formulated for a pair of lines instead of a pair of points.

$$g(\xi_1) \geq 0 \quad \forall \quad \xi_1 \qquad \text{with} \qquad g(\xi_1) := d_{ul}(\xi_1) - R_1 - R_2 \tag{3.47}$$

Instead of the bilateral closest-point projection, the minimal distance problem this time tries to find the closest point ξ_{2c} on the opposing beam while the first point is given as the integration point $\xi_{1,GP}$. Acknowledging this inherent distinction between interaction partners, we refer to the beam with given point ξ_1 as the slave beam (index 1) and the beam projected onto to find ξ_{2c} as the master beam (index 2). This unilateral closest-distance problem may be formulated as

$$d_{\mathrm{ul}}(\xi_1) := \min_{\xi_2} d(\xi_1, \xi_2) = d(\xi_1, \xi_{2c}),$$
$$d(\xi_1, \xi_2) := \|\boldsymbol{r}_1(\xi_1) - \boldsymbol{r}_2(\xi_2)\| \tag{3.48}$$

and solving it is equivalent to solving the following orthogonality condition for ξ_{2c}:

$$\boldsymbol{r}_2'^{T}(\xi_2)\,(\boldsymbol{r}_1(\xi_1) - \boldsymbol{r}_2(\xi_2)) \doteq 0. \tag{3.49}$$

In this manner, the contact normal vector $\boldsymbol{n}$ and thus the direction of applied contact force is always perpendicular to the centerline curve of the master beam 2, but not necessarily to that of the slave beam 1. Finally, a penalty potential per unit length is postulated as

$$\tilde{\pi}_{c\varepsilon_\parallel} = \frac{1}{2}\varepsilon_\parallel \langle g(\xi_1)\rangle^2 \tag{3.50}$$

and the total interaction potential for this pair of beams in contact is evaluated via numerical integration over the slave beam's domain:

$$\Pi_{c\varepsilon_\parallel} = \frac{1}{2}\varepsilon_\parallel \int\limits_0^{l_1} \langle g(\xi_1)\rangle^2 \, \mathrm{d}s_1 \tag{3.51}$$

The integral is evaluated by Gaussian quadrature such that the terms need to be evaluated at a finite number of Gauss points ξ_{1GP}. It is also worth mentioning that a segmentation of the integration domain in order to avoid integration across strong discontinuities turned out to considerably reduce the discretization error [110]. Once again, the variation of this potential yields the contributions to the weak form

$$\delta\Pi_{c\varepsilon_\parallel} = \varepsilon_\parallel \int\limits_0^{l_1} \langle g(\xi_1)\rangle \delta g(\xi_1) \, \mathrm{d}s_1 \tag{3.52}$$

$$\text{with} \quad \delta g(\xi_1) = (\delta\boldsymbol{r}_1(\xi_1) - \delta\boldsymbol{r}_2(\xi_{2c}))^T \boldsymbol{n}(\xi_1). \tag{3.53}$$

Here, the contact line force vector acting on both interacting partners can be identified as

$$\tilde{\boldsymbol{f}}_{c\varepsilon_\parallel}(\xi_1) = \pm\varepsilon_\parallel \langle g(\xi_1)\rangle \boldsymbol{n}(\xi_1), \qquad \boldsymbol{n}(\xi_1) := \frac{\boldsymbol{r}_1(\xi_1) - \boldsymbol{r}_2(\xi_{2c})}{\|\boldsymbol{r}_1(\xi_1) - \boldsymbol{r}_2(\xi_{2c})\|}. \tag{3.54}$$

Finally, the contributions to both elements' residual vectors and stiffness matrices are obtained as a result of spatial discretization of the centerline field as stated in (3.19). All expressions and further details can be found in [110].

3.3.3. Unified approach for beam contact

This section briefly presents the concept of how to combine the point and line contact formulations in order to unite the advantages of both approaches as proposed in [111]. To sum up, the line contact formulation remedies the issue of a non-unique closest-point projection at small mutual angles of the beams. However, its computational cost increases with the enclosed angle, because a higher Gauss point density is required to ensure the detection of contact. It is thus preferable to resort to the point contact formulation as soon as the enclosed angle exceeds a certain value. This combined approach called all-angle beam contact (ABC) allows for a smooth transition between both formulations.

First of all, the definition of the contact angle based on the mutual angle of both tangent vectors shall be given for both point and line contact strategy:

$$\alpha = \arccos(z), \quad z = \frac{|\boldsymbol{r}_1'^T(\xi_{1c})\,\boldsymbol{r}_2'(\xi_{2c})|}{\|\boldsymbol{r}_1'(\xi_{1c})\| \cdot \|\boldsymbol{r}_2'(\xi_{2c})\|} \tag{3.55}$$

$$\alpha(\xi_1) = \arccos(z(\xi_1)), \quad z(\xi_1) = \frac{|\boldsymbol{r}_1'^T(\xi_1)\,\boldsymbol{r}_2'(\xi_{2c})|}{\|\boldsymbol{r}_1'(\xi_1)\| \cdot \|\boldsymbol{r}_2'(\xi_{2c})\|} \tag{3.56}$$

Note that again the short prime denotes a differentiation with respect to the element parameter coordinate, i.e., $\boldsymbol{r}_i'(\xi_i) = \mathrm{d}\,\boldsymbol{r}_i(\xi_i)/\mathrm{d}\,\xi_i$. In order to ensure a smooth transition, a blending of contributions from the point and line contact formulation is applied within an angle interval

$$\alpha \in [\alpha_1; \alpha_2], \quad \alpha_1, \alpha_2 \in [0°; 90°], \quad \alpha_1 < \alpha_2. \tag{3.57}$$

The transition is controlled via a scaling factor $k(z)$ defined as

$$k(z) = \begin{cases} 1, & \alpha < \alpha_1 \\ 0.5\left(1-\cos\left(\pi\frac{z-z_2}{z_1-z_2}\right)\right), & \alpha_2 \ge \alpha \ge \alpha_1. \\ 0, & \alpha > \alpha_2 \end{cases} \tag{3.58}$$

As shown in [111], blending of contact forces instead of the potential contributions according to

$$\delta\Pi_{c\varepsilon} = \underbrace{(1 - k(z_c))\,\varepsilon_\perp\langle g\rangle}_{=:-f_{c\varepsilon\perp}}\delta g$$
$$+ \int_0^{l_1} \underbrace{k(z(\xi_1))\varepsilon_\parallel\langle g(\xi_1)\rangle}_{=:-f_{c\varepsilon\parallel}(\xi_1)}\delta g(\xi_1)\,\mathrm{d}s_1 \tag{3.59}$$

is not variationally consistent and hence does not guarantee conservation of energy because additional contact moment contributions are ignored. By a sensible choice of the ratio of penalty parameters $\varepsilon_\perp/\varepsilon_\parallel$, this effect however is negligible and thus avoids the additional complexity associated with a transition on the level of contact potentials. An estimate for this optimal ratio based on analytical considerations is given by

$$\frac{\varepsilon_\perp}{\varepsilon_\parallel} \approx \frac{4R}{3\sin\bar\alpha_{12}} \quad \text{with} \quad \bar\alpha_{12} := \frac{\alpha_1 + \alpha_2}{2}. \tag{3.60}$$

Once again, refer to the original publication [111] for further details including all required expressions.

Remarks on beam contact

1. Instead of a linear penalty force law used for demonstrating the basic concepts here, it is well established to use a smoothed force-gap relation in the range of very small gap values [43, 111]. Most commonly, a quadratic regularization in the gap value range $g \in [0, \bar{g}]$ with a small, positive regularization gap value $\bar{g} \approx R/10$ is applied to enhance the robustness of the nonlinear solution scheme.

2. Although contact with a beam endpoint is a seemingly rare event, it should be considered by means of a slightly modified variant of the point contact formulation, with the beam endpoint being fixed. Otherwise, in the first place undetected large penetrations might suddenly result in very large contact forces that considerably deteriorate the robustness of the nonlinear solution scheme. Refer to [111] for a discussion of this topic.

3. Rectangular or other piecewise straight cross-section shapes require an individual strategy for each of the possible geometric configurations such as plane-to-plane, edge-to-plane or edge-to-edge and a consistent and robust transition between these regimes (see e.g. [100] for rectangular cross-sections). An extension to more general, parameterized cross-section shapes has been proposed in [56] and demonstrated for the example of superelliptic shapes.

4. Friction in beam-to-beam contact has been accounted for by several publications (see e.g. [24, 44, 57, 99, 101, 167]).

5. Despite the molecular origin of the repulsive forces acting on bodies coming into contact, existing formulations for beam contact have thus far been developed and analyzed from a macroscopic perspective. Bridging this gap between the atomistic understanding of repulsive forces and the experience of contact on the macroscale is considered a valuable and insightful endeavor of future research. First theoretical considerations on this topic will be presented in Section 6.2 and a first numerical example comparing the novel approach to molecular interactions of beams with existing macroscopic beam contact approach will be discussed in Section 4.5.2.

3.3.4. First application of these macroscopic beam contact formulations to KL and SR beam elements: Static and dynamic loading of a helical spring

In the original publication of the ABC formulation [111] (summarized in the preceding Section 3.3.3), the contact formulations have solely been applied in combination with the torsion-free Kirchhoff-Love (TF) element formulation (cf. [107], summarized in Section 3.2.5). In the scope of this work, the ABC formulation has for the first time been applied in combination with the Kirchhoff-Love (KL) beam element (cf. [110], summarized in Section 3.2.4) and the Hermitian Simo-Reissner (SR) element (cf. Section 3.2.2). The content of this section has previously been published in the author's contribution [112].

Beside this proof of concept of combining the beam contact formulations also with KL and SR beam elements, the following numerical example aims at comparing the results of KL and

SR elements based on the characteristics of the structures and the applied boundary conditions. Specifically, it investigates the response of a spring to static as well as dynamic loading. Its initial and stress-free geometry is defined as a helix with linearly increasing slope (see Figure 3.7(d)) via the analytic representation

$$\boldsymbol{r}_0(\beta) = \begin{pmatrix} r_{0x} \\ r_{0y} \\ r_{0z} \end{pmatrix} = R_{h0} \begin{pmatrix} \sin\beta \\ \cos\beta - 1 \\ \frac{6}{81\pi^2}\beta^2 \end{pmatrix}, \tag{3.61}$$

$$R_{h0} = \frac{l}{6\sqrt{\left(\frac{3\pi}{4}\right)^2 + 1} + \frac{27\pi^2}{8}\ln\left(\frac{4}{3\pi} + \sqrt{1 + \left(\frac{4}{3\pi}\right)^2}\right)} \tag{3.62}$$

$$\approx 34.36. \tag{3.63}$$

The radius R_{h0} of the enveloping cylinder of the helix is chosen such that the helix exactly

(a) $u_z = -168$ max. compression

(b) $u_z = -150$

(c) $u_z = -100$

(d) $u_z = 0$: undeformed

(e) $u_z = 125$

(f) $u_z = 250$: max. tension

(g) detail views at $u_z \approx -168$ (central rigid cylinder hidden)
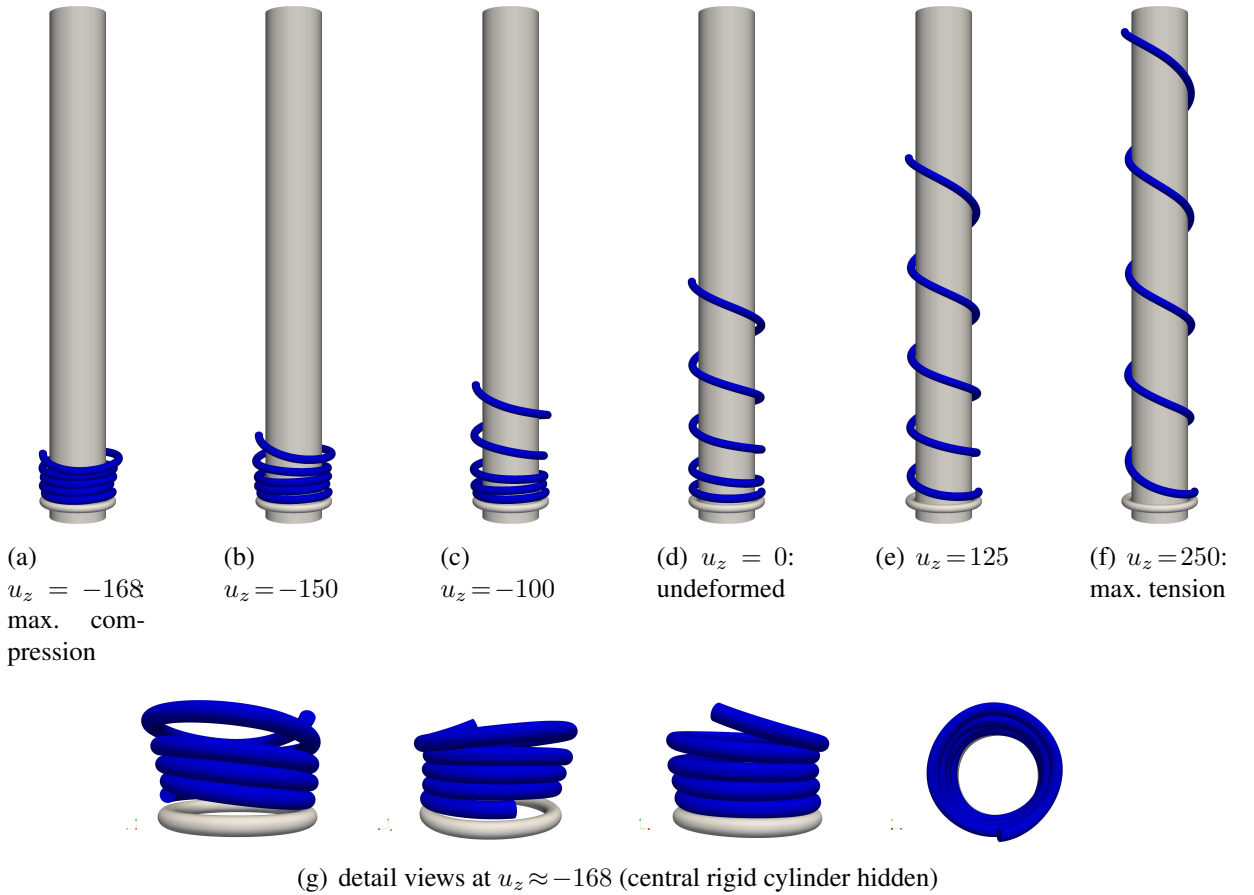
Figure 3.7.: Quasi-static simulation of a helical spring with linearly increasing slope. Taken from the co-authored article [112].

consists of 4.5 coils, i.e. $\beta \in [0; 9\pi]$, along the length of $l = 1000$. A value of $R = 4$ is chosen

for the cross-section radius of the helix which results in a slenderness ratio of $\zeta = 250$. The spring is clamped at one end (bottom in Figure 3.7) and load will be applied to the other end point (top in Figure 3.7). In order to mimic a realistic application of this spring, two additional rigid structures were added in the surrounding of the helix to guide its large deformation under the applied load (see grey colored structures in Figure 3.7). A rigid cylinder of radius $R_{\text{cyl}} = 28$ and length $l_{\text{cyl}} = 500$ is placed along the centerline of the helix, providing a close guidance with an initial closest distance of approximately 2.36 from the surface of the spring. Moreover, a rigid torus with the same cross-section area as the helix is placed such that its centerline contour lies in the $xy-$plane at the vertical position $z = -9.1$.

The material of the spring is modeled by a St. Venant-Kirchhoff law with Young's modulus $E = 1.0$, Poisson's ratio $\nu = 0$ and density $\rho = 1.0 \cdot 10^{-8}$. In case of the shear-deformable SR formulation, the shear correction factor is chosen as $\kappa = 1.0$.

Since small contact angles are prevailing in this example, only the line contact formulation with a linear penalty law and quadratic regularization ([110], summarized in Section 3.3.2) is applied here. Note that a point contact formulation would anyway not be able to model the contact between spring and the central rigid cylinder (aligned with the helix axis), because no unique bilateral closest point exists, which is a prerequisite for this type of formulation. Even though the ABC formulation would automatically resolve this geometrical property in a correct and robust manner, here use has been made of the a priori knowledge that only small contact angles will ocur which makes the point-to-point contact contribution of the ABC formulation obsolete. The corresponding line penalty parameter is chosen as $\varepsilon_{\|} = 10^{-3}$ in the quasi-static simulations and $\varepsilon_{\|} = 10^{-2}$ in the dynamic simulations, and the regularization parameter of the quadratically regularized penalty law are $\bar{g} = 0.05R = 0.2$ and $\bar{g} = 0.25R = 1.0$ respectively. Each beam element is subdivided into twenty 5-point integration segments.

First, a quasi-static loading process will be analyzed. For this purpose, the helical structure is discretized by 16 or 64 beam elements of tangent vector-based KL(-TAN) type or SR type respectively. The tip of the spring is displaced in a Dirichlet controlled way prescribing zero displacement in x- and y-direction $u_x = u_y = 0$ and a piecewise linear displacement in $z-$direction: $u_z = 0 \ldots 250$ for $0 < t < 1$, $u_z = 250 \ldots 0$ for $1 < t < 2$ and $u_z = 0 \ldots -200$ for $2 < t < 3$. Like for a clamped end, all rotations of the beam cross-section at $\beta = 0$ are suppressed by appropriate Dirichlet conditions for the tangential and rotational degrees of freedom in case of KL and SR elements respectively.

Via the defined time curve for the tip displacement u_z, first the tensile and then the compression range of the characteristic displacement-reactions curve of the spring is measured by tracking the reaction forces at the tip. The simulations are conducted with a time step size of $\Delta t = 0.01$ using a Newton-Raphson scheme with step size control that limits the displacement increment per iteration to a maximum value of $0.25R = 0.1$ (see Section F.2 for details). Again, a step adaptivity is employed that repeats a step with half of the original (pseudo-) time step size if convergence fails within the prescribed maximum number of 30 iterations.

Some characteristic configurations are illustrated in Figure 3.7. The simulation ends at the fully compressed state with $u_z \approx -168$ (see Figure 3.7(g)). The resulting displacement-reactions curves are plotted in Figures 3.8(a) and 3.8(b). As expected from Hooke's law, the relationship between displacement in axial direction of the spring u_z and axial reaction force F_z is linear in the regime of moderate displacements (approx. $-100 < u_z < 100$). For large tensile deformations,
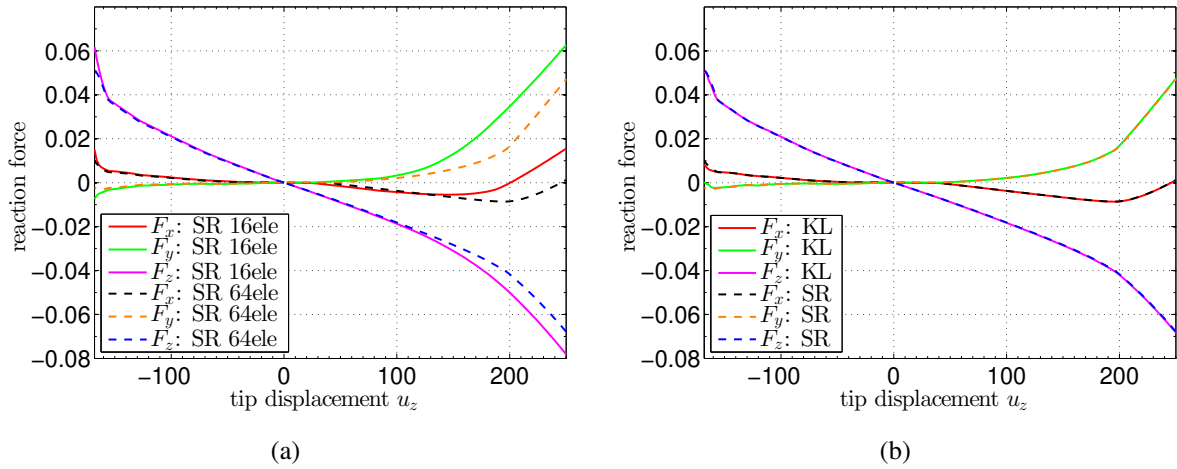
Figure 3.8.: Displacement-reactions curves: (a) 16 SR vs. 64 SR, and (b) 64 KL vs. 64 SR. Taken from the co-authored article [112].

the stiffness of the spring increases smoothly but steadily due to the strong geometrical nonlinearity and the growing influence of stiff axial tension deformation modes. In the compression regime, a strong nonlinear effect, in form of a kink in the load-displacement curve illustrated in Figure 3.8(b), due to the contacting coils can be observed. This compression stiffness is mainly determined by the number of coils in contact and the cross-section stiffness represented by the penalty regularization of the applied beam contact model.

Also for this example of an initially curved elastic fibrous structure, the results from KL and SR elements are in excellent agreement (see Figure 3.8(b)). This meets the expectation of negligible shear deformation for highly slender bodies as it is the case in this example. Furthermore, Figure 3.8(b) reveals that the comparatively rough discretization with 16 SR elements leads to a still visible discretization error as compared to the discretization with 64 finite elements, however, the qualitative behavior is already captured very well.

In order to investigate the influence of shear deformation, a further variant of this example with increased beam cross-section radius shall be investigated. For better comparability, only the value of the cross-section radius occurring in the section constitutive law (3.7) is scaled by a factor of 5, i.e., $\bar{R} = 5R$, leading to correspondingly adapted values of $A, A_2, A_3, I_2, I_3, I_T$, while the external beam geometry, i.e., the cross-section radius occurring in the beam-to-beam contact model, remains unchanged. Again, the simulation is performed in a Dirichlet-controlled manner similar to the first variant. The resulting load-displacement curve is illustrated in Figure 3.9.

Accordingly, due to this artificially increased cross-section radius a clear difference between the results of the shear-free KL elements and the shear-deformable SR elements becomes visible. Consequently, in such a case the Simo-Reissner theory of thick rods might be preferable as compared to the Kirchhoff-Love theory of thin rods.

After this quantitative static analysis, also the dynamic response of the elastic spring shall be investigated in a qualitative as well as quantitative manner. For comparison purposes, the helical structure is discretized by 16 or 64 beam elements of tangent-vector based KL or SR
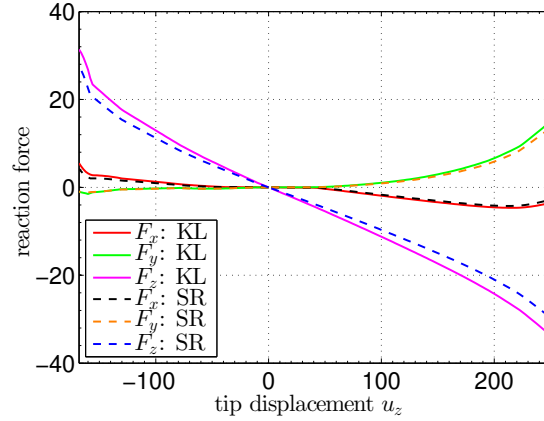
Figure 3.9.: Displacement-reactions curves in case of an increased cross-section radius $\bar{R}=5R$: 64 KL vs 64 SR. Taken from the co-authored article [112].

type respectively. Again, one end of the spring is clamped but now the other end is loaded by a discrete external force $\bar{f}_z$ in z-direction. As the location of load application, i.e. the tip, does not lie on the centerline of the helix, it causes a moment around the x-axis that is (partly, since the tip location changes in time) balanced by an additionally applied discrete external moment $\bar{m}_x = R_0 \bar{f}_z$. Both loads are increased linearly within $0 < t < 4$ and subsequently decreased linearly within $4 < t < 5$. After the release of the applied load, the spring performs a free oscillation and the simulation covers a full cycle up to $t_{\text{end}} = 10$.

The extended generalized-α scheme outlined in Section 3.2.1 with a prescribed spectral radius $\rho_\infty = 0.95$, i.e. a small amount of numerical dissipation, and a constant time step size of $\Delta t = 10^{-3}$ is applied for temporal discretization of the problem.

Figure 3.10 visualizes the deformed geometry at several points in time.

(a) time $t = 0$ (b) time $t = 2$ (c) time $t = 4.5$ (d) time $t = 6$ (e) time $t = 6.5$

(f) time $t = 7$ (g) time $t = 7.5$ (h) time $t = 8$ (i) time $t = 9$ (j) time $t = 10$
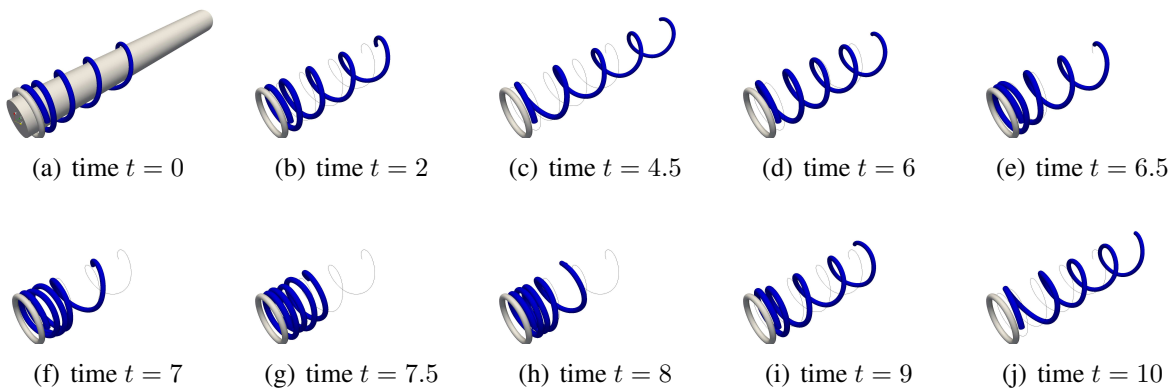
Figure 3.10.: Dynamic simulation of a clamped helical spring loaded by a tip force. Taken from the co-authored article [112].

In the course of the simulation, the spring undergoes large deformations in the tensile as well as the compression regime and shows a highly dynamic motion. Contact interactions with the

rigid guides as well as self contact of the coils occur over the entire simulated time span. Note that in the state of high compression, also the beam endpoints come into contact with other coils such that the contact model for beam endpoints as mentioned in Section 3.3.3 and proposed in [110] is mandatory for this challenging example.

In terms of quantitative analysis, the elastic, kinetic and contact penalty energy is plotted over time in Figure 3.11. The sum of these three contributions is plotted as total system energy

(a) 16 SR vs 64 SR elements

(b) 64 KL vs 64 SR elements
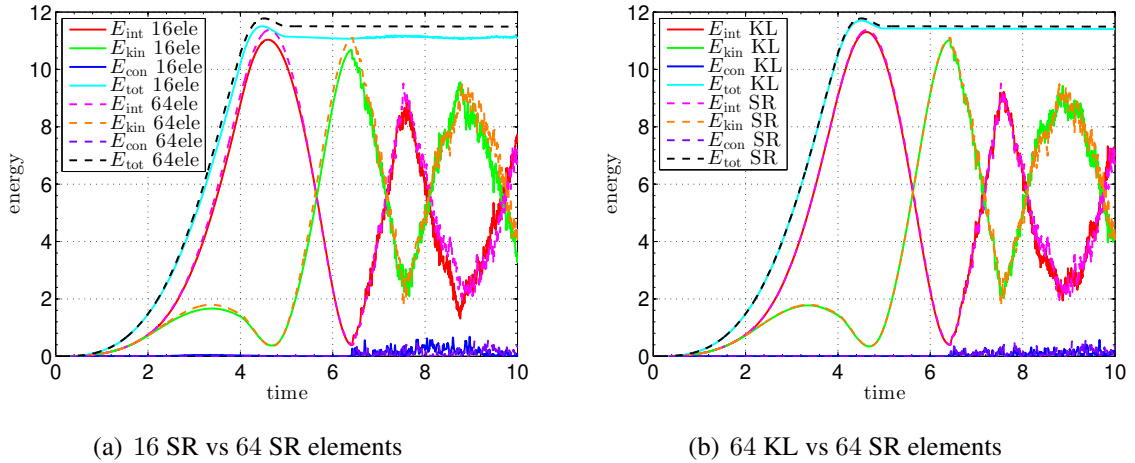
Figure 3.11.: Conservation of total system energy. Taken from the co-authored article [112].

and remains constant with only very little deviations after the external load is released (see Figure 3.11(a)). Already for a rather coarse spatial discretization with 16 beam elements, energy conservation is thus very well fulfilled by the applied beam and contact formulation and the time integration scheme. For a fine discretization of 64 elements, energy is even better conserved and the fluctuations associated with the highly dynamic shocks from self-contacting coils in the compressed state are hardly visible anymore. Even though the total system energy is slightly higher for the SR elements due to the prevalence of additional shear deformation modes, the results for KL and SR elements match excellently well for a sufficiently fine discretization with small spatial discretization error (see Figure 3.11(b)).

4. A Beam-Beam Interaction Formulation Based on Section-Section Interaction Potentials

This chapter aims to develop the first beam-beam interaction model for molecular interactions between curved slender fibers undergoing large deformations in 3D. After a review of related previous work in Section 4.1, the subsequent Section 4.2 will present the general approach without specializing on specific kinds of physical interactions. Section 4.3 turns to specific examples of molecular interactions such as electrostatic, van der Waals (vdW) or repulsive steric forces. Section 4.4 presents the required spatial discretization via finite elements and selected aspects of the algorithmic framework required in the solution procedure. Finally, the set of numerical examples in Section 4.5 aims to verify the effectiveness, accuracy and robustness of the novel interaction models and the chapter will be concluded with a summary and an outlook in Section 4.6. The content of this chapter has previously been published in the author's article [61].

4.1. Literature review

A comprehensive review of the origin, characteristics and mathematical description of intermolecular forces can nowadays be found in (bio)physics textbooks [74, 125] and the relevant aspects for this work have been summarized in Chapter 2. The critical point is to transfer the first principles formulated for the interaction between atoms or single molecules to the interaction between macromolecules such as slender fibers. Here, the analytical approaches to be found in textbooks and also in recent contributions [75, 103, 122, 153] from the field of theoretical biophysics are (naturally) restricted to undeformable, rigid bodies with primitive geometries such as spheres, half spaces or, most relevant in our case, cylinders. Some computational approaches can be found in the literature, but rather aim at including more complex phenomena such as retardation and solvent effects in vdW interactions [42], still limited to rigid bodies. All-atom simulation methods like molecular dynamics do not suffer from this restriction, but their computational cost is by orders of magnitude too high to be applied to the relevant, complex biological systems mentioned in the beginning and thus currently limited to time scales of nano- to microseconds [74].

On the other hand, studying the deformation of elastic, slender bodies has a long history in mechanics and today's geometrically exact finite element formulations for shear-deformable (Simo-Reissner) as well as shear-rigid (Kirchhoff-Love) beams have proven to be both highly

accurate and efficient [29, 76, 113] (see Section 3.2 for a summary). Moreover, contact interaction between beams has been considered in a number of publications, e.g. [23, 43, 56, 86, 87, 98, 110, 111, 161, 163]. However, all these methods are motivated by the macroscopic perspective of non-penetrating solid bodies rather than the microscopic view considering first principles of intermolecular repulsive forces (see Section 3.3 for a summary).

The combination of elastic deformation of general 3D bodies and intermolecular forces has first been considered by Argento et. al. [7] for small deformations, by Sauer and Li [141] for large deformations and finally by Sauer and Wriggers [143] also for three-dimensional problems. In order to reduce the high computational cost associated with the required high-dimensional numerical integrals, a possible model reduction from body to surface interaction in case of sufficiently short-ranged interactions as e.g. predominant in (adhesive) contact scenarios has already been addressed in these first publications and has been the focus of subsequent publications [48, 140]. However, since these formulations aim to describe the interaction between 3D bodies of arbitrary shape, the inherent complexity of the problem still requires a four-dimensional integral over both surfaces in case of surface interactions and a six-dimensional integral over both volumes for volume interactions, respectively. In contrast, beam theory describes a slender body as a 1D Cosserat continuum, such that a further reduction in the dimensionality and thus computational cost can be achieved. So far, this idea has been applied to describing the interaction between a beam and an infinite half-space in 2D as a model for the adhesion of a Gecko spatula on a rigid surface [135, 142] and later also for the interaction of a carbon nanotube with a Lennard-Jones wall in 3D [146]. In both cases, the influence of the rigid half space can be evaluated analytically and formulated as a distributed load on the beam.

To the best of the author's knowledge, no approach for describing molecular interactions between curved 3D beams for arbitrary configurations and large deformations has been proposed so far. Notable previous approaches to similar problems have made simplifying assumptions. Ahmadi and Menon [2] study the clumping of fibers due to vdW adhesion by means of an analytical 2D beam method, yet only include vdW interaction between the hemispherical tips based on an analytical expression for the interaction of two spheres. A numerical study of the influence of inter-fiber adhesion on the mechanical behavior of 2D fiber networks assumes an effective adhesion energy per unit length of perfectly parallel fiber segments and solves for the unknown contact length in a second, nested minimization algorithm [120].

4.2. The section-section interaction potential (SSIP) approach

Based on the fundamentals of molecular interactions (Chapter 2) as well as geometrically exact beam theory (Chapter 3), this section will propose the novel SSIP approach to model various types of molecular interactions between deformable fibers undergoing large deflections in 3D.

4.2.1. Problem statement

For a classical conservative system, the total potential energy of the system can be stated taking into account the internal and external energy Π_{int} and Π_{ext}. The additional contribution from molecular interaction potentials Π_{ia} is simply added to the total potential energy as follows.

$$\Pi_{\text{TPE}} = \Pi_{\text{int}} - \Pi_{\text{ext}} + \Pi_{\text{ia}} \overset{!}{=} \min. \tag{4.1}$$

Note that the existing parts remain unchanged from the additional contribution. One noteworthy difference is that internal and external energy are summed over all bodies in the system whereas the total interaction free energy is summed over all pairs of interacting bodies.

According to the *principle of minimum of total potential energy*, the weak form of the equilibrium equations is derived by means of variational calculus. The very same equation may alternatively be derived by means of the *principle of virtual work* which also holds for non-conservative systems:

$$\delta\Pi_{\text{int}} - \delta\Pi_{\text{ext}} + \delta\Pi_{\text{ia}} = 0 \tag{4.2}$$

Clearly, the evaluation of the interaction potential Π_{ia}, or rather its variation $\delta\Pi_{ia}$, is the crucial step here. Recall from Equation (2.12) that this evaluation generally requires the evaluation of two nested 3D integrals[1]. The direct approach using 6D numerical quadrature turns out to be extremely costly and in fact inhibits any application to (biologically) relevant multi-body systems. See Section 4.4.4 for more details on the complexity and the cost of this naive, direct approach as well as the novel SSIP approach to be proposed in the following.

4.2.2. The key to dimensional reduction from 6D to 2D

Starting from the 6D integration required for the two-body interaction potential in Equation (2.12), a split of the integral into the length dimensions l_1, l_2 on the one hand and the cross-sectional dimensions A_1, A_2 on the other hand is proposed as follows:

$$\Pi_{\text{ia}} = \iint_{l_1, l_2} \underbrace{\iint_{A_1, A_2} \rho_1(\boldsymbol{x}_1)\rho_2(\boldsymbol{x}_2)\Phi(r)\, \mathrm{d}A_2\, \mathrm{d}A_1}_{=:\,\tilde{\tilde{\pi}}(\boldsymbol{r}_{1-2}, \boldsymbol{\psi}_{1-2})}\, \mathrm{d}s_2\, \mathrm{d}s_1 \quad \text{with} \quad r = \|\boldsymbol{x}_1 - \boldsymbol{x}_2\|. \tag{4.3}$$

---

[1]It is important to mention that, assuming additivity of the involved potentials, systems with more than two bodies can be handled by superposition of all pair-wise two-body interaction potentials. It is thus sufficient to consider one pair of beams in the following. The same reasoning applies to more than one type of physical interaction, i.e., potential contribution.

Exploiting the characteristic slenderness of beams, the 4D integration over both undeformable cross-sections shall be tackled analytically and only the remaining two nested 1D integrals along the centerline curves shall be evaluated numerically to allow for arbitrarily deformed configurations. Generally speaking, we follow the key idea of reduced dimensionality from beam theory and thus aim to express the relevant information about the cross-sectional dimensions by the point-wise six degrees of freedom $(\boldsymbol{r}_i, \boldsymbol{\psi}_i)$ of the 1D Cosserat continua without loss of significant information. To this end we need to consider the resulting interaction between all the elementary interaction partners within two cross-sections expressed by an interaction potential $\tilde{\tilde{\pi}}(\boldsymbol{r}_{1-2}, \boldsymbol{\psi}_{1-2})$ that depends on the separation $\boldsymbol{r}_{1-2}$ of the centroid positions and the relative rotation $\boldsymbol{\psi}_{1-2}$ between both material frames attached to the cross-sections. For this reason, the novel approach is referred to as the *section-section interaction potential* (SSIP) approach. The SSIP $\tilde{\tilde{\pi}}$ is a double length-specific quantity in the way that it measures an energy per unit length of beam 1 per unit length of beam 2, which is indicated here by the double tilde. The sought-after total interaction potential Π_{ia} of two slender deformable bodies thus results from double numerical integration of the double length-specific SSIP along both centerline curves:

$$\Pi_{\mathrm{ia}} = \int\limits_{0}^{l_1} \int\limits_{0}^{l_2} \tilde{\tilde{\pi}}(\boldsymbol{r}_{1-2}, \boldsymbol{\psi}_{1-2}) \, \mathrm{d}s_2 \, \mathrm{d}s_1 \tag{4.4}$$

This relation suggests another, alternative interpretation of the SSIP $\tilde{\tilde{\pi}}$. In analogy to the term *inter-surface potential*, introduced by [7], $\tilde{\tilde{\pi}}$ can be understood as an *inter-axis potential*, i.e., describing the interaction of two spatial curves (with attached material frames).
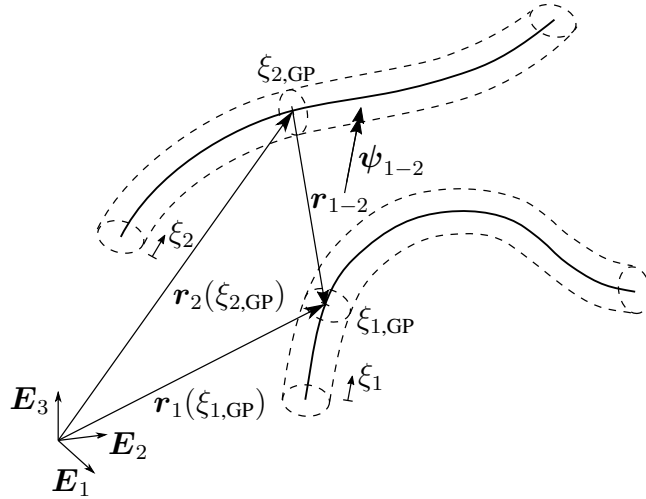
Figure 4.1.: Illustration of the novel SSIP approach: Two cross-sections at integration points $\xi_{1/2,\mathrm{GP}}$ of beam 1 and 2, respectively, their separation $\boldsymbol{r}_{1-2}$ and relative rotation $\boldsymbol{\psi}_{1-2}$. Figure taken from the author's article [61].

To further illustrate this novel concept, a simple, demonstrative example is shown in Figure 4.1. In this scenario of two beams with circular cross-section, the SSIP $\tilde{\tilde{\pi}}(\boldsymbol{r}_{1-2}, \boldsymbol{\psi}_{1-2})$ describes the interaction of two circular disks at arbitrary mutual distance and orientation. To

evaluate the two nested 1D integrals along the beam axes numerically, the SSIP needs to be evaluated for all combinations of integration points (denoted here as Gaussian quadrature points (GP), without loss of generality). For one of these pairs $(\xi_{1,\mathrm{GP}}, \xi_{2,\mathrm{GP}})$, the geometrical quantities are shown exemplarily.

While analytical integration of the inner 4D integral of Equation (4.3) has already been suggested above as one way to find a closed-form expression for the SSIP $\tilde{\tilde{\pi}}$, it is important to stress the generality of the SSIP approach at this point. The question of how to find $\tilde{\tilde{\pi}}$ is independent of the strategy to determine the interaction energy Π_{ia} of two slender bodies via numerical double integration as proposed in this section. This is important to understand because the SSIP $\tilde{\tilde{\pi}}$ will obviously depend on the type of interaction as well as the cross-section shape and a number of other factors and there might also be cases where no analytical solution can be obtained and one wants to resort to relations fitted to experimental data. In the scope of this work, several specific expressions of $\tilde{\tilde{\pi}}$, e.g., for vdW as well as electrostatic interactions, will be derived analytically in the following Section 4.3.

In its most general form $\tilde{\tilde{\pi}}$ will be a function of the relative displacement $\boldsymbol{r}_{1-2}$ and the relative rotation $\boldsymbol{\psi}_{1-2}$ between both cross-sections, i.e., three translational and three rotational degrees of freedom. This becomes clear if one recalls that the position $\boldsymbol{x}_{\mathrm{P}}$ of every material point in a slender body can be uniquely described by the six degrees of freedom of a 1D Cosserat continuum (cf. Equation (3.5)). Thus, keeping one cross-section fixed, the position $\boldsymbol{x}_{\mathrm{P1-P2}}$ of every material point in the second cross-section relative to the (centroid position and material frame of the) first cross-section is again uniquely described by six degrees of freedom $(\boldsymbol{r}_{1-2}, \boldsymbol{\psi}_{1-2})$. This insight naturally leads to the interesting question under which conditions the SSIP $\tilde{\tilde{\pi}}$ can be described by a smaller set of degrees of freedom, thus simplifying the expressions. Rotational symmetry of the interacting cross-sections is one common example where the SSIP would be invariant under rotations around the cross-section's normal axis. We will return to this topic in Section 4.3.1 as a preparation for the following derivation of specific expressions for the SSIP.

Remark on the included special case of surface interactions. It is very convenient that the practically highly relevant case of surface potentials is already included as a simpler, special case in the proposed SSIP approach to model molecular interactions between the entire volume of flexible fibers. In simple words, it is sufficient to omit one spatial dimension of analytical integration on each interacting body in the analytical derivation of the required SSIP $\tilde{\tilde{\pi}}$. More specifically, this means that $\tilde{\tilde{\pi}}$ may be obtained from solving analytically two nested 1D integrals along both, e.g. ring-shaped, contour lines of the fiber cross-sections.

Remark on self-interactions. Note that self-interaction, i.e., the interaction of distinct parts of the same fiber, can be accounted for if we evaluate also interactions between those cross-sections that belong to one and the same beam. Leaving everything else of the SSIP approach unchanged, this is naturally achieved by including those fiber pairs where the first fiber is identical to the second fiber. Including self-interaction in this manner is considered to be important whenever the fibers likely exhibit self-contact or generally speaking whenever distinct (non-neighboring) parts of the same fiber come close to each other. If this is not the case, an alternative modeling strategy is to include these contributions from self-interaction in the constitutive model of the beam theory and thus consider them as part of an effective elastic stiffness as has e.g. been suggested in

[35, 141]. The latter approach has been applied in the numerical examples of Section 4.5. An example for using the SSIP approach to explicitly model self-interactions will be presented in Chapter 9, which studies the conformations of a single mucin filament due to varying line charge distributions.

4.3. Application of the general SSIP approach to specific types of interactions

At this point, let us return to the fact that the SSIP approach proposed in Section 4.2 is general in the sense that it does not depend on the specific type of physical interaction. This section provides the necessary information and formulae to apply the newly proposed, generally valid approach from Section 4.2.2 to certain types of real-world, physical interactions such as electrostatics or vdW. As mentioned above, the approach requires a closed-form expression for the SSIP $\tilde{\tilde{\pi}}$. We basically see two alternative promising ways to arrive at such a reduced interaction law $\tilde{\tilde{\pi}}$:

1. analytical integration, e.g., as presented in Section 4.3.2

2. postulate $\tilde{\tilde{\pi}}$ as a general function of separation $\boldsymbol{r}_{1-2}$ and mutual orientation $\boldsymbol{\psi}_{1-2}$ and determine the free parameters via fitting to

   a) experimental data for specific section-section configurations, i.e., discrete values of separation $\boldsymbol{r}_{1-2}$ and mutual orientation $\boldsymbol{\psi}_{1-2}$

   b) data from (one-time) numerical 4D integration for specific section-section configurations, i.e., discrete values of $\boldsymbol{r}_{1-2}$ and $\boldsymbol{\psi}_{1-2}$

   c) experimental data for the global system response, e.g., of the entire fiber pair or a fiber network

As a starting point we will restrict ourselves to the first option based on analytical integration throughout the remainder of this work. See Section 4.3.2 for an example of the further steps required to derive the final, ready-to-use expressions in case of vdW interactions. To give but one example for a recent experimental work, which could serve as the basis for the second option listed above, the reader is kindly referred to [67] measuring cohesive interactions between a single pair of microtubules. Postulating an SSIP and studying the global system response in numerical simulations could also be used as a verification of theoretical predictions for the system behavior. To give an example, the reader is kindly referred to the work of theoretical biophysicists studying the structural polymorphism of the cytoskeleton resulting from molecular rod-rod interactions [15], which is based on a postulated model potential "that captures the main features of any realistic potential". In summary, one can expect a large number of promising future use cases for the proposed SSIP approach.

4.3.1. Additional assumptions and possible simplification of the most general form of SSIP laws

Recall that the most general form of the SSIP is uniquely described by a set of six degrees of freedom, three for the relative displacement and three for the relative orientation of the two interacting cross-sections, as presented in the preceding Section 4.2.2. The following assumptions turn out to significantly simplify this most general form of the SSIP law by reducing the number of relevant degrees of freedom from six to four, two or even one. This in turn eases the desirable derivation of analytical closed-form solutions of the SSIP $\tilde{\tilde{\pi}}$ based on the point pair potentials $\Phi(r)$ presented in Section 2.2. Specifically, these assumptions are:

1. undeformable cross-sections

2. circular cross-section shapes

3. homogeneous (or, more generally, rotationally symmetric) particle densities ρ_1, ρ_2 in the cross-sections or surface charge densities σ_1, σ_2 over the circumference

The first assumption is typical for geometrically exact beam theory and the second and third assumption are reasonable regarding the applications to biopolymer fibers such as actin or DNA that can often be modeled as homogeneous fibers with circular cross-sections. Based on these three assumptions, we can conclude that the interaction between two cross-sections is geometrically equivalent to the interaction of two homogeneous, circular disks (or rings in case of surface interactions). The rotational symmetry of the circular disks then implies that the interaction potential is invariant under rotations around their own axes and thus reduces the number of degrees of freedom to four. The relative importance of the remaining degrees of freedom, i.e., modes, will be the crucial point in the following discussion, where we turn to the interaction of two slender bodies, i.e., consider the entirety of all cross-section pairs. At this point, recall the fundamental distinction between either short-range or long-range interactions as outlined in Section 2.3.2.
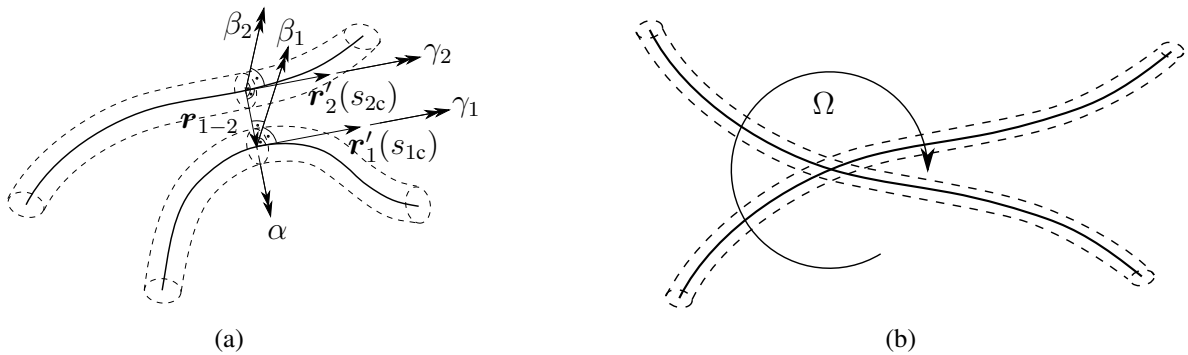

Figure 4.2.: Sketches to illustrate the simplifications resulting for (a) short- and (b) long-range interactions. Figure taken from the author's article [61].

Short-range interactions

In the case of short-range interactions, the cross-section pairs in the immediate vicinity of the mutual closest points of the slender bodies dominate the total interaction. As is known from macroscopic beam contact formulations [110, 111, 163], the criterion for the closest point is that the distance vector $\boldsymbol{r}_{1-2}$ is perpendicular to both centerline tangent vectors $\boldsymbol{r}_i'$, i.e., (assuming small shear angles) the normal vectors of the disks (see Figure 4.2(a)). Since only cross-section pairs in the direct vicinity of the closest points are relevant, arbitrary relative configurations (i.e. separations and relative rotations) between those cross-sections shall in the following be discussed on the basis of six alternative degrees of freedom as illustrated in Figure 4.2(a). By considering the cross-sections A_{1c} and A_{2c} at the closest points as reference, the relative configuration between cross-sections in the direct vicinity of A_{1c} and A_{2c} can be described via (small) rotations of A_{1c} around the axis $\boldsymbol{r}_1'$ (angle γ_1) and $\boldsymbol{r}_{1-2} \times \boldsymbol{r}_1'$ (angle β_1), (small) rotations of A_{2c} around the axes $\boldsymbol{r}_2'$ (angle γ_2) and $\boldsymbol{r}_{1-2} \times \boldsymbol{r}_2'$ (angle β_2), (small) relative rotations between A_{1c} and A_{2c} around the axis $\boldsymbol{r}_{1-2}$ (angle α), and (small) changes in the (scalar) distance $d = \|\boldsymbol{r}_{1-2}\|$. As a consequence of assumptions 1–3 discussed above, the considered interaction potentials are invariant under rotations γ_1 and γ_2. From the remaining four degrees of freedom, the scalar distance d clearly has the most significant influence on the interaction potential because changes in d directly affect the mutual distance r of all point pairs in the body and, most importantly, the smallest surface separation g between both bodies. The second most significant influence is expected for the scalar relative rotation angle α between the cross-section normal vectors, i.e., $\cos(\alpha) = \boldsymbol{n}_1 \cdot \boldsymbol{n}_2 \approx \boldsymbol{r}_1' \cdot \boldsymbol{r}_2'/(\|\boldsymbol{r}_1'\| \|\boldsymbol{r}_2'\|)$. A change in α does not alter the gap g, but influences the distance of all next nearest point pairs in the immediate vicinity of the closest surface point pair. For the remaining two relative rotations β_1 and β_2, arguments for both sides, either significant or rather irrelevant influence on the total interaction potential, can be found at this point. On the one hand, the orthogonality conditions $\boldsymbol{r}_i' \cdot \boldsymbol{r}_{1-2} = 0$, $i = 1, 2$ at the closest points are fulfilled in good approximation also for cross-sections in the direct vicinity of the closest points, such that the influence of $\beta_{1/2}$ could be considered negligible. On the other hand, even small rotations $\beta_{1/2}$ change the smallest separation of any two point pairs in the immediate neighborhood of the closest point pair as soon as the centroid distance vector $\boldsymbol{r}_{1-2}$ rotates out of the two cross-section planes. Therefore, it seems hard to draw a final conclusion with respect to the influence and thus importance of $\beta_{1/2}$ based on the qualitative theoretical considerations of this section.

To summarize, the scalar distance d between the cross-section centroids, the scalar relative rotation angle α between the cross-section normal vectors and possibly also the relative rotation components $\beta_{1/2}$ are supposed to have a perceptible influence on the short-range interaction between slender beams fulfilling assumptions 1–3, with a relative importance which decreases in this order. In favor of the simplest possible model, we will therefore assume at this point that the effect of this scalar relative rotations α, β_1 and β_2 is negligible as compared to the effect of the scalar separation d. This allows us to directly use the analytical, closed-form expression for the disk-disk interaction potential as presented in Section 2.3.2. The error for arbitrary configurations associated with this model assumption will be thoroughly analyzed in Section 4.5.1.1. In this context, it is a noteworthy fact, that the first published method for 2D beam-rigid half space LJ interaction [135] likewise neglects the effect of cross-section orientation. In the subsequent publication [142], the effect of cross-section rotation, i.e., interaction moments, has finally

been included and a quantitative analysis considering a peeling experiment of a Gecko spatula revealed that the differences in the resulting maximum peeling force and bending moment are below 8% and 2%, respectively. However, it is unclear whether this assessment also holds for beam-beam interactions modeled via the proposed SSIP approach. Including the orientation of the cross-sections thus is considered an important step that will be taken in the context of the slightly different beam interaction formulation to be proposed in the following Chapter 5. Because this alternative formulation is specialized in short-ranged interactions, it turns out to be more efficient for this class of interactions and the improvement of the accuracy expected from including the cross-section orientation will therefore be realized in that context first. However, also the SSIP laws considered here would benefit from the increased accuracy and including the cross-section orientation is thus considered a valuable future extension.

Finally, it is emphasized that by the assumptions discussed above, the SSIP law $\tilde{\tilde{\pi}}$ as well as the total two-body interaction potential Π_{ia} can be formulated as pure function of the beam centerlines $\boldsymbol{r}_1$ and $\boldsymbol{r}_2$ without the necessity to consider cross-section orientations via rotational degrees of freedom. This is considered a significant simplification of the most general case of the SSIP approach and thus facilitates both the remaining derivations in the present work as well as potential future applications.

Remark on configurations with non-unique closest points. It is well-known from the literature on macroscopic beam contact that the location of the closest points is non-unique for certain configurations of two interacting beams, e.g., the trivial case of two straight beams, where an infinite number of closest point pairs exists (see e.g. [110]). Note however that the reasoning presented above also holds in these cases, since the cross-section pairs in either one or several of these regions will dominate the total interaction potential.

Long-range interactions

In the case of long-range interactions, the situation is fundamentally different. Recall that here the large number of cross-section pairs with large separation $d \gg R$ outweighs the contributions from those few pairs in the vicinity of the closest point and dominates the total interaction. Thus, the regime of large separations is decisive in this case and it has already been shown in the literature considering disk-disk interaction (see the brief summary in A.1.1) that in this regime the exact orientation of the disks can be neglected as compared to the centroid separation d. In simple terms, this holds because the distance $\boldsymbol{x}_{\text{P1}-\text{P2}}$ between any point in disk 1 and any point in disk 2 may be approximated by the centroid separation d, if d is much larger than the disk radii R_i, which - again - holds for the large majority of all possible cross-section pairs. The validity of this assumption will be thoroughly verified by means of numerical reference solutions in Section 4.5.1.2.

Remark. The following, similar reasoning from the perspective of slender continua comes to the same conclusion. As visualized in Figure 4.2(b), even pure (rigid body) rotations of slender bodies always entail large displacements of the centerline[2] in the region far away from the center

---

[2]Disregarding rotations around its own axis, which are irrelevant here due to rotational symmetry, as mentioned above.

of rotation. The displacement of any material point due to cross-section rotation will be in the order of ΩR, where Ω is the angle of rotation and R denotes the cross-section radius, whereas the displacement due to centerline displacement will be in the order of ΩL, where L is the distance from the center of rotation and thus in the order of the beam length l. Due to the high slenderness $l/R \gg 1$ of beams, the displacement from translation of the centroid will dominate in the region of large separations with $L \gg R$, which is the decisive one here, because it includes the large majority of all possible cross-section pairs, as outlined above. The original, analogous reasoning has been applied to the relative importance of translational versus rotational contributions to the mass inertia of beams.

Conclusions

To conclude, this section has discussed the possibility of defining and using SSIP laws $\tilde{\tilde{\pi}}$ as a function of the scalar separation of the centroids d instead of the six degrees of freedom in the most general form. This significantly simplifies the theory because the analytical solutions for the planar disk-disk interaction from literature can directly be used and the complex treatment of large rotations is avoided. Having considered the additional assumptions above in the context of short-range interactions, the relative importance of cross-section rotations still needs to be verified in the subsequent quantitative analysis of Section 4.5.1.1. In the case of long-range interactions between slender bodies, it has been argued that the application of such simple SSIP laws $\tilde{\tilde{\pi}}(d)$ is expected to be a good approximation, which will be confirmed by the quantitative analysis of Section 4.5.1.2.

4.3.2. Short-range volume interactions such as van der Waals and steric repulsion

In the following, a generic short-range volume interaction described by the point-pair potential law

$$\Phi_{\mathrm{m}}(r) = k_{\mathrm{m}} \, r^{-m}, \; m > 3 \tag{4.5}$$

will be considered, because it includes vdW interaction for exponent $m = 6$ (cf. Equation (2.4)) as well as steric repulsion as modeled by LJ for exponent $m = 12$ (cf. Equation (2.8)). As outlined already in the preceding section, only the regime of small separations is practically relevant in this case of short-range interactions and we neglect the effect of cross-section rotations throughout this article. At this point, we can thus return to the results for the disk-disk scenario obtained in literature on vdW interactions [90] and summarized in Table 2.2. In particular, we make use of expression (2.19) or rather the more general form (A.12). The latter is valid for all power-law point pair interaction potentials with a general exponent $m > 7/2$, i.e., all interactions where the strength decays "fast enough".

First, let us introduce the following abbreviation containing all constants in the lengthy expression:

$$c_{\mathrm{m,ss}} := k_{\mathrm{m}} \rho_1 \rho_2 \frac{2\pi}{(m-2)^2} \quad \sqrt{\frac{2R_1 R_2}{R_1 + R_2}} \quad \frac{\Gamma(m - \frac{7}{2})\Gamma(\frac{m-1}{2})}{\Gamma(m-2)\Gamma(\frac{m}{2} - 1)} \tag{4.6}$$

Using Equation (A.12) in combination with the general SSIP approach (4.4) from Section 4.2.2, we directly obtain an expression for the total interaction potential of two deformable fibers in

the case of short-range interactions:

$$\Pi_{m,ss} = \int_0^{l_1} \int_0^{l_2} \overbrace{c_{m,ss}\, g^{-m+\frac{7}{2}}}^{=:\,\tilde{\tilde{\pi}}_{m,ss}} \mathrm{d}s_2\, \mathrm{d}s_1 \qquad \text{for} \quad m > \tfrac{7}{2} \tag{4.7}$$

$$\text{with} \quad g(s_1, s_2) = \|\boldsymbol{r}_1(s_1) - \boldsymbol{r}_2(s_2)\| - R_1 - R_2 \tag{4.8}$$

In accordance with the key principle of the general SSIP approach, the specific SSIP law $\tilde{\tilde{\pi}}_{m,ss}$ for the generic short-range interactions considered here can be identified as the integrand of this expression. The so-called gap g is the (scalar) surface-to-surface separation, i.e., the beams' centerline curves $\boldsymbol{r}_1(s_1)$ and $\boldsymbol{r}_2(s_2)$ minus the two radii R_i, as visualized in Figure 4.1. In general, the particle densities $\rho_{1/2}$ may depend on the curve parameters $s_{1/2}$, i.e., vary along the fiber, without introducing any additional complexity at this point. For the sake of brevity, these arguments $s_{1/2}$ will be omitted in the remainder of this section.

The variation of the interaction potential required to solve Equation (4.2) finally reads

$$\delta\Pi_{m,ss} = \left(-m + \tfrac{7}{2}\right) \int_0^{l_1} \int_0^{l_2} c_{m,ss} \left(\delta\boldsymbol{r}_1^T - \delta\boldsymbol{r}_2^T\right) \frac{\boldsymbol{r}_1 - \boldsymbol{r}_2}{d} g^{-m+\frac{5}{2}}\, \mathrm{d}s_2\, \mathrm{d}s_1 \quad \text{for} \quad m > \tfrac{7}{2}. \tag{4.9}$$

Here, we used the variation of the gap δg, which is a well-known expression from the literature on macroscopic beam contact [163] and is identical to the variation of the separation of the beams' centerlines δd to be used in (4.13), because the cross-sections are assumed to be undeformable:

$$\delta g = \delta d = \left(\delta\boldsymbol{r}_1^T - \delta\boldsymbol{r}_2^T\right) \frac{\boldsymbol{r}_1 - \boldsymbol{r}_2}{d} \tag{4.10}$$

Solving Equation (4.2) generally requires two further steps of discretization and subsequent linearization of this additional contribution $\delta\Pi_{m,ss}$ to the total virtual work. The resulting expressions will be presented in Section 4.4.1.1 and Appendix C.1.1, respectively. As discussed along with the general SSIP approach in Section 4.2.2, the remaining two nested 1D integrals are evaluated numerically, e.g., by means of Gaussian quadrature. See Section 4.4.4 for details on this algorithmic aspect.

Remark on the regularization of the integrand. The inverse power law in the integrand of Equation (4.9) has a singularity for the limit of zero surface-to-surface separation $g \to 0$. Consequently, a so-called *regularization* of the potential law is needed to numerically handle (the integration of) this term robustly as well as sufficiently accurate. This approach is well-known e.g. from (beam) contact mechanics (see e.g. [45, 110, 140]) and will be further discussed and elaborated in Section 4.4.3.

At the end of this section, we can conclude that a number of specific, ready-to-use expressions for the interaction free energy as well as virtual work of generic short-range interactions described via the SSIP approach have been found. Thus, vdW interaction or steric exclusion of slender, deformable continua can now be modeled in an efficient manner, reducing the numerical integral to be evaluated from six to two dimensions. A detailed quantitative study of the

approximation quality with regard to the assumptions discussed in the preceding Section 4.3.1 is content of Section 4.5.1.1.

Note that speaking about the *proposed* SSIP *laws* in the remainder of this chapter refers to the fact that to the best of the author's knowledge these expressions have not been used as an interaction potential for beam cross-sections before and we thus propose to use specifically these expressions in this new context. In contrast to the general SSIP approach from Section 4.2, the specific expressions exemplarily chosen for the SSIP laws considered throughout this work are not original content of the present work and instead have been carefully selected from the literature and referenced accordingly.

4.3.3. Long-range surface interactions such as electrostatics

Having discussed short-range volume interactions, we now want to consider one example of *long-range surface potentials*. Since electrostatic interaction is the prime example of surface potential interaction and at the same time of high interest for the application to biopolymers we have in mind, we will focus on this case throughout the following section and mostly speak of *point charges* as the elementary interaction partners. However, the required steps and formulae will be presented as general as possible in order to allow for a smooth future transfer to other applications.

Especially in this context, it is important to stress again that within this model the elementary interaction partners, i.e., charges must not redistribute within the bodies. Hence, only non-conducting materials can be modeled with the SSIP approach. This however covers our main purpose to model electrostatic interactions between bio-macromolecules such as protein filaments and DNA because charges are not free to move therein.

According to the SSIP approach proposed in Section 4.2.2, we aim to use analytical expressions for the two inner integrals over the cross-section circumferences, while the integration along the two beam centerlines will be evaluated numerically (cf. Equation (4.3) in combination with the remark on surface interactions at the end of the corresponding section). As discussed in Section 4.3.1, the regime of large separations is the decisive one for beam-beam interactions in this case of long-range interactions and the SSIP law can be simplified in good approximation to depend only on the centroid separation d, which will be confirmed numerically in Section 4.5.1.2.

At this point, we again return to the expressions for the disk-disk interaction based on a generic point pair potential $\Phi_{\mathrm{m}}(r) = k\,r^{-m}$, as derived in the literature on vdW interactions [90] and summarized in Appendix A.1.1. In particular, the relation (A.6) will be used, which is the same approximation used to derive Equation (2.20) that describes the practically rather irrelevant scenario of short-range vdW interactions in the regime of large separations. Note that in the context of electrostatics, this result is well-known as the first term, i.e., zeroth pole or *monopole* of the multipole expansion of the ring-shaped charge distribution on each of the disks' circumference, which represents the effect of the net charge of a (continuous) charge distribution and has no angular dependence (see Section 2.3.1). In simple terms, this monopole-monopole interaction means that the point pair interaction potential $\Phi(r)$ is evaluated only once for the distance between the centers of the distributions $r = d = \|\boldsymbol{r}_1 - \boldsymbol{r}_2\|$ and weighted with the number of all point charges on the two circumferences of the circular cross-sections. The expression for the SSIP law to be used throughout this work would thus be exact for the scenario of the net charge

of each cross-section concentrated at the centroid position (or distributed spherically symmetric around the centroid position). If the accuracy of the SSIP approach needs to be improved beyond the level resulting from this simplified SSIP law (see Section 4.5.1.2 for the analysis), one could simply include more terms from the multipole expansion of the (ring-shaped) charge distributions to the SSIP law, which would take the relative rotation of the cross-sections into account. For the desired applications throughout this work, the simplified SSIP law, which is based on the monopole-monopole interaction of cross-sections, turns out to be an excellent approximation for the true electrostatic interaction law and we thus restrict ourselves to this variant.

Two nested 1D integrals over the beams' length dimensions then yield the two-body interaction potential for two fibers with arbitrary centerline shapes

$$\Pi_{\text{ia,ls}} = \int_0^{l_1} \int_0^{l_2} \overbrace{2\pi R_1 \sigma_1 \, 2\pi R_2 \sigma_2 \, \Phi(r=d)}^{=: \tilde{\tilde{\pi}}_{\text{ls}}} \,\mathrm{d}s_2 \,\mathrm{d}s_1 \tag{4.11}$$

$$\text{with} \quad d(s_1, s_2) = \|\boldsymbol{r}_1(s_1) - \boldsymbol{r}_2(s_2)\| . \tag{4.12}$$

Once again, the specific SSIP law $\tilde{\tilde{\pi}}_{\text{ls}}$ for the generic long-range interactions considered here can here be identified as the integrand of this expression. The surface (charge) densities $\sigma_j, j = 1, 2$ have already been introduced in Equation (2.13). Particularly for the case of electrostatics, the surface charge per unit length can be identified as $\lambda_j = 2\pi R_j \sigma_j, \ j = 1, 2$, and is commonly referred to as *linear charge density*. Note however that Equation (4.11) holds for all long-range point pair potential laws $\Phi(r)$, e.g., all power laws $\Phi_{\text{m}}(r) = k\,r^{-m}$ with $m \leq 3$. In order to obtain the weak form of the continuous problem, the variation of this total interaction energy needs to be derived. This variational form can immediately be stated as

$$\delta\Pi_{\text{ia,ls}} = \int_0^{l_1} \int_0^{l_2} \lambda_1 \lambda_2 \, \frac{\partial\,\Phi(r=d)}{\partial\,d} \, \delta d \,\mathrm{d}s_2 \,\mathrm{d}s_1 \quad \text{with} \quad \delta d = \left(\delta\boldsymbol{r}_1^T - \delta\boldsymbol{r}_2^T\right) \frac{\boldsymbol{r}_1 - \boldsymbol{r}_2}{d} \tag{4.13}$$

as the consistent variation of the separation of the beams' centerlines d, which is well-known from macroscopic beam contact formulations [163]. By inserting the generic (long-range) power law

$$\Phi_{\text{m}}(r) = k\,r^{-m}, \ m \leq 3 \tag{4.14}$$

into (4.13), we obtain the final expression for the variation of the two-body interaction energy of two deformable slender bodies

$$\delta\Pi_{\text{m,ls}} = \int_0^{l_1} \int_0^{l_2} \underbrace{km\,\lambda_1\lambda_2}_{=: c_{\text{m,ls}}} \left(-\delta\boldsymbol{r}_1^T + \delta\boldsymbol{r}_2^T\right) \frac{\boldsymbol{r}_1 - \boldsymbol{r}_2}{d^{m+2}} \,\mathrm{d}s_2 \,\mathrm{d}s_1. \tag{4.15}$$

The specific case of Coulombic surface interactions follows directly for $m = 1$ and $k = C_{\text{elstat}}$ (cf. Equation (2.3)). At this point, we have once again arrived at the sought-after contribution to the weak form (4.2) of the space-continuous problem. The steps of finite element discretization and linearization will again be presented later, in Section 4.4.1.2 and Appendix C.1.2, respectively.

Remark on volume interactions. Note that there is no conceptual difference if long-range volume interactions were considered instead of the long-range surface interactions presented exemplarily in this section. The only difference lies in the constant prefactor $c_{\mathrm{m,ls}}$, which would read $c_{\mathrm{m,ls}} = kmA_1A_2\rho_1\rho_2$ instead. Rather than the spatial distribution of the elementary interaction points in the volume or on the surface, it is the long-ranged nature of the interactions, which is important for the derivations in this section and allows the use of approximations for large separations (refer to the extensive discussion in Section 4.3.1).

4.4. Finite element discretization and selected algorithmic aspects

Having discussed the space-continuous theory in Sections 4.2 and 4.3, we now turn to the step of spatial discretization by means of finite elements. Subsequently, the most important aspects of the required algorithmic framework will be presented briefly and discussed specifically in the light of the novel SSIP approach. This includes the applied regularization technique, multi-dimensional numerical integration, an analysis of the algorithmic complexity as well as the topics of searching for interaction partners and parallel computing.

4.4.1. Spatial discretization based on beam finite elements

At this point, recall the spatial discretization schemes employed in the context of the applied beam finite elements that have been summarized in Section 3.2. The identical centerline interpolation based on cubic Hermite polynomials will be applied to the two-body virtual work contribution from molecular interactions that result from the SSIP approach and reduced interaction laws. The motivation to use Hermite interpolation is that it ensures C_1-continuity, i.e., a smooth geometry representation even across element boundaries. This property turned out to be crucial for the robustness of simulations in the context of macroscopic beam contact methods [112], and is just as important if we include molecular interactions. See [136] for a comprehensive discussion of (non-)smooth geometries and adhesive, molecular interactions using 2D solid elements. Note however that neither the SSIP approach proposed in Section 4.2 nor the specific SSIP laws and resulting expressions for the interaction free energy and the virtual work are limited to this Hermite interpolation scheme. In fact, all of the following discrete expressions will be equally valid for a large number of other beam formulations, where the discrete centerline geometry is defined by polynomial interpolation, which can generally be expressed in terms of the generic shape function matrix $\mathbf{H}$ introduced above.

Recall also that the proposed SSIP laws from Section 4.3 solely depend on the centerline curve description, i.e., the rotation field does not appear in the additional contributions and hence its discretization is not required here. It is therefore sufficient to apply the discretization scheme for the centerline field stated in Equation (3.19) to the expressions for the virtual work contributions $\delta\Pi_{\mathrm{ia}}$ presented in Section 4.3 and finally end up with the discrete element residual vectors $\mathbf{r}_{\mathrm{ia},1/2}$. The latter need to be assembled into the global residual vector $\mathbf{R}$ as it is stan-

dard in the (nonlinear) finite element method. Note that the linearization of all the expressions presented in this Section 4.4.1 is provided in Appendix C.1.

4.4.1.1. Short-range volume interactions such as van der Waals and steric repulsion

Discretization of the centerline curves according to Equation (3.19), i.e., $\boldsymbol{r}_j \approx \boldsymbol{r}_{\mathrm{h},j} = \mathbf{H}_j \hat{\boldsymbol{d}}_j$ and $\delta \boldsymbol{r}_j^{\mathrm{T}} \approx \delta \boldsymbol{r}_{\mathrm{h},j}^{\mathrm{T}} = \delta \hat{\boldsymbol{d}}_j^{\mathrm{T}} \mathbf{H}_j^{\mathrm{T}}$, for both beam elements $j = 1, 2$ transforms the space-continuous form (4.9) of the two-body virtual work contribution from molecular interactions $\delta\Pi_{\mathrm{m,ss}}$ into its discrete counterpart

$$\delta\Pi_{\mathrm{m,ss,h}} = -(m - \tfrac{7}{2}) \int_0^{l_1} \int_0^{l_2} c_{\mathrm{m,ss}} \left(\delta\hat{\boldsymbol{d}}_1^{\mathrm{T}} \mathbf{H}_1^{\mathrm{T}} - \delta\hat{\boldsymbol{d}}_2^{\mathrm{T}} \mathbf{H}_2^{\mathrm{T}} \right) \frac{\boldsymbol{r}_{h,1} - \boldsymbol{r}_{h,2}}{d_h} g_h^{-m+\frac{5}{2}} \, \mathrm{d}s_2 \, \mathrm{d}s_1. \quad (4.16)$$

Refer to Equation (4.6) for the definition of the constant $c_{\mathrm{m,ss}}$. Note that Equation (4.16) only contributes to those scalar residua associated with the centerline, i.e., translational degrees of freedom $\hat{\mathbf{d}}$. This is a logical consequence of the fact that the SSIP law solely depends on the beams' centerline curves, as discussed in detail in Section 4.3. For the sake of brevity, the index 'h' indicating all discrete quantities will be omitted from here on since all following quantities are considered discrete. In Equation (4.16), the discrete element residual vectors of the two interacting elements $j = 1, 2$ can finally be identified as

$$\mathbf{r}_{\mathrm{m,ss,1}} = -(m - \tfrac{7}{2}) \int_0^{l_1} \int_0^{l_2} c_{\mathrm{m,ss}} \mathbf{H}_1^{\mathrm{T}} \frac{(\boldsymbol{r}_1 - \boldsymbol{r}_2)}{d} g^{-m+\frac{5}{2}} \, \mathrm{d}s_2 \, \mathrm{d}s_1 \quad \text{and} \quad (4.17)$$

$$\mathbf{r}_{\mathrm{m,ss,2}} = (m - \tfrac{7}{2}) \int_0^{l_1} \int_0^{l_2} c_{\mathrm{m,ss}} \mathbf{H}_2^{\mathrm{T}} \frac{(\boldsymbol{r}_1 - \boldsymbol{r}_2)}{d} g^{-m+\frac{5}{2}} \, \mathrm{d}s_2 \, \mathrm{d}s_1. \quad (4.18)$$

See Section 4.4.4 for details on the numerical quadrature required to evaluate these expressions.

4.4.1.2. Long-range surface interactions such as electrostatics

In analogy to the previous section, we discretize Equation (4.15) and obtain the discrete element residual vectors

$$\mathbf{r}_{\mathrm{m,ls,1}} = -\int_0^{l_1} \int_0^{l_2} c_{\mathrm{m,ls}} \mathbf{H}_1^{\mathrm{T}} \frac{(\boldsymbol{r}_1 - \boldsymbol{r}_2)}{d^{m+2}} \, \mathrm{d}s_2 \, \mathrm{d}s_1 \quad \text{and} \quad (4.19)$$

$$\mathbf{r}_{\mathrm{m,ls,2}} = \int_0^{l_1} \int_0^{l_2} c_{\mathrm{m,ls}} \mathbf{H}_2^{\mathrm{T}} \frac{(\boldsymbol{r}_1 - \boldsymbol{r}_2)}{d^{m+2}} \, \mathrm{d}s_2 \, \mathrm{d}s_1. \quad (4.20)$$

As mentioned already in Section 4.3.3, the discrete element residual vectors in the specific case of Coulombic interactions follow directly for $m = 1$ and $c_{\mathrm{m,ls}} = C_{\mathrm{elstat}} \lambda_1 \lambda_2$. See Section 2.2.1 for the definition of C_{elstat} and Section 4.3.3 for the definition of the linear charge densities λ_i. Again, as mentioned in Section 4.3.3, the case of long-range *volume* interactions only requires to adapt the constant prefactor via $c_{\mathrm{m,ls}} = k m A_1 A_2 \rho_1 \rho_2$.

4.4.2. Objectivity and conservation properties

It can be shown that the proposed SSIP approach from Section 4.2 in combination with the SSIP laws from Section 4.3 fulfills the essential mechanical properties of objectivity, global conservation of linear and angular momentum as well as global conservation of energy. Due to the equivalent structure of the resulting space-discrete contributions, e.g., Equation (4.16), as compared to the terms obtained in macroscopic beam contact formulations, the reader is kindly referred to the proof and detailed discussion of these important aspects in [111, Appendix B]. The fulfillment of conservation properties will furthermore be verified by means of the numerical examples in Section 4.5.2 and Section 4.5.4.

4.4.3. Regularization of SSIP laws in the limit of zero separation

The singularity of inverse power laws for zero separation is a well-known pitfall when dealing with this kind of interaction laws. See e.g. [74, p.137] for a discussion of this topic in the context of point-point LJ interaction as compared to a hard-sphere model. In numerical methods, one therefore typically applies a regularization that cures the singularity and ensures the robustness of the method. Sauer [136] gives an example for a regularized LJ force law between two half-spaces, where the force is linearly extrapolated below a certain separation, which is chosen as 1.05 times the equilibrium spacing of the two half spaces. Also, existing, macroscopic beam contact formulations rely on the regularization of the seemingly instantaneous and infinite jump in the contact force when two macroscopic beams come into contact (see e.g. [44, 111]).

However, the SSIP laws derived for disk-disk vdW or LJ interaction from Section 4.3.2 have not yet been considered in literature. Note that LJ interaction is the most general and challenging case considered in this work, since strong adhesive forces compete with even stronger repulsive forces whenever two fibers are about to come into contact. To be more precise, it is not only the strength of these competing forces, but also the high gradients in the force-distance relation that lead to a very stiff behavior of the governing partial differential equations. This alone places high demands on the nonlinear solver, which in combination with the already mentioned singularity at zero separation $g = 0$, and the fact that LJ interaction laws are not defined for configurations $g < 0$ where both fibers penetrate each other, makes it extremely demanding to solve the problem numerically.

The results and conclusions discussed throughout this section are mainly based on the extensive numerical peeling and pull-off experiment with two adhesive fibers, which will be presented in Chapter 7. In absence of a regularization, only the pragmatic yet effective approach of applying a very restrictive upper bound of the displacement increment per nonlinear iteration (see Appendix F.2 for details) proved successful to solve for the quasi-static equilibrium configurations without occurrence of any invalid configuration $g \leq 0$ for any integration point pair in any nonlinear iteration. It must be emphasized that even a single occurrence of the latter is fatal and aborts the simulation, such that the mentioned approach is the only way to compute a solution for the full LJ interaction law, which can in turn serve as a reference solution during the validation of the regularization to be proposed and applied. However, the mentioned approach severely deteriorates the convergence behavior and leads to a large number of nonlinear iterations per time step. Thus, the regularization to be proposed in this section is superior in two

respects: it guarantees the avoidance of singular/undefined values and saves a factor of five in the number of iterations of the nonlinear solver.

Specifically, we apply a linear extrapolation of the total LJ force law below a certain separation $g_{\mathrm{reg,LJ}}$ in a manner very similar to [136] with the only difference that it is applied to the length-specific disk-disk force law instead of the force law between two half spaces. Linear extrapolation means that the original expression $(m - 7/2)\,c_{\mathrm{m,ss}}\,g^{-m+\frac{5}{2}}$ in (4.17) and (4.18) is replaced by a linear equation $a\,g + b$ in the gap g for all $g < g_{\mathrm{reg,LJ}}$. The two constants a and b are determined from the requirements that the force value as well as the first derivative of the original and the linear expression are identical for the regularization separation $g = g_{\mathrm{reg,LJ}}$. Figure 4.3 shows both the original (blue) and the regularized (red) LJ disk-disk force law as a function of the smallest surface separation g.
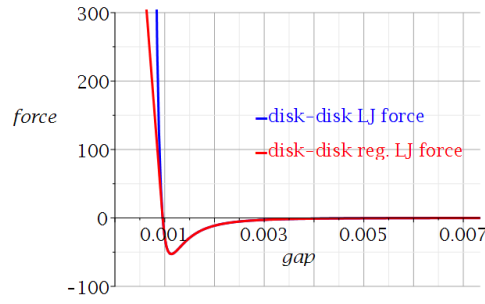
Figure 4.3.: Comparison of regularized (red) and full (blue) LJ disk-disk force law. Here, $g_{\mathrm{reg,LJ}} = g_{\mathrm{LJ,eq,disk\|disk}}$ is shown exemplarily[3]. Note that the same idea has previously been applied in the context of LJ interaction between half spaces [136] instead of disks as considered here. Figure taken from the author's article [61].

The numerical experiment of adhesive fibers studied in Chapter 7 reveals that this regularization yields the already mentioned great enhancement in terms of robustness as well as efficiency without any change in the system response. As will be shown in the comparison of the force-displacement curves in Section 7.3.2, the results obtained with the full LJ and with the regularized LJ force law do indeed coincide down to machine precision. This is reasonable and expected, because of the choice of a regularization parameter $g_{\mathrm{reg,LJ}} \leq g_{\mathrm{LJ,eq,cyl\|cyl}}$ that is smaller than any separation value g occurring anywhere in the system in any converged equilibrium state. Thus, the solution never "sees" the modification to the vdW force law in the interval $g < g_{\mathrm{reg,LJ}}$ and the results are identical. However, since during the nonlinear iterations also non-equilibrium configurations with $g < g_{\mathrm{reg,LJ}}$ occur, the nonlinear solution procedure is influenced in an extremely positive way, leading to an overall saving of a factor of five in the number of nonlinear iterations as compared to the full LJ interaction without any regularization.

---

[3]See Equation (A.29) for an analytical expression of $g_{\mathrm{LJ,eq,disk\|disk}}$.

4.4.4. Numerical evaluation of n-dimensional integrals of intermolecular potential laws

Generally, n nested loops of a 1D Gauss-Legendre quadrature scheme are used, which is the well-established and de-facto standard method in nonlinear finite element frameworks and has been used also in previous publications in the context of molecular interactions [7, 140]. Due to the strong nonlinearity, i.e., high gradients of the power laws, a large number of quadrature points is required in each dimension to achieve sufficient accuracy. This effect is most critical for high exponents of the potential law, i.e., vdW and steric interactions, and small separations of the interacting bodies. We thus implemented the possibility to subdivide the domain of a finite element into n_{IS} integration segments and apply an n_{GP}-point Gauss rule on each of them in order to achieve sufficient density of quadrature points in every case. In this respect, the development and use of more sophisticated numerical quadrature schemes for these challenging integrands consisting of rational functions is considered a promising future step (see e.g. [55]).

4.4.5. Algorithm complexity

Multi-dimensional numerical integration of the intermolecular potential laws as discussed above turns out to be the crucial factor in terms of efficiency. For the following analysis of efficiency, we consider the associated algorithmic complexity. Generally, all possible pairs of elements need to be evaluated, which has $\mathcal{O}\left(n_{\text{ele}}^2\right)$ complexity. Let us assume we apply a total of $n_{\text{GP,tot,ele-length}}$ integration points along the element length and $n_{\text{GP,tot,transverse}}$ integration points in the transversal, i.e., cross-sectional in-plane directions. Thus, the complexity of an approach based on full 6D numerical integration over the 3D volumes of the two interacting bodies (cf. Equation (2.12)) can be stated as

$$\mathcal{O}\left(n_{\text{ele}}^2 \cdot n_{\text{GP,tot,ele-length}}^2 \cdot n_{\text{GP,tot,transverse}}^4\right). \tag{4.21}$$

In contrast to that, the novel SSIP approach proposed in Section 4.2.2 reduces the dimensionality of numerical integration from six to two (cf. Equation (4.4)) and thus yields

$$\mathcal{O}\left(n_{\text{ele}}^2 \cdot n_{\text{GP,tot,ele-length}}^2\right) \tag{4.22}$$

complexity. The resulting difference between both clearly depends on the problem size, type of interaction and other factors. To get an impression, typical numbers for the total number of quadrature points in transverse dimensions based on the numerical examples of Section 4.5 are given as $n_{\text{GP,tot,transverse}} = 10 \ldots 100$. The gain in efficiency thus easily exceeds a factor of 10^4 and can be as large as a factor of 10^8. In addition to this tremendous saving from the inherent algorithmic complexity, the power law integrand has a smaller exponent due to the preliminary analytical integration in case of the SSIP approach. This in turn allows for a smaller number of integration points $n_{\text{ele}} \cdot n_{\text{GP,tot,ele-length}}$ for each of the two nested 1D integrations along the center-line, given the same level of accuracy. To give an example, the vdW interaction force scales with an exponent of -7 if formulated for two points (cf. Equation (2.4)) as compared to an exponent of $-7/2$ for two circular cross-sections (cf. Equation (4.9) for $m = 6$). This makes another significant difference, especially if very small separations – as typically observed for contacting bodies – are considered. The combination of high dimensionality and strong nonlinearity of the

integrand renders the direct approach of six-dimensional numerical quadrature to evaluate Equation (2.12) unfeasible for basically any problem of practical relevance. In fact, even a single evaluation of the vdW potential of two straight cylinders to serve as a reference solution turned out to be too computationally costly below some critical, small separation. See Section 4.5.1.1 for details on this numerical example. Note that although there might be more elaborate numerical quadrature schemes for these challenging integrands consisting of rational functions (see e.g. [55]), the basic problem and the conclusions drawn from this comparison of algorithmic complexities remain the same.

These cost estimates based on theoretical algorithm complexity and the experience from rather small academic examples considered in Section 4.5 show that the SSIP approach indeed makes the difference between feasible and intractable computational problems. This directly translates to the applicability to complex biopolymer as well as synthetic fibrous systems outlined in Section 1.1 and thus significantly extends the range of (research) questions that are accessible by means of numerical simulation.

4.4.6. Search algorithm and parallel computing

In order to find the relevant pairs of interaction partners, the same search algorithms as in the case of macroscopic contact (between beams or 3D solids) may be applied, however, the obvious difference lies in the search radius. For contact algorithms, a very small search radius covering the immediate surrounding of a considered body is sufficient, whereas for molecular interactions the search radius depends on the type of interaction and must be at least as large as the so-called cut-off radius. Only at separations beyond the cut-off radius, the energy contributions from a particular interaction are assumed to be small enough to neglect them. Depending on the interaction potential and partners, the range and thus cut-off radius can be considerably large which underlines the importance of an efficient search algorithm. In the scope of this work, a so-called bucket search strategy has been used, that divides the simulation domain uniformly into a number of cells or buckets and assigns all nodes and elements to these cells to later determine spatially proximate pairs of elements based on the content of neighboring cells. This leads to an algorithmic complexity of $\mathcal{O}(n_{\mathrm{ele}})$ and the search thus turned out to be insignificant in terms of computational cost as compared to the evaluation of pair interactions as discussed in the preceding section. See [164] for an overview of search algorithms in the context of computational contact mechanics.

To speed up simulations of large systems, parallel computing is a well-established strategy of ever increasing importance. Key to this concept is the ability to partition the problem such that an independent and thus simultaneous computation on several processors is enabled. In our framework, this partitioning is based on the same bucket strategy that handles the search for interaction partners. Regarding the evaluation of interaction forces, a pair (or set) of interacting beam elements is assigned to the processor which owns and thus already evaluates the internal and external force contribution of the involved elements. At processor boundaries, i.e., if the two interacting elements are owned by different processors, one processor is chosen to evaluate the interaction forces and the required information such as the element state vector of the element owned by the other processor is communicated beforehand. Upon successful evaluation of the element pair interaction, the resulting contribution to the element residual vector and stiffness

matrix is again communicated for the element whose owning processor was not responsible for the pair evaluation. See Appendix F for a brief overview and discussion of some important aspects of the computational framework used throughout this work.

4.5. Numerical examples

The set of numerical examples studied in this section aims to verify the effectiveness, accuracy and robustness of the proposed SSIP approach and the corresponding SSIP laws as a computational model for either steric repulsion, electrostatic or vdW adhesion and also a combination of those. Supplementary information on the code framework and the algorithms used for the simulations is provided in Appendix F.2.

4.5.1. Verification of the simplified SSIP laws using the examples of two disks and two cylinders

As a follow-up to the general discussion of using simplified SSIP laws in Section 4.3.1 and the proposal of specific closed-form analytic expressions in Sections 4.3.2 and 4.3.3, this section aims to analyze the accuracy in a quantitative manner. The minimal examples of two disks or two cylinders are considered in order to allow for a clear and profound analysis of either the isolated SSIP laws or its use within the general SSIP approach to modeling beam-beam interactions, respectively.

4.5.1.1. Verification for short-range volume interactions such as van der Waals and steric repulsion

Throughout this section, we consider the example of vdW interaction, but analogous results are expected for steric interaction or any other short-range volume interaction. Specifically, we will focus on the approximation quality of the proposed SSIP law from Section 4.3.2, which is based on the assumptions and resulting simplifications discussed in-depth in Section 4.3.1. Recall that, beside the obviously most important surface-to-surface separation g, the rotation of the cross-sections around the closest point α (quantified by the angle enclosed by their tangent vectors) and potentially also the rotation components β_1, β_2 (see Figure 4.2(a)) have been identified as relevant degrees of freedom, yet are neglected in the simplified SSIP law proposed in Section 4.3.2. The influence of these factors, separation and rotation, on the approximation quality will thus be analyzed numerically in the following.

Recall also from the discussions in Sections 4.3.1 and 4.3.2 that only the regime of small separations will be of practical relevance in the case of short-range interactions considered here. However, we include the regime of large separations in the following analyses, mainly because it will be interesting to see the transition from small to large separations and confirm that potential values indeed drop by several orders of magnitude as compared to the regime of small separations. Moreover, it is a question of theoretical interest and has been considered in literature on vdW interactions [90]. This regime of large separations can be treated without any additional

effort as described for the case of long-range interactions in Section 4.3.3 (where this regime is the decisive one) if we take into account the corresponding remark on volume interactions.

As presented in Section 2.3.2, analytical solutions for the special cases of parallel and perpendicular cylinders, for the regime of small and large separations, respectively, can be found in the literature [74, 125] and thus serve as reference solutions in this section. To the best of the author's knowledge, no analytical reference solution has yet been reported for the intermediate regime in between the limits of large and small separations. Another source for reference solutions is the full numerical integration of the point pair potential over the volume of the interacting bodies, however it is limited due to the tremendous computational cost. Only a combination of both analytical and numerical reference solutions thus allows for a sound verification of the novel SSIP approach and the proposed SSIP laws.

In the following analyses, either the SSIP, i.e., the interaction potential per unit length squared $\tilde{\tilde{\pi}}$ of a pair of circular cross-sections, the interaction potential per unit length $\tilde{\pi}$ of a pair of parallel cylinders or the interaction potential Π of a pair of perpendicular cylinders will be plotted as a function of the dimensionless surface-to-surface separation g/R, respectively. For simplicity, the radii of the beams are set to $R_1 = R_2 =: R = 1$.

Parallel disks and cylinders

Figure 4.4(a) shows the SSIP $\tilde{\tilde{\pi}}$ of two disks in parallel orientation, i.e., their normal vectors are parallel with mutual angle $\alpha = 0$, as a function of the normalized separation g/R. This is the simplest geometrical configuration and forms the basis of the proposed SSIP laws from Section 4.3. We thus begin our analysis with the verification of the used analytical solutions in the limit of small (green line, cf. Equation (2.19)) and large (red line, cf. Equation (2.20)) separations by means of a numerical reference solution (black dashed line with diamonds) obtained from 4D numerical integration of the point pair potential law (2.4).

Figure 4.4(a) confirms that both analytical expressions match the numerical reference solution perfectly well in the limit of large and small separations, respectively. As predicted, the interaction potential of two circular disks follows a power law with (negative) exponent 2.5 for small and 6 for large separations[4]. Note that all plots in this section are normalized with respect to the length scale R and the energy scale $\rho_1 \rho_2 C_{\mathrm{vdW}}$. It is remarkable that the obtained values span several orders of magnitude which illustrates the numerical challenges associated with power laws, especially in the context of numerical integration schemes as discussed already in Section 4.4.4. Moreover, it underlines that the regime of large separations is practically irrelevant in the case of short-range interactions, because the potential values are basically zero as compared to those obtained in the small separation regime.

Regarding the full range of separations, one may ask where either of the two expressions may be used given a maximal tolerable error threshold. As can be concluded from Figure 4.4(a), the resulting error is small for separations $g/R < 0.1$ with a relative error below 8% and $g/R > 10$ with a relative error below 7%. In the region of intermediate separations, the analytical solution for small separations seems to yield an upper bound, whereas the one for large separations seems to yield a lower bound for the interaction potential.

---

[4]Note that in the double logarithmic plot, a power law with exponent m is a linear function with slope m.
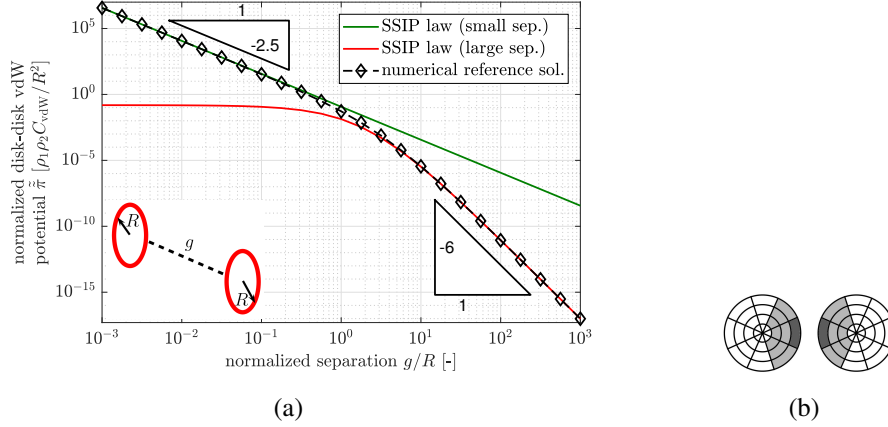
Figure 4.4.: (a) VdW interaction potential per unit length squared $\tilde{\tilde{\pi}}$ of two disks in parallel orientation over normalized surface separation g/R. The analytical expressions (2.19) (green line) and (2.20) (red line) used as SSIP laws throughout this work are verified by means of a numerical reference solution (black dashed line with diamonds). (b) Subdivision of circular cross-sections into integration sectors used to compute numerical reference solution. For rapidly decaying potentials, only the areas highlighted in dark and light gray considerably contribute to the total interaction potential. Figure taken from the author's article [61].

Let us have a look at the efficiency gain from using the analytical solutions. The numerical reference solution requires the evaluation of a 4D integral over both cross-sectional areas for a given separation g and has been carried out in polar coordinates. Assuming Gaussian quadrature with the same number of Gauss points $n_{\text{GP,tot,transverse}}$ in radial and circumferential dimension and for both cross-sections, this requires a total of $(n_{\text{GP,tot,transverse}})^4$ function evaluations. In contrast, the analytical expressions for the large and small separation limit, respectively, require only one function evaluation. This significant gain in efficiency is most pronounced for small separations, where the number of required Gauss points increases drastically due to the high gradient of the power law that needs to be resolved (see Section 4.4.4 for details). If the number of Gauss points is not sufficient, this leads to so-called underintegration and it has been observed that the obtained curve of the numerical reference solution erroneously flattens (because the contribution of the closest-point pair is not captured) or becomes steeper (because the contribution of the closest-point pair is overrated).

For these reasons, the computation of an accurate numerical reference solution shown in Figure 4.4(a) requires quite some effort. The integration domains were subdivided into integration sectors (see Figure 4.4(b)) in order to further increase the Gauss point density. But even in this planar disk-disk scenario requiring only 4D integration, a minimal separation of $g/R \approx 5 \times 10^{-3}$ has been reached, below which the affordable number of Gauss points was not sufficient to correctly evaluate the SSIP $\tilde{\tilde{\pi}}$ by means of full numerical integration[5]. For these very small separations, only the exact analytical dimensional reduction from 4D to 2D according to

---

[5]The maximum number of $n_{\text{GP,tot,transverse}} = 8 \times 32 = 256$ considered in the scope of this work led to several hours of computation time on a desktop PC for the evaluation of $\tilde{\tilde{\pi}}$ as a numerical reference solution for Figure 4.4(a).

Langbein (cf. [90] and Equation (A.7)) allowed to compute an accurate numerical reference solution. The analytical solutions for the disk-disk interaction potential (2.19) (and (2.20)), used as SSIP law in Equation (4.9) (and (4.13)), thus realize a significant increase in efficiency and indeed only enable the accurate evaluation of the interaction potential in the regime of very small separations. Note that such small separations are highly relevant if we consider fibers in contact since surface separations are expected to lie on atomic length scale in this case. For instance, the work of Argento et al. [7] mentions $g = 0.2 \, \text{nm}$ to be a typical value for contacting solid bodies and states that accurate numerical integration thus is the most challenging and in fact limiting factor for the numerical methods based on inter-surface potentials. As a reference value for the applications outlined in Section 1.1, the fiber radius R varies from several nm for DNA to mm for synthetic polymer fibers, resulting in a potentially very small normalized separation g/R. An example for the simulation of adhesive fibers in contact can be found in Chapter 7, which studies the peeling and pull-off behavior of two fibers attracting each other either via vdW or electrostatic forces.

As a next step, the interaction potential per unit length $\tilde{\pi}$ of two parallel straight beams is considered. The length of the beams is chosen sufficiently high such that it has no perceptible influence on the results and meets the assumption of infinitely long cylinders made to derive the analytical reference solution from [90]. Accordingly, a slenderness ratio $\zeta = l/R = 50$ is used in the regime of small separations, whereas $\zeta = l/R = 1000$ is used for large separations. Based
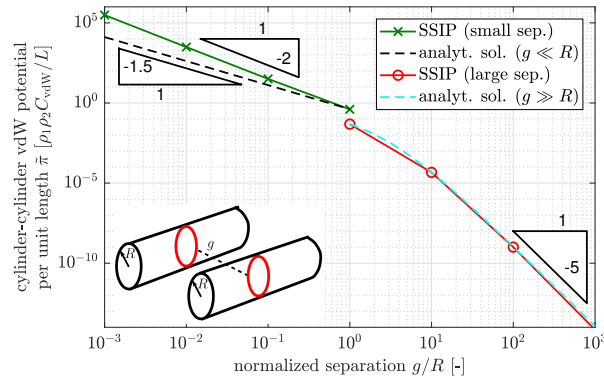
Figure 4.5.: VdW interaction potential per unit length $\tilde{\pi}$ of two parallel cylinders over normalized surface separation g/R. Figure taken from the author's article [61].

on the experience from the disk-disk scenario, it is not surprising that the full 6D numerical integration in this case exceeds the affordable computational resources by orders of magnitude and thus can not serve as a reliable reference solution. In fact, it was not possible to reproduce the theoretically predicted power law scaling in the regime of small separations despite using a number of Gauss points that led to computation times of several days. However, instead of the numerical reference solution, the analytical solution for infinitely long cylinders in the limit of very small (black dashed line, cf. Equation (2.14)) and very large separations (blue dashed line, cf. Equation (2.15)) serves as a reference in Figure 4.5. Note that as compared to the case of two circular disks the exponent of the power laws and thus the slope of the curves drops by one due to the integration over both cylinders' length dimension.

Interestingly, the SSIP approach using the simplified SSIP law from Section 4.3.2 (green line with crosses) does not yield the correct scaling behavior even in this case of parallel cylinders. This confirms the concerns from Section 4.3.1 that the simplified SSIP law neglecting any relative rotations of the cross-sections deteriorates the accuracy of the approach in the case of short-ranged interactions in the regime of small separations. Due to this specific scenario of parallel cylinders, this deterioration can be attributed solely to the rotation components $\beta_{1/2}$ (see Figure 4.2(a)) since the included angle of the cross-section normal vectors α is zero for every of the infinitely many pairs of cross-sections. Despite the correct trend of the resulting interaction potential as an inverse power law of the surface separation, it must thus be stated that the simplified SSIP law overestimates the strength of interaction and that the error increases with decreasing separation [6]. In the regime of large separations, however, the results for the SSIP approach (red line with circles) perfectly match the analytical reference solution (blue dashed line). This confirms the hypothesis from Section 4.3.1 that the relative rotation of cross-sections is negligible in this regime and a high accuracy can be achieved with the simplified SSIP law. Although being of little practical importance here due to the negligible absolute values, this is a first numerical evidence for the validity of the SSIP approach in general and its high accuracy even in combination with simplified SSIP laws in the particular case of long-range interactions to be considered in the following Section 4.5.1.2.

Perpendicular disks and cylinders

Up to now, we have only discussed the situation of parallel orientation of disks and cylinders. In the following, the accuracy of the simplified SSIP laws as well as the SSIP approach for twisted configurations will be analyzed by considering the most extreme configuration of perpendicular disks and cylinders. Again, computing a reference solution by means of full numerical integration was only affordable for the 4D case of two disks. The results for perpendicular disks shown in Figure 4.6(a) confirm that there is no difference between perpendicular and parallel orientation for large separations and the scaling behavior of the numerical reference solution (black dashed line with diamonds) with exponent 6 is met by the simplified SSIP law (red line, cf. Equation (2.20)). On the other hand, there is a remarkable difference in the scaling behavior for small separations. While the interaction potential of two parallel disks, which is the underlying assumption of the proposed SSIP law (green line, cf. Equation (2.19)), follows an inverse 2.5 power law, the numerical reference solution (black dashed line with diamonds) suggests that this behavior changes for perpendicular disks to an inverse 2 power law. This time, the difference in results can be attributed to the relative rotation α, i.e., the angle included by the cross-section normal vectors and again the error of the proposed simplified SSIP law increases with decreasing separation.

Finally, the scenario of perpendicular cylinders is considered in Figure 4.6(b) plotting the total interaction potential Π as a function of the normalized smallest surface separation g/R. As discussed before, the computational cost of the full 6D numerical integration is too high to compute a reliable reference solution in the case of two 3D bodies and we resort to the ana-

---

[6] Note that the numerical integration error has been ruled out as cause for this behavior by choosing a high number of Gauss points $n_{\text{GP,tot,ele-length}} = 2 \times 50 = 100$ for each of the 64 elements used to discretize each cylinder. A further increase of n_{GP} by a factor of five does not change the results using double precision.
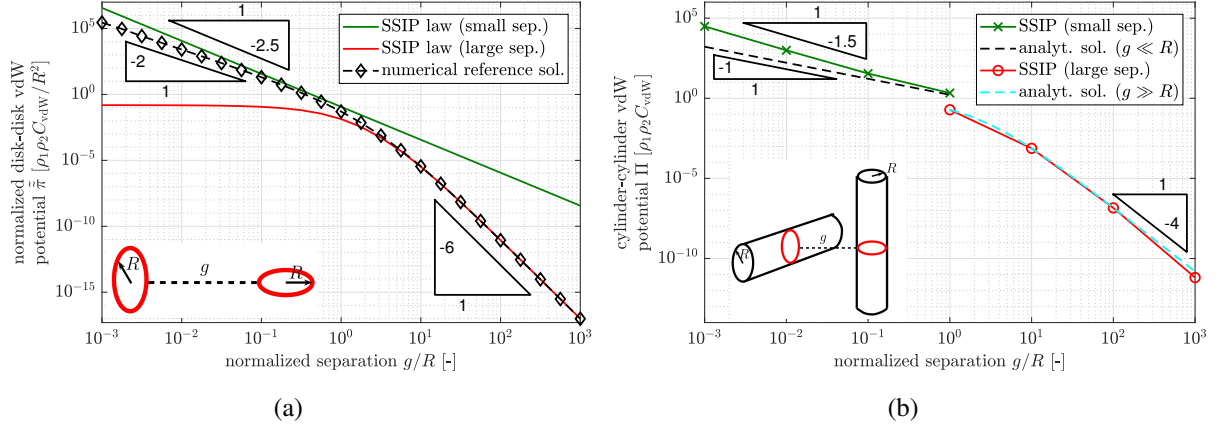
Figure 4.6.: (a) VdW interaction potential per unit length squared $\tilde{\tilde{\pi}}$ of two perpendicular disks and (b) vdW interaction potential Π of two perpendicular cylinders, plotted over the normalized surface separation g/R, respectively. Figure taken from the author's article [61].

lytical solutions for the limits of very small and very large separations, respectively. Note that in contrast to the case of infinitely long *parallel* cylinders (cf. Figure 4.5) the total interaction potential of infinitely long perpendicular cylinders is finite and the result thus has dimensions of energy instead of energy per length. Perpendicular cylinders are worth to consider because they trigger both of the sources of errors that have been analyzed individually so far - neglecting relative rotations α as well as $\beta_{1/2}$ in the simplified SSIP law. In short, the resulting accuracy is similar as for either perpendicular disks or parallel cylinders. In the decisive regime of small separations, the SSIP approach based on the simplified SSIP law (green line with crosses) fails to reproduce the correct scaling behavior of the analytical reference solution (black dashed line, cf. Equation (2.16)), whereas in the regime of large separations, the SSIP approach based on the simplified SSIP law (red line with circles) perfectly matches the analytical reference solution (blue dashed line, cf. Equation (2.17)).

Conclusions

First, this section reveals that full 6D numerical integration to compute the total interaction potential of slender continua is by orders of magnitude too expensive and can thus not reasonably be used as a numerical reference solution even in minimal examples of one pair of cylinders. At most, 4D numerical integration required for disk-disk interactions allows to compute numerical reference solutions for the intermediate regime of separations where no analytical solutions are known. This underlines the importance of reducing the dimensionality of numerical integration to 2D as achieved by the proposed SSIP approach in order to enable the simulation of large systems as well as a large number of time steps.

Second, the thorough analysis of the accuracy resulting from using the proposed simplified SSIP law – neglecting the cross-section rotations – reveals that one has to distinguish between the regime of small and large separations. In the decisive regime of small separations, we find that the scaling behavior deviates from the analytical prediction for perpendicular disks and par-

allel as well as perpendicular cylinders and that the resulting error increases with decreasing separation. An instant remedy of this limitation could be a calibration, i.e., a scaling of the prefactor k in the simple SSIP law, to fit a given reference solution within a small range of separations (e.g. around the equilibrium distance of the LJ potential). For the numerical example studying the peeling and pull-off of adhesive fibers (cf. Section 7.4.5), this pragmatic procedure will be shown to reproduce the global system response very well. Still, it would be valuable to include the relative rotations of the cross-sections in the applied SSIP law to obtain the correct asymptotic scaling behavior. To the best of the author's knowledge, no according analytical closed-form expression has been published yet and the like is far from trivial to derive. The derivation of such an enhanced interaction law including the orientation will be presented in Section 5.2 in the context of the slightly different beam interaction formulation to be proposed in the following Chapter 5. Because this alternative formulation is specialized in short-ranged interactions, it turns out to be more efficient for this class of interactions and the improvement of the accuracy expected from including the cross-section orientation will therefore be realized in that context first. However, also the SSIP laws considered here would benefit from the increased accuracy and including the cross-section orientation is thus considered a valuable future extension. As mentioned before, the regime of large separations is of little practical relevance in the case of short-range volume interactions, however, it is of some theoretical interest and the corresponding findings and conclusions of this regime will hold true also for long-range interactions such as electrostatics to be considered in the following section. Here, the results are in excellent agreement with the theoretically predicted power laws for parallel as well as perpendicular disks and cylinders.

4.5.1.2. Verification for long-range surface interactions such as electrostatics

Turning to long-range interactions, again parallel and perpendicular disks and cylinders will be considered in order to analyze the accuracy of the simplified SSIP law from Section 4.3.3 both individually as well as applied within the general SSIP approach proposed in Section 4.2.2. As before, Coulombic surface interactions are chosen as specific example, however, the conclusions are expected to hold true also for other types of long-range interactions. As compared to the preceding section, the computation of a numerical reference solution simplifies mainly due to the reduction from volume to surface interactions but also due to the smaller gradient values, which need to be resolved in the regime of small separations thus requiring less integration points. This allows for a verification by means of a numerical reference solution also in the case of cylinder-cylinder interaction.

Figure 4.7 shows the results for the simplified SSIP law obtained from the monopole-monopole interaction of two disk-shaped cross-sections in Section 4.3.3 (red line) and a numerical reference solution (black dashed line with diamonds). As expected, the proposed SSIP law excellently matches the reference solution in the regime of large separations, both for the parallel as well as perpendicular configuration. In both cases, the relative error is below 7% already for $g/R = 1$. The most important and remarkable result of this section, however, is the following. The inevitable error of the simplified SSIP law in the regime of small separations does not carry over to beam-beam interactions as shown in Figure 4.8. For both parallel as well as perpendicular cylinders, the results from the SSIP approach using this simplified SSIP law from Section 4.3.3
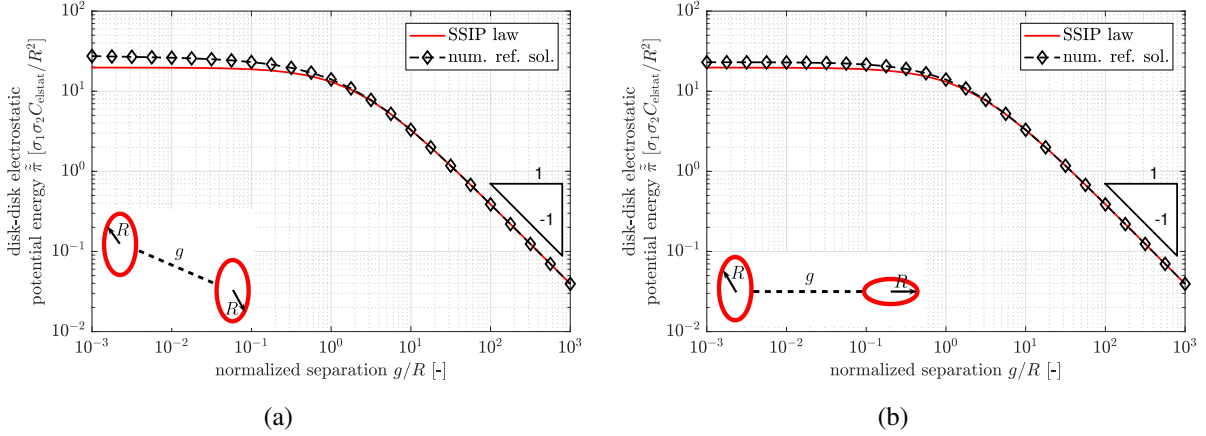
Figure 4.7.: Electrostatic interaction potential per length squared $\tilde{\tilde{\pi}}$ of (a) two parallel disks and (b) two perpendicular disks, plotted over the normalized surface separation g/R, respectively. Figure taken from the author's article [61].

(red line with crosses) agree very well with the numerical reference solution (black dashed line with diamonds) over the entire range of separations. This confirms the theoretical considerations from Section 4.3.1 arguing that the beam-beam interaction will be dominated by the large number of section pairs with large separations, which outweigh the contributions of the few section pairs with smallest separations.

A closer look reveals that the relative error for the parallel cylinders is below 0.3% even for the smallest separation $g/R = 10^{-3}$ considered here. For the presumably worst case of perpendicular cylinders, this deviation is even smaller with a relative error of 0.03%, which can be explained by the following two reasons. First, a comparison of Figure 4.7(a) and 4.7(b) reveals that the accuracy of the simplified SSIP law in the regime of small separations is higher for perpendicular orientation, which can be regarded a happy coincidence. And second, the large majority of all section pairs has a larger separation (which according to Figure 4.7 is the regime of higher accuracy) as compared to the case of parallel cylinders.

Note that – unlike in the case of short-range interactions – here the total interaction potential is considered also for the parallel cylinders. Due to the long range of interactions, the interaction potential per length depends on the length of the cylinders and is thus no representative quantity. For Figure 4.8, a slenderness ratio of $\zeta = L/R = 50$ is chosen exemplarily. The two nested 1D integrals along the cylinder length dimensions are evaluated using $n_{\text{GP,ele-length}} = 5$ Gauss points for each of the 64 elements used to discretize each cylinder. Additionally, $n_{\text{GP,circ}} = 8 \times 32 = 256$ Gauss points over the circumference of each disk are used to compute the numerical reference solution. In all cases, it has been verified that the numerical integration error does not influence the results noticeably.

At this point, recall from Section 4.3.3 that the accuracy of the applied SSIP law can still be increased whenever deemed necessary by including more terms of the multipole expansion of the cross-sections. However, because the results of this section show a high level of accuracy and the resulting simplification is significant, the simplified SSIP law seems to be the best compromise
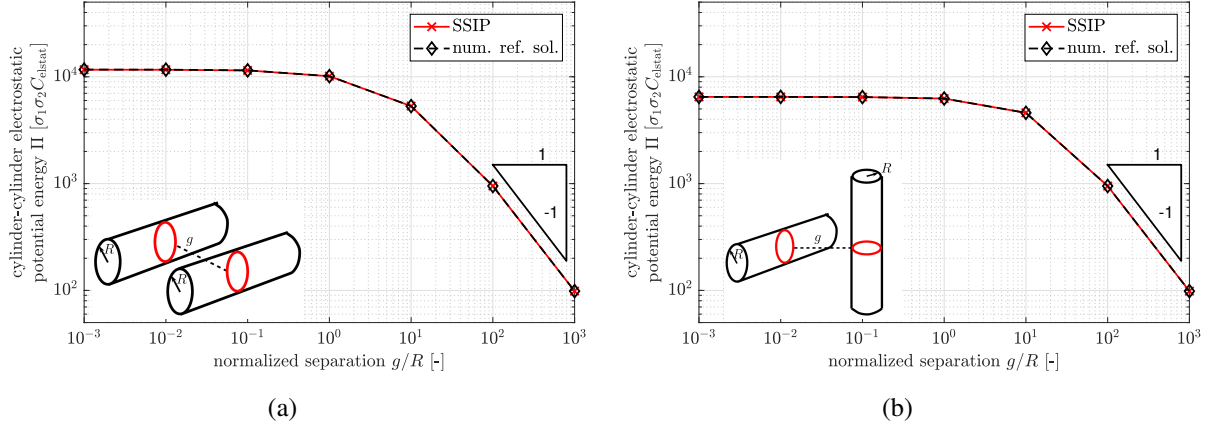
Figure 4.8.: Electrostatic interaction potential Π of (a) two parallel cylinders and (b) two perpendicular cylinders, plotted over the normalized surface separation g/R, respectively. The slenderness ratio of the cylinders is $\zeta = L/R = 50$. Figure taken from the author's article [61].

for our purposes. To conclude this section it can thus be stated that the novel SSIP approach as proposed in Section 4.2.2 in combination with the simplified SSIP law from Section 4.3.3 is a simple, efficient, and accurate computational model for long-range interactions of slender fibers. In the following, it will be applied to first numerical examples of *deformable* slender fibers in Sections 4.5.3 and 4.5.4.

4.5.2. Repulsive steric interaction between two contacting beams

This numerical example aims to demonstrate the general ability of the proposed method to preclude penetration of two slender bodies that come into contact under arbitrary mutual orientation in 3D. No adhesive forces are considered in this example. The setup is inspired by Example 1 in [111] where the macroscopic, so-called all-angle beam contact (ABC) formulation is used to account for the non-penetrability constraint. Here, we model the contact interaction based on the repulsive part of the LJ interaction potential (2.8). More specifically, we apply the novel SSIP approach as proposed in Section 4.2.2 in combination with the SSIP law proposed in Section 4.3.2. The parameter specifying the strength of repulsion is set to be $k\rho_1\rho_2 = 10^{-16}$. To be consistent throughout this chapter, we apply Hermitian Simo-Reissner beam elements instead of the torsion-free Kirchhoff elements used in [111]. As compared to the original example, this requires us to replace the hinged support of the upper beam by clamped end Dirichlet boundary conditions in order to eliminate all rigid body modes in this quasi-static example. The same number of three finite elements for the upper, deformable beam and one element for the lower, rigid beam is used.

A sequence of the resulting simulation snapshots is shown in Figure 4.9. As expected, the two beams do not penetrate each other in any of the various mutual orientations throughout the

(a) initial configuration   (b) time $t = 1.0$ (c) time $t = 1.5$

(d) time $t = 2.0$ (e) time $t = 2.5$ (f) time $t = 3.0$
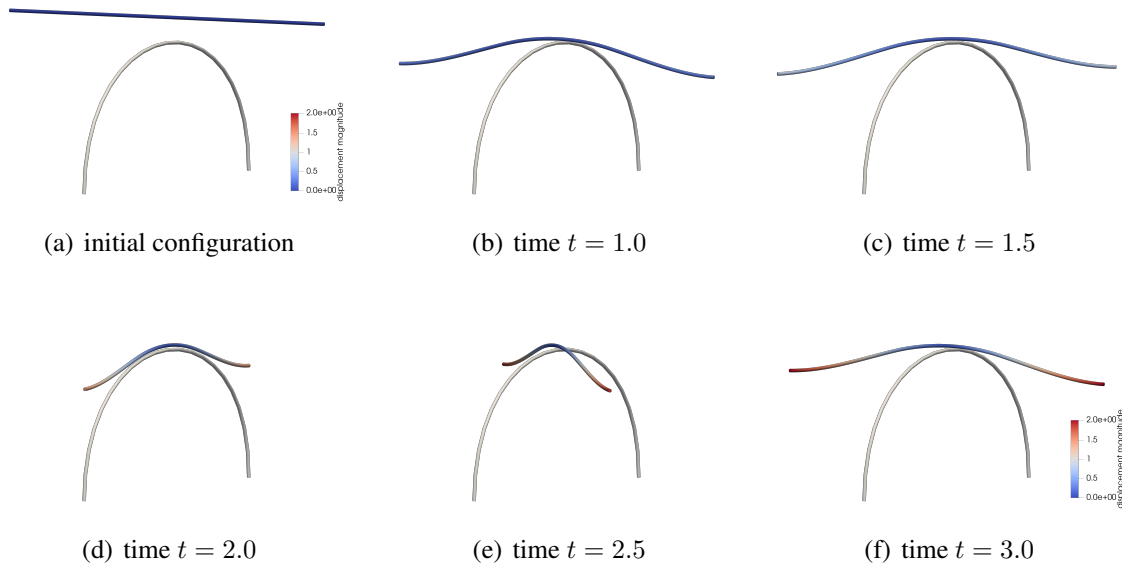
Figure 4.9.: Simulation snapshots: a straight deformable beam rotating on a rigid arc. Figure taken from the author's article [61].

simulation. Figure 4.10 visualizes the contact force distributions[7] in the most interesting time span before the beams reach the parallel orientation at time $t = 2.0$. The force distribution

(a) time $t = 1.95$ (b) time $t = 1.97$ (c) time $t = 1.99$ (d) time $t = 2.0$
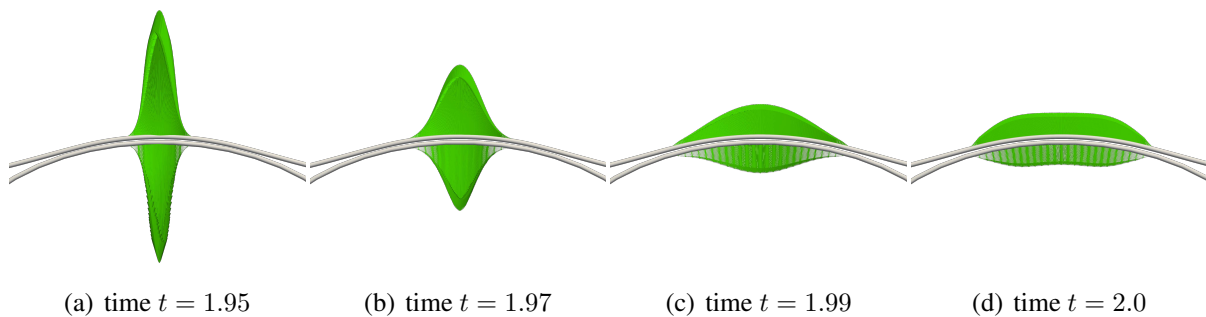
Figure 4.10.: Evolution of contact force distribution in the regime of small contact angles between the beam axes. Each beam element is divided in 100 integration segments with 10 Gauss points each in the simulation shown here. Figure taken from the author's article [61].

quickly changes from a point-like force for large mutual angles to a broad distributed load for parallel beam axes. Note also that the line load has a three dimensional shape where the out-of-plane component decreases with decreasing mutual angle until both beam axes and thus also the

---

[7]More precisely, the vectorial line load with dimensions of force per unit length is visualized as an arrow at each integration point. The force resultant therefore equals the integral over the contour curve defined by the arrows' tips (i.e. the area under this curve), and not the vector sum of all arrows shown. This is important to understand because the number of visible arrows per unit length depends on the discretization and is thus higher for the upper, deformable beam.

line loads lie in one plane at $t = 2.0$. Another remarkable result is the symmetry between the line loads on both fibers. It nicely confirms that the novel approach indeed fulfills the expected *local* equilibrium of interaction forces in good approximation. In contrast to existing, macroscopic formulations for beam contact, this is not postulated a priori in the SSIP approach and hence is a valuable verification at this point. See [140] for a comprehensive discussion of this important topic in the context of contact between 3D solids described by inter-surface potentials. The *global* equilibrium of contact forces on the other hand is fulfilled exactly, as can be concluded from the global conservation of linear momentum that can be shown analytically as outlined in Section 4.4.2. In this numerical example, we found that the sum of all reaction forces in either of the spatial dimensions is indeed zero with a maximal residuum of 10^{-10} throughout all simulations considered here, which confirms the statement numerically.

Figure 4.11 shows the resulting vertical reaction force as well as the interaction potential over time. Due to the inverse-twelve power law and the extremely small separations of the interacting
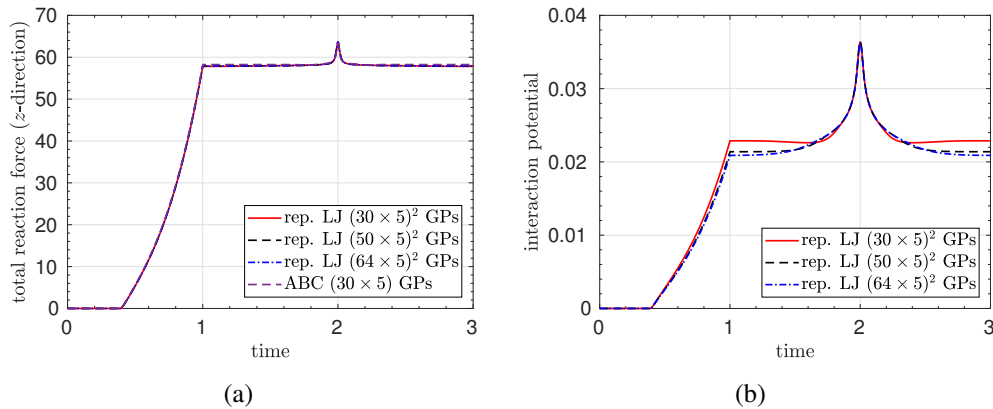
Figure 4.11.: (a) Reaction force and (b) interaction potential over time. Figure taken from the author's article [61].

bodies, the numerical integration of the disk-disk interaction forces is very challenging and we studied the influence of the number of Gauss points. For this purpose, the number of integration segments per element with five Gauss points each is set to 30, 50, or 64, respectively. Interestingly, the interaction potential shown in Figure 4.11(b) seems to be more sensitive with respect to the integration error than the vertical reaction force shown in Figure 4.11(a) despite the fact that the latter has a higher inverse power law exponent. Presumably, this is due to the fact that the reaction force is dominated by the bending deformation of the beams. For reference, the reaction force obtained by using the macroscopic ABC formulation is shown as well and is in excellent agreement with the one resulting from the repulsive part of the LJ interaction potential.

A more comprehensive comparison of this novel SSIP approach to model contact between beams based on (the repulsive part of) the molecular LJ interaction and existing, macroscopic formulations based on heuristic penalty force laws is a highly interesting subject that is worth to investigate in the future. It is expected that both the numerical formulations for the micro- and for the macroscale could benefit from the inspirations of such a comparative analysis. Some first theoretical considerations on this topic will be presented in Section 6.2 resulting in a first

recommendation of which kind of formulation to use in which scenarios. The decision criteria elaborated therein will be followed in the numerical examples and practical applications to be considered throughout the remainder of this work.

4.5.3. Two initially straight, deformable fibers carrying opposite surface charge

The following example consists of two initially straight and parallel, deformable fibers that attract each other due to their surface charge of opposite sign. Its setup is kept as simple as possible to allow for an isolated and clear analysis of the physical effects as well as the main characteristics of the proposed SSIP approach. In a first step presented here, the interplay of elasticity and electrostatic attraction in the regime of large separations is studied. Additionally, the scenario of separating these adhesive fibers starting from initial contact will be considered in the dedicated Chapter 7, because this fundamental problem turned out to show a surprisingly rich and complex system behavior including a variety of different effects that will be investigated in depth.

In this numerical example, we are interested in the static equilibrium configurations for varying attractive strength. As shown in Figure 4.12(a), two straight beams of length $l = 5$ are aligned with the global y-axis at an inter-axis separation $d = 5$. Both are simply supported

(a) Problem setup: undeformed configuration.

(b) Static equilibrium configurations for varying attractive strength. Solution for beam centerlines and corresponding value of the potential law prefactor k shown in the same color.
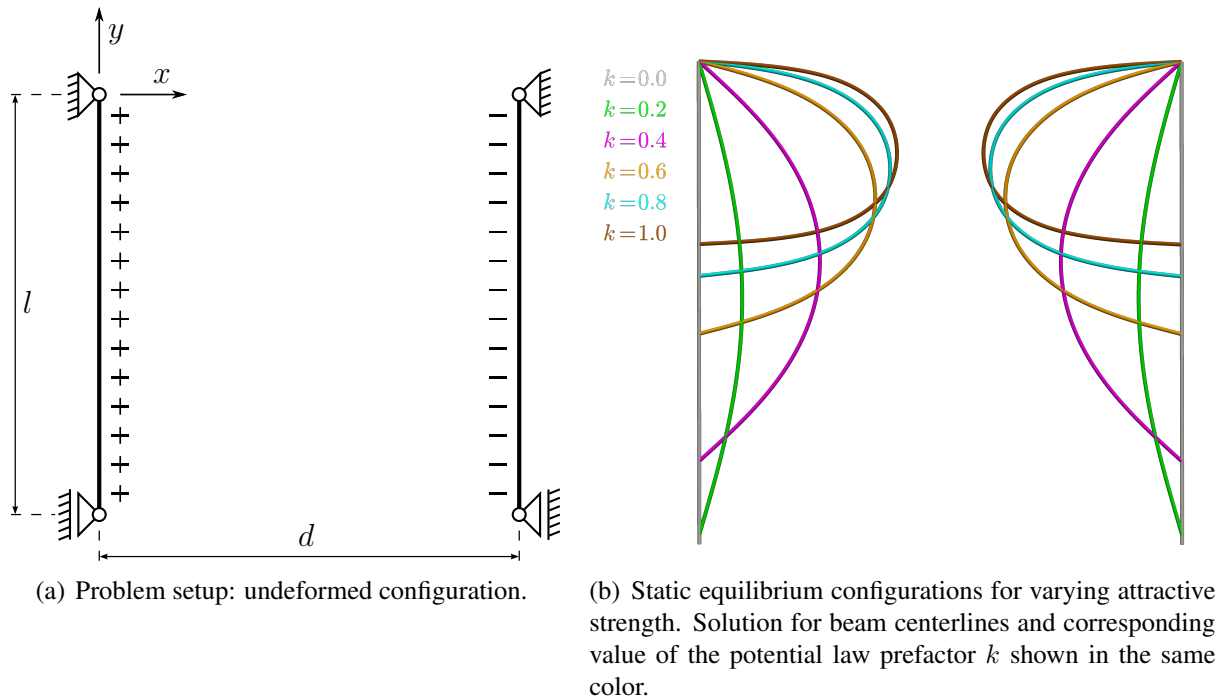
Figure 4.12.: Two parallel beams with constant surface charge density (left beam positive, right beam negative). Figure taken from the author's article [61].

and restricted to move only within the xy-plane and rotate only around the global z-axis. The beams have a circular cross-section with radius $R = 0.02$ which results in a slenderness ratio of $\zeta = 250$. Cross-section area, area moments of inertia and shear correction factor are computed

using standard formula for a circle. A hyperelastic material law with Young's modulus $E = 10^5$ and Poisson's ratio $\nu = 0.3$ is applied. In terms of spatial discretization, we use five Hermitian Simo-Reissner beam elements per fiber (see Section 3.2.2 for details on this element formulation). Electrostatic interaction is modeled via the SSIP approach as presented in Section 4.2.2 and applied to long-range Coulomb interactions in Section 4.3.3. Both beams are nonconducting with a constant surface charge density of $\sigma_1 = 1.0$ and $\sigma_2 = -1.0$, respectively. For simplicity, we vary the prefactor k of the underlying Coulomb law $\Phi(r) = k\,r^{-1}$ to vary the strength of attraction. However, as becomes clear from Equation (4.15), this is equivalent to a variation of surface charge densities because in our case the product of these quantities is a constant prefactor in all relevant equations. In order to evaluate the electrostatic force and stiffness contributions, Gauss quadrature with two integration segments per element and ten Gauss points per integration segment is applied. This turns out to be fine enough to not change the presented results perceptibly. More precisely, the difference in the displacement of the beam midpoint for $n_{\mathrm{GP}} = (2 \times 10)^2$ as compared to $(2 \times 32)^2$ is below 10^{-8}. No cut-off radius is applied here, i.e., the contributions of all Gauss point pairs are evaluated and included.

Figure 4.12(b) finally shows the resulting static equilibrium configurations for different levels of attractive strength. As expected, the beams are increasingly deflected and pulled towards each other if the prefactor of the applied Coulomb law k and thus the attractive strength is increased. Like the problem definition, also all the solutions are perfectly symmetric with respect to the vertical axis of symmetry located at $x = d/2$. Moreover, the centerline curves of each individual solution show a horizontal axis of symmetry defined by the position of the two beam midpoints in the respective deformed state. As a consequence, the vertical force components in the system cancel and the vertical reaction forces vanish. This also becomes clear when looking at the visualization of the resulting electrostatic forces as shown exemplarily for $k = 1.0$ in Figure 4.13(a). Additionally, the forces acting on the Gauss point of one beam caused by the interaction with one finite element of the other beam are visualized individually in Figure 4.13(b). This representation illustrates the nature of the SSIP approach, which is based on two nested 1D numerical integrals that are evaluated element pair-wise. Accordingly, we can identify five force contributions at each Gauss point, one for each of the five beam elements on the opposing fiber. As expected, the magnitude of these individual forces decays with the distance and the contributions of the closest element pair shown in an isolated manner in Figure 4.13(c) constitute the largest part of the total electrostatic load on the beams and are clearly larger than the contributions of the next-nearest element pair shown in Figure 4.13(d). However, the relatively long range of electrostatic forces yields a smooth force distribution along the centerlines and we can identify non-zero force contributions even at the most distant Gauss points right next to the supports in Figure 4.13(a). As mentioned above, a quantitative analysis of the resulting horizontal reaction forces will be presented in Section 7.2.2.

To conclude this example of two charged, attractive beams, we briefly look at the nonlinear solver. Newton's method without any adaptations is used here to allow for a clear and meaningful analysis of nonlinear convergence behavior. The solutions for $k \leq 0.4$ can be found within one load step which is a remarkable result given the resulting large deflection of the beams shown in Figure 4.12(b) and the strong nonlinear nature of the system. For stronger attractive forces, the strength of electrostatic attraction was ramped up in up to ten equal steps $\Delta k = 0.1$. As convergence criteria, it has been enforced that both the Euclidean norm of the residual vector
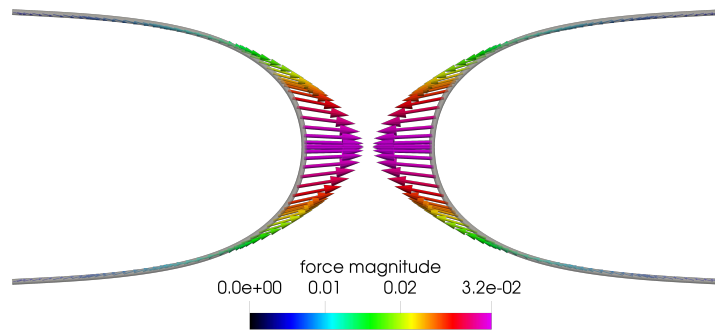
(a) Resulting electrostatic forces evaluated at the Gauss points.
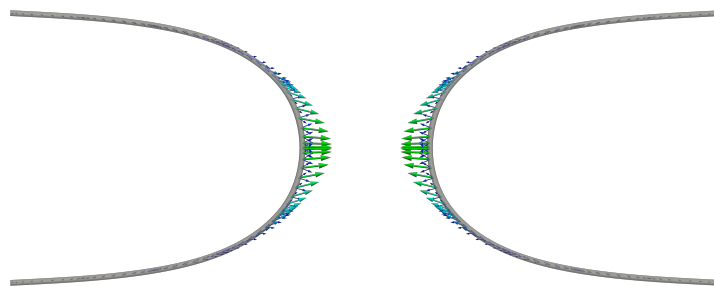
(b) Individual electrostatic force contributions of all element pairs.
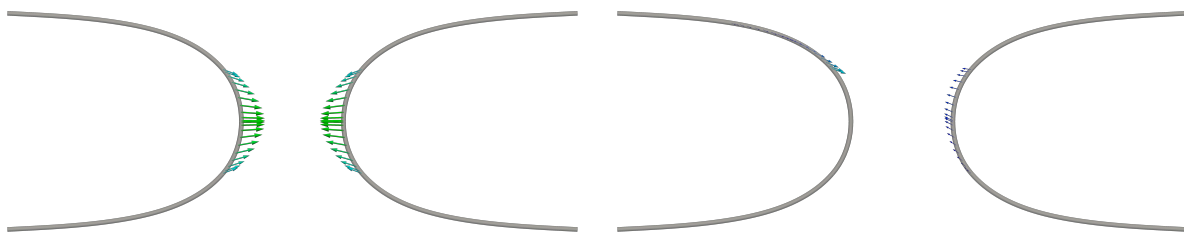
(c) Electrostatic force contributions of the closest element pair.

(d) Electrostatic force contributions of the next-nearest pair.

Figure 4.13.: Electrostatic forces acting on the beams for $k = 1.0$. Color indicates force magnitude. Figure taken from the author's article [61].

fulfills $\|\mathbf{R}\| < 10^{-10}$ and the norm of the iterative displacement update vector fulfills $\|\Delta\mathbf{X}\| < 10^{-8}$. In fact, this combination leads to $\|\mathbf{R}\| < 10^{-12}$ in almost all equilibrium configurations shown here.

4.5.4. Two charged deformable fibers dynamically snap into contact

Due to the high gradients in the inverse power laws, molecular interactions give rise to highly dynamic systems. This is a first, simple example for a dynamic system consisting of two oppositely charged fibers with a hinged support at one end each, that will snap into contact. In the initial configuration shown in Figure 4.14(a), the straight fibers include an angle of $45°$ and their axes are separated by $5R$ in the out-of-plane direction z. With a cross-section radius $R = 0.02$

(a) Problem setup. (b) Energy over time.
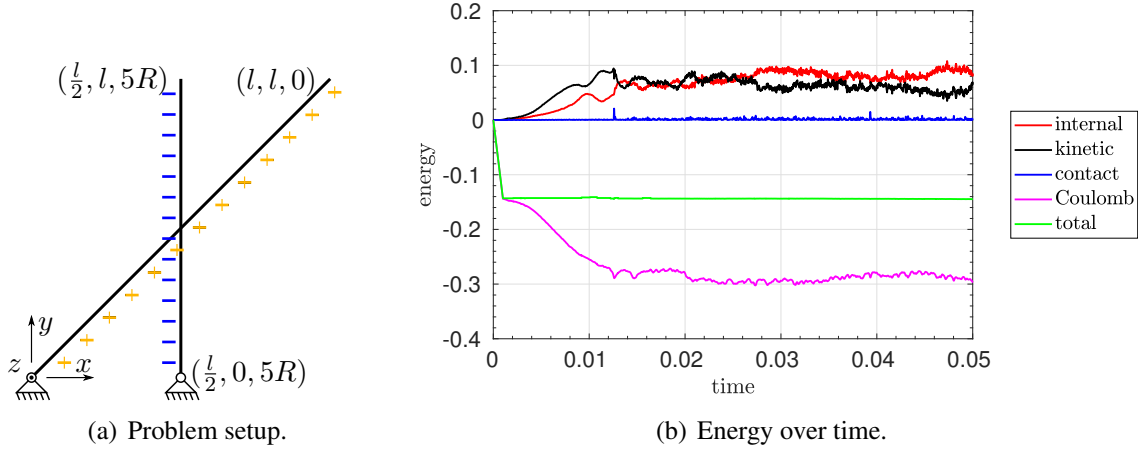
Figure 4.14.: Two oppositely charged, crossed beams dynamically snap into contact. Figure taken from the author's article [61].

and length l set to $l = 5$, they have a high slenderness ratio of $\zeta = 250$ and 354. Each of the fibers is discretized by 10 Hermitian Simo-Reissner beam elements (cf. Section 3.2.2) and the material parameters are chosen to be $E = 10^5$, $\nu = 0.3$, and $\rho = 10^{-3}$. The fibers carry a constant, opposite surface charge $\sigma_{1/2} = \pm 1.0$ and interact via the Coulomb potential law stated in Equation (2.3) with the prefactor set to $C_{\text{elstat}} = 0.4$. In order to start from a stress-free initial configuration, the charge of one of the fibers is ramped up linearly within the first 100 time steps. We apply the SSIP approach as proposed in Section 4.2.2 and applied to long-ranged interactions in Section 4.3.3. A total of 5 integration segments per element with 10 Gauss points each is used to evaluate these electrostatic contributions. The contact interaction between the fibers is modeled by the line contact formulation proposed in [110], using a penalty parameter $\varepsilon = 10^3$ and 20 integration segments per element with 5 Gauss points each for numerical integration. An undetected crossing of the fiber axes is prevented by applying the modified Newton method limiting the maximal displacement increment per nonlinear iteration to $R/2$ (see Appendix F.2 for details).

In terms of temporal discretization, we apply the Generalized-alpha scheme for Lie groups as proposed in [20] and set the spectral radius at infinite frequencies to $\rho_\infty = 0.9$ for small numerical damping. A small time step size of $\Delta t = 10^{-5}$ is applied to account for the highly dynamic behavior of this system.

Figure 4.15 shows a sequence of simulation snapshots where the electrostatic forces on both fibers are visualized as green arrows. We observe a large variety of mutual orientations of the

(a) initial configuration

(b) time $t = 1 \times 10^{-3}$, ramp-up of charge completed

(c) time $t = 5 \times 10^{-3}$

(d) time $t = 1 \times 10^{-2}$

(e) time $t = 2 \times 10^{-2}$

(f) time $t = 4 \times 10^{-2}$

(g) time $t = 6 \times 10^{-2}$

(h) time $t = 8 \times 10^{-2}$

(i) time $t = 1 \times 10^{-1}$
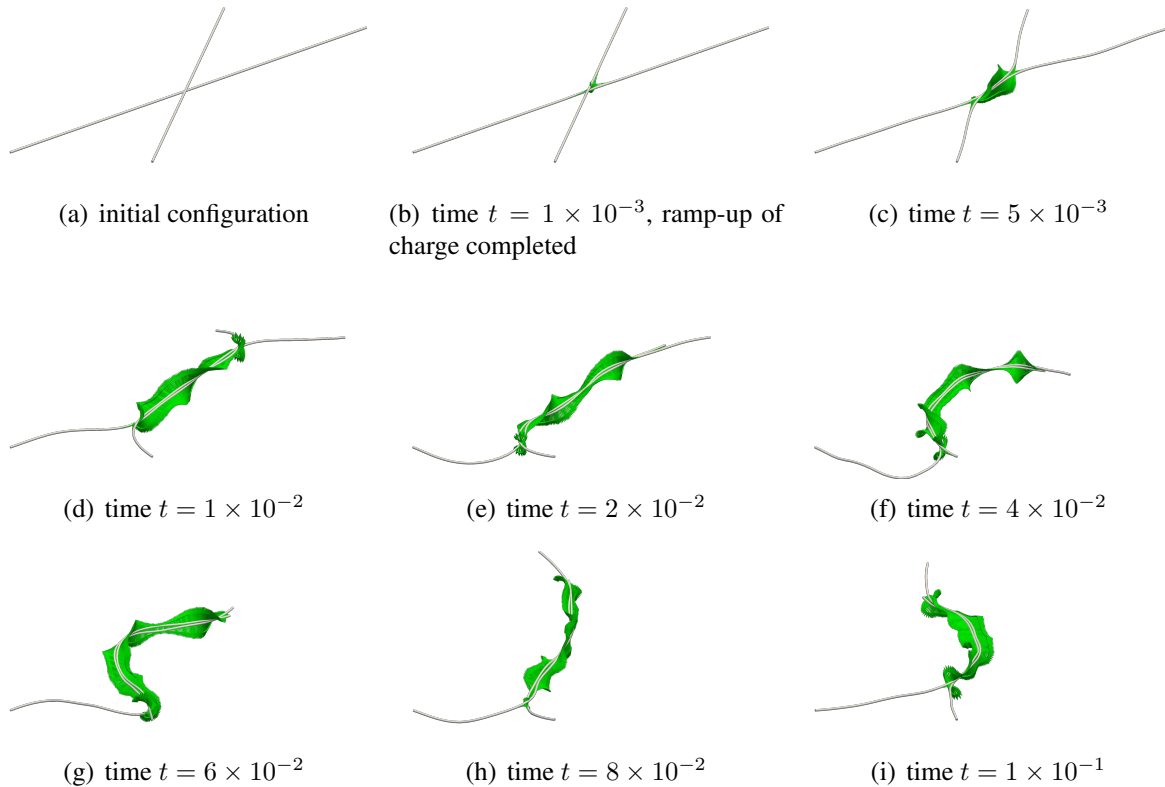
Figure 4.15.: Sequence of simulation snapshots. Electrostatic forces acting on both fibers shown in green. Figure taken from the author's article [61].

two fibers and a strong coupling of adhesive, repulsive and elastic forces that demonstrate the effectiveness and robustness of the proposed SSIP approach. Most importantly, we see that the total system energy is preserved with very little deviation of $\pm 2\%$ as shown in Figure 4.14(b). Note that the negative energy values result from defining the zero level of the interaction potential at infinite separation as described in Section 2.1. Based on this numerical example, it can thus be concluded that the novel SSIP approach proves to be effective as well as robust in a highly dynamic example with large deformations and arbitrary mutual orientations of the fibers in 3D.

4.6. Conclusions and outlook

This chapter proposes the first 3D beam-beam interaction model for molecular interactions such as electrostatic, van der Waals (vdW) or repulsive steric forces between curved slender fibers undergoing large deformations. While the general interaction model is not restricted to a specific beam formulation, in the present work it is combined with the geometrically exact beam theory and discretized via the finite element method. A direct evaluation of the total interaction potential for general 3D bodies requires the integration of contributions from molecule or charge distributions over the volumes of the interaction partners, leading to a 6D integral (two nested 3D integrals) that has to be solved numerically. The central idea of the novel approach is to formulate reduced interaction laws for the resultant interaction potential between a pair of cross-sections of two slender fibers such that only the two 1D integrals along the fibers' length directions have to be solved numerically. This section-section interaction potential (SSIP) approach therefore reduces the dimensionality of the required numerical integration from 6D to 2D and yields a significant gain in efficiency, which only enables the simulation of relevant time and length scales for many practical applications.

Being the key to this SSIP approach, the analytical derivation of the specific SSIP laws is based on careful consideration of the characteristics of the different types of molecular interactions, most importantly their point pair potential law and the range of the interaction. In a first step, the most generic form of the SSIP law, which is valid for arbitrary shapes of cross-sections and inhomogeneous distributions of interacting points (e.g. atoms or charges) within the cross-sections has been presented in Section 4.2 before the focus was laid on specific SSIP law expressions for dedicated applications in Section 4.3. Considering the practically relevant case of homogeneous, disk-shaped cross-sections, Section 4.3.1 has discussed the advantages as well as limitations of possible simplifications of the SSIP law, finally leading to pleasantly simple SSIP laws that solely depend on the scalar separation of the cross-section centroids and in particular neglect the cross-sections' mutual orientation. In this manner, simple SSIP laws for short-range volume interactions such as vdW or steric interactions (Section 4.3.2) and for long-range surface interactions such as Coulomb interactions (Section 4.3.3) are obtained, which have been used and further analyzed in the remainder of the chapter. It should be emphasized that postulating the general structure of the SSIP law and fitting the free parameters to e.g. experimental data is one of the promising alternatives to the strategy of analytical derivation of the SSIP law as applied throughout this work. It is also important to highlight that the general SSIP approach can be seamlessly integrated into an existing finite element framework for solid mechanics. In particular, it does neither depend on any specific beam formulation nor the applied spatial discretization scheme and in the context of the present work, it has exemplarily been used with geometrically exact Kirchhoff-Love as well as Simo-Reissner type beam finite elements. Likewise, it is independent of the temporal discretization and has been used along with static and (Lie group) Generalized-Alpha time stepping schemes as well as inside a Brownian dynamics framework. In order to remedy the characteristic singularity of inverse power interaction laws in the limit of zero separation, a numerical regularization of the LJ SSIP law has been proposed, which leads to a significant increase in robustness and efficiency, saving a factor of five in the number of nonlinear iterations while yielding identical results.

The accuracy of the proposed SSIP laws as well as the general SSIP approach has been studied in a thorough quantitative analysis using analytical as well as numerical reference solutions for the case of vdW as well as electrostatic interactions. It is found that a very high level of accuracy is achieved for long-range interactions such as electrostatics both for the entire range of separations as well as all mutual angles of the fibers from parallel to perpendicular. In the case of short-range interactions, however, the derived SSIP law without cross-section orientation information slightly overestimates the asymptotic power-law exponent of the interaction potential over separation. As a pragmatic solution, a calibration of the simple SSIP law has been proposed to fit a given reference solution in the small yet decisive range of separations around the equilibrium distance of the LJ potential. As will be shown for the fundamental numerical example of peeling two adhesive fibers in Section 7.4.5, this strategy leads to a very good agreement in the force response on the system level. While this accuracy might already be sufficient for certain real world applications, the derivation of reduced interaction laws including the cross-section rotations is considered an important next step. In the present work, the derivation of such an enhanced interaction law including the orientation will be presented in Section 5.2 in the context of the slightly different beam interaction formulation to be proposed in the following Chapter 5. Because this alternative formulation is specialized in short-ranged interactions, it turns out to be more efficient for this class of interactions and the improvement of the accuracy expected from including the cross-section orientation will therefore be realized in that context first. However, also the SSIP laws considered in this chapter would benefit from the increased accuracy (and particularly the exact asymptotic scaling behavior) and including the cross-section orientation is thus considered a valuable future extension.

The presented set of numerical examples in Section 4.5 has finally demonstrated the effectiveness and robustness of the SSIP approach to model steric repulsion, electrostatic or vdW adhesion. Several important aspects such as the influence of the Gauss integration error and the spatial discretization error and local and global equilibrium of forces and conservation of energy are studied in these simulations, including quasi-static and dynamic scenarios as well as arbitrary mutual orientations and separations of the interacting fibers. These first applications of the novel formulations to rather simple, academic examples will be complemented by the comprehensive study of the peeling and pull-off of adhesive elastic fibers in Chapter 7. This simple, fundamental problem turns out to show a surprisingly rich and complex system behavior with a multitude of different effects to be studied in detail. In addition, the SSIP approach will be applied to challenging, real biophysical systems such as the conformations of mucin filaments due to the electrostatic self-interaction under varying line charge distributions to be studied in Chapter 9. A number of further interesting applications including the mechanics of collagen (micro)fibrils (cf. Chapter 11) and DNA origami (cf. Section 12.2) will be outlined in the remainder of this work and are considered highly promising aspects of future research.

5. A Specialized, More Efficient Formulation for Short-Ranged Interactions Based on Section-Beam Interaction Potentials

Following up on the development of the first 3D beam-beam interaction formulation for molecular interactions in the preceding Chapter 4, this chapter aims to develop an enhanced approach for the most challenging case of short-ranged interactions such as the vdW adhesion and the steric repulsion of the LJ interaction. Exploiting the characteristic rapid decay of the interaction potential with increasing distance will lead to a novel formulation that is superior to the SSIP approach (and the applied SSIP laws) in the following two key aspects. First, this specialized formulation will be significantly *more efficient* and second, it will also be significantly *more accurate* than the previous one.

To be more precise, the enhanced efficiency is a result of the different general approach based on the interaction potential of a cross-section interacting with (a surrogate of) the entire opposing beam instead of a pair of cross-sections as considered in the SSIP approach. The resulting section-beam interaction potential (SBIP) approach is proposed in the following Section 5.1. In addition to that, a more sophisticated reduced interaction law including the mutual orientation is derived in Section 5.2, thus achieving the enhanced accuracy as compared to the simple SSIP laws used before. In particular, this will lead to the correct asymptotic scaling behavior in the decisive regime of small separations, which has been identified as the most critical shortcoming when using the simple SSIP law from Section 4.3.2 neglecting the mutual orientation of cross-sections.

These two fundamental novelties – the general SBIP approach and the specific analytical interaction law – will be combined and the resulting virtual work contribution, its discretization based on finite elements, and the consistent linearization is presented in Section 5.3 and Appendix C.2. A suitable numerical regularization of the singularity at zero separation in the reduced interaction law is proposed in Section 5.4 along with the discussion of selected algorithmic aspects such as a criterion to sort out beam element pairs with a larger separation than the cutoff radius before the actual evaluation to save computational resources. Section 5.5 finally presents a comprehensive numerical example studying adhesive nanofiber-grafted surfaces, which confirms the effectiveness, efficiency and robustness of the novel formulation also for large-scale, complex systems with arbitrary mutual configurations and large deformations of the interacting fibers. At the same time, this computational study serves as a proof of principle for the design of bio-inspired artificial adhesive surfaces and delivers insights into the system behavior for dif-

ferent loading scenarios. This chapter will be concluded by the summary and outlook provided in Section 5.6.

5.1. The section-beam interaction potential (SBIP) approach

Consider a point-pair interaction potential with a very steep gradient as for example the inverse power laws with exponent six or twelve from the popular LJ interaction (2.8). The rapid decay of the potential with increasing distance implies that among all possible point pairs between both bodies only those with the smallest separation contribute significantly to the total interaction potential of both bodies. When looking at the interaction of two deformable slender bodies such as fibers, this consideration gives rise to an approach where the geometry of the second body is approximated by a surrogate body with simplified geometry located at the point of closest distance from a given point on the first body. See Figure 5.1 for an illustration of the approach using the example of circular cross-sections and therefore a cylinder-shaped surrogate body. In the region
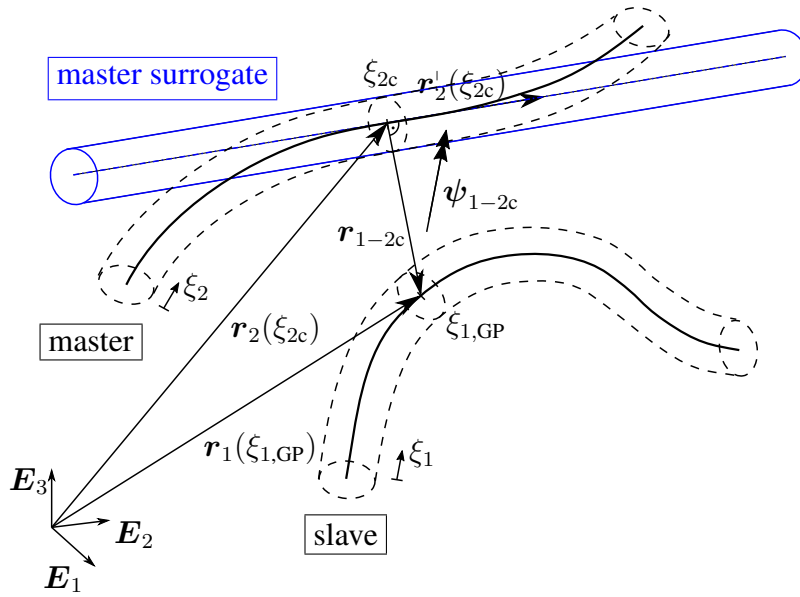
Figure 5.1.: Illustration of the section-beam interaction potential (SBIP) approach. The actual, deformed volume of the second interaction partner ("master") is approximated by a surrogate body (blue) located at the closest point ξ_{2c} to a given integration point $\xi_{1,GP}$ of the first interaction partner ("slave"). Distance vector $\boldsymbol{r}_{1-2c}$ and relative rotation vector $\boldsymbol{\psi}_{1-2c}$ uniquely describe the mutual separation and orientation.

around the closest point, this straight cylinder is expected to be a good approximation for the actual, possibly deformed, beam geometry. Note, however, that the general SBIP approach to

short-ranged beam-beam interactions is not limited to the circular cross-section shape shown in this example.

In accordance with formulations for macroscopic beam contact (see Section 3.3 for a summary), the body which is projected onto, i.e., here the one with approximated geometry is referred to as master beam (indicated by subscript m) whereas the first body is called slave beam (indicated by subscript s). Without loss of generality, the beam with index 1 is assumed to be the slave beam whereas index 2 is used as a synonym for master.

From a mathematical point of view, the geometrical approximation used in this context is equivalent to a Taylor series expansion of the centerline curve $\boldsymbol{r}_2(\xi_{2c})$ of the master beam at the closest point ξ_{2c} truncated after the second, i.e., linear term.

$$\boldsymbol{r}_{2,\text{approx}}(\xi_2) \approx \boldsymbol{r}_2(\xi_{2c}) + \boldsymbol{r}_2^{\shortmid}(\xi_{2c})\,\xi_2 \,(+\,\text{H.O.T.}) \tag{5.1}$$

Here, the linear term represents the orientation of the surrogate body in the direction of the master beam's tangent vector at the closest point $\boldsymbol{r}_2^{\shortmid}(\xi_{2c})$. Recall from Section 3.3.1 that the short prime denotes a differentiation with respect to the element parameter coordinate, i.e., $\boldsymbol{r}_i^{\shortmid}(\xi_i) = \mathrm{d}\,\boldsymbol{r}_i(\xi_i)/\mathrm{d}\,\xi_i$.

Turning to the key question of how to evaluate the two-body interaction potential, we assume a given interaction potential $\tilde{\pi}(\boldsymbol{r}_{1-2c}, \boldsymbol{\psi}_{1-2c})$ for the interaction between all the points within one cross-section of the slave beam and the entire master beam surrogate, i.e., the tangential straight cylinder in the example above. The total interaction potential is then evaluated as an integral along the centerline curve of the slave beam as follows:

$$\Pi_{ia} = \int_0^{l_1} \tilde{\pi}(\boldsymbol{r}_{1-2c}, \boldsymbol{\psi}_{1-2c})\,\mathrm{d}s_1. \tag{5.2}$$

Generally, such a section-beam interaction potential (SBIP) is a length-specific quantity with dimensions of energy per unit length (of the slave beam). It is an analytical expression uniquely defined by the mutual configuration, i.e., the distance vector $\boldsymbol{r}_{1-2c}$ and relative rotation vector $\boldsymbol{\psi}_{1-2c}$ as illustrated in Figure 5.1.

To evaluate the remaining 1D integral in equation (5.2), Gaussian quadrature is applied throughout this work. The reduction starting from 6D integration (cf. Equation (2.12)) to 1D integration already indicates the overall gain in efficiency that will be further analyzed and discussed in Section 5.4.3. Recall also the 2D integral (two nested 1D integrals) resulting for the general SSIP approach to realize the superior efficiency of this novel SBIP approach that will also be verified in the numerical experiments of Section 5.5.

In analogy to the previously presented section-section interaction potential (SSIP) approach from Chapter 4, the question of how to find an analytical, closed-form expression for the reduced interaction law $\tilde{\pi}(\boldsymbol{r}_{1-2c}, \boldsymbol{\psi}_{1-2c})$ can be considered separately from the generally valid SBIP approach proposed in this section. Just as for the SSIP laws discussed in Section 4.3, such an effective SBIP law $\tilde{\pi}$ will depend on the considered type of interaction, the cross-section shape(s) and dimensions, the atom density distributions, and possibly other interaction-specific factors. An example for how to determine this (single) length-specific potential $\tilde{\pi}(\boldsymbol{r}_{1-2c}, \boldsymbol{\psi}_{1-2c})$ analytically by means of 5D integration starting from the point-point interaction potential law

(2.8) in case of LJ interaction is presented in Section 5.2. However, other strategies such as postulating the general form of the SBIP law and fitting of the parameters to experimental results e.g. for the force response in two-fiber systems are considered to be promising alternative ways that could enable a broad variety of future applications of this SBIP approach.

Discussion of the choice of master and slave side. Starting from the problem of two-body interaction that is symmetric with respect to the two interaction partners, the SBIP approach introduces the notion of master and slave, which causes a bias in the formulation and asks for a criterion how to assign these roles. Both from the mathematical description as a linear Taylor approximation and the illustration in Figure 5.1, it becomes clear that the resulting model error and bias will depend on the magnitude of curvature of the master beam's centerline. This would give rise to a criterion that chooses the beam with the smaller (maximum or average) curvature as the master beam. However, such criteria might lead to sudden changes of master and slave over time, which is numerically unfavorable. Alternatively, one could consider to evaluate the pair of beams in two half passes, where the roles of master and slave switch and only the contributions on the slave side are evaluated in each of the passes (see e.g. [124, 140]), such that the bias in the formulation is avoided. However, it can be argued that the model error introduced by the use of the surrogate beam on the master side is negligible, because first, the curvature anyway is assumed to be limited in the underlying beam theory (typically compared to the inverse radius $1/R$ in case of circular cross-sections) and second, the very short range of the considered interactions naturally limits the impact of the master beam's shape deviation from the surrogate shape, because only the immediate surrounding of the expansion point will contribute noticeably to the total interaction. Following this assumption that the corresponding model error will be negligible, we apply the simple heuristic that the beam (element) with the smaller (global) identification number (ID) will generally be the slave beam throughout this work and validate this assumption in the numerical example of Section 7.4. The resulting maximal relative difference in the force response on system level turns out to be below 1.5% even for relatively large curvatures, which is considered to be a reasonably small model error. In addition, this simple criterion based on element IDs ensures a unique decision that does not change in the course of the simulation.

Remark on self-interactions. As already discussed for the SSIP approach in Section 4.2.2, self-interactions, i.e., the interaction of distinct parts of the same beam, can be treated naturally also within the SBIP approach. Leaving everything else unchanged, the search for and evaluation of (non-neighboring) beam element pairs from one and the same physical beam directly allows to incorporate the effect of self-interaction. This is considered to be important for long, flexible fibers showing the tendency to large deformations. An example for the case of long-range electrostatic interactions treated by the SSIP approach will be presented in Chapter 9 studying the conformations of mucin filaments as a result of different line charge distributions.

5.2. Closed-form expression for the disk-cylinder interaction potential

As mentioned before and discussed also in the context of the SSIP laws (cf. Section 4.3), there are different ways to arrive at a closed-form expression for the required SBIP law $\tilde{\pi}$. One of them is the analytical integration of a point-pair potential Φ over all point pairs in the section-beam (surrogate) system. This strategy will be demonstrated here for a generic inverse power law $\Phi_\mathrm{m}(r) = k_\mathrm{m}\, r^{-m}$ with exponent $m \geq 6$. Due to the generality, the resulting reduced interaction law $\tilde{\pi}$ can be used to model both the adhesive vdW part ($m = 6$) and the repulsive part ($m = 12$) of the LJ potential. Moreover, we consider the practically relevant case of circular, undeformable cross-sections and homogeneous densities of the fundamental interacting points in both fibers. From a geometrical point of view, this leads to the scenario of a disk and a cylinder (cf. Figure 5.1) with arbitrary mutual configuration, i.e., separation and orientation.

Note that instead of the six degrees of freedom $(\boldsymbol{r}_{1-2\mathrm{c}}, \boldsymbol{\psi}_{1-2\mathrm{c}})$ in the most general scenario considered in the preceding section, this system consisting of a homogeneous disk and cylinder has three degrees of freedom, which will be discussed in more detail later on. It is of great importance for the accuracy of the SBIP approach that the applied disk-cylinder potential law is accurate for all mutual configurations. To the best of the author's knowledge, no such disk-cylinder interaction potential law $\tilde{\pi}_\mathrm{m,disk\text{-}cyl}$ based on a generic point-pair potential with exponent m and valid for all mutual configurations can be found in the literature. The following Section 5.2.1 thus presents the required steps of the analytical integration and likewise serves as an example for the future derivation of other section-beam interaction potential laws, e.g. for other types of interactions or cross-section shapes. In the subsequent Section 5.2.2, the accuracy of the derived closed-form expression for $\tilde{\pi}_\mathrm{m,disk\text{-}cyl}$ will be verified.

5.2.1. Derivation via 5D analytical integration of the point-pair interaction potential

We aim to find the analytical solution for the disk-cylinder interaction potential

$$\tilde{\pi}_\mathrm{m,disk\text{-}cyl} := \iint_{A_\mathrm{disk}} \rho_1 \overbrace{\iiint_{V_\mathrm{cyl}} \rho_2\, \Phi_\mathrm{m}(r)\, \mathrm{d}V}^{=:\, \Pi_\mathrm{m,pt\text{-}cyl}}\, \mathrm{d}A \tag{5.3}$$

$$\text{with} \quad r = \|\boldsymbol{x}_1 - \boldsymbol{x}_2\| \quad \text{and} \quad \boldsymbol{x}_1 \in A_\mathrm{disk},\ \boldsymbol{x}_2 \in V_\mathrm{cyl}. \tag{5.4}$$

Here, $\boldsymbol{x}_1 \in A_\mathrm{disk}$ denotes any point in the disk, i.e., circular slave cross-section area $A_1 = A_\mathrm{disk} := \{\boldsymbol{x} \in \mathbb{R}^3 \,|\, \boldsymbol{r}_1 + y_1 \boldsymbol{u}_1 + z_1 \boldsymbol{v}_1,\ y_1^2 + z_1^2 \leq R_1^2\}$. This disk area is parameterized via two coordinates y_1, z_1 and its corresponding (for now not further specified) in-plane coordinate vectors $\boldsymbol{u}_1, \boldsymbol{v}_1$. The latter complete the (normalized) slave centerline tangent vector $\boldsymbol{t}_1 = \boldsymbol{r}_1^\mathsf{l} / \|\boldsymbol{r}_1^\mathsf{l}\|$ to form an orthonormal triad $(\boldsymbol{t}_1, \boldsymbol{u}_1, \boldsymbol{v}_1)$ and its definition will be discussed later. Once again, the short prime denotes a differentiation with respect to the element parameter coordinate, i.e., $\boldsymbol{r}_i^\mathsf{l}(\xi_i) = \mathrm{d}\,\boldsymbol{r}_i(\xi_i)/\mathrm{d}\,\xi_i$. On the master side, $\boldsymbol{x}_2 \in V_\mathrm{cyl}$ with $V_\mathrm{cyl} := \{\boldsymbol{x} \in \mathbb{R}^3 \,|\, \boldsymbol{r}_2 + x_2 \boldsymbol{t}_2 + y_2 \boldsymbol{u}_2 + z_2 \boldsymbol{v}_2,\ y_2^2 + z_2^2 \leq R_2^2,\ x_2 \in\,]-\infty, \infty[\}$ denotes any point in the

infinitely long auxiliary cylinder oriented along the (normalized) tangent vector $\boldsymbol{t}_2 = \boldsymbol{r}_2'/\|\boldsymbol{r}_2'\|$. Again, a set of coordinates x_2, y_2, z_2 together with an orthonormal frame $(\boldsymbol{t}_2, \boldsymbol{u}_2, \boldsymbol{v}_2)$ is chosen for parameterizing the geometry. Regarding this second basis $(\boldsymbol{t}_2, \boldsymbol{u}_2, \boldsymbol{v}_2)$, it will turn out that the exact definition does in fact not play a role and is thus left unspecified. Figure 5.2 (left side) illustrates the introduced geometrical quantities.
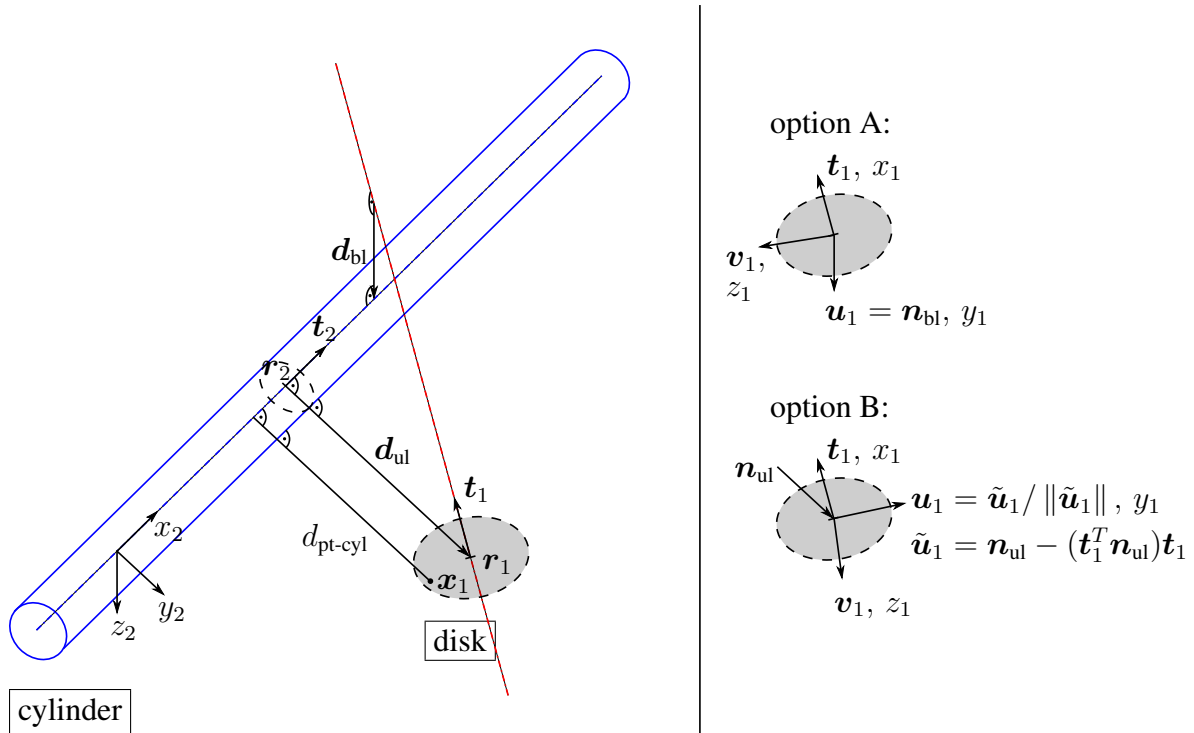
Figure 5.2.: Illustration of the geometrical quantities used to describe the disk-cylinder interaction (left side). In addition, the two different options for the choice of the Cartesian coordinate frame $(\boldsymbol{t}_1, \boldsymbol{u}_1, \boldsymbol{v}_1)$ used for the analytical integration over the disk-shaped slave cross-section are shown on the right side.

General strategy. The general strategy follows the one generally known as point-pairwise summation (see e.g. [74, 125] for details and a discussion) and e.g. applied in [117] for the analytical calculation of vdW forces for certain geometric configurations, e.g., a cylinder and a perpendicular disk. Since already for such specific scenarios, no exact analytical solution can be found for the integrals, also the following derivation will make use of the common approach of series expansions in order to find an analytical, closed-form expression for the integral of the leading term(s) of the series. Due to the rapid decay of the inverse power laws, this approach is known to yield good approximations for the true solution of the integral and in Section 5.2.2 we will

verify the accuracy for the specific expressions derived here.

Fortunately, the point-cylinder scenario for the case $m = 6$ of vdW interaction has already been studied in [117]. It can be generalized for exponents $m \geq 6$ as outlined in Appendix A.1.3.1 and at this point we can make use of the final result that the point-cylinder interaction potential follows the proportionality

$$\Pi_{\text{m,pt-cyl}} \propto g_{\text{pt-cyl}}^{-m+3} \tag{5.5}$$

where $g_{\text{pt-cyl}}$ denotes the *smallest* distance between the point and the cylinder *surface*. For now, we do not need to specify the precise expression for the point-cylinder interaction potential $\Pi_{\text{m,pt-cyl}}$ and in fact we will later investigate two different variants/approximations presented in Appendices A.1.3.1 and A.1.3.2, which deviate by a scalar factor, and discuss its effect on the accuracy of the disk-cylinder interaction potential $\tilde{\pi}_{\text{m,disk-cyl}}$ to be derived.

Due to the orthogonality condition $\boldsymbol{g}_{\text{pt-cyl}} \perp \boldsymbol{t}_2$ for the smallest distance from the master centerline curve $\boldsymbol{r}_2$, $g_{\text{pt-cyl}}$ can be expressed via the smallest distance between a point and the cylinder *axis* $d_{\text{pt-cyl}}$ as

$$g_{\text{pt-cyl}} := d_{\text{pt-cyl}} - R_2, \tag{5.6}$$

which in turn can be written as

$$d_{\text{pt-cyl}} := \|\boldsymbol{d}_{\text{pt-cyl}}\| = \|\boldsymbol{x}_1(s_1, y_1, z_1) - \boldsymbol{r}_2(s_{2c}(s_1, y_1, z_1))\| . \tag{5.7}$$

Again refer to Figure 5.2 for a sketch. Note that $\boldsymbol{r}_2(s_{2c}(s_1, y_1, z_1))$ is the master centerline position at s_{2c}, which results from the unilateral closest-point ("c") projection of the point $\boldsymbol{x}_1$ onto the master centerline curve $\boldsymbol{r}_2$. Therefore, it depends also on the exact coordinates y_1, z_1 of the point within the slave cross-section and not only on the arc-length parameter s_1, i.e., the position along the slave centerline curve $\boldsymbol{r}_1$. This fact can be used to express the decisive distance $d_{\text{pt-cyl}}$ in terms of the primary centerline fields $\boldsymbol{r}_{1/2}$ as well as the slave arc-length parameter s_1 to be used as integration variable in numerical integration (cf. Equation (5.2)) and y_1, z_1 to be used as integration variables for the analytical integration over the disk area. Since $\boldsymbol{g}_{\text{pt-cyl}}$ is perpendicular to $\boldsymbol{t}_2$, Equation (5.7) can equivalently be written as

$$d_{\text{pt-cyl}} = \| (\boldsymbol{x}_1(s_1, y_1, z_1) - \boldsymbol{r}_2(s_{2c}(s_1, y_1, z_1)) \times \boldsymbol{t}_2\| \tag{5.8}$$

$$= \| (\boldsymbol{r}_1(s_1) + y_1\boldsymbol{u}_1(s_1) + z_1\boldsymbol{v}_1(s_1) - \boldsymbol{r}_2(s_{2c}(s_1, 0, 0))) \times \boldsymbol{t}_2\| \tag{5.9}$$

$$= \| (d_{\text{ul}}\boldsymbol{n}_{\text{ul}} + y_1\boldsymbol{u}_1 + z_1\boldsymbol{v}_1) \times \boldsymbol{t}_2\| . \tag{5.10}$$

Here, we have introduced the so-called unilateral inter-axis separation

$$d_{\text{ul}} := \|\boldsymbol{r}_1(s_1) - \boldsymbol{r}_2(s_{2c}(s_1, 0, 0))\| \tag{5.11}$$

and the corresponding unilateral normal vector $\boldsymbol{n}_{\text{ul}}$, which result from the unilateral closest-point projection and are known from macroscopic (line) contact formulations (e.g. [110]). After a few

steps of basic vector algebra and making use of $\boldsymbol{n}_{\mathrm{ul}} \perp \boldsymbol{t}_2$, $\boldsymbol{u}_1 \perp \boldsymbol{v}_1$, $\boldsymbol{v}_1 = \boldsymbol{t}_1 \times \boldsymbol{u}_1$, and $\boldsymbol{t}_2^T \boldsymbol{t}_2 = 1$, we end up with

$$
d_{\text{pt-cyl}}^2 = \underbrace{\left(1 - \left(\boldsymbol{u}_1^T \boldsymbol{t}_2\right)^2\right)}_{=:a_y} y_1^2 + \underbrace{\left(1 - \left(\boldsymbol{t}_1^T \left(\boldsymbol{u}_1 \times \boldsymbol{t}_2\right)\right)^2\right)}_{=:a_z} z_1^2 \underbrace{- 2 \left(\boldsymbol{u}_1^T \boldsymbol{t}_2\right) \left(\boldsymbol{t}_1^T \left(\boldsymbol{u}_1 \times \boldsymbol{t}_2\right)\right)}_{=:a_{yz}} y_1 z_1
$$

$$
+ \underbrace{2 d_{\mathrm{ul}} \left(\boldsymbol{n}_{\mathrm{ul}}^T \boldsymbol{u}_1\right)}_{=:b_y} y_1 + \underbrace{2 d_{\mathrm{ul}} \left(\boldsymbol{t}_1^T \left(\boldsymbol{u}_1 \times \boldsymbol{n}_{\mathrm{ul}}\right)\right)}_{=:b_z} z_1 + \underbrace{d_{\mathrm{ul}}^2}_{=:c}
$$

(5.12)

which aims to express the integrand of Equation (5.3) as polynomial in the integration variables y_1, z_1 to be used for the analytical integration over the disk-shaped cross-section area A_1 on the slave side.

At this point, we return to the pending definition of the coordinate vector $\boldsymbol{u}_1$, which shall serve as an in-plane direction within the slave cross-section and thereby complete the unique definition of the coordinate frame $(\boldsymbol{t}_1, \boldsymbol{u}_1, \boldsymbol{v}_1)$. To briefly outline the procedure, this direction $\boldsymbol{u}_1$ will firstly be used as the first direction of integration over the cross-section area and secondly the associated coordinate y_1 also defines the point of series expansion $(y_1 = -R_1, z_1 = 0)$ to be applied later on. We basically see two reasonable options for the definition of $\boldsymbol{u}_1$ (see Figure 5.2 (right side) for an illustration):

- option A: $\boldsymbol{u}_1 := \boldsymbol{n}_{\mathrm{bl}}$ with $\boldsymbol{n}_{\mathrm{bl}} := (\boldsymbol{t}_1 \times \boldsymbol{t}_2) / \|\boldsymbol{t}_1 \times \boldsymbol{t}_2\|$

- option B: $\boldsymbol{u}_1 := \tilde{\boldsymbol{u}}_1 / \|\tilde{\boldsymbol{u}}_1\|$ with $\tilde{\boldsymbol{u}}_1 := \left(\boldsymbol{I} - \boldsymbol{t}_1 \otimes \boldsymbol{t}_1^T\right) \boldsymbol{n}_{\mathrm{ul}}$

Option A is a natural choice in the sense that the *bilateral* normal vector $\boldsymbol{n}_{\mathrm{bl}}$ will always be perpendicular to $\boldsymbol{t}_1$ and thus lie within the cross-section. Note that its definition in the context of this work deviates from the one known from macroscopic (point) contact models (e.g. [163]). Here, it is defined via the cross product of the normalized tangent vector $\boldsymbol{t}_1$ at the integration point on the slave side, i.e., the vector perpendicular to the disk plane, and the normalized tangent vector $\boldsymbol{t}_2$ at the unilateral closest point on the master side, i.e., the vector defining the axis of the auxiliary cylinder serving as a surrogate for the actual beam geometry on the master side. In contrast to this, point contact formulations for beams define the bilateral normal vector as the result of a bilateral closest-point projection, i.e., the minimization of the mutual distance of both beam centerline curves. This difference is crucial because it carries over to the important topic of non-uniqueness and singularities of the definition (see e.g. [110, 111]). Here, the only critical geometric configuration is the case of parallel disk and cylinder $\boldsymbol{t}_1 \parallel \boldsymbol{t}_2$. In the use case considered here, one could overcome this issue with an alternative definition for this special case $\boldsymbol{t}_1 \parallel \boldsymbol{t}_2$ (similar to the so-called all-angle beam contact (ABC) [111]), however at the cost of an additionally required, smooth transition between both definitions.

In option B, $\boldsymbol{u}_1$ is defined as the projection of the unilateral normal vector $\boldsymbol{n}_{\mathrm{ul}}$ into the slave cross-section plane, which can equivalently be regarded as the construction of an orthonormal frame based on $\boldsymbol{t}_1$ and $\boldsymbol{n}_{\mathrm{ul}}$. This already reveals the singularity in this second possible definition of $\boldsymbol{u}_1$, which now occurs for $\boldsymbol{t}_1 \parallel \boldsymbol{n}_{\mathrm{ul}}$. Fortunately, this scenario is by far less critical than $\boldsymbol{t}_1 \parallel \boldsymbol{t}_2$ and will be discussed in further detail later on.

To sum up, we consider both options A and B as viable choices for $\boldsymbol{u}_1$ and want to further investigate both of them. Therefore, the introduction of generic scalar coefficients $a_y, a_z, b_y, b_z, c \in \mathbb{R}$ in Equation (5.12) conveniently allow us to directly obtain and compare the two different final expressions for the disk-cylinder potential $\tilde{\pi}_{\text{m,disk-cyl}}$ once the analytical 2D integral has been solved as presented in the following steps. For later reference, let us thus state the resulting expressions for these coefficients in both cases. By inserting the definition of $\boldsymbol{u}_1$ according to either option A or B into Equation (5.12), the following final expressions are obtained for the corresponding polynomial coefficients:

$$\text{option A:}\quad a_y = 1,\, a_z = \cos^2\alpha,\, a_{yz} = 0,\, b_y = 2\,d_{\text{ul}}\sqrt{1 - \frac{\cos^2\theta}{\sin^2\alpha}},\, b_z = 2\,d_{\text{ul}}\frac{\cos\theta}{\tan\alpha}, c = d_{\text{ul}}^2 \tag{5.13}$$

$$\text{option B:}\quad a_y = 1 - \frac{\cos^2\alpha}{\tan^2\theta},\, a_z = \frac{\cos^2\alpha}{\sin^2\theta},\, a_{yz} = -2\,\frac{\cos\alpha\,\cos\theta}{\sin^2\theta}\sqrt{\sin^2\alpha - \cos^2\theta}, \tag{5.14}$$
$$b_y = 2\,d_{\text{ul}}\,\sin\theta,\, b_z = 0,\, c = d_{\text{ul}}^2$$

For the sake of both brevity and clarity, here the dot products occurring in the expressions have been replaced by using the corresponding scalar angles enclosed by the vectors as follows.

$$|\boldsymbol{t}_1^T\boldsymbol{t}_2| =: \cos\alpha \quad \text{and} \quad \boldsymbol{t}_1^T\boldsymbol{n}_{\text{ul}} =: \cos\theta \tag{5.15}$$

Remark on the minimal set of degrees of freedom. Note that the chosen set $(d_{\text{ul}}, \alpha, \theta)$ is just one of the many different ways to uniquely describe the *mutual* configuration of the disk-cylinder system. Other choices include e.g. any three of d_{bl}, ϑ with $\cos\vartheta := \boldsymbol{n}_{\text{bl}}^T\boldsymbol{n}_{\text{ul}}$, and the three aforementioned ones. Our choice however avoids the non-uniqueness of the bilateral normal vector $\boldsymbol{n}_{\text{bl}}$ for $\boldsymbol{t}_1 \parallel \boldsymbol{t}_2$ mentioned above and moreover appears to be most natural in the sense of yielding both compact and illustrative expressions.

Remark on the interpretation of the angle θ. Whereas the smallest distance between disk midpoint and cylinder axis d_{ul} and the angle included by the cylinder axis and the disk axis (i.e. the normal to the disk surface) α are straightforward to interpret and visualize, this seems harder for the angle θ. It helps to think of a disk and a cylinder at fixed distance d_{ul} and inter-axis angle $\alpha \neq 0$ (e.g. perpendicular), and then begin to move the disk midpoint on the circle with radius d_{ul} around the closest point on the cylinder axis, while keeping α fixed. This is the interpretation of the third degree of freedom θ. Now consider for instance the cases $\alpha = \pi/2$ and $\theta = 0$ to see that this configuration will not occur for small d_{ul} if we consider the interaction of two (arbitrarily) curved fibers with bounded curvature, because the fibers would penetrate each other. However, only these small values of d_{ul} are decisive for the two-fiber interaction potential, such that we can conclude that certain disk-cylinder configurations are less important for the two-fiber interaction potential. This will be the motivation to later use a further simplified version of the disk-cylinder potential law $\tilde{\pi}_{\text{m,disk-cyl}}$ in the context of the SBIP approach.

Coming back to the problem statement in Equation (5.3), we can now reformulate the initial problem to solve

$$\iint\limits_{A_{\text{disk}}} g_{\text{pt-cyl}}^{-m+3} \, \mathrm{d}A \qquad \text{with} \quad A_{\text{disk}} = \{\,(y_1, z_1) \,|\, y_1^2 + z_1^2 \leq R_1^2\,\} \tag{5.16}$$

using $g_{\text{pt-cyl}}$ from Equation (5.6) and substituting $d_{\text{pt-cyl}}$ from Equation (5.12) to end up with the general expression for the smallest separation of the point and the cylinder *surface*

$$g_{\text{pt-cyl}} = \sqrt{a_y y_1^2 + a_z z_1^2 + a_{yz} y_1 z_1 + b_y y_1 + b_z z_1 + c} - R_2. \tag{5.17}$$

Note that up to this point the two options A and B from above are just two different yet equivalent ways of stating the identical problem. If we could solve the problem defined in either of the two ways in an exact manner, the solution would of course be identical. However, as outlined in the beginning of this section, our strategy to find an approximative solution includes the two steps to first express $g_{\text{pt-cyl}}$ as a multivariate Taylor series expansion and second solve the 2D integral with this simplified integrand analytically. The point of expansion hereby is of crucial importance and due to the nature of the inverse power interaction law, it should be located at the disk point with smallest disk-cylinder surface separation, where the by far largest contributions come from. This is where the two options A and B again come into play, because we choose the point of expansion to be at $(y_1 = -R_1, z_1 = 0)$ in both cases, which means that the point is located on the disk contour and lies either on the bilateral normal direction vector for option A or on the projected unilateral normal direction vector for option B. Both choices will be the optimal choice in terms of being located at the point of smallest surface separation for some mutual configurations, but not for all of them. This motivates the investigation of both of them and a final judgment will later be made based on the resulting accuracy of the disk-cylinder potential for all mutual configurations.

Remark on alternative solution attempts. Note that several other approaches to solve the 2D integral over the circular cross-section area have been investigated, yet did not lead to any exact analytical solutions and thus superior accuracy and simplicity of the final disk-cylinder potential expression. These unsuccessful other attempts include e.g. coordinate transformations in polar coordinates and the description of the projected rotated disk as an ellipse.

The required multivariate series expansion of (5.17) finally reads

$$\text{Lin}\left[g_{\text{pt-cyl}}\right]_{y_1=-R_1, z_1=0} = \overbrace{\beta - R_2}^{=:\tilde{c}} + \overbrace{\frac{1}{2\beta}(b_y - 2a_y R_1)}^{=:\tilde{b}_y}(y_1 + R_1) + \overbrace{\frac{1}{2\beta}(b_z - a_{yz} R_1)}^{=:\tilde{b}_z} z_1 \tag{5.18}$$
$$+ \frac{1}{2}\left(\frac{a_z}{\beta} - \frac{(b_z - a_{yz} R_1)^2}{4\beta^3}\right) z_1^2 + \text{H.O.T.},$$

where the auxiliary variable $\beta := \sqrt{c - b_y R_1 + a_y R_1^2}$ and further abbreviations $\tilde{c}$, $\tilde{b}_y$, $\tilde{b}_z$ have been introduced for the later use. Note also that we have already used the knowledge from the

subsequent accuracy analysis here that the second order term in z_1 is indeed decisive for the overall accuracy whereas neglecting the other second and higher order terms still gives us good results. Continuing from Equation (5.16), the 2D integral can thus be further simplified by

$$\int\limits_{-R_1}^{R_1} \int\limits_{-\sqrt{R_1^2-z_1^2}}^{\sqrt{R_1^2-z_1^2}} g_{\text{pt-cyl}}^{-m+3} \, \mathrm{d}y_1 \, \mathrm{d}z_1 \approx \int\limits_{-R_1}^{R_1} \int\limits_{-\sqrt{R_1^2-z_1^2}}^{\sqrt{R_1^2-z_1^2}} \left(\text{Lin}\left[g_{\text{pt-cyl}}\right]_{y_1=-R_1,z_1=0}\right)^{-m+3} \, \mathrm{d}y_1 \, \mathrm{d}z_1, \quad (5.19)$$

for which a closed-form antiderivative exists for the inner integral in y_1 (see e.g. [19, p.1017]):

$$\int \left(\tilde{b}_y(y_1+R_1)+\dots\right)^{-m+3} \, \mathrm{d}y_1 = \frac{\tilde{b}_y^{-1}}{(-m+4)}(\tilde{b}_y(y_1+R_1)+\dots)^{-m+4}, \quad m \neq 4 \quad (5.20)$$

To keep the expressions simple and enable the subsequent analytical integration in z_1, we once again exploit the fact that the contributions from point-pairs decay rapidly with increasing distance and set the upper integration limit in y_1 to infinity. Following the same reasoning, the lower integration limit is replaced by its second-order Maclaurin series expansion at $z_1 = 0$

$$-\sqrt{R_1^2-z_1^2} \approx -R_1 + z_1^2/(2R_1). \quad (5.21)$$

The error introduced by this approximation is expected to be small because the point of expansion and its immediate vicinity include the most important closest point pair. For a more detailed analysis of the approximation quality, again refer to Section 5.2.2. Finally, the integral in y_1 can be solved as follows:

$$\int\limits_{-\sqrt{R_1^2-z_1^2}}^{\sqrt{R_1^2-z_1^2}} g_{\text{pt-cyl}}^{-m+3} \, \mathrm{d}y_1 \approx \lim_{y_{\max} \to \infty} \int\limits_{-R_1+z_1^2/(2R_1)}^{y_{\max}} \left(\text{Lin}\left[g_{\text{pt-cyl}}\right]_{y_1=-R_1,z_1=0}\right)^{-m+3} \, \mathrm{d}y_1 \quad (5.22)$$

$$= \frac{\tilde{b}_y^{-1}}{(-m+4)}(\tilde{c} + \tilde{b}_z z_1 + \underbrace{\left(\frac{\tilde{b}_y}{2R_1} + \frac{a_z}{2\beta} - \frac{\tilde{b}_z^2}{2\beta}\right)}_{=:\tilde{a}_z} z_1^2)^{-m+4} \quad (5.23)$$

The remaining fifth and final integral to be evaluated analytically is the one in transversal direction z_1 within the disk-shaped cross-section area. Naturally, this last step turns out to be the critical point and many of the mentioned other attempts to find an analytical solution for the disk-cylinder interaction potential $\tilde{\pi}_{\text{m,disk-cyl}}$ failed here. For this specific formulation of the problem described above and the simplifications based on the previously discussed assumptions, an analytical antiderivative exists and is stated in a recursive manner for a generic exponent m (see e.g. [19, p.1019]):

$$\int \underbrace{(\tilde{a}_z z_1^2 + \tilde{b}_z z_1 + \tilde{c})}_{=:Z}^{-m+4} \, \mathrm{d}z_1 = \frac{2\tilde{a}_z z_1 + \tilde{b}_z}{(m-5)\,\Delta} Z^{-m+5} + \frac{2(2m-11)\,\tilde{a}_z}{(m-5)\,\Delta} \int Z^{-m+5} \, \mathrm{d}z_1$$

$$\text{with} \quad (m-4) > 1 \quad (5.24)$$

$$\int Z^{-1} \, \mathrm{d}z_1 = \frac{2}{\sqrt{\Delta}} \arctan\left(\frac{2\tilde{a}_z z_1 + \tilde{b}_z}{\sqrt{\Delta}}\right) \quad \text{for} \quad \Delta > 0$$

Here, the introduced dimensionless quantity $\Delta := 4\tilde{a}_z\tilde{c} - \tilde{b}_z^2$ represents the negative discriminant of the quadratic expression $Z(z_1)$, which can be identified as $\mathrm{Lin}[g_{\mathrm{pt\text{-}cyl}}]$ evaluated at $y_1 = -R_1 + z_1^2/(2R_1)$, i.e., the (approximated) distance between the points on the disk's boundary and the corresponding closest point on the cylinder surface. From this interpretation, we can follow that $\Delta > 0$ will hold true for all physically sensible scenarios, because the distance will always be a positive value, i.e., have no roots and the corresponding discriminant $\tilde{b}_z^2 - 4\tilde{a}_z\tilde{c}$ will be negative.

Substituting Equation (5.23) into Equation (5.19) and making use of the analytical antiderivative (5.24) finally allows us to find a closed-form analytical expression for $\tilde{\pi}_{\mathrm{m,disk\text{-}cyl}}$ for any given exponent $m \geq 6$. The expression will however be lengthy, such that we make a final approximation and replace the exact integration domain $z_1 \in [-R_1, R_1]$ by $z_1 \in\,]-\infty, \infty[$, which significantly simplifies the expression, because all the recursive terms Z^{-m+5} from Equation (5.24) vanish and the arctan-function evaluates to $\pm\pi/2$, respectively. Once again, this is expected to be a good approximation, since only the point pairs in the vicinity of the closest point yield significant contributions to the value of the integral. Finally, the sought-after analytical solution for the disk-cylinder interaction potential with generic exponent thus reads

$$\tilde{\pi}_{\mathrm{m,disk\text{-}cyl}} = \rho_1 K_{\mathrm{m}}\, \tilde{b}_y^{-1}\, \tilde{a}_z^{m-5}\, \Delta^{-m+9/2}, \tag{5.25}$$

where all the constants have been collected in a newly introduced prefactor K_{m}. For the two parts of the LJ potential and using the point-cylinder potential law[1] from Appendix A.1.3.2, these prefactors are given as

$$K_6 := \frac{1}{3}\pi^2\, k_6\, \rho_2 \quad \text{and} \quad K_{12} := \frac{286}{15}\pi^2\, k_{12}\, \rho_2 \tag{5.26}$$

for the adhesive $m = 6$ and repulsive $m = 12$ part, respectively. At this point, we have found an analytical expression for (both parts of) the LJ interaction potential $\tilde{\pi}_{\mathrm{LJ,disk\text{-}cyl}}$ of a disk and a cylinder of infinite length valid for arbitrary mutual orientations α, θ in the decisive regime of small separations $g_{\mathrm{ul}} \ll R_{1/2}$. Now recall the discussion of the two options A and B for the definition of $\boldsymbol{u}_1$ and thus the associated direction of integration in y_1 as well as the point of expansion at $y_1 = -R_1, z_1 = 0$. Re-substitution of the auxiliary variables as follows – together with the general solution of Equation (5.25) – gives a first impression of the complexity of the

---

[1] See Appendix A.1.3.3 for a comparison of the two alternative expressions for the point-cylinder interaction potential $\Pi_{\mathrm{m,pt\text{-}cyl}}$ and the reason for using the one presented in Appendix A.1.3.2.

different expressions for option A and B.

$$
\text{option A:} \quad \beta = \sqrt{d_{\text{ul}}^2 - 2R_1 d_{\text{ul}} \sqrt{1 - \cos^2 \theta / \sin^2 \alpha} + R_1^2}
$$

$$
\tilde{b}_y = \frac{1}{\beta} \left(d_{\text{ul}} \sqrt{1 - \cos^2 \theta / \sin^2 \alpha} - R_1 \right)
$$

$$
\tilde{b}_z = \frac{1}{\beta} d_{\text{ul}} \cos \theta \cos \alpha / \sin \alpha \tag{5.27}
$$

$$
\tilde{a}_z = \frac{\tilde{b}_y}{2R_1} + \frac{\cos^2 \alpha}{2\beta} - \frac{\tilde{b}_z^2}{2\beta}
$$

$$
\tilde{c} = \beta - R_2
$$

$$
\Delta = 4 \tilde{a}_z \tilde{c} - \tilde{b}_z^2
$$

$$
\text{option B:} \quad \beta = \sqrt{d_{\text{ul}}^2 - 2R_1 d_{\text{ul}} \sin \theta + \left(1 - \cos^2 \alpha \cos^2 \theta / \sin^2 \theta \right) R_1^2}
$$

$$
\tilde{b}_y = \frac{1}{\beta} \left(d_{\text{ul}} \sin \theta - \left(1 - \cos^2 \alpha \cos^2 \theta / \sin^2 \theta \right) R_1 \right)
$$

$$
\tilde{b}_z = \frac{1}{\beta} \cos \alpha \, \cos \theta / \sin^2 \theta \, \sqrt{\sin^2 \alpha - \cos^2 \theta} \, R_1 \tag{5.28}
$$

$$
\tilde{a}_z = \frac{\tilde{b}_y}{2R_1} + \frac{\cos^2 \alpha}{2\beta \, \sin^2 \theta} - \frac{\tilde{b}_z^2}{2\beta}
$$

$$
\tilde{c} = \beta - R_2
$$

$$
\Delta = 4 \tilde{a}_z \tilde{c} - \tilde{b}_z^2
$$

Looking at these expressions, we can state that both length and complexity of the terms is similar for both options A and B. As mentioned before, the resulting accuracy will be analyzed in Section 5.2.2 and thus complete the assessment of these two options. At this point, however, let us turn to a possibility to simplify the resulting expressions without significant loss of accuracy. In this respect, the following third option C turned out to be a good compromise between accuracy and simplicity of the expression:

- option C: $\boldsymbol{u}_1 := \boldsymbol{n}_{\text{ul}}$

The main difference to options A and B is that $\boldsymbol{u}_1$ does in general not lie exactly within the disk area, which is why it has not been considered in the first place. However, it will turn out in Section 5.2.2 that the influence of this approximation on the accuracy is rather insignificant.

In analogy to the derivation for the options A and B, the auxiliary variables follow as

$$
\text{option C:} \quad
\begin{aligned}
\beta &= d_{\mathrm{ul}} - R_1 \\
\tilde{b}_y &= 1 \\
\tilde{b}_z &= 0 \\
\tilde{a}_z &= \frac{1}{2R_1} + \frac{\cos^2 \alpha}{2(d_{\mathrm{ul}} - R_1)} \\
\tilde{c} &= d_{\mathrm{ul}} - R_1 - R_2 =: g_{\mathrm{ul}} \\
\Delta &= 4\tilde{a}_z \, g_{\mathrm{ul}},
\end{aligned}
\tag{5.29}
$$

and substitution into the general form of the disk-cylinder interaction potential in Equation (5.25) results in the pleasantly simple expression

$$
\tilde{\pi}_{\mathrm{m,disk\text{-}cyl}} = \rho_1 K_{\mathrm{m}} \, \tilde{a}_z^{-\frac{1}{2}} \left(4\, g_{\mathrm{ul}}\right)^{-m+\frac{9}{2}}.
\tag{5.30}
$$

Note that this option C is equivalent to both options A and B for the special case of $\theta = \pi/2$, i.e., $\cos\theta = \boldsymbol{t}_1^T \boldsymbol{n}_{\mathrm{ul}} = 0$ and thus $\boldsymbol{n}_{\mathrm{ul}} \perp \boldsymbol{t}_1$ and $\boldsymbol{n}_{\mathrm{ul}} \equiv \boldsymbol{n}_{\mathrm{bl}}$. This means that the scalar angle θ has been eliminated and only two degrees of freedom remain. Now recall from the interpretation of the angle θ given above that certain configurations of the disk-cylinder system are more important – and in fact decisive – for the two-fiber interaction potential and others are rather irrelevant. This is the motivation for the special value $\theta = \pi/2$. Consider the fact that $\cos\theta = \sin\alpha \sin\vartheta$ and thus $\theta = \pi/2$ if either $\vartheta = 0$, i.e. $\boldsymbol{n}_{\mathrm{ul}} \parallel \boldsymbol{n}_{\mathrm{bl}}$, which in turn means that we are at the bilateral closest-point pair of the two fibers, or if $\alpha = 0$, i.e., we have parallel beam axes and again a bilateral closest-point pair, which is non-unique in this case. To conclude, all the disk-cylinder configurations that are decisive for the two-fiber interaction will have $\theta \approx \pi/2$. Therefore, the option C disk-cylinder potential law will yield a very high accuracy if applied together with the general SBIP approach on the level of fiber-fiber interactions. In this way, we have eliminated the least relevant degree of freedom in order to obtain a reduced and thus simpler SBIP law.[2]

Note that such a simple SBIP expression is especially desirable for the later use in the resulting virtual work contribution and its linearization in the context of an implicit, nonlinear finite element framework for structural dynamics. In this use case, the required two-fold differentiation of the potential law with respect to the discrete set of primary degrees of freedom can become tedious and at some point unfeasible if the potential law is too complex. The same reasoning applies to the replacement of the exact integration domain in z_1 by $z_1 \in\,]-\infty, \infty[$. In other use cases however, the above presented options A and B of the disk-cylinder interaction potential expressions may still be considered reasonably simple and due to the increased accuracy (especially for those configurations with θ far from $\pi/2$, as discussed above) they may be of great value. For these reasons, they are included here despite the fact that solely the option C will be used in the final beam interaction formulation to be applied in the numerical examples of this work.

---

[2] Note the analogy to the discussion of reduced section-section interaction potential (SSIP) laws in Section 4.3.1.

In this light, one small further simplification can be achieved by recalling the initial restriction to the dominating regime of small separations $g_{\mathrm{ul}} \ll R_{1/2}$ and thus applying

$$d_{\mathrm{ul}} - R_1 = g_{\mathrm{ul}} + R_2 \approx R_2 \tag{5.31}$$

to the coefficients in Equation (5.29), which finally leads to

$$\tilde{\pi}_{\mathrm{m,disk\text{-}cyl}} = \hat{K}_{\mathrm{m}} \, \rho_1 \, \sqrt{\frac{2R_1 R_2}{R_1 \cos^2 \alpha + R_2}} \, g_{\mathrm{ul}}^{-m+\frac{9}{2}} \quad \text{with } \hat{K}_{\mathrm{m}} := 4^{-m+\frac{9}{2}} \, K_{\mathrm{m}}, \quad m \geq 6. \tag{5.32}$$

For convenience in later reference, we explicitly state the most common prefactors for the vdW part $m = 6$ and the repulsive part $m = 12$ of the LJ potential as follows:

$$\hat{K}_6 = \frac{1}{24} \pi^2 \, k_6 \, \rho_2 \quad \text{and} \quad \hat{K}_{12} = \frac{143}{15 \cdot 2^{14}} \pi^2 \, k_{12} \, \rho_2 \tag{5.33}$$

At this point, we have arrived at the final form (5.32) of the disk-cylinder interaction potential to be used as reduced interaction law in the context of the SBIP approach proposed in Section 5.1.

An immediate verification of these expressions for the special case $\alpha = 0$ confirms that both $\tilde{\pi}_{6,\mathrm{disk\text{-}cyl}}$ and $\tilde{\pi}_{12,\mathrm{disk\text{-}cyl}}$ are identical to the independently derived analytical solutions for the interaction potential per unit length $\tilde{\pi}_{6,\mathrm{cyl\|cyl}}$ and $\tilde{\pi}_{12,\mathrm{cyl\|cyl}}$ of two infinitely long, parallel cylinders (cf. Equations (2.14) and (A.15), respectively). This is an important finding, as it shows the consistency of the more general expression (5.32) valid for all mutual angles α with previously derived expressions for the important special case $\alpha = 0$. A much broader and deeper analysis of the accuracy of Equation (5.32) as well as a comparison to the expressions obtained for the other options A and B above will be the content of the following Section 5.2.2.

5.2.2. Verification

This section aims to verify both the general SBIP approach proposed in Section 5.1 and the specific SBIP law $\tilde{\pi}_{\mathrm{m,disk\text{-}cyl}}$ derived in the preceding Section 5.2.1. Let us first recall the underlying assumptions of the general evaluation strategy:

- pair-wise summation

- very short range of interactions and focus on small separation regime $g \ll R_{1/2}$

- linear Taylor expansion of the master beam volume

- choice of master and slave

Moreover, the following assumptions and approximations have been made in order to obtain a closed-form analytical solution for the disk-cylinder interaction potential at arbitrary mutual orientations in the previous section.

- multivariate Taylor expansion of point-cylinder distance, see Equation (5.19)

- Taylor expansion of lower integration limit $y_{\min}(z)$ and set upper integration limit to ∞, see Equation (5.22)

- set integration limits $z_{\text{min/max}}$ to $\pm\infty$, see comment above Equation (5.25)

- use of the point-half space expression $\Pi_{\text{m,pt-hs}}$ as point-cylinder interaction potential $\Pi_{\text{m,pt-cyl}}$, see Equation (A.18)

- further simplification by using option C: $\boldsymbol{u}_1 = \boldsymbol{n}_{\text{ul}}$ and finally $g_{\text{ul}} + R_2 \approx R_2$, see steps above Equation (5.32)

To allow for a clear analysis of the resulting accuracy, the minimal example of two cylinders, which represents the special case of two straight beams with circular cross-section, is considered in the following. In this case, analytical reference solutions are known for the limit of small separations and specifically the influence of the second list of assumptions can be assessed, because the first list is exactly fulfilled.

5.2.2.1. Van der Waals interaction potential of two cylinders for all separations and all mutual angles

The relative configuration of two cylinders is uniquely described by their (bilateral) smallest inter-axis separation d_{bl} and their mutual angle α, as depicted in Figure 5.3. Note that the surface
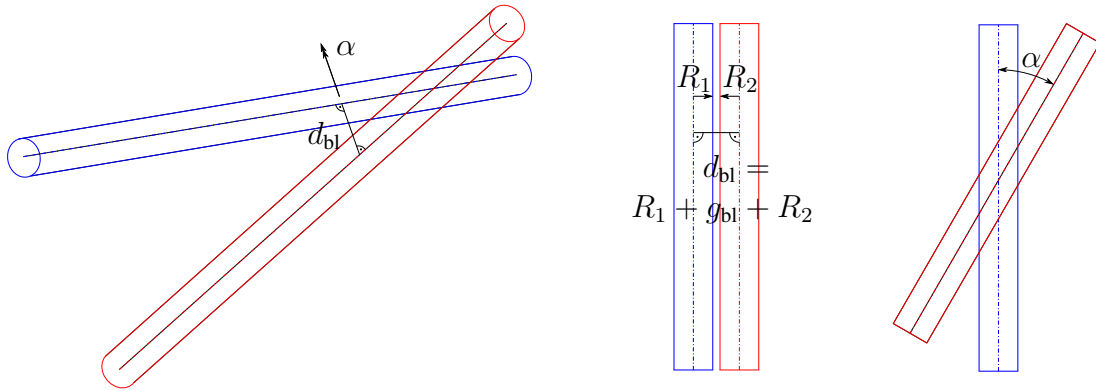
Figure 5.3.: Illustration of the two-cylinder interaction scenario used for verification purposes. Perspective view (left), side view (center), and top view (right) of the cylinders including their smallest inter-axis distance d_{bl} and mutual angle α.

separation also known as gap $g_{\text{bl}} = d_{\text{bl}} - R_1 - R_2$ will often be used instead of the inter-axis separation d_{bl} in the following discussion. Exemplarily, vdW interaction with exponent $m = 6$ of the point pair potential will be considered, however the results are expected to be analogous for the repulsive part of LJ or any other short-ranged interaction. As mentioned before, analytical reference solutions obtained via 6D analytical integration of the point-pair vdW potential Φ_{vdW} for mutual angles $\alpha \in \,]0, \pi/2]$ (see Equation (2.18) and e.g. [125, p. 173]) as well as the special case of parallel cylinders $\alpha = 0$ (see e.g. [125, p. 172] and the summary in Table 2.1) are available from literature. However, keep in mind that these reference solutions are derived for the limit of small separations $g_{\text{bl}} \ll R_{1/2}$ and *infinite* length of the cylinders such that the solution for parallel cylinders is given as interaction potential per unit length $\tilde{\pi}_{\text{vdW,cyl}\|\text{cyl}}$ instead of the

total two-body interaction potential $\Pi_{\text{vdW,cyl-cyl}}$, which would be infinite. For simplicity, a fixed length $L = 20$ and radius $R = 1$ is chosen exemplarily for the numerically evaluated solutions, which turned out to have no noticeable influence as long as the slenderness L/R is sufficiently large.

Figure 5.4 shows a double-logarithmic plot of the dimensionless vdW interaction potential $\Pi_{\text{vdW,cyl-cyl}}$ as a function of the dimensionless surface separation g_{bl}/R at different mutual angles α. The derived analytical expression for the disk-cylinder interaction potential $\tilde{\pi}_{6,\text{disk-cyl}}$ (option C) from Equation (5.32) is numerically integrated along the second cylinder axis (1D) as proposed in the general SBIP approach from Section 5.1 and depicted as red line with triangles.[3] For verification, the analytical reference solutions for parallel and skew cylinders as summarized in Section 2.3.2 are plotted as black dashed line. In addition, the point-half space potential $\Pi_{6,\text{pt-hs}}$ from Equation (A.18), which has been used as point-cylinder potential already in the analytical 5D integration to end up with the disk-cylinder potential $\tilde{\pi}_{6,\text{disk-cyl}}$ is used for 3D numerical integration over the entire volume of the second cylinder and shown as green line with diamonds.[4] This option serves two purposes at the same time. First, Figure 5.4 shows that the two-cylinder interaction potential obtained in this way perfectly matches the analytical reference solutions derived for the limit of small separations. This verifies that the point-half space potential is the consistent approximation for the point-cylinder potential under the assumptions of short-ranged interactions at small separations as discussed and motivated in A.1.3.3 and is thus an important step of verification also of the disk-cylinder interaction potential $\tilde{\pi}_{\text{m,disk-cyl}}$. And second, it is an important numerical reference solution, because it allows to judge the accuracy of the assumptions and simplifications made in the steps of analytically integrating the point-cylinder potential over the disk-shaped slave cross-section (see list of assumptions above). Note also in this respect that obtaining a fully numerical reference solution via 6D numerical integration of the point-pair potential Φ_{vdW} once again failed due to its infeasible computational cost, especially in the decisive regime of small separations. Refer to Section 4.5.1.1 for a more detailed discussion of this topic. The 3D numerical integration of the point-cylinder potential $\Pi_{\text{pt-cyl}}$ therefore is a valuable reference solution for the two-cylinder potential $\Pi_{\text{vdW,cyl-cyl}}$ in the regime of intermediate separations, where no analytical reference solution is known. For the sake of completeness, note that the regime of large separations is covered in Section 4.5.1.1 as well. However, it is of minor practical interest in the case of short-ranged interactions considered here.

Let us now have a detailed look at the most important topic of the accuracy of the analytical disk-cylinder interaction potential $\tilde{\pi}_{6,\text{disk-cyl}}$ (option C) from Equation (5.32). First and foremost, the accuracy is excellent in the case of parallel cylinders shown in Figure 5.4(a), which is no surprise as it has already been stated in an immediate assessment at the end of Section 5.2.1 that $\tilde{\pi}_{\text{m,disk-cyl}}$ coincides with the analytical reference solution for the interaction potential per unit length of parallel cylinders $\tilde{\pi}_{\text{m,cyl}\|\text{cyl}}$. As a consequence, the asymptotic scaling behavior

---

[3] Gaussian quadrature with 5 integration points has been applied in each of the 40 integration segments, which were chosen increasingly fine around the bilateral closest point of the cylinders, and it has been verified that a further increase of the number of integration points has no noticeable influence on the results.

[4] In addition to the 1D integration scheme above, we applied Gaussian quadrature with 12 integration segments in z_1- and 16 segments in y_1-direction (see Figure 5.2 for the definition of the coordinates), once again with adaptive fineness and 5 integration points each, and verified that a further increase of the number of integration points has no noticeable influence on the results.

(a) Mutual angle $\alpha = 0°$

(b) Mutual angle $\alpha = 2.8125°$

(c) Mutual angle $\alpha = 11.25°$

(d) Mutual angle $\alpha = 22.5°$

(e) Mutual angle $\alpha = 45°$
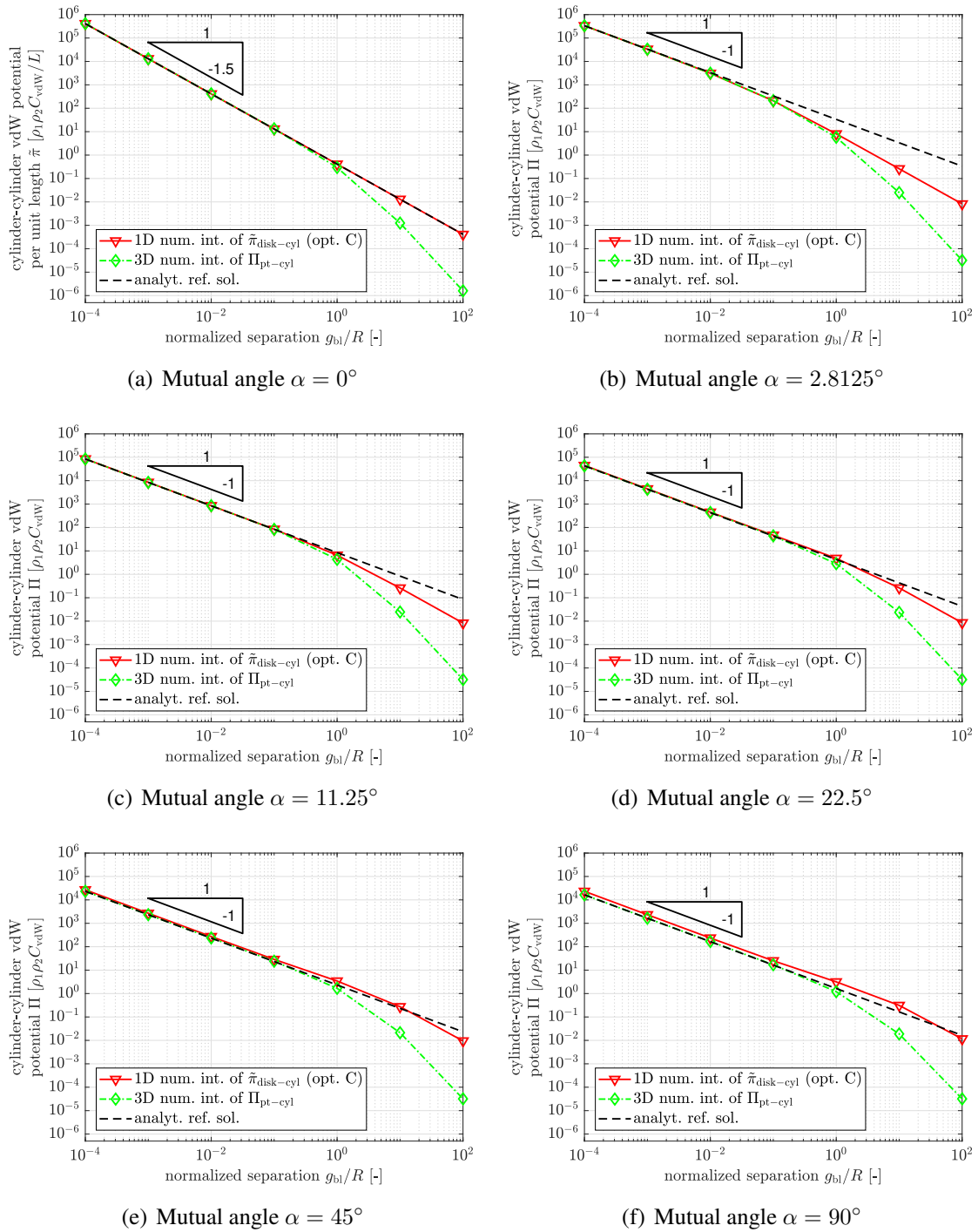
(f) Mutual angle $\alpha = 90°$

Figure 5.4.: Interaction potential of two cylinders as a function of the dimensionless minimal surface separation g_{bl}/R at different mutual angles α. Verification of the analytical expression for the disk-cylinder potential $\tilde{\pi}_{6,\text{disk-cyl}}$ from Equation (5.32) (used together with the SBIP approach from Section 5.1; red line with triangles) by means of a numerical reference solution obtained via 3D Gaussian quadrature of the point-half space potential $\Pi_{6,\text{pt-hs}}$ from Equation (A.18) (green line with diamonds) and by means of analytical reference solutions summarized in Section 2.3.2 (black dashed line).

being an inverse power-law with exponent 1.5 is correctly reproduced. Taking into account also the reference from 3D numerical integration, the accuracy is found to be excellent even for $g_{bl}/R \lesssim 1$, which is already well into the region of intermediate separations and the interaction potential values have dropped by several orders of magnitude. To give a number, the relative error is approx. 2.3% for $g_{bl}/R = 0.1$, increases to approx. 39% for $g_{bl}/R = 1$, and decreases as expected with decreasing separation. Considering the next plot 5.4(b) for $\alpha = \pi/64$, it is striking to see that the asymptotic scaling behavior now follows the g_{bl}^{-1} law as theoretically predicted for skew cylinders $\alpha \neq 0$ in Equation (2.18). Despite this sharp transition between both cases $\alpha = 0$ and $\alpha \neq 0$, the SBIP approach with the "option C" disk-cylinder law $\tilde{\pi}_{m,disk-cyl}$ again shows the correct asymptotic scaling behavior and agrees very well with the 3D numerical reference solution up to separations of $g_{bl}/R \lesssim 1$. The same statements hold for all other mutual angles shown in Figure 5.4(c) - 5.4(f), although one important point requires some more discussion. It is clearly visible for $\alpha = \pi/2$ and noticeable above $\alpha \approx \pi/4$ that the "option C" disk-cylinder law $\tilde{\pi}_{m,disk-cyl}$ no longer approaches the correct level of the asymptotic solution for small separations, however still shows the correct g_{bl}^{-1} scaling behavior. This deviation from the analytical as well as numerical reference solution by an almost constant factor of e.g. approx. 1.5 for the worst case $\alpha = \pi/2$ can be attributed to the additional simplifications made for option C of $\tilde{\pi}_{m,disk-cyl}$ and is not observable for the more accurate yet more complex option A and B expressions as will be shown in a subsequent analysis further down. At this point, the most important conclusion to take away from analyzing the accuracy of the "option C" disk-cylinder potential $\tilde{\pi}_{m,disk-cyl}$ as a reduced interaction law within the general SBIP approach therefore is that the accuracy is best for the regime of small separations $g_{bl}/R \lesssim 1$ and particularly for small angles, which is by far the most important one, because the interaction potential values are by far the highest. Note also in this respect that the only stable equilibrium configuration of two adhesive fibers is the one of straight parallel fibers and it seems especially important to achieve the highest accuracy at and around this special configuration. Finally, and maybe even most important is the finding that the correct asymptotic scaling behavior $g_{bl}^{-1.5}$ and g_{bl}^{-1} is met for both distinctive cases $\alpha = 0$ and $\alpha \neq 0$, respectively.

Specific investigation of the scaling behavior with respect to the mutual angle
Having observed the sharp transition between the cases $\alpha = 0$ and $\alpha \neq 0$ above it seems worth to have a more specific look at the angle dependency and especially the $\sin \alpha^{-1}$ scaling behavior as theoretically predicted by Equation (2.18) for the limit of small separations. The double-logarithmic plots in Figure 5.5 thus complement the analysis above by showing the dimensionless interaction potential as a function of the sine of the mutual angle α for various separations. Note the different scales on the vertical axes, which once again underline the importance of the small separation regime. The considered scenario of two cylinders and the three different solutions for the two-cylinder interaction potential are identical to the previous Figure 5.4. Most importantly, the theoretically predicted scaling behavior is confirmed by the numerical reference solution and reproduced by the disk-cylinder potential law $\tilde{\pi}_{6,disk-cyl}$ (option C) from Equation (5.32). Moreover, one can clearly observe the limits of validity of the analytical reference solution (2.18) and particularly the predicted $1/\sin \alpha$ scaling due to the underlying assumptions of small separations and $\alpha \neq 0$. In order to include also the special value $\alpha = 0$ of parallel

(a) Surface separation $g_{\mathrm{bl}}/R = 10^{-3}$

(b) Surface separation $g_{\mathrm{bl}}/R = 10^{-2}$

(c) Surface separation $g_{\mathrm{bl}}/R = 10^{-1}$

(d) Surface separation $g_{\mathrm{bl}}/R = 1$
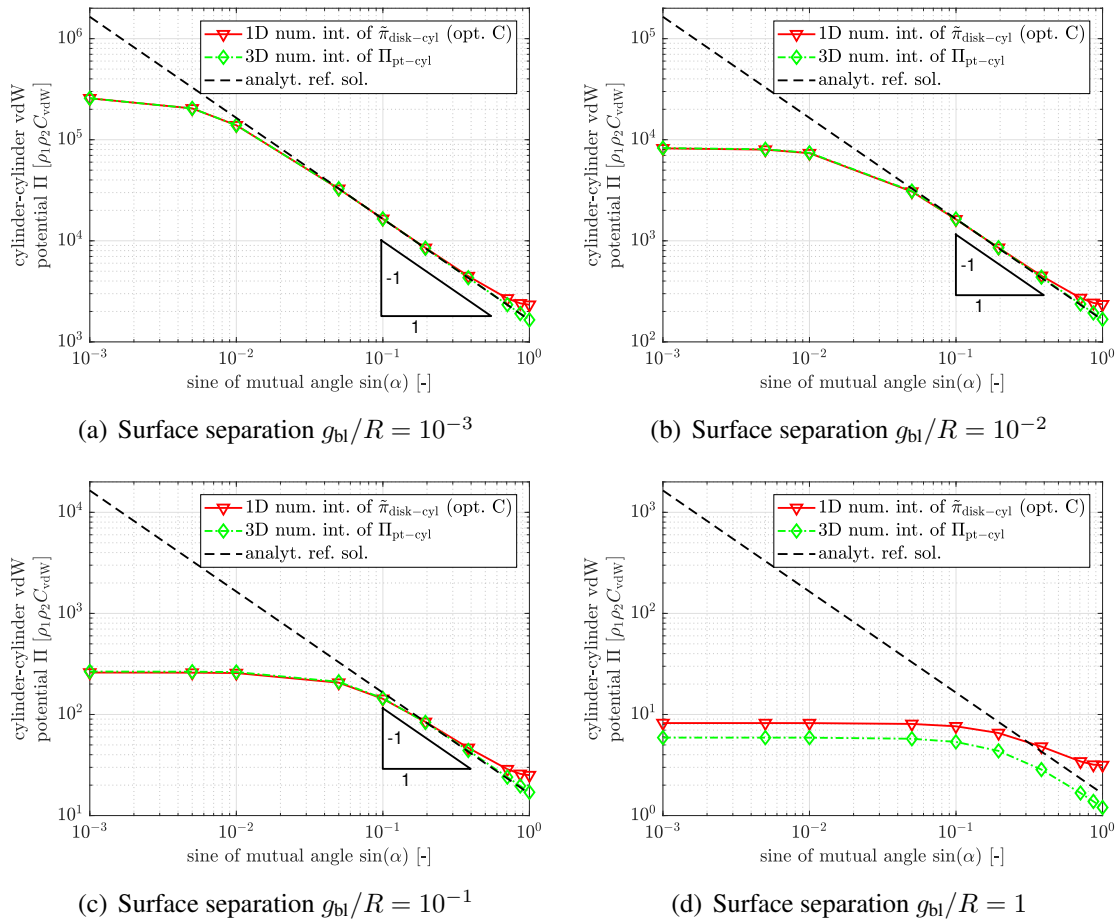
Figure 5.5.: Interaction potential of two cylinders as a function of the sine of the mutual angle at different smallest surface separations g_{bl}/R. Verification of the analytical expression for the disk-cylinder potential $\tilde{\pi}_{6,\mathrm{disk\text{-}cyl}}$ from Equation (5.32) (used together with the SBIP approach from Section 5.1; red line with triangles) by means of a numerical reference solution obtained via 3D Gaussian quadrature of the point-half space potential $\Pi_{6,\mathrm{pt\text{-}hs}}$ from Equation (A.18) (green line with diamonds) and by means of analytical reference solutions summarized in Section 2.3.2 (black dashed line).

cylinders and to get a more intuitive impression of the change of the interaction potential over the angle $\alpha \in [0, \pi/2]$, the equivalent plots as function of the angle α and in semi-logarithmic style are provided in Appendix D (cf. Figure D.2).

Comparison of options A, B and C

Figure 5.6 specifically compares the different options A, B and C of the disk-cylinder interaction potential derived in Section 5.2.1. Again, additional plots as function of the angle α and in semi-logarithmic style are provided in Appendix D (cf. Figure D.1). For parallel as well as perpendicular cylinders, option A and B are identical, as follows directly from the definition in Equations (5.25) and either (5.27) or (5.28). In all other cases, option B is closer to the numerical reference solution than option A and is thus the most accurate variant. Most important, however, is the fact that both options A and B perfectly match the asymptotic solution for small separations for all mutual angles up to $\alpha = \pi/2$ (see e.g. Figure 5.6(d) and Figure D.1(a)), which has been identified as the most noticeable inaccuracy of the option C potential law above. Therefore, future applications of the presented analytical disk-cylinder interaction potential laws with a strong focus on minimizing the approximation error and less restrictions with respect to the complexity of the equations probably want to use the option B expressions from Equations (5.25) and (5.28). As outlined above, in the scope of this work the differences are considered small and irrelevant enough to use the significantly simpler option C expression from Equation (5.32) as the reduced interaction law within the SBIP approach proposed in Section 5.1.

Comparison with the previously used SSIP interaction law $\tilde{\tilde{\pi}}_{\mathrm{m,disk\|disk}}$ without orientation information

As a last aspect of this comprehensive accuracy analysis, Figure 5.7 demonstrates that the novel SBIP law $\tilde{\pi}_{\mathrm{m,disk\text{-}cyl}}$ from Equation (5.32) in combination with the general SBIP approach from Section 5.1 is significantly more accurate than the previous method using the SSIP law $\tilde{\tilde{\pi}}_{\mathrm{m,disk\|disk}}$ from Equation (4.7) in combination with the general SSIP approach as proposed in Chapter 4. Recall the important result of the SSIP verification in Section 4.5.1 that the simple and readily available section-section interaction law $\tilde{\tilde{\pi}}_{\mathrm{m,disk\|disk}}$ from Equation (4.7) does not yield the correct asymptotic scaling behavior in the limit of small separations, which is decisive in case of short-ranged interactions, and that the orientation of the (disk-shaped) cross-sections would need to be included in the reduced interaction law $\tilde{\tilde{\pi}}$ to improve this crucial characteristic. With the alternative SBIP approach specialized on short-range interactions and the derived SBIP law $\tilde{\pi}_{\mathrm{m,disk\text{-}cyl}}$, the goal of reproducing the correct asymptotic scaling behavior has finally been accomplished.

Conclusions

The conclusions to take away from this important accuracy analysis are summarized as follows. To begin with, the point-half space potential used as point-cylinder potential to compute the 3D numerical reference solution yields the correct asymptotic scaling behavior and allows to verify the two-cylinder potential in the range of intermediate separations where no analytical solution is known. This is an important finding, because the same point-half space potential is used in the analytical derivations of the disk-cylinder potential $\tilde{\pi}_{\mathrm{m,disk\text{-}cyl}}$ of which all three considered options have been analyzed in this section. The pleasantly simple option C (cf. Equation (5.32))

(a) Mutual angle $\alpha = 0°$

(b) Mutual angle $\alpha = 2.8125°$

(c) Mutual angle $\alpha = 45°$

(d) Mutual angle $\alpha = 90°$

(e) Surface separation $g_{\text{bl}}/R = 10^{-3}$

(f) Surface separation $g_{\text{bl}}/R = 10^{-1}$

Figure 5.6.: Interaction potential of two cylinders as a function of the dimensionless minimal surface separation g_{bl}/R at different mutual angles α (first and second row) and as a function of $\sin\alpha$ at different minimal surface separations g_{bl}/R (third row). Comparison of the options A (Equations (5.25) with (5.27); brown line with big diamonds), B (Equations (5.25) with (5.28); blue dashed line with pluses) and C (Equation (5.32); red line with triangles) of the analytical expression for the disk-cylinder potential $\tilde{\pi}_{6,\text{disk-cyl}}$ (used together with the SBIP approach from Section 5.1). The numerical reference solution obtained via 3D Gaussian quadrature of the point-half space potential $\Pi_{6,\text{pt-hs}}$ from Equation (A.18) (green line with diamonds) and the analytical reference solutions summarized in Section 2.3.2 (black dashed line) are plotted as reference.

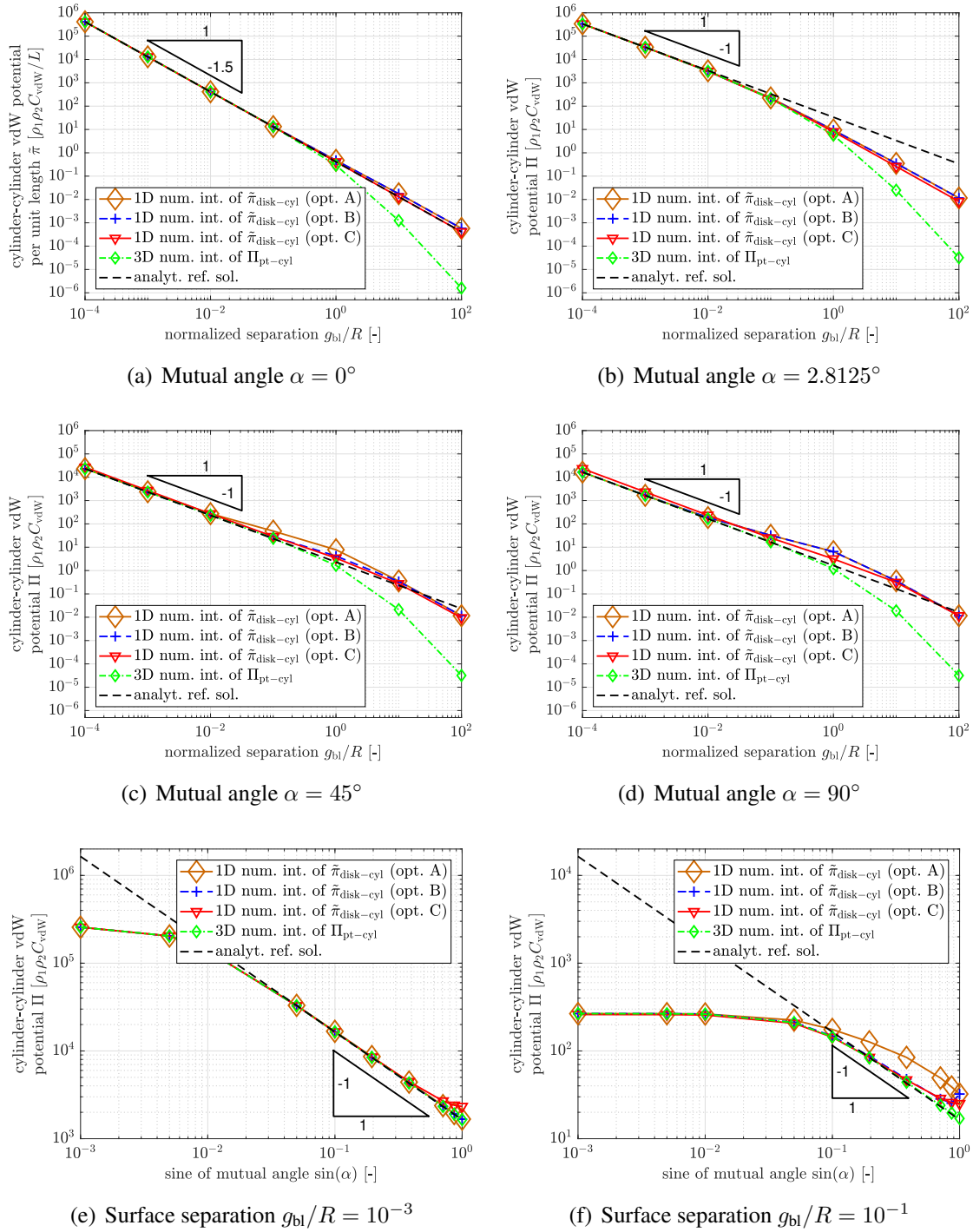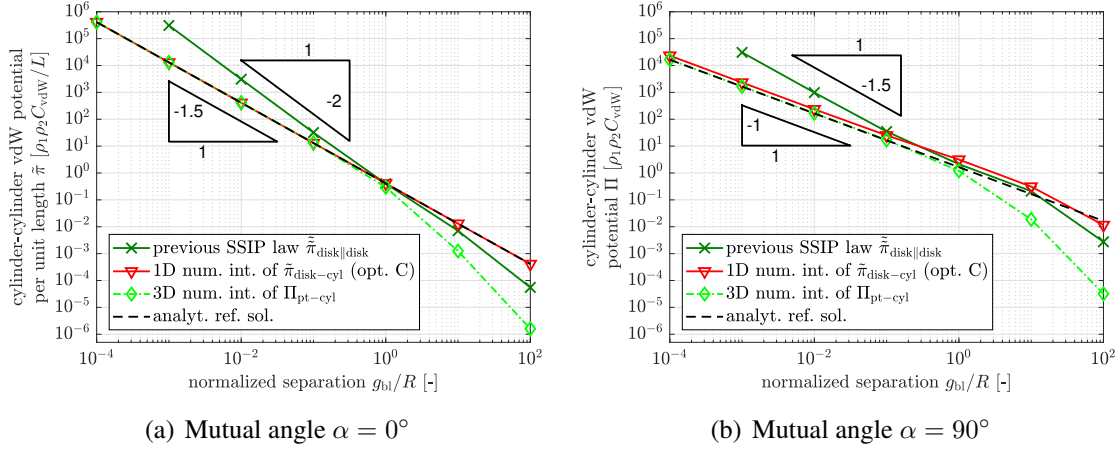(a) Mutual angle $\alpha = 0°$ (b) Mutual angle $\alpha = 90°$

Figure 5.7.: Interaction potential of two cylinders as a function of the dimensionless minimal surface separation g_{bl}/R at different mutual angles α. Comparison of the previously used SSIP law $\tilde{\tilde{\pi}}_{6,\mathrm{disk}\|\mathrm{disk}}$ from Equation (4.7) (used together with the SSIP approach from Section 4.2; dark green line with crosses) with the final option C (Equation (5.32); red line with triangles) of the analytical expression for the disk-cylinder potential $\tilde{\pi}_{6,\mathrm{disk\text{-}cyl}}$ (used together with the SBIP approach from Section 5.1). The numerical reference solution obtained via 3D Gaussian quadrature of the point-half space potential $\Pi_{6,\mathrm{pt\text{-}hs}}$ from Equation (A.18) (green line with diamonds) and the analytical reference solutions summarized in Section 2.3.2 (black dashed line) are plotted as reference.

shows the correct asymptotic scaling behavior in the decisive regime of small separations and small angles and is thus considered the optimal compromise between accuracy and complexity of the expression for the purposes of this work. In particular, also the theoretically predicted $1/\sin\alpha$ angle dependence (for non-parallel cylinders $\alpha \neq 0$) has been successfully verified. In addition to that, options A (Equations (5.25) with (5.27)) and B (Equations (5.25) with (5.28)) also ensure the correct scaling behavior for large angles (and small separations) and thus achieve an increased accuracy at the prize of an increased complexity of the expressions. Taking into account the entire configuration space of separations and angles, option B shows the highest accuracy and is thus recommended for future applications with less or no restrictions in terms of the complexity of the expressions.

As compared to the simple SSIP law $\tilde{\tilde{\pi}}_{\mathrm{m,disk}\|\mathrm{disk}}$ neglecting cross-section orientations previously applied within the SSIP approach from Section 4.2, the use of the derived SBIP law $\tilde{\pi}_{\mathrm{m,disk\text{-}cyl}}$ (option C) within the SBIP approach is significantly more accurate and particularly ensures the correct asymptotic scaling behavior. To conclude this entire Section 5.2, it is a great achievement of the analytical 5D integration using series expansions that the problem of vdW/LJ interaction between a disk and a cylinder can be described by an analytical closed-form expression $\tilde{\pi}_{\mathrm{m,disk\text{-}cyl}}$ instead of the otherwise required 3D/5D numerical integration (of a numerically unfavorable inverse power law in the regime of small separations) and that such a high accuracy is achieved.

5.3. Virtual work contribution

Recall from Equation (4.2) that it is the variation of the two-body interaction energy $\delta\Pi_{\text{ia}}$, which needs to be evaluated to incorporate the effects of molecular interactions into both the theoretical and computational framework of nonlinear continuum mechanics. According to the general SBIP approach proposed in Section 5.1 combined with (any of the variant A, B or C of) the generic disk-cylinder interaction potential law $\tilde{\pi}_{\text{m,disk-cyl}}$ derived in Section 5.2.1, the variation of the two-fiber interaction energy reads

$$\delta\Pi_{\text{ia}} = \int_0^{l_1} \delta\tilde{\pi}_{\text{m,disk-cyl}} \, \mathrm{d}s_1. \tag{5.34}$$

Note that $\delta(\mathrm{d}s_1)$ vanishes due to the fact that $\mathrm{d}s_1 = \|\boldsymbol{r}_{01}'(\xi_1)\| \, \mathrm{d}\xi_1$ only depends on the element parameter coordinate ξ_1 and the initial ("0") configuration of the slave beam, but not on the current configuration, i.e., current values of the primary degrees of freedom. As argued in the previous Section 5.2, the final expression $\tilde{\pi}_{\text{m,disk-cyl}}(g_{\text{ul}}, \alpha)$ from Equation (5.32) (cf. option C) is considered to be the best compromise between accuracy and complexity and will thus be used for the numerical examples. For the sake of brevity, the subscripts "m" and "disk-cyl" as well as the function arguments (g_{ul}, α) of $\tilde{\pi}$ will be omitted in the remainder of this section. The variation of $\tilde{\pi}$ consists of the following four parts

$$\delta\Pi_{\text{ia}} = \int_0^{l_1} \frac{\mathrm{d}\,\tilde{\pi}}{\mathrm{d}\,g_{\text{ul}}} \delta g_{\text{ul}} + \frac{\mathrm{d}\,\tilde{\pi}}{\mathrm{d}(\cos\alpha)} \delta(\cos\alpha) \, \mathrm{d}s_1, \tag{5.35}$$

which will be determined subsequently in the next steps. First, the derivatives of $\tilde{\pi}$ can be conveniently expressed in a recursive manner as follows:

$$\frac{\mathrm{d}\,\tilde{\pi}}{\mathrm{d}\,g_{\text{ul}}} = \frac{\left(-m + \frac{9}{2}\right)}{g_{\text{ul}}} \tilde{\pi} \tag{5.36}$$

$$\frac{\mathrm{d}\,\tilde{\pi}}{\mathrm{d}(\cos\alpha)} = -\frac{R_1 \cos\alpha}{R_1 \cos^2\alpha + R_2} \tilde{\pi} \tag{5.37}$$

Note that the remaining two parts δg_{ul} and $\delta(\cos\alpha)$ are known from the macroscopic line contact formulation proposed in [110] and its combination with a point contact formulation presented in a unified ABC formulation [111], respectively. Both are reproduced here for the sake of completeness and a unified notation.

$$\delta g_{\text{ul}} = \delta d_{\text{ul}} = \delta\boldsymbol{d}_{\text{ul}}^T \boldsymbol{n}_{\text{ul}} = \left(\delta\boldsymbol{r}_1^T(\xi_1) - \delta\boldsymbol{r}_2^T(\xi_{2\text{c}})\right) \boldsymbol{n}_{\text{ul}} \tag{5.38}$$

$$\delta(\cos\alpha) = \left(\delta\boldsymbol{r}_1'^T(\xi_1) \boldsymbol{v}_{\alpha 1} + \delta\left(\boldsymbol{r}_2'^T(\xi_{2\text{c}})\right) \boldsymbol{v}_{\alpha 2}\right) \operatorname{sgn}(\boldsymbol{t}_1^T \boldsymbol{t}_2) \tag{5.39}$$

In the last equation, we have introduced the auxiliary vectors

$$\boldsymbol{v}_{\alpha 1} := \frac{1}{\|\boldsymbol{r}_1'\|} \left(\boldsymbol{I}_{3\times 3} - \boldsymbol{t}_1 \otimes \boldsymbol{t}_1^T\right) \boldsymbol{t}_2 \quad \text{and} \quad \boldsymbol{v}_{\alpha 2} := \frac{1}{\|\boldsymbol{r}_2'\|} \left(\boldsymbol{I}_{3\times 3} - \boldsymbol{t}_2 \otimes \boldsymbol{t}_2^T\right) \boldsymbol{t}_1. \tag{5.40}$$

Note the difference between $\delta\left(\boldsymbol{r}_2^{\shortmid}(\xi_{2c})\right)$ and $\delta\boldsymbol{r}_2^{\shortmid}(\xi_{2c})$ in Equation (5.39), which originates from the fact that ξ_{2c} is the result of a (closest) point-to-curve projection. In contrast to δg_{ul} in Equation (5.38)[5], here the additional contribution from $\delta\xi_{2c}$ must actually be computed and included to ensure a variationally consistent formulation. Also for the later reference, all the expressions required in this respect are given here as

$$\delta(\boldsymbol{r}_2(\xi_{2c})) = \delta\boldsymbol{r}_2(\xi_{2c}) + \boldsymbol{r}_2^{\shortmid}(\xi_{2c})\,\delta\xi_{2c} \tag{5.41}$$

$$\delta(\boldsymbol{r}_2^{\shortmid}(\xi_{2c})) = \delta\boldsymbol{r}_2^{\shortmid}(\xi_{2c}) + \boldsymbol{r}_2^{\shortparallel}(\xi_{2c})\,\delta\xi_{2c} \tag{5.42}$$

and finally

$$\delta\xi_{2c} = \frac{1}{p_{2,\xi_2}}\Big(-\delta\boldsymbol{r}_1^T\boldsymbol{r}_2^{\shortmid} + \delta\boldsymbol{r}_2^T\boldsymbol{r}_2^{\shortmid} - \delta\boldsymbol{r}_2^{\shortmid T}\underbrace{(\boldsymbol{r}_1 - \boldsymbol{r}_2)}_{=\,\boldsymbol{d}_{\mathrm{ul}}}\Big), \tag{5.43}$$

where the derivation of the scalar orthogonality condition $p_2 := \boldsymbol{r}_2^{\shortmid T}\boldsymbol{d}_{\mathrm{ul}} \overset{!}{=} 0$ with respect to ξ_2 reads

$$p_{2,\xi_2} = \boldsymbol{r}_2^{\shortparallel T}\boldsymbol{d}_{\mathrm{ul}} - \boldsymbol{r}_2^{\shortmid T}\boldsymbol{r}_2^{\shortmid}. \tag{5.44}$$

At this point, we have gathered all the required pieces that allow us to evaluate the virtual work contribution from molecular interactions $\delta\Pi_{\mathrm{ia}}$ according to Equation (5.34). As discussed along with the general SBIP approach in Section 5.1, the 1D integral along the slave beam is evaluated numerically, e.g., by means of Gaussian quadrature. Note that the correctness of the presented and implemented expressions of this section has been verified to be consistent with the corresponding interaction energy Π_{ia} (see Equations (5.2) with (5.32)) by means of an automatic differentiation tool [66].

Solving the nonlinear system of equations (4.2) generally requires two further steps of discretization and subsequent linearization of this additional contribution $\delta\Pi_{\mathrm{ia}}$. The discrete counterpart $\delta\Pi_{\mathrm{ia,h}}$ of the space-continuous form $\delta\Pi_{\mathrm{ia}}$ is obtained via substitution of the centerline interpolation scheme from Equations (3.19) and (3.20) into Equation (5.35). This allows to identify the discrete residual vectors $\mathbf{r}_{\mathrm{ia,i}}$ of the interacting beam elements $i = \{1, 2\}$ that finally result from the molecular interactions. As a last step, the linearization of these residual vectors $\Delta[\delta\Pi_{\mathrm{ia}}]$ with respect to the vector of primary degrees of freedom $\hat{\mathbf{d}}$ is presented in Appendix C.2.

Discussion of the special treatment required for master beam endpoints.
Recall from the derivation of the disk-cylinder potential law $\tilde{\pi}_{\mathrm{m,disk\text{-}cyl}}$ in Section 5.2.1 that the cylinder used as the surrogate for the master beam has been assumed to have an infinite length. Due to the very short range of the interactions considered here, this is an excellent approximation in almost all cases. In the special case that the result of the closest-point projection is a master beam endpoint, however, this approximation overestimates the true contribution to the interaction potential approximately by a factor of two. Again, given the short range of interactions

---

[5] In the final step of Equation (5.38), the orthogonality condition $\boldsymbol{r}_2^{\shortmid T}(\xi_{2c})\,\boldsymbol{n}_{\mathrm{ul}} \equiv 0$ has been exploited and the additional contribution from the variation of the (closest-point) arc-length coordinate on the master side $\delta\xi_{2c}$ vanishes.

considered here, the resulting model error can be interpreted as if the master beam was slightly longer[6] than it actually should be.

Due to this short range of interactions and the rarity of this event involving the endpoints of slender fibers among all those cases involving the points between the endpoints, the influence of this model error on the total two-body interaction potential is expected to be negligible in almost all applications. Nevertheless, we can think of the worst case scenario, where two straight, parallel, adhesive fibers of finite length (with equilibrium inter-axis separation) slide along each other in axial direction and the only effective force would be the one at the fiber endpoints, where the influence of the second beam on an exemplarily considered cross-section of the first beam rapidly decreases, because the second beam ends. Whereas the unmodified SBIP approach using $\tilde{\pi}_{\mathrm{m,disk\text{-}cyl}}$ would yield zero force, it could be augmented by a special treatment of master beam endpoints that subtracts half of the interaction potential contribution at any integration point where the result of the closest-point projection is a master beam endpoint. This procedure probably needs to be smooth such that the transition from the full disk-cylinder interaction potential contribution to half that value at the master beam endpoint needs to be smeared out over a small, yet finite length of the beam. Due to the expected negligible effect in almost all applications, this augmentation of the SBIP approach is left for future work, but this discussion as well as the described worst-case scenario should be useful when implementing, calibrating and verifying this model enhancement.

5.4. Regularization and selected algorithmic aspects

This section discusses the numerical regularization scheme as well as further algorithmic aspects that are of special importance for the application of the novel SBIP approach and the proposed interaction law $\tilde{\pi}$.

5.4.1. Regularization of the reduced disk-cylinder interaction law in the limit of zero separation

Due to the inherent singularity of molecular interaction potentials in the limit of zero separation, a numerical regularization is required in order to solve the governing, nonlinear system of equations resulting from (4.2) in a robust manner. See Section 4.4.3 for a detailed discussion of the motivation, the strategy as well as the effect of a suitable regularization. Generally, such a numerical regularization is a standard approach in (beam) contact formulations (see e.g. [44, 111]) and in the specific context of the LJ potential considered here, it has first been applied in [136]. In analogy to the regularization of the section-section interaction potential law in Section 4.4.3, a quadratic/linear extrapolation of the section-beam interaction potential/force law will be applied here in the range of very small gap values $g_{\mathrm{ul}} < g_{\mathrm{ul,reg}}$ below a certain regularization parameter $g_{\mathrm{ul,reg}} \in \mathbb{R}^+$. It has already been argued in Section 4.4.3 that if this regularization parameter is chosen sufficiently small, which means smaller than any gap value occurring in any

---

[6] by the length of the cut-off radius longer, to be more precise

converged configuration of any time/load step throughout the entire simulation, such a regularization scheme will not influence the results at all and can thus be considered a mere auxiliary means to enable and improve the iterative process of solving the nonlinear system of equations. The equation describing the mentioned quadratic extrapolation below $g_{\text{ul,reg}}$ for a general section-beam interaction potential law $\tilde{\pi}$ is given as follows:

$$
\tilde{\pi}_{\text{reg}} = \begin{cases} \tilde{\pi}(g_{\text{ul,reg}}) + \dfrac{\mathrm{d}\,\tilde{\pi}}{\mathrm{d}\,g_{\text{ul}}}\bigg|_{g_{\text{ul,reg}}} (g_{\text{ul}} - g_{\text{ul,reg}}) + \dfrac{1}{2}\dfrac{\mathrm{d}^2\,\tilde{\pi}}{\mathrm{d}\,g_{\text{ul}}^2}\bigg|_{g_{\text{ul,reg}}} (g_{\text{ul}} - g_{\text{ul,reg}})^2, & g_{\text{ul}} < g_{\text{ul,reg}} \\[3mm] \tilde{\pi}(g_{\text{ul}}), & g_{\text{ul}} \geq g_{\text{ul,reg}} \end{cases}
\tag{5.45}
$$

Note that the required derivatives of this regularized potential law $\tilde{\pi}_{\text{reg}}$ accordingly change to

$$
\frac{\mathrm{d}\,\tilde{\pi}_{\text{reg}}}{\mathrm{d}\,g_{\text{ul}}} = \begin{cases} \dfrac{\mathrm{d}\,\tilde{\pi}}{\mathrm{d}\,g_{\text{ul}}}\bigg|_{g_{\text{ul,reg}}} + \dfrac{\mathrm{d}^2\,\tilde{\pi}}{\mathrm{d}\,g_{\text{ul}}^2}\bigg|_{g_{\text{ul,reg}}} (g_{\text{ul}} - g_{\text{ul,reg}}), & g_{\text{ul}} < g_{\text{ul,reg}} \\[3mm] \dfrac{\mathrm{d}\,\tilde{\pi}}{\mathrm{d}\,g_{\text{ul}}}(g_{\text{ul}}), & g_{\text{ul}} \geq g_{\text{ul,reg}} \end{cases}
\tag{5.46}
$$

$$
\frac{\mathrm{d}^2\,\tilde{\pi}_{\text{reg}}}{\mathrm{d}\,g_{\text{ul}}^2} = \begin{cases} \dfrac{\mathrm{d}^2\,\tilde{\pi}}{\mathrm{d}\,g_{\text{ul}}^2}\bigg|_{g_{\text{ul,reg}}}, & g_{\text{ul}} < g_{\text{ul,reg}} \\[3mm] \dfrac{\mathrm{d}\,\tilde{\pi}}{\mathrm{d}\,g_{\text{ul,reg}}}(g_{\text{ul}}), & g_{\text{ul}} \geq g_{\text{ul,reg}} \end{cases}
\tag{5.47}
$$

$$
\frac{\mathrm{d}\,\tilde{\pi}_{\text{reg}}}{\mathrm{d}(\cos\alpha)} = \begin{cases} \dfrac{\mathrm{d}\,\tilde{\pi}}{\mathrm{d}(\cos\alpha)}\bigg|_{g_{\text{ul,reg}}} + \dfrac{\mathrm{d}^2\,\tilde{\pi}}{\mathrm{d}(\cos\alpha)\,\mathrm{d}\,g_{\text{ul}}}\bigg|_{g_{\text{ul,reg}}} (g_{\text{ul}} - g_{\text{ul,reg}}) \ldots \\[3mm] \qquad + \dfrac{1}{2}\dfrac{\mathrm{d}^3\,\tilde{\pi}}{\mathrm{d}(\cos\alpha)\,\mathrm{d}\,g_{\text{ul}}^2}\bigg|_{g_{\text{ul,reg}}} (g_{\text{ul}} - g_{\text{ul,reg}})^2, & g_{\text{ul}} < g_{\text{ul,reg}} \\[3mm] \dfrac{\mathrm{d}\,\tilde{\pi}}{\mathrm{d}(\cos\alpha)}(g_{\text{ul}}), & g_{\text{ul}} \geq g_{\text{ul,reg}} \end{cases}
\tag{5.48}
$$

$$
\frac{\mathrm{d}^2\,\tilde{\pi}_{\text{reg}}}{\mathrm{d}(\cos\alpha)\,\mathrm{d}\,g_{\text{ul}}} = \begin{cases} \dfrac{\mathrm{d}^2\,\tilde{\pi}}{\mathrm{d}(\cos\alpha)\,\mathrm{d}\,g_{\text{ul}}}\bigg|_{g_{\text{ul,reg}}} + \dfrac{\mathrm{d}^3\,\tilde{\pi}}{\mathrm{d}(\cos\alpha)\,\mathrm{d}\,g_{\text{ul}}^2}\bigg|_{g_{\text{ul,reg}}} (g_{\text{ul}} - g_{\text{ul,reg}}), & g_{\text{ul}} < g_{\text{ul,reg}} \\[3mm] \dfrac{\mathrm{d}^2\,\tilde{\pi}}{\mathrm{d}(\cos\alpha)\,\mathrm{d}\,g_{\text{ul}}}(g_{\text{ul}}), & g_{\text{ul}} \geq g_{\text{ul,reg}} \end{cases}
\tag{5.49}
$$

$$\frac{\mathrm{d}^2\,\tilde{\pi}_{\mathrm{reg}}}{\mathrm{d}(\cos\alpha)^2} = \begin{cases} \left.\dfrac{\mathrm{d}^2\,\tilde{\pi}}{\mathrm{d}(\cos\alpha)^2}\right|_{g_{\mathrm{ul,reg}}} + \left.\dfrac{\mathrm{d}^3\,\tilde{\pi}}{\mathrm{d}(\cos\alpha)^2\,\mathrm{d}\,g_{\mathrm{ul}}}\right|_{g_{\mathrm{ul,reg}}} (g_{\mathrm{ul}} - g_{\mathrm{ul,reg}}) \ldots \\ \qquad + \dfrac{1}{2}\left.\dfrac{\mathrm{d}^4\,\tilde{\pi}}{\mathrm{d}(\cos\alpha)^2\,\mathrm{d}\,g_{\mathrm{ul}}^2}\right|_{g_{\mathrm{ul,reg}}} (g_{\mathrm{ul}} - g_{\mathrm{ul,reg}})^2, & g_{\mathrm{ul}} < g_{\mathrm{ul,reg}} \\ \dfrac{\mathrm{d}^2\,\tilde{\pi}}{\mathrm{d}(\cos\alpha)^2}(g_{\mathrm{ul}}), & g_{\mathrm{ul}} \geq g_{\mathrm{ul,reg}}. \end{cases} \quad (5.50)$$

These expressions for the regularized general interaction potential $\tilde{\pi}$ and its first and second derivatives replace the original expressions presented in the context of Sections 5.2.1 and 5.3 and Appendix C.2, respectively. For the specific disk-cylinder interaction potential from Equation (5.32), most of the derivatives required on the right hand side of these equations have already been presented in Section 5.3 and Appendix C.2, and the additionally required third and fourth derivative follow (recursively) as

$$\frac{\mathrm{d}^3\,\tilde{\pi}_{\mathrm{m,disk\text{-}cyl}}}{\mathrm{d}(\cos\alpha)^2\,\mathrm{d}\,g_{\mathrm{ul}}} = \left(-m + \frac{9}{2}\right)\frac{1}{g_{\mathrm{ul}}}\frac{\mathrm{d}^2\,\tilde{\pi}_{\mathrm{m,disk\text{-}cyl}}}{\mathrm{d}(\cos\alpha)^2}, \qquad (5.51)$$

$$\frac{\mathrm{d}^3\,\tilde{\pi}_{\mathrm{m,disk\text{-}cyl}}}{\mathrm{d}(\cos\alpha)\,\mathrm{d}\,g_{\mathrm{ul}}^2} = \left(-m + \frac{9}{2}\right)\left(-m + \frac{7}{2}\right)\frac{1}{g_{\mathrm{ul}}^2}\frac{\mathrm{d}\,\tilde{\pi}_{\mathrm{m,disk\text{-}cyl}}}{\mathrm{d}(\cos\alpha)} \qquad (5.52)$$

and

$$\frac{\mathrm{d}^4\,\tilde{\pi}_{\mathrm{m,disk\text{-}cyl}}}{\mathrm{d}(\cos\alpha)^2\,\mathrm{d}\,g_{\mathrm{ul}}^2} = \left(-m + \frac{9}{2}\right)\left(-m + \frac{7}{2}\right)\frac{1}{g_{\mathrm{ul}}^2}\frac{\mathrm{d}^2\,\tilde{\pi}_{\mathrm{m,disk\text{-}cyl}}}{\mathrm{d}(\cos\alpha)^2}. \qquad (5.53)$$

Note that this regularization needs to be applied to both the adhesive $m = 6$ and the repulsive $m = 12$ part of the LJ potential law. Altogether, the necessity of a suitable regularization scheme due to its significantly positive effect on robustness and efficiency (mentioned already in Section 4.4.3 for the SSIP laws) will be confirmed also in the context of the proposed SBIP approach and corresponding reduced interaction law $\tilde{\pi}$ by the numerical examples to be presented in Sections 5.5 and 7.4.

5.4.2. Objectivity and conservation properties

Recall from Section 5.3 that the final contributions to the discrete element residual vectors $\mathbf{r}_{\mathrm{ia}}$ resulting from the general SBIP approach in combination with the reduced interaction law derived in Section 5.2.1 have the same abstract form as in the case of macroscopic beam contact formulations [111]. Most importantly, they are functions of the unilateral gap g_{ul} and the mutual angle of the tangent vectors α. Due to this fact, the proofs presented in [111, Appendix B] likewise hold in this case and it is thus straightforward to conclude that also the SBIP approach in combination with the here proposed reduced interaction law fulfills objectivity, global conservation of linear and angular momentum as well as global conservation of energy.

5.4.3. Algorithm complexity

The following discussion focuses on the part of evaluating the total interaction potential $\delta\Pi_{\mathrm{ia}}$ (and likewise its linearization $\Delta[\delta\Pi_{\mathrm{ia}}]$) as this is the one determined by the computational approach to

molecular interactions of fibers. Depending on many other factors, this part may or may not be the dominating one in the entire algorithmic framework required for a nonlinear finite element solver in structural dynamics. Based on the experiences with the novel SBIP approach, the previously proposed SSIP approach from Chapter 4, and the attempt of directly evaluating $\delta\Pi_{ia}$ via 6D numerical integration (see Equation (2.12)), it can however be stated that in a best case scenario the computational cost of evaluating this part is still a considerable one and in the worst case scenario – using direct 6D numerical integration – it becomes so costly that it is actually unfeasible for any system of practical relevance. This initial general assessment shows both the urgent need for an efficient approach and also the high leverage of any potential improvement in this respect, which has actually been the main motivation for the development of the novel SBIP approach.

To narrow the broad topic of algorithm efficiency further down, this analysis can be restricted to the evaluation of one element pair, because the number of interacting element pairs can be considered a fixed number for now. This number mainly depends on the spatial distribution of the fibers and the range of interaction, i.e., the cut-off radius, which means that it will be limited due to both the short range of interactions considered in this chapter and the non-penetrability constraint restricting the closest packing of fibers. Note that the associated important question of an efficient search for element pairs and the selection of element pairs to be finally evaluated will be discussed in the following Sections 5.4.4 and 5.4.5.

At this point, recall from the previous analysis in Section 4.4.5 that the algorithm complexity of the evaluation of one element pair in case of direct 6D numerical integration of Equation (2.12) will be $\mathcal{O}(n_{\text{GP,tot,ele-length}}^2 \cdot n_{\text{GP,tot,transverse}}^4)$. Here, $n_{\text{GP,tot,ele-length}}$ and $n_{\text{GP,tot,transverse}}$ denote the number of integration points in axial and transverse direction, respectively. The SSIP approach already reduces this complexity significantly to $\mathcal{O}(n_{\text{GP,tot,ele-length}}^2)$ due to the replacement of the 4D numerical integration over the cross-section areas by an effective section-section interaction potential law. By the novel SBIP approach, this is finally reduced even further and for the remaining 1D integral along the slave beam (cf. Equation (5.2)), we obtain

$$\mathcal{O}\left(n_{\text{GP,tot,ele-length}}\right) \tag{5.54}$$

complexity. Bearing in mind the typically large number of integration points required to integrate the (short-ranged) molecular interaction laws with its high gradients with sufficient accuracy, this linear complexity makes a significant difference as compared to the quadratic complexity of the SSIP approach. Based on the experience of the numerical examples studied throughout this work, typical values are given as $n_{\text{GP,tot,ele-length}} = 50\ldots100$, which is thus the factor we can expect to save from this reduced dimensionality of numerical integration. However, this comes at the cost of the closest point-to-curve projection required in case of the novel SBIP approach. This projection consists of solving the scalar nonlinear orthogonality condition (cf. Equation (5.44)) e.g. by means of Newton's method, which however turns out to be rather insignificant as compared to evaluating the terms of the integrand. The net saving will thus be slightly smaller than the number of (axial) integration points per element, but still significant.

In addition to that, there is another positive effect to be considered. Due to the additional analytical integration step in the derivation of the reduced SBIP law from Section 5.2.1 as compared to the SSIP laws presented in Section 4.3.2, the (inverse) exponent of the effective interaction

law and thus integrand is reduced by one: cf. $-m + 9/2$ in Equation (5.32) vs. $-m + 7/2$ in Equation (4.7), for $m \geq 6$. In turn, this makes the integrand smoother and less integration points are required to achieve the same accuracy of the numerical integration. Especially for the short-ranged interactions e.g. from the LJ interaction with $m = 6$ and $m = 12$, this makes a significant difference in the decisive regime of small separations and contributes to the superior efficiency of the SBIP approach as compared to the SSIP approach or even the direct 6D numerical integration.

In this respect, it seems noteworthy to point out the clear separation of the general SSIP/SBIP approach and the applied reduced interaction law. Generally, the complexity of the specific expression does not necessarily depend on whether it is a SSIP or SBIP law. However, some conclusions like the one just made for the resulting exponent of the power law – if consistently derived from a inverse-power point pair potential law – are possible. Likewise, assuming homogeneous, circular cross-sections we can state that the mutual configuration of the disk-disk system has four degrees of freedom (cf. Section 4.3.1) whereas the disk-cylinder system can be described by three degrees of freedom as discussed in Section 5.2.1. However, this does not allow to estimate the complexity of the specific expressions even in the hypothetical case of exact analytical interaction laws. Given the concrete examples of expressions for short-range interactions presented in Section 5.2.1 and 4.3.2, respectively, it is important to underline that they are based on different simplifying assumptions and thus naturally have a different accuracy as discussed in Section 5.2.2. The fact that the SSIP law expressions from Section 4.3 are simpler than their SBIP law counterparts must thus be seen in the light of this tradeoff between simplicity and accuracy. Nevertheless, when comparing the performance in the numerical example to be presented in Section 7.4, one will notice this effect of less operations being required to evaluate the simpler yet less accurate specific SSIP law as compared to the SBIP law.[7] This contrary effect diminishes the observable net speed-up resulting from the superior efficiency of the general SBIP approach over the general SSIP approach described above.

To conclude this important assessment of the algorithm's efficiency, it can be stated that the general SBIP approach is significantly more efficient than the SSIP approach (which in turn is still significantly more efficient than a direct 6D numerical integration). This holds even despite the superior accuracy of the applied SBIP law (5.32), which is therefore also slightly more complex as compared to the simple SSIP law (4.7). In the numerical example of peeling two adhesive fibers to be presented in Section 7.4, the combination of the novel SBIP approach and the specific SBIP law turns out to be approximately a factor of 3.8 faster than its SSIP counterpart.

---

[7] Note that actually the evaluation of the discrete residual vector and, predominantly, the tangent stiffness matrix should be considered when comparing simplicity of expressions and number of required operations. For the sake of clarity, however, this argument is made on the level of reduced interaction laws knowing well that the judgment holds true also for the resulting residual vector and stiffness matrix. In fact, the differences in simplicity increase due to the two differentiation steps.

5.4.4. Search for interacting pairs and partitioning for parallel computing

The search for interacting beam element pairs follows an efficient standard algorithm commonly referred to as bucket search (see e.g. [164] for details), which has already been used in combination with the SSIP approach (cf. Section 4.4.6). Due to the very short range of the interactions such as vdW and repulsive steric forces considered in this chapter, the requirements for the search algorithm are very similar to those from macroscopic (beam) contact formulations. The resulting small cut-off radius is beneficial with respect to both minimizing the number of interaction pairs to be evaluated and an effective partitioning of the problem to parallelize the evaluation on multiple processors without excessive cost for communication between the processors. Hereby, the partitioning of the problem is based on the spatial arrangement of the beam elements and uses the same subdivision of the computational domain into buckets already obtained from the search algorithm. A repartitioning and thus redistribution of the interaction pairs to the processors is done only if the spatial distribution of the beam elements has changed so much that – considering the cut-off radius – there is a chance that new interaction pairs need to be identified and evaluated. Generally, the computational cost of these steps of search and partitioning turned out to be insignificant as compared to the evaluation of the interaction pairs. Therefore, the parallelization of the pair evaluation on multiple processors indeed reduces the overall computation time significantly.

5.4.5. A criterion to sort out element pairs separated further than the cut-off radius before the actual evaluation

The following is applied as an additional step after the search for spatially proximate and thus potentially interacting element pairs. Motivated by the critical influence of the pair evaluation on the overall computational cost, this additional filtering step aims to sort out element pairs that are identified by the rather rough and conservative bucket search algorithm, but are further separated than the cut-off radius and will thus not contribute to the total interaction energy. The key idea is thus to skip the entire evaluation of the element pair, i.e., the loop over the integration points on the slave side, which otherwise would only after the closest point-to-curve projection check the cut-off radius and skip the evaluation of terms for this specific integration point.

To achieve high net savings, the applied criterion must be cheap to evaluate and is thus only based on the nodal positions and an estimate of the actual, deformed centerline geometry of the elements by means of so-called spherical bounding boxes. A very similar filter criterion has been applied in the context of macroscopic beam contact [111], where all details can be found. The only difference lies in the distance threshold value that is used. Here, we skip the pair evaluation if the minimal distance between the spherical bounding boxes is more than twice the cut-off radius, which should be on the safe side to not miss any contributions also in the case of strongly deformed elements. Still, the resulting decrease in the overall runtime observed for the numerical examples from Section 5.5 was up to 30%, which is quite remarkable and underlines the effectiveness of this additional filtering step. As an additional benefit, it has been observed that the number of non-unique or ill-posed closest point-to-curve projections

significantly decreased and in fact vanished for the numerical examples considered in the context of this work.

5.5. Numerical examples

All presented formulations and algorithms have been implemented in C++ and integrated into the existing computational framework outlined in Appendix F. Note that the implementation of the SBIP approach as well as the disk-cylinder potential has been verified by means of a second, independent implementation in MATLAB [157] used also for the accuracy analysis in Section 5.2.2. Furthermore, the correct implementation of the discrete element residual vectors as well as tangent stiffness matrices has been verified by means of an automatic differentiation tool provided by the package Sacado, which is part of the Trilinos project [66].

At this point, it is also important to emphasize that the novel SBIP approach nicely integrates into an existing nonlinear finite element solver for solid and structural mechanics. It does neither depend on any specific beam (finite element) formulation nor time discretization scheme, which underlines the versatility of this novel approach and shall be demonstrated also by the following numerical examples.

The numerical examples are chosen to demonstrate the general functionality, validity and versatility of the novel SBIP approach as well as the proposed disk-cylinder potential to be used as effective SBIP law for both the adhesive (vdW) as well as repulsive part of the LJ potential. A first set of numerical examples will be presented in the following section and another one in the context of the comprehensive computational study of the peeling and pull-off behavior of elastic fibers in Section 7.4.

5.5.1. Adhesive nanofiber-grafted surfaces: A proof of principle

This set of numerical examples deals with bioinspired adhesive surfaces, which have recently gained a lot of attention (see e.g. [17] for a review). Generally, this topic is motivated by the fascinating skills of geckos [8], spiders [84], mussels [92], and other animals to stick to surfaces and defy significant detachment forces such as for instance their body weight when sitting on the ceiling or steeply inclined surfaces. The origin of this extraordinary adhesion is known to lie on the molecular scale and vdW forces between hierarchical arrays of nano-hairs and the surface have been shown to play a major role [9, 53]. In this context, powerful simulations tools based on both accurate and efficient nano-/micromechanical models are expected to contribute to both the understanding and imitation of the underlying physical mechanisms, which are crucial steps on the way to leverage these natural phenomena in human-made technical applications such as in the field of robotics (see e.g. [93] for a review). In the long run, such simulation tools could prove useful to streamline the design and manufacturing process of industrial products.

In addition to this long-term perspective and motivation, this numerical example serves two immediate purposes. On the one hand, it demonstrates the capability of the novel SBIP approach to handle arbitrary mutual configurations of fibers in 3D by means of an initially curved spatial geometry as well as large, non-trivial deformations of fibers. Also the efficiency of the novel approach will be showcased by applying it to a large-scale system regarding both the number of

fibers and time steps. On the other hand, this computational study suggests and analyzes a possible design for artificial adhesive surfaces based on grafted helical nanofibers. Hereby, nature's ubiquitous pattern of helical fibers is used to achieve the desired large ratio of strong adhesion and easy removal of surfaces, depending on the respective needs. The idea is to maximize the total length of parallel, adhesive contact between fibers if helices from both surfaces match and use twisting of surfaces to initiate the relatively easy separation via peeling of fibers, thereby using also the lever arm of the surfaces' large in-plane dimensions. To demonstrate this working principle, we will thus measure the force-displacement curves of both normal, i.e., out-of-plane loading and the removal process in numerical experiments. After considering a minimal setup, the system will be upscaled in Section 5.5.1.3.

5.5.1.1. Setup and parameters

Figure 5.8 shows the setup of this numerical example from different view angles. As mentioned

(a) Perspective view with translucent top surface.
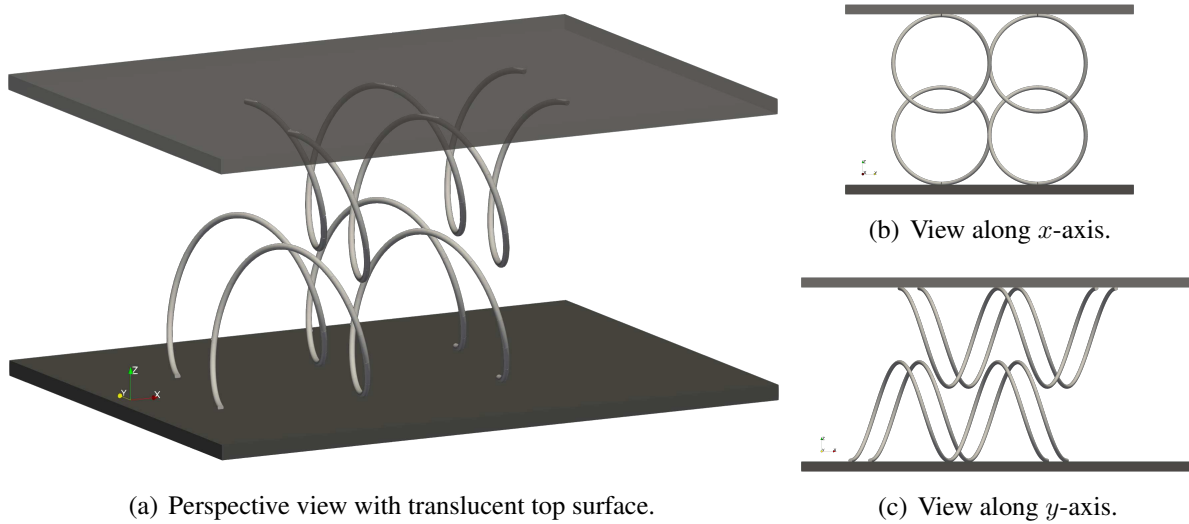
(b) View along x-axis.

(c) View along y-axis.

Figure 5.8.: Initial, undeformed configuration of the numerical experiments studying adhesive nanofiber-grafted surfaces.

above, the system is mainly composed of helical fibers with a helix diameter of $D_h = 2R_h = 1$ and a pitch, i.e., height of one complete turn, of $P_h = 1$, respectively. The grafting onto surfaces is modeled by respective Dirichlet boundary conditions applied to the fibers and the dark colored surfaces shown in Figure 5.8 are only used for visualization and not considered in the simulation. In this first minimal setup, 2x2x2 fiber loops are considered, which refers to 2 surfaces with 2 helices each with 2 complete turns, i.e., loops each. The offset in axial direction of the helices, i.e., along the global x-axis, is best seen in Figure 5.8(c) and chosen to be $0.2P_h$ between the helices on the same surface, and $0.5P_h$ between helices on opposite surfaces. As can be seen from Figure 5.8(b), the helix axes on each surface are separated by D_h in y-direction, and those helix axes on opposite surfaces are separated by $0.75P_h$ in the surface normal, i.e., z-direction.

The individual fibers have a circular cross-section with radius of $R = 0.02$ and a hyperelastic material with axial, shear, torsional and bending stiffness of $EA = 250$, $G\bar{A} = 100$,

$GI_\mathrm{T} = 0.03$, $EI = 0.05$, respectively is considered, which resembles the values for a biopolymer filament such as actin. The effect of inertia is neglected as commonly assumed on the micro- and nanoscale. Velocity-proportional viscous forces and moments on the fibers are modeled as proposed in [32] and can be interpreted either as the fibers' interaction with a quiescent background fluid or an artificial damping, which is beneficial for the iterative solution procedure of the nonlinear system of equations in order to deal with the challenging physical instabilities that are inherent in adhesive contact problems. In the latter case, the quasi-static system behavior is recovered in the limit of negligible velocity, i.e., very small displacement as well as rotation increments per time step, which has already been made use of in [60]. Specifically, we choose a viscosity of $\eta = 10^{-3}$, which corresponds to water, and apply a backward Euler time integration scheme with a default step size of $\Delta t = 0.01$ and adaptive time step size reduction as described in Appendix F.2. The spatial discretization of the fibers is given as 16 Hermitian Simo-Reissner beam elements (see Section 3.2.2 for details) per complete turn of a helix, which leads to 128 elements for the smallest 2x2x2 loop system considered in the beginning.

As the key component of this numerical experiment, both the adhesive vdW and the repulsive steric part of the LJ potential are considered for the interactions of all individual fibers, including those on the same surface. The LJ parameters are chosen as $k_6 = -10^{-6}$ and $k_{12} = 10^{-23}$ and atom densities are set to $\rho = 1$, which corresponds to an equilibrium spacing $g_\mathrm{LJ,eq,cyl\|cyl} \approx 0.08\,R$ and a minimal LJ force per unit length $\tilde{f}_\mathrm{min,LJ} \approx -1.36$ (cf. Equations (7.2) and (7.3)). These LJ interactions are modeled via the SBIP approach proposed in Section 5.1 and the disk-cylinder interaction law $\tilde{\pi}_\mathrm{m,disk\text{-}cyl}$ from Equation (5.32). Gaussian quadrature with five integration segments per element and 10 integration points each is applied to evaluate the integral along the slave element. The regularization strategy proposed in Section 5.4.1 is applied with a regularization separation $g_\mathrm{ul,reg} = 8 \times 10^{-4} = 0.04 \cdot R$, which is smaller than any given above. The short range of the LJ interactions is exploited by applying a cut-off radius of $r_c = 0.1 = 5R$.

Getting back to the original idea behind this numerical example, two different scenarios are considered in the following. The first scenario represents the actual use case of an adhesive bond between two surfaces, i.e., the surfaces are first brought together and afterwards pulled apart. To be more precise, the numerical experiment is conducted in a displacement-controlled manner and the reaction force-displacement curve is determined. Here, the bottom plate is considered fixed, whereas the top plate is moved down and then up in z-direction such that the plates remain parallel. As mentioned above, the plates are not considered in the simulation and the displacement boundary conditions are directly applied to the respective beam nodes, where we assume that the fibers are grafted onto the surface every second turn of the helix. This first scenario – referred to as "Pull" scenario in the remainder of this section – is thus defined by prescribing zero displacement and zero rotation to those nodes grafted onto the bottom plate and prescribing zero rotation, zero displacement in x- and y-direction and the following displacement curve in z-direction to the nodes grafted onto the top plate:

$$\text{"Pull"}: \quad u_z(t) = \begin{cases} -u_{z,\mathrm{max}}\,t, & 0 \leq t < 1 \\ -u_{z,\mathrm{max}}, & 1 \leq t < 2 \\ -u_{z,\mathrm{max}} + u_{z,\mathrm{max}}\,t, & 2 \leq t < 5 \end{cases}$$

Here, the maximal displacement magnitude in negative z-direction is chosen as $u_{z,\mathrm{max}} = 0.71\,R_h$ such that the smallest separation of the fiber surfaces g_{min} is smaller than the equilibrium separation $g_{\mathrm{LJ,eq,cyl\|cyl}}$ and thus leads to repulsive forces in the closest mutual distance of the surfaces, yet is slightly larger than the regularization separation $g_{\mathrm{ul,reg}}$ given above. The second scenario on the other hand represents the desired easy removal mechanism of the adhesive bond and relies on a mutual twisting of the surfaces before pulling them apart, thus referred to as "Twist & Pull". Again, the bottom surface is fixed, while the following z-displacement as well as rotation around the z-axis is prescribed at the nodes grafted onto the top surface:

$$\text{``Twist \& Pull'':}\quad u_z(t) = \begin{cases} -u_{z,\mathrm{max}}\,t, & 0 \le t < 1 \\ -u_{z,\mathrm{max}}, & 1 \le t < 4, \\ -u_{z,\mathrm{max}} + u_{z,\mathrm{max}}\,t, & 4 \le t < 7 \end{cases}$$

$$\psi_z(t) = \begin{cases} 0, & 0 \le t < 2 \\ \phi_{z,\mathrm{max}}/2\,(t-2), & 2 \le t < 4 \\ \phi_{z,\mathrm{max}}, & 4 \le t < 7 \end{cases}$$

Here, the center of rotation is assumed to be the midpoint of the fiber array on the top surface and thus follows as $\boldsymbol{r}_{\mathrm{M}} = [1.35\,R_h, 0.5\,R_h, (.)]^T$ and the maximal rotation angle is given as $\phi_{z,\mathrm{max}} = 75°$. Note that a shifted z-displacement $\bar{u}_z = u_z - u_{z,\mathrm{max}}$, which is zero when the fiber surfaces are closest, is used in some parts of the following analysis as a more natural and thus intuitive quantity when discussing the pull-off behavior starting from fibers in contact.

5.5.1.2. Results and discussion

Figure 5.9 shows selected simulation snapshots for the normal loading referred to as "Pull" scenario. The configuration in Figure 5.9(a) corresponds to the end of the approach (and equilibration) phase at $t = 2$, where the helical fibers of both surfaces are perfectly aligned and their surfaces touch. In the subsequent pull-off phase shown in Figure 5.9(b) - 5.9(d), the fibers are continuously peeled and the contact length decreases while the fibers are strongly deformed. Only after approximately $t = 4.09$, the last contact points of the fibers detach and the separation process is completed.

Figure 5.10 likewise shows selected simulation snapshots for the "Twist & Pull" scenario. Note that until time $t = 2$, this scenario is identical to the previously discussed "Pull" scenario shown in Figure 5.9. Figure 5.10(a) - 5.10(d) cover the twisting phase and show that twisting the surfaces by $75°$ indeed separates the fibers almost entirely, which agrees with the idea of a subsequent, relatively easy separation of surfaces in normal direction. A closer look reveals that the strength of adhesion suffices to keep the fibers in contact almost along the entire length up to approximately $37.5°$, which leads to quite large and complex deformations of the fibers. Note also that Figure 5.10(d) shows a limitation of our modeling approach in a way that the fibers can penetrate the surfaces, because the surfaces are not explicitly included in the simulation and only accounted for by means of Dirichlet boundary conditions on the grafted fiber endpoints as discussed above. This is however not expected to have a major influence on the pull-off forces

(a) $t = 2$, $u_z = -u_{z,\text{max}}$: minimum separation of surfaces

(b) $t = 2.5$, $u_z = -0.5\,u_{z,\text{max}}$: early stage of pulling surfaces apart

(c) $t = 3.5$, $u_z = 0.5\,u_{z,\text{max}}$: intermediate stage of pulling surfaces apart

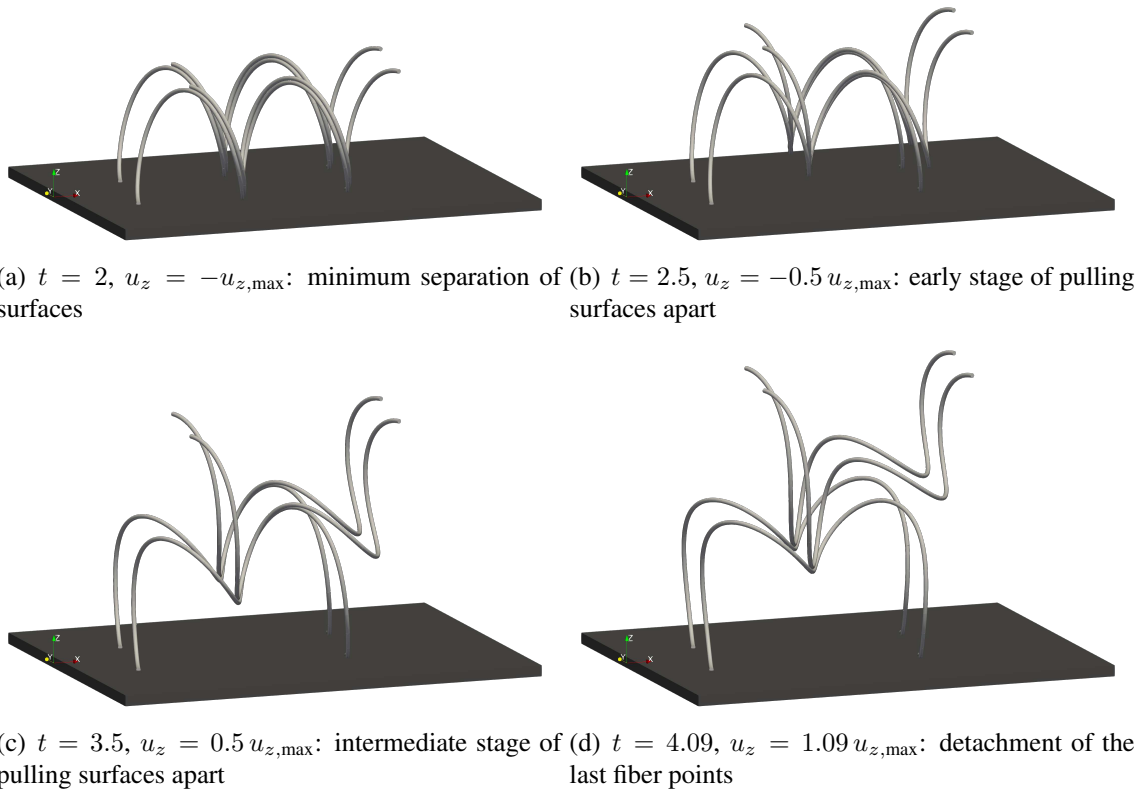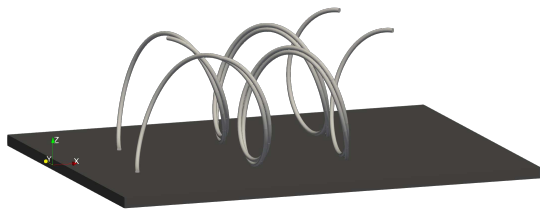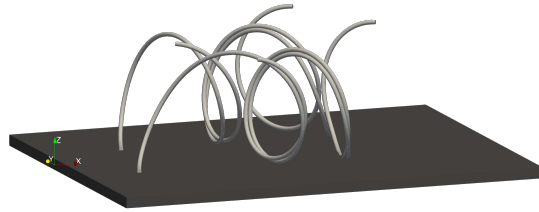(d) $t = 4.09$, $u_z = 1.09\,u_{z,\text{max}}$: detachment of the last fiber points
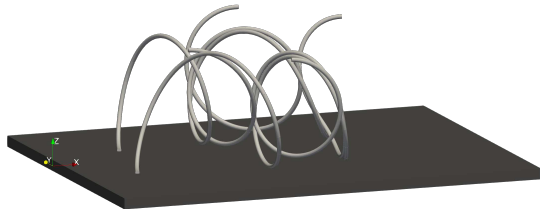
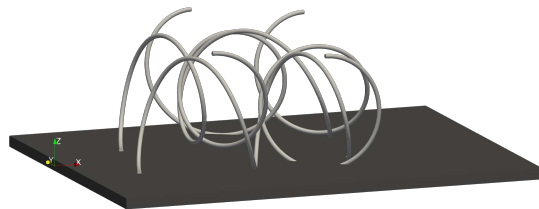Figure 5.9.: Sequence of simulation snapshots of the "Pull" scenario. Top surface is hidden for better visibility of the fibers.

(a) $t = 2.5$, $\psi_z = 18.75°$: early stage of twisting surfaces

(b) $t = 3$, $\psi_z = 37.5°$: intermediate stage of twisting surfaces

(c) $t = 3.5$, $\psi_z = 56.25°$: intermediate stage of twisting surfaces

(d) $t = 4$, $\psi_z = 75°$: final twisted configuration
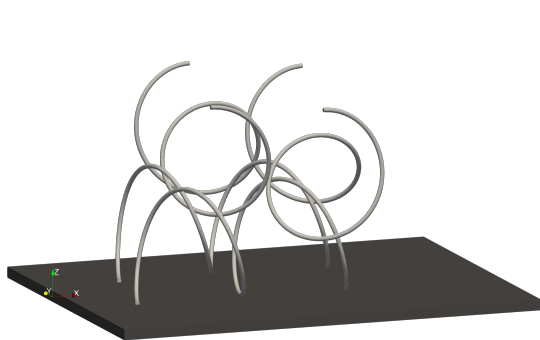
(e) $t = 5$, $u_z = 0$: intermediate stage of pulling surfaces apart
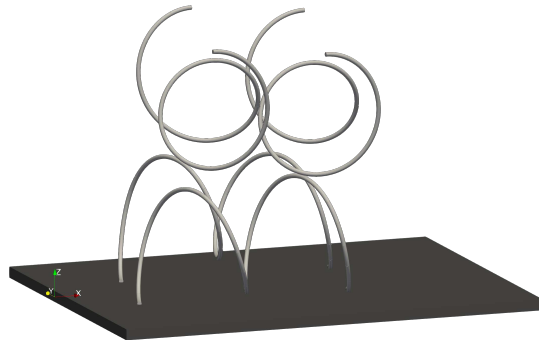
(f) $t = 5.72$, $u_z = 0.72\,u_{z,\text{max}}$: detachment of the last fiber points

Figure 5.10.: Sequence of simulation snapshots of the "Twist & Pull" scenario. Top surface is hidden for better visibility of the fibers. Note that until time $t = 2$, this scenario is identical to the "Pull" scenario shown in Figure 5.9.

to be discussed next, as it occurs rather rarely and from Figure 5.10(d) it can be estimated that a preclusion of the observed penetration would not change the overall deformed shape of the fibers in a significant manner.

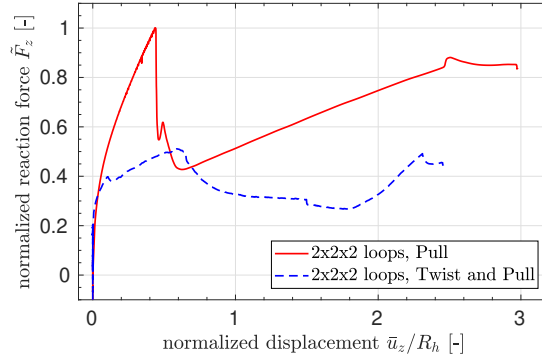Finally, the force-displacement curves for both scenarios are shown in Figure 5.11. Specifi-

Figure 5.11.: Force-displacement curves for the decisive phase, i.e., $2 \leq t < 5$ in the "Pull" scenario and $2 \leq t < 7$ in the "Twist & Pull" scenario. Force values are normalized with respect to the maximal pull-off force $F_{z,\text{max}}$.

cally, the reaction force component F_z in the surface normal, i.e., z-direction, is summed over all nodes grafted onto the top surface and normalized by means of the maximum force $F_{z,\text{max},2x2x2} \approx 0.356$ that is observed for this 2x2x2 loop system to ease the subsequent comparison to larger system sizes. As desired, the adhesive connection of surfaces is able to withstand approximately two times larger pull-off forces in the normal loading scenario (red line) as compared to the scenario meant to be used for the removal of surfaces (blue dashed line). While it is quite obvious that the maximal pull-off force for normal loading will scale linearly with the surface area, it will be interesting to see how this ratio between the maximal forces in the loading and removal scenario behaves if we scale up the system size in the following section. Generally, a rich and highly nonlinear system behavior can be observed from these force-displacement curves, which reflects the complex interplay of strongly adhesive LJ interactions and large and complex structural deformations in 3D. Particularly for the "Pull" scenario, some characteristics of the fundamental problem of peeling two initially straight adhesive fibers (cf. Chapter 7) such as the sharp force peak, the extended pull-off phase and the sudden snap-free are however still recognizable. Note also the considerable compressive forces that occur in the "Twist & Pull" for $\bar{u}_z = 0$, i.e., during the twisting phase $2 \leq t < 7$. In this context, it seems worth mentioning that the reaction forces in x- and y-direction are below 0.1 and thus another factor of two smaller than the maximal pull-off force observed in this scenario.

5.5.1.3. Upscaling of the computational experiment

Increasing the size of the system is important to judge both the performance of the novel SBIP approach for modeling the LJ interactions, but also the scaling of the maximal pull-off forces of the adhesive surfaces. Therefore, a 2x8x8 loop system (see Figure 5.12(a) - 5.12(c)) and a 2x16x16 loop system (see Figure 5.12(d) - 5.12(f)) is considered in the following. With respect

(a) 2x8x8 loops: Perspective view with hidden top surface.

(b) 2x8x8 loops: View along x-axis.

(c) 2x8x8 loops: View along y-axis.

(d) 2x16x16 loops: Perspective view with hidden top surface.

(e) 2x16x16 loops: View along x-axis.

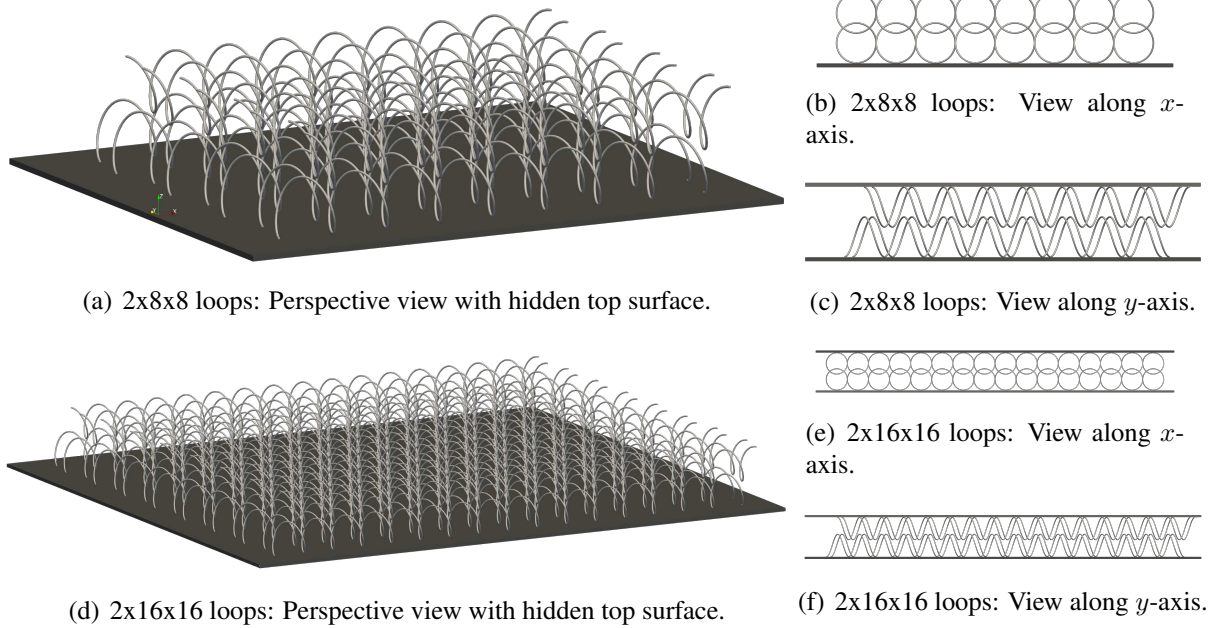(f) 2x16x16 loops: View along y-axis.

Figure 5.12.: Initial, undeformed configuration of the 2x8x8 and 2x16x16 loops setup used to study adhesive nanofiber-grafted surfaces.

to the original 2x2x2 loop system, this corresponds to a scaling factor of 16 and 64, respectively, which leads to a total of 2048 elements / 4112 nodes and 8192 elements / 16416 nodes, respectively. Except for the system size, the setup and parameters stated in Section 5.5.1.1 remain unchanged.

Figures 5.13 and 5.14 show selected simulation snapshots for the "Pull" scenario of the scaled systems and confirm that the periodicity in the problem setup is also observable in the resulting deformed configurations. Note however that the problem setup differs at the boundaries in x-direction such that only the solution sufficiently far from these boundary conditions, i.e., in the interior region, is truly periodic and the aforementioned linear scaling of the pull-off force with the surface area is expected to be slightly altered by this fact. But also in y-direction, the neighboring rows of helical fibers come into contact and the solution at the boundary fibers will thus slightly different as compared to the middle rows. This influence of the boundaries on the periodicity of the solution is particularly clear in the side views of the system, e.g. in Figure 5.14(d) for the 2x16x16 loops system.

Figure 5.15(a) shows the comparison of the force-displacement curves for the three different system sizes. The curve for the 2x16x16 loops system (black dash-dotted line) and the 2x8x8 loops system (pink dashed line) clearly show qualitative similarities and the maximal normalized force values deviate by a factor of 4.04, which supports the argument of linear scaling with the area of the surfaces that deviates by a factor of 4. The comparison of the 2x8x8 loops system with the smallest considered 2x2x2 loops system however is still influenced by the boundary effects discussed above and results in a disproportionately high increase of the maximal pull-off force

(a) $t = 3.4$, $u_z = 0.5\,u_{z,\mathrm{max}}$: maximum force

(b) $t = 3.4$ (view along y-axis)

(c) $t = 4$, $u_z = u_{z,\mathrm{max}}$

(d) $t = 4$ (view along y-axis)

Figure 5.13.: Selected simulation snapshots of the "Pull" scenario with 2x8x8 loops. Top surface is hidden for better visibility of the fibers.

(a) $t = 3.5$, $u_z = 0.5\,u_{z,\mathrm{max}}$: maximum force

(b) $t = 3.5$: (view along y-axis)

(c) $t = 4.25$: detachment of the last fibers
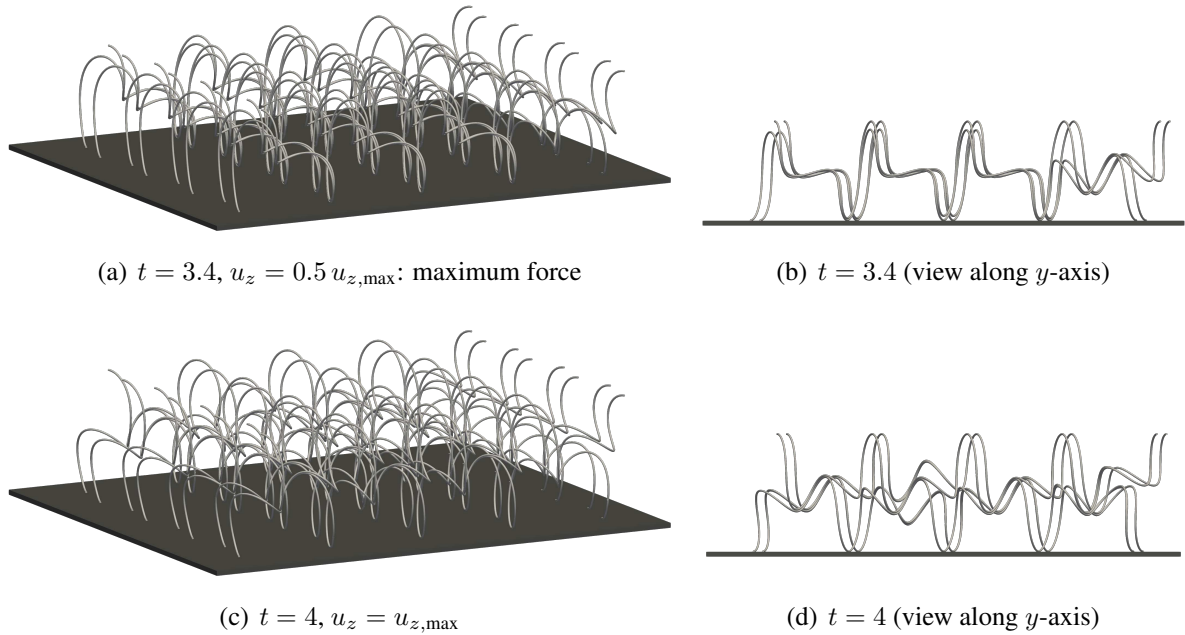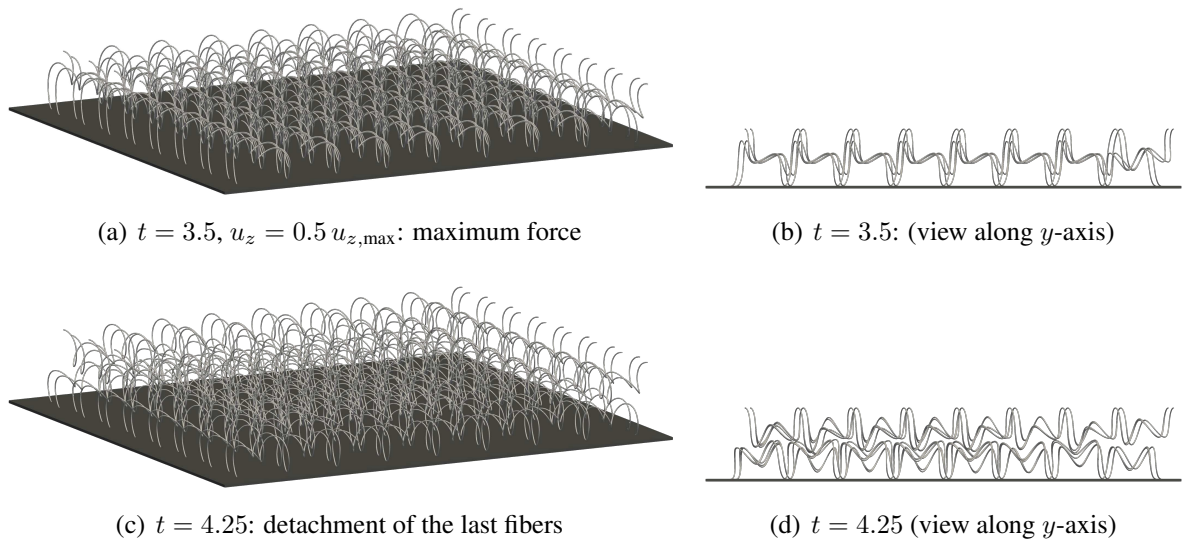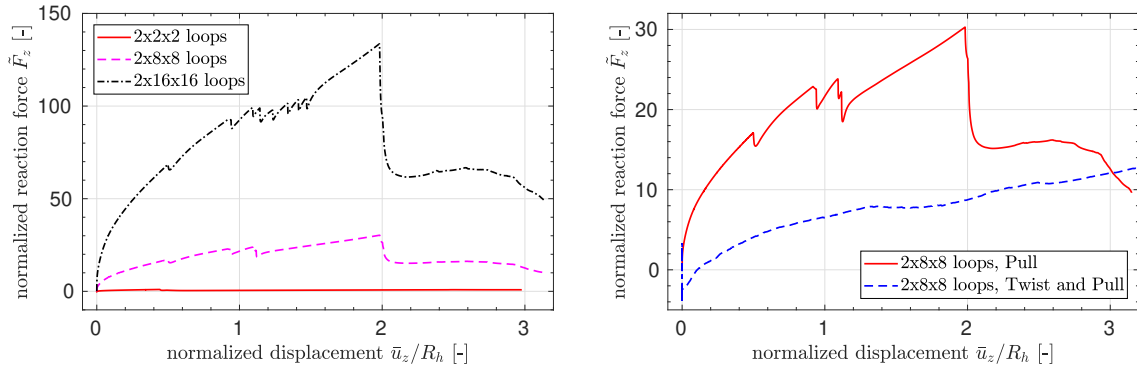
(d) $t = 4.25$ (view along y-axis)

Figure 5.14.: Selected simulation snapshots of the "Pull" scenario with 2x16x16 loops. Top surface is hidden for better visibility of the fibers.

(a) Comparison of the "Pull" scenario with 2x2x2, 2x8x8 and 2x16x16 loops, respectively.

(b) Comparison of "Pull" and "Twist & Pull" scenario with 2x8x8 loops.

Figure 5.15.: Force-displacement curves for the decisive phase, i.e., $2 \leq t < 5$ in the "Pull" scenario and $2 \leq t < 7$ in the "Twist & Pull" scenario. Force values are normalized with respect to the maximal pull-off force $F_{z,\max}$ occurring for 2x2x2 loops.

by a factor of approximately 30 and noticeable differences both in the maximal displacement before snapping free as well as the displacement value where the maximal force occurs.

5.5.1.4. Entanglement of fibers

Turning to the second considered scenario including the twisting of surfaces, an unintended entanglement of fibers has been observed, which has a noticeable influence on the force-displacement curve (blue dashed line) shown in Figure 5.15(b). This can be traced back to the (unphysical) behavior that during the twisting phase the outermost loop from the top surface dives under the fiber endpoint grafted onto the bottom surface and thus leaves the fibers entangled for the remaining course of the simulation, as can be seen from the simulation snapshots in Figure 5.16. While this is obviously neither physically correct nor desirable in the initial context of separating the adhesive fibers from each other, it still demonstrates the effectiveness and robustness of the proposed SBIP approach even for highly complex, large 3D deformations in large-scale systems that include a broad variety of mutual orientations and separations of fibers. In order to investigate the actual differences in the force response between the "Pull" and "Twist & Pull" scenario also in the upscaled 2x8x8 and 2x16x16 scenario, the computational experiments should be repeated with a slightly larger array of fibers on the bottom surface such that the fiber endpoints can not be reached by the fiber loops of the top surface. It will be interesting to see how the ratio of maximum loading force and required separation force scales with the system size.

(a) $t = 3$, $\psi_z = 37.5°$: intermediate stage of twisting surfaces

(b) $t = 4$, $\psi_z = 75°$: final twisted configuration

(c) $t = 5.5$

(d) $t = 7$: final configuration

(e) $t = 3$, $\psi_z = 37.5°$ (view from the top)

(f) $t = 4$, $\psi_z = 75°$ (view from the top)

(g) $t = 7$ (view along y-axis)
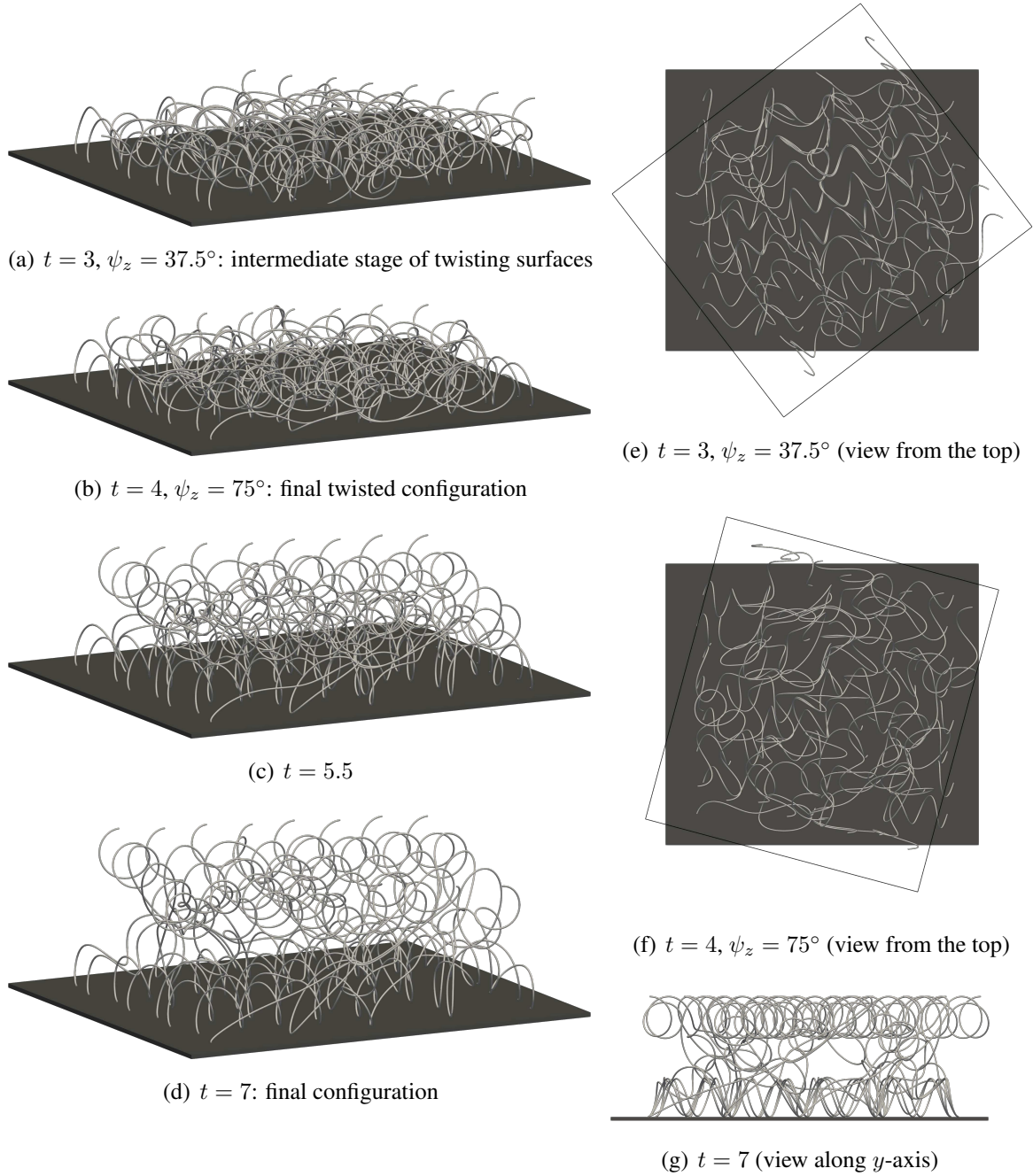
Figure 5.16.: Sequence of simulation snapshots of the "Twist & Pull" scenario with 2x8x8 loops. Top surface is hidden for better visibility of the fibers.

5.6. Conclusions and outlook

Following up on the development of the first 3D beam-beam interaction formulation for molecular interactions (the so-called SSIP approach) in the preceding Chapter 4, this chapter proposes an enhanced approach specializing on the most challenging case of short-ranged interactions such as the vdW adhesion and the steric repulsion of the LJ interaction. Exploiting the characteristic rapid decay of the interaction potential with increasing distance allows to further reduce the dimensionality of the beam-beam interaction problem and thus achieve a significantly more efficient approach than the more general SSIP approach. The key idea is to approximate the second, arbitrarily deformed beam by a surrogate body with trivial geometry, which is located at the closest point from a given point on the first beam and oriented according to the centerline tangent vector of the second beam. Mathematically, this surrogate body is the linear series expansion of the second, so-called master beam around the closest point. In this manner, the interaction of the entire second beam with a given section of the first, so-called slave beam can be described by an analytical, closed-form interaction potential law, which replaces the numerical integration along the master beam by a single function evaluation. This novel, specialized approach is therefore called the section-beam interaction potential (SBIP) approach.

In addition to being significantly more efficient, the novel formulation developed in this chapter is also significantly more accurate than the one used before if short-ranged interactions are considered. This is due to the fact that the reduced interaction law is superior to the previously used simple SSIP law, because it includes the relative rotation, i.e., the orientation of the interacting bodies in addition to their scalar separation. This SBIP law has been derived in Section 5.2 considering the case of circular, homogeneous cross-sections and a generic inverse power law with exponent $m \geq 6$ as fundamental point-pair interaction potential. The required derivation of the resulting disk-cylinder interaction potential is based on 5D analytical integration using appropriate series expansions and is valid for arbitrary mutual orientations of the two bodies. A comprehensive analysis of the accuracy of the disk-cylinder potential allowed to choose the optimal compromise between accuracy and simplicity of the expression. In particular, the SBIP law ensures the correct asymptotic scaling behavior in the decisive regime of small separations, which has been identified as the most critical aspect when using the simple SSIP law from Section 4.3.2 neglecting the mutual orientation of cross-sections.

These two fundamental novelties – the general SBIP approach from Section 5.1 and the specific analytical interaction law from Section 5.2 – have been combined in Section 5.3 to obtain the resulting virtual work contribution. The subsequent discretization via finite elements and its consistent linearization finally give rise to a novel beam-beam interaction formulation that can be seamlessly integrated in an existing nonlinear finite element framework for structural or solid mechanics. In this respect, it is important to point out that the approach does neither depend on a specific beam (element) formulation nor time integration scheme and is thus considered to be highly versatile. Further methodological aspects such as a suitable numerical regularization of the singularity at zero separation in the reduced interaction law and a criterion to sort out beam element pairs with a larger separation than the cutoff radius before the actual evaluation to save computational resources have been presented in Section 5.4.

Section 5.5 finally presents a comprehensive numerical example studying adhesive nanofiber-grafted surfaces, which confirms the effectiveness, efficiency and robustness of the novel for-

mulation also for large-scale, complex systems with arbitrary mutual configurations and large deformations of the interacting fibers. In addition, the computational experiments demonstrate the working principle of the proposed design of the nanofiber-grafted surfaces based on arrays of helical fibers by showing the desired large ratio of strong adhesive connection under load and easy removal of the surfaces if desired. This showcases how suitable simulation tools such as the one developed in this chapter could contribute to the design and manufacturing of bioinspired artificial adhesives in the long run.

By means of the additional numerical example studying the peeling and pull-off behavior of elastic adhesive fibers to be presented in Chapter 7, the higher efficiency of the novel, specialized SBIP approach as compared to the previous, more general SSIP approach will be quantified. As it will turn out, the novel approach is by about a factor of 4 faster than the previous approach. This holds even despite the aforementioned superior accuracy of the derived SBIP law (Equation (5.32)), which is therefore also more complex than the simple SSIP law (Equation (4.7)). To conclude, the combination of a better accuracy and higher efficiency leads to a drastically improved applicability – for instance with respect to the maximum feasible system size and time scales – and therefore opens the door to tackle a multitude of yet intractable problems in science and technology.

A future derivation of other SBIP laws for instance for the case of screened electrostatics or hydrophobic/-philic interactions would further extend the range of applications of the novel SBIP approach. Given the importance of the mentioned interaction types in many biological systems on the nano- and microscale, this is considered a highly promising extension of the work presented in this chapter. In addition to an analytical derivation of SBIP laws, the identification and fitting of such reduced interaction laws based on experimental results (such as the force-displacement curves for simple characteristic setups with two interacting fibers) would be an interesting and worthwhile avenue of future research that could be of great benefit to the prediction quality of computational experiments.

6. Beam Interaction Formulations from a Meta-Level Perspective

This chapter aims to take a step back and look at beam interaction formulations from a meta-level perspective in order to get an overall picture of both the previously existing approaches and the new ones proposed in the last two chapters. After the classification and comparison to be presented in the following Section 6.1 and a detailed discussion of the differences and applicability between formulations for macroscopic contact and molecular steric repulsion in Section 6.2, the last section of this chapter provides an overview of formulations for interactions of beams with special types of interaction partners of reduced dimensionality, which turn out to be derivable as special cases of the beam-beam interaction formulations.

6.1. Classification and comparison of approaches for beam-beam interactions

After reviewing the first principles of molecular interactions (Section 2) as well as existing formulations for macroscopic contact between beams (Section 3.3), two fundamentally new formulations of beam-beam interactions have been developed in Chapter 4 and Chapter 5. This asks for a classification and comparison of all these approaches, which is presented in Figure 6.1.

The leftmost column depicts the approach of point-pairwise summation – or corresponding nested volume integration – of the fundamental interaction potentials for pairs of charges or charges. The second and third column shows the formulations based on section-section interaction potentials (SSIP) proposed in Chapter 4, and based on section-beam interaction potentials (SBIP) proposed in Chapter 5, respectively. Finally, the rightmost column depicts a possible further dimensional reduction of the problem to the interaction of two beam surrogates, which would allow to evaluate the two-body interaction potential by a single function evaluation. From left to right, the resolution of details decreases and likewise the algorithmic complexity determined by the dimensionality of the underlying problem decreases. This overview of four distinct, logical categories of beam-beam interaction formulations therefore illustrates the tradeoff between resolution of details ranging from atomistic view to trivial meso/macroscopic bodies on the one hand and the dimensionality and thus main driver for the computational cost on the other hand. The ultimate goal for the derivation and choice of (a class of) formulations however is to outsmart this natural conflict of objectives by a consistent dimensional reduction of the fully resolved problem (on the left) to the minimal possible description that is yet able to reproduce the most important, characteristic features. Based on the detailed theoretical considerations in
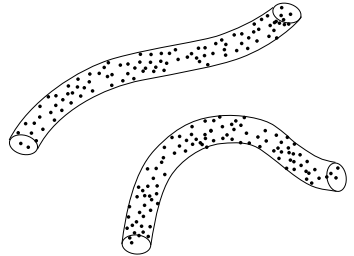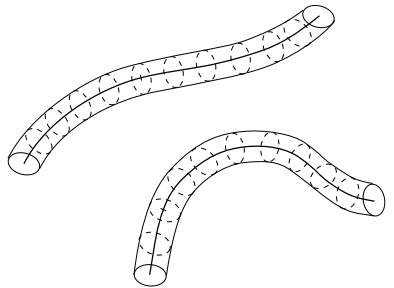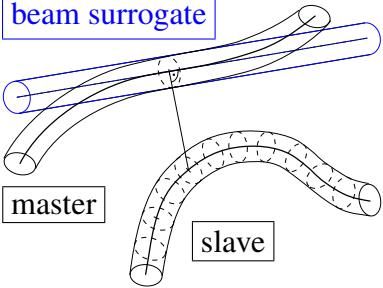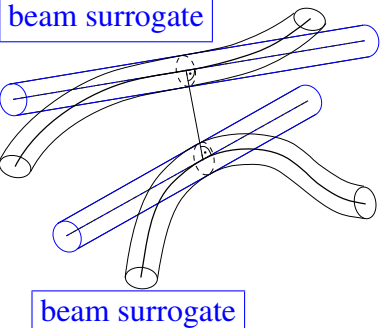
point-point	section-section	section-beam surrogate	beam surrogate-beam surrogate
$3D \times 3D = 6D$	$1D \times 1D = 2D$	$1D \times 0D = 1D$	$0D \times 0D = 0D$
$\Pi_{ia} = \sum_{i \in \mathcal{B}_1} \sum_{j \in \mathcal{B}_2} \Phi(r_{ij})$ $\Pi_{ia} = \int\limits_{V_1} \int\limits_{V_2} \rho_1 \rho_2 \Phi(r) \, dV_2 \, dV_1$ $r = \|\boldsymbol{x}_1 - \boldsymbol{x}_2\|$	$\Pi_{ia} = \int\limits_0^{l_1} \int\limits_0^{l_2} \tilde{\tilde{\pi}}(\boldsymbol{r}_{1-2}, \boldsymbol{\psi}_{1-2}) \, ds_2 \, ds_1$	$\Pi_{ia} = \int\limits_0^{l_1} \tilde{\pi}(\boldsymbol{r}_{1-2c}, \boldsymbol{\psi}_{1-2c}) \, ds_1$	$\Pi_{ia} = \Pi_{ia}(\boldsymbol{r}_{1c-2c}, \boldsymbol{\psi}_{1c-2c})$
atomistic resolution Section 2.3	long-/short-range interactions Chapter 4	short-range interactions Chapter 5	-
-	-	macroscopic line contact [110], Section 3.3.2	macroscopic point contact [163], Section 3.3.1

Figure 6.1.: Classification of formulations for beam-beam interactions.

Chapter 4 and Chapter 5, this optimal choice is given as the SSIP approach for long-range and the SBIP approach for short-range molecular interactions of beams.

This new overall picture of beam interaction formulations also allows to classify previous approaches to macroscopic contact of beams and interpret them in the context of molecular interactions, which are also the origin of the macroscopic contact forces and resulting non-penetrability of objects that we observe in everyday life. Interestingly, the very first numerical formulation of (macroscopic)) beam contact is based on the concept of determining the one bilateral closest-point pair between both beams and evaluating an heuristic penalty force law as a function of the closest point-pair separation in order to preclude any (noticeable) penetrations ([163], summarized in Section 3.3.1). Given this new overall picture of beam interaction formulations, such an approach can be interpreted as the consistent, most extreme dimensional reduction of the problem motivated by the short range of interactions and the resulting possibility to evaluate the total interaction potential for a pair of surrogate bodies approximating the shape of the actual beams. However, this new perspective likewise reveals the well-known limitations of this kind of approach with respect to describing arbitrary mutual configurations as the illustrative examples of two parallel straight beams or one straight beam and a surrounding helical beam demonstrate (see e.g. the discussion in [110]). The non-uniqueness of the bilateral closest-point pair in such situations is a confirmation of the oversimplification of the general beam-beam interaction problem by such an approach. Nevertheless, this category of surrogate-surrogate interaction formulations is the most efficient theoretically possible class of formulations and due to its validity for a certain range of mutual orientations, this efficiency can be exploited in combined approaches such as the ABC formulation ([111], summarized in Section 3.3.3) that handle the problematic mutual configurations differently. This recognition of the superior efficiency of the existing, combined macroscopic contact formulation asks for a more detailed discussion of the applicability of such an heuristic approach to preclude penetration also in microscopic problem settings, which will thus be given in the following section.

6.2. Brief comparison of micro- and macroscopic approaches to beam contact

Modeling the steric repulsion that prevents a penetration of distinct fibers has a long history in the field of computational contact mechanics and has first been addressed in [163]. The paradigm of these macroscopic continuum models is that the smallest surface separation or gap must be equal to or greater than zero which is formulated as an inequality constraint. With the development of the novel SSIP and SBIP approaches to molecular interactions of fibers, an alternative modeling strategy has arisen, which is motivated by the rather microscopic perspective of LJ interactions between all material points in the slender continua. In this work, both kind of approaches will be applied, which asks for a brief assessment and comparison of the modeling approaches.

On the one hand, penalty-based models for beam contact are well-established formulations with optimized efficiency as well as robustness. On the other hand, the SSIP and SBIP approaches are based on first principles in form of the LJ law and are thus expected to better resolve the actual contact force distributions, especially in the case of nano- to micro-scale applications.

This becomes obvious if we recall the purely heuristic nature of the penalty force law and the resulting (small) negative gap values, i.e., tolerated penetrations. It will most likely depend on the specific application whether the associated model error has a significant or rather negligible influence on the results. In order to answer this question with respect to the studies of this work, it seems most important to look at the adhesive force laws to be applied in combination with the models for steric repulsion. The SSIP law (4.11) modeling long-ranged electrostatic attraction is an inverse power law in the inter-axis separation d rather than the smallest surface separation $g = d - R_1 - R_2$ and thus expected not to be very sensitive to small changes in the gap values in case of contacting fibers $g \approx 0$. On the contrary, the SSIP law (4.7) as well as the SBIP law (5.32) modeling the short-range vdW adhesion are inverse power laws in the gap itself and therefore highly sensitive with respect to the gap g. Indeed, the thorough validation of both adhesion models using the example of two straight slender fibers in Section 4.5 as well as an unsuccessful attempt to use penalty beam contact in combination with vdW adhesion for the peeling simulation[1] to be presented in Section 7.3 confirm these considerations. Moreover, refer to Section 4.4.3 for a detailed discussion of the importance to correctly resolve the regime of small gap values by means of a suitable regularization strategy to remedy the inherent singularity of the vdW SSIP law (4.7) for zero separation $g \to 0$.

To conclude, the choice of a proper computational model for steric repulsion between contacting fibers is closely linked to the type of adhesion and most probably even depends on the specific application. For the reasons outlined above, the penalty-based line contact formulation will be applied together with the SSIP law for electrostatic attraction, whereas the SSIP/SBIP approach based on the repulsive part of the LJ law will be applied in combination with the SSIP/SBIP law for vdW adhesion, respectively. Nevertheless, a more detailed analysis of the similarities and differences of existing, macroscopic beam contact formulations and the novel approaches based on molecular steric repulsion is considered a interesting aspect of future work in this field.

6.3. Approaches derivable as special cases of beam-beam interactions

In the context of the overall picture of beam-beam interaction formulations presented in this chapter, it becomes evident that certain related scenarios of similarly high practical relevance can be regarded as dimensionally reduced, special cases of the beam-beam interaction and thus treated by means of similar formulations that are derivable as special cases from the general beam-beam case. One example is the interaction between a a rigid, infinite half-space or rigid wall that has been considered in the literature as a model for the adhesion of a Gecko spatula on a rigid surface [135, 142] and later also for the interaction of a carbon nanotube with a Lennard-Jones wall in 3D [146]. In these cases, the influence of the rigid half space or wall can be evaluated analytically and formulated as a distributed load on the beam. Recalling the SSIP approach to beam-beam interaction presented in Chapter 4, this can be interpreted as an analytical section-rigid half space interaction potential law, where the contributions of all points

---

[1]The resulting peeling force values showed a noticeable unphysical dependence on both the type of the penalty force law and the value of the penalty parameter ε.

in the half space are included by means of analytical integration over this rigid body with trivial geometry.

This reveals the key characteristic of these special cases addressed in this section, namely that the contributions of all elementary interacting points (e.g. charges or atoms) can be evaluated by means of analytical integration and therefore the influence of the second interacting body on the beam may be expressed in a closed-form, analytical expression, which reduces the dimensionality of the problem. In addition to the example of rigid half spaces or walls, the interaction of a beam with a rigid sphere turned out to be another scenario of high practical relevance in the context of studying the mobility of particles in fibrous networks to be presented in Chapter 10. Since this beam-rigid sphere interaction has not been described in the literature before, the resulting expressions will be presented in the following subsection. Another related scenario is the interaction of a beam with a fixed background potential field, which will be applied in Chapter 8 to study the effect of prestress in biopolymer networks and motivates the brief presentation of the used formulation of the interaction to be presented in Section 6.3.2. Figure 6.2 illustrates these different considered scenarios by means of exemplarily chosen simulation snapshots. Finally,

(a)   (b)   (c)
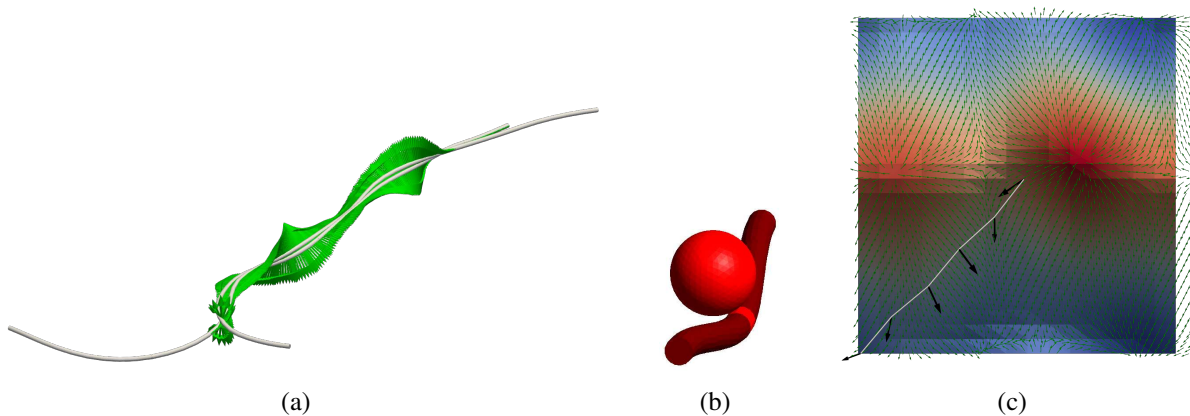
Figure 6.2.: Simulation snapshots illustrating the classification of beam interactions by the type of interacting partners. (a) Beam-beam interaction (e.g. Section 4.5.4), (b) beam-rigid sphere interaction (Chapter 10), (c) beam-static potential field interaction (Chapter 8).

also the self-interaction of a beam should be noted as a very special case of beam-beam interaction, where the second beam is identical to the first one. Refer to the concluding remarks in Section 4.2.2 and Section 5.1 for a discussion of this topic and to Chapter 9 for an application of self-interaction to study the conformation of a mucin filament as a result of varying line charge distributions.

6.3.1. Beam interacting with a rigid sphere

To the best of the author's knowledge, the problem of a beam interacting with a rigid sphere has not been considered in literature before. In the scope of this work, it will be applied to study the hindered mobility of spherical particles due to steric repulsive as well as electrostatic interaction with a fibrous, biopolymer network to be presented in Chapter 10. Following the idea

of deriving this case from the general beam-beam interaction, both a formulation to describe molecular interactions based on beam-sphere interaction potentials as well as a beam-to-sphere penalty contact formulation will be briefly presented in the following. Here, the sphere will be considered as a rigid, homogeneous body that can thus be uniquely described by its midpoint position r_s and its radius R_s.

6.3.1.1. Beam-sphere interaction potential approach

The two-body interaction potential of a beam-sphere pair will be described as

$$\Pi_{ia} = \int\limits_0^l \tilde{\pi}_\text{section-sphere}(\boldsymbol{r}_\text{b-s}, \boldsymbol{\psi}_\text{b-s}) \, \mathrm{d}s, \tag{6.1}$$

where a reduced, effective section-sphere interaction potential law $\tilde{\pi}_\text{section-sphere}$ has been introduced that potentially depends on the relative distance vector $\boldsymbol{r}_\text{b-s}$ of the section midpoint $\boldsymbol{r}_\text{b}(s)$ and sphere midpoint $\boldsymbol{r}_\text{s}$ as well as the relative orientation $\boldsymbol{\psi}_\text{b-s}$. Note the close analogy to both the SSIP law and the SBIP law from Equations (4.3) and (5.2), respectively.

To give one specific example for the section-sphere interaction potential law $\tilde{\pi}_\text{section-sphere}$, we consider the case of the long-range Coulomb interaction that will be applied in the computational study in Chapter 10. Again in close analogy to the careful choice of the SSIP law for this kind of interaction (see Section 4.3.3), the following section-sphere interaction potential law is obtained:

$$\tilde{\pi}_\text{section-sphere} = \lambda_\text{b} \, Q_\text{s} \, \Phi(d), \quad \text{with} \ \ d = \|\boldsymbol{r}_\text{b} - \boldsymbol{r}_\text{s}\| \tag{6.2}$$

Here, λ_b denotes the line charge density of the beam and Q_s denotes the total charge of the sphere. Following the detailed theoretical considerations from Section 4.3.1, the section-sphere interaction potential law $\tilde{\pi}_\text{section-sphere}$ may be expressed solely be the scalar separation of the section and sphere midpoint positions. According to the detailed study of the accuracy of this simple kind of interaction law in Section 4.5.1.2, this turned out to be a very good approximation in the case of circular, homogeneous cross-sections and long-range interactions as considered here.

The required variation of Equation (6.1) to obtain the corresponding virtual work contribution and subsequent spatial discretization of the beam centerline to arrive at the discrete element force vector for both the beam and the sphere as well as the consistent linearization of these terms follows in close analogy to the SSIP approach and will thus not be presented here.

6.3.1.2. Beam-to-sphere penalty contact formulation

Following the argumentation of Section 6.2, a macroscopically motivated, heuristic penalty contact formulation will be applied in Chapter 10 to model the steric repulsive forces between the fibers and the spherical particle. For this reason, the line contact formulation ([110], summarized in Section 3.3.2) will be adapted here to match the case of beam-sphere interaction.

Postulating a beam-sphere penalty force law as a linear function of the minimal surface-surface separation (i.e. gap) $g_\text{b-s}$ with constant scalar prefactor (i.e. penalty parameter) $\varepsilon_\text{b-s}$ yields

the two-body interaction potential

$$\Pi_{c\varepsilon,\text{b-s}} = \frac{1}{2}\varepsilon_{\text{b-s}} \int_0^l \langle g_{\text{b-s}}(s) \rangle^2 \, \mathrm{d}s, \tag{6.3}$$

where the crucial difference to the beam-beam scenario lies in the way how the gap g is computed. Whereas a unilateral closest-point projection is required in the beam-beam scenario, the problem simplifies significantly in the case of a rigid sphere, because the minimal surface separation between the current beam cross-section and the sphere may be expressed in good approximation as

$$g_{\text{b-s}}(s) = \|\boldsymbol{r}_\text{b} - \boldsymbol{r}_\text{s}\| - R_\text{b} - R_\text{s}. \tag{6.4}$$

As in the previous section, the required variation of Equation (6.3) to obtain the corresponding virtual work contribution and subsequent spatial discretization of the beam centerline to arrive at the discrete element force vector for both the beam and the sphere as well as the consistent linearization of these terms follows in close analogy to the beam-beam scenario and will thus not be presented here. The evaluation of the virtual work contribution generally requires numerical integration along the beam centerline curve such as Gaussian quadrature. In the computational study to be presented in Chapter 10, this numerical integration has been replaced by a summation over so-called collocation points, which is expected to be an equivalent formulation as long as sufficiently many collocation points are used.

6.3.2. Beam interacting with a static background potential field

This scenario of a beam interacting with a static background potential field $\Psi(\boldsymbol{x})$ will be applied in Chapter 8 to study the effect of prestress in biopolymer networks. As mentioned before, this interaction scenario can be interpreted as a special, dimensionally reduced case derivable from the more general beam-beam interaction. Starting from the first principles for atoms or charges and assuming that the background potential field $\Psi(\boldsymbol{x})$ acts on every material point of the beam thus yields the total interaction potential

$$\Pi_{\text{ia}} = \int_V \rho(\boldsymbol{x}) \, \Psi(\boldsymbol{x}) \, \mathrm{d}V \tag{6.5}$$

Note the analogy to Equation (2.12) describing beam-beam interactions, where the influence of the second beam on the first one may be interpreted as a configuration-dependent spatial potential field acting on every material point of the first beam. Following the key idea of the general SSIP approach, a split of the volume integral into one part along the centerline curve and the other over the cross-section leads us to

$$\Pi_{\text{ia}} = \int_0^l \underbrace{\int_A \rho(\boldsymbol{x}) \, \Psi(\boldsymbol{x}) \, \mathrm{d}A}_{=:V(\boldsymbol{r},\boldsymbol{\psi})} \, \mathrm{d}s. \tag{6.6}$$

The resulting, effective potential $V(\boldsymbol{r}, \boldsymbol{\psi})$ acting on the beam centerline has dimensions of energy per length. Once again, note the analogy to the reduced interaction potential laws, either in form of an SSIP law $\tilde{\tilde{\pi}}(\boldsymbol{r}_{1-2}, \boldsymbol{\psi}_{1-2})$ or SBIP law $\tilde{\pi}(\boldsymbol{r}_{1-2c}, \boldsymbol{\psi}_{1-2c})$, that naturally result for the beam-beam interaction in Equations (4.3) and (5.2), respectively.

To ease the following notation and discussion, and because only this case will be required in the application in Chapter 8, we now restrict ourselves to an effective potential field $V(\boldsymbol{r})$ that solely depends on the centerline midpoint positions $\boldsymbol{r}(s)$ and not on the orientation of the cross-section expressed by the rotation vector $\boldsymbol{\psi}(s)$. At this point, the problem can alternatively be seen as a line Neumann load that results from the corresponding force field $-\nabla V(\boldsymbol{r})$ of the potential $V(\boldsymbol{r})$ and in general depends on the current configuration of the beam.

Its contribution to the virtual work required for the weak, variational formulation of the problem can thus be stated as

$$\delta\Pi_{\mathrm{ia}} = - \int_0^l \left(\nabla V(\boldsymbol{r}(s))\right)^T \delta\boldsymbol{r}(s) \; \mathrm{d}s \tag{6.7}$$

where $\boldsymbol{r} \in \mathbb{R}^3$ is the centerline position and $s \in [0, l]$ denotes the arclength coordinate in the stress-free reference configuration of the beam. The evaluation of the virtual work contribution generally requires numerical integration along the beam centerline curve such as Gaussian quadrature. Subsequent discretization of the admissible centerline variations $\delta\mathbf{r}$ according to the finite element method (see Section 3.2) yields the contributions to the discrete element force vector.

7. Peeling and Pull-off Behavior of Adhesive Elastic Fibers

The objective of this chapter is two-fold: On the one hand, it studies the fundamental problem of separating two adhesive elastic fibers to foster the understanding of the underlying physical mechanisms, which has only been made possible by the development of the beam interaction formulations in Chapters 4 and 5. Specifically, it covers the peeling and pull-off process starting from fibers contacting along its entire length to fully separated fibers (and the reverse order) including all intermediate configurations and the well-known physical instability of snapping into contact and snapping free. On the other hand, the computational study of this chapter serves as a proof of concept for the application of the novel computational models, thus facilitating future applications including also larger and increasingly complex systems of slender fibers. Apart from the results considering the case of vdW adhesion by means of the SBIP approach in Section 7.4, the content of this chapter has previously been published in the author's article [60].

7.1. Motivation and background

This fundamental problem of separating two adhesive, elastic fibers seems to be intractable for purely analytical approaches due to the interplay of adhesion, repulsion and structural resistance against deformation, i.e., elasticity within the highly nonlinear regime of large deformations. For the same reasons, it is challenging also for a computational approach and in fact the numerical treatment brings a number of further challenges with it (see [137] for a summary) which will be addressed in this chapter. Several contributions to related problems can be found in the literature. The adhesion of a Gecko spatula to solid surfaces has inspired the development of computational models to study and optimize the peeling behavior of thin elastic films and strips [114, 115, 134, 138, 142]. The corresponding model system of a beam interacting with a rigid half-space via the Lennard-Jones (LJ) potential shows certain similarities with the system of two deformable adhesive fibers to be studied in this chapter and this comparison will thus be addressed in the discussion of the results. Also the contribution by Sauer [139], where the peeling of two flexible strips is modeled via a 2D solid finite element formulation that combines a so-called cohesive zone model with a penalty contact formulation, will serve as source for comparison. The problem studied in [139] differs from the one in the present work in terms of the specific geometry, boundary conditions, type of interactions and not at least in terms of the specific modeling and discretization approach. It will thus be interesting to see how these differences carry over to the resulting force responses. Two approaches to investigate the undesirable effect of clumping in fibrillar arrays used for bio-inspired dry adhesives are presented in [2]. The analytical approach aims to predict the critical fiber length leading to tip-tip contact by calculating the vdW force

between assumed spherical tips of the fibers and applying it as a tip load in Euler-Bernoulli beam theory for a 2D cantilever. This is complemented by a finite element approach using 2D solid elements and an effective inter-element vdW force based on the inverse-sixth power law. The computational model proposed and applied in [120] focuses on the effect of inter-fiber adhesion at the level of 2D fiber networks. It thus abstains from resolving the exact kinematics of adhesion and contact at the fiber scale and applies an effective energy gain per unit length of contacting parallel fiber segments and solves for the corresponding bundle segment lengths as additional unknowns. Finally, an example for the electrostatic interaction of a double-clamped microbeam with a flat rigid electrode in a microelectromechanical system is given in [148].

The present study extends these previously published results for related problems with respect to the following aspects. To the best of the author's knowledge, this is the first study of the peeling behavior of two elastic fibers interacting via attractive electrostatic or vdW forces. Compared to previous peeling studies, it also includes the pull-off phase, the intermediate regime around the physical instability of snapping into contact and snapping free, as well as the separated state of fibers. Moreover, we investigate the scenario of peeling from both ends of the fibers, which turns out to show a similar behavior in the peeling phase yet a fundamentally different behavior in the pull-off phase as compared to the peeling from one side considered in the related problems of strip-rigid surface LJ interaction [138] and double-strip debonding [139]. Eventually, we analyze the resulting force-displacement curve revealing a rich, highly nonlinear system behavior and investigate the underlying physical mechanisms arising from the interplay of adhesion, mechanical contact interaction and structural resistance against (axial, shear and bending) deformation. Furthermore, the influence of different material and interaction parameters such as Young's modulus as well as type (e.g. electrostatic or vdW) and strength of adhesion on the resulting force-displacement relationship is studied by varying these parameters over two orders of magnitude.

In addition to the physical system behavior, the decisive numerical aspects required to simulate this challenging computational problem in a robust and accurate manner will be discussed in this chapter. From a computational point of view, the major challenges resulting from the physical system characteristics are the delicate task of determining equilibrium configurations in the direct vicinity of the mentioned physical instability, the control of spatial discretization and numerical integration error such that the high gradients of short-range interaction potentials are represented with sufficient accuracy, and the regularization of inverse power laws to eliminate the singularity at zero separation. For the employed reduced interaction laws, such a regularization procedure has been proposed in Sections 4.4.3 and 5.4.1, which will turn out to enable a considerable increase in numerical robustness and efficiency at identical accuracy when applied to the highly challenging example of LJ interaction as considered in the present application.

7.2. Electrostatic attraction

The system considered in the simulation consists of two initially straight and parallel, deformable fibers that attract each other due to their constant surface charge of opposite sign. Its setup is kept as simple as possible to allow for an isolated and clear analysis of the physical effects as well as the characteristics of the computational model. Note that the static equilibrium configurations as

a result of different surface charge densities at a fixed, large separation of the fibers have already been studied in Section 4.5.3. The study of the peeling and pull-off process to be presented in this section can thus be considered the more advanced continuation of this analysis in order to obtain the full picture of the system behavior from fibers clinging together along their entire length to fully separated fibers.

7.2.1. Setup and parameters

As shown in Figure 7.1(a), two straight fibers of length $l = 5$ are aligned with the global y-axis and are simply supported at their endpoints. Additionally, both fibers are restricted to move only within the xy-plane and rotate only around the global z-axis. The fibers have a circular cross-section with radius $R = 0.02$, which results in a slenderness ratio of $\zeta = l/R = 250$. The initial configuration is chosen such that the fiber surfaces are in contact, i.e., the fiber centerlines are placed with an inter-axis separation $d_0 = 2R$. Starting from this initial state, a horizontal displacement u_x will be prescribed to both supports of the right fiber and the total resulting horizontal force $F_x = F_x^{tr} + F_x^{br}$ will be analyzed. Cross-section area, area moments of inertia and shear correction factor are computed using standard formula for a circle. A hyperelastic material law with Young's modulus $E = 10^5$ and Poisson's ratio $\nu = 0.3$ is applied.
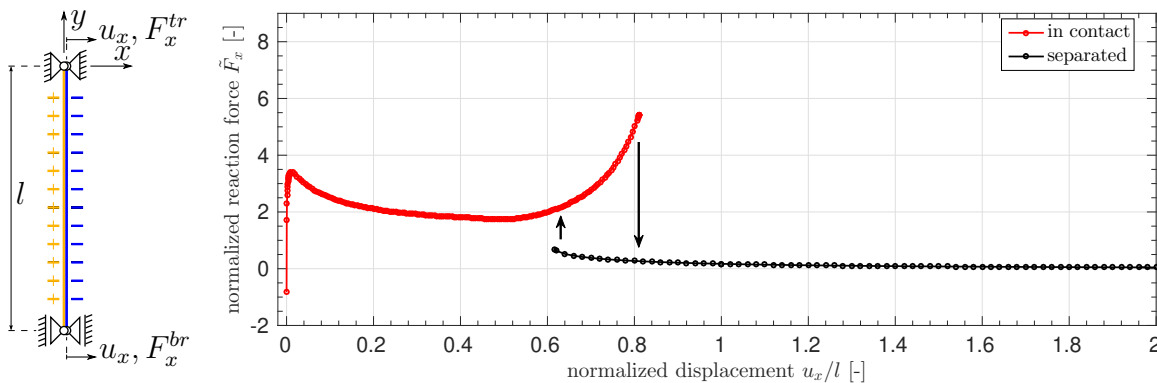
(a) Problem setup   (b) Quasi-static force-displacement curve. Force values to be interpreted as multiple of a reference point load that causes a deflection of $l/4$ if applied at the fiber midpoint.

Figure 7.1.: Numerical peeling and pull-off experiment with two adhesive elastic fibers. Figure taken from the author's article [60].

Electrostatic interaction is accounted for via the SSIP approach as presented in Section 4.3.3. Both fibers are nonconducting with a constant surface charge density of $\sigma_1 = 1.0$ and $\sigma_2 = -1.0$, respectively. Note that the hereby considered immobility of charges in nonconducting material is consistently assumed also during the contact of fibers, such that no charge transfer occurs and the constant surface charge densities of opposite sign will remain unchanged. The strength of attraction is controlled via the prefactor k of the Coulomb law $\Phi(r) = kr^{-1}$ and set to $k = 0.1$ for the first part of this study. An analysis of the effect of parameter value variation will be the content of Section 7.2.4.

The repulsive contact forces are modeled by means of the frictionless line penalty contact formulation as presented in Section 3.3.2.[1] In particular, a quadratically regularized linear penalty law with line penalty parameter $\varepsilon = 100$ and regularization parameter $\bar{g} = R/10$ is applied here. Recall at this point, that the surface-to-surface separation – or gap – g is defined as $g = d - R_1 - R_2$ and thus negative gap values indicate a penetration, whereas positive gap values imply physical separation of the bodies. The applied regularization therefore means that contact forces smoothly increase in the regime of small positive gaps $0 < g < \bar{g}$, starting from a force value as well as slope of zero at $g = \bar{g}$. As a result of the simulations, it will turn out that these exemplarily chosen parameter values lead to a slightly positive equilibrium spacing $g_{eq} \approx 2.28 \times 10^{-4} \approx R/100$, where the repulsive contact forces balance the adhesive electrostatic forces. The initial state of the system with zero separation $g_0 = d_0 - 2R = 0$ along the entire length of the fibers will thus lie in the compressive, i.e., repulsive regime with negative reaction force values $\tilde{F}_x < 0$.

For the following quantitative analysis, we use a fine spatial discretization of $n_{\mathrm{ele}} = 16$ Hermitian Simo-Reissner beam elements (see Section 3.1 for details) per fiber to ensure that the discretization error has no perceptible effect on the results. For the same reason, we choose a high number of Gauss points for the numerical integration of contact as well as electrostatic forces. Two integration segments per element with ten Gauss points each are used for electrostatic forces and 20 integration segments per element with five Gauss points each are used for contact forces. This turns out to be fine enough to not change the presented results perceptibly. A closer look at mesh refinement and the undesirable effect of too coarse meshes follows at the end of this section.

Obviously, the competition of attractive and repulsive forces of which both are strongly deformation dependent leads to a complex system behavior. The associated nonlinearity and stiffness are highly demanding with respect to solving the nonlinear system of equations. We thus apply Newton's method in combination with a displacement increment control as described in Appendix F.2. The upper bound of the displacement increment per iteration is chosen as $|\Delta u|_{\max} = R/2$ here, which prevents an undetected crossing of fibers.

7.2.2. Results

The resulting force-displacement curve shown in Figure 7.1(b) reveals a rich and interesting system behavior. Most obvious, there are two distinct branches of static equilibrium configurations that do not merge. On the one hand, starting from zero displacement and illustrated in red, we see the branch where the fibers are in contact and on the other hand, for large separations, there is another branch depicted in black where the fibers are separated. The transition between both states as indicated with arrows will always be a dynamic process and will be discussed in further detail later on. Simulation snapshots for some characteristic displacement values are provided in Figure 7.2.

Let us first look at the left part of the force-displacement plot where the fibers are in contact. Note that the force values are normalized and to be interpreted as multiple of a reference point load that causes a deflection of l/4 if applied at the fiber midpoint. At zero displacement and thus

---

[1] See Section 6.2 for a discussion of the applicability of penalty contact formulations in this context.

(a) $u_x/l = 0$ (b) $u_x/l = 0.01$ (c) $u_x/l = 0.2$ (d) $u_x/l = 0.4$ (e) $u_x/l = 0.5$

(f) $u_x/l \approx 0.62$: in contact   (g) $u_x/l = 0.8$: in contact   (h) $u_x/l \approx 0.8105$: rightmost red data point in Fig. 7.1(b), ultimately before fibers would snap free

(i) $u_x/l \approx 0.62$: leftmost black data point in Fig. 7.1(b), ultimately before fibers would snap in contact   (j) $u_x/l = 0.8$: separated   (k) $u_x/l = 1.2$: separated
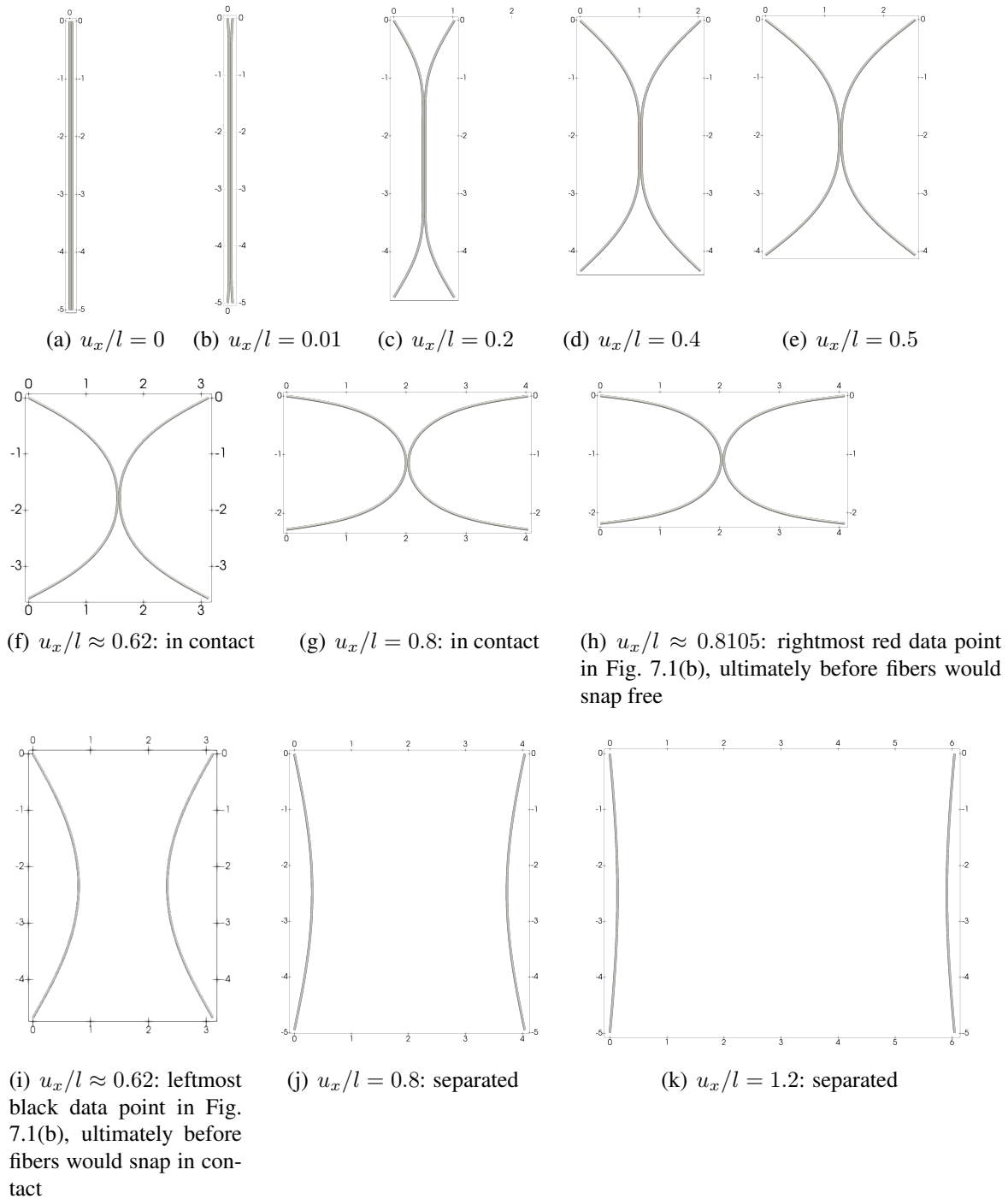
Figure 7.2.: Simulation snapshots of the peeling and pull-off experiment of two adhesive elastic fibers. Note that all configurations are symmetric with respect to a vertical as well as horizontal axis. This also implies $F_x^{\text{tl}} = F_x^{\text{bl}} = -F_x^{\text{tr}} = -F_x^{\text{br}}$, $F_y \equiv 0$ for the reaction force components acting on the left (l) and right (r) fiber's endpoints at the top (t) or bottom (b), respectively. Note that (a) - (h) show configurations on the red branch, (i) - (k) on the black branch of Figure 7.1(b), respectively. Figure taken from the author's article [60].

zero separation of the fiber surfaces, the fibers repel each other as a resistance against penetration which results in a negative reaction force $\tilde{F}_x \approx -0.8$. From the second data point onwards, we identify the tensile regime with positive, rapidly increasing force values. At $u_x/l \approx 0.01$, the force reaches a local maximum value of $\tilde{F}_x \approx 3.9$ and then decreases until it reaches a local minimal value of $\tilde{F}_x \approx 1.74$ at $u_x/l \approx 0.5$. Upon further displacement, the force increases again until the fibers suddenly snap free at some point. The exact point of snapping free strongly depends on the dynamics of the system and can thus not be determined in this quasi-static analysis. However, it is very interesting to see that for a certain range of separation $0.6 \lessapprox u_x/l \lessapprox 0.8$ two different static equilibrium configurations exist - one with contacting fibers and one with separated fibers. See also the corresponding simulation snapshots in Figure 7.2(g) and Figure 7.2(j), respectively. The largest horizontal separation of the supports for which we could find a static equilibrium configuration with the fibers being still in contact, i.e., the rightmost red data point yields $\tilde{F}_x \approx 5.4$ at $u_x/l \approx 0.81$. Beyond this point, Newton's method fails to converge. This is reasonable because the nearest solution of the nonlinear system of equations looks similar to Figure 7.2(j) whereas the last converged configuration and thus initial guess for Newton's method is Figure 7.2(h).

The second branch of static equilibrium with separated fibers is much more intuitive and some qualitative aspects have already been discussed in Section 4.5.3, where the resulting equilibrium configurations for varying attractive strength at a fixed, large separation $u_x/l = 1$ have been studied. Here, we also present the quantitative analysis of the resulting force values as a function of the displacement and particularly include the intermediate range of separations $0.6 \lessapprox u_x/l \lessapprox 0.8$. Due to the long range of electrostatic forces, we still observe a perceptible force and deflection for separated fibers. Nevertheless, as expected, force values decay and approach zero for large separation. Most interesting however is once again the range of $0.6 \lessapprox u_x/l \lessapprox 0.8$. Here, no static equilibrium could be found with Newton's method as fibers tend to jump into contact and so the equilibrium states are unstable. Instead, we conducted dynamic simulations with artificial viscous damping forces and waited until the system had reached its steady state[2]. The method used to compute the viscous forces has been proposed in [32] and models the interaction of a semi-flexible filament with a quiescent background fluid. In this manner, we could determine further (unstable) static equilibrium configurations in the range of $0.616 \lessapprox u_x/l \lessapprox 0.9$. As discussed earlier for the pull-off, also the exact point of jump-into-contact will depend on the dynamics of the system.

Since the separation of the fiber axes/surfaces is a non-trivial result of the competing attractive and repulsive forces, it is worth to have a closer look at the gap values. From Figure 7.2, one can already tell that contacting fibers neither show large penetrations nor a visible gap between the surfaces and as such meet our expectations. In Figure 7.3, points of active contact are visualized as spheres and coloring indicates the gap values g/R, i.e., normalized with respect to the fiber radius. We find that $g/R \gtrapprox -0.15$, i.e., the maximal penetration is less than 15% of the fiber radius throughout the entire simulation from zero displacement to separation. In the context of penalty-based models for beam contact, this is considered a reasonable small value and may be interpreted as a model for the cross-section deformation, which is otherwise precluded in the

---

[2] The steady state has been defined in a way that the magnitude of every velocity and acceleration component in the system has fallen below a threshold value of 10^{-10}.
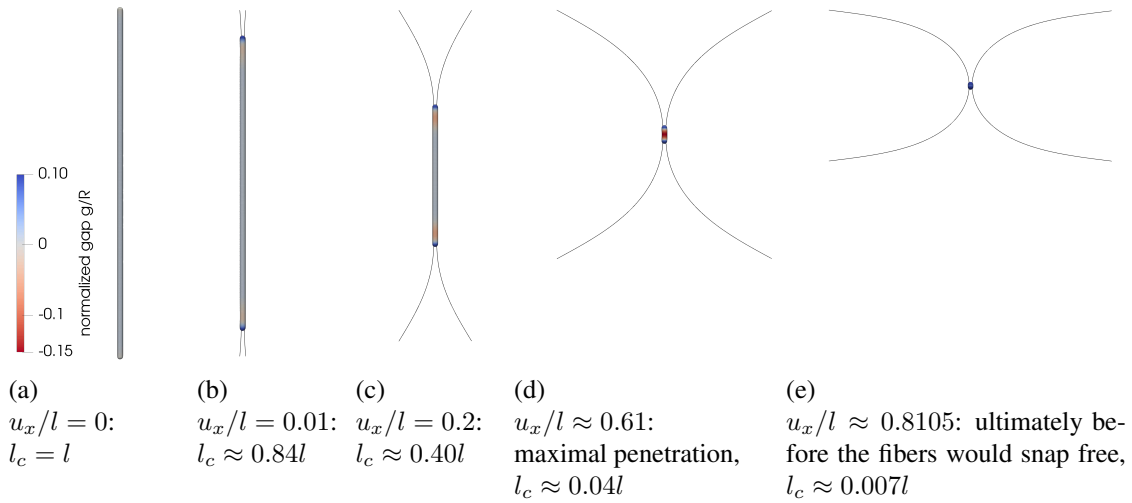
(a)
$u_x/l = 0$:
$l_c = l$

(b)
$u_x/l = 0.01$:
$l_c \approx 0.84l$

(c)
$u_x/l = 0.2$:
$l_c \approx 0.40l$

(d)
$u_x/l \approx 0.61$:
maximal penetration,
$l_c \approx 0.04l$

(e)
$u_x/l \approx 0.8105$: ultimately be-
fore the fibers would snap free,
$l_c \approx 0.007l$

Figure 7.3.: Visualization of surface-to-surface separation during the peeling and pull-off exper-
iment of two adhesive elastic fibers. Fibers represented by their centerlines and active contact
pairs illustrated as spheres located halfway between interacting points on fibers. Color indicates
gap values normalized with the fiber radius g/R. Negative gap values indicate penetration. Here,
l_c denotes the length of the contact line. Figure taken from the author's article [60].

applied beam theory. Note also that the maximal penetration only occurs for a very short time
interval at $u_x/l \approx 0.61$ in the spatially confined region around the fiber midpoints.

Remark on the reference force value   At $u_x/l = 0.5$, the deflection of the fiber mid-
point(s) is the same as in the experiment to determine the reference force used for normalization.
The corresponding force value of $\tilde{F}_x \approx 1.7$ can thus be interpreted as a surplus of deformation
as compared to the simple reference experiment with a point load applied to the midpoint.

7.2.3. Discussion

In the following discussion, a deeper understanding of the observed system behavior will be
elaborated. Particularly, the underlying mechanisms of the complex force-displacement curve
from zero displacement to full separation of the fibers shall be elucidated. To this end, one has
to discuss the attractive as well as repulsive forces between both fibers along with the internal
elastic forces and moments in the fibers. Generally, the prevalent mode of fiber deformation is
bending, i.e., curvature of fiber axes. Axial elongation and shear deformation remain small and
no torsional deformation occurs due to the planar setup. Concerning the interaction forces, it is
most plausible to look at a net interaction line load acting on each of the fibers. To begin with,
we basically identify three distinct phases that are discussed individually in the following.

Phase a) initiation of fiber deformation and detachment (here: $0 < u_x/l < 0.01$): The displace-
ment of the fiber endpoints initiates a curvature in a locally confined region towards the
endpoints of the fiber. Accordingly, the first surface point pairs begin to separate, leave the

equilibrium spacing and cause an adhesive force. Since the fiber axes are almost parallel and the fibers show a resistance against bending deformation, a considerable number of surface point pairs must detach at once. This explains the steep increase of the pulling force in the leftmost part of the force-displacement diagram. The major part in the middle of the fibers however remains parallel in an equilibrium state of balanced contact and adhesive forces. The two limiting cases would be rigid fibers, where the entire length of the fiber needs to detach at once and rope-like fibers, i.e., with negligible bending stiffness, where one point pair after another could detach. It is thus a competition of elastic deformation and electrostatic adhesion, that will be further analyzed in a parameter study with varying Young's modulus at the end of this section. Figure 7.2(b) illustrates the configuration corresponding to the local force maximum which can be considered as the end of this initial phase.

Phase b) peeling (here: $0.01 < u_x/l < 0.5$): Subsequently, the contact zone continuously decreases as more and more surface point pairs detach which can be identified as peeling. Especially in the beginning of this peeling phase, the opening angle between the fiber axes increases and likewise the pulling force decreases. This is due to the known effect, that a larger angle requires less point pairs to detach at the same time. Additionally, the lever arm in form of the already detached, free part of the fiber becomes longer, such that the reaction force at the supports decreases. The combination of the increasing opening angle and the decreasing effective stiffness of the longer free fiber parts are presumably the most important effect in this phase. From the perspective of fiber deformation, the radius of curvature increases as compared to the initially induced strong local curvature. Still, the middle part of the fibers remains parallel whereas the end parts are bent. Interestingly, a closer look at the gap values shown in Figure 7.3(c) reveals that the resulting centerline shape resembles a very slight "w". In the course of the peeling phase, the opening angle as well as the free fiber length and likewise the pulling force approaches a constant value. This constant peeling force over displacement is well-known from thin film peeling in the limit of zero bending stiffness [138] as predicted analytically by [83].

Phase c) pull-off (here: $0.5 < u_x/l < 0.8$): The end of the peeling and begin of the pull-off phase can be identified as the point from which on the pulling force increases again. As can be seen from Figure 7.2(e) and 7.3(d), the centerline shape now resembles a "c", i.e., is convex. Accordingly, the contact zone diminished to a short region in the middle of the fibers that can not easily be peeled any further because it would require a strong local curvature of the fibers. During the entire pull-off phase, the adhesive forces acting on the fibers change only marginally because there is not much change in the mutual distance of the most important closest parts of the fibers. However, the repulsive contact forces decrease and therefore the net interaction force increases considerably. So the remarkable increase in the external pulling force before the fibers finally snap free results from the compensation of the diminishing contact forces. The maximum value of the tensile force that is required during the separation of adhesive bodies is commonly referred to as *pull-off force* and is of highest relevance in many practical applications. Looking at this phase from the different perspective of elastic deformation, the fibers undergo a high

curvature in the middle part and increasing axial tension towards the endpoints in order to conform with the ever increasing separation u_x/l, such that in the end each fiber resembles a "u"-shape[3]. The high axial stiffness of the fibers leads to an increase in the reaction force until it ultimately reaches the maximum value that can be transferred by the adhesive connection.

Note that the given range of displacement values is not meant to be the universal characteristic property of the identified phases. Instead, the fundamental qualitative features of the force-displacement curve and the revealed underlying mechanisms motivate the presented distinction into three phases, while the specific displacement values separating these three phases depend on the considered system parameters as will be shown in Section 7.2.4.

When comparing these results to those obtained for the related scenario of the one-sided peeling of a thin elastic film adhering to a rigid surface via vdW forces in the previous study [138], a number of similarities can be identified. In both of the aforementioned phases a) and b), the resulting force-displacement curves have the same characteristic shape, i.e., a steep initial slope towards a sharp force peak followed by gradually decreasing force values eventually approaching a plateau-like regime of almost constant peeling forces thus representing a strongly nonlinear, deformation-dependent system behavior that arises from the interplay of elasticity, adhesion and mechanical contact interaction. This also holds true for the double-strip peeling modeled via 2D solid elements and a cohesive zone model studied in [139], which underlines the universality of both the results itself as well as of the thorough analysis of the underlying physical mechanisms. Neither the differences in the physical origin (and computational modeling) of adhesion nor the slightly different setup with respect to loading and support, i.e., the different boundary conditions, seem to change this fundamental system response during peeling and the initiation thereof. We will get back to this topic in the discussion of the results for the parameter variation in Section 7.2.4 and for the case of vdW adhesion in Section 7.3.2.

Turning to the differences in the results as well as its reasons, the most obvious observation from Figure 7.1(b) is the pronounced pull-off phase described above. As compared to the mentioned previous studies, this can be attributed to the application of pulling forces at both ends of the fibers, which results in a two-sided instead of a one-sided peeling. While the pull-off displacement and force in case of one-sided peeling strongly depend on the properties and modeling of the fiber endpoints, the two-sided peeling setup shifts the focus to the interaction of the fibers' middle parts. The observed significant increase of the force over an extended range of displacement values $0.5 < u_x/l < 0.8$ before snapping free is therefore considered to be characteristic for the two-sided peeling setup, which is an important finding with implications concerning the assessment of real-world systems of adhesive fibers.

Following up on this, the most striking fact is that the global force maximum occurs at the end of this pull-off phase c), ultimately before snapping free. As the results for the case of vdW attraction will show, this appears to be a distinguishing feature of the long range of electrostatic attraction considered here. In view of the fact that the global force maximum will be the decisive feature in biological as well as bio-inspired synthetic dry adhesives, a clear understanding of how the maximum force value and the corresponding displacement or, more generally, system state depends on the elementary system properties is certainly of the highest importance.

---

[3] This shape will be even more pronounced for a smaller value of Young's modulus, cf. Figure 7.5(b).

Thus, the following section investigates the effect of varying the principal parameters, and subsequently the fundamentally different type of adhesion arising from vdW interactions will be studied in Section 7.3.

7.2.4. Influence of the strength of adhesion and Young's modulus

Having studied the interplay of elasticity and adhesion for one set of parameters, now the effect of parameter variation will be considered. As has been noted already by Sauer [138] in the scenario of peeling a thin film with finite bending stiffness from a rigid surface, the decisive parameter is the ratio of Young's modulus and adhesive strength. The simulations conducted in the scope of this section confirmed that this holds true also for the case of two adhesive elastic fibers studied here. In the following, the prefactor of the point potential law $k = 0.1$ is thus left unchanged and Young's modulus E will be varied by a factor of 0.1 and 10, respectively, thus covering a range of two orders of magnitude.
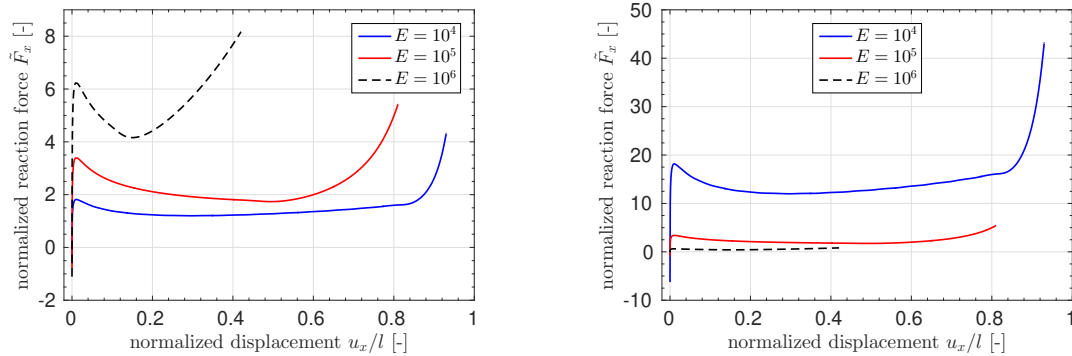
(a) Quasi-static force-displacement curves. Force values to be interpreted as multiple of a reference point load that causes a deflection of $l/4$ if applied at the fiber midpoint. Here, the same reference force value - the one which is obtained for Young's modulus $E = 10^5$ - is used for all three curves.

(b) Quasi-static force-displacement curves with alternative normalization: Force values are again to be interpreted as multiple of a reference point load that causes a deflection of $l/4$ if applied at the fiber midpoint, but here an individual reference force value, which is obtained for the corresponding value of Young's modulus $E = 10^4, 10^5, 10^6$, respectively, is used for each of the three curves.

Figure 7.4.: Comparison of results for ten times larger and ten times smaller value for Young's modulus E. Figure taken from the author's article [60].

The resulting force-displacement curves are shown in Figure 7.4(a). Accordingly, the static equilibrium configurations for one exemplarily chosen displacement value $u_x/l = 0.4$ are compared in Figure 7.5(a) and the configurations ultimately before snapping free, i.e., corresponding to the rightmost data point of each curve, are visualized in Figure 7.5(b). Note the two different variants of normalization of force values shown in Figure 7.4(a) and Figure 7.4(b). On the one hand, using the same reference force for all scenarios allows to compare the absolute force levels in Figure 7.4(a). It is found that the force peak associated with the initiation of fiber deformation is more pronounced for higher values of Young's modulus and thus bending stiffness of the

fibers, as expected from the discussion of this initiation phase above. Directly related to this, the subsequent peeling phase shows higher force values and passes over to the final pull-off phase at smaller displacement values. The force plateau, which is characteristic for peeling with zero bending resistance, is not observable at all for the highest value of Young's modulus $E = 10^6$ considered here, but is very pronounced for $E = 10^4$. In the final pull-off phase, fibers with higher Young's modulus again show higher force values, however with a less sharp increase just before snapping free. Altogether, the system behavior shows some analogy to the failure of brittle and ductile material.
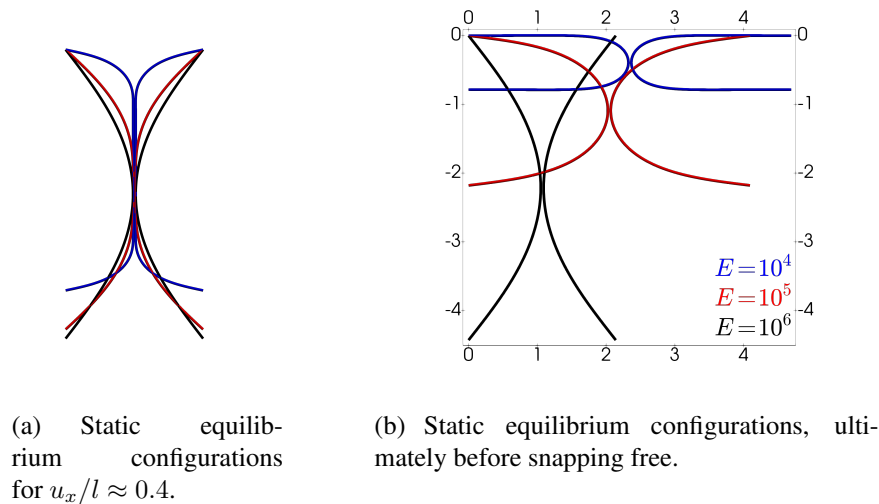

(a) Static equilibrium configurations for $u_x/l \approx 0.4$.

(b) Static equilibrium configurations, ultimately before snapping free.

Figure 7.5.: Comparison of equilibrium configurations for ten times larger and ten times smaller value for Young's modulus E. Figure taken from the author's article [60].

Alternatively, one can compute an individual reference force for each of the three curves with the corresponding value for the Young's modulus $E = 10^4, 10^5, 10^6$, respectively (see Figure 7.4(b)). As expected, this reference force in the case of the ten times smaller / larger value of Young's modulus will be ten times smaller / larger than the reference force originally obtained for $E = 10^5$ and used in Figure 7.4(a), respectively. This alternative normalization nicely illustrates the relative strength of the electrostatic interaction forces as compared to the forces that would typically result from large elastic bending deformation as represented by the scenario to compute the reference force. It can be observed that the pull-off force in the case of the most flexible fibers with $E = 10^4$ exceeds this reference force by an impressive factor of more than 40.

Getting back to the comparison with the previous study of one-sided peeling of a thin film adhering to a rigid surface via vdW forces [138], the results from variation of the relative adhesive strength over two orders of magnitude basically confirm the conclusions drawn above for the reference value. The initial steep increase of the force and subsequent decrease in the initiation and peeling phase can be identified as unifying characteristics throughout all setups. In addition, the trends of increasing force peak values and decreasing plateau width with increasing Young's modulus, i.e., decreasing relative strength of adhesion are observable both for the system here

as well as for one-sided peeling of a thin film from a rigid substrate. Also, the distinct pull-off phase with increasing force values including the global force maximum is reproduced here for all values of the relative strength of adhesion whereas it is not present for any of the parameter values in the one-sided peeling scenario of [138]. This confirms the causal link between peeling from two sides and such a pronounced pull-off phase as suggested and explained above.

7.2.5. Discussion of parameter values and the transfer of results to specific real-world systems

Dimensional analysis by means of the Buckingham π theorem shows that the quasi-static problem considered in this section can be described by three dimensionless parameters. Apart from the slenderness ratio $\zeta := L/R$ of the fibers, which is well known from beam theory to be the key parameter concerning the elastic deformation of fibers under load, the ratio $\sigma^2 \, k_{\mathrm{elstat}}/E =: C_{\mathrm{adh}}$ is obtained as the dimensionless parameter governing the interplay of adhesive electrostatic forces and structural stiffness/compliance of the fibers. The third dimensionless parameter involving the penalty contact parameter ε is obtained as $\varepsilon/(\sigma^2 \, k_{\mathrm{elstat}} \, R)$, which can be interpreted as a measure for the normalized equilibrium distance that results from the competition of repulsive steric and attractive electrostatic forces.[4] For a given slenderness ratio ζ, the ratio $C_{\mathrm{adh}} = \sigma^2 \, k_{\mathrm{elstat}}/E$ of adhesive strength and fiber stiffness is the decisive parameter for the peeling and pull-off behavior observed and discussed here, as has already been mentioned above and has been the motivation to vary Young's modulus of the fibers while keeping the strength of adhesion fixed. Regarding the further use, it seems reasonable to refer to this characteristic dimensionless quantity C_{adh} as the "adhesive compliance" of fibers.

This theoretical analysis has been verified by additional simulation runs, where all three quantities E, k_{elstat} and ε have been multiplied by a factor of 10^5 such that the ratios $\varepsilon/(\sigma^2 \, k_{\mathrm{elstat}} \, R)$ and $\sigma^2 \, k_{\mathrm{elstat}}/E$ remain unchanged and the resulting normalized force-displacement curves for Young's modulus $E = \{10^9, 10^{10}, 10^{11}\}$ are indeed identical to the ones shown in Figure 7.4. Note also in this respect that intentionally no units are specified in this entire study, because the computed results hold true for any consistent system of units. For example, for a system of μm, mg and s as often used in micromechanics, the numbers given for Young's modulus $E = \{10^4, 10^5, 10^6\}$ in the parameter study above correspond to values of $\{10\,\mathrm{kPa}, 100\,\mathrm{kPa}, 1\,\mathrm{MPa}\}$, respectively. However, other choices are equally valid.

Now that the adhesive compliance C_{adh} has been identified as the decisive dimensionless quantity, it can be stated that the three values used for Young's modulus $E = \{10^4, 10^5, 10^6\}$ correspond to parameter values $C_{\mathrm{adh}} = \{10^{-5}, 10^{-6}, 10^{-7}\}$, respectively, and that these values turn out to cover the entire range from "relatively strong adhesion/relatively soft fibers" to "relatively weak adhesion/relatively stiff fibers". Based on the trends in the force-displacement curves in Figure 7.4, one also gets an impression of the system behavior in both limits of "dominant strength of adhesion/negligible stiffness" (cf. adhesion between ideal ropes) and "negligible

---

[4] Since the penalty contact formulation is considered to be a numerical regularization of the non-penetration constraint rather than a physically motivated repulsive force law (refer to the discussion in Section 6.2), it is suggested to keep this ratio $\varepsilon/(\sigma^2 \, k_{\mathrm{elstat}} \, R)$ fixed when varying the adhesive strength, such that an increased adhesive strength does not lead to an increased violation of the non-penetration constraint.

strength of adhesion/almost rigid fibers" (cf. adhesion between rigid rods), respectively. In this manner, the present study delivers basic insights for any set of real parameter values.

Finally, in order to draw conclusions for a specific real system or compare the results to experimental results, one would need to quantify both the strength of adhesion and the stiffness of the real fibers to determine their adhesive compliance C_{adh}. To give a real-world example, consider the mucin filaments to be studied in Chapter 9. First, note that the slenderness ratio $\zeta = 250$ considered in this computational study is in the range of values $\zeta \in [150, 400]$ that can be estimated for mucin filaments [132, 149]. Second, taking into account the reported values for the surface charge density[5] [105] and persistence length [132, 149] allows to estimate $C_{adh} \in [10^{-6}, 10^{-1}]$. Due to these rather high values for the adhesive compliance as compared to the values considered in this computational study $[10^{-7}, 10^{-5}]$, mucin is thus expected to lie in the regime of "strong adhesion/soft fibers" of the observed spectrum of system responses and show considerable structural deformations due to the electrostatic interactions. This behavior will indeed be observed in the computational experiments investigating the (self-)interaction of mucin filaments in Chapter 9.

7.2.6. Discussion of the numerical approximation quality

At the end of this Section 7.2 considering electrostatic adhesion, the important numerical aspects of spatial discretization as well as numerical integration error shall be briefly analyzed. Generally, peeling simulations are known to be extremely sensitive to non-smoothness and coarseness of the spatial discretization and considerable effort has been made in the past to tackle this issue by surface enrichment strategies for 2D solid elements [136, 139]. As outlined in Section 3.1, here, third-order Hermite interpolation of the beam centerline has been used, which directly ensures C^1-continuity and needs no smoothing in the first place. This carries over to a smooth representation of the inter-axis separation and hence the interaction force field. In turn, relatively coarse meshes can be applied, which are limited with respect to the inherent spatial approximation error rather than non-smoothness at the element boundaries. Figure 7.6 shows the results of the mesh refinement study. For each of the values for Young's modulus used above, three different levels of mesh refinement are shown. One of them obviously is too coarse and leads to artificial oscillations in the force values as typically observed in this case. For the second and third discretization, the difference in results is already very small such that the second refinement level can arguably be regarded as a fine enough discretization for the purposes of this study. To rule out the error from numerical quadrature as the decisive factor for the oscillations, each of the three simulations has been repeated with the coarsest mesh and twice the number of Gauss points per element from $n_{GP,tot,ele-length} = 20$ to 40, which did not eliminate the oscillations. From these results, it also becomes obvious that more elements are needed for smaller values of the Young's

---

[5] Although using the precise sequence of amino acids of the mucin macromolecule would lead to a much more complex line charge distribution than the homogeneous charge density considered in this study, the corresponding line charge densities are known to lie in the range of $\lambda = 2\pi R\sigma \in [1e/1.2nm, 1e/10nm]$. Bearing in mind the neglect of charge screening effects (as typically observed in electrolyte solutions under physiological conditions), the parameters of the current computational model should be interpreted as *effective* charge densities and the values for the real charge densities obtained from analysis of the sequence of amino acids would need to be decreased to account for this modeling assumption.
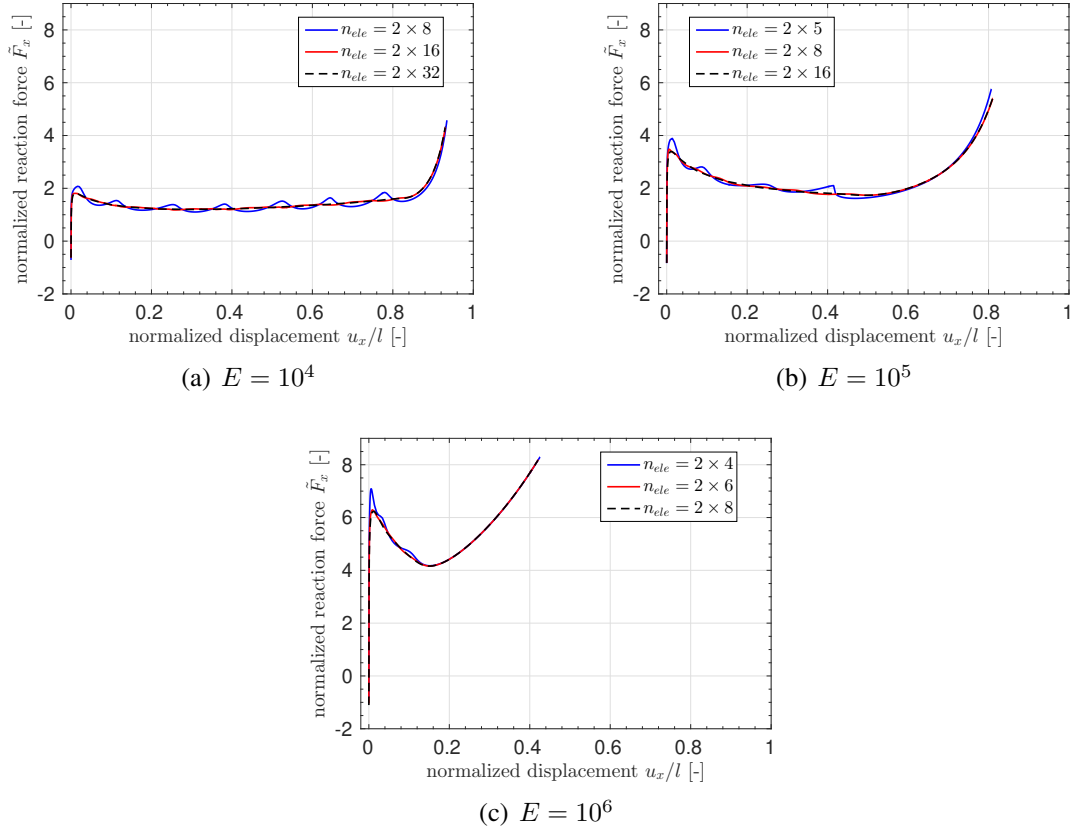
(a) $E = 10^4$

(b) $E = 10^5$

(c) $E = 10^6$

Figure 7.6.: Effect of mesh refinement depending on Young's modulus E. Too coarse discretizations lead to artificial oscillations in the force-displacement curves. Two integration segments per element with ten Gauss points each, i.e., $n_{\text{GP,tot,ele-length}} = 20$ are used in all simulations. However, doubling $n_{\text{GP,tot,ele-length}}$ did not eliminate the oscillations for each of the three coarsest discretizations, such that the error from numerical quadrature is ruled out as the decisive factor. Here, the same normalization for the force values as in Figure 7.4(a) is used. Figure taken from the author's article [60].

modulus, i.e., more flexible fibers. This can be explained by the degree of fiber deformation as visible e.g. from Figure 7.5(b). In order to limit the spatial discretization error to a minimum and ensure comparability of results, 32 elements per fiber were used for all simulations in Figure 7.4. We can thus conclude that the smooth, cubic centerline representation used in combination with the SSIP approach throughout this study allows for robust and accurate peeling simulations even with relatively coarse meshes.

7.3. Van der Waals attraction modeled by the SSIP approach

The aim of this section is to repeat the peeling experiment of Section 7.2 with a fundamentally different type of attractive forces, namely vdW forces. This allows us to analyze the differences and similarities in the force response of the system and also to discuss the differences in the numerical methods used to model the two phenomena. Furthermore, this section will start with the application of the SSIP approach and simple reduced interaction law neglecting mutual orientations of the cross-sections before Section 7.4 will repeat the numerical peeling experiment using the SBIP approach and the more sophisticated SBIP law including orientation information. This again allows for a clear analysis of the differences of the two computational approaches on the global level of this two fiber system.

7.3.1. Setup and parameters

As mentioned above, the setup of this numerical experiment shown in Figure 7.7(a) is almost identical to the one discussed in the preceding Section 7.2. The most important difference is

(a)
Problem setup: undeformed configuration.

(b) Quasi-static force-displacement curve. Force values to be interpreted as multiple of a reference point load that causes a deflection of $l/4$ if applied at the fiber midpoint.
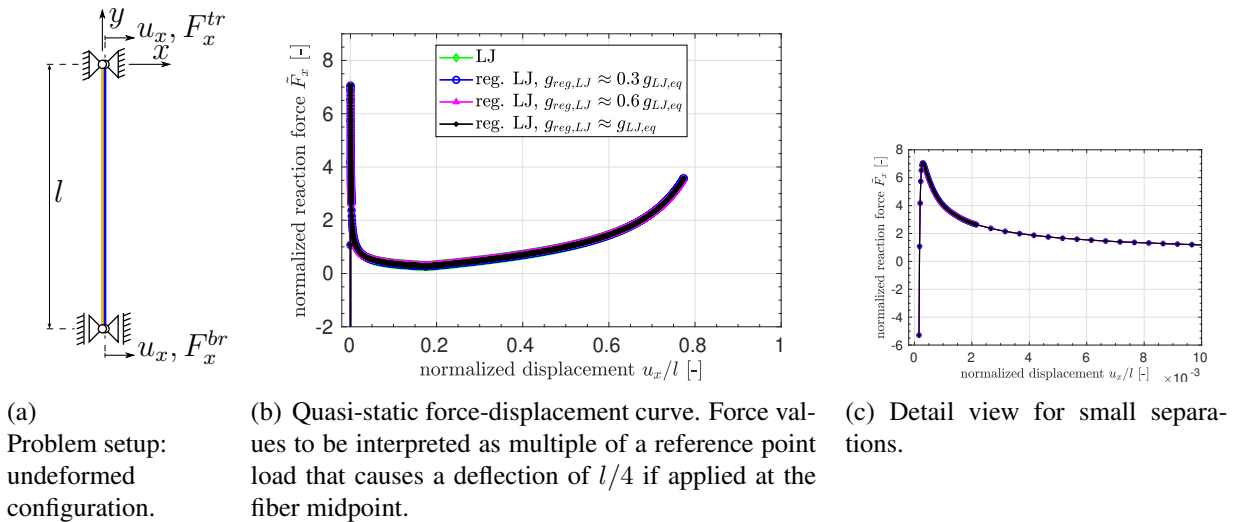
(c) Detail view for small separations.

Figure 7.7.: Numerical peeling experiment with two adhesive elastic fibers interacting via the LJ potential. Figure taken from the author's article [60].

the fact that the fibers interact via a LJ potential instead of the electrostatic one. Specifically, the LJ interaction is evaluated using the SSIP approach proposed in Section 4.2 and applying the simple SSIP law presented in Section 4.3.2 with exponent 6 for the attractive vdW and exponent 12 for the repulsive part. The parameter values of the LJ point pair potential law are chosen exemplarily as $k_{\text{vdW}} = -10^{-7}$ and $k_{\text{repLJ}} = 5 \times 10^{-25}$ such that the resulting reaction forces are of the same order of magnitude as for the electrostatic adhesion. Obviously, this is an arbitrary choice and the comparison of force-displacement curves between electrostatic and

LJ interaction, later on, will only be a qualitative one. The particle densities are assumed to be constant and set to $\rho_{1/2} = 1.0$. Due to the rapid decay of both the adhesive vdW and even more the repulsive part of the LJ potential, the interaction has an extremely short range and it is essential to ensure a fine resolution of these small length scales. Thus, a large number of 64 elements per fiber and five integration segments with ten Gauss points each is used for the discretization and numerical integration of the contributions from LJ interaction and it has been verified that a further refinement does not change the results perceptibly. To reduce the computational cost, the very short range of the interactions has been exploited by using a cut-off radius $r_c = 0.1 = 5R$ which again did not change the results perceptibly. See Section 7.2.1 for all geometric and material parameter values. Specifically, the original value $E = 10^5$ for the Young's modulus is used again, which has been varied in the parameter study at the end of the preceding section. The one, yet important difference in the geometric setup of the problem is the initial separation of the fibers in the first step of the simulation that turns out to be crucial in order to be close enough to a static equilibrium configuration such that the nonlinear solver converges. For this reason, an analytical solution for the equilibrium separation $g_{\text{LJ,eq,cyl}\|\text{cyl}}$ of two parallel, infinitely long cylinders interacting via the LJ potential has been derived in Appendix A.2.2 (cf. Equation (A.35)) and is repeated here for the reader's convenience:

$$g_{\text{LJ,eq,cyl}\|\text{cyl}} = \left(-5\,\tilde{k}_{\text{cyl,12}}/\tilde{k}_{\text{cyl,6}}\right)^{\frac{1}{6}} \approx 0.571\,69\,r_{\text{LJ,eq}} \tag{7.1}$$

Here, $r_{\text{LJ,eq}}$ denotes the equilibrium spacing of a point pair interacting via the LJ potential, which is related to the alternative set of parameters used in this work according to $r_{\text{LJ,eq}} = \left(-2\,k_{\text{repLJ}}/k_{\text{vdW}}\right)^{1/6}$ and $\tilde{k}_{\text{cyl,6}}$ and $\tilde{k}_{\text{cyl,12}}$ are used as abbreviations for the constant prefactors of the cylinder-cylinder LJ interaction potential law. Refer to Appendix A for the required derivation of the cylinder-cylinder LJ interaction potential as well as force law starting from the point-point LJ potential law. For the parameters listed above, we obtain $g_{\text{LJ,eq,cyl}\|\text{cyl}} \approx 4.2 \times 10^{-2} \cdot R \approx 1.7 \times 10^{-4} \cdot l$. In order to include also the repulsive regime, a slightly smaller initial separation, i.e., displacement $u_x/l = 1.6 \times 10^{-4}$ is chosen here. Note, however, that in contrast to infinitely long cylinders considered in the theory of Equation (7.1), the force-free equilibrium configuration for this pair of deformable fibers with finite length l is not straightforward to find. In particular, it is not the trivial case of two straight fibers at a constant surface-to-surface spacing g along their length.

7.3.2. Results and discussion

Figure 7.7(b) finally shows the resulting force-displacement curve. In addition, the most interesting range of very small displacement values $u_x/l < 10^{-2}$ is magnified and shown in a separate plot in Figure 7.7(c). Let us first leave the different variants of numerical regularization aside, since all of them yield identical results and will be discussed later. As suggested by the analytical solution for the equilibrium spacing of infinitely long, parallel cylinders, the first data point with the slightly smaller initial separation lies in the repulsive regime with $\tilde{F}_x < 0$, whereas all subsequent data points yield positive, i.e., tensile reaction forces. The qualitative comparison with the electrostatic attraction shown in Figure 7.8 reveals a substantial difference in the system response, most obvious in terms of the much sharper and also higher force peak during the

initiation of the peeling process. Interestingly, after quickly dropping to a much smaller value, the adhesive vdW force effectively keeps the fibers in contact up to a comparable separation of the fibers' endpoints as in the electrostatic case (see again Figure 7.2(g) for a visualization of the corresponding system state).
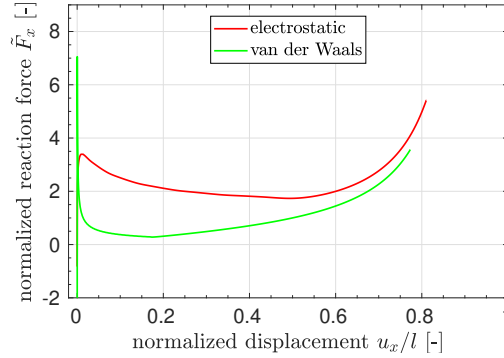

Figure 7.8.: Comparison of the quasi-static force-displacement curves obtained for electrostatic and vdW attraction. Force values to be interpreted as multiple of a reference point load that causes a deflection of $l/4$ if applied at the fiber midpoint. Figure taken from the author's article [60].

At this point, recall the known limitation of the applied simple SSIP law for vdW adhesion in terms of accuracy that has been revealed in Section 4.5.1. To ensure that the model error does not alter the qualitative results nor the following conclusions, we have repeated the simulations employing the SBIP approach proposed in Section 5.1 together with the derived SBIP law from Section 5.2.1 (cf. Equation (5.32)). This alternative modeling approach has been shown to achieve the correct asymptotic scaling behavior and thus significantly enhanced accuracy (cf. Section 5.2.2). The results of applying the SBIP approach will be presented in the following Section 7.4 and confirm that the strength of adhesion resulting from the given value of k_{vdW} is overestimated here (which is expected also from the analysis in Section 4.5.1), leading to a higher force peak and larger pull-off displacement. However, the characteristic shape of the force-displacement curve and thus all the following conclusions remain valid. These insights are important to decide about potential future applications of the most simple (SSIP) laws neglecting the mutual orientation and thus accepting the loss in accuracy.

In fact, it can be shown that the prefactor k_{vdW} of the simple SSIP law can be calibrated in a manner such that the resulting overall force-displacement curve is in excellent agreement with the corresponding force-displacement curve resulting from the enhanced computational model using the SBIP law (5.32). Note also that the applied set of parameter values k_{vdW}, k_{repLJ} for the LJ interaction is chosen based on the heuristic criterion that the resulting reaction forces are of the same order of magnitude as in the case of electrostatic adhesion considered in Section 7.2, such that this comparison between both cases naturally is a qualitative rather than quantitative one. In the specific context of this section – and bearing the limitations in mind – the approach using the simple SSIP law from Section 4.3.2 may still be a valuable computational model. Nevertheless, the resulting quantitative inaccuracy on the system level will be critically analyzed

in Section 7.4.5 to show the differences between the simple SSIP law and the more sophisticated SBIP law.

Following up on the analyses of the previous sections, we can conclude that the characteristic shape of the force-displacement curve in the initiation and peeling phases is obtained here as well, although the force peak is higher, sharper and shifted to smaller displacement values, which is most likely a result of the shorter range of adhesive forces. Once again, also the pronounced pull-off phase is observed (despite the shorter range of interaction), which supports the argument that it can be attributed to the symmetric two-sided peeling from both fiber endpoints. As a final and most important result, however, it has to be pointed out that the maximum force value in the entire separation process occurs during initiation of the peeling in the case of vdW adhesion considered here, whereas it occurs in the final pull-off phase ultimately before snapping free in the case of electrostatic attraction studied in Section 7.2. This noteworthy finding can again be explained by the fundamental difference between the short and long range of these interaction types.

7.3.3. Discussion of the numerical regularization of the Lennard-Jones interaction law

A suitable regularization strategy to remedy the inherent singularity of the LJ SSIP law has been proposed in Section 4.4.3. The concrete numerical example of this section allows us to study and quantify its significant positive impact on the performance of the nonlinear solver and in this way complement the theoretical considerations made in Section 4.4.3. The LJ potential applied here shows both very high gradients in the force-distance law as well as the singularity in the SSIP law for zero separation $g = 0$ and is thus the more challenging case with respect to the nonlinear solver as compared to electrostatic interaction. In order to find a solution of the non-linear system of equations in every load step, we apply Newton's method in combination with a displacement increment control as outlined in Section F.2. Using a very strict upper bound for the displacement increment per iteration of $|\Delta u|_{\max} = R/20$ allowed to compute the solution for the LJ interaction without any modification of the SSIP laws stated in Section 4.3.2 and 4.3.2 for the vdW and repulsive part, respectively. This effectively avoids the singularity in any uncon-verged state, however comes at the tremendous computational cost of an average of 46.2 required Newton iterations in each of the approximately 1600 steps required to compute the entire force-displacement curve shown in Figure 7.7(b) (green line with diamonds). These numbers underline the urgent need for the regularization of the LJ law in the limit of zero separation $g \to 0$ as pro-posed in Section 4.4.3 for the SSIP law and previously applied in the context of solid bodies in [136]. Applying the proposed linear extrapolation of the section-section interaction force law below a certain separation $g_{\mathrm{reg,LJ}}$ indeed considerably improves the performance of the nonlinear solver. The average number of Newton iterations per step decreases to 10.2, which is almost a factor of five, while the results shown in Figure 7.7(b) (blue, pink, and black line) coincide with the full LJ solution (green line) down to machine precision. This remarkable reduction of computational cost while obtaining identical results is exactly the same for all three values of the regularization parameter $g_{\mathrm{reg,LJ}} = \{0.3, 0.6, 1.0\} \times g_{\mathrm{LJ,eq,cyl\|cyl}}$ that we applied. As outlined in the theoretical considerations of Section 4.4.3, this is reasonable and expected, because we choose

a regularization parameter $g_{\mathrm{reg,LJ}} \leq g_{\mathrm{LJ,eq,cyl\|cyl}}$ that is smaller than (or equal to) any separation value g occurring anywhere in the system in any converged state. Thus, the solution never "sees" the modification of the LJ force law in the interval $g < g_{\mathrm{reg,LJ}}$ and the results are identical. If, on the contrary, the regularization parameter is chosen as $g_{\mathrm{reg,LJ}} = 1.2 \times g_{\mathrm{LJ,eq,cyl\|cyl}} > g_{\mathrm{LJ,eq,cyl\|cyl}}$, we observed that the nonlinear solver failed to converge at $u_x/l \approx 0.17$ and the obtained force values in the range $u_x/l \lesssim 0.17$ deviate from those for the unmodified LJ SSIP law. This underlines the importance of the correct choice of the regularization parameter and the knowledge of the theoretical equilibrium spacing $g_{\mathrm{LJ,eq,cyl\|cyl}}$ stated in Equation (7.1).

7.4. Van der Waals attraction modeled by the SBIP approach

As mentioned above, the numerical peeling experiment of the preceding section is revisited here to compare the results and computational cost of the SSIP and the SBIP approach in a minimal example of adhesive contact between fibers. The unmodified problem setup consisting of two parallel, straight fibers interacting via a LJ potential is shown in Figure 7.7(a). The idea is to study the entire process of separating these adhesive fibers starting from contact along the entire length up to the point where they would suddenly snap free. Therefore, a displacement u_x in x-direction is prescribed at both ends of the right fiber and the sum of the reaction forces $F_x := F_x^{\mathrm{tr}} + F_x^{\mathrm{br}}$ in this direction is measured in order to obtain the characteristic, quasi-static force-displacement curve.

7.4.1. Setup and parameters

At this point, only the differences in the setup will be presented. Refer to Section 7.2 and Section 7.3.1 for a complete presentation of the setup, numerical methods and parameter values. Most importantly, the LJ interaction between the fibers is modeled by means of the novel SBIP approach from Section 5.1 in combination with the proposed disk-cylinder interaction potential law $\tilde{\pi}_{\mathrm{m,disk\text{-}cyl}}$ from Equation (5.32), which is used for both the attractive $m = 6$ as well as the repulsive $m = 12$ part of the LJ interaction. The two prefactors k_6 and k_{12} specifying the LJ point-pair potential law will be varied to study their influence on the system response. Instead of using these prefactors, however, it seems more meaningful and intuitive in this context to use an equivalent set of parameters, which describe the equilibrium spacing $g_{\mathrm{LJ,eq,cyl\|cyl}}$ and the minimal (i.e. maximal adhesive) force per unit length $\tilde{f}_{\mathrm{min,LJ,cyl\|cyl}}$ of straight, parallel fibers. According to the theoretical work for the scenario of infinitely long and parallel rigid cylinders presented in Appendix A.2.2, these two alternative sets of two LJ parameters are bi-uniquely related[6] as follows:

$$g_{\mathrm{LJ,eq,cyl\|cyl}} \approx 1.1434 \, (-k_{12}/k_6)^{\frac{1}{6}} \tag{7.2}$$

$$\tilde{f}_{\mathrm{min,LJ,cyl\|cyl}} \approx 0.7927 \, \rho_1 \rho_2 \sqrt{\frac{2R_1 R_2}{R_1 + R_2}} \, k_6 \, (-k_6/k_{12})^{\frac{5}{12}} \tag{7.3}$$

---

[6] taking into account the atom densities ρ_i and radii R_i of the fibers $i = 1, 2$

Again refer to Appendix A.2.2 for the rather lengthy exact expressions of the scalar prefactors that are given here in their approximate floating point representation. For the sake of brevity, the subscript "cyl∥cyl" will be omitted in the remainder of this section, however, keep in mind that these quantities describe the academic case of infinitely long and parallel, rigid cylinders. Since the meaning of these two parameters is much more intuitive in the context of fiber adhesion, it can now be argued that the equilibrium surface spacing $g_{\mathrm{LJ,eq}}$ is a fundamental property of the type of physical interaction (and maybe also the material combination of both fibers and surrounding media) and it can thus be kept fixed for now with an exemplarily chosen value of $g_{\mathrm{LJ,eq}} = 10^{-3} = 0.05 \cdot R = 2 \times 10^{-4} \cdot l$, which corresponds to five percent of the fiber radius. The minimal LJ force per unit length $\tilde{f}_{\mathrm{min,LJ}}$ on the other hand is a viable measure for the strength of adhesion and will be varied to study this important influence on the system behavior. Unless otherwise stated, two integration segments with ten Gauss points each are used for numerical integration of the LJ contributions in each of the 64 beam elements per fiber. It has been verified by means of refinement studies that the influence of the spatial discretization error and numerical integration error is negligible for all results to be presented in the following. The regularization strategy proposed in Section 5.4.1 has been applied with a regularization separation $g_{\mathrm{ul,reg}} = 8 \times 10^{-4} = 0.04 \cdot R$, which is smaller than the equilibrium spacing $g_{\mathrm{LJ,eq}}$ given above and thus – as has been argued in Section 5.4.1 – led to identical results as compared to the non-regularized interaction law, yet ensures robustness and a significant reduction of the number of required nonlinear iterations by a factor of approximately 4.5. In order to further reduce the computational cost, the very short range of the LJ interaction has been exploited by applying a cut-off radius of $r_c = 0.1 = 5R$, which again had no influence on the results. As mentioned above, all other parameters including the geometrical and material properties of the fibers remain unchanged as compared to the preceding sections.
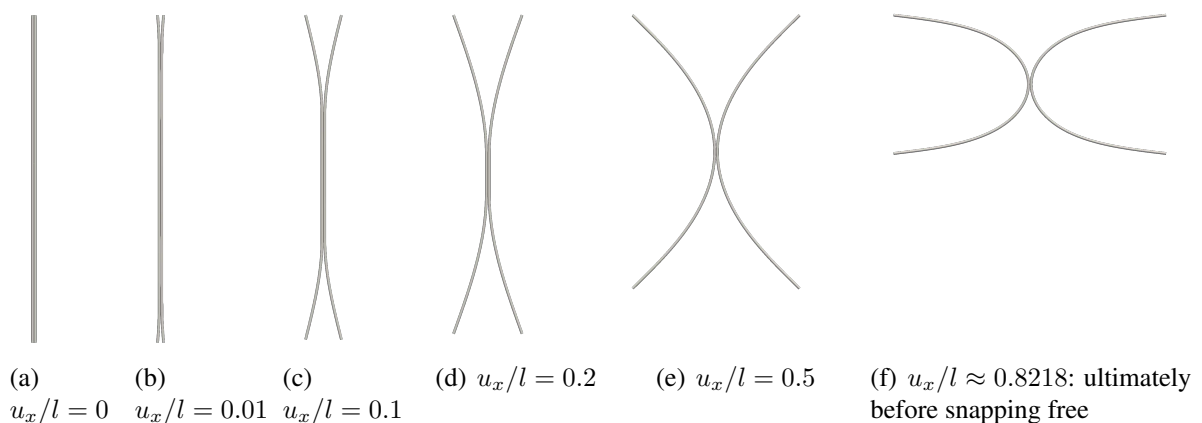
7.4.2. Resulting qualitative system behavior

(a)
$u_x/l = 0$

(b)
$u_x/l = 0.01$

(c)
$u_x/l = 0.1$

(d) $u_x/l = 0.2$

(e) $u_x/l = 0.5$

(f) $u_x/l \approx 0.8218$: ultimately before snapping free

Figure 7.9.: Characteristic equilibrium configurations obtained for the case $\tilde{f}_{\mathrm{min,LJ}} = -1$.

Let us first look at the case of $\tilde{f}_{\mathrm{min,LJ}} = -1$, which is the strongest attractive strength considered in this numerical experiment. The resulting equilibrium configurations for exemplarily

chosen displacement values u_x are shown in Figure 7.9. Note that the configurations are symmetric with respect to both a vertical and a horizontal middle axis, which also implies for the individual reaction force components on the left/right ("l"/"r") side and top/bottom ("t"/"b") that $F_x^{\text{tl}} = F_x^{\text{bl}} = F_x^{\text{tr}} = F_x^{\text{br}}$ and $F_y \equiv 0$, as expected from the symmetric setup of the experiment and already observed in Section 7.2.2. The corresponding force-displacement curve is shown in Figure 7.10(a) (blue line) and a magnified view of the small displacement value range is provided in Figure 7.10(b). Overall, the shape of the curve is very similar to the one
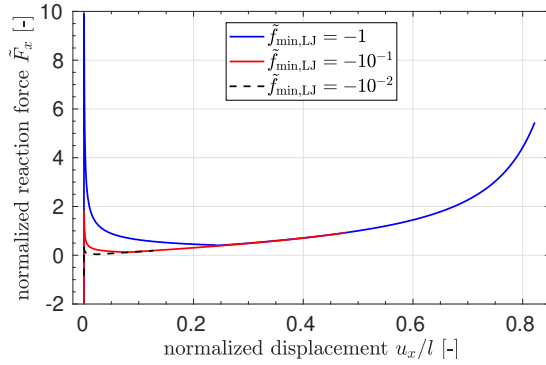
(a) Quasi-static force-displacement curve. Force values to be interpreted as multiple of a reference point load that causes a deflection of $l/4$ if applied at the fiber midpoint.
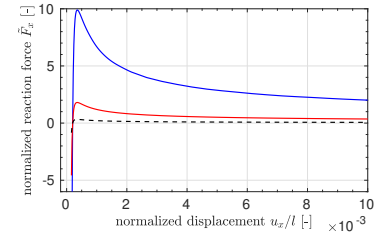
(b) Detail view for small displacement values.

Figure 7.10.: Numerical peeling experiment with two adhesive elastic fibers interacting via the LJ potential.

obtained using the previous SSIP approach in Section 7.3.2 and also the three characteristic phases of *initiation of fiber deformation*, *peeling*, and *pull-off* as obtained and analyzed for the case of electrostatic attraction in Section 7.2.3 are recognizable here. Moreover, the sharp force maximum for a very small displacement value in the initiation phase is confirmed by this study using the novel SBIP approach and more accurate disk-cylinder interaction law $\tilde{\pi}_{\text{m,disk-cyl}}$. It can thus be concluded that the known limitation regarding the accuracy of the previously applied, simple SSIP law $\tilde{\tilde{\pi}}$ from Section 4.3.2 does not affect the qualitative analysis and conclusions drawn in the previous Section 7.2. A detailed comparison, including a quantitative analysis of the differences in the global system response for the identical set of parameter values will follow in a dedicated section below. Following up on the qualitative results, note that the very short range of the LJ interactions leads to the fact that fibers interact almost exclusively if or where they are in contact and that there is no perceptible far range effect as observed and measured in form of a second branch ("separated fibers") in the force-displacement plot, e.g., for the case of electrostatic attraction in Figure 7.1(b). This observation is also in agreement with the common notion that short-ranged interactions such as vdW adhesion only have an influence on the state of being/remaining in contact, and not the process of coming into contact from an initially separated state. A quantitative analysis of the results will be given in the following section discussing the influence of the strength of adhesion, however, two brief aspects are stated here as an immediate verification of the results. First, the specified parameter value for the equilibrium gap

of infinitely long and parallel, rigid cylinders $g_{\text{LJ,eq}} = 10^{-3}$ is indeed recovered as a simulation result in the middle parts of the fibers wherever they are approximately parallel. And second, as can be seen from the visualization of the resulting LJ force distributions in Figure 7.11, the maximum magnitude of the observed interaction forces per unit length agrees very well with the specified parameter value $\tilde{f}_{\text{min,LJ}} = -1$.

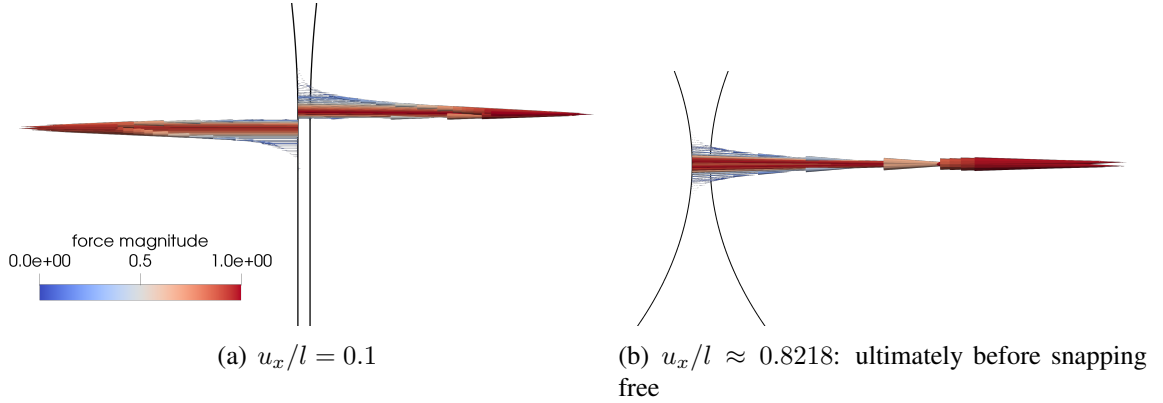(a) $u_x/l = 0.1$ (b) $u_x/l \approx 0.8218$: ultimately before snapping free

Figure 7.11.: Detail study of the resulting line force distributions for two displacement values obtained for the case $\tilde{f}_{\text{min,LJ}} = -1$. For clarity, the fibers are depicted as their centerlines and forces are shown for the left fiber only. Note that both pictures show details of the entire system and are not to scale.

7.4.3. Influence of the strength of adhesion

A more general, theoretical study of parameter influences in systems of adhesive fibers by means of nondimensionalization of the governing partial differential equations is provided in Appendix B. Here, it is complemented by a numerical study considering the influence of the adhesive strength for this fundamental two-fiber peeling and pull-off example. Thus, keeping all other parameters unchanged, the minimal LJ force per unit length of infinitely long and parallel cylinders $\tilde{f}_{\text{min,LJ}}$ is varied over two orders of magnitude such that both limits of "strong adhesion/low fiber stiffness" and "weak adhesion/high fiber stiffness" can be observed. The resulting force-displacement curves for $\tilde{f}_{\text{min,LJ}} = \{-1, -0.1, -0.01\}$ (blue solid line, red solid line, black dashed line) are shown in Figure 7.10(a) and 7.10(b) and the corresponding final equilibrium configurations ultimately before snapping free are displayed in Figure 7.12. As expected, an increase of the adhesive strength generally leads to increased reaction force values and higher displacement values before the fibers would finally snap free. Specifically, we obtain normalized force peak values of $\tilde{F}_{x,\text{max}} \approx 0.32$ at $u_x/l \approx 3.4 \times 10^{-4}$ for $\tilde{f}_{\text{min,LJ}} = -0.01$, $\tilde{F}_{x,\text{max}} \approx 1.8$ at $u_x/l \approx 3.6 \times 10^{-4}$ for $\tilde{f}_{\text{min,LJ}} = -0.1$, and $\tilde{F}_{x,\text{max}} \approx 9.9$ at $u_x/l \approx 3.6 \times 10^{-4}$ for $\tilde{f}_{\text{min,LJ}} = -1$. The peak force values thus increase by a factor of approximately 5.6 and 31 if the minimal LJ force per unit length is increased by a factor 10 and 100, respectively. However, the location of the force peak is not influenced by the varying adhesive strength, which meets our expectations from keeping the equilibrium surface separation $g_{\text{LJ,eq}}$ fixed. Finally, the maximum normalized displacement values $u_{x,\text{max}}/l$ before the fibers would snap free are observed to be
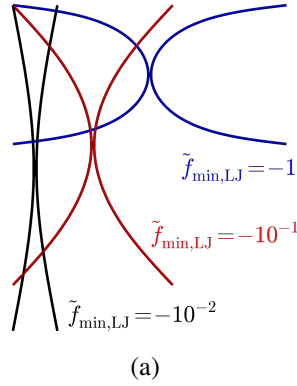
(a)

Figure 7.12.: Comparison of the final configurations before snapping free for different values of the minimal LJ force per unit length $\tilde{f}_{\mathrm{min,LJ}}$.

approximately 0.13, 0.48, and 0.82 for $\tilde{f}_{\mathrm{min,LJ}} = \{-0.01, -0.1, -1\}$, respectively. Note however that these maximum displacement values are the result of a quasi-static analysis and that the exact point of snapping free will depend on the dynamics of the system. A final interesting observation based on the force-displacement curves in Figure 7.10(a) is that both pairs of curves for $\tilde{f}_{\mathrm{min,LJ}} = \{-0.01, -0.1\}$ and $\tilde{f}_{\mathrm{min,LJ}} = \{-0.1, -1\}$ approximately correspond to each other in a certain, limited displacement range $u_x/l \approx [0.08, 0.13]$ and $u_x/l \approx [0.25, 0.48]$, respectively, before the system with weaker adhesive strength would snap free.

7.4.4. Influence of the choice of master and slave

Following up on the discussion of how to assign the roles of master and slave in Section 5.1, this numerical example is used to study the influence of this choice and thus bias in the SBIP approach. For this sake, all three cases shown in Figure 7.10(a) have been repeated with switched roles of master and slave and the resulting differences in the reaction force-displacement curves have been evaluated. The maximal relative differences along the entire curve are approximately $\{4 \times 10^{-6}, 5 \times 10^{-6}, 3 \times 10^{-5}\}$ for $\tilde{f}_{\mathrm{min,LJ}} = \{-0.01, -0.1, -1\}$, respectively, and thus are of the same order of or even smaller than the spatial discretization error that has been verified by doubling the number of elements. These results meet our expectations, since the entire problem is symmetric and the resulting bias should thus be negligible. To quantify the model error associated with replacing the master beam by a surrogate cylinder, the setup of the example is now slightly modified by constraining the left fiber's deformation to zero and thus preserving the initial straight cylinder shape. Using the left fiber as the master beam will thus eliminate the corresponding model error and serves as a reference solution for the subsequent simulation run with switched roles of master and slave. This results in maximal relative differences of approximately $\{0.13\%, 0.43\%, 1.42\%\}$ for $\tilde{f}_{\mathrm{min,LJ}} = \{-0.01, -0.1, -1\}$, once again measured along the entire force-displacement curve. Given the considerable magnitude of curvature for the highest adhesion force value, which is even slightly more than in the original example visualized in Figure 7.12, this is considered to be a reasonably small error level, which will presumably be negligible in most practical applications of the novel SBIP approach.

7.4.5. Comparison of SSIP and SBIP approach and corresponding reduced interaction laws

At this point, recall from the prior analysis of the model accuracy using the example of two cylinders in Section 5.2.2 that the previously used simple SSIP law $\tilde{\tilde{\pi}}_{\mathrm{m,disk\|disk}}$ from Section 4.3.2 overestimates both the total interaction potential and force in the decisive regime of small separations and that the novel SBIP law $\tilde{\pi}_{\mathrm{m,disk\text{-}cyl}}$ from (5.32) on the contrary ensures the correct scaling behavior and is thus significantly more accurate. The influence of this model error on the global system behavior shall be briefly investigated by means of the numerical peeling and pull-off experiment considered in this section. Figure 7.13 shows the corresponding force-displacement curves for the original set of LJ parameters $k_6 = -10^{-7}$, $k_{12} = 5 \times 10^{-25}$ from Section 7.3, using either the SSIP law $\tilde{\pi}_{\mathrm{m,disk\text{-}cyl}}$ from Section 4.3.2 (red solid line) or the proposed SBIP law $\tilde{\pi}_{\mathrm{m,disk\text{-}cyl}}$ from (5.32) (blue solid line). The results confirm the assessment summarized above
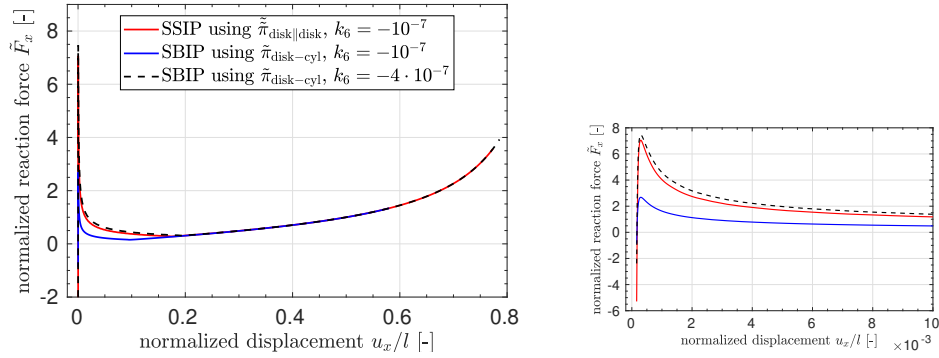
(a) Quasi-static force-displacement curve. Force values to be interpreted as multiple of a reference point load that causes a deflection of $l/4$ if applied at the fiber midpoint.

(b) Detail view for small separations.

Figure 7.13.: Comparison of the results obtained in Section 7.3 via the SSIP law $\tilde{\tilde{\pi}}_{\mathrm{m,disk\|disk}}$ from Section 4.3.2 with the results for the SBIP law $\tilde{\pi}_{\mathrm{m,disk\text{-}cyl}}$ from (5.32) and corresponding approach from Section 5.1.

because the peak force value $\tilde{F}_{x,\mathrm{max}}$ is overestimated by a factor of approximately 2.6 and the maximum displacement value before snapping free $u_{x,\mathrm{max}}/l$ is overestimated by a factor of approximately 1.3 if using the simple SSIP law from Section 4.3.2. On the other hand, the location of the force peak at $u_x/l \approx 3.0 \times 10^{-4}$, which is determined by the ratio of adhesive and repulsive contributions, is identical for both approaches. Most importantly, however, is that the qualitative shape of the force-displacement curve is very similar for both approaches and indeed almost the identical force-displacement curve can be obtained from the consistent SBIP law $\tilde{\pi}_{\mathrm{m,disk\text{-}cyl}}$ if a different parameter value set $k_6 = -4 \times 10^{-7}$, $k_{12} = 2 \times 10^{-24}$ is used (black dashed line). This confirms the argument given in Section 7.3.2 that the simple SSIP law $\tilde{\tilde{\pi}}_{\mathrm{m,disk\|disk}}$ can be calibrated to compensate for the overestimation of the interaction potential in the small yet decisive range of separations around the equilibrium separation of the LJ potential. In this manner, the simple SSIP law $\tilde{\tilde{\pi}}_{\mathrm{m,disk\|disk}}$ from Section 4.3.2 yields results, which excellently agree with the

consistent SBIP law on the system level, e.g., the reaction force-displacement curve studied in this numerical example.

After the accuracy, let us now briefly compare the efficiency of both approaches, which has been discussed on the theoretical level of algorithmic complexity in Section 5.4.3, by looking at the computational cost for one simulation run of the numerical example considered here. Keeping in mind the general limitations of such a simple performance comparison and especially the unoptimized implementation of both approaches, we found that the SBIP approach is approximately a factor of 3.8 faster than the SSIP approach.[7] The advantage of the SBIP approach that less integration points will be required for the same level of numerical integration error due to the smaller exponent of the reduced interaction law as argued in Section 5.4.3 has not been exploited in this comparison to isolate the net effect of the decreased algorithmic complexity of the approaches on the one hand and increased complexity of the reduced interaction law on the other hand. It is thus confirmed by this numerical experiment that the novel SBIP approach in combination with the proposed disk-cylinder interaction law $\tilde{\pi}_{\mathrm{m,disk\text{-}cyl}}$ is significantly more efficient than the previous SSIP approach from Chapter 4 for the case of short-ranged interactions.

7.5. Conclusions and outlook

This chapter studies the fundamental problem of separating two adhesive elastic fibers based on numerical simulation employing the novel beam-beam interaction formulations developed in Chapter 4 and 5. Specifically, it covers the peeling and pull-off process starting from fibers contacting along its entire length to fully separated fibers (and also the reverse order) including all intermediate configurations and the well-known physical instability of snapping into contact and snapping free. In order to study the key influences, the strength of adhesion relative to the Young's modulus of the fibers has been varied over a broad range of values spanning two orders of magnitude, and also two different types of attractive forces resulting either from van der Waals (vdW) interactions or the electrostatic interaction of oppositely charged non-conducting fibers are considered. The analysis of the resulting force-displacement curve reveals a rich, highly nonlinear system behavior and the underlying physical mechanisms arising from the interplay of adhesion, mechanical contact interaction and structural resistance against (axial, shear and bending) deformation have been thoroughly investigated. Based on the differences in these fundamental mechanisms, the three distinct phases of a) initiation of fiber deformation and peeling, b) the actual peeling, and c) a final pull-off phase have been identified. The initiation phase is characterized by a steep initial increase towards a sharp force peak and followed by the peeling phase with gradually decreasing force values eventually approaching a plateau-like regime of almost constant peeling force. The unitary nature of these first two phases in the peeling of adhesive elastic structures is confirmed by the comparison with previous studies and across all considered variants in this study. On the contrary, the presence of the pull-off stage as a third distinct phase of the separation process, that is characterized by a significant increase of the force

---

[7] Average computation time per nonlinear iteration for each of the approximately 1.7×10^4 iterations of the full run of either "SSIP using $\tilde{\pi}_{\mathrm{disk\|disk}}$, $k_6 = -10^{-7}$" or "SBIP using $\tilde{\pi}_{\mathrm{disk-cyl}}$, $k_6 = -4 \cdot 10^{-7}$" from Figure 7.13. Apart from these two values identical set of parameters, identical code framework, build, system environment, number of processors including parallel distribution and hardware.

over an extended range of displacement values before finally snapping free, was not observed in the aforementioned one-sided peeling studies and can thus be attributed to the application of pulling forces at both ends of the fibers, which results in a two-sided instead of a one-sided peeling. Moreover, the practically highly relevant global maximum of the pulling force is found to occur at the end of the initiation phase in case of short-ranged vdW attraction, whereas it occurs in the final pull-off phase ultimately before snapping free in the case of the long-ranged electrostatic attraction.

The complexity of the physical effects of adhesion, contact and elasticity in the regime of large deformations – individually and particularly in combination – carries over to the computational models and numerical solution methods required for this study. In addition to the physical behavior of the system, therefore, the decisive aspects regarding robustness and accuracy of the simulations have been discussed. Here, the major challenges include the delicate task of determining equilibrium configurations in the direct vicinity of the mentioned physical instability, the control of spatial discretization and numerical integration error such that the high gradients of short-range interaction potential laws are represented with sufficient accuracy as well as the regularization of these inverse power laws to remedy the singularity at zero separation. Concretely, the regularization procedure for the employed beam-beam interaction models, which have been proposed in Section 4.4.3 and 5.4.1, have proven to significantly enhance robustness and efficiency at identical accuracy by saving a factor of five in the number of nonlinear iterations when applied to the highly challenging example of Lennard-Jones interaction. Besides the insights gained into the peeling and pull-off behavior of the specific two-fiber system, the present study thus serves as a proof of concept facilitating future applications of the employed beam-beam interaction models to increasingly complex systems of slender fibers.

Subsequent fundamental studies may include e.g. the dynamics of the peeling and pull-off process or further scenarios of loading and support of the fibers, e.g. twisting and out-of-plane bending, all of which is directly accessible by means of the computational models and methods applied in this work. In the wider context of the continued work on (the computational study of) fibrous biophysical systems on the microscale (cf. Chapters 8, 9 and 10 and e.g. [118, 119]) a multitude of specific applications come to mind. In particular, investigating the influence of adhesion on the conformation, self-assembly and mechanical behavior of biological fibrillar assemblies such as collagen (cf. Chapter 11) or muscle fibers is considered a highly relevant subject of future research.

8. Conformation of a Filament in a Static Random Potential Field

This chapter presents the computational study of a single filament's conformation in a static random potential field. The system is considered to be an abstract model for the interactions of a semiflexible filament with the surrounding biopolymer network and allows to investigate the effect of prestress in such self-assembled network structures. From a computational point of view, this scenario can be regarded a special case of the general beam-beam interaction, where one beam is replaced by an effective, static background potential field as has been discussed in Section 6.3.2. The study thus represents the first application of this numerical formulation to a relevant biophysical problem. It is a result of a collaborative research project combining the theoretical work by V. Slepukhin and A. Levine (UCLA) with the computational work by K. Müller and the author (TUM) and has previously been published in the joint article [152].

8.1. Motivation

Transiently cross-linked networks of semiflexible biopolymer filaments are well-known to include elastically deformed, e.g., curved and stretched, filaments. This can be attributed to the thermal fluctuations of the filaments and the stochastic formation of cross-links that couple certain parts of the deflected filaments to other filaments and therefore effectively trap their deformation. Due to the dynamic nature of both the formation and the continuous re-organization of these networks, the resulting structures are not necessarily in a state of mechanical equilibrium, thus leading to some excess elastic deformation also known as prestress of the network structure. This in turn influences the fundamental rheological behavior of biopolymer networks (see e.g. [18, 118]) and can thus be expected to have major implications on a number of processes and functions in the human body such as cell division and migration.

Motivated by this important role of prestress in biopolymer gels, this study aims to foster the understanding of the underlying mechanisms and decisive influences by developing and investigating a model system both in theory and simulation. As mentioned above, the abstract model consists of a single semiflexible filament immersed in a thermal bath at temperature T and interacting with a random static potential field mimicking the (binding to the) surrounding network. The spatial correlation length of the pinning potential hereby serves as a model for the mesh size of the network and will be varied to study its influence on the amount of prestress. Moreover, three different distributions of the random potential field will be considered and the influence of the persistence length of the filament will be analyzed.

8.2. Computational model and methods

The established computational framework for the Brownian dynamics of semiflexible filaments proposed in [33] and used e.g. in [118] has been extended to account for forces resulting from the random potential field. Both model components will be briefly presented in the following.

8.2.1. Brownian motion of a semiflexible filament

A single filament is modeled by nonlinear, geometrically exact, 3D Simo-Reissner beam theory and discretized in space using the finite element formulation [29, 76] (summarized in Section 3). In terms of the structural rigidity of the filament, we thus account for axial, torsional, bending, and shear deformation. To model the Brownian motion, we include viscous drag as well as thermal forces, each distributed along the entire filament length as proposed in [33]. More precisely, viscous forces and moments are computed assuming a quiescent background fluid and individual damping coefficients for translations parallel and perpendicular to the filament axis as well as rotation around the filament axis, respectively. Thermal forces are determined from the stochastic Wiener process in accordance with the fluctuation-dissipation theorem. Finally, an implicit Backward-Euler scheme is used to discretize in time and a Newton-Raphson algorithm solves the resulting nonlinear system of equations.

8.2.2. Random potential field

As discussed in Section 6.3.2, the interaction of a beam with a static background potential field can be interpreted as a special, dimensionally reduced case derivable from the more general beam-beam interaction. Alternatively, it may be seen as a Neumann boundary condition, i.e., a line load that results from the corresponding force field of the potential and thus generally depends on the current configuration of the beam. The resulting virtual work contribution is given in Equation 6.7. Specifically, the trapezoidal rule is applied in each finite element to numerically evaluate the integral along the filament. Regardless of the fact that only the planar problem is considered in this chapter, the entire simulation framework as well as Equation 6.7 is capable of modeling arbitrary filament configurations in 3D. Note that the potential exerts forces on the filament, however, as it models a surrounding network, it is assumed to be independent of the motion of the filament. This is commonly denoted as one-way coupling. In the remainder of this section, the definition and generation process of the different variants of the potential field V will be presented.

Definition of the pinning potential.
Three different probability distributions are considered in the following. The first one is defined via

$$\mathcal{P}_{\mathrm{V}}(V) = \frac{1}{P_0} \exp\left\{ -\frac{1}{2V_0^2} \int d^2x \left[(\nabla V)^2 + \xi^{-2} V^2 \right] \right\} \tag{8.1}$$

and generates an ensemble of random potentials in which the amplitude of each Fourier mode is selected as an independent Gaussian random variable from a distribution with zero mean and

a width that depends on the magnitude of the wavenumber $k = |\mathbf{k}|$. Here, V_0 is used to set the energy scale and ξ denotes the spatial correlation length.

As a second option, the correlation length ξ may be assigned on the force level instead of the potential level, which results in a probability distribution given as

$$\mathcal{P}_{\mathrm{F}}(V) \sim \exp\left[-\frac{1}{2V_0^2} \int d^2x \, \xi^2(\nabla^2 V)^2 + (\nabla V)^2\right]. \tag{8.2}$$

In the following, this distribution will thus be referred to as the force-controlled distribution whereas the one defined in Equation (8.1) is the energy-controlled distribution. The advantage of the force-controlled distribution is that the correlation length ξ can be varied without changing the level of the force magnitudes and thus allows for a systematic analysis of its influence. In contrast, the energy-controlled distribution leads to quite large forces on the filament for short correlation lengths, because the gradient of the potential is proportional to V_0/ξ.

A third variant of the pinning potential follows from the idea of an exponential suppression of the higher Fourier modes. Expressing the potential in the alternative form of the probability distribution of these Fourier components illustrates and defines this third variant to be considered in the analysis:

$$P(V_{k_x,k_y}) \propto \exp\left\{-\frac{L_x L_y}{\xi^2}\frac{V_{k_x,k_y}^2}{8V_0^2}\exp\left(\xi^2(k_x^2 + k_y^2)\right)\right\} \tag{8.3}$$

Here, the rectangular area $A = L_x \times L_y$ has been introduced. This third and last class of random potential fields turns out to be particularly suitable for the simulations since the resulting force field is much smoother as compared to the ones resulting for the energy- or force-controlled distribution. The energy- and force-controlled distributions, however, are much more suitable for analytical calculations, which is the reason why all three distributions have been included in this study. See Figure 8.1 for one random realization of each of the three distributions and Figure 8.2 for the corresponding force fields. As becomes clear from Figure 8.1(A), the energy-controlled distribution leads to a complex force landscape with very short ranged correlations, which is why the corresponding force vector field is omitted in Figure 8.2.

Finally, the generation of random realizations of these potential fields is conducted in a pre-processing step before the actual simulation runs. To be more precise, applying a random number generator and a discrete Fourier transformation yields the potential field V and a subsequent numerical differentiation via finite differences allows to compute the required force field $-\nabla V$ on a sufficiently fine grid in the entire simulation domain. In each iteration, these precomputed grid values are finally interpolated to calculate $-\nabla V$ at the current position of each node and evaluate Equation 6.7 element-wise.

8.3. Simulation setup and parameterization

The specific simulation setup consists of a single filament with initial length $L_0 = 20\mu$m and persistence length $\ell_p \approx 14\mu$m. Its initial, stress-free reference configuration is chosen straight and parallel to the global x-axis, as shown in Figure 8.3(A). By means of Dirichlet boundary conditions, the filament is constrained to the xy-plane and simply supported, i.e., free to rotate at
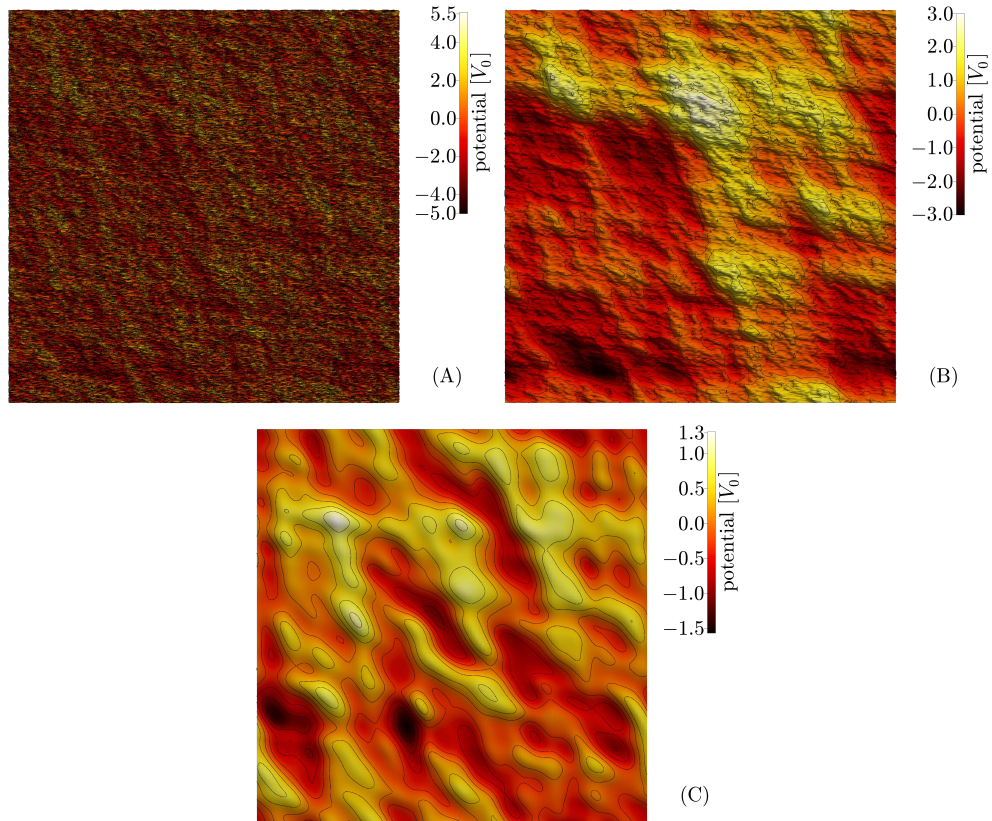
Figure 8.1.: Examples of the random potentials $V(x, y)$ (shown as a heat map with contour lines) selected from different distributions: (A) Energy-controlled distribution. (B) Force-controlled distribution. (C) Exponential suppression of high modes. The correlation length is fixed in all three so that $L_x/\xi = 20$. Figure taken from the co-authored article [152].
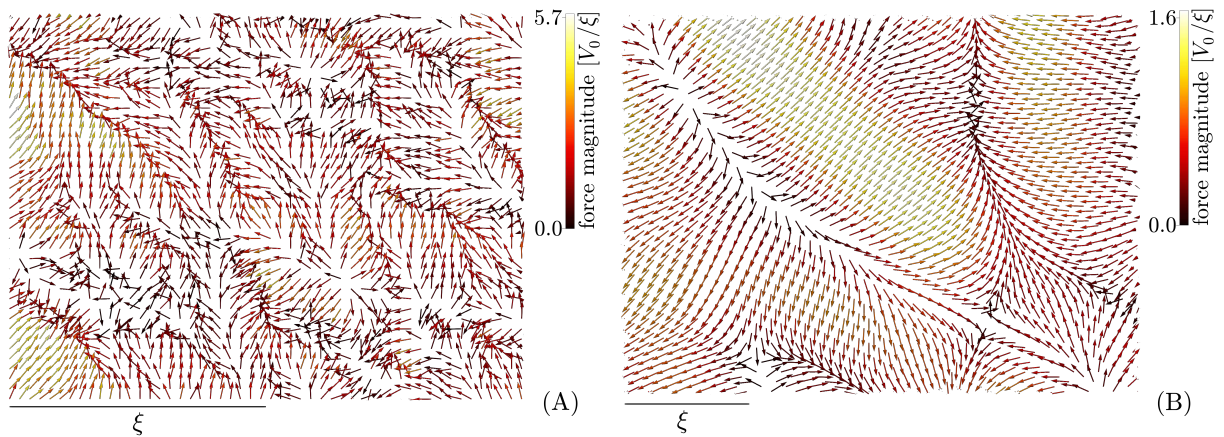

Figure 8.2.: Detail views of the force fields resulting due to the random pinning potentials shown in Fig. 8.1. (A) Force-controlled distribution. (B) Exponential suppression of high modes. Figure taken from the co-authored article [152].
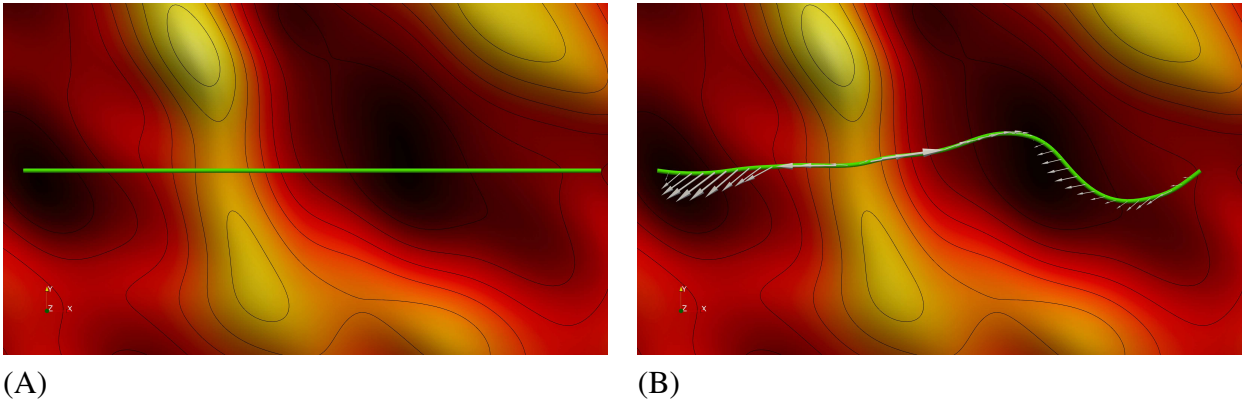
(A)   (B)

Figure 8.3.: (A) Simulation snapshot of the initial setup. An initially straight, stress-free filament is constrained to the xy-plane and simply supported at its endpoints. It interacts with a random potential $V(x, y)$ that is shown as a heat map with contour lines. (B) Simulation snapshot of a deformed configuration showing the forces on the filament resulting from the pinning potential. Figure taken from the co-authored article [152].

both ends, however only free to move in x-direction at one endpoint. Its circular cross-section is specified by the area $A = 1.9 \times 10^{-5} \mu m^2$, area moment of inertia $I = 4.3 \times 10^{-12} \mu m^4$ and polar moment of inertia $I_p = 8.6 \times 10^{-12} \mu m^4$. The material is defined by the Young's modulus $E = 1.3 \times 10^{10} pN/\mu m^2$ and the Poisson's ratio $\nu = 0.3$. Temperature is set to $T = 293K$ and the dynamic viscosity of the quiescent background fluid to $\eta = 10^{-3} \, Pa\, s$. The filament is discretized in space using 400 linear beam finite elements and the time step size is chosen as $\Delta t = 0.01s$.

8.4. Results and discussion

Most of the results of the theoretical work by V. Slepukhin and A. Levine (UCLA) will not be presented here and the reader is kindly referred to the original joint publication [152]. Only those aspects relevant for the interpretation of and comparison with the simulation results will be reproduced in a concise form for the reader's convenience. Two variants of the potential field have been considered in simulations. First, the potential with exponential suppression of high Fourier modes defined by Equation 8.3 and second, the force-controlled distribution defined by Equation 8.2.

8.4.1. Results for the potential with exponential suppression of high wavenumber modes

Figure 8.4 shows a typical simulation snapshot of three tensed filaments interacting with the pinning potential, which is illustrated as a heat map with brighter colors representing higher potential energies. This snapshot showcases characteristic features of the filament conformations that result from the interaction with the static background potential field. Generally, the filament axis follows the valleys of the potential landscape and thus adapts to the externally imposed
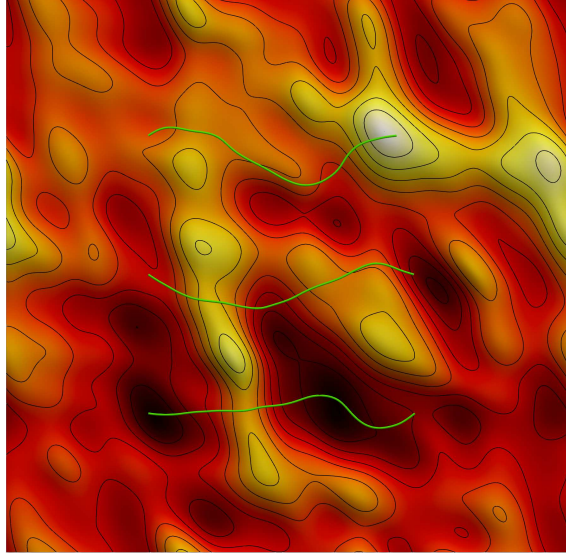
Figure 8.4.: Simulation snapshot of three tensed filaments interacting with the pinning potential, shown as a heat map with brighter colors representing higher potential energies. The lowest filament traverses a saddle between local potential maxima. On the right of that saddle point it curves into a deep potential minimum (dark). Similar features may be seen in the other filaments. Figure taken from the co-authored article [152].

spatial structure by means of elastic bending and axial tension. This is an expected result, which serves as a first verification of the computational model and simulation setup.

To study the effect of tension τ on the prestress of a filament, let us define the excess arclength ΔL as a measure for the (axial) prestress:

$$\Delta L = [\langle L \rangle] - L_0 \quad \text{with} \quad L_0 = \langle L \rangle|_{V_0=0} \,. \tag{8.4}$$

In the simulations, the tension was applied via a single point force $\tau \in [10^{-2}, 50]\text{pN}$ in global x-direction to the (right) endpoint of the filament that is free to move in this direction. For the results shown in Figure 8.5, we used the potential with exponential suppression of high Fourier modes from Equation 8.3, using 3096 Fourier modes, a correlation length of $\xi \approx 1.6\mu\text{m}$ and $V_0 = 0.175\text{pN}$. Each simulation was run for 5×10^4 time steps until $t_{\text{end}} = 500\text{s}$. To speed up simulations, we made use of parallelization and simulated systems of five filaments at a vertical spacing much larger than ξ and without any interactions between the filaments to ensure independent results for each filament. Each data point in Figure 8.5 results from the statistical ensemble of 70 to 100 such systems with five filaments each, depending on the deviation in results that was higher for the small tension values.

Figure 8.5 shows the simulation results (blue dots with errorbars) and includes a fit to the theoretical predictions for the regime of low tension (green line) and high tension (orange, dashed line). All details on these theoretical predictions can be found in the original publication [152]. Most importantly, Figure 8.5 shows a decrease in the excess arclength ΔL of the filament with increasing tension τ. This can be explained by the fact that high tension leads to a straightening
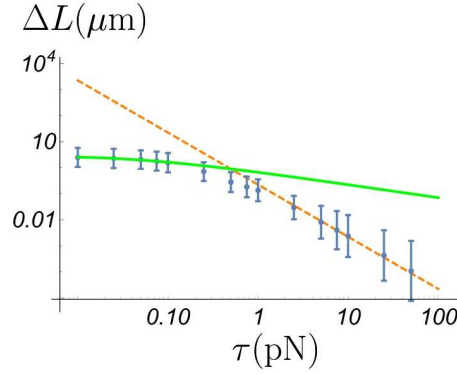
Figure 8.5.: The excess arclength ΔL (see Equation 8.4) of a semiflexible filament in the quenched pinning potential (with persistence length $\ell_P \approx 14\mu m$) as a function of tension τ. The (blue) dots with errorbars represent simulation results and the errors show the standard deviations of about four hundred filaments. At high tension (orange, dashed line) the filament cannot track the bottom of potential valleys, while at low tension (green line) or small bending modulus the filament does track the potential valleys with higher fidelity. For details on these theoretical predictions, refer to the original publication [152] where this figure is taken from.

of the filament and prevents it from following the (valleys of the) potential landscape. Specifically, the double-logarithmic plot shows that the behavior in the two distinct regimes of low and high tension can be described by two different power laws. The theoretical predictions of these power laws have been derived assuming the force-controlled distribution whereas the simulations used the potential with exponential suppression of high Fourier modes. To obtain the fit, the curvature and correlation length of the valley assumed in theory has been freely adjusted. To allow for a direct comparison of theory and simulations, the simulation results presented in the following section use the force-controlled distribution. As mentioned before, this distribution leads to less smooth potential fields (see Figure 8.1) and force fields (see Figure 8.2) and is thus numerically more challenging.

8.4.2. Results for the force-controlled distribution

Two parameter sets have been considered: one representing the case of large tension and another one representing the case of large bending and zero tension. Both shall be directly compared to the theory elaborated in the original publication [152] and repeated here for the reader's convenience. First, in the limit of a short correlation length $\xi/L_0 \ll 1$ and large tension $L_0\sqrt{\frac{\tau}{\kappa}} \gg 1$, the prediction is

$$\Delta L = \frac{V_0^2 L_0^2}{12\tau^2\xi}. \tag{8.5}$$

Second, in the limit of large bending $L_0\sqrt{\frac{\tau}{\kappa}} \ll 1$, the prediction is

$$\Delta L = \frac{V_0^2 L_0^6}{1890\kappa^2\xi}. \tag{8.6}$$

The first parameter set is given as $V_0 = 1/256^2$ pN, $\tau = 0.006$ pN, $\xi = 1\mu$m, $L_0 = 5\mu$m. The simulation gives us $\langle \Delta L \rangle = 2.0 \pm 0.6 \times 10^{-5}\mu$m, while Equation 8.5 predicts $\Delta L \approx 1.3 \times 10^{-5}\mu$m. The second parameter set is $V_0 = 1/256^2$ pN, $\tau = 0$, $\xi = 1\mu$m, $L_0 = 5\mu$m, $\kappa \approx 0.0125$ pN μm^2. Here, the result from the simulations is $\langle \Delta L \rangle = 2.2 \pm 0.4 \times 10^{-5}\mu$m, while Equation 8.6 predicts $\Delta L \approx 1.2 \times 10^{-5}\mu$m. In total, sixteen simulation runs have been performed for each parameter set.

9. Conformation of Mucin Filaments Subject to Varying Charge Conditions

This chapter studies the effect of different charge distributions on the conformation of a single mucin filament. Besides the primary purpose of delivering results and insights of biophysical relevance, it serves as an example of how the SSIP approach from Chapter 4 can be applied to model the (electrostatic) self-interaction of a slender fiber, i.e., the interaction of distinct, charged parts of the filament. Accurate, efficient, and versatile computational models for all kinds of molecular self-interactions are considered to be important, because tertiary and quaternary structures of proteins are a result of the complex interplay of this self-interaction and the intramolecular forces giving rise to an elastic stiffness, which is in our case modeled by the hyperelastic constitutive law within classical beam theory. Especially for highly slender fibers that show a tendency to undergo large 3D deformations, self-interaction due to intermolecular forces is thus expected to play a crucial role, which highlights the practical relevance of the proposed computational approaches.

9.1. Motivation

Mucins are a family of glycoproteins that are the key constituent of mucus hydrogels and thus abundant in the human nose, mouth, eyes, lung, the gastrointestinal tract and the female genital region. They are known to have extraordinary properties e.g. in terms of lubrication and selective permeability, which allow them to fulfill central tasks such as reducing friction to avoid irritation and wear on sliding surfaces and hindering pathogens from entering the body whilst ensuring the effective transport of useful physiological substances [10, 95, 162]. Refer also to Section 10 for a computational study of the hindered mobility of particles in hydrogels due to steric and electrostatic interactions. The computational investigation of this section studies the influence of electrostatic interactions on the conformation of individual mucin filaments and thus aims to contribute to the still ongoing exploration of mucin's fundamental properties. In the long run, this should lead to a detailed understanding of diseases caused by malfunction of the related body functions and thus allow for novel therapeutic approaches, but also enable the transfer of the underlying biophysical mechanisms to human-made, technical applications.

More specifically, this computational study is concerned with the question how the conformation of mucin changes due to a varying charge distribution along the filament as a result of an altered molecular architecture e.g. in the form of removed side chains, but possibly also as a result of different pH conditions. Based on first in-vitro experimental results of our collaborators

Theresa Lutz and Oliver Lieleg (TUM), this is expected to have significant implications regarding the interaction of mucin with other molecules. These investigations have been stimulated by the observations of a previous study dealing with the charge-dependent transport of molecules into and across mucin hydrogels [105] and suggesting that transient binding is the key influence on the penetration speed and depth. In this context, it was found that the removal of negatively charged side chains (i.e., sialic acids and sulfate groups) from mucin filaments does not increase the binding affinity of negatively charged dextrans as one would expect from the decreased repulsive forces. A possible explanation for this surprising behavior would be a conformational change of mucin, for instance some kind of folding or coiling, that restricts the access to the positively charged amino acid side chains in the terminal regions. The hypothesis to be tested in this computational study is that changes in the effective line charge distribution of mucin induced by different pH conditions lead to the mentioned change in the conformation of the filament. Such insights with respect to muco-adhesion are expected to contribute to an improved design of pharmaceuticals and drug carrier objects that need to overcome the barrier of the mucus layer in order to arrive and take effect at their intended destination.

9.2. Setup of the computational model and methods

Geometry, material and spatial discretization. The system consists of a single, initially straight filament of length $L = 1.155\,\mu\text{m}$ with a circular cross-section of radius $R = 7\,\text{nm}$, which is a simple model for the actual molecular architecture of a mucin filament [132, 149] and yields a slenderness ratio of $\zeta = 165$. The structural constitutive parameters for the bending, torsional, axial and shear stiffness are set to $EI = 2 \times 10^{-4}\,\text{pN}\mu\text{m}^2$, $GI_{\text{T}} = 2 \times 10^{-4}\,\text{pN}\mu\text{m}^2$, $EA = 2 \times 10^1\,\text{pN}$, $G\bar{A} = 2 \times 10^1\,\text{pN}$. These values correspond to experimentally determined values for the persistence length $L_{\text{p}} = EI/(k_{\text{B}}T) \approx 50\,\text{nm}$ reported in literature [132, 149]. A total of 68 Hermitian Simo-Reissner beam elements (see Section 3.2.2 for details) are used to discretize the filament in space, which is a result of dividing the extended glycosolated domain consisting of 2380 amino acids in the middle of the filament into 50 amino acids per element and treating the two terminal regions of the filament individually according to the molecular domain structure. The resulting discretization consists of 47 elements with a length of $17.5\,\text{nm}$ in the extended glycosolated domain, 1 element for the remaining amino acids in this domain, and 10 elements each for the N- and C-terminal region. This definition of the finite element domains will also be reflected in the determination of the line charge distribution and a precise definition thus follows further down.

Brownian dynamics and temporal discretization. Thermal excitation and viscous damping of the filament due to the implicitly modeled surrounding fluid are incorporated via the micromechanical continuum approach to Brownian dynamics proposed in [33]. The thermal energy used to compute the random thermal forces on the filaments is set to $k_{\text{B}}T = 4.04 \times 10^{-3}\,\text{aJ}$, which corresponds to room temperature and the viscous drag forces acting along the filament are computed based on the viscosity $\eta = 1 \times 10^{-3}\,\text{Pa}\,\text{s}$ of water and individual damping coefficients for translations parallel and perpendicular to the filament axis as well as rotation around the filament axis that are computed based on the cylindrical shape of the filament. A Backward Euler scheme is used to discretize the problem in time and a base time step size of $\Delta t = 1 \times 10^{-3}\,\text{s}$ is applied.

This is augmented by the adaptive time stepping scheme described in Section F.2, in which however the stochastic thermal forces are kept constant over an interval of $\Delta t_{\mathrm{stoch}} = 1 \times 10^{-2}\,\mathrm{s}$ each in order to allow the system to converge to the corresponding dynamic equilibrium configuration.

Electrostatic interactions. Being the key model component, the electrostatic self-interaction is modeled via the SSIP approach from Section 4.2.2 and the SSIP law for Coulomb-type surface interaction from Section 4.3.3. The constant prefactor $C_{\mathrm{elstat}}^{\mathrm{true}} \approx 1.12 \times 10^2\,\mathrm{aJ\mu mfC^{-2}}$ directly follows from assuming the dielectric permittivity of water (at room temperature) for the surrounding fluid. In order to not significantly overestimate the effect of Coulomb interactions due to not considering the screening of charges in our computational model, the actual applied prefactor $C_{\mathrm{elstat}} = 0.1 \cdot C_{\mathrm{elstat}}^{\mathrm{true}}$ has been reduced by a factor of ten, which is of course only a rough model correction and would need to be verified by a more detailed model including the counterions in the surrounding electrolyte either explicitly or via a (Debye) screening model. As mentioned above, the focus of this study lies on the role of the complex line charge distribution λ along the filament, which varies due to manipulations of the molecular microstructure – to be more specific the removal of the sialic acids (SA) and/or the sulfate groups (SO_4^{2-}), and also due to the two different considered pH values of 4 and 7. In a first step, the full sequence of the porcine Mucin-5AC protein (A0A287ANG4_PIG) was obtained from UniProt [158] and the number of elementary charges at pH 4 and 7 was analyzed for each of the 4192 amino acids by our collaboration partner Theresa Lutz. To arrive at the concrete input parameter values for the simulation, the net charge for the specific region of each finite beam element was computed and applied as an element-wise constant line charge density $\lambda(s)$ along the filament. The complete data set used in the simulation setup for each of the different scenarios to be compared later on is provided in Table E.1 in Appendix E.1 of this work. Finally, the contributions from electrostatic interactions are evaluated by Gaussian quadrature using five integration points per element.

As a consequence of applying the electrostatic self-interactions, the filament with an initially straight, stress-free reference configuration defined above will experience locally confined axial tension as well as compression, which is equilibrated in ten additional time steps in the beginning of each simulation during which no thermal forces are applied. This turned out to be crucial for a successful iterative solution of the nonlinear system of equations, because otherwise physical instabilities in form of local buckling was induced by the combination of strong, inverse-distance dependent electrostatic forces and small undulations of the straight fiber axis due to thermal forces. Both the resulting equilibrium configurations at the end of this equilibration phase and the definition of the stress-free reference configuration in the presence of electrostatic self-interaction will be discussed in the subsequent result section.

Repulsive steric interactions. Due to the possibly strong attractive electrostatic forces, it is particularly important to account for self-contact of the filament in order to preclude an unphysical interpenetration of distinct parts of the filament, which would also lead to a singularity in the inverse-distance dependent SSIP law for electrostatic interactions. Following the reasoning in Section 6.2, a macroscopic beam contact formulation is applied that is summarized in Section 3.3.2. The line penalty parameter is set to $\varepsilon_\parallel = 1 \times 10^5\,\mathrm{pN\mu m^{-2}}$, which – in combination with a quadratic regularization in the gap value range $[0, 2\,\mathrm{nm}]$ – turns out to be sufficiently large to effectively preclude any noticeable penetration in any (dynamic) equilibrium configuration. This is supplemented by the Newton increment control algorithm described in Section F.2 in order to preclude also unphysical crossings, i.e., passing of distinct parts of the filament through

each other's volume in between two iterations of the nonlinear solver due to an overly large displacement increment per nonlinear iteration.

Boundary conditions. One end of the filament is hinged by means of Dirichlet boundary conditions in order to comply with the in-vitro experimental setup. Due to a lack of knowledge and control over the fact which terminus of the filament is hinged in the in-vitro experiments, the N-terminus is chosen to be pinned in all the simulations, but no noticeable changes in the statistical quantities of interest are expected if instead the C-terminus was pinned or even if the filament was entirely free to move. Still, there is no conceptual restriction in the computational model or framework and repeating all simulations with a pinned C-terminus or free filament in order to study the influence on the results would be straightforward to do.

Quantities of interest. Since we are interested in the conformation of this filament, the quantities of interest to be measured in the computational experiments will be the time- and configuration-averaged end-to-end distance L_{e2e} and radius of gyration R_g. To ensure a sufficient sampling of these statistical quantities, the total simulation time is set to $t_{end} = 2s$ and five random realizations for each scenario, i.e., set of parameters will be computed. Note that the radius of gyration is computed in a spatially discrete manner, i.e., the contributions are evaluated at the 69 nodes used for the centerline discretization, which should however be sufficiently accurate especially since we are interested in relative changes of this quantity over the different scenarios to be considered.

9.3. Results and discussion

The average values of the root-mean-squared end-to-end distance $< L_{e2e}^2 >^{1/2}$ and radius of gyration $< R_g^2 >^{1/2}$ over the five random realizations each are shown in the bar plot in Figure 9.1. Accordingly, the error bars indicate the standard deviation of the mean over these five simulation runs conducted for each of the six considered scenarios. As a reference, both the trivial analytical solution for a rigid mucin filament, i.e., a cylinder with identical dimensions as the undeformed state of mucin (black dashed line), and the simulation results for an uncharged mucin filament with otherwise identical properties are included in these plots.

Comparison of results for pH 4 and pH 7

Let us first focus on the results for the two different pH conditions, one being acidic with a pH value of 4 and the other being neutral with pH 7. With an end-to-end distance of $< L_{e2e}^2 >^{1/2} \approx 0.29 \pm 0.038 \, \mu m$ for pH 4 vs. $< L_{e2e}^2 >^{1/2} \approx 0.98 \pm 0.017 \, \mu m$ for pH 7 as well as radius of gyration of $< R_g^2 >^{1/2} \approx 0.21 \pm 0.0086 \, \mu m$ for pH 4 vs. $< R_g^2 >^{1/2} \approx 0.33 \pm 0.0019 \, \mu m$, we obtain significantly smaller values for the acidic conditions as compared to neutral conditions. These values indicating a more compact shape for pH 4 as compared to a more elongated, linear conformation for pH 7 can be explained by the illustrative simulation snapshots shown in Figure 9.2. In these plots, the filament axis (blue line), the center of mass (red point), and the radius of gyration (gray sphere around the center of mass) are visualized for two characteristic conformations of pH 4 (top row) and pH 7 (bottom row), respectively. The difference in both the end-to-end distance and radius of gyration can be observed very clearly and traced back to the
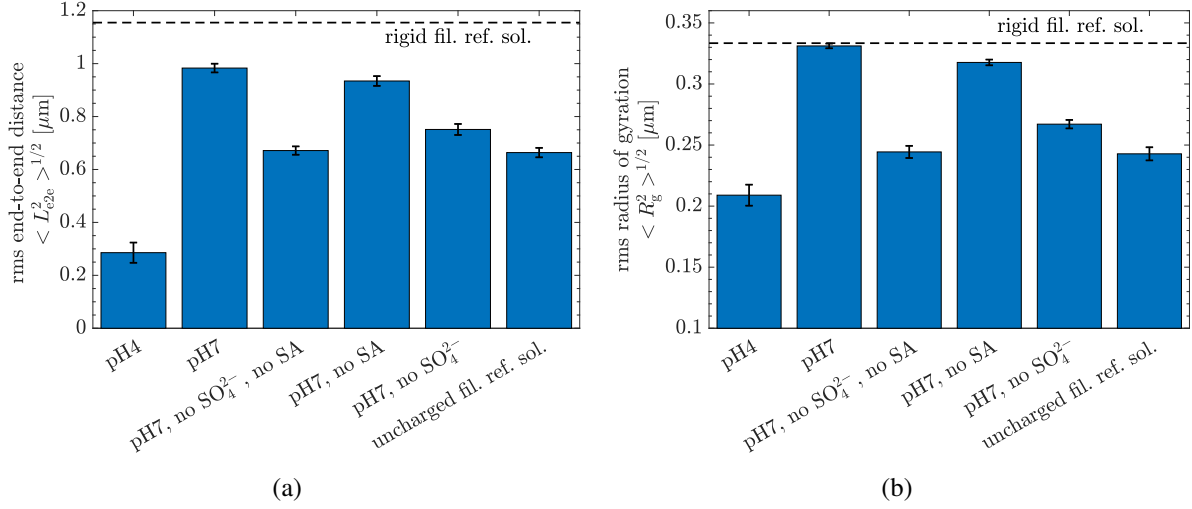
Figure 9.1.: Mean of (a) the root-mean-square (rms) end-to-end distance $< L_{\text{e2e}}^2 >^{1/2}$ and (b) rms radius of gyration $< R_{\text{g}}^2 >^{1/2}$ over five random realizations of each of the six considered scenarios. Error bars indicate the standard deviation of the mean.

fact that both ends of the filament are folded onto the extended glycosolated domain in the middle of the filament in case of pH 4. Looking at the prescribed line charge distributions provided in Table E.1 reveals that both are identical and strongly negatively charged in the extended glycosolated domain, however both terminal regions are positively charged at pH 4, whereas they are negatively charged at pH 7. The resulting attraction of unlike charges and repulsion of like charges explains both the folding of the terminal regions for pH 4 and the relatively unflexible behavior for pH 7.

Figure 9.3 shows additional, detailed simulation snapshots revealing the axial strains, the repulsive contact force distribution and the electrostatic force distribution along the mucin filament at exemplarily chosen steps in time. Once again, the difference between the compact, folded conformation at pH 4 and the elongated, stretched conformation at pH 7 is clearly visible. The highly negative charged extended glycosolated domain leads to considerable axial strains of up to 10% in both scenarios. Whereas the adhesive self-contact observed in Figures 9.3(a) and 9.3(b) occurs in almost all time steps for the pH 4 case, it is basically non-existent in the simulations for pH 7. From a computational point of view, the adhesive self-contact is the most challenging aspect, because it requires a fine temporal resolution (i.e. smaller time steps) to resolve the contact dynamics and prevent noticeable penetrations along the entire filament as well as it complicates the iterative solution of the nonlinear system. The presented simulation results involving a lot of adhesive self-contact in this highly dynamic system are therefore considered to be a proof of the effectiveness and robustness of the applied computational model and methods.

Getting back to the interpretation of the biophysical system behavior, a comparison of both scenarios with the reference solutions $< L_{\text{e2e}}^2 >^{1/2} \approx 0.66 \pm 0.018 \, \mu\text{m}$ and $< R_{\text{g}}^2 >^{1/2} \approx 0.24 \pm 0.0054 \, \mu\text{m}$ obtained from simulations of the uncharged filament (again refer to Figure 9.1) shows that the electrostatic self-interaction has two different effects, which can be studied separately
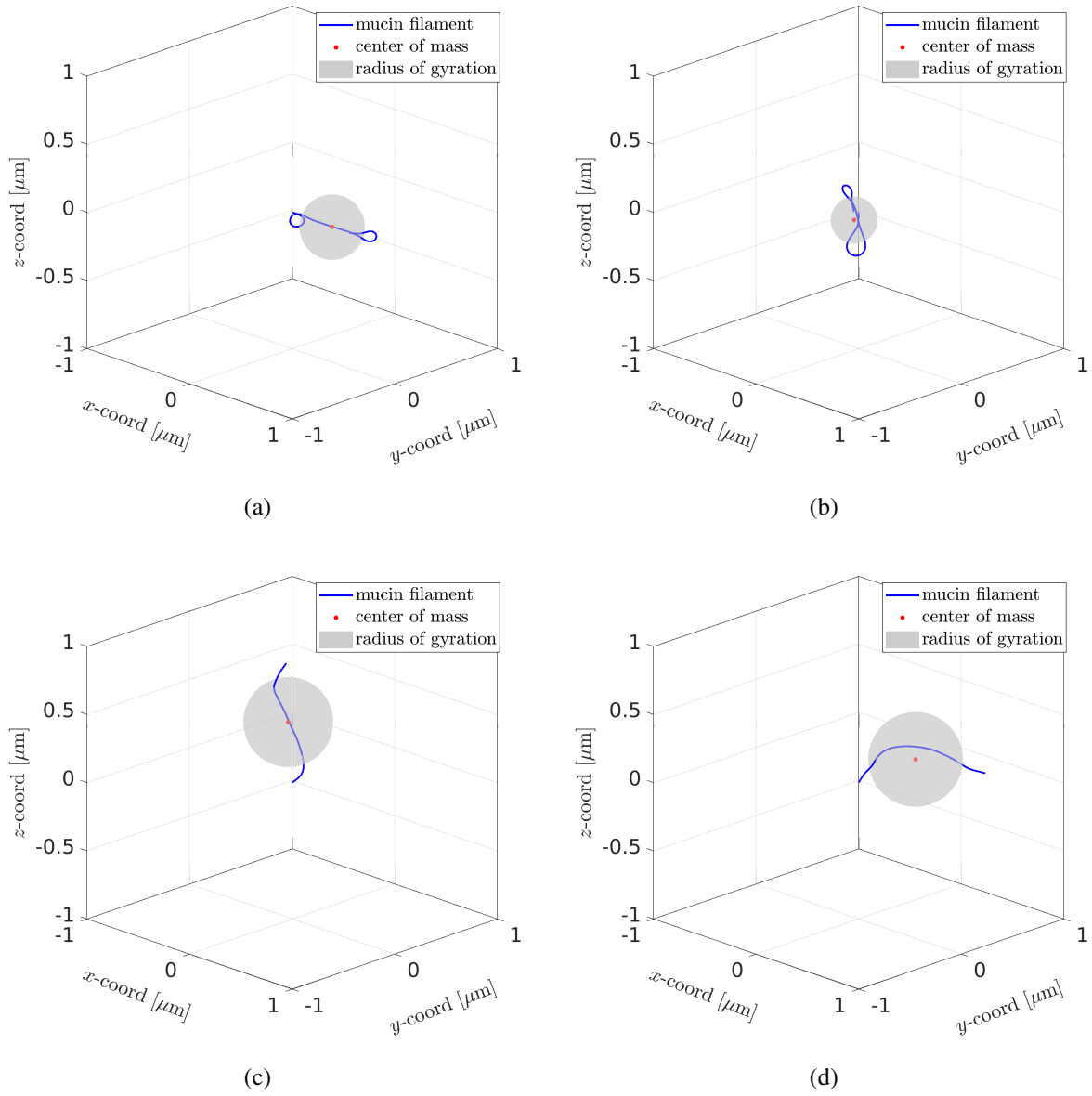
(a)

(b)

(c)

(d)

Figure 9.2.: Exemplarily chosen simulation snapshots for the case of pH4 (top row) and pH7 (bottom row) showing the centerline of mucin, the center of mass and the radius of gyration.
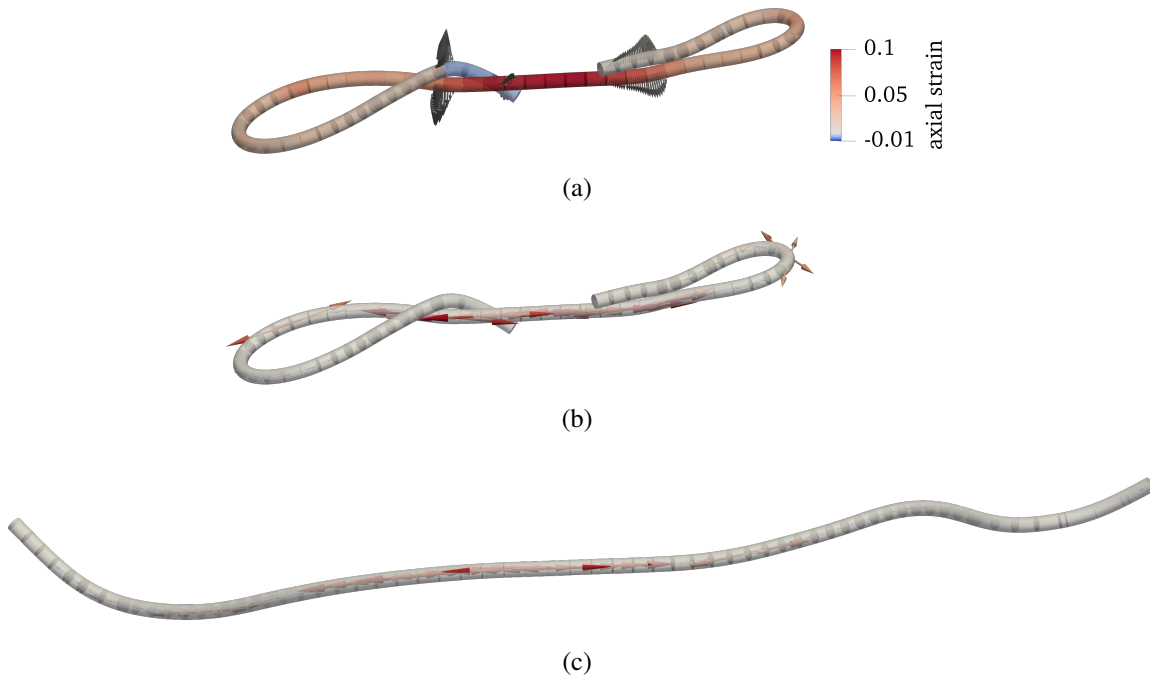
Figure 9.3.: Simulation snapshots showing (a) the axial strains (red color indicates tension, blue color compression) and contact force distributions along the mucin filament for the case of pH 4; (b) the distribution of electrostatic forces for the case of pH 4; (c) the distribution of electrostatic forces for the case of pH 7.

and isolated here. It can either lead to a stiffer and thus more rod-like behavior of the filament as compared to the pure elastic stiffness as observed for the almost entirely negative and thus like charges in case of pH 7, or it can lead to a seemingly less stiffer behavior, which in fact is rather a compact, folded and relatively stable conformation with still quite stiff mechanical properties. The latter is also confirmed by the plots over time of the end-to-end distance L_{e2e} and the radius of gyration R_g for one run of each scenario shown in Figure 9.4. Starting from the initially straight configuration, the data for mucin at pH 4 (red line) reveals two distinctive, abrupt changes in the conformation, which can be traced back to the subsequent folding of the two ends, and finally remains in the most compact, twice folded state for over a second. Moreover, the data shows very little fluctuations around these distinct folded states as compared to all other scenarios, which might be surprising after the larger standard deviations obtained for this case as shown in Figure 9.1. Note also that the folding of ends in case of pH 4 manifests itself in terms of a more drastic reduction and thus bigger difference in the end-to-end distance than in the radius of gyration if compared to pH 7 or the charge-free reference, respectively.

Comparison of results for the modified molecular structure of mucin

Let us now turn to the results for the scenarios, where either of or both of the SA and SO_4^{2-} groups are removed from the extended glycosolated domain of the mucin filament, thus leading to three more different line charge distributions (again cf. Table E.1) to be analyzed. Figure 9.1 shows that the removal of both types of side groups leads to a behavior that is almost identical to
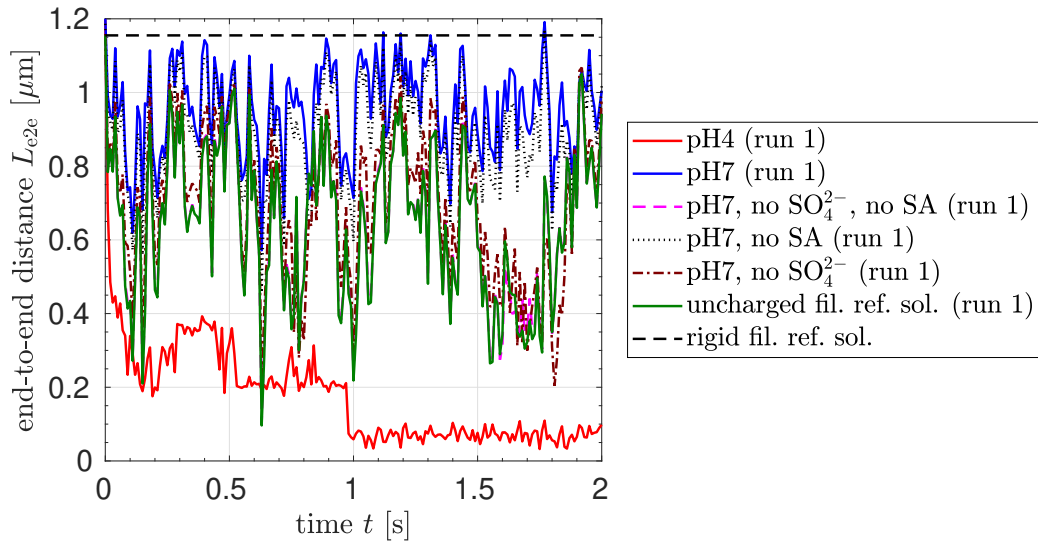
(a)
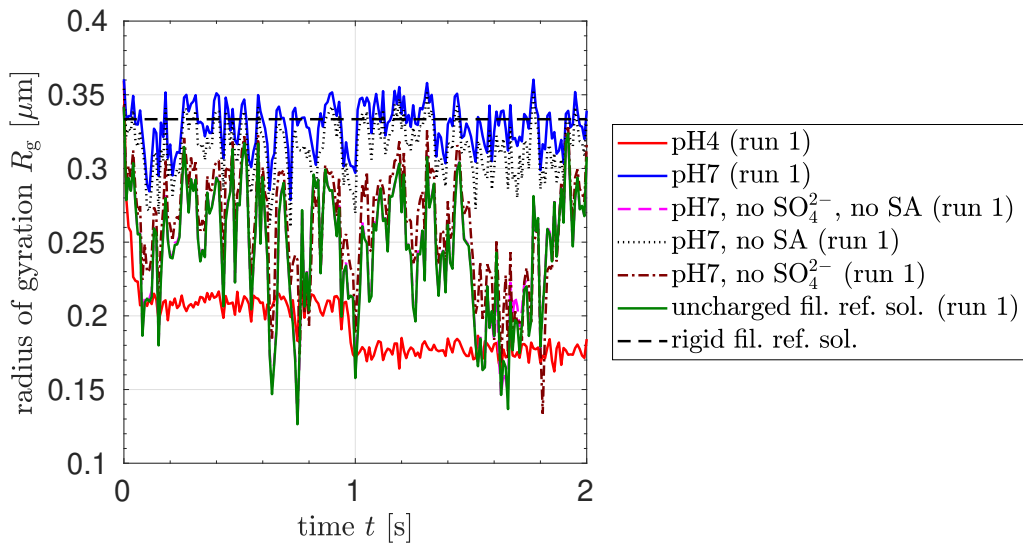
(b)

Figure 9.4.: End-to-end distance (top) and radius of gyration (bottom) over time for one random realization of each of the six considered scenarios. The data for the remaining four simulation runs of each scenario is provided as supplementary material in Appendix E.2.

the reference solution obtained for an uncharged filament, which is expected due to the almost complete removal of charges in the middle part of the filament that can be seen already in Table E.1. As compared to the unmodified mucin filament at the same pH value 7, the removal of these side groups and thus charges therefore causes a significant difference in the conformation of the filament. The remaining question is which fraction of this effect is attributed to which type of the side groups. Once again, the data for both the end-to-end distance L_{e2e} and the radius of gyration R_g gives an unambiguous answer in that the significantly larger part of the difference comes from the removal of the SO_4^{2-} groups, which is again expected based on the corresponding line charge distributions listed in Table E.1.

Discussion of the stress-free reference configuration

In this study, we have treated the experimentally determined values for dimensions and constitutive parameters as if these were measured in absence of any electrostatic (and other types of) (self-)interactions and defined the stress-free reference configuration of the beam accordingly. Enabling the electrostatic interactions in the simulation will then lead to an equilibrated configuration that slightly differs both in dimensions and effective structural stiffness of the filament due to the induced deformations. These deformations in the equilibration phase are observed to be small and are thus expected to not significantly change the results obtained for the statistical quantities of interest. However, it would be desirable to further investigate and quantify the impact of this simple modeling strategy. To this end, the results obtained here should be compared to those obtained for a different set of parameters, which is obtained from fitting the experimentally determined contour as well as persistence length of mucin to the ones resulting from the computational model including electrostatic self-interaction *after* the equilibration phase.

9.4. Conclusions and outlook

The results of this computational study reveal a significant influence of the electrostatic self-interactions on the conformation of the mucin filament. As compared to the reference solutions obtained from simulations of a hypothetical, charge-free filament, the different line charge distributions characterizing the different considered scenarios of mucin at pH 4, at pH 7, and at pH 7 with removal of either or both of the SA and SO_4^{2-} side groups, had a major impact on both the end-to-end distance and the radius of gyration. The removal of both types of side groups and therefore the majority of the charges from the extended middle domain of the filament led to significantly smaller values for the end-to-end distance and the radius of gyration. This is associated with a more flexible behavior as compared to the unmodified mucin filament at pH 7, where the mutual repulsion of the big amount of negative charges distributed almost along the entire filament contributes to the effective bending stiffness. At pH 4, the mucin filament shows a persistent folding of both terminal regions onto the extended glycosolated domain, which can be explained by the mostly positively charged terminal regions in this case and gives rise to a fundamentally different conformation as compared to the stretched out, semi-flexible conformation observed at pH 7.

In addition to these relevant biophysical results, the present computational study serves as the first proof of principle for modeling (electrostatic) self-interaction of fibers via the novel

SSIP approach from Chapter 4. The large number of simulation runs and time steps and the variety of different configurations generated both due to different sets of input parameters and the stochastic thermal forces prove the effectiveness and robustness of the SSIP approach itself as well as its combination with the macroscopic beam contact formulation. Especially the case of pH 4 with self-contact of the bent ends occurring in almost all time steps needs to be highlighted as the most challenging scenario in this respect.

Promising aspects of future work include the incorporation of charge screening effects in the computational model, e.g., in form of a different SSIP law based on the theory of Poisson-Boltzmann and its solution by Debye-Hückel, and its influence on the resulting conformation of mucin. Moreover, the consideration of hydrophobic interactions both in the computational model and its effect on the presented results would be highly interesting and is expected to play a role especially in the case of removed SA and SO_4^{2-} side groups, because the hydrophobic terminal regions might show the tendency to fold onto each other in these cases, where the effective bending stiffness of the filament is drastically reduced.

10. Hindered Mobility of Charged Particles in Hydrogels

This chapter both proposes and applies a novel computational model to study the mobility of particles in hydrogels, i.e., cross-linked networks of biological or synthetic polymers immersed in aqueous solution. Due to steric and electrostatic interactions with polymer fibers, the dynamics of particles significantly differs from the classical random walk observed for free diffusion. In the overall context of this work, this chapter serves as the first application of the fiber-sphere interaction models both for electrostatic and repulsive steric interactions that have been proposed in Section 6.3.1 as special cases of the general SSIP approach from Chapter 4. The following Section 10.1 first highlights the biophysical background as well as the practical relevance of the problem and briefly reviews existing experimental studies and computational models to point out the motivation for the novel modeling approach. Section 10.2 presents all aspects of this computational model and the required numerical methods, thereby relating to the broader context of this work in terms of versatile, accurate and efficient modeling of molecular interactions of deformable fibers. After the presentation and discussion of the results in Section 10.3, this chapter will be concluded with a summary of the findings and an outlook to promising aspects of future research in Section 10.4.

10.1. Motivation

The remarkable ability of biological hydrogels to individually control the mobility of diffusing particles is of crucial importance for numerous functions of the human body and can likewise be observed in a variety of other creatures. See e.g. [162] for a recent review of this topic. On the one hand, this selective permeability gives rise to the protection of the organism against pathogens such as viruses and bacteria that are effectively hindered from invading and traversing the organism. On the other hand, it ensures the effective transport of a broad variety of substances that are useful and important for the organism. Examples for such biological hydrogels include mucus (cf. Section 9), the extracellular matrix (ECM), the cytoplasm, and biofilms and can thus be found throughout the entire human body and in countless other places in nature. The high practical relevance of this topic originates from its implications and associated prospects in several fields ranging from medical diagnosis to therapy of body malfunctions and targeted drug release, and carries over to yet unimagined possibilities in technical applications such as filters.

A large number of experimental studies has investigated the origin of this selective filtering. Meanwhile, there is strong evidence that – besides the most obvious mechanism to filter by size – also the surface charge of the particles plays an important role (see e.g. [1, 4, 6, 26, 37, 81, 95–97, 165, 168] and again the review article [162]). This new paradigm thus suggests filtering

not (only) by size but a combination of other particle properties such as charge, hydrophobicity or binding affinity and is thus commonly referred to as interaction filtering. Despite the considerable scientific effort in this field, many aspects concerning the underlying mechanisms and specific conditions are, however, yet unknown. To a large extent, this can be explained by the great complexity of the many different biological systems both in number and diversity of components, e.g. with respect to their molecular architecture, as well as the lack of an in-depth understanding of physical and chemical interactions on the molecular scale, and not least by the challenges and limitations with respect to experimental preparation and measurement techniques when it comes to the required high spatial and temporal resolution, especially over considerable time spans of several seconds. At this point, computational studies are expected to contribute to the scientific progress in this field.

As compared to the large body of literature reporting on experimental work, relatively few computational studies have been published so far. Most of the early and also some of the recent work concentrated solely on the so-called excluded volume effect of the fibers, i.e., the repulsive steric interactions with the network fibers that hindered the free diffusion of a (hard) spherical particle (see e.g. [77, 80, 121, 126, 144, 154]). Saxton [145] was the first to include and study other than steric interactions in the form of a binding model in his Monte Carlo simulations. Since the recognition of the dominant role of electrostatic and possibly other types of molecular interactions as outlined above, several computational studies included electrostatic effects and confirmed the trends observed in experiments and shed light on the underlying mechanisms [64, 65, 116, 155, 168, 169]. Particularly the recent works published by Hansing et al. [65] and Hansing and Netz [64] were very successful in analyzing the influences of particle size, fiber volume fraction, particle charge, and the comparison of oppositely vs. similarly charged particles and networks. They also found good agreement of the simulation results with several sets of experimental data, which confirms the validity of such a modeling approach.

The computational model to be proposed in this work aims to improve especially on the modeling of the fiber network, which has been modeled in a strongly simplified manner in all previous studies. Either a square array of straight and parallel, rigid fibers oriented along one spatial dimension [155] or a cubic lattice consisting of either linearly aligned hard spheres [116] or consisting of straight rigid fibers [65, 168] has been assumed. Zhou and Chen [169] likewise applied a cubic lattice consisting of beads placed at the vertices and connected by linear spring elements. Hansing and Netz [64] were the first to break the strong geometrical order in all these models, however only allowed for a variation of the spacing of the still straight and infinitely long, rigid fibers with mutually orthogonal orientation. Yet they found a significant and fundamental difference in the trapping mechanism of ordered and disordered fiber lattices, which can be attributed to locally denser regions of the network in the case of attractive particle-network interactions. This is a strong motivation to work towards a more realistic modeling of the fiber network as a crucial part of biological hydrogels as will be outlined in the following.

First, the individual fibers will be explicitly modeled by geometrically exact 3D beam theory, thus allowing for arbitrarily curved initial shapes of the fibers and possibly large deformations including all six modes of axial strain, (2x) shear, torsion, and (2x) bending. Second, the initial spatial distribution, orientation and interconnection of fibers will be modeled as a random 3D Voronoi network, thus mimicking several important geometrical features of real biopolymer networks such as a random, spatially variable mesh size distribution, a random fiber length

distribution, random mutual orientations of the fibers, and arbitrary connectivity between the fibers. Several of these attributes are expected to play an important role when it comes to both purely steric interactions and the combination with electrostatic interactions and will be studied in Section 10.3. A similar approach to network generation based on Voronoi tessellation has previously been applied in a number of publications, e.g., to study cell-cell communication in a 2D network of linearly elastic springs [71].

Applying such a sophisticated model for the individual fibers and the network they constitute comes at the cost of an increased complexity and size of the system of equations to be solved in the simulations. However, the same modeling strategy based on geometrically exact beam finite elements describing the biopolymer fibers has previously been applied to model the Brownian dynamics of individual semiflexible filaments (cf. [32], Chapters 8 and 9) and has been proven to be accurate and also efficient enough to study large-scale problems such as the process of self-assembly of (different morphologies of) transiently cross-linked biopolymer networks [34, 35] as well as their (high- and low-frequency) rheology [118]. On the one hand, this confirms the feasibility of the novel modeling approach to study the hindered mobility of particles in hydrogels and on the other hand this already outlines the long-term opportunities and motivation. Using the self-assembled network configurations, e.g., for an actin bundle network, can readily replace the Voronoi-type network applied in a first step in the present study. Moreover, the dynamics of the network including the reorganization of the transient cross-links could be included and would be highly interesting since there is experimental evidence that particles larger than the mesh size of the particle can still diffuse through the network by locally breaking inter-fiber links [89]. This has also been confirmed to be an effective transport mechanism in a first computational model [58]. Another example for the dynamics of hydrogel networks is given by the self-renewal process of a mucus layer [105, 162].

In general, the mathematical description of the problem and therefore also the numerical methods required to solve it as well as the code framework substantially differs from the ones used by previous computational studies listed above, which is an inevitable consequence of the aforementioned explicit modeling of biopolymer fibers as elastically deformable, geometrically exact beams. In the present model, a set of well-established numerical formulations for beams (see Section 3) is combined with the beam-sphere interaction models (see Section 6.3.1) derived as a special case of the general SSIP approach to fiber-fiber interactions proposed in Chapter 4 of this work. The solution strategy follows the one commonly used in nonlinear finite element frameworks for structural dynamics and – in short – it consists of the following steps. According to the principle of virtual work the weak form of the mechanical balance equations is derived and subsequently discretized in space and time. Given a proper set of initial and boundary conditions, a load/time stepping scheme is applied and in every step the solution of the resulting discrete system of nonlinear equations is found iteratively by means of Newton's method. Refer to Appendix F for an overview of the computational framework as well as a discussion of selected aspects of the applied algorithms and libraries.

## 10.2. Setup of the computational model and methods

Given the broad variety of biological hydrogels mentioned above, the ECM gel(s) used in the comprehensive experimental studies of particle mobility by Lieleg et al. [96] and Arends et al. [4] are chosen to serve as the main reference for the specific setup and parametrization of the versatile computational model. For these gels, an additional, subsequent characterization in terms of their biophysical properties has been conducted [5] that proves helpful with respect to model setup and parametrization. The key components of the computational model are the fiber network, the diffusing particle, and their mutual interactions. All these components will be presented individually in the following sections before selected further aspects of the simulation setup such as boundary conditions and post-processing of the results will be discussed.

10.2.1. Biopolymer fiber network

As outlined above, the initial, stress-free configuration of the fiber network is the result of a 3D Voronoi tessellation of the cubic simulation box (size $10 \times 10 \times 10\,\mu\text{m}$) generated via the open source library voro++ [133]. Figure 10.1(a) shows an example of the resulting network architecture. The main input of this preprocessing step are the randomly chosen locations of a number of n_{VP} so-called Voronoi points[1]. The output are the vertices and edges of a random, irregular, polygonal network that are used to define the position and orientation of the initially straight beam segments as well as their interconnections. For Voronoi-based tessellation, the connectivity number, i.e., the number of fibers branching off at each junction point, is 4, which agrees well with values of 3 to 4 reported for ECM gels [166]. This parameter could also be adapted by randomly removing or adding fibers to match other hydrogel architectures in the future. At each junction, the beam endpoint positions and rotations are coupled, which is a model assumption based on the expected mechanical behavior of the chemical binding between the fibers, and once again is straightforward to adapt e.g. to hinged connections in the future. To be able to use the simulation box as a representative volume element (RVE) with periodic boundary conditions (details see below), the Voronoi tessellation and thus the resulting network geometry is chosen to be periodic in space. Altogether, a simple visual comparison with electron microscopy images of real biological hydrogels in Figure 10.1 reveals a high similarity both in terms of the random, irregular, polygonal structure as well as its characteristic properties such as the distribution of pore sizes, fiber segment length, and connectivity.

The individual fibers are modeled by 3D geometrically exact beam theory assuming a circular shape of the cross-section and a hyperelastic material law (see Section 3.1.1 for details). Further specifications such as the dimensional and constitutive parameters are chosen to mimic collagen I as the key constituent of the targeted class of ECM hydrogels, however, all these parameters can easily be adapted to study their influences or model specific other fiber species. In the present study, the cross-section diameter is set to $D_{\text{f}} = 75\,\text{nm}$, Poisson's ratio is set to $\nu = 0.3$, and Young's modulus is varied from as low as $E = 0.1\,\text{MPa}$ up to the theoretical limit of rigid fibers to study the influence of the fiber stiffness. Note that experimental results for collagen I

---

[1]Note that the original term Voronoi *particles* from [133] is not used here to avoid confusion with the diffusing particle(s).
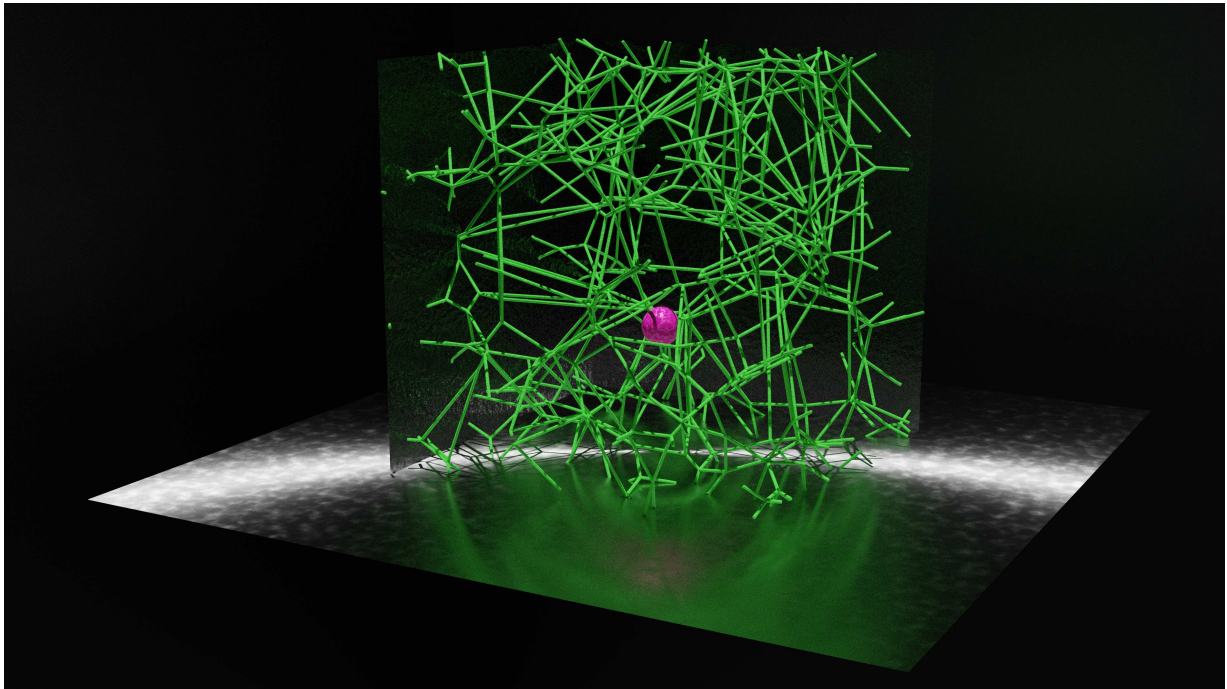
(a)
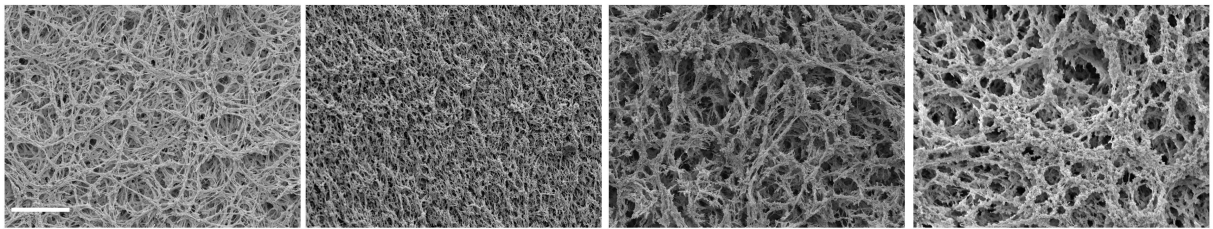
(b)
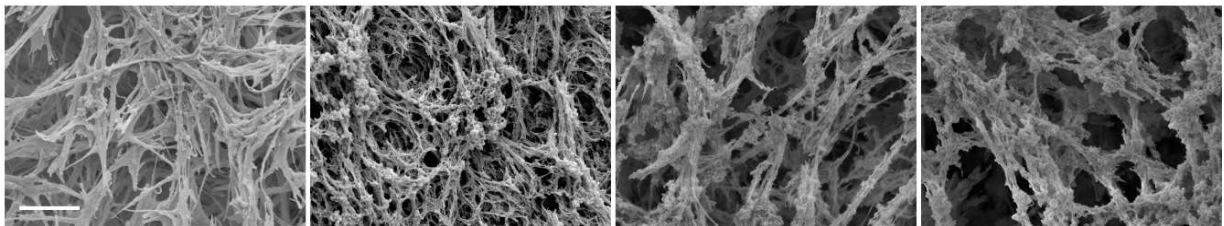
(c)

Figure 10.1.: Network architectures (a) resulting as one example of the random, periodic Voronoi tessellation and used as initial, stress-free configuration in the computational model (box size is $10 \times 10 \times 10\,\mu m$, rendered using Blender [14]); and (b)-(c) observed in SEM images of four different basal lamina gels used by in vitro experiments studying particle mobility (scale bars indicate (b) $25\,\mu m$ and (c) $5\,\mu m$, reprinted from [5]).

suggest values in the order of $E = 0.1 - 1\,\mathrm{GPa}$ [160], which are covered by the wide range of values considered here. As it will turn out from the results in Section 10.3.3, the influence of the fiber stiffness on the particle mobility in the problem setup considered here is negligible for the realistic range of values for Young's modulus E and a noticeable difference in results is observed only below values of $E = 1\,\mathrm{MPa}$. It can therefore be assumed that the specific values for the fiber material are of minor importance and that the deformation of fibers will only become important if the dynamics of the network reorganization will be included as outlined above or if much thinner and softer, i.e., much more compliant fibers are considered e.g. in the context of a different kind of hydrogel (e.g. mucin or F-actin) or a dysregulation of fiber stiffness.

To characterize the generated fiber networks, Figure 10.2 shows the resulting values of the mean and standard deviation of the fiber volume fraction $\bar{V}_{\mathrm{f}}$ and the minimum / average / maximum cell diameters[2] as a function of the number of Voronoi points n_{VP}. For this statistical

| (a) | (b) |
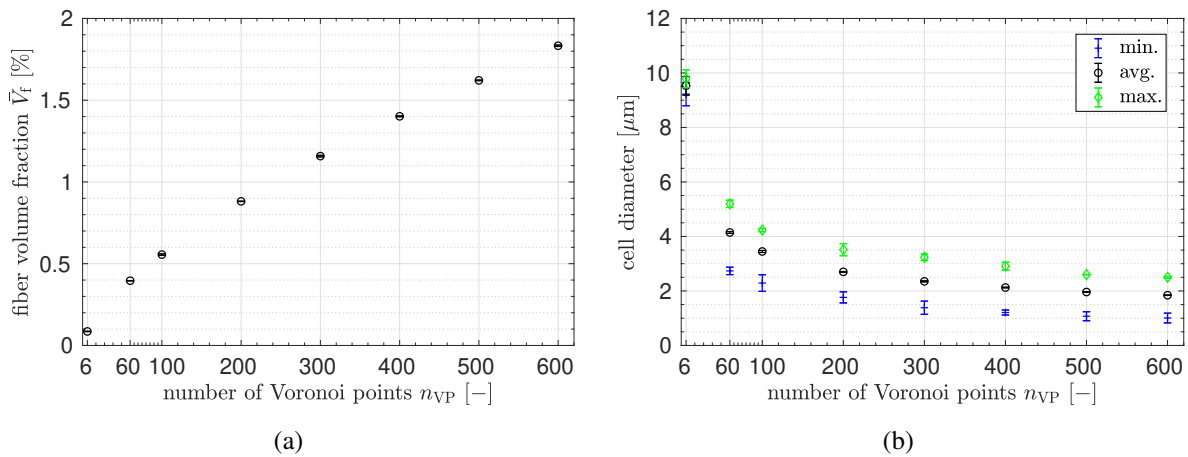
Figure 10.2.: Mean and standard deviation of (a) the fiber volume fraction (black circles with errorbars) and (b) the minimum (blue pluses with errorbars) / average (black circles with errorbars) / maximum (green diamonds with errorbars) cell diameter obtained for three random network geometries for each of the considered numbers of Voronoi points n_{VP}.

analysis of the random network geometries, a box size of $10 \times 10 \times 10\,\mu\mathrm{m}$ and a fiber diameter $D_{\mathrm{f}} = 75\,\mathrm{nm}$ as stated above is assumed. A number of $n_{\mathrm{VP}} = 60$ Voronoi points results in a fiber volume fraction $\bar{V}_{\mathrm{f}} \approx 0.4\%$ and a range of cell diameters of approx. $2.7 - 5.2\,\mu\mathrm{m}$. This turns out to match the typical *mesh* size of $2 - 3\,\mu\mathrm{m}$ reported in [96] quite well and is thus chosen as the default value for most of the simulations conducted in this work (once again refer to Figure 10.1 for a visual comparison of model and real hydrogels). The densest network to be considered in this work is given as $n_{\mathrm{VP}} = 600$ and thus results in a high fiber volume fraction $\bar{V}_{\mathrm{f}} \approx 1.8\%$ and cell diameters in the range of approx. $1.0 - 2.5\,\mu\mathrm{m}$. An example is shown in Figure 10.3 along with electron microscopy images of the ECM hydrogel from the human amniotic basal membrane [166], which appears to be much denser than the one considered above and thus motivates this second considered value of the network parameter $n_{\mathrm{VP}} = 600$.

---

[2]Here, the cell diameter for each of the n_{VP} cells in the network has been computed as an approximated inscribed sphere of the irregular polyhedron based on the shortest distance of the Voronoi point to each of the cell edges.
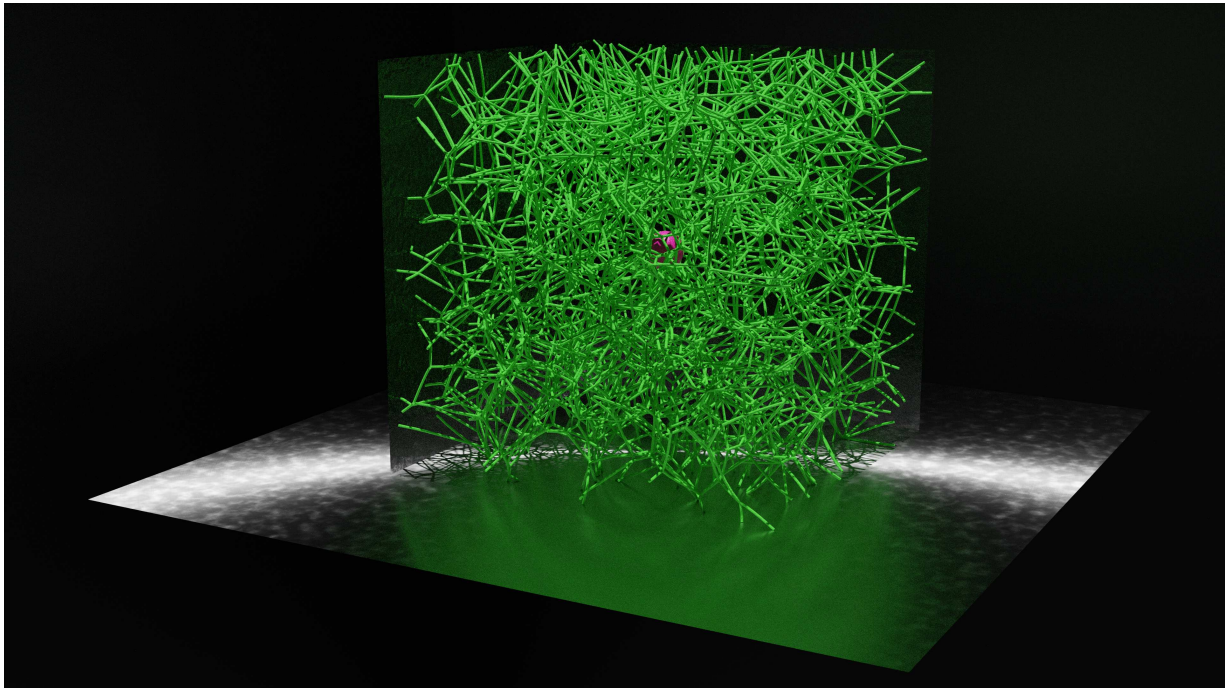
(a)
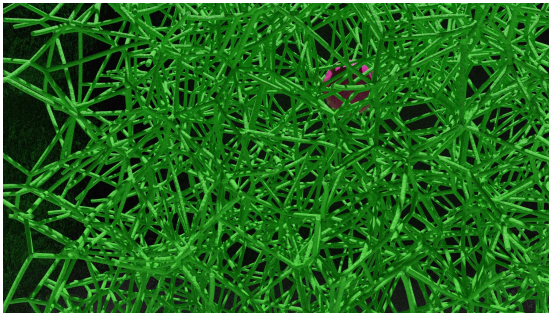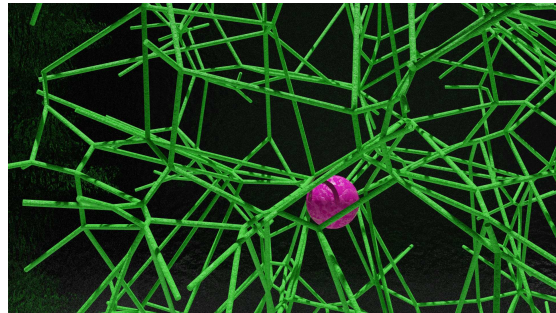
(b)   (c)
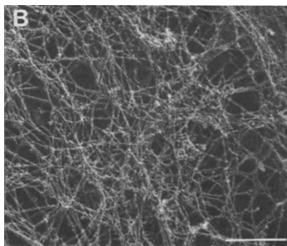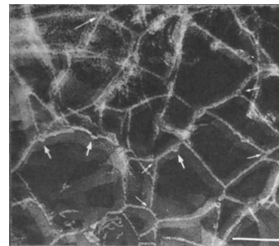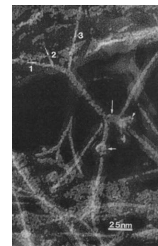
(d)   (e)   (f)

Figure 10.3.: (a) Image of an example network resulting for a second, very high value for the fiber volume fraction $\bar{V}_\mathrm{f} \approx 1.8\%$ considered in the simulations (box size is $10 \times 10 \times 10\,\mu\mathrm{m}$, rendered using Blender [14]). Comparison of (b) a magnified part of this network with (c) a magnified part of the network with the default fiber volume fraction $\bar{V}_\mathrm{f} \approx 0.4\%$ (shown in Figure 10.1(a)). (d)-(f) Electron microscopy images of human amniotic basement membranes (scale bars indicate $250\,\mathrm{nm}$, $50\,\mathrm{nm}$ and $25\,\mathrm{nm}$, reprinted from [166]).

In order to investigate and average out the influence of the specific network geometry, 5 different realizations of the random network generation process will be considered as input for the simulations for each – otherwise identical – set of input parameters in Sections 10.3.2 and 10.3.3, respectively. In contrast to the spherical particle, which will be discussed next, the fibers are assumed to be athermal because the lengths of the individual fiber segments are generally much smaller than their persistence length $\ell_p \approx 39\,\mu\mathrm{m}$ (resulting from the parameters for the bending stiffness given above and the thermal energy at room temperature $k_B T \approx 4 \times 10^{-3}\,\mathrm{aJ}$) and thermal undulations will therefore be negligible. However, for another network architecture with longer fiber segments or a different species of thinner and thus more flexible fibers such as mucin or F-actin, this effect might become important and may be included in the novel computational model by means of the formulation proposed in [32].

Finally, the spatial discretization of the fibers makes use of the geometrically exact Hermitian Simo-Reissner beam elements presented in Section 3.2.2. Its centerline interpolation by means of cubic Hermite polynomials ensures both a high accuracy in terms of spatial approximation and a C^1-continuous geometry representation. This is particularly important for smooth contact kinematics and smooth interaction force distributions as has been shown in the context of beam-beam interactions e.g. in Section 4.5 and 7. When creating the finite element discretization for each of the random network configurations, a default element length $l_{\mathrm{ele}} = 1\,\mu\mathrm{m}$ is used for each straight fiber segment and one additional shorter beam element is created for the remainder of the random segment length if needed. Based on the previous experience (from challenging scenarios with large deformations such as presented in Section 4.5) with this kind of beam finite element featuring fourth order spatial convergence, this is considered to be a sufficiently fine spatial resolution for the magnitude of deformations observed throughout this computational study such that the influence of the spatial approximation error on the results is expected to be negligible. To conclude, this strategy typically leads to a number of fiber segments $n_f \approx 800$, a number of beam elements $n_{\mathrm{ele}} \approx 1600$, and a number of nodes $n_{\mathrm{node}} \approx 4000$ for $n_{\mathrm{VP}} = 60$. Likewise, for the densest network with $n_{\mathrm{VP}} = 600$, we obtain $n_f \approx 6200$, $n_{\mathrm{ele}} \approx 6200$, and $n_{\mathrm{node}} \approx 18700$.

10.2.2. Spherical particle

The particle is modeled as a rigid sphere and therefore uniquely described by its midpoint position $\boldsymbol{r}_p(t) \in \mathbb{R}^3$ as a function of the time t as well as its diameter $D_p = 1\,\mu\mathrm{m}$ that is chosen to comply with the experimental studies presented in [4, 97]. As in several of the aforementioned previous computational studies (e.g. [64, 65]), the Brownian dynamics of the particle is modeled by the Langevin equation (see e.g. [40]) including the stochastic thermal as well as viscous drag forces that are repeated here for the reader's convenience. The velocity-proportional drag force $\boldsymbol{f}_{\mathrm{s,visc}}$ implicitly models a quiescent surrounding fluid and makes use of the friction coefficient of a sphere $\gamma = 3\pi\eta D_p$ according to Stokes

$$\boldsymbol{f}_{\mathrm{s,visc}} = \gamma \boldsymbol{I}_{3\times3}\,\dot{\boldsymbol{r}}_p. \tag{10.1}$$

Here, $\dot{\boldsymbol{r}}_p$ denotes the particle velocity and the fluid viscosity is chosen as $\eta = 1\,\mathrm{mPa\,s}$, which corresponds to the viscosity of water at room temperature and has been found to be in good agreement with experimental tracer studies of freely diffusing particles [4]. Following the consistent

modeling of the Brownian dynamics of slender biopolymers within the space- and time-discrete theoretical framework of the nonlinear finite element method according to [32], the stochastic thermal forces acting on the sphere are given as

$$\boldsymbol{f}_{\text{s,stoch}} = \sqrt{2k_{\text{B}}T}\,\gamma\boldsymbol{I}_{3\times3}\,\frac{\partial^2\,\mathcal{W}(x,t)}{\partial\,x\,\partial\,t}. \tag{10.2}$$

Here, the thermal energy is set to $k_{\text{B}}T = 4.1\times10^{-3}\,\text{aJ}$ corresponding to room temperature and the last term describes the space-time white noise resulting from a two-dimensional Wiener process $\mathcal{W}(x,t)$. Both contributions from viscous and stochastic forces on the spherical particle are added to the total virtual work of the system, which other than that includes the contributions from internal elastic forces of the fibers and the contributions from the particle-fiber interactions that will be discussed next. Afterwards, the temporal discretization and time stepping scheme will be presented in Section 10.2.4.

10.2.3. Interactions between particle and fiber network

In view of the central research questions described above, the interactions between the spherical particle and the fiber network are the key component of this computational model. In accordance with the sophisticated, explicit modeling of elastic fibers, these interactions are modeled on the level of individual particle-fiber pairs and evaluated as a fully resolved, resulting line force distribution on the fiber. At this point, it becomes clear that the sophisticated fiber model including potentially large 3D deformations, which is a unique feature of this novel computational model, carries over to the interaction modeling in form of additional challenges to accurately and efficiently describe the sphere-fiber interactions for arbitrarily deformed fiber configurations and mutual orientations. Since the conclusion of previous experimental as well as computational studies is that the combination of repulsive steric and (attractive) electrostatic effects is the main reason for the effective selective filtering of biological hydrogels (see e.g. [4, 64, 97]), both interaction types are accounted for in the present model.

The key idea of the applied modeling approaches hereby is to consider the sphere-beam interaction as a simpler, special case of the beam-beam interaction, for which well-established formulations for (macroscopic) contact exist (cf. Section 3.3) and novel computational approaches for molecular interactions have been developed in Chapter 4 and Section 5. The resulting, derived formulations for contact as well as electrostatic interactions between a rigid sphere and a beam are presented in Section 6.3.1. Note in this respect that the most critical limitation of the computational model is the use of a Coulomb interaction potential law, which neglects the presence of counterions in the electrolyte solution and the associated screening of charges that in turn significantly reduces the range of electrostatic interactions in biological hydrogels. This can be seen as a pragmatic, simplified model chosen due to the current lack of a sphere-beam or beam-beam interaction formulation for screened electrostatic interactions and the implications will be discussed in the following paragraph.

Discussion of the neglect of screening effects.
Regarding the impact of this model assumption on the results of this computational study, it is

expected that the effect of charges in general and particularly the range of interaction is overestimated and that the simple applied Coulomb interaction model is thus not able to predict the particle mobility in a quantitatively correct manner. However, the qualitative behavior of the particle and the trends in the statistical quantities of interest such as the mean squared displacement (MSD) of the particle over time for varying charge density is expected to be meaningful and thus allow for both valuable insights in the biophysical system behavior and mechanisms as well as a first proof of principle for this novel computational modeling approach in general. Based on the experimental observations and in anticipation of the obtained simulation results, this reasoning is supported by the fact that the most effective trapping mechanism is the one of a persistent, strongly adhesive contact between the particle and the oppositely charged network fibers, which is a scenario with minimal surface separation and thus minimal screening effect. Therefore, the behavior of a particle with medium to large distance to the nearest fibers is thus expected not to be reproduced correctly by the Coulomb interaction model whereas in contrast the practically much more important regime of small separations should be represented with sufficient qualitative accuracy in order to allow for the aforementioned analysis of trends and basic mechanisms. In order to still account for the screening of charges, the cutoff distance of the interaction is set to $r_{\text{cutoff}} = 2\,\mu\text{m}$, which is defined via the separation of the sphere and fiber midpoint position and thus effectively neglects any interaction forces beyond particle-fiber surface separations of $g_{\text{cutoff}} \approx 0.96\,\mu\text{m}$. Finally, despite the fact that the development of a screened electrostatic interaction formulation for instance based on the Debye-Hückel approximation of the Poisson-Boltzmann theory would go beyond the scope of this computational study, it is clearly considered an important and promising future extension of the present model that should be used for both subsequent verification of the drawn conclusions and specific analysis of the influence of salt concentration as well as ion-specific effects observed in experiments [4].

The parametrization used throughout this study is given as follows. Based on assuming the dielectric permittivity of water (at room temperature) for the surrounding fluid, the constant prefactor of the Coulomb interaction potential law is obtained as $C_{\text{elstat}} \approx 1.12 \times 10^2\,\text{aJ}\mu\text{mfC}^{-2}$. As a first step and in accordance with all previous computational studies, the surface charge density of the fibers as well as of the particle is assumed to be homogeneous and constant along the fibers. In view of the complex, inhomogeneous molecular architecture and thus charge distribution of individual biopolymer filaments (cf. Section 9) and moreover the complex constitution of a real biological hydrogel, this model assumption is once again expected to have a significant influence on the quantitative accuracy of the results. However, it should still allow for qualitative analysis of trends and mechanisms, as argued above in the context of the electrostatic interaction model. Concerning a potential improvement on this point, it is rather a question of parametrization as the current sphere-beam interaction model is capable of describing varying line charge distributions along the filaments as has been demonstrated in Section 9. Here, a constant, homogeneous line charge density of the fibers $\lambda_{\text{f}} = -0.25\,\text{fC}\mu\text{m}^{-1}$ is assumed and the positive surface charge of the particle will be varied in Section 10.3.2 to study its influence on the particle mobility. Finally, a total of 10 integration points per beam element is used to evaluate the contributions of the electrostatic line force distribution along the fibers by means of Gaussian quadrature.

Turning to the repulsive steric interactions and following the reasoning in Section 6.2, it seems appropriate to apply a penalty contact formulation that effectively precludes any noticeable pen-

etration of particle and fibers. Throughout this study, a linear penalty law and a constant penalty parameter $\varepsilon = 100\,\mathrm{pN\mu m}^{-1}$ is chosen, which turned out to be sufficiently large such that the maximum penetration of particle and fiber is smaller than 5% of the fiber diameter D_f even in the most challenging scenarios of strongly adhesive contact and sudden stochastic forces on the particle in the direction towards the fiber. Finally, 15 collocation points per beam element are used for the evaluation of the contact line force distribution along the fibers.

At the end of this section, note that fiber-fiber interactions (apart from the obvious rigid connections of endpoints at the network vertices) are generally neglected, because they are assumed to be negligible due to the fact that their mutual separation and orientation is almost entirely fixed by the chemical binding at their endpoints. However, beam-beam interaction formulations for both steric repulsive and electrostatic interactions are readily available (cf. Section 3.3, Chapter 4, and Section 5) and could be incorporated without any conceptual difficulties as a future extension of this computational model.

10.2.4. Temporal discretization

In addition to the already discussed spatial discretization of the fibers via beam finite elements, the problem is discretized in time via finite differences. Specifically, the resulting system of first order stochastic partial differential equations in time is discretized by means of a Backward Euler scheme, as proposed in [32]. Starting from a default time step size of $\Delta t = 10^{-3}\mathrm{s}$, an adaptive time stepping scheme is applied, which is especially important to resolve the highly nonlinear dynamics during (adhesive) contact interactions and potentially large sudden changes in the magnitude and direction of the thermal forces. The total simulation time per run is set to $t_\mathrm{end} = 20\,\mathrm{s}$, which generally leads to a required number of time steps in the range of $n_\mathrm{step} \in [2 \times 10^5, 3 \times 10^5]$. In order to account for the stochastic nature of the thermal forces driving the particle motion, generally two or more random realizations for each – otherwise identical – set of input parameters (i.e. identical, random network geometry and interaction parameters) are computed and considered in the analyses to be presented in Section 10.3.

10.2.5. Boundary conditions

Periodic boundary conditions are applied at each side of the simulation box shown in Figure 10.3(a). Thus, once the particle as well as (parts of) fibers leave the representative volume element at any side, they reenter it on the opposing side. Moreover, the steric as well as electrostatic interactions are evaluated also across periodic boundaries. In the majority of the simulations considered in Section 10.3, no other boundary conditions are applied. However, in a certain batch of simulations, the entire network of fibers will be fixed by means of Dirichlet boundary conditions in order to serve as a reference solution mimicking the limiting case of rigid fibers.

10.2.6. Postprocessing and quantities of interest

Since this study focuses on the (hindered) diffusive mobility of particles, the most important raw data obtained from the simulations is the particle midpoint position in every time step. From

this point on, the postprocessing procedure is equivalent to experiments that track the motion of individual fluorescent tracer particles (e.g. [4, 96, 97]). Based on the discrete time sequence of particle positions, the mean squared displacement (MSD) $< \Delta r_{\mathrm{p}}^2 >$ is computed for the range of time intervals $\tau \in [\Delta t, t_{\mathrm{end}}]$ observable in one simulation run as follows.

$$< \Delta r_{\mathrm{p}}^2 > = \frac{1}{N_\tau} \sum_{i=0}^{N_\tau} \left(\boldsymbol{r}_{\mathrm{p}}(i\Delta t + \tau) - \boldsymbol{r}_{\mathrm{p}}(i\Delta t) \right)^2 \tag{10.3}$$

Here, N_τ denotes the number of all distinct (but possibly overlapping) time intervals τ obtained for one simulation run. Because the number of *independent* samples obtained for large time intervals is naturally limited, only the first 10% of the maximal possible time intervals, i.e., $\tau \in [\Delta t, 0.1 \cdot t_{\mathrm{end}}]$, will be considered in the statistical analyses. However, the remaining data is included and indicated by a gray background in all the MSD plots to be presented. Moreover, the mean and standard deviation of the MSD obtained for several realizations of the random network geometry as well as several realizations of the stochastic process of thermal forces will be considered. As the majority of the considered scenarios shows a subdiffusive behavior, the MSD curves over the time interval will be presented and discussed instead of the (apparent) diffusion constant, which obviously depends on the considered time interval and could still be computed from the MSD curves if desired. Other simulation results such as the resulting axial strains of the fibers will be presented and discussed for a few specific investigations wherever needed for the interpretation of the system behavior.

10.3. Results and discussion

The following discussion of simulation results is divided into three parts. First, in Section 10.3.1, we study the influence of collisions of the particle with the fiber network on the particle mobility. Second, the effect of additional attractive electrostatic interactions between the particle and the fiber network will be investigated in Section 10.3.2. Finally, Section 10.3.3 analyzes the special role of the fiber stiffness in the case of the most effective hindrance mechanism observed in the simulations.

10.3.1. The effect of solely repulsive steric interactions

To begin with, the double-logarithmic plot of the particle's MSD $< \Delta r_{\mathrm{p}}^2 >$ as a function of the time interval τ shown in Figure 10.4(a) confirms the validity of the applied Brownian dynamics model, because the results obtained for free diffusion of the particle (red line with circles and error bars) excellently match the analytical reference solution (black dashed line). Moreover, the standard deviation of the mean over ten random realizations as indicated by the error bars is negligible within the first 10% of the time interval range (indicated by the white background) that is considered in the following analyses.

(a)

(b)

(c)
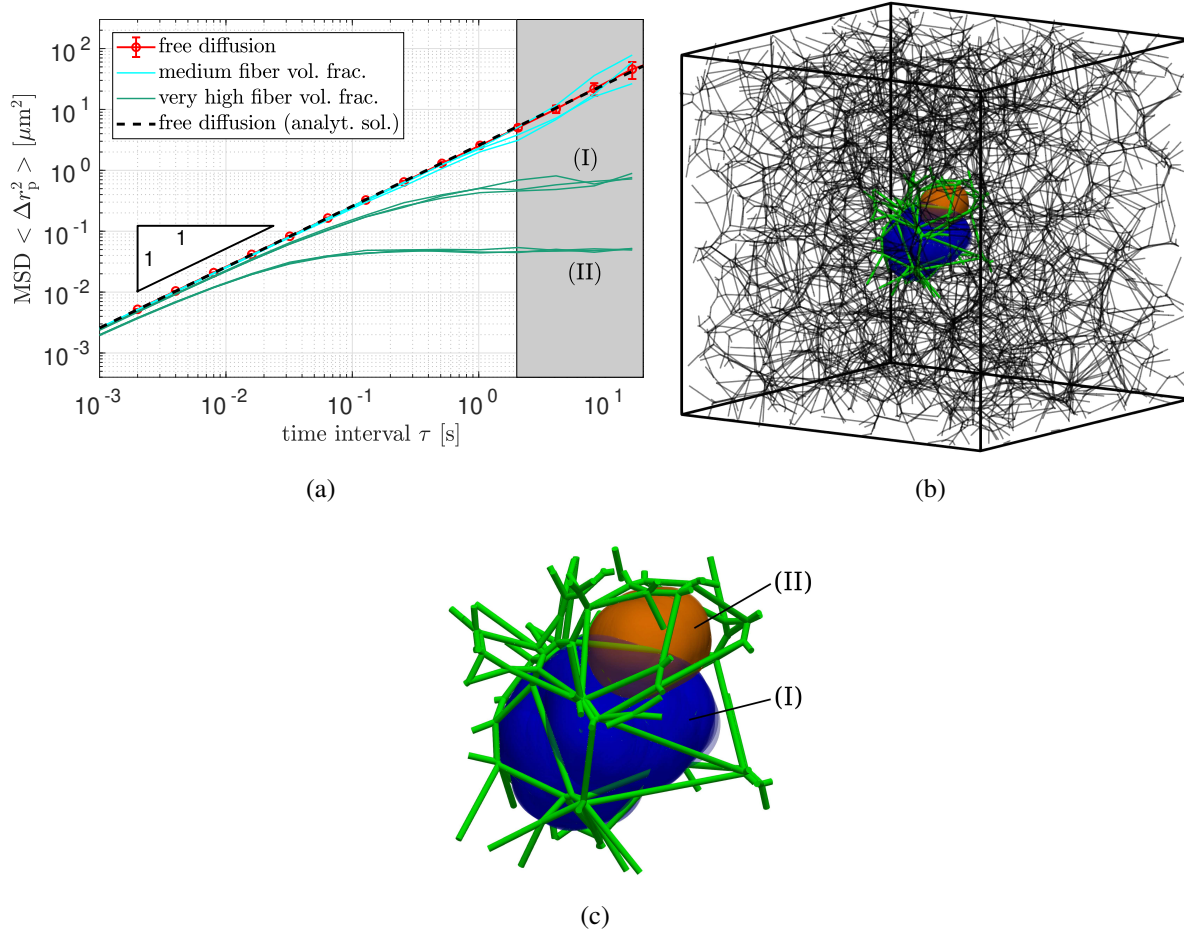
Figure 10.4.: (a) Mean squared displacement (MSD) $< \Delta r_p^2 >$ as a function of the time interval τ: Mean and standard deviation over ten random realizations for the case of free diffusion (red line with circles and error bars), three individual random realizations for a medium fiber volume fraction $\bar{V}_f \approx 0.4\%$ resulting from tessellation with $n_{VP} = 60$ Voronoi points (cyan lines), two sets of three individual random realizations each for a very high fiber volume fraction $\bar{V}_f \approx 1.8\%$ resulting from tessellation with $n_{VP} = 600$ Voronoi points (green lines). The analytical solution for the case of free diffusion is plotted as a reference (black dashed line). The gray background indicates the range of time intervals above 10% of the simulation time, where only few independent samples are available for computing the MSD. (b) Network with very high fiber volume fraction $\bar{V}_f \approx 1.8\%$ and overlay of all observed particle positions in one simulation run corresponding to either the high MSD plateau value (I, blue) or the low value (II, orange). (c) Magnified detail showing the two compartments with irregular polygonal shape that the particle can not leave.

Steric hindrance is insignificant as long as particle diameters are smaller than the smallest mesh sizes.

Turning to the influence of repulsive steric interactions, i.e., collisions of the particle with the fiber network, Figure 10.4(a) shows that a medium fiber volume fraction $\bar{V}_f \approx 0.4\%$ (cyan lines, see Figure 10.1(a) for an example of the network) has almost no perceptible influence on the MSD. Only above approximately $\tau = 0.5$ s, a very subtle subdiffusive behavior is observable for the three individual realizations plotted here, which is insignificant, but however indicates the occurrence of a few collisions if the particle travels over longer periods in time. On the one hand, this behavior of almost free diffusion of the particle is expected from the range of cell diameters $2.7 - 5.2\,\mu$m of this irregular polygonal network compared to the particle diameter $D_p = 1\,\mu$m. Moreover, previous experimental studies have made very similar observations for almost neutral particles or high salt concentrations that effectively shield any electrostatic interactions [4, 96, 97]. However, this is the first computational study with a realistic, irregular polygonal fiber network geometry and thus an important confirmation that the effect of solely steric hindrance is indeed negligible in this regime where the ratios of network mesh sizes and particle diameter are greater than one.

Particles with diameters in the range of the mesh sizes are caged in polygonal compartments of random size and show confined diffusive behavior.

To push this to the limit where purely steric hindrance and thus filtering by particle size will become significant, a ten times larger number of Voronoi points $n_{VP} = 600$ corresponding to a fiber volume fraction of $\bar{V}_f \approx 1.8\%$ and cell diameters of $1.0 - 2.5\,\mu$m, i.e., in the order of the particle diameter $D_p = 1\,\mu$m, has been applied. An example of the resulting network architecture is illustrated in Figure 10.3(a). To probe the most extreme effect of steric hindrance, the fibers are completely fixed in space for these two sets of three random realizations each. The results are plotted in Figure 10.4(a) (green lines). One of the sets shows close to normal diffusive behavior on very small time scales up to approximately $\tau = 0.05$ s and eventually reaches a plateau value of $< \Delta r_p^2 > \approx 0.7\,\mu$m^2 beyond $\tau \approx 1$ s. The other set, which are random realizations using the identical fiber network geometry, but a different initial position of the particle, shows a significantly subdiffusive behavior already for the smallest considered time intervals and quickly reaches a plateau value of $< \Delta r_p^2 > \approx 0.05\,\mu$m^2 for any time interval longer than $\tau \approx 0.1$ s.

This is an expected behavior for the diffusion of particles in an irregular network with cell diameters of the same order as the particle diameter and therefore randomly connected sufficiently large cells that together form a polygonal volume surrounding the initial position of the particle, which the particle can not leave at all. The specific compartments that the particle is able to explore starting from either of the two initial positions in the identical network are illustrated in Figure 10.4(b) and 10.4(c). Here, the overlay of all particle positions throughout the entire simulation is shown in dark blue for the case of the higher MSD plateau value (I) and in orange for the case of the lower MSD plateau value (II) observed in Figure 10.4(a). This behavior is known as confined diffusion and has been theoretically described and experimentally observed e.g. in the context of studying cadherin molecule mobility in plasma membranes [88]. As discussed e.g. in [162], such a filtering mechanism based on size clearly has a very effective selectivity and is applied by organisms to strictly preclude the access of any objects larger than the characteristic

mesh size, e.g. of the nasal mucous membrane.

However, there are still open questions concerning the mobility of (medium to) large objects in biological hydrogels taking into account the continuous reorganization of biopolymer networks based on both (de-)polymerization and the transient nature of crosslinks. Such a transport mechanism for relatively large particles has been observed in experiments [89] and recently been investigated also in a theoretical and computational model [58], where crosslink binding dynamics are influenced by the diffusing particle. It is also suggested that this kind of mechanism could play a role in the selective permeability of the nuclear pore complex, for which the governing principles are still under debate (see e.g. the review article [162]). Replacing the Voronoi-type network in the present computational model by the one of a transiently cross-linked, self-assembled network driven by Brownian motion [34, 35] is thus considered a promising future step.

10.3.2. The effect of additional attractive electrostatic interactions

In addition to repulsive steric interactions, attractive electrostatic interactions due to uniformly distributed, opposite charges on the particle and the fibers will now be considered. This has been confirmed to be the most effective hindrance mechanism for particles smaller than the mesh sizes both in experiments (e.g. [4, 96, 97]) and simulations (e.g. [64, 65]).

On average, the degree of subdiffusion increases with the strength of attraction.
The resulting MSD curves for a low (green), medium (cyan), and high (red) value of the particle's surface charge Q_p are shown in Figure 10.5 and compared to the analytical reference solution for free diffusion (black dashed line). The fiber volume fraction $\bar{V}_f \approx 0.4\%$ is identical for all simulation runs and 5 different random network geometries with 2 random realizations of the stochastic forces each have been simulated for each of the three different charge values. Figure 10.5(b) shows these 10 independent realizations for each particle charge value and the corresponding mean values and standard deviations are plotted in Figure 10.5(a). On average, the degree of subdiffusion increases with the strength of attractive interaction, which has been suggested by previous experiments (e.g. [4, 96]), and has been confirmed by previous computational studies using ordered (e.g. [65, 116]) and unordered arrays of straight, rigid, mutually orthogonal fibers [64]. Here, the smallest charge value $Q_p = 0.125 \times 10^{-3}$ fC leads to a very small degree of subdiffusion, which is in fact quite similar to the one observed in the limit of no charge shown in Figure 10.4(a). In contrast, medium (cyan) and high charge values (red), which are a factor of 8 and 64 higher, significantly hinder the diffusion of the particles already on (very) small time scales $\tau < 0.1$ s. In this regime, the slopes of the MSD curves are however close to one, which suggests normal diffusive behavior with a decreased diffusion constant.

The variability of MSD values and slopes increases for longer time intervals, which indicates that particles randomly switch between distinct motion patterns.
This almost normal diffusive behavior with slope values close to one on very small time scales changes drastically for longer time intervals $\tau > 0.1$ s, where the individual realizations exhibit slopes in the broad range from zero to one, and even some examples for superdiffusive behavior with a slope greater than one can be observed for medium charge values. Such a significant

(a)　　　　　　　　　　　　　　　　(b)
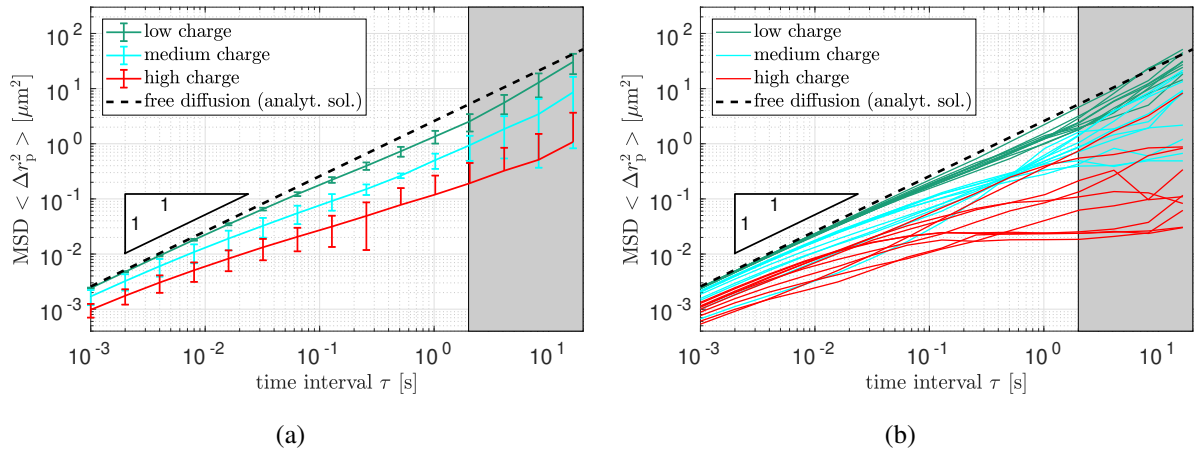
Figure 10.5.: Mean squared displacement (MSD) $< \Delta r_\mathrm{p}^2 >$ as a function of the time interval τ: (a) Mean and standard deviation over five random network geometries and two random realizations each and (b) corresponding individual realizations for three different values of the particle's surface charge: Low charge $Q_\mathrm{p} = 0.125 \times 10^{-3}$ fC (green), medium charge $Q_\mathrm{p} = 10^{-3}$ fC (cyan), and high charge $Q_\mathrm{p} = 8 \times 10^{-3}$ fC (red). The fiber volume fraction $\bar{V}_\mathrm{f} \approx 0.4\%$ is identical for all these realizations. The analytical solution for the case of free diffusion is plotted as a reference (black dashed line). The gray background indicates the range of time intervals above 10% of the simulation time, where only few independent samples are available for computing the MSD.

increase in the variation of MSD values as well as slopes is in excellent agreement with the experimental results from [4]. Their subsequent analysis of squared displacement values over time revealed the existence of sudden trapping and escape events of particles switching between an almost free, a loosely bound, and a tightly bound state. This hypothesis is confirmed by the simulation results shown in Figure 10.6(a), where very similar motion patterns can be observed.

(Strongly) charged particles jump between local aggregates of fibers, i.e., opposite charges. While the causal link of trapped states and local aggregation of fibers, i.e., charge patches of opposite sign, has already been suggested in several experimental studies (e.g. [4, 96]), the limited spatio-temporal resolution of single particle tracking and imaging has so far precluded a direct proof. The particle trajectory shown in Figure 10.6(b) and the detail view of the fiber aggregates corresponding to the three observed trapped states illustrated in Figure 10.6(c) clearly confirm this causality. Related observations have been made in the recently published computational study [64], which for the first time considered disorder in the still rigid, straight, mutually orthogonal fibers and described a resulting, so-called dense-region trapping. In the present study, the random, irregular polygonal network structure very similar to the one of real biological hydrogels (cf. Figures 10.1 and 10.3) allows for a more detailed analysis of this trapping mechanism. Particularly, these fiber aggregates are found at network vertices and small polygonal faces in the network that have a lateral spatial extension smaller than the particle diameter. Figure 10.6 also suggests that the magnitude of the remaining thermal fluctuations observed in the squared
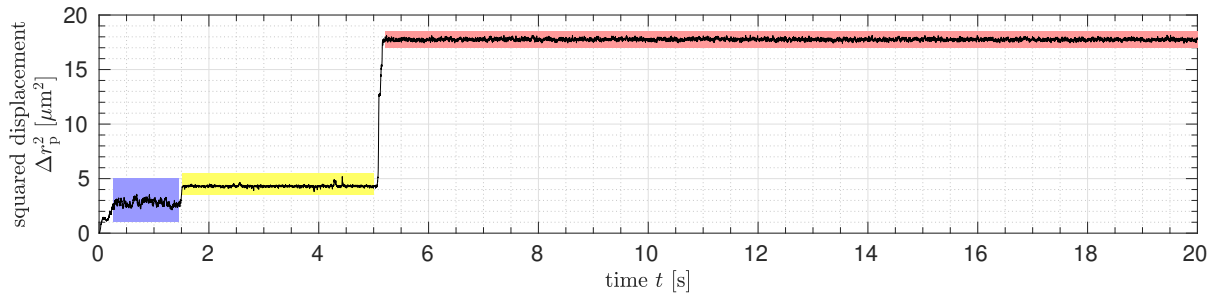
(a)
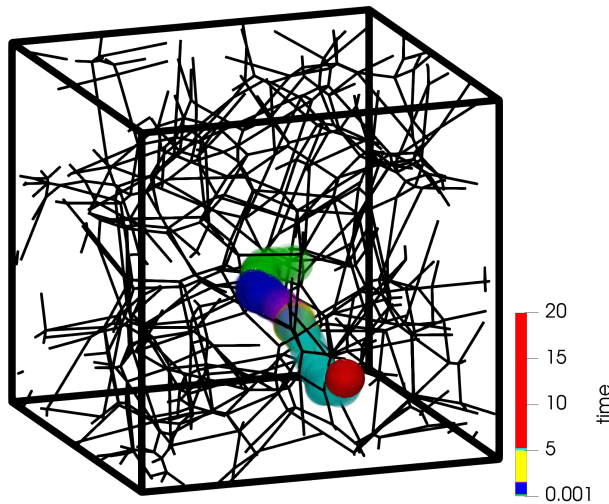
(b)
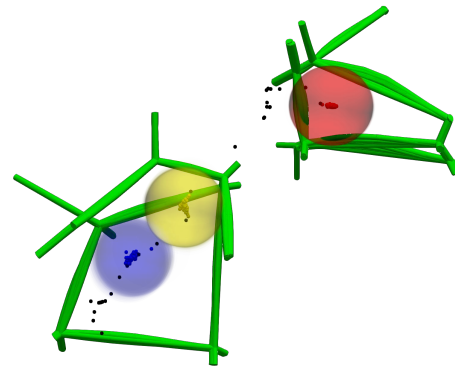
(c)

Figure 10.6.: One realization with high charge $Q_\mathrm{p} = 8 \times 10^{-3}\,\mathrm{fC}$ and medium fiber volume fraction $\bar{V}_\mathrm{f} \approx 0.4\%$ that exhibits three distinct trapped states with sudden transitions ("jumps") between them. (a) Squared displacement Δr_p^2 over the simulation time t. (b) Particle trajectory with color indicating the characteristic intervals of simulation time where the particle is either trapped or jumps between the trapped states. (c) Detail view showing an overlay of the particle positions in the three distinct trapped states and an overlay of the (oppositely charged) fiber aggregates that are responsible for the effective trapping. Colors indicate the corresponding time intervals in (a) and (b).

displacement of the particle are a measure for the strength of the trapping and that this strength is proportional to the local fiber, i.e., charge, density. Finally, the results suggest that the stronger the particle is immobilized, i.e., the smaller the fluctuations in the squared displacement are, the longer will the particle remain at this location.

The irregularity in the fiber/charge distribution gives rise to three distinct motion patterns, one of which allows the particle to travel via successive jumps.
From a mechanical point of view, the spatially varying distribution of fibers and thus charges gives rise to a random 3D potential field to be explored by the particle (similar to the one used in Chapter 8 to study the effect of filament prestress in biopolymer networks). The location and values of the (local) minima in the potential field as well as the potential barrier and paths connecting them strongly depend on the characteristic geometrical properties of the network such as connectivity, distribution of fiber segment lengths and the resulting distribution of cell and mesh sizes. Considering real biological hydrogels further extends the list of crucial influencing factors by the type and fractions of load-carrying components and their specific surface charge distributions. All these factors shaping the characteristic potential landscape will determine whether and how the stochastic thermal excitation causes the particle to either (1) remain at one location being completely immobilized, (2) cycle between neighboring minima being restricted to a certain region, or (3) travel through the hydrogel via jumps – potentially also over long distances.

Among the realizations shown in Figure 10.5(b), all three motion patterns (1)–(3) can be identified. For long time intervals $\tau > 0.1\,\mathrm{s}$, both patterns (1) and (2) lead to a similar behavior of confined diffusion as obtained for the case of caged particles considered in the previous section[3]. The plateau MSD value thus allows to draw conclusions with respect to the volume enclosed by the particle's initial position and the location(s) of the potential minimum/minima (i.e. fiber/charge agglomerations) that the particle has visited. By looking at the sequence of snapshots over the entire simulation time, it has been verified that those four (highly charged) particles with the smallest MSD plateau values of $< \Delta r_\mathrm{p}^2 > \approx 2 \times 10^{-2}\,\mathrm{\mu m^2}$ are completely immobilized at one single location in the network (cf. motion pattern (1)). In contrast, those medium and highly charged particles with intermediate values for the MSD slopes jump or smoothly transit between local fiber agglomerations in cycles (cf. motion pattern (2)) such as observed in the example shown in Figure 10.7. Finally, also motion pattern (3) has been identified in the set of individual realizations, as already shown in Figure 10.6 for a particle with high surface charge. This case can easily be identified among the MSD curves plotted in Figure 10.5(b) as the one with the largest MSD values for long time intervals.

To conclude this section it can be stated that strong attractive forces mostly lead to motion patterns (1) and (2) that effectively immobilize the particles in a confined volume. However, the motion pattern (3) allows – at least theoretically – for a travel of particles over considerable distances by means of a series of successive jumps. The effectiveness of this transport mechanism depends on the irregularity of the fiber/charge distribution in space and in particular the (relative) height of the potential barriers between the fiber/charge agglomerations. While the specific ex-

---

[3]Note however the difference in the diffusive behavior for small time intervals $\tau < 0.1\,\mathrm{s}$ that allows to differentiate between purely steric hindrance (cf. Figure 10.4(a)) and additional attractive interactions (cf. Figure 10.5(b)).
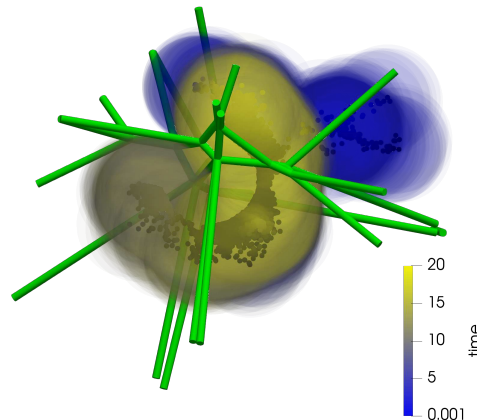
Figure 10.7.: Particle trajectory for one realization with medium charge $Q_{\mathrm{p}} = 1 \times 10^{-3}\,\mathrm{fC}$ and medium fiber volume fraction $\bar{V}_{\mathrm{f}} \approx 0.4\%$ that smoothly cycles around a region of fiber/charge agglomeration. Color indicates the course of the simulation time t.

ample observed in Figure 10.6 seems to be completely immobilized after two consecutive jumps, one might think of another, special design of the fiber/charge distribution with a certain degree of periodicity that could lead to an effective transport of the particle also over large distances and in small time intervals. One could speculate that such a directed motion might even lead to superdiffusive behavior.

Altogether, the results of this section indicate that the irregularity of the potential landscape has a crucial influence on the overall effectiveness of particle immobilization and therefore on the selectivity of hydrogels. The aforementioned factors shaping the effective potential field explored by the particle are known to vary substantially between the multitude of different biological hydrogels (see e.g. [162]). Therefore, a systematic parametrization (and if required also extension) of the present computational model with respect to other classes of gels is expected to be a valuable means for studying the species-specific variations of the general behavior and principles observed so far. In the long run, this might even lead to simulation-based prediction tools enabling a case-specific choice or design of drug delivery vehicles.

Brief discussion of computational aspects.
In total, 60 simulations with at least 2×10^4 time steps each have been conducted and evaluated for the results shown in this section (cf. Figure 10.5(b) for all the realizations). One simulation typically took 2–4 days if run in parallel on 16 cores[4] on a Linux cluster. The main drivers for the computational cost are the fiber volume fraction and the presence and strength of electrostatic interactions leading to a complex interplay of repulsive steric and attractive electrostatic forces that require a fine temporal resolution (i.e. smaller time steps) and make the nonlinear problem more challenging to solve.

---

[4]AMD Opteron 6128

10.3.3. The influence of fiber stiffness/compliance

Up to this point, we haven't discussed the influence of the fiber stiffness, which mainly influences the amount of fiber deformations and – besides the realistic network geometry – is the second unique feature of the present computational model. In the problem setup considered here, fiber deformations originate exclusively from contact and/or electrostatic interactions with the Brownian particle. Thus, the highest particle charge $Q_p = 8 \times 10^{-3}$ fC will be considered in this section, because the most frequent and strongest interactions can be expected in this case. To explore the point where fiber deformations begin to change the results, the value for Young's modulus has been varied systematically starting from the theoretical limit of rigid fibers as outlined already in Section 10.2.1. In the following, the results for rigid fibers will thus be compared to those obtained for a value of $E = 0.1$ MPa where first differences are observable, and to the ones obtained for a ten times larger value $E^* = 10 \cdot E = 1$ MPa, which are basically identical to the case of rigid fibers.

Figure 10.8 compares the MSD curves obtained for the low fiber stiffness resulting for Young's modulus E (red lines) with the ones obtained for a ten times higher value for Young's modulus E^* (yellow lines) and the ones obtained for the limit of rigid fibers (cyan dashed lines). Apart
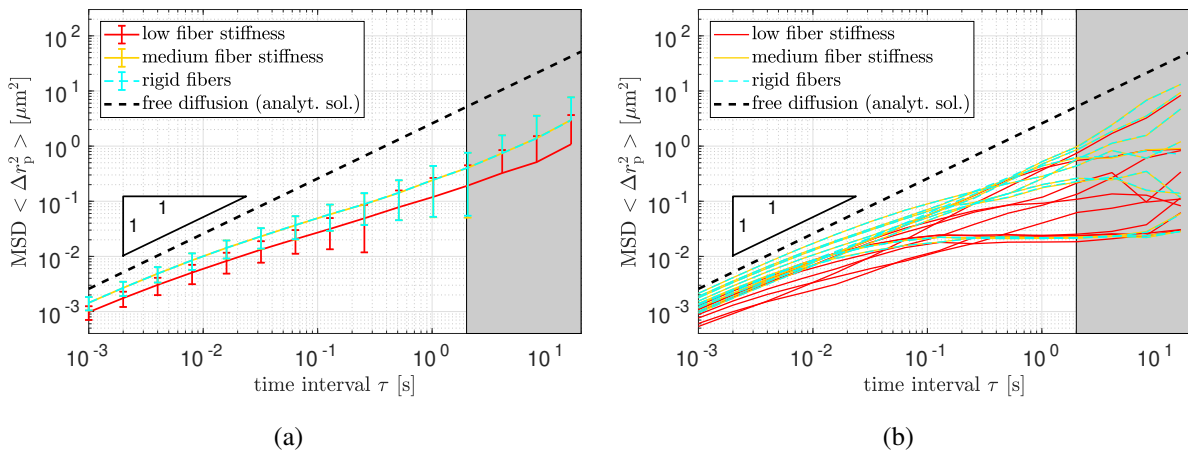
Figure 10.8.: Mean squared displacement (MSD) $< \Delta r_p^2 >$ as a function of the time interval τ: (a) Mean and standard deviation over five random network geometries and two random realizations each and (b) corresponding individual realizations for different levels of fiber stiffness: Low value for Young's modulus $E = 0.1$ MPa (red, see also Figure 10.5), medium value for Young's modulus $E^* = 1$ MPa (yellow), and the limit of rigid fibers (cyan). The fiber volume fraction $\bar{V}_f \approx 0.4\%$ and particle's surface charge $Q_p = 8 \times 10^{-3}$ fC is identical for all these realizations. The analytical solution for the case of free diffusion is plotted as a reference (black dashed line). The gray background indicates the range of time intervals above 10% of the simulation time, where only few independent samples are available for computing the MSD.

from the fiber stiffness, the compared sets of ten realizations are identical, notably with respect to the 5 different random network geometries and the 2 different sequences of the random stochas-

tic forces each.

The influence of fiber compliance on the particle mobility is insignificant for realistic values of Young's modulus.
There is no perceptible difference between the results for the medium fiber stiffness using E^* and those for the limiting case of rigid fibers. Recall from Section 10.2.1 that the value E^* is already a factor of 100 smaller than the reported values for ECM gels and has been chosen here solely to show the limit above which the results will be (almost) identical to the ones for rigid fibers. For the lowest considered fiber stiffness E, the curves are slightly shifted towards smaller MSD values, however, the difference is insignificant due to the considerable variability observed already in the results of the last section. This becomes even more clear if three pairs of otherwise identical realizations, i.e., particularly with identical network geometry and identical sequence of stochastic forces, yet different fiber stiffness are exemplarily compared in detail as shown in Figure 10.9. The first pair of realizations with otherwise identical parameters (both marked with
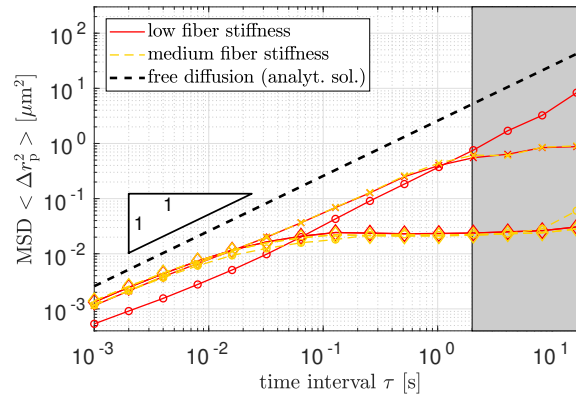
Figure 10.9.: Mean squared displacement (MSD) $< \Delta r_\mathrm{p}^2 >$ as a function of the time interval τ for three individual realizations (circles, crosses, and diamonds) of each value for the fiber stiffness (red: E, yellow: E^*). The analytical solution for the case of free diffusion is plotted as a reference (black dashed line).

crosses) shows almost identical results for E (red) and E^* (yellow). The second pair of realizations, i.e. using a second sequence of stochastic forces, with otherwise identical parameters (both marked with circles) leads to entirely different results for E (red) and E^* (yellow). This leads to the conclusion that tiny differences in the fiber behavior can trigger entirely different particle trajectories in individual realizations of the stochastic process. However, the deviations between these individual realizations are large also for identical fiber stiffness (cf. Figure 10.8(b)) and on average, there is no significant influence of the fiber stiffness on the particle mobility as becomes clear from Figure 10.8(a). Still, these results allow to conclude that – for the given set of parameters – a value below E^* will begin to influence the simulation results. To investigate the trends to be expected for even softer fibers, the third and last pair of realizations shall prove useful.

For very soft fibers, the MSD values are shifted to lower values in short time intervals and to higher values on long time intervals.
This third pair of realizations with otherwise identical parameters considered in Figure 10.9 (both marked with diamonds) once again shows the identical *qualitative* behavior for E (red) and E^* (yellow). However, the MSD values for the stiffer fibers E^* are slightly smaller on long time intervals and slightly larger on short time intervals. This interesting detail reveals the expected behavior of compliant fibers as will be further analyzed and discussed in the following. To begin with, it is an intuitive result that the stiffer fibers constrain the particle motion more effectively on long time intervals, because the compliant fibers deform due to the thermal forces acting on the trapped particle as illustrated in Figures 10.10(a) and 10.10(b) showing an overlay of fiber configurations for all time steps. On short time intervals, however, the opposite effect

<div align="center">(a)   (b)   (c)</div>
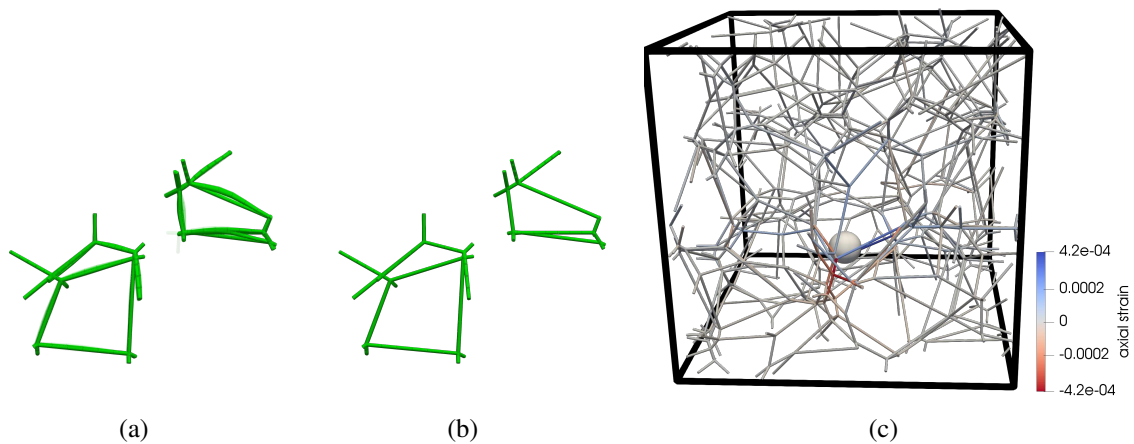
Figure 10.10.: Comparison of the amount of fiber deformations visualized by an overlay of the configurations from all time steps: (a) low fiber stiffness E leading to noticeable fiber deformations; (b) ten times larger fiber stiffness $E^* = 10 \cdot E$ preventing basically any deformations. (c) Visualization of the magnitude and distribution of axial strains in the fiber network resulting from the thermal excitation of the particle for a low fiber stiffness E.

can be observed and the stiffer fibers allow for slightly larger fluctuations of the particle and thus MSD values. This is most likely due to the fact that the increased effective drag coefficient of the compound consisting of the sticky particle and the surrounding, deformable fibers leads to a decreased diffusion constant and thus smaller MSD values. The plot of the axial strains in the network (at an arbitrarily chosen point in time) shown in Figure 10.10(c) allows to judge the amount of axial deformation and how this perturbation spreads across the fiber network. It confirms that the surrounding fibers are deformed due to the interaction with the thermally excited particle and that both tension and compression occurs and decays with increasing distance from the particle, however, the magnitude of strains is generally negligible.

To conclude this section, it can be stated that the influence of fiber deformation on the particle mobility is negligible in the here considered scenario and for realistic parameter values of the fiber stiffness in ECM gels. If very soft fibers are considered, the fiber compliance leads

to a decrease of MSD values on short time intervals and an increase of MSD values on long time intervals (for particles that are effectively trapped sticking to oppositely charged fiber agglomerations). In real systems, these trends might be observable as a result of dysregulated fiber stiffness or for certain (biological) hydrogels with very thin or soft and therefore compliant filaments such as mucin or F-actin.

10.4. Conclusions and outlook

This chapter presents the first computational study of the diffusive mobility of particles in hydrogels with a realistic fiber network model. It proposes a novel computational approach based on, most notably, the modeling of deformable fibers via beam theory, a Voronoi tessellation of the periodic simulation box to obtain random, irregular network geometries, and the beamsphere interaction model for contact and electrostatic interactions from Section 6.3.1. After a model validation and the investigation of only repulsive steric interactions in Section 10.3.1, the particularly important effect of additional attractive electrostatic forces has been studied in Section 10.3.2. Finally, a specific look at the role of fiber deformations has been presented in Section 10.3.3.

In the case of only repulsive steric interactions, it is found that the hindrance of the particle mobility is insignificant as long as the mesh sizes of the fiber network are larger than the particle diameter. If, however, the mesh sizes are in the order of the particle diameter, the particle is effectively caged in a polygonal fiber hull of random shape and size and shows a behavior known as confined diffusion and characterized by a plateau in the MSD curve for long time intervals. Within the given problem setup and the focus on relatively small particles, these are expected results validating the novel approach. However, this effect of steric hindrance will become highly relevant if the effective transport of relatively large particles as observed in experiments [89] is considered. In this context, including the dynamics of the fiber network such as its self-assembly driven by Brownian motion and transient reorganization of cross-links (as demonstrated for the directly compatible computational model applied in [34, 35]) might be an important model component as suggested by recent findings in the context of the nuclear pore complex [26, 58] or the dynamic secretion and shedding of mucus layers [105].

Turning to the effect of additional electrostatic interactions between the fibers and the oppositely charged particle, the prevailing notion that the degree of hindrance on average increases with the strength of attraction has been confirmed by the numerical experiments with five different network geometries and two random realizations each. Moreover an increased variability of the particle's mean squared displacement values and slopes in the regime of long time intervals has been observed and excellently agrees with previous experimental results from [4]. A detailed look at the 3D particle trajectories within the fiber network provides a first direct proof for the existence of distinct motion patterns of the particles that explain the variability in the MSD curves. As hypothesized before in [4], the particles stick to oppositely charged fiber/charge aggregations experiencing more or less strong trapping and eventually escape due to the continuous thermal excitation only to be quickly attracted to another fiber/charge aggregation. While some particles remain completely immobilized at one and the same location for the entire 20s of simulation time, others smoothly or rapidly cycle between two local minima in the potential landscape.

Both of these motion patterns lead to a behavior on longer time intervals that is very similar to the confined diffusion described for caged particles above, however the diffusive mobility on short time intervals is significantly reduced as well due to sticking to the fibers. A third observed motion pattern is the one of several successive jumps that – at least theoretically – could be a transport mechanism also over longer distances if the potential landscape is formed accordingly and e.g. shows some degree of periodicity and directional preference.

Altogether, these findings indicate that the precise shape of the effective 3D potential field explored by the particle has a crucial influence on its mobility. In view of the broad variety of biopolymer hydrogels with diverse chemical compositions and biophysical properties, the current computational model could thus be leveraged to study the individual selective filtering behavior for a large number of particle-hydrogel property combinations. Based on the recognized importance of the precise fiber/charge distribution in the system, two points seem to be of particular importance to achieve a case-specific, highly accurate and reliable prediction. First, the inhomogeneous charge distribution along the fiber should be both determined (e.g. by analyzing the molecular architecture) and applied in the model as demonstrated for the example of mucin in Chapter 9. Second, the specific composition and geometry of fiber networks should be determined (e.g. by processing of electron microscopy images) and applied in the model. Also the inclusion of the dynamic self-assembly and reorganization of networks mentioned above would be worth considering in this respect.

As a last particular aspect investigated in this study, fiber deformations have been found to be negligible for the range of realistic values for the fiber stiffness. To be more precise, varying the value for the Young's modulus over the range of reported values for the considered ECM gels has led to identical results as obtained for the theoretical limit of rigid fibers. If, however, very soft fibers are considered, the fiber compliance caused a decrease of MSD values on short time intervals and an increase of MSD values on long time intervals (for particles that are effectively trapped sticking to oppositely charged fiber agglomerations). In real systems, these trends might be observable as a result of dysregulated fiber stiffness or for certain (biological) hydrogels with very thin or soft and therefore compliant filaments such as mucin or F-actin.

In addition to the specific numerical results and gained insights, this study provides an extensive proof of concept for the application of the novel computational model. As outlined above, many important findings especially for various particle/hydrogel-specific behaviors and mechanisms can be expected from different parametrizations and the suggested model extensions in the short to mid-term. In the long term, further advances of the present computational model towards a truly predictive tool could ultimately lead to a case- and patient-specific choice (or design) of pharmaceuticals and assessment of infection risk.

11. Towards a Versatile, Powerful, and Comprehensible Nano-/Micromechanical Model for Collagen Fibrils

This chapter demonstrates how the novel computational approaches to molecular interactions of slender fibers from Chapter 4 and Chapter 5 could be used as the decisive model components of a versatile, powerful, and comprehensible computational model for collagen fibrils, which is based on an explicit modeling of the individual collagen molecules by geometrically exact 3D beam theory.

11.1. Motivation

Collagen type I is the most abundant protein in the human body and for instance is the key component of soft matter such as connective tissue, tendon, ligament, cornea or lung parenchyma, but also occurs in extremely stiff material such as bone and tooth dentin, where it acts as matrix within a mineralized nanocomposite. Its crucial role as the main load-bearing structure providing support and protection has stimulated vast and intensive research projects over the last decades, leading to a huge body of literature on this topic, parts of which are summarized in a comprehensive textbook format [49]. As a result of this still ongoing research efforts, we nowadays know the link of collagen-related disorders to severe diseases such as osteogenesis imperfecta ("brittle bone disease") [49], pulmonary fibrosis [78], aortic aneurysms and dissection [69], and cancer metastasis [27] to name just a few. Another major achievement of the intense previous scientific work is that the hierarchical fibrous structure from molecular polypeptide chains on the scale of a few nanometers up to fibers, fiber bundles and fibrous networks on the scale of millimeters is meanwhile quite well understood [49, 50, 82] and schematically depicted for the example of tendon in Figure 11.1.

This insight into the hierarchical fibrous structure leads us to the specific motivation of this work by exposing both the need and the solution approach. The variety and complexity of collageneous material both in terms of number and diversity of individual components as well as the range of involved length scales from molecular scales to tens of microns and the involved range of time scales from nanoseconds to tens of years of a human life is a tremendous challenge for existing theoretical, computational as well as experimental techniques. Therefore, a large number of both unanswered urgent questions and unforeseen crucial aspects yet remain to be investigated. This work proposes a versatile, powerful, and comprehensible computational
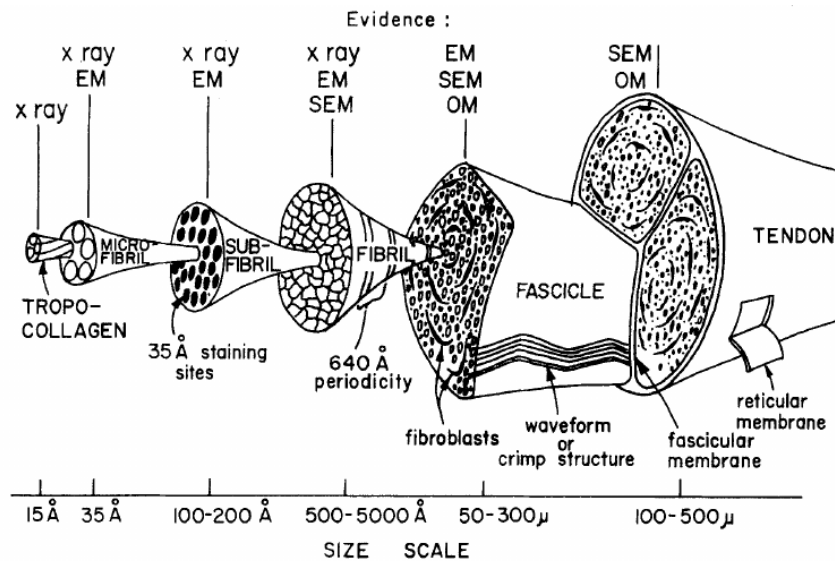
Figure 11.1.: Hierarchical fibrous structure of tendon. Image reprinted from [82].

model for collagen microfibrils that has the potential to study a variety of effects on the microfibrillar, fibrillar and fiber scale that are yet inaccessible both to atomistic (e.g. [21, 54]) and macroscale continuum mechanical approaches (e.g. [63, 70, 106]). The central idea of the novel computational model is the explicit modeling of the slender tropocollagen molecules by means of geometrically exact 3D beam theory (cf. Section 3) as well as applying the novel, efficient approaches to molecular interactions between fibers (cf. Chapter 4 and Chapter 5) both integrated within the versatile (theoretical and code) framework for nonlinear finite element methods in structural mechanics (cf. Section F). A previously published mesoscale model with a similar intention as the present work applies a bead-spring theory based on coarse-graining of the atomistic structure, which uses (bi)linear springs to account for translational as well as rotational deformations of the bead sequence as well as a LJ potential for intermolecular interactions and cross-links with a bilinear force-displacement relationship [21, 38]. Another related article applied 3D solid finite elements to fully resolve a mineralized microfibril geometry by means of 35000 tetrahedral elements and explicitly modeled cross-links via nonlinear springs [62]. To give a first specific example, the model to be proposed here will be used to investigate the origin of the highly tunable nature of fibril stiffness even on very short time scales that has been revealed in recent experiments [3].

In this concluding paragraph, the key modeling concept of this work will be motivated and the specific objectives as well as the mid- and long-term goals will be highlighted. Inspired by an in silico reconstitution of the collagen microfibril, the individual model components such as geometrically exact, nonlinear elasticity of the slender molecules, their spatial arrangement, (transient) mechanical links between them, and intermolecular effects such as steric repulsive and vdW forces will be assembled in a flexible, modular manner. This allows for an isolated, critical review and verification of their individual mechanical behavior compared to experimental results of real collagen molecules and (micro-)fibrils, which in turn will lead to an in-depth understanding of the collagen (micro-)fibril, fiber, and fibrous system behavior from the perspec-

tive of a (bio-)mechanical systems, including all decisive influences and parameter sensitivities. In the long term, this could contribute to the development of innovative therapeutical approaches for the aforementioned diseases as well as to the design and manufacturing of novel materials both based on biological and synthetic (polymer) filaments. In addition, the continued enhancement of computational approaches such as the one to be proposed might lead us to powerful simulation tools that can predict the course of a disease on a case- and patient-specific level and can thus also predict the effectiveness of different available options of treatment and lead to an informed, optimal decision.

11.2. Computational reconstitution of a collagen microfibril: Setup of models and methods

Inspired by the recent experimental study [3] of our collaborator P. Thurner (TU Wien), an in silico reconstitution of the collagen microfibril with the aim to investigate fundamental properties of collagen fibrils and its key influences is elaborated in this section. In accordance with the versatile modular approach above, the individual model components will be presented in the following sections. Note that although the present model focuses on collagen type I as the most abundant one, the modification of the model towards other fibrillar types of collagen is considered a feasible and promising subject of future research and would allow to investigate both similarities as well as differences between the different types and its implications for the various use cases in the human body. The parametrization and validation of the model by means of experimental results for single collagen molecules as well as (micro-)fibrils is a work in progress and will thus not be discussed.

11.2.1. Tropocollagen molecules immersed in a thermal bath

As mentioned above, the individual tropocollagen molecules with a diameter of approximately $1.5\,\text{nm}$ and a length of approximately $300\,\text{nm}$ [49] are modeled by the geometrically exact 3D beam theory as summarized in Section 3, which accounts for the six deformation modes of axial strain, (2x) shear, torsion, and (2x) bending and is known to accurately and efficiently describe potentially large elastic deformations in 3D. An important aspect will be the relevance of bilinear or nonlinear constitutive laws that probably depends on the magnitude of (axial) deformation to be expected and observed in the numerical experiments. Whereas the experimental determination of mechanical properties of individual tropocollagen molecules is still challenging and limited in this specific respect [102, 156], atomistic simulation of collagen-like peptide chains [21] suggest a nonlinearity in the axial strain-force relation only in the regime of very large strains above approximately 30%.

The thermal excitation as well as viscous drag that the molecules experience due to the surrounding fluid is modeled implicitly by means of the finite element formulation for Brownian dynamics proposed in [32] and previously applied in the context of polymer dynamics e.g. in [34, 118] and Chapters 8 and 9.

11.2.2. Assembly of molecules into (micro-)fibrils

The slender collagen molecules are known to self-assemble into fibrillar structures with diameters ranging from 20 to 300 nm and lengths up to hundreds of microns [79, 94]. Due to a characteristic band pattern observed in different imaging techniques, there is a clear understanding of the axial staggering of the individual molecules that is given as a periodic repetition of gap-overlap regions with a periodicity of 67 nm [49]. This repeated pattern gives rise to defining the unit building block of fibrils as five axially staggered collagen molecules, commonly referred to as microfibril. Although the spatial resolution of the fibril cross-sections remains to be a far more challenging task as compared to the axial direction, the current understanding of the lateral packing of collagen molecules is that the parallel molecules arrange in a lattice with quasi-hexagonal ordering [123]. Finally, the formation of covalent cross-links is known to stabilize this assembled fibril structure (refer to the following Section 11.2.3 for the modeling of cross-links). This leads to the prevailing notion of collagen fibrils as a large number of axially staggered, laterally densely packed, parallel collagen molecules. However, Section 11.3 will present a computational study of the dynamic self-assembly process of collagen molecules / microfibrils into fibrils driven by Brownian motion and the transient formation of cross-links that challenges this prevailing notion of the fibril structure. Leaving this special topic aside for now and sticking to the just presented fibril structure, Figure 11.2(a) shows the resulting geometry of a microfibril in its initial, stress-free configuration as applied in the present computational model.

(a)

(b)
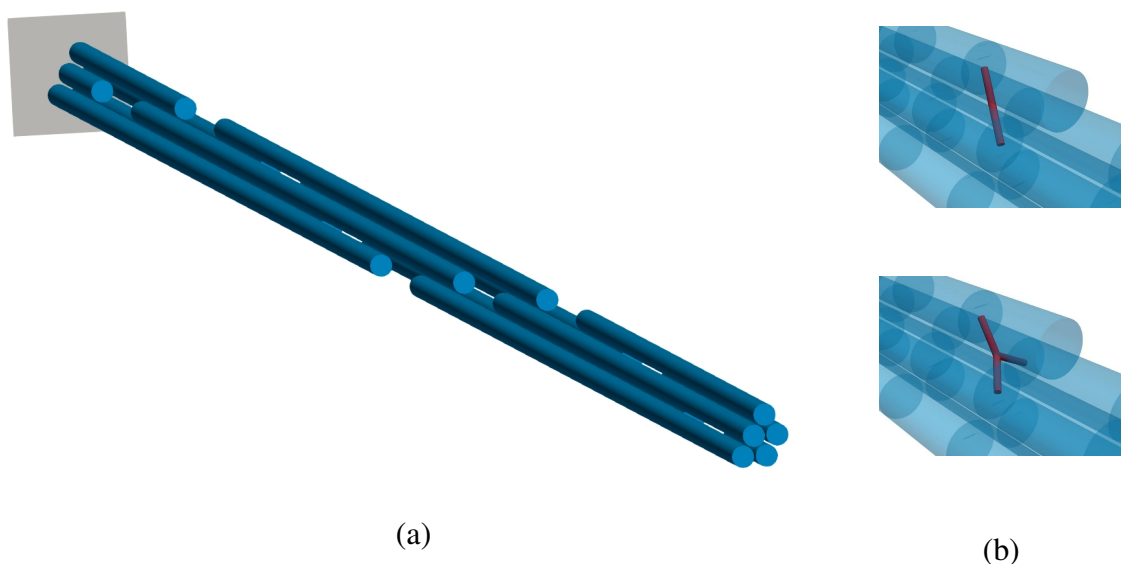
Figure 11.2.: (a) Initial, stress-free configuration of the microfibril model consisting of axially staggered collagen molecules in a quasi-hexagonal lateral arrangement. (b) Divalent (top) and trivalent (bottom) cross-links connecting the individual collagen molecules (cf. Section 11.2.3 for details).

11.2.3. Covalent cross-links between molecules

Two distinct mechanisms of cross-linking in form of either enzymatic lysyl oxidase or non-enzymatic glycosylation / glycation are known to stabilize the fibrillar assemblies of collagen molecules. While the former play an important role in the fibril formation process and form covalent bonds at both telopeptide ends, the latter type of cross-links is far less specific regarding both the time of formation as well as the location [47]. In the present computational model, cross-links are treated as additional beam elements that connect the collagen molecules at distinct binding spots and bind (and potentially unbind) at specified rates. The corresponding numerical formulation has been proposed in [119] and applied to study the self-assembly process of biopolymer networks driven by Brownian motion and mediated by transient cross-linking. A special aspect regarding collagen fibril formation is that divalent enzymatic cross-links (connecting two molecules) are known to undergo a transition to mature, trivalent cross-links over time [47]. The resulting bi- and trivalent cross-links in the present computational model are shown in Figure 11.2(b).

11.2.4. Intermolecular forces between molecules

A specific focus of the present computational model lies on the intermolecular forces, mainly repulsive steric forces and adhesive vdW forces. This is due to the fact that the recently observed tunable nature of collagen fibril stiffness is believed to have its origin in the varying lateral separation of collagen molecules and thus varying strength of the inverse-distance dependent intermolecular forces [3]. In order to investigate this behavior in computational experiments, intermolecular forces are thus included in the model via the novel beam-beam interaction formulations developed in Chapter 4 and Chapter 5.

As a very first step of model parametrization and validation using a minimal problem setup, two initially straight, parallel collagen molecules with a fixed lateral separation and interacting via attractive vdW forces are pulled apart in axial direction. In order to model the inhomogeneous molecular sequence along the collagen molecule, the atom densities ρ_1, ρ_2 are assumed to alternate between two distinct, constant values. Figure 11.3(a) shows the resulting force-displacement curves for different values of the lateral separation of the molecule surfaces. On the one hand, this demonstrates that the novel mesoscale model is capable of reproducing the qualitative behavior of pulling two collagen molecules apart as predicted via atomistic simulations [54]. On the other hand, the decreasing maximal force values with increasing lateral separation, i.e., hydration of the molecules is a first sign that the tunable nature of collagen fibrils might indeed result from the varying strength of attraction via intermolecular forces. However, these preliminary results clearly need to be handled with care and a profound parametrization and validation of the present computational model is still a work in progress. As a final remark on this part of the model considering intermolecular forces, the influence of hydrogen bonds and hydrophobic effects should be clarified and included if needed.

(a)   (b)
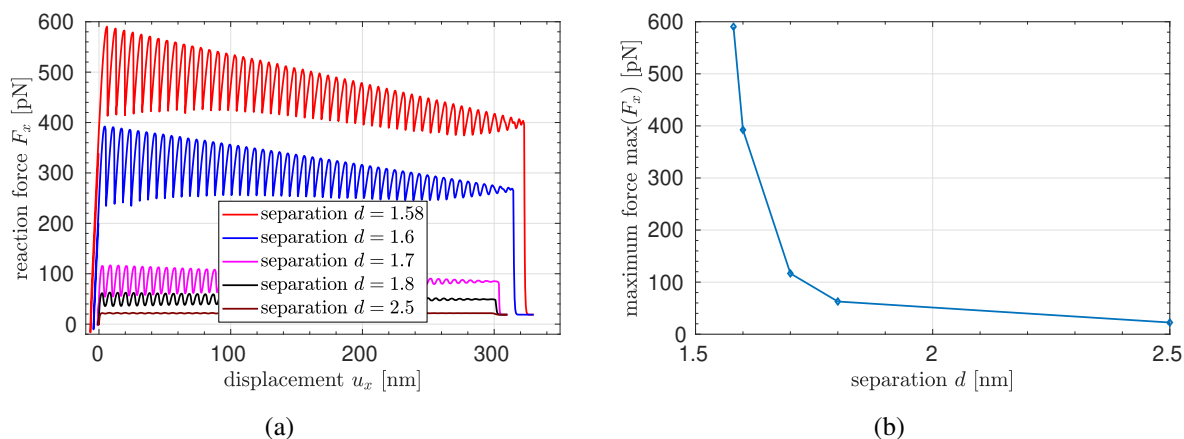
Figure 11.3.: (a) Reaction force-displacement curves of a first minimalistic computational experiment pulling two parallel collagen molecules with fixed lateral surface separation apart in axial direction. (b) Corresponding maximal force values as a function of the lateral surface separation of the molecules.

11.3. Self-assembly of collagen fibrils and fibers

This section provides some first insights into the preliminary results of a computational study of the dynamic self-assembly process of collagen fibrils and fibers driven by Brownian motion and the formation of lateral cross-links as briefly outlined in the previous section. It is motivated by the observation of localized high curvature of collagen fibers in recent experiments (Q. Hu and E. Botvinick, UCI, unpublished material) using fluorescence imaging [41]. Surprisingly, these bends and kinks appear to be long-living, metastable states that occur even in absence of external loads, which challenges the prevailing notion of the strictly parallel alignment and quasi-hexagonal lateral packing of collagen molecules outlined in Section 11.2.2.

In order to investigate this in computational experiments, we consider initially straight and parallel, semiflexible beams, apply the Brownian dynamics finite element formulation outlined in Section 11.2.1, and include the transient cross-links outlined in Section 11.2.3. Some snapshots of the resulting self-assembled bundle structures are shown in Figure 11.4. The full bundle consisting of six initially straight, semiflexible filaments is shown in Figure 11.4(a) and a detail thereof in Figure 11.4(b). These snapshots reveal a wavy and kinked bundle geometry that results from braiding of filaments and is stabilized by the cross-link formation such that it persists over considerable time intervals of tens of seconds. A reduction of the 3D problem via projection to 2D and consideration of only two filaments is shown in Figure 11.4(c). Again, we observe stabilized topological defects such as braiding of filaments and a bubble, i.e., trapped filament length without any cross-links. All the observed mechanisms appear to be meta-stable states that survive tens of seconds and occur in many different, independent simulation runs.

These observations in experiments as well as simulation has stimulated theoretical work on this topic, which aims to describe these topological defects mathematically and predict their frequency of occurrence as well as dynamics in order to analyze their stability (V. Slepukhin and
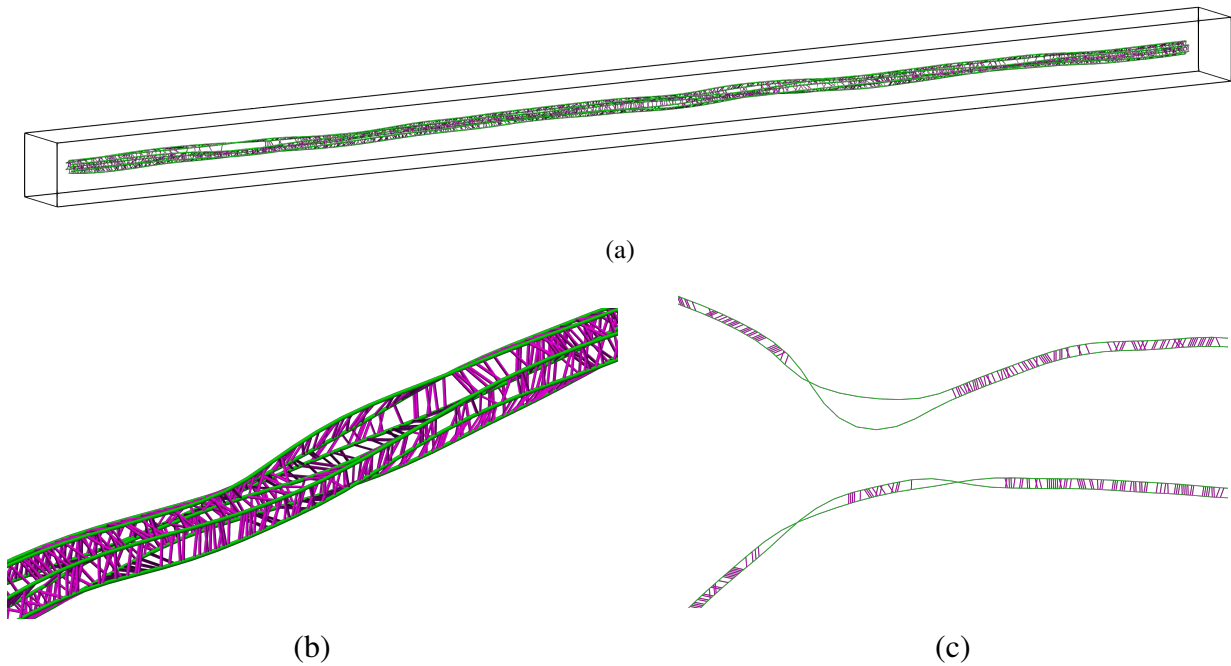
Figure 11.4.: Simulation snapshots of a self-assembled, randomly cross-linked bundle of six initially straight, semiflexible filaments undergoing Brownian motion. (a) The entire bundle of six individual filaments, (b) a detail thereof showing the filaments in green and cross-links in pink, (c) two examples for a minimalistic setup of two filaments in 2D that can be interpreted as a projection of the full bundle in 3D. Both braids and bubbles, i.e., trapped filament length without any cross-links can be observed.

A. Levine, UCLA, unpublished material). To conclude, the presented results indicate that the stress-free configuration of collagen fibrils and fibers might not follow the strict and simple pattern of a straight, ordered bundle as it is currently believed. Therefore, the observed localized regions of high curvature might be meta-stable, stress-free states instead of the result of external loads such as buckling effects. This would have far-reaching implications with respect to the mechanics of collagen fibrils and fibers, because it gives rise to a much richer mechanical behavior than the current understanding of its stress-free state as a straight, homogeneous bundle of regularly arranged, straight filaments would suggest.

Motivated by these observations and insights of highest practical relevance, the future collaborative research on this topic will focus on a detailed analysis of the effects such as the cross-link distributions, frequency of occurrence as well as dynamics of topological effects, and corresponding influences of parameters such as the number and binding rate of cross-linker molecules. In the long term, the mechanical behavior of such self-assembled bundles of filaments is expected to be an important and promising topic of future research.

12. Summary and Outlook

Following the overall structure of this work, this concluding chapter is split into two major parts. First, the outcome of the methodological work presented in Chapter 4 to 6 will be summarized and second, the most important findings of its application to specific biophysical systems in Chapter 7 to 11 will be recapitulated in Section 12.2. Promising future extensions and further applications of the present work will be outlined in several suitable places.

12.1. Computational models and methods

The first part of this thesis is dedicated to the development of efficient and accurate computational models and methods for molecular interactions of deformable fibers. In a first step, the fundamentals of intermolecular forces and potentials such as electrostatic, van der Waals (vdW) and repulsive steric interactions have thus been reviewed and those aspects of high relevance with respect to the later work have been selected from the vast body of literature on this topic. The resulting **Chapter 2** and Appendix A have proven to be a valuable source of reference throughout the remainder of this work. As an additional preparatory step, the fundamentals of geometrically exact beam theory, the corresponding finite element formulations, and existing computational approaches to macroscopic contact between beams have been studied and extended with respect to a few, but decisive details (**Chapter 3**). Most importantly, the extension of the well-established Simo-Reissner beam element formulation developed by Crisfield and Jelenić [29, 76] to the smooth, C^1-continuous centerline interpolation using cubic Hermite polynomials has to be mentioned in this respect. Another important prerequisite for the actual scientific progress made in this work has been the thorough revision of the existing code framework as outlined in Appendix F.

The first primary objective of this work has been accomplished in **Chapter 4**, which proposes the first 3D beam-beam interaction formulation for molecular interactions between curved slender fibers undergoing large deformations. It has been published in the author's article [61]. While the general interaction model is not restricted to a specific beam formulation, in the present work it is combined with the geometrically exact beam theory and discretized via the finite element method. The central idea of the novel approach is to formulate reduced interaction laws for the resultant interaction potential between a pair of cross-sections of two slender fibers such that only the two 1D integrals along the fibers' length directions have to be solved numerically. This section-section interaction potential (SSIP) approach therefore reduces the dimensionality of the required numerical integration from 6D (two nested 3D integrals) to 2D and yields a significant gain in efficiency, which only enables the simulation of relevant time and length scales for many practical applications.

Being the key to this SSIP approach, the analytical derivation of the specific SSIP laws is based on careful consideration of the characteristics of the different types of molecular interactions, most importantly their point pair potential law and the range of the interaction. In a first step, the most generic form of the SSIP law, which is valid for arbitrary shapes of cross-sections and inhomogeneous distributions of interacting points (e.g. atoms or charges) within the cross-sections has been presented in Section 4.2 before the focus was laid on specific SSIP law expressions for dedicated applications in Section 4.3. Considering the practically relevant case of homogeneous, disk-shaped cross-sections, Section 4.3.1 has discussed the advantages as well as limitations of possible simplifications of the SSIP law, finally leading to pleasantly simple SSIP laws that solely depend on the scalar separation of the cross-section centroids and in particular neglect the cross-sections' mutual orientation. In this manner, simple SSIP laws for short-range volume interactions such as vdW or steric interactions (Section 4.3.2) and for long-range surface interactions such as Coulomb interactions (Section 4.3.3) are obtained, which have been used and further analyzed in the remainder of the chapter. In order to remedy the characteristic singularity of inverse power interaction laws in the limit of zero separation, a numerical regularization of the LJ SSIP law has been proposed, which leads to a significant increase in robustness and efficiency, saving a factor of five in the number of nonlinear iterations while yielding identical results.

The accuracy of the proposed SSIP laws as well as the general SSIP approach has been studied in a thorough quantitative analysis using analytical as well as numerical reference solutions for the case of vdW as well as electrostatic interactions. It is found that a very high level of accuracy is achieved for long-range interactions such as electrostatics both for the entire range of separations as well as all mutual angles of the fibers from parallel to perpendicular. In the case of short-range interactions, however, the derived SSIP law without cross-section orientation information slightly overestimates the asymptotic power-law exponent of the interaction potential over separation. As a pragmatic solution, a calibration of the simple SSIP law has been proposed to fit a given reference solution in the small yet decisive range of separations around the equilibrium distance of the Lennard-Jones (LJ) potential. As has been shown for the fundamental numerical example of peeling two adhesive fibers in Section 7.4.5, this strategy leads to a very good agreement in the force response on the system level. While this accuracy might already be sufficient for certain real world applications, the derivation of reduced interaction laws including the cross-section rotations is considered an important next step. In the present work, the derivation of such an enhanced interaction law including the orientation has been exemplified in the context of the alternative beam-beam interaction formulation, which has been developed with a focus on short-ranged interactions in Chapter 5 and will be summarized in the following. However, also the SSIP laws considered in Chapter 4 would benefit from the increased accuracy (and particularly the exact asymptotic scaling behavior) and including the cross-section orientation is thus considered a valuable future extension.

In an effort to further improve the efficiency in the most challenging case of very short-ranged interactions such as vdW adhesion and steric repulsion, a second fundamental approach to molecular interactions of deformable fibers has been developed in **Chapter 5**. Exploiting the characteristic rapid decay of the interaction potential with increasing distance allows to further reduce the dimensionality of the beam-beam interaction problem and thus achieve an even more

efficient approach than the previously developed, more general SSIP approach. The key idea is to approximate the second, arbitrarily deformed beam by a surrogate body with trivial geometry, which is located at the closest point from a given point on the first beam and oriented according to the centerline tangent vector of the second beam. Mathematically, this surrogate body is the linear series expansion of the second, so-called master beam around the closest point. In this manner, the interaction of the entire second beam with a given section of the first, so-called slave beam can be described by an analytical, closed-form interaction potential law, which replaces the numerical integration along the master beam by a single function evaluation. This novel, specialized approach is therefore called the section-beam interaction potential (SBIP) approach.

In addition to being significantly more efficient, the SBIP formulation is also significantly more accurate if short-ranged interactions are considered. This is due to the fact that the reduced interaction law is superior to the previously used, simple SSIP law, because it includes the relative rotation, i.e., the orientation of the interacting bodies in addition to their scalar separation. This SBIP law has been derived in Section 5.2 considering the case of circular, homogeneous cross-sections and a generic inverse power law with exponent $m \geq 6$ as fundamental point-pair interaction potential. The required derivation of the resulting disk-cylinder interaction potential is based on 5D analytical integration using appropriate series expansions and is valid for arbitrary mutual orientations of the two bodies. A comprehensive analysis of the accuracy of the disk-cylinder potential allowed to choose the optimal compromise between accuracy and simplicity of the expression. In particular, the SBIP law ensures the correct asymptotic scaling behavior in the decisive regime of small separations, which has been identified as the most critical deficiency when using the simple SSIP law from Section 4.3.2, which neglects the mutual orientation of cross-sections. To anticipate the result of a specific numerical example in Chapter 7, the SBIP approach is found to be by about a factor of 4 more efficient than the more general SSIP approach. This holds even despite the aforementioned superior accuracy of the derived SBIP law (Equation (5.32)), which is therefore also more complex than the simple SSIP law (Equation (4.7)).

The two fundamental novelties – the general SBIP approach from Section 5.1 and the specific analytical SBIP law from Section 5.2 – have been combined in Section 5.3 to obtain the resulting virtual work contribution. As for the SSIP approach above, it needs to be underlined that also the SBIP approach to beam-beam interactions does neither depend on any specific beam formulation nor the applied spatial discretization or time integration scheme and is thus considered to be highly versatile. The required steps of discretization and consistent linearization have been presented for all aforementioned variants of general approach and reduced interaction law. The implementation of the resulting, ready-to-use expressions has proven that the novel beam-beam interaction formulations can be seamlessly integrated in an existing nonlinear finite element framework for structural or solid mechanics as outlined in Appendix F. In the context of the present work, they have exemplarily been used with geometrically exact Kirchhoff-Love and Simo-Reissner type beam finite elements, and in combination with quasi-static or (Lie group) Generalized-Alpha time stepping schemes or a Brownian dynamics framework.

The set of first numerical examples in Section 4.5 and Section 5.5 has finally demonstrated the effectiveness and robustness of the novel approaches to model molecular interactions such as electrostatics, vdW adhesion, and steric repulsion, and a combination thereof. Several impor-

tant aspects such as the influence of the numerical integration error and the spatial discretization error, local and global equilibrium of forces, and conservation of energy have been validated by these simulations. They include quasi-static and dynamic scenarios, and arbitrary deformations, mutual orientations and separations of the interacting fibers. To highlight just one particularly challenging example, Section 5.5 studies adhesive nanofiber-grafted surfaces and demonstrates the working principle of a proposed design of the nanofiber-grafted surfaces based on arrays of helical fibers by showing the desired large ratio of strong adhesive connection under load and easy removal of the surfaces if desired. This showcases how suitable simulation tools such as the ones developed here could contribute to the design and manufacturing of bioinspired artificial adhesives in the long run.

In addition to the aforementioned inclusion of the cross-section orientations in the SSIP laws, a future derivation of SSIP and SBIP laws, e.g. for the case of screened electrostatics or hydrophobicity, would further extend the range of applications of the novel formulations. Given the importance of the mentioned interaction types in many biological systems on the nano- and microscale, this is considered a highly promising extension of this work. As an alternative to the analytical derivation of SSIP and SBIP laws, the identification and fitting of such reduced interaction laws based on experimental results (such as the force-displacement curves for simple characteristic setups with two interacting fibers) would be another interesting and worthwhile avenue of future research that is considered to be of great benefit to the quantitative prediction quality of computational experiments. Furthermore, a generalization of the formulations with respect to the interacting bodies as considered e.g. for the beam-sphere interaction in the scope of this work is deemed to be a desirable direction of future work. Once again inspired from biological systems, the interaction of biopolymer filaments with lipid bilayers and the interaction of cells with the extracellular matrix (ECM) immediately come to mind as an example for beam-membrane and beam-solid interactions, respectively.

The first major part of this thesis dealing with the development of novel computational approaches has finally been wrapped up with a concluding overview of beam interaction formulations from a meta-level perspective in **Chapter 6**. It suggests a new classification of beam-beam interaction formulations spanning the full range from the fully resolved, yet computationally costly point-pairwise (atomistic) perspective to the most efficient, yet least accurate method of evaluating a fully reduced, analytical interaction law derived on the basis of two surrogate beams. While the former generally requires the aforementioned 6D numerical integration of all possible point-pair potential contributions, the latter can be associated with the well-established, so-called point contact formulation that postulates a penalty law for one pair of closest points. In this context, the novel approaches developed in this thesis thus bridge the gap between these two extremes and can retrospectively be regarded as the consistent intermediate steps in the spectrum from fully resolved to maximally reduced formulations. Taking into account the either long or short range of the interactions, the approach based on section-section interaction laws from Chapter 4 or the one based on section-beam interaction laws from Chapter 5 appears to be the most efficient, yet detailed enough and thus generally valid approach.

To conclude, the combination of high efficiency and high accuracy leads to a significantly improved applicability to complex, large-scale fibrous systems as compared to the previously

existing, fundamental approaches reviewed in Section 1.3. If, e. g., compared to molecular dynamics, the applied modeling of fiber-like, slender structures and their molecular interactions on the level of fibers allows for drastically increased feasible system sizes and time scales and therefore opens the door to tackle a multitude of so far intractable problems in science and technology. These include, but are not limited to, the specific biological systems that have been studied in the second major part of this work and will be summarized in the following.

12.2. Biophysical applications

The second major part of this thesis from Chapter 7 to 11 is dedicated to the application of the novel computational approaches to biophysical systems on the nano- and microscale. These applications have motivated the development of models and methods in the beginning and have served the need of ambitious, yet achievable targets that inspired and pushed the successive enhancement of the methodological part of this work. In addition to driving the progress and innovation in the field of computational mechanics, the applications allow for valuable insights into real biological systems of high relevance with respect to physiology and pathophysiology. An overview of the second part of this thesis is given as follows. In the beginning, the rather small and simple model systems have been considered, which represent the characteristics of real biological systems on an abstract level. On the one hand, these reduced, academic examples are particularly useful for the systematic analysis and advancement of the computational approaches and on the other hand, they allow for the investigation of the fundamental properties and behavior that many real systems have in common. Towards the end, more and more specific, realistic systems have been studied, which has led to the aforementioned immediate gain of knowledge about these particular biological systems.

The first extensive computational study presented in **Chapter 7** investigates the fundamental problem of separating two adhesive elastic fibers and large parts of it have been published in the author's article [60]. Specifically, it covers the peeling and pull-off process starting from fibers contacting along its entire length to fully separated fibers (and also the reverse order) including all intermediate configurations and the well-known physical instability of snapping into contact and snapping free. In order to study the key influences, the strength of adhesion relative to the Young's modulus of the fibers has been varied over a broad range of values spanning two orders of magnitude, and also two different types of attractive forces resulting either from vdW interactions or the electrostatic interaction of oppositely charged, non-conducting fibers are considered. The analysis of the resulting force-displacement curve has revealed a surprisingly rich, highly nonlinear system behavior.

In an effort to understand and explain this behavior, the underlying physical mechanisms arising from the interplay of adhesion, mechanical contact interaction and structural resistance against (axial, shear and bending) deformation have been thoroughly investigated. Based on the differences found in these fundamental mechanisms, the three distinct phases of a) initiation of fiber deformation and peeling, b) the actual peeling, and c) a final pull-off phase have been identified. The initiation phase is characterized by a steep initial increase towards a sharp force peak and followed by the peeling phase with gradually decreasing force values eventually approach-

ing a plateau-like regime of almost constant peeling force. The unitary nature of these first two phases in the peeling of adhesive elastic structures is confirmed by the comparison with previous studies and across all considered variants in this study. On the contrary, the presence of the pull-off stage as a third distinct phase of the separation process, that is characterized by a significant increase of the force over an extended range of displacement values before finally snapping free, was not observed in the previous, one-sided peeling studies and can thus be attributed to the application of pulling forces at both ends of the fibers, which results in a two-sided instead of a one-sided peeling. Moreover, the practically highly relevant global maximum of the pulling force has been found to occur at the end of the initiation phase in case of short-ranged vdW attraction, whereas it occurs in the final pull-off phase ultimately before snapping free in the case of the long-ranged electrostatic attraction. Subsequent studies may include the dynamics of the peeling and pull-off process or further scenarios of loading and support of the fibers, e.g., twisting and out-of-plane bending, all of which is directly accessible by means of the computational models and methods developed and applied in this work.

Chapter 8 presents the computational study of a filament's conformation in a static random potential field while undergoing thermal fluctuations. It is the result of a collaborative research project combining the theoretical work by V. Slepukhin and A. Levine (UCLA) with the computational work by K. Müller and the author (TUM) and has been published in the joint article [152]. The system is considered to be an abstract model for the interactions of a semiflexible filament with the surrounding biopolymer network and allows to investigate the fundamental effect of prestress in self-assembled network structures such as the cytoskeleton. Due to the dynamic nature of both the formation and the continuous re-organization of these networks, the resulting structures are not necessarily in a state of mechanical equilibrium, thus leading to some excess elastic deformation also known as prestress of the network. From a computational point of view, this scenario can be regarded a special case of the general beam-beam interaction, where one beam is replaced by an effective, static background potential field as has been discussed in Section 6.3.2. The results of this computational study show a decrease in the excess arclength of the filament with increasing externally applied tension. This can be explained by the fact that high tension leads to a straightening of the filament and prevents it from following the (valleys of the) potential landscape. Specifically, the simulation results have confirmed the previous theoretical prediction that the behavior in the two distinct regimes of low and high tension can be described by two different power laws.

Chapter 9 studies the effect of different charge distributions on the conformation of a single mucin filament. Mucins are a family of glycoproteins that are the key constituent of mucus hydrogels, which cover all wet epithelia in the human body and are known to have extraordinary properties, e.g., in terms of selective permeability (cf. Chapter 10) and lubrication. This computational study of mucin's conformation is inspired by the observations of a previous experimental study [105] and additional, so far unpublished in-vitro experiments of our collaborators T. Lutz and O. Lieleg (TUM). According to these experiments, changes in the effective line charge distribution along the mucin filament are expected to have an influence on the conformation and in turn on the interaction of mucin with other molecules such as dextrans.

From a computational point of view, this study serves as an example of how the SSIP approach from Chapter 4 can be applied to model the (electrostatic) self-interaction of a slender fiber, i.e., the interaction of distinct, charged parts of the filament. In general, accurate, efficient, and versatile computational models for all kinds of molecular self-interactions are considered to be important, because tertiary and quaternary structures of proteins are a result of the complex interplay of these self-interactions and the intramolecular forces giving rise to an elastic stiffness. Especially for highly slender fibers that show a tendency to undergo large 3D deformations, self-interaction due to intermolecular forces is expected to play a crucial role, which highlights the practical relevance of the novel computational approaches.

The results of this computational study have revealed a significant influence of the electrostatic self-interactions on the conformation of the mucin filament. As compared to the reference solutions obtained from simulations of a hypothetically charge-free filament, the different line charge distributions characterizing the different considered scenarios of mucin at pH 4, at pH 7, and at pH 7 with removal of either or both of the SA and SO_4^{2-} side groups, had a major impact on both the end-to-end distance and the radius of gyration. The removal of both types of side groups and therefore the majority of the charges from the extended middle domain of the filament led to significantly smaller values for the end-to-end distance and the radius of gyration. This is associated with a more flexible behavior as compared to the unmodified mucin filament at pH 7, where the mutual repulsion of the big amount of negative charges distributed almost along the entire filament contributes to the effective bending stiffness. At pH 4, the mucin filament shows a persistent folding of both terminal regions onto the extended glycosolated domain, which can be explained by the mostly positively charged terminal regions in this case and gives rise to a fundamentally different conformation as compared to the stretched out, semi-flexible conformation observed at pH 7.

Chapter 10 proposes and applies a novel computational model to study the mobility of particles in hydrogels, i.e., cross-linked networks of biological or synthetic polymers immersed in aqueous solution. Due to steric and electrostatic interactions with polymer fibers, the dynamics of particles significantly differs from the classical random walk observed for free diffusion as has been shown in several experimental studies including, e.g., the ones by our collaboration partner O. Lieleg (TUM) [96, 97], which inspired this work. The remarkable ability of biological hydrogels (e.g., mucus, ECM) to individually control the mobility of diffusing particles is of crucial importance for numerous processes in the human body. The high practical relevance of this topic originates from its significant implications e.g. with respect to the design of pharmaceuticals and vesicles for targeted drug release.

As compared to previous numerical studies of the diffusive mobility of particles in hydrogels, the model developed in the present work is the first computational approach with a realistic fiber network model. Most notably, it is based on the modeling of elastically deformable fibers via beam theory and a Voronoi tessellation of the periodic simulation box to obtain random, irregular network geometries. This approach has only been made possible by the novel beam-sphere interaction models from Section 6.3.1. After a model validation and the investigation of only repulsive steric interactions in Section 10.3.1, the particularly important effect of additional attractive electrostatic forces has been studied in Section 10.3.2. Finally, the role of fiber deformations has been analyzed for the first time in Section 10.3.3.

In the case of only repulsive steric interactions, it is found that the hindrance of the particle mobility is insignificant as long as the mesh sizes of the fiber network are larger than the particle diameter. If, however, the mesh sizes are in the order of the particle diameter, the particle is effectively caged in a polygonal fiber hull of random shape and size and shows a behavior known as confined diffusion and characterized by a plateau in the mean squared displacement (MSD) curve for long time intervals. Within the given problem setup and the focus on relatively small particles, these are expected results validating the novel approach. However, this effect of steric hindrance will become highly relevant if the surprisingly effective transport of relatively large particles is considered that has been observed in experiments [89]. In this context, including the dynamics of the fiber network such as its self-assembly driven by Brownian motion and transient reorganization of cross-links (as demonstrated for the compatible computational model applied in [34, 118]) might be an important model component as suggested by recent findings in the context of the nuclear pore complex [26, 58] or the secretion and shedding of mucus layers [105].

Turning to the effect of additional electrostatic interactions between the fibers and the oppositely charged particle, the prevailing notion that the degree of hindrance on average increases with the strength of attraction has been confirmed by the numerical experiments with five different network geometries and two random realizations each. Moreover an increased variability of the particle's MSD values and slopes in the regime of long time intervals has been observed and excellently agrees with previous experimental results from [4]. A detailed look at the 3D particle trajectories within the fiber network provides a first direct proof for the existence of distinct motion patterns of the particles that explain the variability in the MSD curves. As hypothesized before in [4], the particles stick to oppositely charged fiber/charge aggregations experiencing more or less strong trapping and eventually escape due to the continuous thermal excitation only to be quickly attracted to another fiber/charge aggregation. While some particles remain completely immobilized at one particular location for the entire 20 seconds, others smoothly or rapidly cycle between two local minima in the potential landscape. Both of these motion patterns lead to a behavior on longer time intervals that is very similar to the confined diffusion described for caged particles above, however the diffusive mobility on short time intervals is significantly reduced as well due to sticking to the fibers. A third observed motion pattern is the one of several successive jumps that – at least theoretically – could be a transport mechanism also over longer distances if the potential landscape is formed accordingly and e.g. shows some degree of periodicity and directional preference.

Altogether, these findings indicate that the precise shape of the effective 3D potential field explored by the particle has a crucial influence on its mobility. In view of the broad variety of biopolymer hydrogels with diverse chemical compositions and biophysical properties, the current computational model could thus be leveraged to study the individual selective filtering behavior for a large number of particle-hydrogel property combinations. Based on the recognized importance of the precise fiber/charge distribution in the system, two points seem to be of particular importance to achieve a case-specific, highly accurate and reliable prediction. First, the inhomogeneous charge distribution along the fiber should be both determined (e.g. by analyzing the molecular architecture) and applied in the model as demonstrated for the example of mucin in Chapter 9. Second, the specific composition and geometry of fiber networks should be determined (e.g. by processing electron microscopy images) and applied in the model. Also the

inclusion of the dynamic self-assembly and reorganization of networks mentioned above would be worth considering in this respect.

As a last particular aspect investigated in this study, fiber deformations have been found to be negligible for the range of realistic values for the fiber stiffness. To be more precise, varying the value for the Young's modulus over the range of reported values for the considered ECM gels has led to identical results as obtained for the theoretical limit of rigid fibers. If, however, very soft fibers are considered, the fiber compliance causes a decrease of MSD values on short time intervals and an increase of MSD values on long time intervals (for particles that are effectively trapped sticking to oppositely charged fiber agglomerations). In real systems, these trends might be observable as a result of dysregulated fiber stiffness or for certain (biological) hydrogels with very thin or soft and therefore compliant filaments such as mucin or F-actin.

As outlined above, further insights especially with respect to the variety of particle/hydrogel-specific behaviors and mechanisms can be expected from different parametrizations and the suggested model extensions in the short to mid-term. In the long term, further advances of the present computational model towards a truly predictive tool could ultimately lead to a case- and patient-specific choice (or design) of pharmaceuticals and assessment of infection risk.

As the last application considered in the present work, **Chapter 11** already outlines the path to promising future work in this field. It demonstrates how the novel computational approaches to molecular interactions of slender fibers could be used as components of a versatile, powerful, and comprehensible computational model for collagen fibrils, which is based on an explicit modeling of the individual collagen molecules by geometrically exact 3D beam theory. Collagen is the most abundant protein in the human body and type I collagen fibers are the key component of both soft matter (e.g., connective tissue, tendon, lung parenchyma) and stiff material (e.g., bone, dentin). The variety of collageneous material is a result of its complex, hierarchical fibrous structure from nanometers up to the millimeter scale. In combination with the involved range of time scales from nanoseconds to several years of a human life, this is a tremendous challenge for existing theoretical, computational, and experimental techniques. Therefore, a large number of both unanswered urgent questions and unforeseen crucial aspects yet remain to be investigated. This is underlined by the already known causal links of collagen-related disorders to severe diseases such as osteogenesis imperfecta (i.e., brittle bone disease) [49], pulmonary fibrosis [78], aortic aneurysms and dissection [69], and cancer metastasis [27] to name just a few.

Inspired by the recent experimental study [3] of our collaborator P. Thurner (TU Wien), an in silico reconstitution of the collagen microfibril with the aim to investigate fundamental properties of collagen fibrils and its key influences is currently a work in progress. Section 11.2 has presented the first steps of including the individual model components such as geometrically exact, nonlinear elasticity of the slender molecules, their spatial arrangement, (transient) mechanical links between them, and intermolecular effects such as steric repulsive and vdW forces.

As a second, related line of exploration, an ongoing computational study of the dynamic self-assembly process of fiber bundles such as collagen fibrils and fibers, driven by Brownian motion and the formation of lateral cross-links, has finally been outlined in Section 11.3. It is motivated by the observation of localized high curvature of collagen fibers in recent experiments (Q. Hu and E. Botvinick, UCI, unpublished material) and has stimulated also theoretical work by our collaborators V. Slepukhin and A. Levine (UCLA), which aims to describe these topological

defects mathematically to predict their frequency of occurrence and their dynamics in order to analyze their stability. Surprisingly, these bends and kinks appear to be long-living, metastable states that occur even in absence of external loads, which challenges the prevailing notion of the strictly parallel alignment and quasi-hexagonal lateral packing of collagen molecules outlined in Section 11.2.2. This would have far-reaching implications with respect to the mechanics of collagen fibrils and fibers, because it gives rise to a much richer mechanical behavior than the current understanding of its stress-free state as a straight, homogeneous bundle of regularly arranged, straight filaments would suggest.

In summary, the presented applications in the second major part of this thesis provide an extensive proof of concept regarding the developed beam-beam interaction models and methods as well as the overall theoretical and computational framework outlined in Appendix F. In particular, the large number of scenarios, simulation runs and time steps, and the variety of different configurations resulting both from the many different sets of input parameters and the random thermal forces demonstrate their robustness and effectiveness beyond one fortunate set of input parameters. This work should therefore encourage and facilitate further applications, also to increasingly complex systems of fiber-like structures on the nano- and microscale.

Recalling the abundance and relevance of slender structures and its interactions in biological nano- and microscale systems as described in the introductory Section 1.1, a multitude of promising future research topics come to mind. Besides a number of other aspects, the selective permeability of the nuclear pore complex has already been mentioned above. Moreover, the topic of DNA origami would be worth considering, because a fast and reliable prediction of the final tertiary structures by employing computational tools such as the ones developed in this work would streamline the design process of the nanoscale objects. As a consequence of the generality and versatility of the proposed approaches, the future fields of applications need not remain limited to biological systems and may be extended to the investigation, design, and manufacturing of synthetic fibrous systems involving e.g. cellulose, polymer, glass, and carbon nanofibers. The range of technological applications on these molecular length scales is expected to grow significantly with the ongoing progress of understanding the basic design and working principles as well as the manufacturing of such microscale systems.

In the long run, computational tools based on the long and successful history of beam theory, which have been extended towards (molecular) interactions within this thesis, might become widely-used, valuable tools in several fields of science, engineering, and medicine. This includes, but is not limited to the visionary goals outlined both initially in Section 1.1 and throughout this concluding chapter.

Appendices

A. Examples for the Derivation and Analysis of the Two-Body Interaction Potential and Force Laws for Parallel Disks and Cylinders

The aim of this appendix is to present the mathematical background of analytical solutions for two-body interaction potential as well as force laws. Generally, the strategy of pairwise summation, i.e., integration of a point pair potential, is applied. See Section 2.3.2 for a discussion of the applicability of this approach. Exemplarily, we consider the interaction between two parallel disks and two parallel cylinders since these scenarios proved to be most important throughout the derivation of SSIP laws as well as their verification in Section 4.3 and 4.5.1, respectively. In addition, the point-cylinder interaction will be considered and used in the context of deriving a closed-form analytical expression for the disk-cylinder interaction potential law in Section 5.2.1. For all these scenarios, an inverse power law with generic exponent m will be assumed for the point-pair potential law in order to obtain general expressions that can be applied to both vdW as well as repulsive steric interactions. These results are then used as soon as we turn to the total LJ interaction potential and force law in the limit of small separations, because the regularization proposed in Section 4.4.3 is based on these theoretical considerations. Finally, also the equilibrium spacing $g_{\text{LJ,eq,cyl}\|\text{cyl}}$ of two infinitely long cylinders interacting via the LJ potential will be derived and has proven helpful in order to choose an almost stress-free initial configuration of two deformable, straight fibers e.g. in Chapter 7 studying the peeling and pull-off behavior. Major parts of this appendix have previously been published in the author's article [61].

A.1. A generic interaction potential described by an inverse power law

Instead of $\Phi_{\text{vdW}}(r)$ from (2.4) or any other particular interaction type, here, we rather use the more general power law $\Phi_m(r) = k_m\, r^{-m}$ for the point pair potential. As noted already in [90], this does not introduce any additional complexity in the derivations and the solutions can directly be used for other exponents m. We will make use of this fact when considering LJ interaction between two disks and two cylinders analytically in Appendix A.2.1 and A.2.2, respectively.

These findings are to be used in the context of deriving a proper regularization of the potential laws in Section 4.4.3.

A.1.1. Disk-disk interaction

The following refers to the analytical solutions for the disk-disk vdW interaction potential from literature that is summarized in Section 2.3.2. Let us first state the underlying mathematical problem. We would like to find an analytical solution for the required 4D integral C_m over the circular area of each disk

$$C_m := \iint_{A_1, A_2} \Phi_m(r) \, \mathrm{d}A_2 \, \mathrm{d}A_1 \qquad \text{with} \quad \Phi_m(r) = k_m \, r^{-m} \tag{A.1}$$

in order to arrive at the disk-disk interaction potential

$$\tilde{\tilde{\pi}}_m = \rho_1 \rho_2 \, C_m. \tag{A.2}$$

Details on 2(a) in Section 2.3.2: The regime of large separations

For the limit of large separations $g \gg R_1, R_2$, the solution is quite straightforward and can be explained in simple words as follows. The distance of any point in a disk to its center is of order $\mathcal{O}(R)$ and thus much smaller than the disks' surface-to-surface separation g:

$$\tilde{r}_{1/2} = \mathcal{O}(R_{1/2}) \ll \mathcal{O}(g) \tag{A.3}$$

Figure A.1 illustrates the introduced geometrical quantities. The distance r between any two
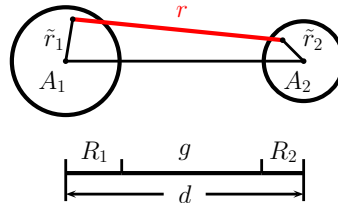
Figure A.1.: Two circular cross-sections, i.e. disks in parallel alignment. Figure taken from the author's article [61].

points $\boldsymbol{x}_1$ in disk 1 and $\boldsymbol{x}_2$ in disk 2 may therefore be approximated by the inter-axis distance $d = g + R_1 + R_2$:

$$r = \|\boldsymbol{x}_1 - \boldsymbol{x}_2\| = \|\boldsymbol{r}_1 + \tilde{\boldsymbol{r}}_1 - \boldsymbol{r}_2 - \tilde{\boldsymbol{r}}_2\| \approx \|\boldsymbol{r}_1 - \boldsymbol{r}_2\| = d \tag{A.4}$$

Double integration over both disks is hence equivalent to a multiplication with the disks' areas A_1, A_2

$$C_{m,\mathrm{ls}} \approx A_1 A_2 \, \Phi_m(r = d) \tag{A.5}$$

and finally we end up with the sought-after expression for the general disk-disk interaction potential in the limit of large separations

$$\tilde{\tilde{\pi}}_{m,\mathrm{disk}\|\mathrm{disk},\mathrm{ls}} \approx \rho_1 \rho_2 \, A_1 A_2 \, \Phi_m(r = d). \tag{A.6}$$

Note that this approximation is valid for arbitrary pair interaction functions $\Phi(r)$. Moreover, this solution does not even depend on the parallel orientation of the disks. It is valid for all mutual angles of the disks which is important because we will apply it to arbitrary configurations of deflected beams. For the special case of parallel disks, this result can alternatively be obtained by the sound mathematical derivation of [90, Equation (10)]. The leading term of his hypergeometric series is identical to the right hand side of equation (A.6).

Details on 1(a) in Section 2.3.2: The regime of small separations

Now, we consider the limit of small separations $g \ll R_1, R_2$. The problem has been studied by Langbein [90] in the context of vdW attraction of rigid cylinders, rods or fibers. In the following, we will briefly present the central mathematical concept of his derivations. The basic idea is to
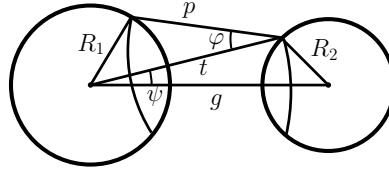
Figure A.2.: Integration over the cross-sections at small separations. Figure taken from [90] with adapted notation.

choose a favorable set of integration variables p, t, φ, ψ as shown in Figure A.2. In this way, the four dimensional integral (A.1) can be reduced to a double integral because the integrand $\Phi_m(p)$ does not depend on the angles φ and ψ:

$$C_m = \int_{A_1} \int_{A_2} \Phi_m(p) \, \mathrm{d}A_2 \, \mathrm{d}A_1 = \int_p \int_t \int_\varphi \int_\psi \Phi_m(p) \, \mathrm{d}\psi \, \mathrm{d}\varphi \, \mathrm{d}t \, \mathrm{d}p$$

$$= \int_p \int_t \Phi_m(p) \, 2p\varphi(p,t) \, 2t\psi(p,t) \, \mathrm{d}t \, \mathrm{d}p \tag{A.7}$$

$$\text{where} \quad \cos(\varphi) = \frac{p^2 + t^2 - R_1^2}{2pt}, \quad \cos(\psi) = \frac{t^2 + d^2 - R_2^2}{2td}, \quad d = g + R_1 + R_2$$

For a general potential law $\Phi_m(r = p) = k_m p^{-m}$, this reads

$$C_m = 4k_m \int_p \int_t p^{-m+1} \varphi t \psi \, \mathrm{d}t \, \mathrm{d}p \tag{A.8}$$

Making use of $g \ll R_1, R_2$ and introducing reduced variables $\bar{p} = p/g$ and $\bar{t} = t/g$ leads to

$$C_{m,\mathrm{ss}} = 4k_m \sqrt{\frac{2R_1 R_2}{R_1 + R_2}} \int_g^{g+2R_1+2R_2} p^{-m+1} \int_g^p \sqrt{t - g} \arccos\left(\frac{t}{p}\right) \mathrm{d}t \, \mathrm{d}p \tag{A.9}$$

$$= 4k_m \sqrt{\frac{2R_1 R_2}{R_1 + R_2}} g^{-m+7/2} \int_1^\infty \bar{p}^{-m+1} \int_1^{\bar{p}} \sqrt{\bar{t} - 1} \arccos\left(\frac{\bar{t}}{\bar{p}}\right) \mathrm{d}\bar{t} \, \mathrm{d}\bar{p} \tag{A.10}$$

Another substitution of variables $x = \bar{t}/\bar{p}$ and interchanging the order of integration finally yields the solution[1]

$$C_{m,\text{ss}} = g^{-m+\frac{7}{2}} \; \frac{2k_m\pi}{(m-2)^2} \; \sqrt{\frac{2R_1R_2}{R_1+R_2}} \; \frac{\Gamma(m-\frac{7}{2})\,\Gamma(\frac{m-1}{2})}{\Gamma(m-2)\,\Gamma(\frac{m}{2}-1)} \qquad \text{for} \quad m > \tfrac{7}{2} \qquad \text{(A.11)}$$

Here, Γ denotes the gamma function which is defined by $\Gamma(z) = \int_0^\infty w^{z-1}e^{-w}\,\mathrm{d}w$.

Multiplication with the particle densities finally results in the sought-after general disk-disk interaction potential for the regime of small separations

$$\tilde{\tilde{\pi}}_{m,\text{disk}\|\text{disk,ss}} = \rho_1\rho_2\,C_{m,\text{ss}} \qquad \text{for} \quad m > \tfrac{7}{2} \qquad\qquad\qquad \text{(A.12)}$$

that can be further specified by means of $m = 6$ and $k_6 = -C_{\text{vdW}}$ to end up with $\tilde{\tilde{\pi}}_{\text{vdW,disk}\|\text{disk,ss}}$ as in (2.19).

Remarks

1. Note that this solution is valid for exponents $m > 7/2$ only. This is in contrast to the approximation for large separations (A.6) which is valid for arbitrary forms of the pair interaction potential $\Phi(r)$.

2. Note however the conceptual similarity of this expression to the one valid for the limit of large separations (A.6). Here, we also find a power law, however in the surface-to-surface distance g instead of the inter-axis distance d and with a different exponent.

A.1.2. Cylinder-cylinder interaction

Considering the case of two parallel cylinders, we are interested in the length-specific interaction potential

$$\tilde{\pi}_{m,\text{cyl}\|\text{cyl}} = \lim_{l_1\to\infty} \frac{1}{l_1} \int_{-l_1/2}^{l_1/2} \int_{-\infty}^{\infty} \iint_{A_1,A_2} \rho_1\rho_2\,\Phi_m(r)\,\mathrm{d}A_2\,\mathrm{d}A_1\,\mathrm{d}s_2\,\mathrm{d}s_1 \qquad \text{with} \quad \Phi_m(r) = k_m\,r^{-m}.$$

$$\text{(A.13)}$$

The integral over $s_1 = -l_1/2 \ldots l_1/2$ yields a factor of l_1 since the integrand is constant along s_1 and thus immediately cancels with the normalization factor $1/l_1$.

Exemplarily, we want to discuss the more interesting and challenging regime of small separations here. Following [90, p.63], one can interchange the order of integration, solve the integral over the infinitely long cylinder length analytically in a first step, and then make use of the generic solution for $C_{m,\text{ss}}$ from (A.11), but this time with reduced exponent $m - 1$, to end up

---

[1] Note that in the original article [90], the final form of C_m (Equation (15) on p. 65) seems to be incorrect. A comparison with [125, p. 172] for the case of vdW potential with $m = 6$ confirms the solution presented here. Additionally, this solution is verified by means of numerical quadrature in Section 4.5.1.1 (cf. Figure 4.4(a)).

with

$$\tilde{\pi}_{m,\text{cyl}\|\text{cyl},ss} = \iint_{A_1,A_2} \int_{-\infty}^{\infty} \rho_1 \rho_2 \, \Phi_m(r) \, \mathrm{d}s_2 \, \mathrm{d}s_1 \, \mathrm{d}A_2 \, \mathrm{d}A_1 \tag{A.14}$$

$$= \frac{3\pi}{8} \, \rho_1 \rho_2 \, k_m \, \frac{C_{m-1,\text{ss}}}{k_{m-1}}. \tag{A.15}$$

Plugging in $m = 6$ for vdW interaction directly yields the two-body interaction potential per unit length for two parallel cylinders in the regime of small separations $\tilde{\pi}_{\text{vdW,cyl}\|\text{cyl,ss}}$ as stated in Equation (2.14). This generic expression (A.15) will be exploited when deriving the total LJ interaction law in A.2.2.

A.1.3. Point-cylinder interaction

We aim to find an expression for the interaction potential $\Pi_{\text{m,pt-cyl}}$ of a single point, i.e. molecule, and an infinite cylinder of radius R and atom density ρ via analytical pair-wise summation of the generic point-pair potential Φ_{m}:

$$\Pi_{\text{m,pt-cyl}} = \int_{V_{\text{cyl}}} \rho \, \Phi_{\text{m}}(r) \, \mathrm{d}V, \quad \text{with} \quad \Phi_{\text{m}}(r) = k_{\text{m}} \, r^{-m}, \quad m \geq 6. \tag{A.16}$$

Its solution shall serve as the basis for the disk-cylinder interaction potential $\tilde{\pi}_{\text{m,disk-cyl}}$ as indicated in Equation (5.3). To the best of the author's knowledge, no exact (closed-form) analytical solution exists for this problem, however, as commonly applied in this context, good approximate analytical solutions for the dominating regime of small separations can be found by means of series expansion and truncation. This solution approach will be exemplified in the remainder of this section, where we present two alternative solutions and finally compare their accuracy to choose the one to be used in the derivation of $\tilde{\pi}_{\text{m,disk-cyl}}$ in Section 5.2.

A.1.3.1. Generalization of the solution by Montgomery et al. for the case of vdW interaction

We start from the following expression for the van der Waals, i.e. $m = 6$, interaction potential as obtained by Montgomery et al. [117]:

$$\Pi_{6,\text{pt-cyl}}(g_{\text{pt-cyl}}) = \frac{1}{8}\pi^2 k_6 \rho \left(\frac{1}{g_{\text{pt-cyl}}^3} - \frac{1}{(g_{\text{pt-cyl}} + 2R)^3} + \text{H.O.T.} \right) \tag{A.17}$$

Here, $g_{\text{pt-cyl}}$ denotes the closest distance between the point and the cylinder surface. Since we are interested in the limit of small separations $g_{\text{pt-cyl}}/R \ll 1$, the second and all higher order terms will be substantially smaller as compared to the first term and we will restrict ourselves to this leading term, resulting in

$$\Pi_{6,\text{pt-cyl}}(g_{\text{pt-cyl}}) = \frac{1}{8}\pi^2 k_6 \rho \, g_{\text{pt-cyl}}^{-3}. \tag{A.18}$$

All the steps of the derivation in [117], basically solving three nested integrals over the cylinder volume, can be generalized from the vdW case $m = 6$ to a generic exponent $m \geq 6$. Mainly due to the recursive nature of the following antiderivative (see e.g. [19, p.1020]) required for one of the integrals

$$\int X^{-(n+1)} \, \mathrm{d}x = \frac{x}{2na^2} X^{-n} + \frac{2n-1}{2na^2} \int X^{-n} \, \mathrm{d}x \quad \text{with} \quad X = a^2 + x^2 \tag{A.19}$$

$$\int X^{-1} \, \mathrm{d}x = \frac{x}{a} \arctan\left(\frac{x}{a}\right), \tag{A.20}$$

writing down the final expression for generic exponents m however is quite tedious. For the later reference, at this point we therefore present the general form of the solution

$$\Pi_{m,\text{pt-cyl}} = K_{m,\text{pt-cyl}} \, g_{\text{pt-cyl}}^{-m+3}, \quad m \geq 6 \tag{A.21}$$

and only provide the exact prefactors $K_{m,\text{pt-cyl}}$ for the two cases of vdW ($m = 6$) and repulsive part ($m = 12$) of the LJ potential, which are actually applied in the numerical examples of this work:

$$K_{6,\text{pt-cyl}} = \frac{1}{8}\pi^2 k_6 \rho \qquad \text{and} \qquad K_{12,\text{pt-cyl}} = \frac{7}{256}\pi^2 k_{12}\rho \tag{A.22}$$

A.1.3.2. Alternative solution obtained from the point-half space interaction

As compared to the point-cylinder interaction scenario from the previous section, the geometry of an (infinite) half space is a much simpler integration domain and thus even an exact analytical solution can be found and stated in closed form also for a general inverse power law exponent m (see e.g. [74, p.210]):

$$\Pi_{m,\text{pt-hs}} = K_{m,\text{pt-hs}} \, g_{\text{pt-hs}}^{-m+3}, \quad \text{with} \quad K_{m,\text{pt-hs}} = \frac{2}{(m-2)(m-3)}\pi k_m \rho \tag{A.23}$$

This expression shall serve as an alternative approximate solution for the sought-after point-cylinder interaction potential

$$\Pi_{m,\text{pt-cyl}} \approx \Pi_{m,\text{pt-hs}} \tag{A.24}$$

and its approximation quality will be investigated in the following section.

A.1.3.3. Investigation of the accuracy of both alternatives

This section aims to compare the accuracy of the variants Equation (A.21) and Equation (A.24) presented above. At first sight, the expression derived for the point-cylinder geometry (A.21) appears to be the more natural choice. However, as shown in more detail in Section 5.2.2.1, the resulting cylinder-cylinder interaction potential $\tilde{\pi}_{6,\text{cyl-cyl}}$ based on the approximate solution (A.21) deviates from the one obtained via analytical 6D integration. To be more precise, the solutions deviate by a constant scalar factor in the asymptotic behavior for very small separations,

which turns out to be independent of the mutual angle of the cylinders. Interestingly, exactly the same difference by a factor of $3/4\,\pi \approx 2.356$ has already been identified for the asymptotic case $R \to \infty$, i.e., when comparing the result to the one for point-half space interaction in the original publication [117]. This initially motivated the investigation of the alternative solution for the point-cylinder interaction potential presented in Appendix A.1.3.2. Using this alternative solution, the resulting disk-cylinder interaction potential applied within in the SBIP approach indeed yields the asymptotically correct solution for the cylinder-cylinder interaction (cf. again Sections 5.2.1 and 5.2.2 for the details), such that the difference in the results is tracked down to the underlying solution for $K_{6,\text{pt-cyl}}$ stated above. To this end, this assessment has been verified by means of a numerical reference solution obtained from 3D integration of the vdW point-pair potential over a cylinder volume in Maple [104]. For the relevant regime of small separations $g \ll R$, the numerical reference solution excellently agrees with the analytical solution obtained from the point-half space interaction in Appendix A.1.3.2. This rather counterintuitive result appears reasonable if we think of the two radii of curvature of the cylinder surface $R_{\text{c}1} = R$ and $R_{\text{c}2} = \infty$, of which both are much greater than the surface separation in the considered regime $g_{\text{pt-cyl}} \ll R$, such that the interacting point faces an almost flat surface. Finally, in the limit $g_{\text{pt-cyl}}/R \to 0$, this scenario coincides with the one of the point-half space interaction, which is the illustrative explanation why the corresponding analytical solution is the consistent one and therefore to be used in the derivation of Section 5.2.1.

A.2. Lennard-Jones force laws in the regime of small separations

As compared to the preceding sections, we now want to turn to the LJ interaction consisting of two power law contributions, one adhesive and one repulsive, respectively. Our motivation is to study the characteristics of the resulting, superposed force laws for disk-disk as well as cylinder-cylinder interactions by means of theoretical analysis of the analytical expressions. These findings shall prove valuable when deriving an effective yet accurate regularization of the LJ potential law for the limit of zero separation in Section 4.4.3. We therefore focus on the regime of small separations throughout this section.

Coming from the expressions for the two-body interaction potential $\tilde{\tilde{\pi}}_{m,\text{disk}\|\text{disk,ss}}$ and $\tilde{\pi}_{m,\text{cyl}\|\text{cyl,ss}}$ derived for a generic point pair potential Φ_m in A.1, we will now sum the adhesive contribution $m = 6$ and the repulsive contribution $m = 12$ and differentiate once to arrive at the desired LJ force laws.

A.2.1. Disk-disk interaction

As outlined above, we make use of (A.12) for both parts of the LJ interaction and immediately obtain

$$\tilde{\tilde{\pi}}_{\text{LJ,disk}\|\text{disk,ss}} = \tilde{k}_6\,g^{-\frac{5}{2}} + \tilde{k}_{12}\,g^{-\frac{17}{2}} \tag{A.25}$$

where the following abbreviations for the constant prefactors have been introduced:

$$\tilde{k}_6 := \frac{\pi}{8} k_6 \rho_1 \rho_2 \sqrt{\frac{2R_1 R_2}{R_1 + R_2}} \Gamma^2\left(\frac{5}{2}\right) \qquad \text{and} \qquad \tilde{k}_{12} := k_{12} \rho_1 \rho_2 \sqrt{\frac{2R_1 R_2}{R_1 + R_2}} 5.30 \times 10^{-3} \tag{A.26}$$

For later use in the analysis of the force law, let us restate the conversion from one set of parameters k_6, k_{12} specifying the point pair LJ potential to the other commonly used set $\Phi_{\text{LJ,eq}}, r_{\text{LJ,eq}}$ according to (2.8):

$$k_6 = 2\Phi_{\text{LJ,eq}} r_{\text{LJ,eq}}^6 \qquad \text{and} \qquad k_{12} = -\Phi_{\text{LJ,eq}} r_{\text{LJ,eq}}^{12} \tag{A.27}$$

Differentiation with respect to the separation yields the disk-disk LJ force law

$$\tilde{\tilde{f}}_{\text{LJ,disk}\|\text{disk,ss}} = -\frac{\mathrm{d}\,\tilde{\tilde{\pi}}_{\text{LJ,disk}\|\text{disk,ss}}}{\mathrm{d}\,g} = \frac{5}{2}\tilde{k}_6\,g^{-\frac{7}{2}} + \frac{17}{2}\tilde{k}_{12}\,g^{-\frac{19}{2}}. \tag{A.28}$$

See Section 4.4.3 for a plot of the function. This expression allows us to determine some very interesting, characteristic quantities like the equilibrium spacing $g_{\text{LJ,eq,disk}\|\text{disk}}$, i.e., the distance where the force vanishes:

$$g_{\text{LJ,eq,disk}\|\text{disk}} = \left(-\frac{17}{5}\frac{\tilde{k}_{12}}{\tilde{k}_6}\right)^{\frac{1}{6}} \approx 0.653\,513\,r_{\text{LJ,eq}}. \tag{A.29}$$

Due to the fact, that repulsive contributions from proximate point pairs decay faster than the adhesive contributions, we obtain a smaller equilibrium spacing as compared to the scenario of a point pair. Another differentiation allows us to determine the value of the force minimum, i.e., the maximal adhesive force, and the corresponding separation

$$\tilde{\tilde{f}}_{\text{LJ,disk}\|\text{disk,min}} \approx 0.904\,115\,\rho_1 \rho_2 \sqrt{\frac{2R_1 R_2}{R_1 + R_2}}\,r_{\text{LJ,eq}}^{\frac{5}{2}}\,\Phi_{\text{LJ,eq}} \tag{A.30}$$

$$g_{\tilde{\tilde{f}}_{\text{LJ,disk}\|\text{disk,min}}} = \left(-\frac{323}{35}\frac{\tilde{k}_{12}}{\tilde{k}_6}\right)^{\frac{1}{6}} \approx 0.771\,844\,8\,r_{\text{LJ,eq}} \approx 1.181\,07\,g_{\text{LJ,eq,disk}\|\text{disk}}. \tag{A.31}$$

These quantities turn out to be decisive for the choice of a regularized, i.e., altered force law that is to be used instead of the original one in order to cure the numerical problems that come with the singularity at zero separation $g = 0$.

In summary, we have found an analytical, closed-form expression for the disk-disk LJ force law (A.28), valid in the regime of small separations and for parallel disks. By means of elementary algebra, we were thus able to determine analytical expressions for the characteristic equilibrium spacing as well as value and spacing of the force minimum.

A.2.2. Cylinder-cylinder interaction

As in the previous section (A.1.2), we want to restrict ourselves to parallel, infinite cylinders and consider the length-specific interaction potential as well as force law. Again, starting from the

expression for a generic interaction potential (A.15), superposition yields

$$\tilde{\pi}_{\text{LJ,cyl}\|\text{cyl,ss}} = \tilde{k}_{\text{cyl,6}}\, g^{-\frac{3}{2}} + \tilde{k}_{\text{cyl,12}}\, g^{-\frac{15}{2}} \tag{A.32}$$

where the following abbreviations have been introduced:

$$\tilde{k}_{\text{cyl,6}} := \frac{\pi^2}{24} k_6 \rho_1 \rho_2 \sqrt{\frac{2R_1 R_2}{R_1 + R_2}} \qquad \text{and} \qquad \tilde{k}_{\text{cyl,12}} := 5.818\,68 \times 10^{-4}\, k_{12} \pi^2 \rho_1 \rho_2 \sqrt{\frac{2R_1 R_2}{R_1 + R_2}} \tag{A.33}$$

Differentiation with respect to the separation yields the cylinder-cylinder LJ force law

$$\tilde{f}_{\text{LJ,cyl}\|\text{cyl,ss}} = -\frac{\text{d}\,\tilde{\pi}_{\text{LJ,cyl}\|\text{cyl,ss}}}{\text{d}\,g} = \frac{3}{2}\,\tilde{k}_{\text{cyl,6}}\, g^{-\frac{5}{2}} + \frac{15}{2}\,\tilde{k}_{\text{cyl,12}}\, g^{-\frac{17}{2}}. \tag{A.34}$$

that shall be further analyzed in the following. To begin with, the equilibrium spacing for two parallel cylinders interacting via a LJ potential can be derived as

$$g_{\text{LJ,eq,cyl}\|\text{cyl}} = \left(-5\, \frac{\tilde{k}_{\text{cyl,12}}}{\tilde{k}_{\text{cyl,6}}} \right)^{\frac{1}{6}} \approx 0.571\,69\, r_{\text{LJ,eq}}. \tag{A.35}$$

This is an extremely interesting and important result, since it leads the way to the non-trivial stress-free configuration of two flexible, initially straight fibers. We make use of this knowledge e.g. in Chapter 7. Again, since the repulsive contribution of proximate point pairs decays faster than the adhesive contribution, this equilibrium spacing is smaller than $g_{\text{LJ,eq,disk}\|\text{disk}}$ for the disks, that in turn is smaller than $r_{\text{LJ,eq}}$ in the fundamental case of a point pair. The very same value of 57% of the point pair equilibrium spacing has already been mentioned as a side note by Langbein [90, p. 62], however, without presenting the detailed, comprehensive derivation. In addition to the equilibrium spacing, we can again determine and look at the value and location of the force minimum

$$\tilde{f}_{\text{LJ,cyl}\|\text{cyl,min}} \approx 2.116\,34\, \rho_1 \rho_2 \sqrt{\frac{2R_1 R_2}{R_1 + R_2}}\, r_{\text{LJ,eq}}^{\frac{7}{2}}\, \Phi_{\text{LJ,eq}} \tag{A.36}$$

$$g_{\tilde{f}_{\text{LJ,cyl}\|\text{cyl,min}}} = \left(-\frac{255}{15}\, \frac{\tilde{k}_{\text{cyl,12}}}{\tilde{k}_{\text{cyl,6}}} \right)^{\frac{1}{6}} \approx 0.701\,04\, r_{\text{LJ,eq}} \approx 1.226\,25\, g_{\text{LJ,eq,cyl}\|\text{cyl}}. \tag{A.37}$$

Here, we find that the force minimum, i.e., the maximal adhesive force is slightly shifted towards a smaller separation as compared to the disk-disk interaction. However, expressed in terms of the respective equilibrium spacing $g_{\text{LJ,eq,cyl}\|\text{cyl}}$, the value is slightly larger as compared to $1.18\, g_{\text{LJ,eq,disk}\|\text{disk}}$ from (A.31). With these results we conclude the derivation and analysis of LJ force laws in the regime of small separations and summarize the most important results in the following concluding section to serve as a quick access reference.

A.2.3. Summary

The following table gives an overview of some important quantities characterizing the LJ force laws for point-point, parallel disk-disk, and parallel cylinder-cylinder interaction.

	equilibrium spacing $r_{\text{LJ,eq}}$ / $g_{\text{LJ,eq}}$	location of force min. $r_{f_{\text{LJ,min}}}$ / $g_{f_{\text{LJ,min}}}$	min. force value $f_{\text{LJ,min}}$ / $\tilde{\tilde{f}}_{\text{LJ,min}}$ / $\tilde{f}_{\text{LJ,min}}$
point-point	$1\,[r_{\text{LJ,eq}}]$	$1.11\,[r_{\text{LJ,eq}}]$	$2.69\,\left[\frac{\Phi_{\text{LJ,eq}}}{r_{\text{LJ,eq}}}\right]$
disk$\parallel$disk	$0.65\,[r_{\text{LJ,eq}}]$	$0.77\,[r_{\text{LJ,eq}}]$	$0.90\,\left[\rho_1\rho_2\sqrt{\frac{2R_1R_2}{R_1+R_2}}\,r_{\text{LJ,eq}}^{\frac{5}{2}}\,\Phi_{\text{LJ,eq}}\right]$
cylinder$\parallel$cylinder	$0.57\,[r_{\text{LJ,eq}}]$	$0.70\,[r_{\text{LJ,eq}}]$	$2.12\,\left[\rho_1\rho_2\sqrt{\frac{2R_1R_2}{R_1+R_2}}\,r_{\text{LJ,eq}}^{\frac{7}{2}}\,\Phi_{\text{LJ,eq}}\right]$

Table A.1.: Comparison of characteristic quantities of LJ force laws for a pair of points, parallel disks and parallel cylinders.

B. Dimensionless key parameters of a system with (LJ) adhesive elastic fibers

This aim of this appendix is to identify the dimensionless parameters that govern the fundamental behavior of a mechanical system with elastic, adhesive fibers. Considering the space-continuous, static problem without external loads, the governing equation for the total potential energy (4.1) simplifies to the internal energy contributions from elastic forces and moments Π_{int}, which is well-known from beam theory, and the energy contribution from the interaction Π_{ia}. For the latter, we use the most general form (2.12) based on two nested volume integrals of the point-pair potential $\Phi(r)$ and consider the LJ potential with its adhesive and repulsive component as an example. The entire set of parameters carrying units is thus given by the length L and radius R of the fibers, its Young's modulus E, the atom density ρ, and finally the prefactors of the adhesive and repulsive part of the LJ law k_6 and k_{12}, respectively. Note that instead of these two prefactors, an equivalent set of parameters $r_{\text{LJ,eq}}$ and $\Phi_{\text{LJ,eq}}$ specifying the equilibrium distance and the corresponding minimal potential value of the LJ law is commonly used. Nondimensionalization of this equation by means of normalization of the primary variables with suitable length measures allows to identify the following (non-unique) set of dimensionless parameters:

$$\frac{L}{R} =: \zeta \qquad\qquad\qquad\qquad \text{slenderness ratio} \qquad (\text{B.1})$$

$$\frac{k_{12}}{|k_6|\,L^6} \quad \text{or} \quad \frac{r_{\text{LJ,eq}}}{R} \qquad\qquad \text{normalized equilibrium distance} \qquad (\text{B.2})$$

$$\frac{\rho^2\,|k_6|}{E\,L^3} \quad \text{or} \quad \frac{\rho^2\,|\Phi_{\text{LJ,eq}}|\,L^3}{E} \qquad \text{adhesive compliance} \qquad (\text{B.3})$$

The slenderness ratio ζ is known to be the only dimensionless parameter of the static elastic problem of beams and e.g. determines the amount and thus relevance of shear deformation. The second and third parameter are specific for the interactions between beams and given for the two alternative sets of LJ parameters mentioned above. Using $r_{\text{LJ,eq}}$ and $\Phi_{\text{LJ,eq}}$, these parameters nicely disclose their meaning as equilibrium distance measure and measure for the strength of adhesion relative to the fibers' structural rigidity. The latter is thus named "adhesive compliance", because it will determine how much the fibers will deform due to the exposure to adhesive interactions with other fibers. As expected, this compliance will increase with increasing strength of adhesion, i.e., increasing atom density and increasing depth of the LJ potential minimum and decrease with increasing structural stiffness, i.e., increasing Young's modulus and decreasing fiber length. Such a ratio has before been reported to crucially influence the peeling

behavior of thin films from rigid surfaces [138] and likewise the peeling and pull-off behavior of two adhesive fibers (see Chapter 7). An illustrative analogy for this adhesive compliance may be found as the ratio of fiber length L and persistence length l_p, which is commonly used in (bio-)polymer physics to measure the amount of deformation of filaments to be expected due to thermal excitation in the context of Brownian dynamics and thus characterizes filaments to be either flexible, semi-flexible, or rather stiff (see e.g. [40]). Finally, note that these dimensionless parameters are not unique and other recombinations of the ones given above are possible. Our approach of normalizing the governing equation as described above has been verified by means of the formalized dimensional analysis based on the Buckingham π theorem, which in addition to the three dimensionless parameters suggests a fourth dimensional group $\rho\,L^3$, which can be interpreted as the number of atoms in a cube with edge length L.

C. Linearization of Virtual Work Contributions

This appendix provides the required linearization of the discrete virtual work contributions for both the SSIP and SBIP approach. The content of Appendix C.1 has previously been published in the author's article [61].

C.1. Expressions required for SSIP approach

Generally, the discrete residual vectors $\mathbf{r}_{\mathrm{ia},j}$ from molecular interactions between two beam elements $j = 1, 2$ depend on the primary variables $\hat{\mathbf{x}}_k$ of both beam elements $k = 1, 2$. Consistent linearization thus yields the following four sub-matrices $\mathbf{k}_{jk}$ to be considered and assembled into the global stiffness matrix, i.e., system Jacobian $\mathbf{K}$:

$$\mathbf{k}_{11} := \frac{\mathrm{d}\,\mathbf{r}_{\mathrm{ia},1}}{\mathrm{d}\,\hat{\mathbf{x}}_1}, \quad \mathbf{k}_{12} := \frac{\mathrm{d}\,\mathbf{r}_{\mathrm{ia},1}}{\mathrm{d}\,\hat{\mathbf{x}}_2}, \quad \mathbf{k}_{21} := \frac{\mathrm{d}\,\mathbf{r}_{\mathrm{ia},2}}{\mathrm{d}\,\hat{\mathbf{x}}_1}, \quad \mathbf{k}_{22} := \frac{\mathrm{d}\,\mathbf{r}_{\mathrm{ia},2}}{\mathrm{d}\,\hat{\mathbf{x}}_2} \tag{C.1}$$

Note that the linearization with respect to the primary variables $\hat{\mathbf{x}}_k$ of both interacting beam elements simplifies due to the fact that the residuals $\mathbf{r}_{\mathrm{ia},j}$ do not depend on the cross-section rotations as discussed along with the derivation of the specific SSIP laws in Section 4.3. Thus, only the linearization with respect to the centerline degrees of freedom $\hat{\mathbf{d}}_k$ yields non-zero entries and are therefore presented in the remainder of this section.

C.1.1. Short-range volume interactions such as van der Waals and steric repulsion

The linearization of the residual contributions with respect to the primary variables $\hat{\mathbf{x}}$ of both interacting beam elements is directly obtained from differentiation of Equation (4.17) and (4.18):

$$\mathbf{k}_{\mathrm{m,ss},11} = (m - \tfrac{7}{2}) \int_0^{l_1} \int_0^{l_2} c_{\mathrm{m,ss}} \left(-d^{-1}\, g^{-m+\frac{5}{2}}\, \mathbf{H}_1^{\mathrm{T}} \mathbf{H}_1 + \right.$$
$$\left. \left(d^{-3}\, g^{-m+\frac{5}{2}} + (m - \tfrac{5}{2})\, d^{-2}\, g^{-m+\frac{3}{2}} \right) \mathbf{H}_1^{\mathrm{T}}\, (\boldsymbol{r}_1 - \boldsymbol{r}_2) \otimes (\boldsymbol{r}_1 - \boldsymbol{r}_2)^T\, \mathbf{H}_1 \right) \mathrm{d}s_2\, \mathrm{d}s_1$$
$$\tag{C.2}$$

$$\mathbf{k}_{\mathrm{m,ss},12} = (m - \tfrac{7}{2}) \int_0^{l_1} \int_0^{l_2} c_{\mathrm{m,ss}} \left(d^{-1}\, g^{-m+\frac{5}{2}}\, \mathbf{H}_1^{\mathrm{T}} \mathbf{H}_2 - \right.$$
$$\left. \left(d^{-3}\, g^{-m+\frac{5}{2}} + (m - \tfrac{5}{2})\, d^{-2}\, g^{-m+\frac{3}{2}} \right) \mathbf{H}_1^{\mathrm{T}}\, (\boldsymbol{r}_1 - \boldsymbol{r}_2) \otimes (\boldsymbol{r}_1 - \boldsymbol{r}_2)^T\, \mathbf{H}_2 \right) \mathrm{d}s_2\, \mathrm{d}s_1 \tag{C.3}$$

$$\mathbf{k}_{\text{m,ss,21}} = (m - \tfrac{7}{2}) \int_0^{l_1} \int_0^{l_2} c_{\text{m,ss}} \left(d^{-1} g^{-m+\frac{5}{2}} \, \mathbf{H}_2^{\text{T}} \mathbf{H}_1 - \right.$$
$$\left. \left(d^{-3} g^{-m+\frac{5}{2}} + (m - \tfrac{5}{2}) d^{-2} g^{-m+\frac{3}{2}} \right) \mathbf{H}_2^{\text{T}} (\boldsymbol{r}_1 - \boldsymbol{r}_2) \otimes (\boldsymbol{r}_1 - \boldsymbol{r}_2)^T \mathbf{H}_1 \right) \text{d}s_2 \, \text{d}s_1 \tag{C.4}$$

$$\mathbf{k}_{\text{m,ss,22}} = (m - \tfrac{7}{2}) \int_0^{l_1} \int_0^{l_2} c_{\text{m,ss}} \left(-d^{-1} g^{-m+\frac{5}{2}} \, \mathbf{H}_2^{\text{T}} \mathbf{H}_2 + \right.$$
$$\left. \left(d^{-3} g^{-m+\frac{5}{2}} + (m - \tfrac{5}{2}) d^{-2} g^{-m+\frac{3}{2}} \right) \mathbf{H}_2^{\text{T}} (\boldsymbol{r}_1 - \boldsymbol{r}_2) \otimes (\boldsymbol{r}_1 - \boldsymbol{r}_2)^T \mathbf{H}_2 \right) \text{d}s_2 \, \text{d}s_1. \tag{C.5}$$

See Equation (4.6) for the definition of the constant $c_{\text{m,ss}}$ and Equation (3.19) for the definition of the shape function matrices $\mathbf{H}_j$. Note that the 'mixed' matrix products $\mathbf{H}_1^{\text{T}}(\ldots)\mathbf{H}_2$ and $\mathbf{H}_2^{\text{T}}(\ldots)\mathbf{H}_1$ lead to off-diagonal entries in the tangent stiffness matrix of the system which couple the corresponding degrees of freedom. This is reasonable and necessary because these couplings represent the interaction between the respective bodies.

C.1.2. Long-range surface interactions such as electrostatics

In analogy to the previous section, differentiation of Equation (4.19) yields

$$\mathbf{k}_{\text{m,ls,11}} = -\int_0^{l_1} \int_0^{l_2} c_{\text{m,ls}} \, \mathbf{H}_1^{\text{T}} \frac{1}{d^{2m+4}} \left(\mathbf{H}_1 d^{m+2} - (m+2) d^m (\boldsymbol{r}_1 - \boldsymbol{r}_2) \otimes (\boldsymbol{r}_1 - \boldsymbol{r}_2)^T \mathbf{H}_1 \right) \text{d}s_2 \, \text{d}s_1$$
$$= \int_0^{l_1} \int_0^{l_2} c_{\text{m,ls}} \left(-\frac{1}{d^{m+2}} \mathbf{H}_1^{\text{T}} \mathbf{H}_1 + \frac{(m+2)}{d^{m+4}} \mathbf{H}_1^{\text{T}} (\boldsymbol{r}_1 - \boldsymbol{r}_2) \otimes (\boldsymbol{r}_1 - \boldsymbol{r}_2)^T \mathbf{H}_1 \right) \text{d}s_2 \, \text{d}s_1 \tag{C.6}$$

$$\mathbf{k}_{\text{m,ls,12}} = \int_0^{l_1} \int_0^{l_2} c_{\text{m,ls}} \left(\frac{1}{d^{m+2}} \mathbf{H}_1^{\text{T}} \mathbf{H}_2 - \frac{(m+2)}{d^{m+4}} \mathbf{H}_1^{\text{T}} (\boldsymbol{r}_1 - \boldsymbol{r}_2) \otimes (\boldsymbol{r}_1 - \boldsymbol{r}_2)^T \mathbf{H}_2 \right) \text{d}s_2 \, \text{d}s_1 \tag{C.7}$$

$$\mathbf{k}_{\text{m,ls,21}} = \int_0^{l_1} \int_0^{l_2} c_{\text{m,ls}} \left(\frac{1}{d^{m+2}} \mathbf{H}_2^{\text{T}} \mathbf{H}_1 - \frac{(m+2)}{d^{m+4}} \mathbf{H}_2^{\text{T}} (\boldsymbol{r}_1 - \boldsymbol{r}_2) \otimes (\boldsymbol{r}_1 - \boldsymbol{r}_2)^T \mathbf{H}_1 \right) \text{d}s_2 \, \text{d}s_1 \tag{C.8}$$

$$\mathbf{k}_{\text{m,ls,22}} = \int_0^{l_1} \int_0^{l_2} c_{\text{m,ls}} \left(-\frac{1}{d^{m+2}} \mathbf{H}_2^{\text{T}} \mathbf{H}_2 + \frac{(m+2)}{d^{m+4}} \mathbf{H}_2^{\text{T}} (\boldsymbol{r}_1 - \boldsymbol{r}_2) \otimes (\boldsymbol{r}_1 - \boldsymbol{r}_2)^T \mathbf{H}_2 \right) \text{d}s_2 \, \text{d}s_1 \tag{C.9}$$

See again Equation (3.19) for the definition of the shape function matrices $\mathbf{H}_j$. As mentioned before, the discrete element residual vectors in the specific case of Coulombic interactions directly follow for $m = 1$ and $c_{\text{m,ls}} = C_{\text{elstat}} \lambda_1 \lambda_2$. See Section 2.2.1 for the definition of C_{elstat} and Section 4.3.3 for the definition of the linear charge densities λ_i. Again, as mentioned already in Section 4.3.3, the case of long-range *volume* interactions only requires to adapt the constant prefactor via $c_{\text{m,ls}} = km A_1 A_2 \rho_1 \rho_2$.

C.2. Expressions required for SBIP approach

In order to solve the nonlinear system of equations resulting from discretization of (4.2) by means of Newton's method, the linearization, i.e., the tangent stiffness matrix, of the virtual work contribution (5.35) is required. Its derivation is a mere application of differentiation rules and presented in the following. Differentiation of the discrete residual vector resulting from Equation (5.35) reads

$$\Delta[\delta\Pi_{\mathrm{ia}}] = \int_0^{l_1} \Delta[\frac{\mathrm{d}\,\tilde{\pi}}{\mathrm{d}\,g_{\mathrm{ul}}}]\,\delta g_{\mathrm{ul}} + \frac{\mathrm{d}\,\tilde{\pi}}{\mathrm{d}\,g_{\mathrm{ul}}}\,\Delta[\delta g_{\mathrm{ul}}] \tag{C.10}$$

$$+ \Delta[\frac{\mathrm{d}\,\tilde{\pi}}{\mathrm{d}(\cos\alpha)}]\,\delta(\cos\alpha) + \frac{\mathrm{d}\,\tilde{\pi}}{\mathrm{d}(\cos\alpha)}\,\Delta[\delta(\cos\alpha)]\,\mathrm{d}s_1,$$

where $\Delta[.] := \frac{\mathrm{d}}{\mathrm{d}\,\hat{\mathbf{d}}}[.]\,\Delta\hat{\mathbf{d}}$ denotes the incremental change of a quantity expressed by an incremental change of the vector of degrees of freedom $\hat{\mathbf{d}}$. Refer to Equation (3.19) for the definition of this vector consisting of all those discrete degrees of freedom $\hat{\mathbf{d}} = [\hat{\mathbf{d}}_1^T, \hat{\mathbf{d}}_2^T]^T$, which are required for the centerline discretization of both elements $i = 1, 2$, and the definition of the correspondingly assembled matrix of shape functions $\mathbf{H}$. Therefore,

$$\Delta\boldsymbol{r}_1 = [\mathbf{H}_1, \mathbf{0}]\,\Delta\hat{\mathbf{d}},\; \Delta\boldsymbol{r}_1' = [\mathbf{H}_1', \mathbf{0}]\,\Delta\hat{\mathbf{d}}, \tag{C.11}$$

$$\Delta\boldsymbol{r}_2 = [\mathbf{0}, \mathbf{H}_2]\,\Delta\hat{\mathbf{d}},\; \Delta\boldsymbol{r}_2' = [\mathbf{0}, \mathbf{H}_2']\,\Delta\hat{\mathbf{d}},\; \text{and}\; \Delta\boldsymbol{r}_2'' = [\mathbf{0}, \mathbf{H}_2'']\,\Delta\hat{\mathbf{d}}$$

and the four $\Delta[.]$ terms from Equation (C.10) will now be expressed by means of these basic quantities. To begin with,

$$\Delta[\frac{\mathrm{d}\,\tilde{\pi}}{\mathrm{d}\,g_{\mathrm{ul}}}] = \frac{\mathrm{d}^2\,\tilde{\pi}}{\mathrm{d}\,g_{\mathrm{ul}}^2}\,\Delta g_{\mathrm{ul}} + \frac{\mathrm{d}^2\,\tilde{\pi}}{\mathrm{d}\,g_{\mathrm{ul}}\,\mathrm{d}(\cos\alpha)}\,\Delta[\cos\alpha], \tag{C.12}$$

where

$$\Delta g_{\mathrm{ul}} = \boldsymbol{n}_{\mathrm{ul}}^T(\Delta\boldsymbol{r}_1 - \Delta\boldsymbol{r}_2) \tag{C.13}$$

and

$$\Delta[\cos\alpha] = \left(\boldsymbol{v}_{\alpha 1}^T\,\Delta\boldsymbol{r}_1' + \boldsymbol{v}_{\alpha 2}^T\,\Delta\boldsymbol{r}_2' + (\boldsymbol{r}_2''^T\boldsymbol{v}_{\alpha 2})\,\Delta\xi_{2\mathrm{c}}\right)\,\mathrm{sgn}(\boldsymbol{t}_1^T\boldsymbol{t}_2) \tag{C.14}$$

are analogous to the variations of these quantities given in Equations (5.38) and (5.39). The required second derivatives of the disk-cylinder interaction potential $\tilde{\pi}$ from Equation (5.32) can – like the first derivatives in Equations (5.36) and (5.37) – be conveniently expressed in recursive manner as

$$\frac{\mathrm{d}^2\,\tilde{\pi}}{\mathrm{d}\,g_{\mathrm{ul}}^2} = (-m + \frac{7}{2})\frac{1}{g_{\mathrm{ul}}}\frac{\mathrm{d}\,\tilde{\pi}}{\mathrm{d}\,g_{\mathrm{ul}}} \quad \text{and} \tag{C.15}$$

$$\frac{\mathrm{d}^2\,\tilde{\pi}}{\mathrm{d}\,g_{\mathrm{ul}}\,\mathrm{d}(\cos\alpha)} = (-m + \frac{9}{2})\frac{1}{g_{\mathrm{ul}}}\frac{\mathrm{d}\,\tilde{\pi}}{\mathrm{d}(\cos\alpha)}. \tag{C.16}$$

Furthermore,

$$\Delta\left[\frac{\mathrm{d}\,\tilde{\pi}}{\mathrm{d}(\cos\alpha)}\right] = \frac{\mathrm{d}^2\,\tilde{\pi}}{\mathrm{d}\,g_{\mathrm{ul}}\,\mathrm{d}(\cos\alpha)}\,\Delta g_{\mathrm{ul}} + \frac{\mathrm{d}^2\,\tilde{\pi}}{\mathrm{d}(\cos\alpha)^2}\,\Delta[\cos\alpha], \tag{C.17}$$

and the missing second derivative of $\tilde{\pi}$ with respect to $\cos\alpha$ reads

$$\frac{\mathrm{d}^2\,\tilde{\pi}}{\mathrm{d}(\cos\alpha)^2} = \left(-\frac{R_1}{R_1\cos\alpha + R_2} + \frac{3\,R_1^2\cos^2\alpha}{(R_1\cos\alpha + R_2)^2}\right)\tilde{\pi}. \tag{C.18}$$

The linearization of the variation of the unilateral gap is obtained as

$$\Delta[\delta g_{\mathrm{ul}}] = \left(\delta r_1^T - \delta r_2^T\right)\Delta n_{\mathrm{ul}} - \delta r_2^{|T} n_{\mathrm{ul}} \otimes \Delta\xi_{2\mathrm{c}}, \tag{C.19}$$

where in turn the linearization of the unilateral unit normal vector

$$\Delta n_{\mathrm{ul}} = \frac{1}{d_{\mathrm{ul}}}\left(I_{3\times 3} - n_{\mathrm{ul}} \otimes n_{\mathrm{ul}}\right)\Delta d_{\mathrm{ul}} \tag{C.20}$$

and unilateral distance vector

$$\Delta d_{\mathrm{ul}} = \Delta r_1 - \Delta r_2 - r_2^{|} \otimes \Delta\xi_{2\mathrm{c}} \tag{C.21}$$

are required. In these equations, the linearization of the (closest-point) arc-length coordinate on the master side $\Delta\xi_{2\mathrm{c}}$ appears, which is a result from the fact that $\xi_{2\mathrm{c}}$ is determined via a closest-point-to-curve projection and thus depends on the current configuration, i.e., primary degrees of freedom. For this reason, we need

$$\Delta[r_2(\xi_{2\mathrm{c}})] = \Delta r_2(\xi_{2\mathrm{c}}) + r_2^{|}(\xi_{2\mathrm{c}})\,\Delta\xi_{2\mathrm{c}} \tag{C.22}$$

$$\Delta[r_2^{|}(\xi_{2\mathrm{c}})] = \Delta r_2^{|}(\xi_{2\mathrm{c}}) + r_2^{||}(\xi_{2\mathrm{c}})\,\Delta\xi_{2\mathrm{c}} \tag{C.23}$$

with

$$\Delta\xi_{2\mathrm{c}} = \frac{1}{p_{2,\xi_2}}\left(-r_2^{|T}\Delta r_1 + r_2^{|T}\Delta r_2 - d_{\mathrm{ul}}^T\Delta r_2^{|}\right). \tag{C.24}$$

Note the analogy to the corresponding variation $\delta\xi_{2\mathrm{c}}$ from Equation (5.41) and the definition of p_{2,ξ_2} given in Equation (5.44).

Remark. Up to this point, the number and complexity of the expressions is comparable to the ones required in the macroscopic line contact formulation proposed in [110] and the combination, i.e., blending[1] thereof with a point contact formulation in [111] (see Section 3.3 for a summary). Indeed, only the expressions that depend on the applied disk-cylinder interaction potential law deviate from the line contact case, where most commonly a quadratic penalty potential $\tilde{\pi} = 0.5\,\varepsilon_{\|}\,g_{\mathrm{ul}}^2$ is used. This is an interesting insight contributing to the broader topic of comparing macroscopic beam contact formulations and the approaches based on the steric

---

[1] on contact force level

repulsion of molecules developed in the scope of this work. See Sections 6.1 and 6.2 for a classification and brief comparison of these different approaches to beam-beam interactions.

Here, the additional expression for the linearization of the variation of the cosine of the mutual angle

$$\Delta[\delta(\cos\alpha)] = \left(\delta\boldsymbol{r}_1^{|T}\Delta\boldsymbol{v}_{\alpha1} + \delta\boldsymbol{r}_2^{|T}\Delta\boldsymbol{v}_{\alpha2} + \delta\xi_{2c}\left(\boldsymbol{r}_2^{\|T}\Delta\boldsymbol{v}_{\alpha2} + \boldsymbol{v}_{\alpha2}^T\Delta[\boldsymbol{r}_2^{\|}(\xi_{2c})]\right)\right. \tag{C.25}$$
$$\left. + \boldsymbol{v}_{\alpha2}^T\Delta[\delta\boldsymbol{r}_2^{|}] + (\boldsymbol{r}_2^{\|T}\boldsymbol{v}_{\alpha2})\Delta[\delta\xi_{2c}]\right)\,\mathrm{sgn}(\boldsymbol{t}_1^T\boldsymbol{t}_2)$$

is required for a consistent linearization and in fact most of the complexity comes from this contribution or, to be more precise, from the linearization of the variation of the element parameter of the closest-point on the master side

$$\Delta[\delta\xi_{2c}] = \frac{1}{p_{2,\xi_2}^2}\left(\delta\boldsymbol{r}_1^T\boldsymbol{r}_2^{|} - \delta\boldsymbol{r}_2^T\boldsymbol{r}_2^{|} + \delta\boldsymbol{r}_2^{|T}\boldsymbol{d}_{\mathrm{ul}}\right)\Delta[p_{2,\xi_2}] \tag{C.26}$$
$$+ \frac{1}{p_{2,\xi_2}}\left(-\delta\boldsymbol{r}_1^T\Delta[\boldsymbol{r}_2^{|}(\xi_{2c})] + \delta\boldsymbol{r}_2^T\Delta[\boldsymbol{r}_2^{|}(\xi_{2c})] - \delta\boldsymbol{r}_2^{|T}\Delta\boldsymbol{d}_{\mathrm{ul}} + \boldsymbol{r}_2^{|T}\Delta[\delta\boldsymbol{r}_2] - \boldsymbol{d}_{\mathrm{ul}}^T\Delta[\delta\boldsymbol{r}_2^{|}]\right).$$

In addition, the following quantities have been introduced in these last two equations.

$$\Delta[\boldsymbol{v}_{\alpha1}] = -\frac{1}{\|\boldsymbol{r}_1^{|}\|^2}\left(\left((\boldsymbol{I}_{3\times3} - \boldsymbol{t}_1\otimes\boldsymbol{t}_1^T)\boldsymbol{t}_2\right)\otimes\boldsymbol{r}_1^{|T}\right)\Delta\boldsymbol{r}_1^{|} \tag{C.27}$$
$$+ \frac{1}{\|\boldsymbol{r}_1^{|}\|}\left(\boldsymbol{I}_{3\times3} - \boldsymbol{t}_1\otimes\boldsymbol{t}_1^T\right)\Delta\boldsymbol{t}_2 - \frac{1}{\|\boldsymbol{r}_1^{|}\|}\left((\boldsymbol{t}_1^T\boldsymbol{t}_2)\boldsymbol{I}_{3\times3} + \boldsymbol{t}_1\otimes\boldsymbol{t}_2^T\right)\Delta\boldsymbol{t}_1$$

$$\Delta[\boldsymbol{v}_{\alpha2}] = -\frac{1}{\|\boldsymbol{r}_2^{|}\|^2}\left(\left((\boldsymbol{I}_{3\times3} - \boldsymbol{t}_2\otimes\boldsymbol{t}_2^T)\boldsymbol{t}_1\right)\otimes\boldsymbol{r}_2^{|T}\right)\Delta[\boldsymbol{r}_2^{|}(\xi_{2c})] \tag{C.28}$$
$$+ \frac{1}{\|\boldsymbol{r}_2^{|}\|}\left(\boldsymbol{I}_{3\times3} - \boldsymbol{t}_2\otimes\boldsymbol{t}_2^T\right)\Delta\boldsymbol{t}_1 - \frac{1}{\|\boldsymbol{r}_2^{|}\|}\left((\boldsymbol{t}_1^T\boldsymbol{t}_2)\boldsymbol{I}_{3\times3} + \boldsymbol{t}_2\otimes\boldsymbol{t}_1^T\right)\Delta\boldsymbol{t}_2$$

$$\Delta[\boldsymbol{r}_2^{\|}(\xi_{2c})] = \Delta\boldsymbol{r}_2^{\|}(\xi_{2c}) + \boldsymbol{r}_2^{\|\prime}(\xi_{2c})\,\Delta\xi_{2c} \tag{C.29}$$

$$\Delta[\delta\boldsymbol{r}_2^{|}] = \delta\boldsymbol{r}_2^{\|}\otimes\Delta\xi_{2c} \tag{C.30}$$

$$\Delta\boldsymbol{t}_i = \frac{1}{\|\boldsymbol{r}_i^{|}\|}\left(\boldsymbol{I}_{3\times3} - \boldsymbol{t}_i\otimes\boldsymbol{t}_i^T\right)\Delta[\boldsymbol{r}_i^{|}(\xi_i)], \quad \text{with } i = 1, 2 \tag{C.31}$$

Note that the correctness of the presented and implemented analytical linearization has been verified by means of automatic differentiation [66] of the virtual work expression (5.35). Due to the high complexity of $\Delta[\delta\xi_{2c}]$, it would be interesting to investigate how a neglect of this contribution would influence the computational cost on the one hand and the performance of the nonlinear solver on the other hand. In the context of this work, however, always the fully consistent linearization has been used.

D. Supplementary plots for the verification of the SBIP approach

This appendix provides additional plots that analyze the accuracy of the disk-cylinder interaction potential law $\tilde{\pi}_{\text{m,disk-cyl}}$ derived in Section 5.2.1 and its use within the general SBIP approach proposed in Section 5.1. In particular, Figure D.2 shows the vdW interaction potential of two cylinders as a function of the enclosed angle in a semi-logarithmic fashion and is thus closely related to Figure 5.5 using double-logarithmic plots to confirm the $1/\sin\alpha$-scaling. Similarly, Figure D.1 shows the supplementary plots to Figure 5.6(e) – 5.6(f).
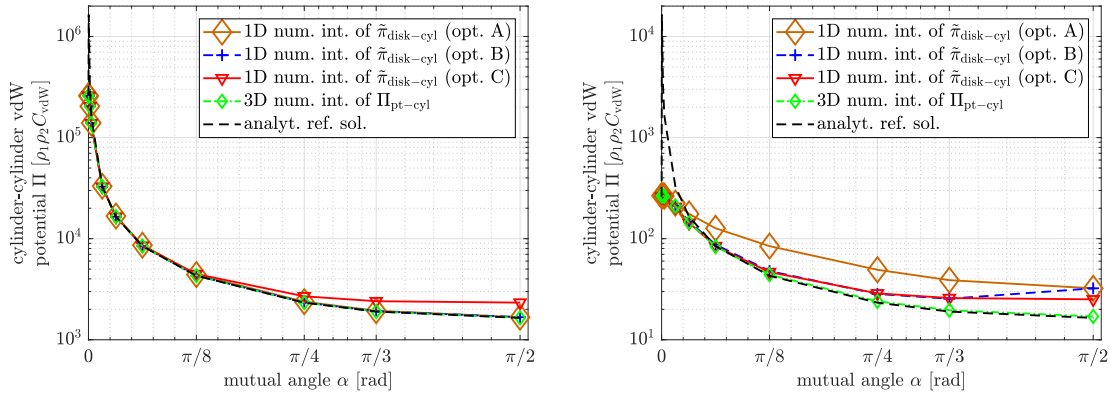
(a) Surface-to-surface separation $g_{\text{bl}}/R = 10^{-3}$ (b) Surface-to-surface separation $g_{\text{bl}}/R = 10^{-1}$

Figure D.1.: Interaction potential of two cylinders as a function of the mutual angle at different minimal surface separations g_{bl}/R. Comparison of the options A (Equations (5.25) with (5.27); brown line with big diamonds), B (Equation (5.25) with (5.28); blue dashed line with pluses) and C (Equation (5.32); red line with triangles) of the analytical expression for the disk-cylinder potential $\tilde{\pi}_{6,\text{disk-cyl}}$ (used together with the SBIP approach from Section 5.1). The numerical reference solution obtained via 3D Gaussian quadrature of the point-half space potential $\Pi_{6,\text{pt-hs}}$ from Equation (A.18) (green line with diamonds) and the analytical reference solutions summarized in Section 2.3.2 (black dashed line) are plotted as reference.

(a) Surface-to-surface separation $g_{\mathrm{bl}}/R = 10^{-3}$

(b) Surface-to-surface separation $g_{\mathrm{bl}}/R = 10^{-2}$

(c) Surface-to-surface separation $g_{\mathrm{bl}}/R = 10^{-1}$

(d) Surface-to-surface separation $g_{\mathrm{bl}}/R = 1$

Figure D.2.: Interaction potential of two cylinders as a function of the enclosed angle at different smallest surface separations g_{bl}/R. Verification of the analytical expression for the disk-cylinder potential $\tilde{\pi}_{6,\mathrm{disk\text{-}cyl}}$ from Equation (5.32) (used together with the SBIP approach from Section 5.1; red line with triangles) by means of a numerical reference solution obtained via 3D Gaussian quadrature of the point-half space potential $\Pi_{6,\mathrm{pt\text{-}hs}}$ from Equation (A.18) (green line with diamonds) and by means of analytical reference solutions summarized in Section 2.3.2 (black dashed line).

E. Supplementary information for the computational study of mucin conformations

This appendix provides the complete data set used for the definition of the line charge distribution along the filament and additional result data showing the end-to-end distance as well as radius of gyration over time for each of the five random realizations simulated for each of the six different considered scenarios.

E.1. Line charge distribution data set used in the computational study of mucin

Table E.1 provides the data specifying both the spatial discretization of the mucin filament by means of 68 beam elements and the corresponding constant charge density values per finite element, which are given in terms of the net number of elementary charges for all the considered scenarios. As mentioned in Section 9.2, the charge data is the result of an analysis of the full sequence of the porcine Mucin-5AC protein (A0A287ANG4_PIG, obtained from UniProt [158]) conducted by our collaboration partner Theresa Lutz (TUM). The elements with IDs 1–10 cover the 185 amino acids of the N-terminus, elements with IDs 11–58 cover the 2380 amino acids of the extended glycosolated domain, and the last ten elements with IDs 59–68 cover the 137 amino acids of the C-terminus.

element ID	element length [nm]	net number of elementary charges				
		pH 4	pH 7	pH 7, no SO_4^{2-}	pH 7, no SA	pH 7, no SO_4^{2-}, no SA
1	25	11	8	8	8	8
2	6	-5	-8	-8	-8	-8
3	26.5	4	-3	-3	-3	-3
4	26.5	1	-6	-6	-6	-6
5	6	13	-2	-2	-2	-2
6	22.25	2	0	0	0	0
7	22.25	0	-2	-2	-2	-2
8	22.25	0	-4	-4	-4	-4

element ID	element length [nm]	net number of elementary charges				
		pH 4	pH 7	pH 7, no SO_4^{2-}	pH 7, no SA	pH 7, no SO_4^{2-}, no SA
8	22.25	2	-1	-1	-1	-1
10	6	6	-4	-4	-4	-4
11	17.5	-5	-5	-1	-4	-6
12	17.5	-1	-1	0	-1	0
13	17.5	-8	-8	-3	-5	-3
14	17.5	-8	-8	-1	-7	-1
15	17.5	-19	-19	-5	-14	4
16	17.5	-9	-9	-3	-6	-5
17	17.5	-4	-4	0	-4	-1
18	17.5	-16	-16	-5	-11	2
19	17.5	-20	-20	-5	-15	-1
20	17.5	-6	-6	-1	-5	0
21	17.5	-5	-5	-2	-3	-3
22	17.5	-23	-23	-6	-17	0
23	17.5	-8	-8	-2	-6	-2
24	17.5	-1	-1	-1	0	2
25	17.5	-23	-23	-4	-19	0
26	17.5	-36	-36	-6	-30	0
27	17.5	-14	-14	-4	-10	-2
28	17.5	-2	-2	0	-2	0
29	17.5	-23	-23	-7	-16	0
30	17.5	-18	-18	-3	-15	-2
31	17.5	-3	-3	-1	-2	1
32	17.5	-17	-17	-4	-13	0
33	17.5	-31	-31	-6	-25	2
34	17.5	-32	-32	-7	-25	1
35	17.5	-29	-29	-5	-24	0
36	17.5	-33	-33	-8	-25	1
37	17.5	-32	-32	-6	-26	0
38	17.5	-30	-30	-6	-24	0
39	17.5	-30	-30	-5	-25	0
40	17.5	-31	-31	-6	-25	0
41	17.5	-33	-33	-6	-27	1
42	17.5	-30	-30	-5	-25	0
43	17.5	-33	-33	-6	-27	1
44	17.5	-30	-30	-8	-22	0
45	17.5	-23	-23	-6	-17	0
46	17.5	-16	-16	-3	-13	-2

element ID	element length [nm]	net number of elementary charges				
		pH 4	pH 7	pH 7, no SO$_4^{2-}$	pH 7, no SA	pH 7, no SO$_4^{2-}$, no SA
47	17.5	-3	-3	0	-3	0
48	17.5	-12	-12	-4	-8	2
49	17.5	-26	-26	-7	-19	0
50	17.5	-8	-8	-1	-7	0
51	17.5	-2	-2	-1	-1	0
52	17.5	-20	-20	-5	-15	1
53	17.5	-30	-30	-6	-24	0
54	17.5	-23	-23	-6	-17	0
55	17.5	-11	-11	-2	-9	2
56	17.5	-11	-11	-2	-9	1
57	17.5	-8	-8	-2	-6	2
58	10.5	-6	-6	-1	-5	2
59	6	8	-7	-7	-7	-7
60	20	0	-4	-4	-4	-4
61	20	0	-3	-3	-3	-3
62	4	3	-5	-5	-5	-5
63	12	2	-3	-3	-3	-3
64	4	2	-4	-4	-4	-4
65	17.75	5	-2	-2	-2	-2
66	17.75	6	4	4	4	4
67	17.75	5	0	0	0	0
68	17.75	4	-3	-3	-3	-3

Table E.1.: Data specifying the line charge distribution along the mucin filament for all the considered scenarios.

E.2. Supplementary figures

Figures E.1 and E.2 show the simulation results obtained for the end-to-end distance L_{e2e} and the radius of gyration R_g over time, thereby including all five simulation runs conducted for each of the six different considered scenarios and the trivial analytical reference solution obtained for a rigid mucin filament with the same dimensions as defined in the initial, stress-free state of the filament.
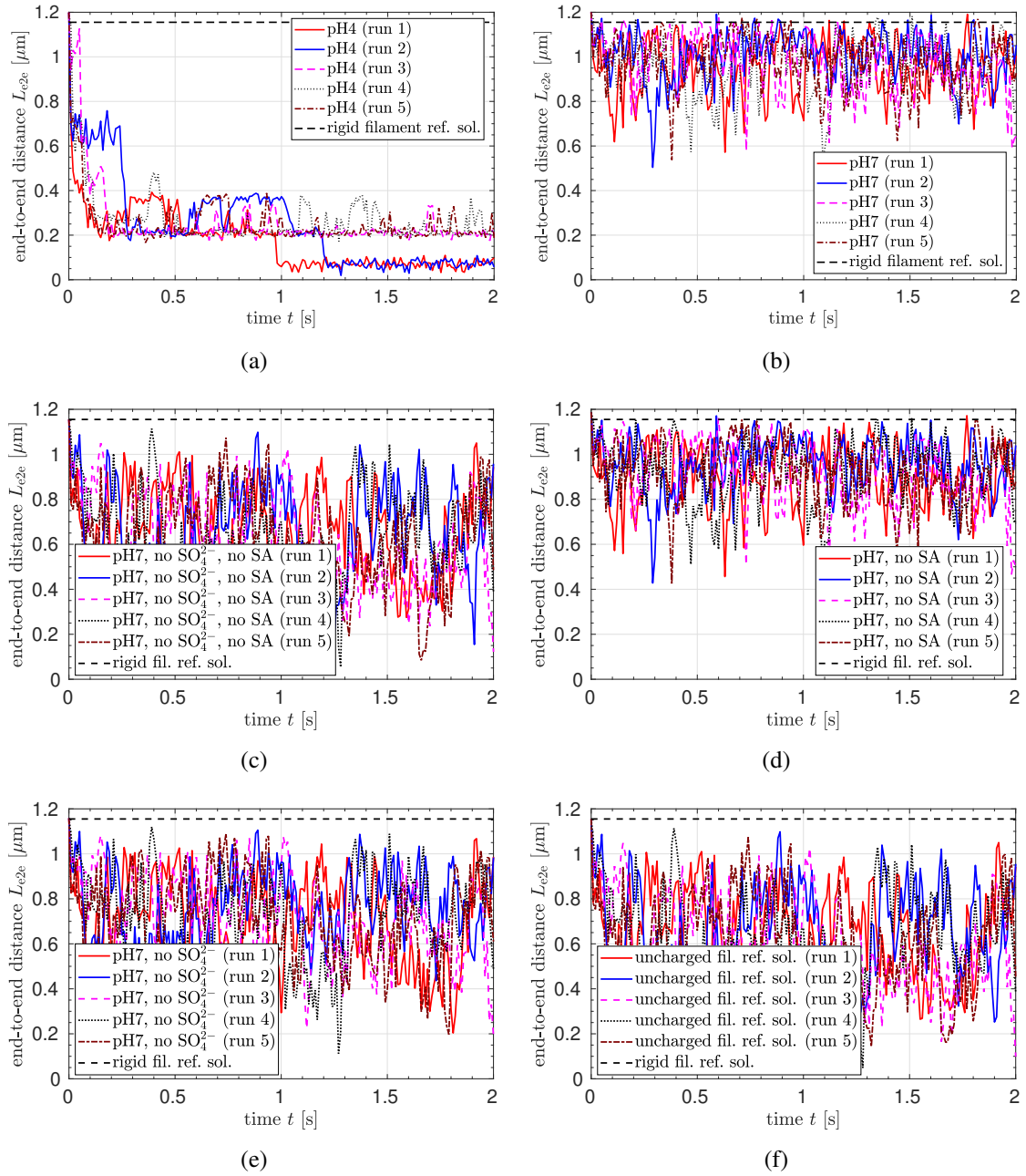
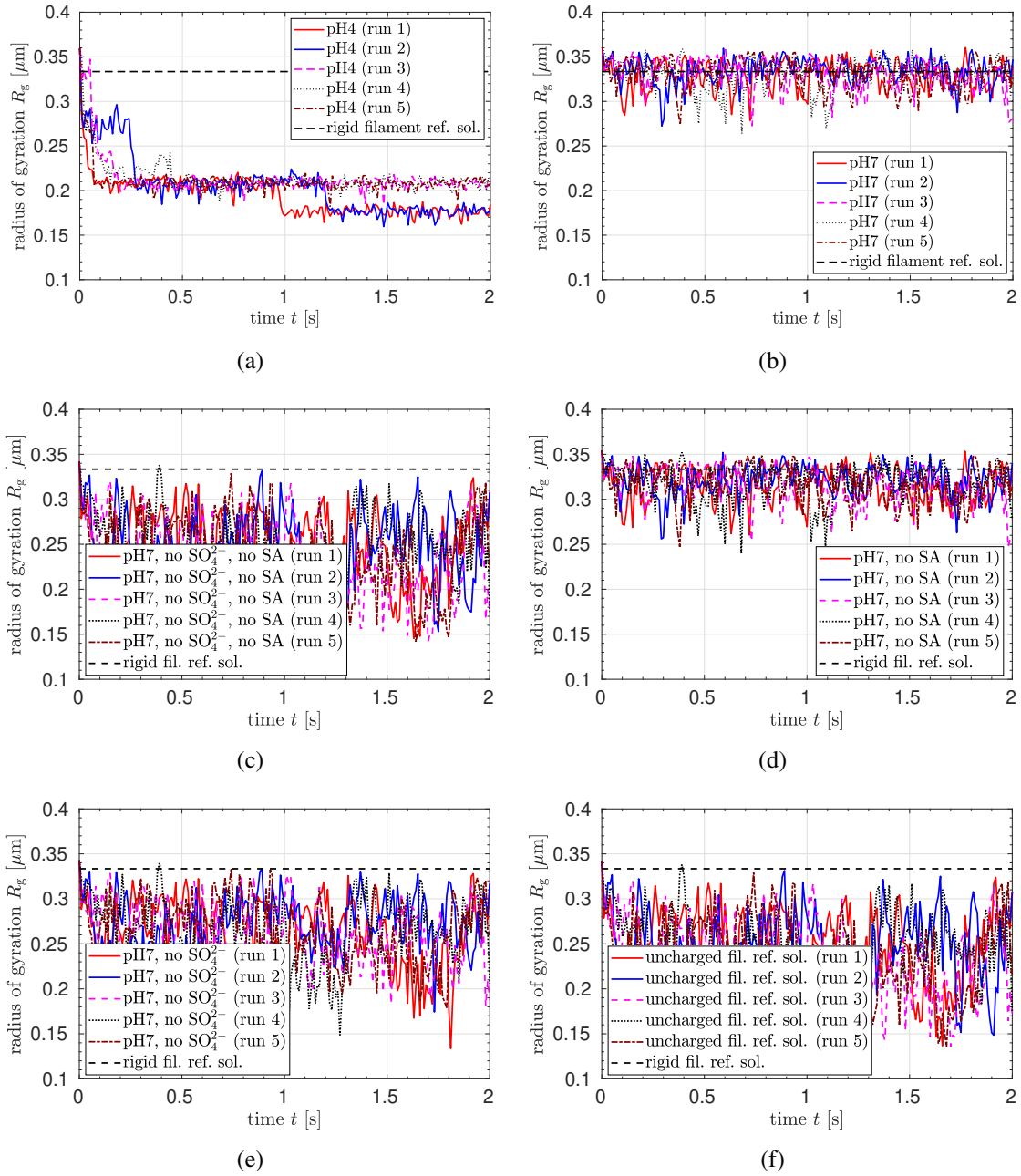Figure E.1.: End-to-end distance over time for the five random realizations simulated for each scenario.

Figure E.2.: Radius of gyration over time for the five random realizations simulated for each scenario.

F. The Comprehensive, Versatile and Powerful Computational Framework for Beam-Related Models and Methods

The software used for all the simulations presented in this work is the parallel, multi-physics, in-house research code BACI [73]. It is written in C++ and aims to solve a multitude of problems by means of cutting-edge numerical methods from the field of computational mechanics. Over many years, BACI has been and still is actively developed and maintained by a group of researchers working on advanced finite element methods, (hybridizable) discontinuous Galerkin methods, discrete element methods, mesh-free methods as well as other approaches. The aim of this appendix is to provide a brief overview of one specific part of BACI dealing with the mechanics of beams. In the context of this work, it has been thoroughly revised and extended as will be outlined in the following.

At the beginning of this PhD project, much of the extensive beam-related simulation framework to be presented in the next section has been readily available, mainly as a result of the previous PhD projects by Christian Cyron, Kei Müller, and Christoph Meier (TUM). However, a thorough revision of the entire beam-related code framework has been undertaken by the author in close collaboration with Jonas Eichinger (TUM), leading to the present state as summarized in the following section. The primary goal of this revision was the modularization of existing functionality, leading to a more versatile, extensible and maintainable code base. Further goals were an improved overall performance and particularly in terms of parallelization as a preparation for the intended use and extension within this and other PhD projects. Besides the daily maintenance and clean-up work and other minor contributions, the following list summarizes the author's major contributions to BACI:

- Implementation of the general SSIP approach and the interaction laws (cf. Chapter 4)

- Implementation of the general SBIP approach and the interaction laws (cf. Chapter 5)

- Design and implementation of a new code framework for all kinds of interactions between beams

- Introduction of a beam base element that unifies the common functionality of all beam element formulations

- Extension of the Simo-Reissner beam element to Hermite centerline interpolation (cf. Section 3.2.2)

- Implementation of the analytical linearization for the Kirchhoff-Love beam element

- Combination of the existing macroscopic beam contact formulations with the Simo-Reissner and Kirchhoff-Love beam elements (cf. Section 3.3.4)

- Combination of the Brownian dynamics formulation with Hermitian Simo-Reissner beam element, Kirchhoff-Love beam element, and torsion-free Kirchhoff-Love beam element

- Combination of the cross-linking formulation with Hermitian Simo-Reissner beam element, Kirchhoff-Love beam element, and torsion-free Kirchhoff-Love beam element

- Migration of large parts of the existing beam-related functionality to a new code framework for solid and structural mechanics

- Implementation of a module writing output in VTK format at runtime

In addition, the author has been a member of the steering committee of BACI and thus acted as one of the lead developers for more than three years.

F.1. Overview of implemented modules and overall integration

The overall integration follows the theoretical framework of the nonlinear finite element method applied to solve the nonlinear continuum mechanics of solids and structures. The novel approaches developed in this work can be integrated very well into such a framework. In particular, they do not depend on a specific beam (finite element) formulation and have been used with geometrically exact Kirchhoff-Love as well as Simo-Reissner beam elements. Also, they are independent of the temporal discretization and has been used along with statics, Lie group Generalized-Alpha as well as Brownian dynamics. This versatility is reflected in the code architecture such that the many different combinations of the available models and methods allows to tackle a multitude of problems including but not limited to the complex biophysical systems on the nano- and microscale studied in this work.

In the following, a brief overview of the implemented functionality and its organization in logical modules is provided. Selected aspects of special importance for the numerical examples of this work will be discussed in further detail in the following Section F.2.

Beam element formulations

- Simo-Reissner, Kirchhoff-Love, and torsion-free Kirchhoff-Love: each including . . .

- internal (elastic) forces and moments, and

- inertia forces and moments.

Boundary conditions

- external point/line forces and moments via Neumann boundary conditions

- Dirichlet point/line boundary conditions

- periodic boundary conditions

Brownian dynamics of beams

- viscous drag forces and moments

- stochastic thermal forces (and moments)

Interactions between beams

- macroscopic beam contact: point contact, line contact, and ABC formulation

- (molecular) interactions based on the SSIP or SBIP approach

- (cross-)links / connections

- search algorithm and problem partitioning used by all these interaction types

- coupling of degrees of freedom at a set of nodes

Load/time stepping

- (Lie group) Generalized-α time integration

- One-step-θ time integration

- Statics

- each including load/time step size adaptation

Nonlinear solver

- Newton-Raphson scheme with a special update of the multiplicative increments of rotational degrees of freedom

- Newton step size control

- Pseudo-transient continuation

Linear solver

- direct: UMFPACK [36]

- iterative: GMRES with different preconditioning strategies

F.2. Supplementary information on selected algorithms and external packages

The content of this section has previously been published in the author's article [61].

Load/time stepping Either a fixed step size or an automatic step size adaption is applied, which shall be outlined in the following. Starting from a given initial step size, a step is repeated with half of the previous step size if and only if the nonlinear solver did not converge within a prescribed number of iterations. This procedure may be repeated until convergence is achieved (or until a given finest step size is reached which aborts the algorithm). After four subsequent converging steps with a new, small step size, the step size is doubled. Again, this is repeated until the initial step size is reached.

Nonlinear solver The Newton-Raphson algorithm used throughout this work is based on the package NOX, which is part of the Trilinos project [66]. Unless otherwise stated, the Euclidean norms of the displacement increment vector and of the residual vector are used as convergence criteria. Typically, the corresponding tolerances were chosen as 10^{-10} and 10^{-7}, respectively. In some of the numerical examples, an additional Newton step size control is applied. It restricts the step size such that a specified upper bound of the displacement increment per nonlinear iteration is not exceeded. In simple terms, it is meant to prevent any two points on two beams from moving too far and eventually crossing each other without being detected from one iteration to the other. For this reason, the value for this upper bound is typically chosen as half of the beam radius.

Linear solver Throughout this work, the algorithm UMFPACK [36] has been applied. It is a direct solver for sparse linear systems of equations based on LU-factorization and included in the package Amesos, which is part of the Trilinos project [66].

Parallel computing The implementation of the novel methods supports parallel computing and is based on the package Epetra, which is part of the Trilinos project [66]. See Section 4.4.6 for details on the partitioning of the problem in the context of the search algorithm applied to identify spatially proximate interaction partners.

F.3. Post-processing and visualization

The post-processing of raw simulation data and plotting of results was done by means of self-written scripts using MATLAB [157]. Most visualizations of the simulation results were generated using Paraview [85] and the underlying file formats VTU for the beam geometries and VTP for the interaction forces, which will be briefly summarized in the following.

Concerning the beam geometry, two major challenges associated with the special properties of beam finite element formulations shall be outlined. Recall that the primary variables and thus raw simulation results are given as the nodal centerline positions and triads of the beams. The first challenge therefore is to visualize the actual, three-dimensional volumetric shape of the slender bodies based on nodal centerline and triad data. In the context of this work, a workflow

has been developed that uses the available *Tube* filter in Paraview [85] to generate the tube-like surface geometry of a beam with circular cross-sections as applied throughout this work. Specifically, the radius of each beam element is previously written as part of the simulation output and automatically applied as the radius of the tube in a customized Paraview filter. The second challenge is associated with the cubic Hermite polynomials that are used for the centerline interpolation of all beam element formulations applied throughout this work. As opposed to the more common Lagrange polynomials, these Hermite polynomials are not natively supported in Paraview [85], which means that the actual centerline curve between the nodal positions is not correctly obtained from the built-in interpolation scheme. As an alternative, the centerline curve is subdivided into a sufficiently large number of straight line segments already in the output routine in BACI and the VTK cell type *polyline* is written as output for each beam element. Consequently, the centroid positions and base vectors are written as point data for each of these polyline cells. Based on the experience of this work, a number of five straight subsegments per element already results in a sufficiently smooth visual impression of the geometry in almost all cases, i.e., for typical meshes and deformation magnitudes. Further result data can be written depending on the specific needs and include deformation measures (axial and shear strains, twist, curvature), resulting stresses (axial and shear forces, torsion and bending moments), internal and kinetic energy contributions (for individual modes) as well as the aforementioned radius of the circular cross-section.

Only where a particularly realistic and visually appealing representation of the simulated systems was intended, the scenes were rendered with the specialized computer graphics software Blender [14]. For this sake, the geometry data for all time steps was exported from Paraview [85] in STL format and imported and processed in Blender [14]. See Figures 10.1 and 10.3 for examples of this advanced visualization strategy.

As the most important quantity resulting from the novel approaches for molecular interactions of beams, it is highly desirable to also visualize the interaction force distributions. This is achieved by writing a set of point positions and associated force vectors at each of the integration points (and projected closest points in case of the SBIP approach). In Paraview [85], this result data set can then be processed using the *Glyph* filter to be finally depicted as individual force arrows and as an ensemble form the line force distributions along the beam axes[1]. The identical strategy has been applied to visualize the contact forces from the existing macroscopic beam contact formulations. Finally, the cross-links connecting two beams are visualized in a similar manner by writing its midpoint positions and a direction vector indicating its axis orientation. In Paraview [85], the application of the *Glyph* filter with a cylinder that is oriented according to this direction vector therefore allows to visualize the doubly bound cross-links in its current state and geometry.

---

[1]Note also the remark on the correct interpretation of the force visualization given in Section 4.5.2.

Bibliography

[1] M. Abdulkarim, N. Agulló, B. Cattoz, P. Griffiths, A. Bernkop-Schnürch, S. G. Borros, and M. Gumbleton, Nanoparticle diffusion within intestinal mucus: Three-dimensional response analysis dissecting the impact of particle surface charge, size and heterogeneity across polyelectrolyte, pegylated and viral particles, *European Journal of Pharmaceutics and Biopharmaceutics* **97**, 230–238, 2015.

[2] S. Ahmadi and C. Menon, A new model for predicting fiber clumping phenomenon in bio-inspired dry adhesives, *Journal of Adhesion* **90**, 135–155, 2014.

[3] O. G. Andriotis, S. Desissaire, and P. J. Thurner, Collagen Fibrils: Nature's Highly Tunable Nonlinear Springs, *ACS Nano* **12**, 3671–3680, 2018.

[4] F. Arends, R. Baumgärtel, and O. Lieleg, Ion-Specific Effects Modulate the Diffusive Mobility of Colloids in an Extracellular Matrix Gel, *Langmuir* **29**, 15965–15973, 2013.

[5] F. Arends, C. Nowald, K. Pflieger, K. Boettcher, S. Zahler, and O. Lieleg, The biophysical properties of basal lamina gels depend on the biochemical composition of the gel, *PLoS ONE* **10**, e0118090, 2015.

[6] F. Arends, H. Chaudhary, P. Janmey, M. M. A. E. Claessens, and O. Lieleg, Lipid Head Group Charge and Fatty Acid Configuration Dictate Liposome Mobility in Neurofilament Networks, *Macromolecular Bioscience* **17**, 1600229, 2017.

[7] C. Argento, A. Jagota, and W. C. Carter, Surface formulation for molecular interactions of macroscopic bodies, *Journal of the Mechanics and Physics of Solids* **45**, 1161–1183, 1997.

[8] K. Autumn, Y. A. Liang, S. T. Hsieh, W. Zesch, W. P. Chan, T. W. Kenny, R. Fearing, and R. J. Full, Adhesive force of a single gecko foot-hair, *Nature* **405**, 681–685, 2000.

[9] K. Autumn, M. Sitti, Y. A. Liang, A. M. Peattie, W. R. Hansen, S. Sponberg, T. W. Kenny, R. Fearing, J. N. Israelachvili, and R. J. Full, Evidence for van der Waals adhesion in gecko setae, *Proceedings of the National Academy of Sciences* **99**, 12252 – 12256, 2002.

[10] R. Bansil and B. S. Turner, Mucin structure, aggregation, physiological functions and biomedical applications, *Current Opinion in Colloid & Interface Science* **11**, 164–170, 2006.

[11] Y. Basar and D. Weichert, *Nonlinear Continuum Mechanics of Solids*, Springer, Berlin, Heidelberg, 2000.

[12] K.-J. Bathe, *Finite element procedures*, Klaus-Jürgen Bathe, Watertown, MA, 2nd Edition, 2014.

[13] K.-J. Bathe and S. Bolourchi, Large displacement analysis of three-dimensional beam structures, *International Journal for Numerical Methods in Engineering* **14**, 961–986, 1979.

[14] Blender Foundation. Blender 2.80, 2019.

[15] I. Borukhov, R. F. Bruinsma, W. M. Gelbart, and A. J. Liu, Structural polymorphism of the cytoskeleton: A model of linker-assisted filament aggregation, *Proceedings of the National Academy of Sciences of the United States of America* **102**, 3673–3678, 2005.

[16] S. L. Brenner and V. A. Parsegian, A physical method for deriving the electrostatic interaction between rod-like polyions at all mutual angles, *Biophysical Journal* **14**, 327–334, 1974.

[17] D. Brodoceanu, C. T. Bauer, E. Kroner, E. Arzt, and T. Kraus, Hierarchical bioinspired adhesive surfaces - A review, *Bioinspiration and Biomimetics* **11**, 051001, 2016.

[18] C. P. Broedersz, M. Depken, N. Y. Yao, M. R. Pollak, D. A. Weitz, and F. C. MacKintosh, Cross-Link-Governed Dynamics of Biopolymer Networks, *Physical Review Letters* **105**, 238101, 2010.

[19] I. N. Bronshtein, K. A. Semendyayev, G. Musiol, and H. Muehlig, *Handbook of mathematics*, Springer Science & Business Media, 4th Edition, 2003.

[20] O. Brüls and A. Cardona, On the Use of Lie Group Time Integrators in Multibody Dynamics, *Journal of Computational and Nonlinear Dynamics* **5**, 031002, 2010.

[21] M. J. Buehler, Atomistic and continuum modeling of mechanical properties of collagen: Elasticity, fracture, and self-assembly, *Journal of Materials Research* **21**, 1947–1961, 2006.

[22] A. Cardona and M. Geradin, A beam finite element non-linear theory with finite rotations, *International Journal for Numerical Methods in Engineering* **26**, 2403–2438, 1988.

[23] M. Chamekh, S. Mani-Aouadi, and M. Moakher, Stability of elastic rods with self-contact, *Computer Methods in Applied Mechanics and Engineering* **279**, 227–246, 2014.

[24] M. Chamekh, M. A. Latrach, and Y. Renard, Frictional self-contact problem of elastic rods, *Journal of King Saud University - Science*, 2019.

[25] J. Chung and G. M. Hulbert, A Time Integration Algorithm for Structural Dynamics With Improved Numerical Dissipation: The Generalized-α Method, *Journal of Applied Mechanics* **60**, 371, 1993.

[26] L. J. Colwell, M. P. Brenner, and K. Ribbeck, Charge as a Selection Criterion for Translocation through the Nuclear Pore Complex, *PLOS Computational Biology* **6**, e1000747, 2010.

[27] T. R. Cox, D. Bird, A.-M. Baker, H. E. Barker, M. W.-Y. Ho, G. Lang, and J. T. Erler, LOX-Mediated Collagen Crosslinking Is Responsible for Fibrosis-Enhanced Metastasis, *Cancer Research* **73**, 1721 – 1732, 2013.

[28] M. A. Crisfield, A consistent co-rotational formulation for non-linear, three-dimensional, beam-elements, *Computer Methods in Applied Mechanics and Engineering* **81**, 131–150, 1990.

[29] M. A. Crisfield and G. Jelenić, Objectivity of strain measures in the geometrically exact three-dimensional beam theory and its finite-element implementation, *Proceedings of the Royal Society of London. Series A: Mathematical, Physical and Engineering Sciences* **455**, 1125–1147, 1999.

[30] L. A. Crivelli and C. A. Felippa, A three-dimensional non-linear Timoshenko beam based on the core-congruential formulation, *International Journal for Numerical Methods in Engineering* **36**, 3647–3673, 1993.

[31] C. J. Cyron and W. A. Wall, Finite-element approach to Brownian dynamics of polymers, *Physical Review E* **80**, 66704, 2009.

[32] C. J. Cyron and W. A. Wall, Consistent finite-element approach to Brownian polymer dynamics with anisotropic friction, *Physical Review E* **82**, 66705, 2010.

[33] C. J. Cyron and W. A. Wall, Numerical method for the simulation of the Brownian dynamics of rod-like microstructures with three-dimensional nonlinear beam elements, *International Journal for Numerical Methods in Engineering* **90**, 955–987, 2012.

[34] C. J. Cyron, K. W. Müller, K. M. Schmoller, A. R. Bausch, W. A. Wall, and R. F. Bruinsma, Equilibrium phase diagram of semi-flexible polymer networks with linkers, *Europhysics Letters* **102**, 38003, 2013.

[35] C. J. Cyron, K. W. Müller, A. R. Bausch, and W. A. Wall, Micromechanical simulations of biopolymer networks with finite elements, *Journal of Computational Physics* **244**, 236–251, 2013.

[36] T. A. Davis, Algorithm 832: UMFPACK V4.3 – an unsymmetric-pattern multifrontal method, *ACM Transactions on Mathematical Software* **30**, 196–199, 2004.

[37] M. Dellian, F. Yuan, V. S. Trubetskoy, V. P. Torchilin, and R. K. Jain, Vascular permeability in a human tumour xenograft: molecular charge dependence, *British Journal of Cancer* **82**, 1513–1518, 2000.

[38] B. Depalle, Z. Qin, S. J. Shefelbine, and M. J. Buehler, Influence of cross-link structure, density and mechanical properties in the mesoscale deformation mechanisms of collagen fibrils, *Journal of the Mechanical Behavior of Biomedical Materials* **52**, 1–13, 2015.

[39] J. F. Dobson and T. Gould, Calculation of dispersion energies, *Journal of Physics Condensed Matter* **24**, 2012.

[40] M. Doi and S. F. Edwards, *The theory of polymer dynamics*, Oxford university press, 1988.

[41] A. D. Doyle, Generation of 3D Collagen Gels with Controlled Diverse Architectures, *Current Protocols in Cell Biology* **72**, 10.20.1–10.20.16, 2016.

[42] D. M. Dryden, J. C. Hopkins, L. K. Denoyer, L. Poudel, N. F. Steinmetz, W.-Y. Ching, R. Podgornik, A. Parsegian, and R. H. French, van der Waals Interactions on the Mesoscale: Open-Science Implementation, Anisotropy, Retardation, and Solvent Effects, *Langmuir* **31**, 10145–10153, 2015.

[43] D. Durville, Simulation of the mechanical behaviour of woven fabrics at the scale of fibers, *International Journal of Material Forming* **3**, 1241–1251, 2010.

[44] D. Durville, Contact-friction modeling within elastic beam assemblies: an application to knot tightening, *Computational Mechanics* **49**, 687–707, 2012.

[45] D. Durville, Finite Element Simulation of Textile Materials at Mesoscopic Scale, In *Finite element modelling of textiles and textile composites*, pages 1–14, Saint-Petersbourg, Russian Federation, 2007.

[46] S. R. Eugster, C. Hesch, P. Betsch, and C. Glocker, Director-based beam finite elements relying on the geometrically exact beam theory formulated in skew coordinates, *International Journal for Numerical Methods in Engineering* **97**, 111–129, 2014.

[47] D. R. Eyre and J.-J. Wu, Collagen Cross-Links, In J. Brinckmann, H. Notbohm, and P. K. Müller (eds.), *Collagen. Topics in Current Chemistry*, pages 207–229, Springer Berlin Heidelberg, Berlin, Heidelberg, 2005.

[48] H. Fan and S. Li, A three-dimensional surface stress tensor formulation for simulation of adhesive contact in finite deformation, *International Journal for Numerical Methods in Engineering* **107**, 252–270, 2016.

[49] P. Fratzl, *Collagen*, Springer US, Boston, MA, 2008.

[50] P. Fratzl and R. Weinkamer, Nature's hierarchical materials, *Progress in Materials Science* **52**, 1263–1334, 2007.

[51] R. H. French, V. A. Parsegian, R. Podgornik, R. F. Rajter, A. Jagota, J. Luo, D. Asthagiri, M. K. Chaudhury, Y. M. Chiang, S. Granick, S. Kalinin, M. Kardar, R. Kjellander, D. C. Langreth, J. Lewis, S. Lustig, D. Wesolowski, J. S. Wettlaufer, W. Y. Ching, M. Finnis,

F. Houlihan, O. A. Von Lilienfeld, C. J. Van Oss, and T. Zemb, Long range interactions in nanoscale science, *Reviews of Modern Physics* **82**, 1887–1944, 2010.

[52] D. Frenkel and B. Smit, *Understanding molecular simulation: from algorithms to applications*, Academic Press, 2001.

[53] H. Gao, X. Wang, H. Yao, S. Gorb, and E. Arzt, Mechanics of hierarchical adhesion structures of geckos, *Mechanics of Materials* **37**, 275–285, 2005.

[54] A. Gautieri, M. I. Pate, S. Vesentini, A. Redaelli, and M. J. Buehler, Hydration and distance dependence of intermolecular shearing between collagen molecules in a model microfibril, *Journal of Biomechanics* **45**, 2079–2083, 2012.

[55] W. Gautschi, The use of rational functions in numerical quadrature, *Journal of Computational and Applied Mathematics* **133**, 111–126, 2001.

[56] A. Gay Neto, P. M. Pimenta, and P. Wriggers, A master-surface to master-surface formulation for beam to beam contact. Part I: Frictionless interaction, *Computer Methods in Applied Mechanics and Engineering* **303**, 400–429, 2016.

[57] A. Gay Neto, P. M. Pimenta, and P. Wriggers, A master-surface to master-surface formulation for beam to beam contact. Part II: Frictional interaction, *Computer Methods in Applied Mechanics and Engineering* **319**, 146–174, 2017.

[58] C. P. Goodrich, M. P. Brenner, and K. Ribbeck, Enhanced diffusion by binding to the crosslinks of a polymer gel, *Nature Communications* **9**, 4348, 2018.

[59] M. Griebel, S. Knapek, and G. Zumbusch, *Numerical Simulation in Molecular Dynamics*, Springer Berlin Heidelberg, 2007.

[60] M. J. Grill, C. Meier, and W. A. Wall, Investigation of the peeling and pull-off behavior of adhesive elastic fibers via a novel computational beam interaction model, *The Journal of Adhesion*, 2019 (accepted), https://doi.org/10.1080/00218464.2019.1699795.

[61] M. J. Grill, W. A. Wall, and C. Meier, A computational model for molecular interactions between curved slender fibers undergoing large 3D deformations with a focus on electrostatic, van der Waals, and repulsive steric forces, *International Journal for Numerical Methods in Engineering*, 2020 (accepted), https://doi.org/10.1002/nme.6309.

[62] R. Hambli and A. Barkaoui, Physically based 3D finite element model of a single mineralized collagen microfibril, *Journal of Theoretical Biology* **301**, 28–41, 2012.

[63] K. M. Hamdia, M. Marino, X. Zhuang, P. Wriggers, and T. Rabczuk, Sensitivity analysis for the mechanics of tendons and ligaments: investigation on the effects of collagen structural properties via a multiscale modelling approach., *International Journal for Numerical Methods in Biomedical Engineering* **35**, e3209, 2019.

[64] J. Hansing and R. R. Netz, Particle Trapping Mechanisms Are Different in Spatially Ordered and Disordered Interacting Gels, *Biophysical Journal* **114**, 2653–2664, 2018.

[65] J. Hansing, C. Ciemer, W. K. Kim, X. Zhang, J. E. DeRouchey, and R. R. Netz, Nanoparticle filtering in charged hydrogels: Effects of particle size, charge asymmetry and salt concentration, *European Physical Journal E* **39**, 53, 2016.

[66] M. A. Heroux and J. M. Willenbring, A New Overview of the Trilinos Project, *Scientific Programming* **20**, 83–88, 2012.

[67] F. Hilitski, A. R. Ward, L. Cajamarca, M. F. Hagan, G. M. Grason, and Z. Dogic, Measuring cohesion between macromolecular filaments one pair at a time: Depletion-induced microtubule bundling, *Physical Review Letters* **114**, 138102, 2015.

[68] G. A. Holzapfel, *Nonlinear Solid Mechanics*, John Wiley & Sons, 2000.

[69] G. A. Holzapfel and R. W. Ogden, Biomechanical relevance of the microstructure in artery walls with a focus on passive and active components, *American Journal of Physiology-Heart and Circulatory Physiology* **315**, H540–H549, 2018.

[70] G. A. Holzapfel, R. W. Ogden, and S. Sherifova, On fibre dispersion modelling of soft biological tissues: a review, *Proceedings of the Royal Society A: Mathematical, Physical and Engineering Sciences* **475**, 20180736, 2019.

[71] D. L. Humphries, J. A. Grogan, and E. A. Gaffney, Mechanical Cell - Cell Communication in Fibrous Networks: The Importance of Network Geometry, *Bulletin of Mathematical Biology* **79**, 498–524, 2017.

[72] A. Ibrahimbegovic, On finite element implementation of geometrically nonlinear Reissner's beam theory: three-dimensional curved beam elements, *Computer Methods in Applied Mechanics and Engineering* **122**, 11–26, 1995.

[73] Institute for Computational Mechanics (Technical University of Munich). BACI: A multiphysics simulation environment, 2020.

[74] J. N. Israelachvili, *Intermolecular and surface forces*, Academic press, Oxford, 3rd Edition, 2011.

[75] R. P. Jaiswal and S. P. Beaudoin, Approximate Scheme for Calculating van der Waals Interactions between Finite Cylindrical Volume Elements, *Langmuir* **28**, 8359–8370, 2012.

[76] G. Jelenić and M. A. Crisfield, Geometrically exact 3D beam theory: implementation of a strain-invariant finite element for statics and dynamics, *Computer Methods in Applied Mechanics and Engineering* **171**, 141–171, 1999.

[77] L. Johansson and J. E. Löfroth, Diffusion and interaction in gels and solutions. 4. Hard sphere Brownian dynamics simulations, *The Journal of Chemical Physics* **98**, 7471–7479, 1993.

[78] M. G. Jones, O. G. Andriotis, J. J. W. Roberts, K. Lunn, V. J. Tear, L. Cao, K. Ask, D. E. Smart, A. Bonfanti, P. Johnson, A. Alzetani, F. Conforti, R. Doherty, C. Y. Lai, B. Johnson, K. N. Bourdakos, S. V. Fletcher, B. G. Marshall, S. Jogai, C. J. Brereton, S. J. Chee, C. H. Ottensmeier, P. Sime, J. Gauldie, M. Kolb, S. Mahajan, A. Fabre, A. Bhaskar, W. Jarolimek, L. Richeldi, K. M. A. O'Reilly, P. D. Monk, P. J. Thurner, and D. E. Davies, Nanoscale dysregulation of collagen structure-function disrupts mechano-homeostasis and mediates pulmonary fibrosis, *eLife* **7**, e36354, 2018.

[79] K. Kadler, D. Holmes, J. Trotter, and J. Chapman, Collagen fibril formation, *Biochemical Journal* **316**, 1–11, 1996.

[80] N. Kamerlin and C. Elvingson, Tracer diffusion in a polymer gel: Simulations of static and dynamic 3D networks using spherical boundary conditions, *Journal of Physics Condensed Matter* **28**, 2016.

[81] B. T. Käsdorf, F. Arends, and O. Lieleg, Diffusion Regulation in the Vitreous Humor, *Biophysical Journal* **109**, 2171–2181, 2015.

[82] J. Kastelic, A. Galeski, and E. Baer, The multicomposite structure of tendon, *Connective Tissue Research* **6**, 11–23, 1978.

[83] K. Kendall, Thin-Film Peeling - The Elastic Term, *Journal of Physics D: Applied Physics* **8**, 1449–1452, 1975.

[84] A. B. Kesel, A. Martin, and T. Seidl, Adhesion measurements on the attachment devices of the jumping spider Evarcha arcuata, *Journal of Experimental Biology* **206**, 2733 – 2738, 2003.

[85] Kitware Inc. Paraview 5.4.1.

[86] A. Konyukhov, O. Mrenes, and K. Schweizerhof, Consistent Development of a Beam-To-Beam Contact Algorithm via the Curve-to-Solid Beam Contact - Analysis for the Nonfrictional Case, *International Journal for Numerical Methods in Engineering* **113**, 1108–1144, 2018.

[87] A. Kulachenko and T. Uesaka, Direct simulations of fiber network deformation and failure, *Mechanics of Materials* **51**, 1–14, 2012.

[88] A. Kusumi, Y. Sako, and M. Yamamoto, Confined lateral diffusion of membrane receptors as studied by single particle tracking (nanovid microscopy). Effects of calcium-induced differentiation in cultured epithelial cells, *Biophysical Journal* **65**, 2021–2040, 1993.

[89] S. K. Lai, D. E. O'Hanlon, S. Harrold, S. T. Man, Y.-Y. Wang, R. Cone, and J. Hanes, Rapid transport of large polymeric nanoparticles in fresh undiluted human mucus, *Proceedings of the National Academy of Sciences* **104**, 1482 – 1487, 2007.

[90] D. Langbein, Van der Waals attraction between cylinders, rods or fibers, *Physik der kondensierten Materie* **15**, 61–86, 1972.

[91] D. Langbein, Theory of Van der Waals attraction, In *Springer Tracts in Modern Physics Vol. 72*, pages 1–139, Springer, Berlin, Heidelberg, 1974.

[92] H. Lee, B. P. Lee, and P. B. Messersmith, A reversible wet/dry adhesive inspired by mussels and geckos, *Nature* **448**, 338–341, 2007.

[93] Y. Li, J. Krahn, and C. Menon, Bioinspired Dry Adhesive Materials and Their Application in Robotics: A Review, *Journal of Bionic Engineering* **13**, 181–199, 2016.

[94] Y. Li, A. Asadi, M. R. Monroe, and E. P. Douglas, pH effects on collagen fibrillogenesis in vitro: Electrostatic interactions and phosphate binding, *Materials Science and Engineering: C* **29**, 1643–1649, 2009.

[95] O. Lieleg and K. Ribbeck, Biological hydrogels as selective diffusion barriers, *Trends in Cell Biology* **21**, 543–551, 2011.

[96] O. Lieleg, R. M. Baumgärtel, and A. R. Bausch, Selective filtering of particles by the extracellular matrix: an electrostatic bandpass, *Biophysical Journal* **97**, 1569–1577, 2009.

[97] O. Lieleg, I. Vladescu, and K. Ribbeck, Characterization of Particle Translocation through Mucin Hydrogels, *Biophysical Journal* **98**, 1782–1789, 2010.

[98] P. Litewka, The penalty and Lagrange multiplier methods in the frictional 3d beam-to-beam contact problem, *Civil and Environmental Engineering Reports* **1**, 189–207, 2005.

[99] P. Litewka, Frictional beam-to-beam multiple-point contact finite element, *Computational Mechanics* **56**, 243–264, 2015.

[100] P. Litewka and P. Wriggers, Contact between 3D beams with rectangular cross-sections, *International Journal for Numerical Methods in Engineering* **53**, 2019–2041, 2002.

[101] P. Litewka and P. Wriggers, Frictional contact between 3D beams, *Computational Mechanics* **28**, 26–39, 2002.

[102] H. H. Lovelady, S. Shashidhara, and W. G. Matthews, Solvent specific persistence length of molecular type I collagen, *Biopolymers* **101**, 329–335, 2014.

[103] H. Maeda and Y. Maeda, Orientation-Dependent London-van der Waals Interaction Energy between Macroscopic Bodies, *Langmuir* **31**, 7251–7263, 2015.

[104] Maplesoft. Maple 2015.

[105] M. Marczynski, B. T. Käsdorf, B. Altaner, A. Wenzler, U. Gerland, and O. Lieleg, Transient binding promotes molecule penetration into mucin hydrogels by enhancing molecular partitioning, *Biomaterials Science* **6**, 3373–3387, 2018.

[106] M. Marino and G. Vairo, 5 - Computational modeling of soft tissues and ligaments, In Z. B. T. Jin (ed.), *Computational Modelling of Biomechanics and Biotribology in the Musculoskeletal System*, pages 141–172, Woodhead Publishing, 2014.

[107] C. Meier, A. Popp, and W. A. Wall, A locking-free finite element formulation and reduced models for geometrically exact Kirchhoff rods, *Computer Methods in Applied Mechanics and Engineering* **290**, 314–341, 2015.

[108] C. Meier, *Geometrically Exact Finite Element Formulations for Slender Beams and Their Contact Interaction*, Dissertation, Technical University of Munich, 2016.

[109] C. Meier, A. Popp, and W. A. Wall, An objective 3D large deformation finite element formulation for geometrically exact curved Kirchhoff rods, *Computer Methods in Applied Mechanics and Engineering* **278**, 445–478, 2014.

[110] C. Meier, A. Popp, and W. A. Wall, A finite element approach for the line-to-line contact interaction of thin beams with arbitrary orientation, *Computer Methods in Applied Mechanics and Engineering* **308**, 377–413, 2016.

[111] C. Meier, W. A. Wall, and A. Popp, A unified approach for beam-to-beam contact, *Computer Methods in Applied Mechanics and Engineering* **315**, 972–1010, 2017.

[112] C. Meier, M. J. Grill, W. A. Wall, and A. Popp, Geometrically exact beam elements and smooth contact schemes for the modeling of fiber-based materials and structures, *International Journal of Solids and Structures* **154**, 124–146, 2018.

[113] C. Meier, A. Popp, and W. A. Wall, Geometrically Exact Finite Element Formulations for Slender Beams: Kirchhoff-Love Theory Versus Simo-Reissner Theory, *Archives of Computational Methods in Engineering* **26**, 163–243, 2019.

[114] J. C. Mergel and R. A. Sauer, On the optimum shape of thin adhesive strips for various peeling directions, *Journal of Adhesion* **90**, 526–544, 2014.

[115] J. C. Mergel, R. A. Sauer, and A. Saxena, Computational optimization of adhesive microstructures based on a nonlinear beam formulation, *Structural and Multidisciplinary Optimization* **50**, 1001–1017, 2014.

[116] T. Miyata, Brownian Dynamics Simulation of Self-Diffusion of Ionic Large Solute Molecule in Modeled Polyelectrolyte Gel, *Journal of the Physical Society of Japan* **81**, SA010, 2012.

[117] S. W. Montgomery, M. A. Franchek, and V. W. Goldschmidt, Analytical Dispersion Force Calculations for Nontraditional Geometries., *Journal of colloid and interface science* **227**, 567–584, 2000.

[118] K. W. Müller, R. F. Bruinsma, O. Lieleg, A. R. Bausch, W. A. Wall, and A. J. Levine, Rheology of Semiflexible Bundle Networks with Transient Linkers, *Physical Review Letters* **112**, 238102, 2014.

[119] K. W. Müller, C. Meier, and W. A. Wall, Resolution of sub-element length scales in Brownian dynamics simulations of biopolymer networks with geometrically exact beam finite elements, *Journal of Computational Physics* **303**, 185–202, 2015.

[120] V. Negi and R. C. Picu, Mechanical behavior of cross-linked random fiber networks with inter-fiber adhesion, *Journal of the Mechanics and Physics of Solids* **122**, 418–434, 2018.

[121] P. A. Netz and T. Dorfmüller, Computer simulation studies of diffusion in gels: Model structures, *The Journal of Chemical Physics* **107**, 9221–9233, 1997.

[122] H. Ohshima and A. Hyono, Electrostatic interaction between two cylindrical soft particles, *Journal of Colloid and Interface Science* **333**, 202–208, 2009.

[123] J. P. R. O. Orgel, T. C. Irving, A. Miller, and T. J. Wess, Microfibrillar structure of type I collagen in situ, *Proceedings of the National Academy of Sciences* **103**, 9001 – 9005, 2006.

[124] P. Papadopoulos, R. E. Jones, and J. M. Solberg, A novel finite element formulation for frictionless contact problems, *International Journal for Numerical Methods in Engineering* **38**, 2603–2617, 1995.

[125] V. A. Parsegian, *Van der Waals forces: a handbook for biologists, chemists, engineers, and physicists*, Cambridge University Press, Cambridge, UK, 2005.

[126] H. Pei, S. Allison, B. M. H. Haynes, and D. Augustin, Brownian Dynamics Simulation of the Diffusion of Rods and Wormlike Chains in a Gel Modeled as a Cubic Lattice: Application to DNA, *The Journal of Physical Chemistry B* **113**, 2564–2571, 2009.

[127] K. Prytz, *Electrodynamics: The Field-Free Approach*, Springer, 2015.

[128] R. F. Rajter, R. Podgornik, V. A. Parsegian, R. H. French, and W. Y. Ching, Van der Waals-London dispersion interactions for optically anisotropic cylinders: Metallic and semiconducting single-wall carbon nanotubes, *Physical Review B - Condensed Matter and Materials Physics* **76**, 1–16, 2007.

[129] E. Reissner, On finite deformations of space-curved beams, *Zeitschrift für Angewandte Mathematik und Physik (ZAMP)* **32**, 734–744, 1981.

[130] I. Romero, The interpolation of rotations and its application to finite element models of geometrically exact rods, *Computational Mechanics* **34**, 121–133, 2004.

[131] I. Romero, A comparison of finite elements for nonlinear beams: the absolute nodal coordinate and geometrically exact formulations, *Multibody System Dynamics* **20**, 51–68, 2008.

[132] A. N. Round, M. Berry, T. J. McMaster, S. Stoll, D. Gowers, A. P. Corfield, and M. J. Miles, Heterogeneity and Persistence Length in Human Ocular Mucins, *Biophysical Journal* **83**, 1661–1670, 2002.

[133] C. Rycroft, Voro++: a three-dimensional Voronoi cell library in C++, Technical report, United States, 2009.

[134] R. A. Sauer, An atomic interaction-based rod formulation for modelling Gecko adhesion, *Proceedings in Applied Mathematics and Mechanics* **8**, 10193–10194, 2008.

[135] R. A. Sauer, Multiscale modelling and simulation of the deformation and adhesion of a single gecko seta, *Computer Methods in Biomechanics and Biomedical Engineering* **12**, 627–640, 2009.

[136] R. A. Sauer, Enriched contact finite elements for stable peeling computations, *International Journal for Numerical Methods in Engineering* **87**, 593–616, 2011.

[137] R. A. Sauer, Challenges in computational nanoscale contact mechanics, In D. Mueller-Hoeppe, S. Loehnert, and S. Reese (eds.), *Recent Developments and Innovative Applications in Computational Mechanics*, pages 39–46, Springer, Berlin, Heidelberg, 2011.

[138] R. A. Sauer, The peeling behavior of thin films with finite bending stiffness and the implications on gecko adhesion, *Journal of Adhesion* **87**, 624–643, 2011.

[139] R. A. Sauer, Local finite element enrichment strategies for 2D contact computations and a corresponding post-processing scheme, *Computational Mechanics* **52**, 301–319, 2013.

[140] R. A. Sauer and L. De Lorenzis, A computational contact formulation based on surface potentials, *Computer Methods in Applied Mechanics and Engineering* **253**, 369–395, 2013.

[141] R. A. Sauer and S. Li, A contact mechanics model for quasi-continua, *International Journal for Numerical Methods in Engineering* **71**, 931–962, 2007.

[142] R. A. Sauer and J. C. Mergel, A geometrically exact finite beam element formulation for thin film adhesion and debonding, *Finite Elements in Analysis and Design* **86**, 120–135, 2014.

[143] R. A. Sauer and P. Wriggers, Formulation and analysis of a three-dimensional finite element implementation for adhesive contact at the nanoscale, *Computer Methods in Applied Mechanics and Engineering* **198**, 3871–3883, 2009.

[144] M. Saxton, Anomalous diffusion due to obstacles: a Monte Carlo study, *Biophysical Journal* **66**, 394–401, 1994.

[145] M. Saxton, Anomalous diffusion due to binding: a Monte Carlo study, *Biophysical Journal* **70**, 1250–1262, 1996.

[146] M. G. Schmidt, A. E. Ismail, and R. A. Sauer, A continuum mechanical surrogate model for atomic beam structures, *International Journal for Multiscale Computational Engineering* **13**, 413–442, 2015.

[147] M. Schulz and F. C. Filippou, Non-linear spatial Timoshenko beam element with curvature interpolation, *International Journal for Numerical Methods in Engineering* **50**, 761–785, 2001.

[148] M. Shavezipur, G. H. Li, I. Laboriante, W. J. Gou, C. Carraro, and R. Maboudian, A finite element technique for accurate determination of interfacial adhesion force in MEMS using electrostatic actuation, *Journal of Micromechanics and Microengineering* **21**, 115025, 2011.

[149] R. Shogren, T. A. Gerken, and N. Jentoft, Role of glycosylation on the conformation and chain dimensions of O-linked glycoproteins: light-scattering studies of ovine submaxillary mucin, *Biochemistry* **28**, 5525–5536, 1989.

[150] J. C. Simo, A Finite Strain Beam Formulation. The Three-Dimensional Dynamic Problem. Part I, *Computer Methods in Applied Mechanics and Engineering* **49**, 55–70, 1985.

[151] J. C. Simo and L. Vu Quoc, A Three Dimensional Finite Strain Rod Model Part II: Computational Aspects, *Computer Methods in Applied Mechanics and Engineering* **58**, 79–116, 1986.

[152] V. M. Slepukhin, M. J. Grill, K. W. Müller, W. A. Wall, and A. J. Levine, Conformation of a semiflexible filament in a quenched random potential, *Physical Review E* **99**, 042501, 2019.

[153] T. Stedman, D. Drosdoff, and L. M. Woods, Van der Waals interactions between nanostructures: Some analytic results from series expansions, *Physical Review A* **89**, 012509, 2014.

[154] T. Stylianopoulos, B. Diop-Frimpong, L. L. Munn, and R. K. Jain, Diffusion Anisotropy in Collagen Gels and Tumors: The Effect of Fiber Network Orientation, *Biophysical Journal* **99**, 3119–3128, 2010.

[155] T. Stylianopoulos, M.-Z. Poh, N. Insin, M. G. Bawendi, D. Fukumura, L. L. L. Munn, and R. K. Jain, Diffusion of Particles in the Extracellular Matrix: The Effect of Repulsive Electrostatic Interactions, *Biophysical Journal* **99**, 1342–1349, 2010.

[156] Y.-L. Sun, Z.-P. Luo, A. Fertala, and K.-N. An, Direct quantification of the flexibility of type I collagen monomer, *Biochemical and Biophysical Research Communications* **295**, 382–386, 2002.

[157] The MathWorks Inc. MATLAB R2017b.

[158] The UniProt Consortium, UniProt: a worldwide hub of protein knowledge, *Nucleic Acids Research* **47**, D506–D515, 2018.

[159] S. Timoshenko, LXVI. On the correction for shear of the differential equation for transverse vibrations of prismatic bars, *The London, Edinburgh, and Dublin Philosophical Magazine and Journal of Science* **41**, 744–746, 1921.

[160] J. A. J. van der Rijt, K. O. van der Werf, M. L. Bennink, P. J. Dijkstra, and J. Feijen, Micromechanical Testing of Individual Collagen Fibrils, *Macromolecular Bioscience* **6**, 697–702, 2006.

[161] O. Weeger, B. Narayanan, L. De Lorenzis, J. Kiendl, and M. L. Dunn, An isogeometric collocation method for frictionless contact of Cosserat rods, *Computer Methods in Applied Mechanics and Engineering* **321**, 361–382, 2017.

[162] J. Witten and K. Ribbeck, The particle in the spider's web: transport through biological hydrogels, *Nanoscale* **9**, 8080–8095, 2017.

[163] P. Wriggers and G. Zavarise, On contact between three-dimensional beams undergoing large deflections, *Communications in Numerical Methods in Engineering* **13**, 429–438, 1997.

[164] P. Wriggers, *Computational Contact Mechanics*, Springer, 2nd Edition, 2006.

[165] Q. Xu, N. J. Boylan, J. S. Suk, Y.-Y. Wang, E. A. Nance, J.-C. Yang, P. J. McDonnell, R. A. Cone, E. J. Duh, and J. Hanes, Nanoparticle diffusion in, and microrheology of, the bovine vitreous ex vivo, *Journal of Controlled Release* **167**, 76–84, 2013.

[166] P. D. Yurchenco and G. C. Ruben, Basement membrane structure in situ: evidence for lateral associations in the type IV collagen network., *The Journal of Cell Biology* **105**, 2559–2568, 1987.

[167] G. Zavarise and P. Wriggers, Contact with friction between beams in 3D space, *International Journal for Numerical Methods in Engineering* **49**, 977–1006, 2000.

[168] X. Zhang, J. Hansing, R. R. Netz, and J. E. DeRouchey, Particle Transport through Hydrogels Is Charge Asymmetric, *Biophysical Journal* **108**, 530–539, 2015.

[169] H. Zhou and S. B. Chen, Brownian dynamics simulation of tracer diffusion in a cross-linked network, *Physical Review E* **79**, 21801, 2009.

[170] O. Zienkiewicz, R. Taylor, and J. Z. Zhu, *The Finite Element Method: Its Basis and Fundamentals*, Butterworth-Heinemann, 7th Edition, 2013.

Verzeichnis der betreuten Studienarbeiten

Im Rahmen dieser Dissertation entstanden am Lehrstuhl für Numerische Mechanik (LNM) in den Jahren von 2015 bis 2017 unter wesentlicher wissenschaftlicher, fachlicher und inhaltlicher Anleitung des Autors die im Folgenden aufgeführten studentischen Arbeiten. Der Autor dankt allen Studierenden für ihr Engagement bei der Unterstützung dieser wissenschaftlichen Arbeit.

Studierender	Studienarbeit
Dominik Gau	*Modeling and simulation of single collagen fibril mechanics based on beam finite elements*, Semesterarbeit, 2017, eingeflossen in Kapitel 11.2
Patrick Praegla	*Simulation of frictional beam-to-beam contact based on geometrically exact beam finite element formulations*, Bachelorarbeit, 2017
Jonas Koban	*Simulation of hindered diffusion of particles in biological hydrogels due to contact and electrostatic interaction*, Bachelorarbeit, 2017, eingeflossen in Kapitel 10
Daniel Paukner	*Simulation of the Brownian dynamics of slender biopolymers using beam finite elements*, Semesterarbeit, 2017
Reimar Weißbach	*Development of a finite element method for short-range potential-based interactions of thin fibers*, Bachelorarbeit, 2015, eingeflossen in Kapitel 5